

High Resolution Infrared Spectroscopy of van der Waals and Hydrogen Bonded
Clusters: Pairwise and Nonpairwise Additive Intermolecular Forces in $\text{Ar}_n\text{HF/DF}$
and $(\text{HF})_n$ complexes.

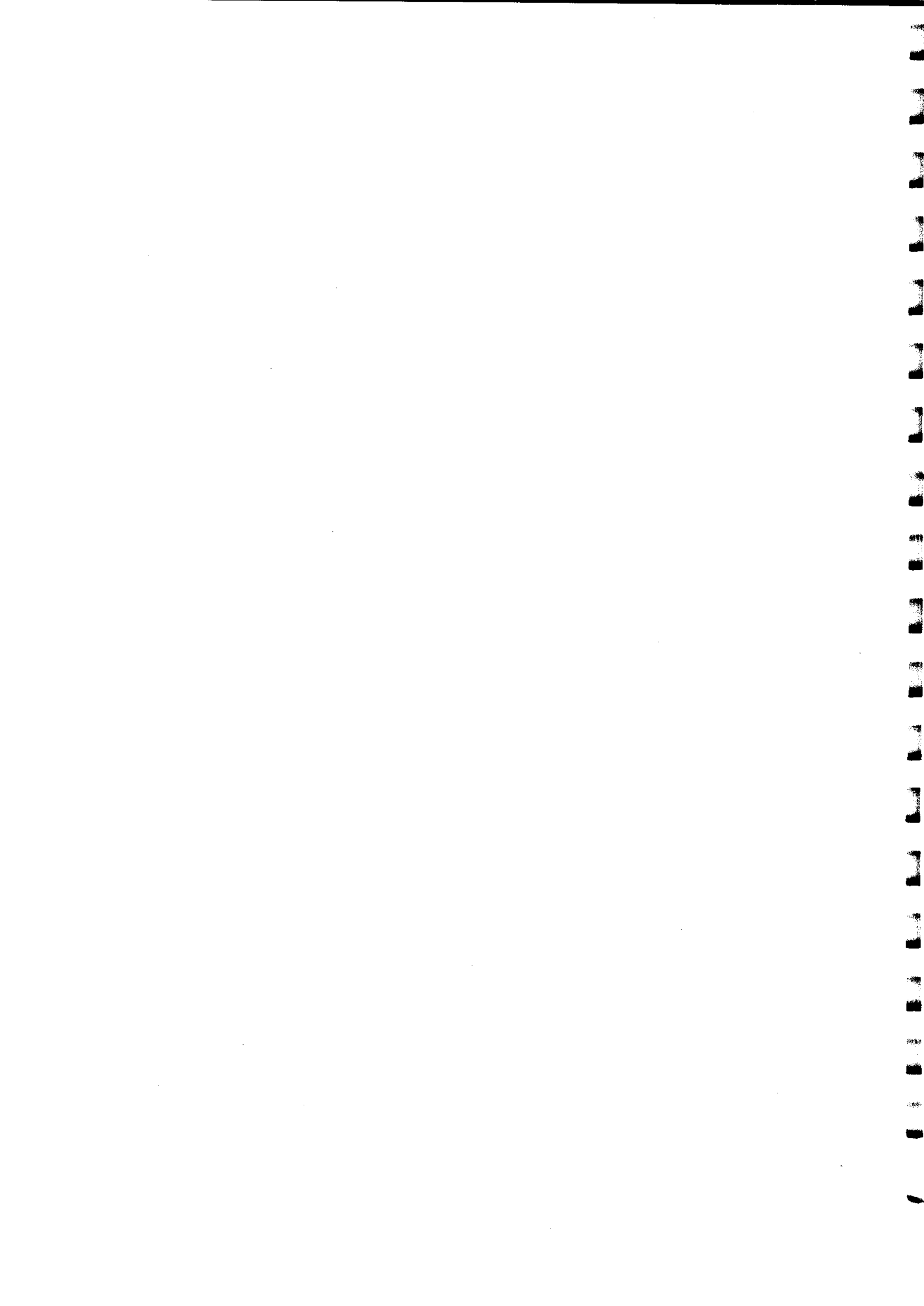
by

John T. Farrell, Jr.

B. S., Purdue University, 1990

A Thesis submitted to the
Faculty of the Graduate School of the
University of Colorado in partial fulfillment
of the requirements for the degree of
Doctor of Philosophy
Department of Chemistry

1995



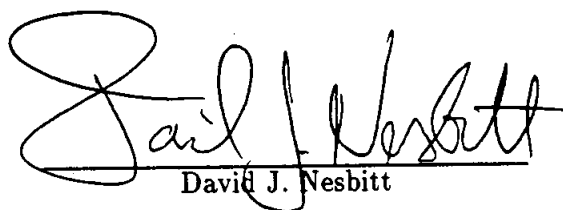
This thesis for the Doctor of Philosophy degree by

John T. Farrell, Jr.

has been approved for the program in

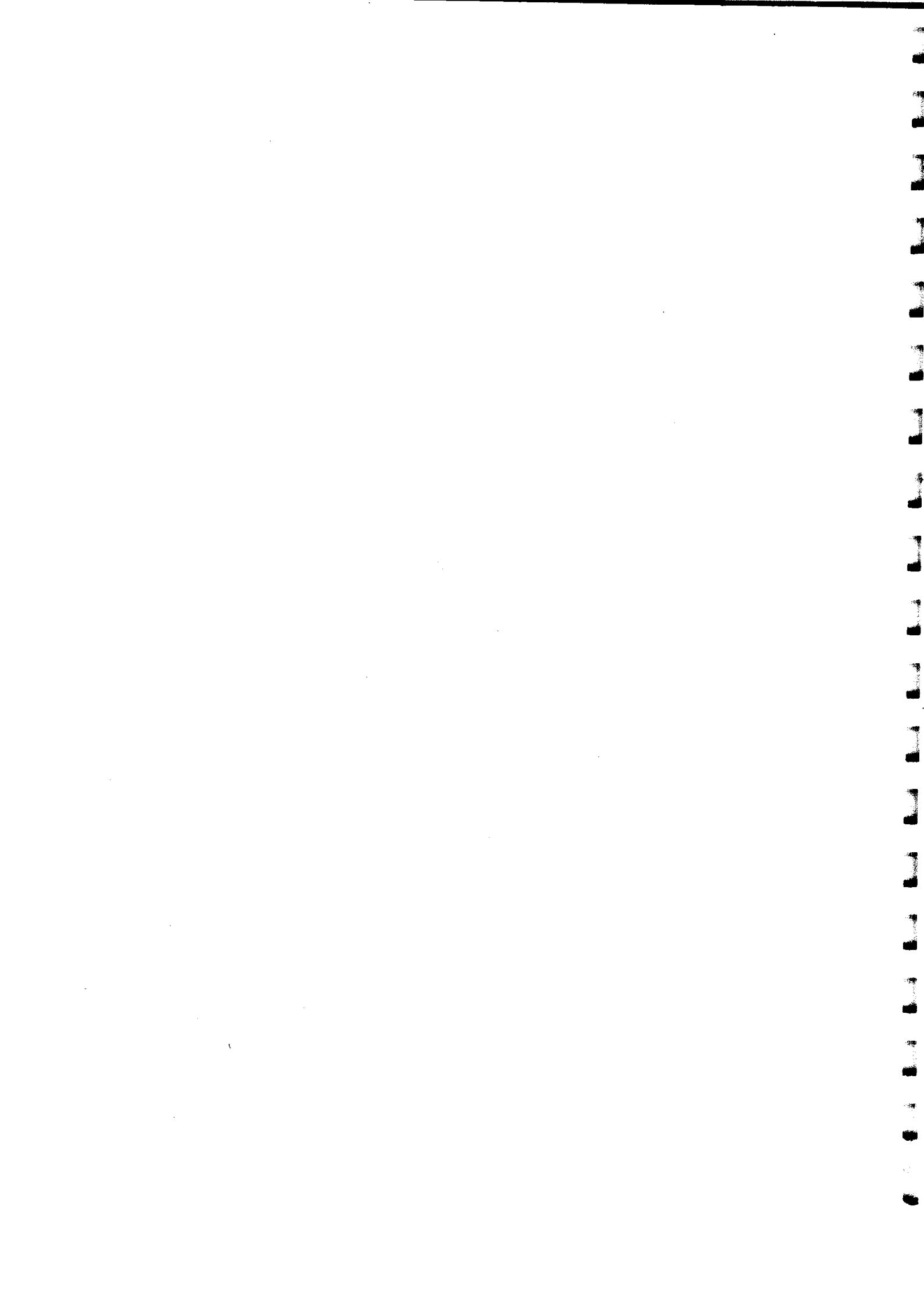
Physical Chemistry

by


David J. Nesbitt


Eric A. Cornell

Date 5/25/95



Farrell, Jr., John T. (Ph. D., Chemistry)

High Resolution Infrared Spectroscopy of van der Waals and Hydrogen Bonded Clusters: Pairwise and Nonpairwise Additive Intermolecular Forces in $\text{Ar}_n\text{HF/DF}$ and $(\text{HF})_n$ complexes.

Thesis directed by Adjoint Professor David J. Nesbitt.

This dissertation describes studies of intermolecular and intramolecular dynamics in weakly bound van der Waals and hydrogen bonded complexes. The complexes are synthesized in the low temperature ($T = 5\text{--}15\text{ K}$) environment of a slit supersonic expansion. The slit geometry provides i) a high number density, ii) an ≈ 5 -fold increase in peak absorption vs pinhole expansions through suppression of Doppler broadening along the laser axis, and iii) a long absorption pathlength amenable to direct absorption techniques. Together with the advantages of sensitive dual beam detection of high resolution ($< 0.0005\text{ cm}^{-1}$) tunable IR laser light, this technique provides a very sensitive method for studying the spectroscopy and dynamics of weakly bound molecular species at a state-to-state level.

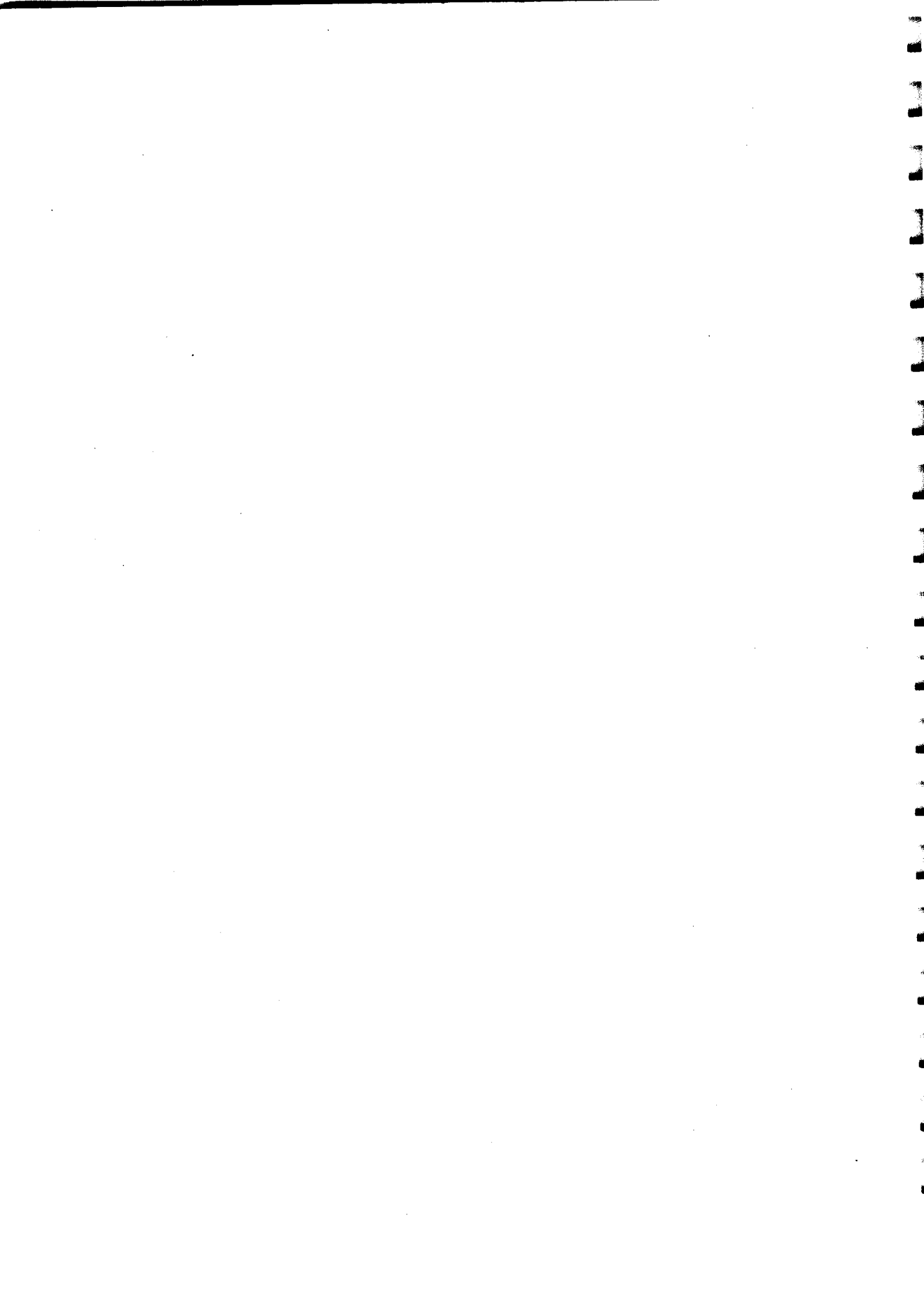
The underlying goal of these studies is to provide information about the potential energy surfaces which govern weak intermolecular interactions. Several investigations are reported for the prototypical Ar-HF system. The spectroscopic characterization of intermolecular bending and stretching states of ArHF excited in combination with the $\nu_{\text{HF}} = 2 \leftarrow 0$ stretch provides information on the angular and radial anisotropy of the intermolecular potential in an excited intramolecular vibrational level. In addition, the near-IR spectra of Ar_nDF ($n=1\text{--}3$) provide a glimpse into the dynamics of a DF rotor sequentially "solvated" by a well defined number of argon

atoms. The observation of intermolecular bending states of Ar_2HF and Ar_2DF allow a detailed assessment of the importance of nonpairwise additive, or many body, terms to the intermolecular potential.

The effects of intramolecular excitation on intermolecular dynamics are investigated for the HF-HF and N_2 -HF systems. The vibrational frequency shifts and predissociation lifetimes for HF-HF and N_2 -HF in the $\nu_{\text{HF}}=2$ vibrational level provide detailed information on the coupling between the intermolecular and intramolecular degrees of freedom. This is probed at a more subtle level for the HF-HF system, by characterizing how the vibrational frequencies and lifetimes change upon isotopic substitution (to form the deuterated isotopomers HF-DF, DF-HF, and DF-DF) in the $\nu_{\text{HF,DF}}=1$ manifold. The infrared spectra of $(\text{DF})_3$ affords a unique opportunity for investigating the role of intramolecular vibrational relaxation in a photoinitiated unimolecular ring opening.

DEDICATION

To Esther, Lauren, and Jason.



ACKNOWLEDGMENTS

It is somewhat of an injustice that only a couple pages are set aside to recognize and thank the large number of people who made the research described in this thesis possible. My advisor David Nesbitt of course deserves special recognition for the time and interest he has invested in my scientific training. David not only provided a world-class experiment on which to work, but more importantly, the guidance necessary to squeeze physical insight from what could have easily remained a jumble of dreary spectroscopic perturbations and molecular constants. His standard of scientific rigor, integrity, and enthusiasm continue to inspire me, as does his commitment to clarity in oral and written communication.

I would also like to acknowledge Eberhard Riedle and Martin Suhm for their many contributions. I would still be designing and debugging many of the electronic circuits described in Chapter II had it not been for Eberhard's expert guidance and assistance. In addition, the improved quality of life provided by the generous donation of his data analysis and simulation programs cannot be overstated. Martin is inextricably linked to the insightful analysis of the HF dimer system described in Chapters VI-VIII. I am deeply grateful for his patient answers to more stupid questions than anyone should have inflicted upon them.

During the past five years, I've had the good fortune of having Bill Chapman as a cohort in skiing, hiking, and squash indulgences, as well as the occasional Irish whiskey or two. Well, *mostly* good fortune. There's still that issue of Bill dragging me down Outhouse at Mary Jane on only my second day on skis; of course, I was able to retaliate when I tried to catch some air in my car on Rabbit Ears pass on the way

to Steamboat. Nevertheless, he and his wife Judy have been (and remain) valuable friends to whom Esther and I owe a great debt of gratitude.

The other members of the Nesbitt group are also due appreciation for their friendship and assistance. In particular I'd like to thank all those wacky postdocs who called B212 home (for however short a time) during my stay here, i.e., Martin Suhm, Ofer Sneh, Steve Ashworth, and Dave Anderson. Steve gets a special tip of the cap for all the improvements he made to the system, in particular the dye laser locking servo described in Chapter II. Thanks also to Scott Davis, my favorite long-haired, trailer-park-living, motorcycle-riding, tatoo-covered, vegetarian, speed-metal/punk rock-and-rollin' lab pardner. Thanks also to Dave Plusquellic for letting me mooch all those beers from you at Brandy's (RIP?) and other choice locales. Further thanks go out to Miles Weida, Aram Schiffman, Jeanette Sperhac, and Ondrej Votava, for the occasional ski trip or pilgrimage to Denver to pay homage to Dictator Tot.

I am also grateful for all the assistance provided by the support staff at JILA. In particular, I'd like to thank Ed Holliness, Patti Krog, Marilyn Greve, Paul Beckingham, and Terry Brown for their expert help and guidance. A hearty thanks goes out to Lorraine Volsky in the Scientific Reports Office (and more recently Mary Eberle and Sandy Rush) for taking care of many essential tasks that are all too often unappreciated.

And, saving the most important acknowledgement for last, I'd like to express deep appreciation to my wife Esther, whose understanding and patience made this whole ordeal much easier than it could have been. A special thanks also goes out to my daughter Lauren and my son Jason, who have brought me innumerable smiles and laughs.

CONTENTS

I	Introduction	1
1.1	General Introduction	1
1.2	An introduction to intermolecular potential energy surfaces	3
1.3	High resolution IR spectroscopy as a probe of intermolecular forces	18
II	Experimental	24
2.1	Introduction	24
2.2	Overview of difference frequency generation	27
2.2.1	Generation of difference frequency light	32
2.2.2	Dye laser servo control	34
2.2.3	LiNbO ₃ thermal control	38
2.2.4	Formation of weakly bound complexes in a slit supersonic expansion	45
2.2.5	Data acquisition and storage	57
2.2.6	Frequency measurements	59
2.3	HeNe-stabilized transfer cavity and stabilization of Ar ⁺ laser	63
2.3.1	Basic Considerations	64
2.3.2	The FPI as a transfer cavity	67
2.3.3	Possible limitations of performance for the HeNe-stabilized cavity	71
2.3.4	Locking of the transfer cavity to the HeNe laser	74

2.3.5	Frequency control of the Ar ⁺ laser	77
2.3.6	Optical and electronic tests	79
2.3.7	Spectroscopic measurements	80
2.4	Conversion to 1.2–2.2 μm region	82
2.5	Appendices	90
2.5.1	Dye laser lock	90
2.5.2	Marker Cavity	98
2.5.3	Ar ⁺ laser stabilization circuit	106
III	High-resolution infrared overtone spectroscopy of ArHF	112
3.1	Introduction	112
3.2	Experimental	117
3.3	Results and Analysis	118
3.3.1	ArHF HF stretch overtone (2000) \leftarrow (0000)	118
3.3.2	ArHF internal rotor states from $j_{\text{HF}} = 1$: (2100) \leftarrow (0000) Σ bend and (2110) \leftarrow (0000) Π bend	124
3.4	Discussion	131
3.4.1	Overtone vibrational red shifts in ArHF	131
3.4.2	Angular and radial potential-energy surface dependence on ν_{HF}	133
3.4.3	Overtone line strengths and Coriolis mixing in ArHF	137
3.4.4	Predissociation lifetimes in the ArHF ($\nu_{\text{HF}} = 2$) level	143
3.5	Summary	146
IV	Pairwise and nonpairwise additive forces in weakly bound complexes: High resolution infrared spectroscopy of Ar _n DF ($n = 1,2,3$)	148

4.1	Introduction	148
4.2	Experimental	152
4.3	Results and Analysis	154
4.3.1	ArDF	155
4.3.2	Ar ₂ DF	157
4.3.3	Ar ₃ DF	164
4.4	Discussion	169
4.4.1	Ar _n DF Vibrationally Averaged Geometries and Nonpairwise Additive Effects	170
4.4.2	Vibrational Redshifts	178
4.4.3	Vibrational Predissociation Lifetimes	184
4.5	Summary	186
V	Near-IR spectroscopy of Ar ₂ HF and Ar ₂ DF intermolecular van der Waals modes: Detailed probes of nonadditive intermolecular forces.	190
5.1	Introduction	190
5.2	Experimental	196
5.3	Results and Analysis	197
5.3.1	Ar ₂ DF in-plane bend	198
5.3.2	Ar ₂ DF out-of-plane bend	204
5.3.3	Ar ₂ HF in-plane bend	207
5.3.4	Ar ₂ HF out-of-plane bend	212
5.3.5	Coriolis and anharmonic perturbations to the Ar ₂ HF in-plane and out-of-plane bends	216

5.4	Discussion	224
5.4.1	Comparison with 2-D angular calculations	226
5.4.2	Comparison with 5-D calculations	235
5.4.3	Assessment of Ar ₂ HF nonadditivity from <i>ab initio</i> calculations	245
5.5	Summary	247
VI High resolution 1.3 μm overtone spectroscopy of HF dimer in a slit jet: $K_a =$		
	$0 \leftarrow 0$ and $K_a = 1 \leftarrow 0$ subbands of $\nu_{\text{acc}} = 2 \leftarrow 0$	249
6.1	Introduction	249
6.2	Experimental	254
6.3	Spectroscopic results and analysis	255
6.4	Vibrational predissociation measurements	262
6.5	Discussion	268
6.5.1	Vibrational overtone assignment in the $v=2$ triad	268
6.5.2	Tunneling splittings and exchange symmetries	274
6.5.3	Symmetry and K -state dependent perturbations	277
6.5.4	Vibrational predissociation and H-atom exchange dynamics	283
6.6	Conclusions	285
VII High resolution infrared spectroscopy of DF-DF, HF-DF, and DF-HF: Near-		
	resonant intermolecular energy transfer dynamics	287
7.1	Introduction	287
7.2	Experimental	296
7.3	Rovibrational analysis	297
7.3.1	DF-excited dimer complexes	298

7.3.2	HF-excited dimer complexes	311
7.4	Tests of potential energy surfaces	318
7.4.1	Isotopic frequency shifts	319
7.4.2	Vibrational predissociation	323
7.5	Further tests of potential energy surfaces: The difference in binding energy for HF-DF and DF-HF	328
7.6	Energy transfer in the mixed HF/DF dimers	332
7.6.1	Comparison of full and half-collision dynamics	332
7.6.2	Near-resonant state mixing between HF- and DF-excited mixed dimers	335
7.7	Summary	341
VIII High-resolution slit jet spectroscopy and vibrational dynamics of the degen- erate DF stretching fundamental ν_5 in $(DF)_3$		343
IX High resolution infrared overtone spectroscopy of N_2 -HF: Vibrational red- shifts and predissociation rates as a function of HF stretching quanta.		359
9.1	Introduction	359
9.2	Experimental	364
9.3	Results and Analysis	366
9.4	Discussion	371
9.4.1	Vibrational Redshifts	371
9.4.2	Rotational Constants	376
9.4.3	Vibrational Predissociation	379
9.5	Summary	385

TABLES

3.1	Observed transitions for the (2000) \leftarrow (0000), (2100) \leftarrow (0000), and (2110) \leftarrow (0000) bands of ArHF.	120
3.2	Observed transitions for the (2002) \leftarrow (0000) band of ArHF.	121
3.3	Molecular constants obtained from analysis of the four ArHF bands in Table 3.1 (in cm^{-1}).	123
4.1	Observed transition frequencies for the $\nu_{\text{DF}} = 1 \leftarrow 0$ transition in Ar_2DF .	160
4.2	Spectroscopic constants (in cm^{-1}) derived from a simultaneous least-squares fit of the Ar_2DF infrared and microwave data	163
4.3	Transition frequencies for the $\nu_{\text{DF}} = 1 \leftarrow 0$ transition in Ar_3DF	166
4.4	Spectroscopic constants (in cm^{-1}) derived from a least-squares fit of the microwave (Ref. [153]) and infrared Ar_3DF data	167
4.5	Comparison of the Ar_2HF and Ar_2DF rotational constants with those predicted by quantum mechanical variational calculations.	176
4.6	Experimental vibrational redshifts for DF and HF with sequential addition of argon "solvent" atoms.	180
5.1	Observed transition frequencies for the $\nu_{\text{DF}} = 1 \leftarrow 0 +$ in-plane bend transition in Ar_2DF	201

5.2	Spectroscopic constants (in cm^{-1}) derived from least-squares fitting of the Ar_2DF in-plane and out-of-plane bend data to an A-reduction Watson Hamiltonian using the I' representation.	203
5.3	Observed transition frequencies for the $\nu_{\text{DF}} = 1 \leftarrow 0 +$ out-of-plane bend transition in Ar_2DF . The numbers in parentheses represent (observed-calculated) values using the constants listed in Table 5.2.	206
5.4	Observed transition frequencies for the $\nu_{\text{HF}} = 1 \leftarrow 0 +$ in-plane bend transition in Ar_2HF	209
5.5	Spectroscopic constants (in cm^{-1}) derived from least-squares fitting of the Ar_2HF in-plane and out-of-plane bend data to an A-reduction Watson Hamiltonian using the I' representation.	211
5.6	Observed transition frequencies for the $\nu_{\text{HF}} = 1 \leftarrow 0 +$ out-of-plane bend transition in Ar_2HF	214
5.7	Spherical harmonic expansion coefficients (in cm^{-1}) for the intermolecular potentials used in the 2-D $\text{Ar}_n\text{HF/DF}$ calculations.	229
5.8	Vibrational energies (cm^{-1}) of $\text{Ar}_n\text{HF/DF}$ ($n=1-4$) intermolecular rotor states in the $\nu_{\text{HF/DF}} = 1$ manifold.	233
5.9	Frequencies (in cm^{-1}) for the in-plane and out-of-plane internal rotor states of Ar_2DF and Ar_2HF	236
5.10	Comparison of the experimental rotational constants for the in-plane and out-of-plane bends of Ar_2HF and Ar_2DF with those calculated on a pairwise additive potential.	238

6.1	The observed and fitted transitions of the $K = 0 \leftarrow 0$ and $K = 1 \leftarrow 0$ subbands of $(\text{HF})_2$	258
6.2	Spectroscopic constants from a weighted least squares fit to the $(\text{HF})_2$ transition frequencies.	261
6.3	Predissociation linewidths measured for upper states of transitions in HF dimer.	266
6.4	Tunneling splittings in ground state, fundamental, and overtone excited $(\text{HF})_2$	268
7.1	Transition frequencies (in cm^{-1}) for $K = 0 \leftarrow 0$ of $^*\text{DF-DF}$	299
7.2	Molecular constants (in cm^{-1}) obtained from least-squares analysis of the $K = 0 \leftarrow 0$ transitions of $^*\text{DF-DF}$	301
7.3	Transition frequencies (in cm^{-1}) for DF-HF	304
7.4	Molecular constants (in cm^{-1}) obtained from least-squares analysis of DF-HF	305
7.5	Transition frequencies (in cm^{-1}) for HF-DF	308
7.6	Q branch transition frequencies (in cm^{-1}) for HF-DF	309
7.7	Molecular constants (in cm^{-1}) obtained from least-squares analysis of HF-DF	310
7.8	Experimental and calculated vibrational redshifts (in cm^{-1}) for $K = 0 \leftarrow 0$ transitions in HF-HF , DF-DF , HF-DF , and DF-HF	319
7.9	Mode and isomer specific predissociation linewidths for the mixed HF/DF dimers.	325

7.10	Vibrational origin and rotational constants (in cm^{-1}) used in modeling the perturbations to the rovibrational frequencies of $^*\text{HF-DF } K = 0 \leftarrow 0.340$	
8.1	Spectroscopic constants obtained in the band shape fit of the $(\text{DF})_3$ spectrum.	350
8.2	Harmonic vibrational frequencies for DF trimer based on the quantum Monte Carlo calculations discussed in the text.	356
9.1	Observed transitions to the $2\nu_1$ level of $\text{N}_2\text{-HF}$	368
9.2	Molecular constants obtained from least-squares analysis of the $\text{N}_2\text{-HF } 2\nu_1$ transitions.	369
9.3	Average predissociation linewidths for P and R branch transitions of $2\nu_1$ of $\text{N}_2\text{-HF}$	371
9.4	Vibrational redshifts (in cm^{-1}) of van der Waals complexes containing HF for which rotationally resolved overtone data have been reported. .	372
9.5	Vibrational relaxation channels for vibrational predissociation following $v = 1$ and $v = 2$ excitation of $\text{N}_2\text{-HF}$	382

FIGURES

1.1	Figure of the face centered cubic lattice.	2
1.2	Intermolecular coordinates for Ar_2 , ArHF , and $(\text{HF})_2$	7
1.3	Ar-Ar internuclear potential	8
1.4	Angular wavefunctions for three states of ArDF	9
1.5	1-D radial potential for HF/DF	11
1.6	Surface and contour plot of the $\text{H6}(4,3,2)$ ArHF potential in the $\nu_{\text{HF}}=1$ manifold	12
1.7	Two-dimensional slice of the $(\text{HF})_2$ potential.	14
1.8	Equilibrium geometries for $\text{Ar}_n\text{HF}/\text{DF}$, $n=1-4$	16
1.9	Equilibrium geometry for $(\text{DF})_3$	17
1.10	Three experimental scans of an Ar/HF sample over the frequency region between $R(0)$ and $P(1)$ of HF	20
2.1	Frequency coverage provided by cw infrared lasers in the $1-4 \mu\text{m}$ region.	26
2.2	The index ellipsoid for a birefringent material demonstrating the vary- ing index of refraction as a function of θ , the angle between the Poynting vector S and the optic (extraordinary) axis.	31
2.3	Schematic of the experimental apparatus used for the difference fre- quency generation of $2.2-4.2 \mu\text{m}$ infrared light.	33
2.4	Simplified representation of the dye laser locking scheme.	35

2.5	Circuit diagrams for visible detectors.	36
2.6	Typical experimental scan showing the TAC signal, the etalon fringes, and the IR signal.	39
2.7	LiNbO ₃ oven controller circuit	41
2.8	IR power as a function of time, demonstrating temperature stability of the oven of $\approx \pm 0.02^\circ\text{C}$ over 20 minutes.	44
2.9	The pulsed slit valve used to generate the weakly bound complexes.	46
2.10	Circuit for pulsed valve driver.	47
2.11	Schematic of the gas handling system for the pulsed slit jet spectrometer.	48
2.12	Temporal profiles of ArDF absorbance vs backing pressure.	50
2.13	Absorbance vs backing pressure for ArDF, Ar ₂ DF, and Ar ₃ DF.	52
2.14	Boltzmann plot for Ar ₂ DF (encompassing $J'=1-19$), demonstrating the high degree of rotational equilibration. Experimental conditions: 0.8% DF in a 60:40 mixture of Ar:first run Ne at 500 Torr backing pressure.	54
2.15	A time trace of a typical absorption signal from the difference frequency spectrometer.	58
2.16	Schematic of the "lambda-meter," i.e., the traveling Michelson interfer- ometer used to measure the frequencies of the dye and Ar ⁺ lasers.	60
2.17	Schematic diagram of the optical setup used for stabilization of a dif- ference frequency spectrometer.	68
2.18	Schematic diagram of the electronic scheme used to stabilize the transfer cavity onto the stabilized HeNe laser.	70
2.19	Part of the RQ_0^- branch of the HF dimer free hydrogen stretch funda- mental (ν_{acc}) at 3893 cm^{-1} recorded at sub-Doppler resolution.	81

2.20	Frequency drift of the difference frequency spectrometer as a function of relative time.	83
2.21	Series of scans over part of the ν_1 , $K = 1 \leftarrow 0$ Q branches of $(DF)_2$, taken over the course of one week.	84
2.22	Experimental schematic for 1.2-2.2 μm difference frequency generation.	86
2.23	The temperature of the LiNbO_3 crystal necessary for 90° , type I phase matching vs the difference frequency obtained from the subtraction of the 1.06 μm radiation of a cw Nd:YAG from the tunable output of a ring dye laser operating on Rhodamine 6G (R6G).	87
2.24	Frequency drift of the Nd:YAG laser as a function of time.	89
2.25	Circuit diagram for servo for locking the dye laser.	91
2.26	Page 2 of circuit diagram for servo for locking the dye laser.	92
2.27	Page 3 of circuit diagram for servo for locking the dye laser.	93
2.28	Page 4 of circuit diagram for servo for locking the dye laser.	94
2.29	Circuit diagram for servo for locking the marker cavity.	100
2.30	Page 2 of circuit diagram for servo for locking the marker cavity.	101
2.31	Page 3 of circuit diagram for servo for locking the marker cavity.	102
2.32	Ar^+ laser stabilization circuit diagram.	108
3.1	Coordinates used for defining the intermolecular potential of a rare-gas hydrogen halide van der Waals complex.	114
3.2	Spectrum of the ArHF (2000)-(0000) HF overtone stretch, constructed of overlapping 1.5 cm^{-1} scans, averaging 15 pulses per 18 MHz frequency step.	119

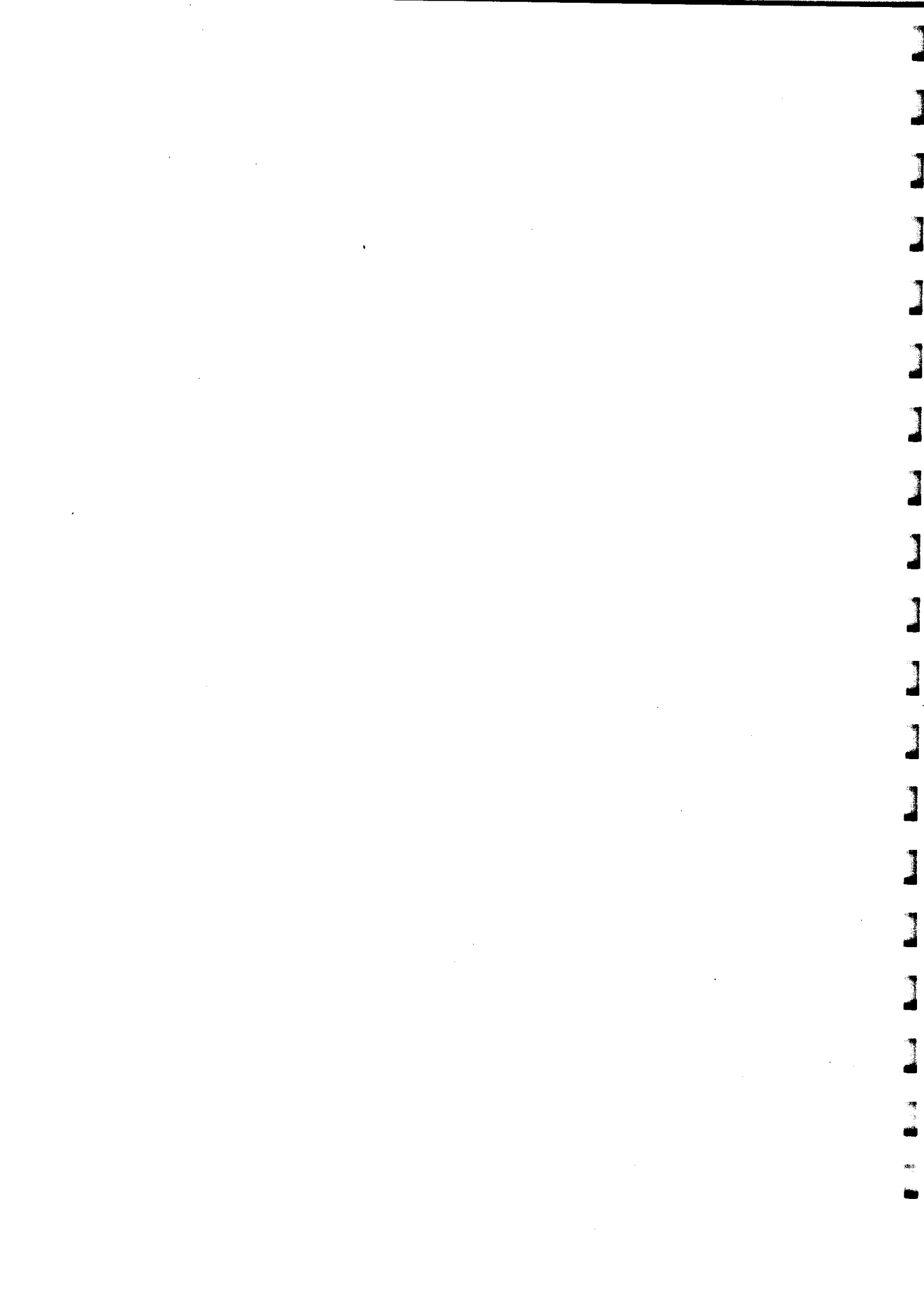
3.3	Spectrum of the ArHF (2100) \leftarrow (0000) Σ bend.	125
3.4	Spectrum of the ArHF (2110) \leftarrow (0000) Π bend	127
3.5	Energies of the ArHF Σ bend, Π bend, and doubly-excited van der Waals stretch vs quanta of stretch excitation in the HF.	134
3.6	ArHF rotational constants for the first three vibrational levels of the HF, including combination bands.	136
3.7	One-dimensional slices through the ArHF intermolecular potential of Hutson at angular orientations of $\theta=0^\circ$, 90° , and 180° for the first three vibrational levels of the HF.	138
3.8	Boltzmann plots of the P and R branch intensities for the (2000) level, (2110) Π bend, and (2100) Σ bend.	142
4.1	Pictorial representation of the equilibrium geometries for Ar_nDF , $n=1-3$.	153
4.2	Overview scan of the region to the red of the ArDF origin near 2898 cm^{-1}	156
4.3	Experimental and calculated spectra for Ar_2DF near the band origin.	158
4.4	Experimental spectrum near the $\text{Ar}_3\text{DF } \nu_{\text{DF}} = 1 \leftarrow 0$ origin, and spec- tral simulations of Ar_2DF and Ar_3DF calculated at a rotational tem- perature of 8.5 K.	165
4.5	Pictorial representations of the two lowest energy isomers for $\text{Ar}_4\text{HF/DF}$.	174
4.6	Vibrational origins for complexes of DF/HF and argon as a function of n , the number of Ar atoms in the complex.	181
4.7	Fractional vibrational redshifts for Ar_nHF and Ar_nDF as a function of n .	183

4.8	Representative Voigt lineshape deconvolutions for $v = 1 \leftarrow 0$ transitions of Ar_2DF	187
5.1	$\text{Ar}_2\text{HF}/\text{DF}$ intermolecular degrees of freedom expressed in Jacobi (scattering) coordinates.	194
5.2	Sample experimental and calculated spectra for the Q branch region of the Ar_2DF in-plane bend.	199
5.3	Sample experimental and calculated spectra for the Q branch region of the out-of-plane bend of Ar_2DF	205
5.4	Region near the origin of the Ar_2HF in-plane bend.	208
5.5	Experimental and calculated spectra for the region of the Ar_2HF out-of-plane bend just to the blue of the vibrational origin.	213
5.6	Intermolecular bending and stretching states for Ar_2HF ($v_{\text{HF}}=1$).	218
5.7	States correlating to $j_{\text{HF}/\text{DF}}=1$ for HF/DF , ArHF/DF , and $\text{Ar}_2\text{HF}/\text{DF}$	225
5.8	Polar plot of the Ar_2HF ($v_{\text{HF}}=1$) potential obtained from expanding the sum of two pairwise ArHF potentials in spherical harmonics.	230
5.9	Two dimensional (radially averaged) wave functions for the lowest four vibrational states of Ar_2HF and Ar_2DF	231
5.10	Pictorial representation of the nonadditive terms that are found to be necessary for reproducing spectroscopic data on $\text{Ar}_2\text{HF}/\text{DF}$	241
5.11	Comparison of experimental and calculated vibrational energies for the in-plane and out-of-plane bends for Ar_2HF and Ar_2DF	244
6.1	Q branches of the $K = 1 \leftarrow 0$ subbands of $2\nu_{\text{acc}}$ ($T_{\text{rot}} = 11 \pm 1 \text{ K}$).	257
6.2	Voigt fits to selected $(\text{HF})_2$ transitions.	265

6.3	Predissociation lifetimes and tunneling splittings as a function of K .	269
6.4	Energy level dyad and triad for $(\text{HF})_2$ fundamental and overtone transitions.	271
7.1	Ground state geometries and Jacobi coordinates for DF/HF dimers.	288
7.2	Wavefunctions ($\Psi(R, \theta_1)$) for the ground state of DF-DF and the two lowest energy isomers of HF-DF/DF-HF.	294
7.3	Experimental scan of $K = 0 \leftarrow 0$ transitions of *DF-DF and *DF-HF.	300
7.4	Spectral region near the origin of $K = 1 \leftarrow 0$ of *DF-HF.	303
7.5	Spectrum of $K = 0 \leftarrow 0$ of HF-*DF.	306
7.6	P branch transitions for $K = 0 \leftarrow 0$ of DF-*HF.	311
7.7	Spectrum of the $K = 0 \leftarrow 0$ transitions of *HF-DF.	313
7.8	Spectrum of the $K = 1 \leftarrow 0$ transition of *HF-DF.	314
7.9	Residuals from the fit of the $K = 0 \leftarrow 0$ transitions of HF-*DF vs $K = 1 \leftarrow 0$ of *HF-DF.	316
7.10	Vibrational origins for $K' = 0$ and 1 of HF-HF, DF-DF, HF-DF, and DF-HF in both the HF and DF stretching regions.	321
7.11	Representative rovibrational lineshapes for $K = 0 \leftarrow 0$ transitions of the HF/DF dimers.	326
7.12	Predissociation linewidths for $K = 0 \leftarrow 0$ and $K = 1 \leftarrow 0$ of *HF-DF, demonstrating the pronounced J' dependence of these bands. The highly localized broadening is attributed to interactions with DF-excited dimer vibrations as described in the text.	327

7.13	Energy diagram showing a possible origin of the "resonance state" which perturbs and gains intensity from $K = 1 \leftarrow 0$ of *HF-DF.	330
7.14	An energy level diagram showing the predicted intermolecular bending and stretching levels built on DF-excited HF-DF and DF-HF.	337
7.15	Residuals (observed - calculated) deviations for *HF-DF $K = 0 \leftarrow 0$ transitions.	339
8.1	Pictorial representation of the IR induced unimolecular opening of the (DF) ₃ ring.	345
8.2	Survey spectrum over ν_5 of (DF) ₃	348
8.3	Comparison of the observed spectra for two τQ branches with simulations assuming no IVR and assuming $\rho_{\text{rovib}}^{\text{exp}} = 200 \times (2J' + 1)$ states per cm^{-1}	351
8.4	Two scans over the τQ (assigned to be $K = 7 \leftarrow 6$) demonstrating the reproducibility of the fine spectral structure	352
8.5	The dissociation energetics for (DF) ₂ and (DF) ₃	354
8.6	The dissociation energetics for (HF) ₂ and (HF) ₃	355
9.1	Spectrum of N ₂ -HF excited to the first overtone stretching level of the HF.	367
9.2	Vibrational redshifts vs the quanta of stretch excitation in the infrared chromophore of all complexes for which rotationally resolved data have been reported in an overtone level.	373

9.3 One-dimensional potential curves for N_2 -HF generated by inversion of the rotational and centrifugal distortion constants using a rotational-RKR technique.	378
--	-----



CHAPTER I

Introduction

1.1 General Introduction

Four centuries ago, Johannes Kepler took a break from his extraterrestrial concerns and pondered the following question: what is the most efficient way to arrange a collection of spheres so as to minimize the total volume? His conjecture (which has been proven only recently [180]) is that this could be achieved by arranging the objects into what is now referred to as the face-centered cubic (fcc) structure (see Figure 1.1). A similar problem confronts the chemist interested in understanding the "packing" of atoms or molecules held together by weak van der Waals or hydrogen bonds. Indeed, many atomic (Ne, Ar, Kr, and Xe) and molecular (HCl, H₂S, and SiF₄) species exploit the high packing efficiency of the fcc lattice in their solid state. Unlike macroscopic spheres, however, the structures adopted by an aggregate of atoms depend sensitively on a delicate balance of attractive and repulsive forces, both angular and radial. A detailed understanding of the nature of these interatomic and intermolecular forces allows us to predict not only crystal structures, but other phenomena as well that are governed by these weak forces. For instance, processes such as solvation,

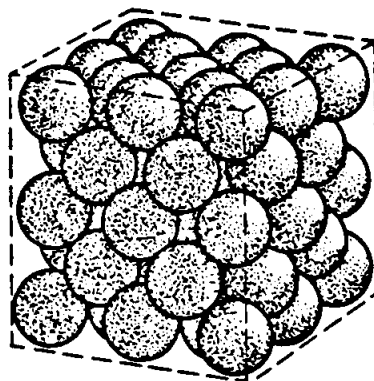


Figure 1.1: Figure of the face centered cubic lattice (from Ref. [199], page 276).

phase transitions, the folding of biomolecules, micelle formation, and collisional energy transfer are all strongly affected by the strength and anisotropy of the intermolecular forces between the constituents.

Although the computational sophistication necessary to address the above processes varies greatly, an essential element of the calculations is a potential energy surface from which the forces acting between the constituents can be derived. While in some instances the “potential” only needs to be known to an accuracy of a few percent to reproduce the properties of interest, many fundamental processes (e.g. vibrational predissociation, energy transfer) depend critically on small details of the potential. All the experiments described in this thesis are motivated by the need to increase our understanding of weak intermolecular forces, and to provide the experimental data necessary to test theoretical potentials rigorously. These data include both structural (rotational constants) and dynamical (inter- and intramolecular vibrational energy levels, vibrational predissociation lifetimes) properties. Because of the central importance of the potential energy surface in these experiments, we consider

specific contributions and examples.

1.2 An introduction to intermolecular potential energy surfaces

The interatomic and intermolecular forces that play the dominant role in van der Waals and hydrogen bonding are electromagnetic in origin. The components of the potential energy can be classified as either electrostatic, induction, dispersion, or exchange (overlap) interactions. The first three are the most important at long distances, while the last dominates at short separations. Each of these is discussed briefly below, and the reader is referred to Refs. [174, 78, 193, 260] for more detailed accounts.

Electrostatic forces arise from the interaction of the permanent multipole moments (e.g. charge, dipole, quadrupole, etc.) of the isolated molecules. Examples include the dipole-dipole interaction between two HCl molecules or the dipole-quadrupole interaction between HCl and CO₂. Induction forces arise from the interaction of permanent multipole moments of one species with the polarizable electron cloud of another. For example, a dipolar species will induce a dipole moment in a rare gas atom, and will increase the permanent dipole moment of another species when oriented head-to-tail. Dispersion (also known as London) forces are purely quantum mechanical in origin, and have no classical analogue. They exist for all species, both polar and nonpolar. Stated most simply, they arise from the concerted fluctuations in electron density between two (or more) species. An instantaneous dipole on one member polarizes a second, and induces in it an instantaneous dipole. The head-to-tail orientation of the two fluctuating dipoles is always energetically favorable, thereby

lowering the energy of the system. As the direction and magnitude of the dipole moment of the first species changes (so as to give a time average of zero), that of the second will follow. Consequently, the time-averaged interaction results in a net attraction. The overlap energy is responsible for the repulsive interactions at short range. When two species get close enough so that their electron clouds overlap, the electrons distort away from the region directly between the nuclei. This is a manifestation of the Pauli exclusion principle, which forbids two electrons from occupying the same (spin-orbital) state. The decrease in electron density reduces the shielding between the (positively-charged) nuclei, resulting in a repulsive interaction which increases rapidly as the separation between the nuclei decreases.

The potential energy surface consists of the combined energy from each of these interactions at all nuclear configurations. The task of obtaining the potential as a function of all $3N-6$ degrees of freedom is quite formidable. Fully *ab initio* potentials are in principle capable of high accuracy, and indeed have been presented for a wide range of weakly bound systems (see, for example, Ref. [68] and references cited therein). One common implementation is the "supermolecule" approach, in which the interaction energy is given by the difference between the energy of the complex (the "supermolecule") and the isolated monomers [68]. However, because the intermolecular energy is often quite small compared to the monomer energies, it is necessary to use large, carefully chosen basis sets and high levels of electron correlation to obtain accurate results. In addition, fitting the points to a functional form to enhance computational convenience is both laborious and subject to bias [348]. Nevertheless, *ab initio* potentials with near-spectroscopic accuracy been reported recently for several important prototypical weakly bound systems such as HeHCN [105], NeHF [292], and

the dimer complexes of Ar with HF [353], H₂O [353], and NH₃ [353].

Experimental data has of course played a central role in extracting information about intermolecular potentials. Studies of the macroscopic properties of gases such as second virial coefficients and transport coefficients (viscosity, diffusion, thermal conductivity, and thermal diffusion factor) have been carried out for many decades, and have provided much insight into the forces between pairs of molecules. However, these quantities involve significant averaging over impact parameters and rovibrational energy levels, which precludes a quantum state specific modeling of the interaction. Although it has been possible to generate relatively accurate potentials for rare gas-rare gas systems from the "inversion" of the transport coefficient data, similar calculations for more complicated molecular systems are quite difficult and often require drastic approximations [260].

Spectroscopic measurements of a weakly bound dimer constitutes a much more direct probe of the intermolecular potential than the transport coefficients. In recent years, high resolution spectroscopy of van der Waals and hydrogen bonded complexes has emerged as a powerful method for characterizing the bound ($E < D_0$) region of the intermolecular potential. In addition, the theoretical methodology necessary to construct potentials from inversion of spectroscopic data has become increasingly sophisticated. Presently, the most accurate potentials available for prototypical systems such as Ar-HF [190], Ar-HCl [191], Ar-H₂O [85], and Ar-NH₃ [328] have been constructed from inversion of the spectroscopic data. Ideally, data that samples the repulsive wall of the potential (e.g., from state-resolved rotational energy transfer scattering experiments) would also be incorporated in order to characterize the full potential. For regions of the potential which are poorly sampled by the available

experimental data, *ab initio* calculations can be used to "fill in the holes."

As an illustrative example of systems for which accurate potentials have been constructed based on spectroscopy of complexes, consider the Ar dimer shown in Figure 1.2a. The atoms have no rotational or vibrational degrees of freedom, and consequently the potential depends only on their separation. Because the Ar atoms have no permanent multipole moments, the long range attractive forces are due entirely to dispersion. Inversion of high resolution UV spectroscopic data on the Ar dimer has provided sufficient information to construct a potential that reproduces vibrational frequencies, rotational constants, scattering cross sections, and second virial coefficients to near-spectroscopic accuracy.

The most accurate potential curve currently available [15] is shown in Figure 1.3. The shallow well depth ($D_e \approx 100 \text{ cm}^{-1}$ or 0.3 kcal/mole) highlights the very weak nature of the interaction, and the correspondingly high demands on the theoretical techniques used to model the potential. Because of the relative simplicity of this system, it has served as an important testing ground for understanding interatomic van der Waals forces for nearly 50 years, and now constitutes perhaps the best characterized weakly bound system.

The next step up in complexity beyond the atom-atom system is the atom-diatom, illustrated schematically in Figure 1.2b. The intermolecular potential is a function of the center of mass radial separation (R) as for the atom-atom system, but in addition depends on the intramolecular radial coordinate (r) and the diatom bending coordinate (θ). Consequently, mapping out the potential requires spectroscopic data that provides information on all three of these coordinates. Figure 1.4 shows angular wavefunctions for several vibrational states of the ArDF complex. In the van der

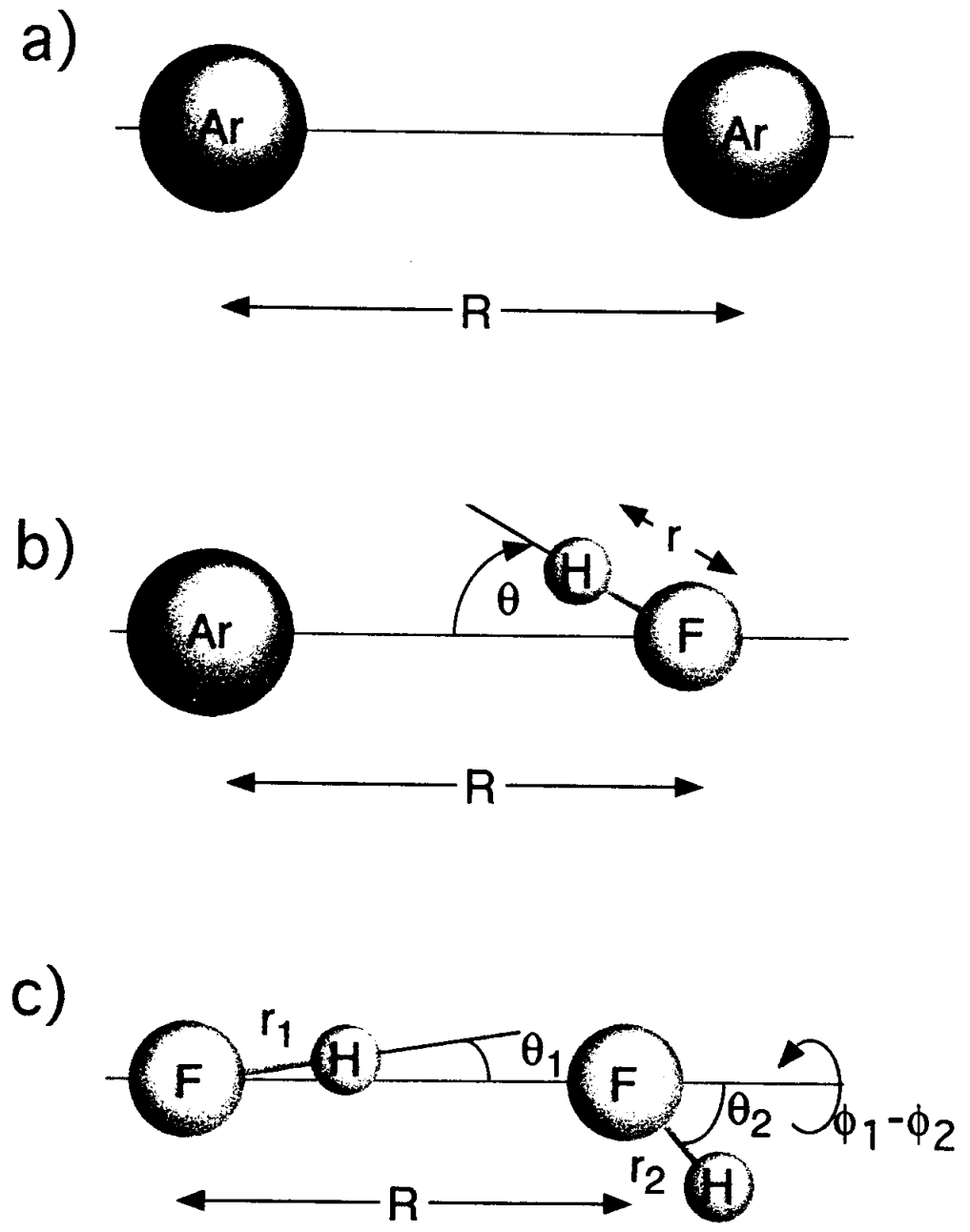


Figure 1.2: Intermolecular coordinates for a) Ar_2 , b) ArHF , and c) $(\text{HF})_2$

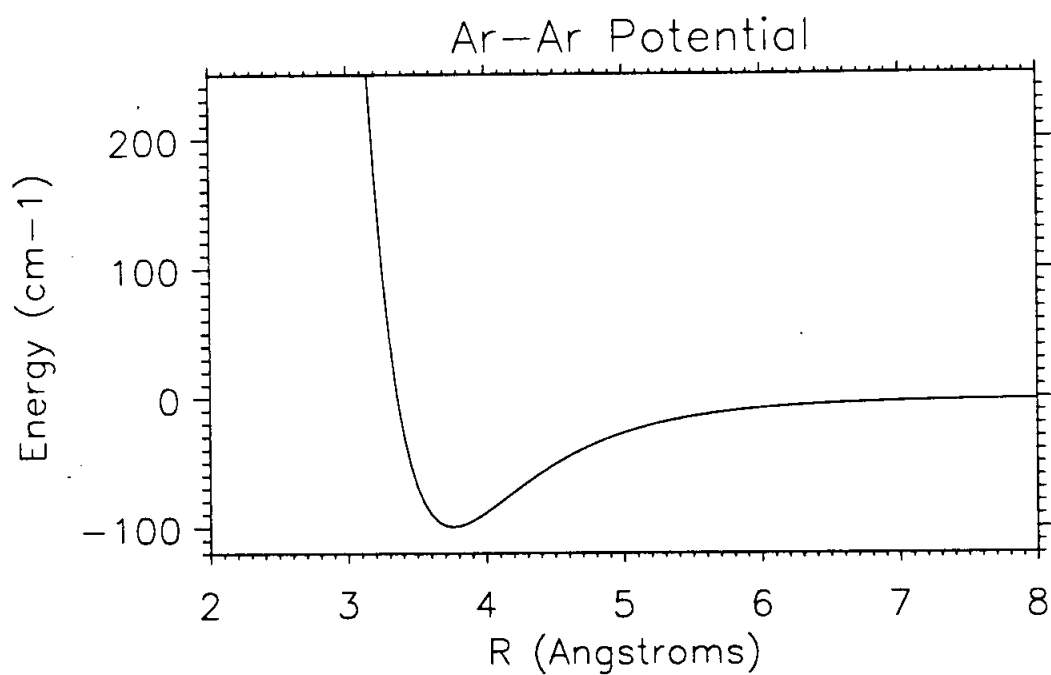


Figure 1.3: Ar-Ar potential from Ref. [15].

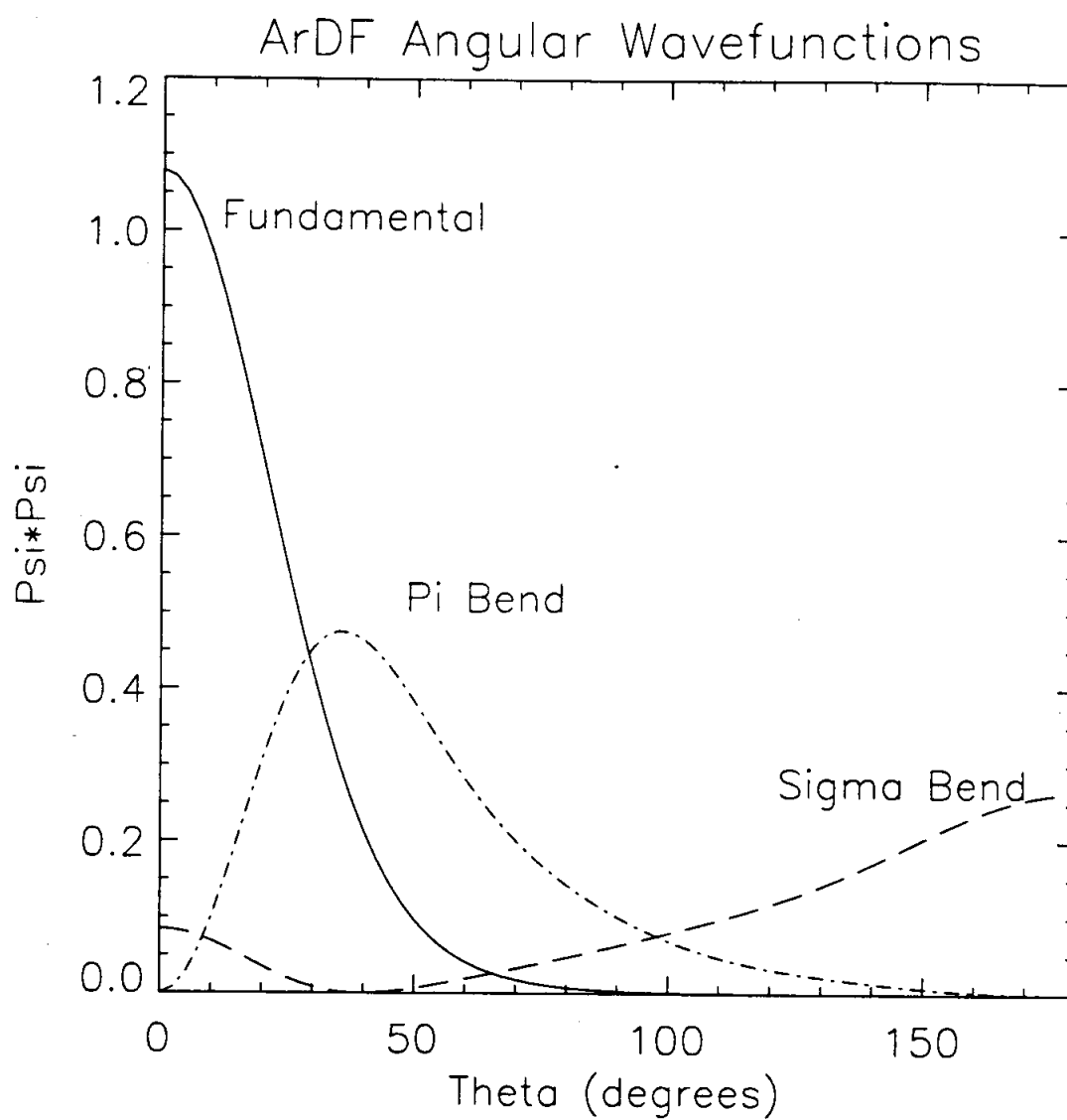


Figure 1.4: Angular wavefunctions for three states of ArDF.

Waals ground state (labeled the "fundamental" in the figure), the DF executes large amplitude zero point bending motion that samples angles of $|\theta| \approx 0-40^\circ$. However, the wavefunctions for the two lowest energy intermolecular bends (labeled the " Σ " and " Π " bends) are peaked at angles of $\theta=40^\circ$ and 180° respectively, demonstrating that a large region of the angular potential can be sampled with a relatively small number of intermolecular vibrational states. In a similar manner, van der Waals stretch excitation allows different regions of the *intermolecular* radial potential to be accessed. One means of probing the dependence of the potential on the *intramolecular* radial coordinate is through excitation of the high frequency stretch, e.g. the HF/DF stretch for the case of ArHF/DF. The excitation of an intramolecular degree of freedom alters the intermolecular potential because properties such as the multipole moments and polarizability of the monomer change upon vibrational excitation. Alternatively, isotopic substitution can also be used to infer the dependence of the potential on the intramolecular coordinate. As shown in Figure 1.5 for the particular example of DF vs HF substitution, the reduced zero-point motion of the heavier isotopomer leads to sampling of different regions of the intramolecular potential. A large body of data has been amassed for ArHF/DF, which has permitted the construction of a potential that depends explicitly on the van der Waals distance R and angle θ , and parametrically on the intramolecular coordinate r . Figure 1.6 shows a surface plot of this potential in the $v_{\text{HF}}=1$ manifold.

Just as Ar-Ar and Ar-HF have served as important prototypes for understanding interatomic and intermolecular van der Waals forces, $(\text{HF})_2$ (see Fig. 1.2c) has played an analogous role for hydrogen bonding. The interaction of two polar diatoms constitutes the simplest model of hydrogen bonding, yet encompasses many of

HF/DF RADIAL WAVEFUNCTIONS

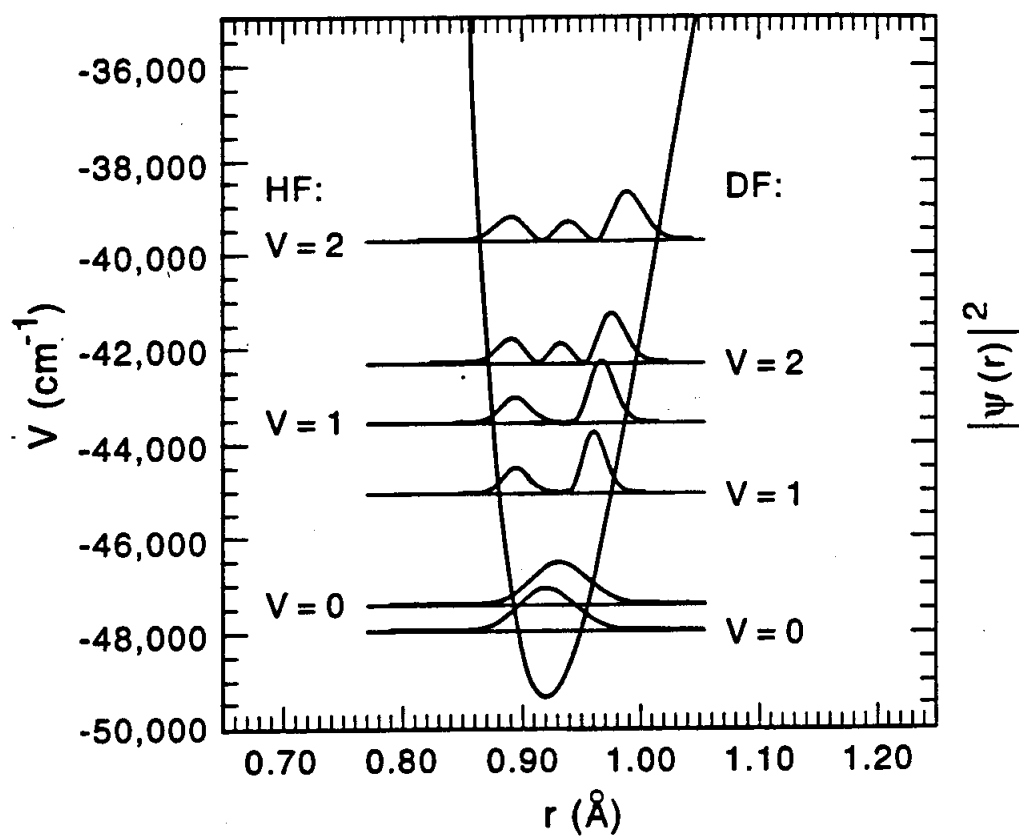


Figure 1.5: 1-D radial potential for HF/DF emphasizing the differences in zero point energy and thus the different r dependent information this provides about the potential.

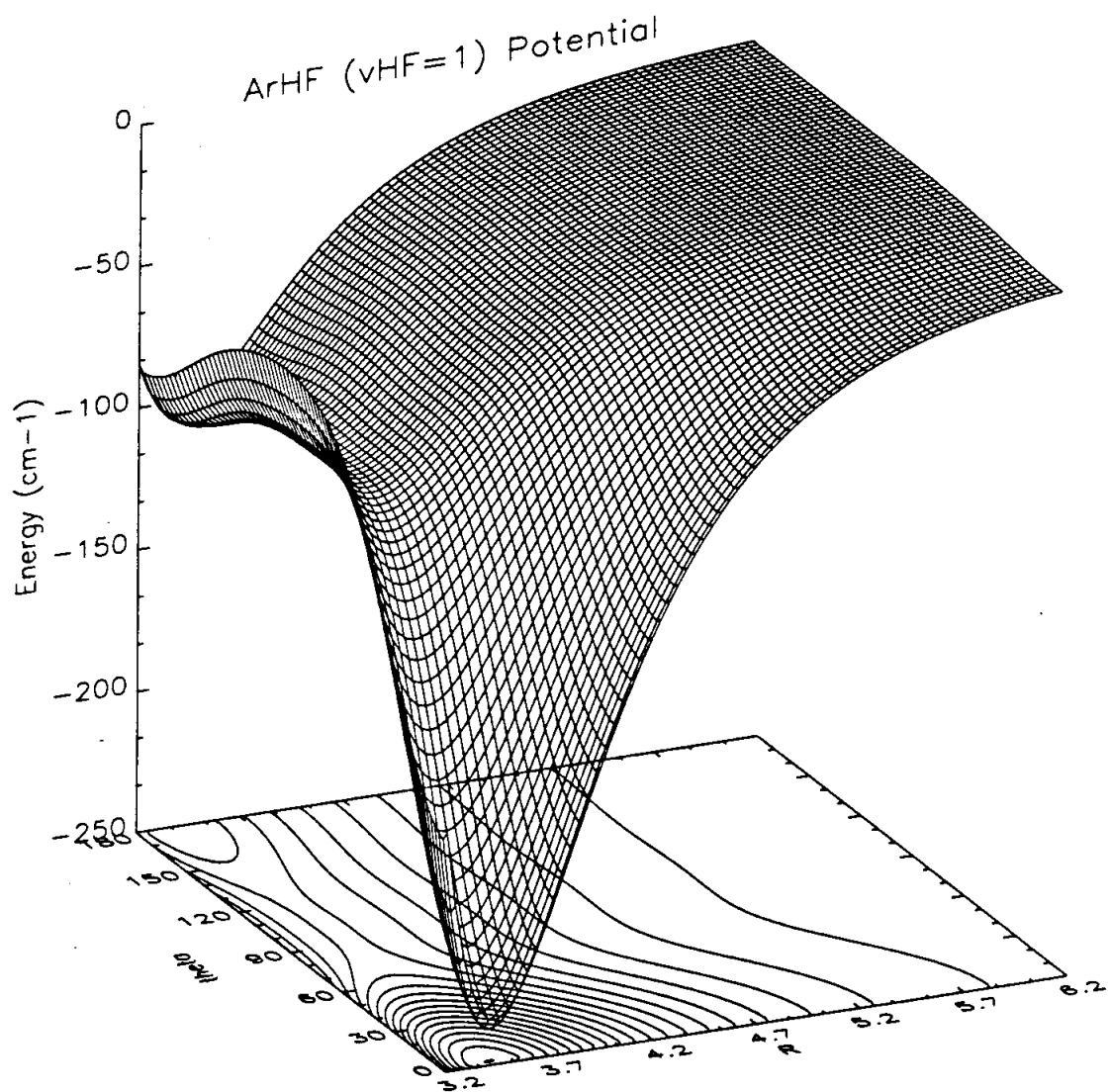


Figure 1.6: Surface and contour plot of the H6(4,3,2) ArHF potential in the $v_{HF}=1$ manifold (from Ref.[190]).

the important dynamics of more complicated systems. The small number of electrons (20) and the reduced dimensionality (6 degrees of freedom) makes $(\text{HF})_2$ an attractive system to study from both a computational and experimental standpoint. The most accurate potential currently available [311] is a full-dimensional 6-D *ab initio* potential, with constraints imposed to reproduce key experimental results such as the dissociation energy and ground state rotational constants. A 2-dimensional slice of this potential is shown in Figure 1.7 as a function of the two HF bending angles θ_1 and θ_2 .

Calculations of intermolecular vibrational frequencies and product state distributions following photodissociation on this potential have demonstrated good agreement with experiment [361, 389].

The three dimer systems discussed above, i.e., Ar-Ar, Ar-HF, and HF-HF have played a seminal role in furthering our understanding of weak intermolecular forces. The accuracy of the “pair potentials” constructed for these systems is sufficiently high that they can be used to model the structure and dynamics of larger complexes. For example, the simplest description of the potential for a large aggregate of Ar atoms is constructed from summing all the pair interactions. Within this “pairwise-additive” approximation, the total potential is represented as

$$V_{\text{total}} = \sum_N V_{\text{Ar-Ar}} \quad (1.1)$$

However, properties of solid Ar such as the binding energy calculated on the pairwise additive potential are poorly reproduced. It is reasonable to expect that the potential describing the interaction of a pair of atoms changes in the presence of a third (or fourth, etc.). The importance of these “3-body” and higher n -body (collectively desig-

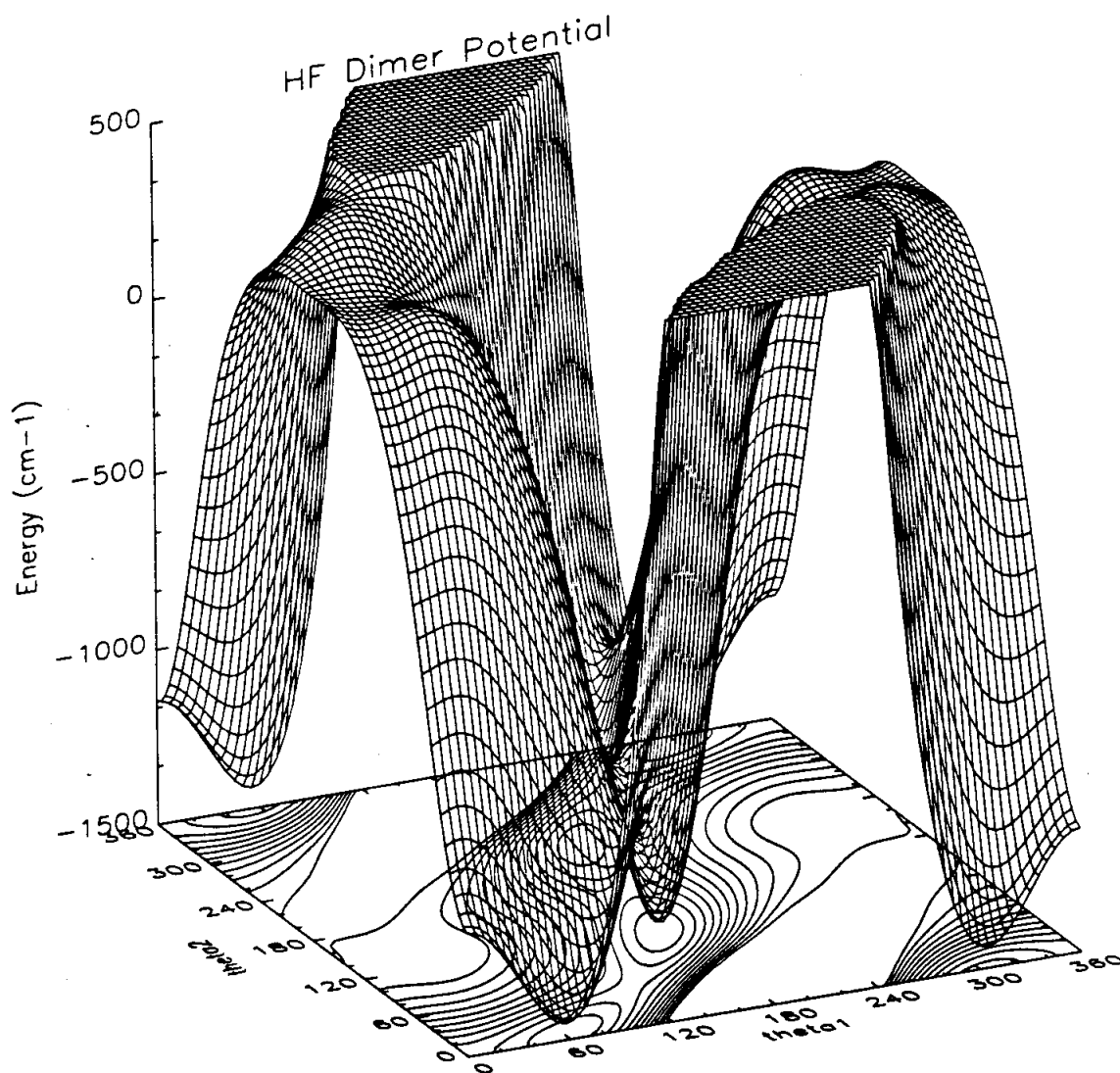


Figure 1.7: Two-dimensional slice of the $(\text{HF})_2$ potential of Ref.[311]. In this figure, the bending angles of the two HF molecules are varied, keeping the two HF bond lengths fixed at 0.935 \AA , the intermolecular radial separation fixed at 2.789 \AA , and $\Delta\phi = 180^\circ$.

nated "nonadditive") terms can be significant. For example, theoretical calculations of HF clusters [313] on an *ab initio*-based potential indicate that cooperative nonadditive effects increase the binding-energy of $(\text{HF})_4$ by 25%. Although increasing theoretical attention is being devoted to the nonadditivity in molecular systems, experimental data that is highly sensitive to these effects are relatively scarce.

Trimers represent the simplest systems for which nonadditive intermolecular forces are present. Given the wealth of knowledge accrued for the dimer systems discussed above, trimers that utilize these dimers as building blocks represent natural systems to study for insight into nonadditive intermolecular forces. $\text{Ar}_n\text{HF}/\text{DF}$ ($n=2-4$) (shown in Figure 1.8) and $(\text{DF})_3$ (Figure 1.9) are two systems discussed in this thesis that provide detailed information into the relative importance of nonadditive terms. The subject of nonadditive intermolecular forces has been reviewed recently [115] and consequently only a brief discussion is provided. Perhaps the best known nonadditive term is the Axilrod-Teller triple dipole dispersion term (denoted DDD), which is the leading (3-body) nonadditive term in a perturbative expansion of the intermolecular potential. Higher order treatment gives other long-range nonadditive terms such as (DDQ), (DQQ), (QQQ), etc., where D and Q stand for dipole and quadrupole, respectively. The DDD energy is attractive when the three species are arranged collinear because the induced dipoles can maintain favorable orientations for all directions of a given inducing dipole moment. Conversely, an equilateral triangular orientation gives rise to a repulsive DDD contribution, although the overall dispersion energy is still attractive.

Another nonadditive term which exhibits a similar geometric dependence is the exchange nonadditivity. However, it is the equilateral triangular geometry for

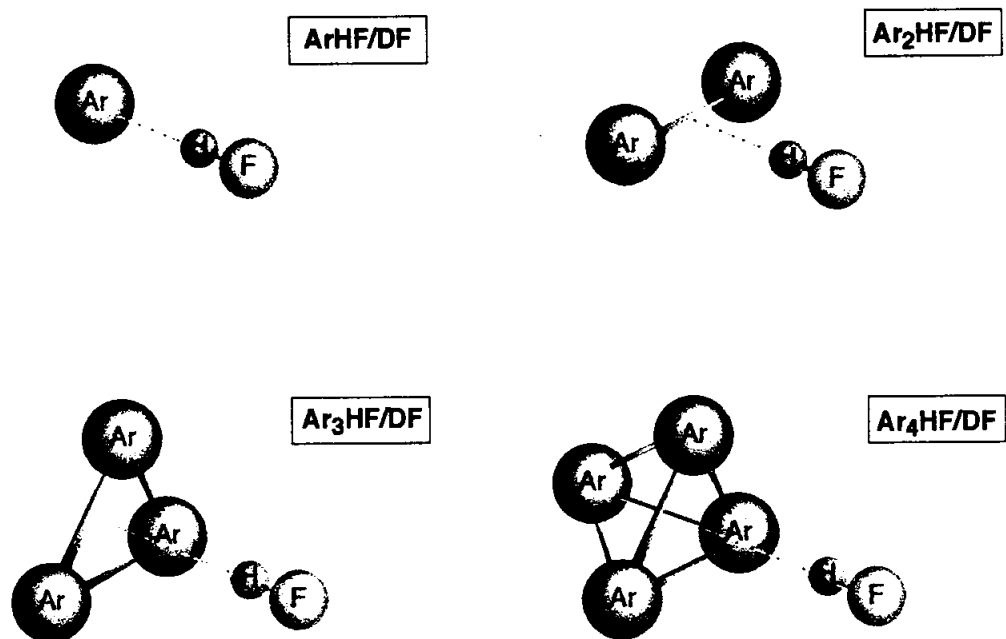


Figure 1.8: Equilibrium geometries for $\text{Ar}_n\text{HF/DF}$, $n=1-4$.

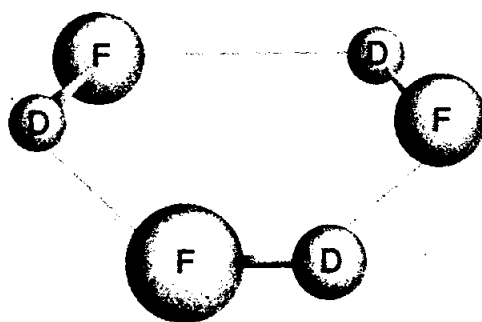


Figure 1.9: Equilibrium geometry for $(DF)_3$.

which this energy is attractive while the collinear is repulsive. This effect can be understood by considering that the exchange interaction between two atoms in a dimer causes the electron clouds to distort away from the region between the nuclei. When a third atom is placed on-axis, it restricts the amount of this distortion, leading to a repulsive 3-body contribution [88]. Conversely, the equilateral triangular orientation does not restrict this redistribution, and consequently leads to an attractive nonadditive energy.

The above two terms do not require a permanent multipole moment in the constituents, and are thus present in both atomic and molecular systems. When one of the partners does have a permanent multipole moment, additional nonadditive terms become important. For instance, the permanent multipole moments on one member will induce multipole moments in its neighbors. These induced moments can themselves interact to give a nonadditive contribution to the total energy which is either attractive or repulsive depending on the relative orientations of the moments. Similarly, permanent multipole moments of a member may interact with the moments induced

by other species. For example, the two argon atoms in Ar_2 generate a quadrupole moment between them; if another species with a permanent dipole or quadrupole approaches, its interaction with this induced quadrupole moment will constitute a nonadditive interaction.

The experimental demands for extracting detailed information about pairwise additive and nonadditive intermolecular forces are quite high. We therefore address the relevant experimental issues in more detail for the specific case of IR spectroscopy of complexes formed in supersonic expansions.

1.3 High resolution IR spectroscopy as a probe of intermolecular forces

The basic premise of the experiments described in this thesis is quite simple. High resolution infrared laser light is passed through a gaseous sample containing the weakly bound complexes, and is monitored on a detector. When the light is tuned to a resonant frequency of a complex, the detector records an attenuation of the light. The amount of light reaching the detector is monitored as the laser is scanned in frequency and yields the spectrum. Although simple in principle, the implementation of the experiment is quite challenging. There are two integral components of the apparatus that provide the unique capability of measuring the spectra of weakly bound complexes, i) the IR laser source and ii) the pulsed slit jet used to synthesize the molecular complexes. While each of these components will be described in more detail in the following chapter, it is instructive to examine the benefits realized through implementation of these two components.

Figure 1.10 shows a series of three scans over approximately the same spec-

tral region near the $v = 1 \leftarrow 0$ origin of HF. The top spectrum is recorded with a conventional IR spectrometer with a static gas cell containing HF and Ar at room temperature [360]. The spectral structure between $R(0)$ and $P(1)$ is the induced Q branch of HF, or equivalently arises from absorption by complexes of Ar and HF. However, the relatively low resolution of the spectrometer (0.5 cm^{-1}), coupled with the large Doppler and pressure broadening of a room temperature high pressure gas sample, prevent rotational structure of the complexes from being resolved.

The second spectrum demonstrates the dramatic improvement in resolution realized upon the incorporation of an infrared laser as the light source [135]. The broad structure near the HF $v = 1 \leftarrow 0$ origin which is unresolved in Figure 1.10a is seen to be composed of a large number of transitions corresponding to rotational progressions of ArHF and high- J states of $(\text{HF})_2$. In addition, reduced Doppler and pressure broadening is realized by virtue of the lower temperature and pressure employed in these experiments.

The full benefits of low temperature and pressure are demonstrated in Fig 1.10c, which shows the ArHF spectrum recorded using a laser similar to that used in Figure 1.10b, but with a pulsed slit supersonic expansion as the cluster source [251]. The rotational temperature of the complex in the supersonic expansion is approximately 10 K, which leads to a significant simplification of the spectrum by virtue of the decreased number of quantum states populated. This has the added benefit of increasing the number of molecules per quantum state, leading to a much greater detection sensitivity. Together with the concomitant narrowing of transitions due to reduced Doppler broadening and the elimination of pressure broadening, the use of an IR laser coupled with the slit supersonic expansion source lead to a unique ability to

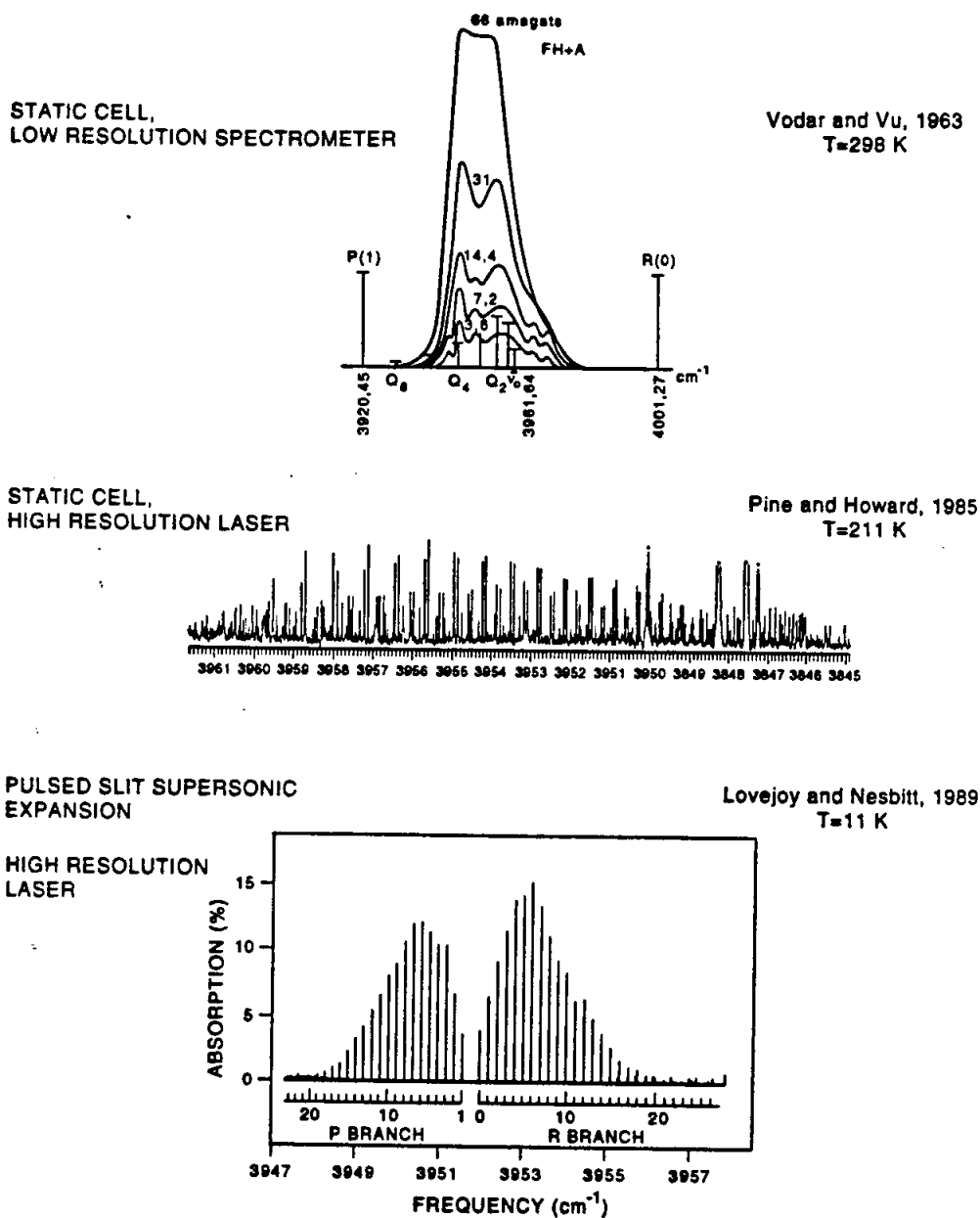


Figure 1.10: Three experimental scans over the frequency region between $R(0)$ and $P(1)$ of HF. a) Low frequency spectrum of an Ar/HF mixture in a room temperature, static gas cell [360]. b) An expanded frequency region, recorded in a 211 K cell but with a high resolution IR laser [135] demonstrating the dramatic improvement in resolution (note the inverted frequency scale and progression of doublets from high- J (HF)₂ transitions). c) Similar frequency region as b), but with a slit jet supersonic expansion as the cluster source [251]. The very low temperature and pressure of the supersonic expansion lead to a dramatic simplification of the spectrum as discussed in the text.

characterize the spectroscopy and dynamics of weakly bound systems.

It might be questioned, however, how it is possible to obtain rotationally resolved spectra of complexes with binding energies of $\approx 100 - 1000 \text{ cm}^{-1}$ (0.3–3 kcal) following excitation by a $2500 - 10000 \text{ cm}^{-1}$ photon. If the complexes were to fall apart soon after photon absorption (say after tens of monomer vibrations), then the associated lifetime broadening of the transitions ($\Delta\nu \propto 1/\tau$) would be so large that rotational state resolution would be precluded. Thus, the mere acquisition of rotationally resolved spectra for a complex requires that the energy remain localized in the intramolecular coordinates for at least several hundreds of picoseconds. That this is the case indicates that the coupling between the intramolecular and intermolecular coordinates is indeed quite weak. If the complex falls apart (predissociates) on the timescale of $\approx 200 \text{ ps} - 70 \text{ ns}$, then the associated lifetime broadening can be extracted from an analysis of the rovibrational lineshapes (as will be described in more detail in the following chapter) and provides important information on the timescale for energy transfer within the complex.

An additional asset of near-IR spectroscopy in studying weakly bound systems is the relative ease of scanning large spectral regions. The complete $1-4 \mu\text{m}$ coverage of our IR laser not only provides access to fundamental and overtone vibrations of species C-H, N-H, O-H, or X-H (X=F,Cl) substituent, but also permits extensive searches for *intermolecular* vibrations excited in conjunction with the *intramolecular* stretch. These "combination bands" are typically only $10-500 \text{ cm}^{-1}$ higher than the van der Waals ground states, and are readily accessed with only minor experimental modifications. As discussed above, it is these intermolecular vibrations which sample large regions of the angular and radial parts of the intermolecular potential that

provide the most detailed information on the potential.

The rest of this thesis is organized as follows. Chapter 2 presents a detailed description of the experimental technique. Results from the study of ArHF in the $\nu_{\text{HF}}=2$ manifold are given in Chapter 3, which have been used in the construction of a potential for ArHF/DF that depends on all internal degrees of freedom. This potential has been instrumental in interpreting the results from Chapter 4, which presents data for Ar_nDF ($n=1-3$) complexes. Calculations on a pairwise-additive potential constructed by summing the Ar-Ar and Ar-DF pair contributions have provided information about nonadditive forces for the prototypical $\text{Ar}_n\text{HF/DF}$ system. Chapter 5 describes the analysis of two intermolecular bending states of Ar_2HF and Ar_2DF , which permit a much more detailed assessment of nonadditivity by virtue of the much larger region of the angular potential accessed by these vibrations. Chapters 6-8 investigate the intramolecular dynamics of the hydrogen fluoride dimer and trimer. Excitation of the $\nu_{\text{HF}}=2$ stretch in the dimer described in Chapter 6 provides important information about the intramolecular dynamics of the complex, and suggests an intriguing mixing between the three components of the $\nu_{\text{HF}}=2$ triad (*vide infra*). Chapter 7 presents results for $\nu_{\text{HF/DF}}=1$ excitation of the HF/DF isotopomers; as well as elucidating important information about the intramolecular dynamics in the $\nu_{\text{HF}}=1$ manifold, interesting state-mixing in the HF-excited HF-DF and DF-HF dimers are identified and attributed to interactions with highly excited intermolecular states built on the $\nu_{\text{DF}}=1$ stretch. The first high resolution IR spectra for a HF oligomer larger than the dimer is described in Chapter 8, which confirms the cyclic equilibrium ground state geometry, and further establishes intriguing ring opening dynamics following photon absorption. Chapter 9 describes data for N_2HF excited to the $\nu_{\text{HF}}=2$ manifold. In

addition to establishing a strong dependence of the vibrational predissociation rate to quanta of HF excitation, information about the intermolecular radial potential is extracted through rotational-RKR analysis of the rotational constants.

CHAPTER II

Experimental

2.1 Introduction

The pulsed slit jet infrared spectrometer used in the experiments described in this thesis had already demonstrated an unparalleled sensitivity in spectroscopically characterizing weakly bound complexes at the time I started my graduate work (see, for example, Refs. [254, 266, 330]). The basic components of the experiment have remained the same during the past five years, although a large number of modifications and improvements have been implemented. Consequently, the primary emphasis of this chapter is to describe the near infrared spectrometer in its current incarnation, with most of the attention devoted to describing in detail the changes that have been made.

The infrared light used in these experiments is generated from the nonlinear mixing of a tunable dye laser and a fixed frequency Ar⁺ or Nd:YAG laser. Although many sources of infrared light are available to the experimentalist, our laboratory utilizes difference frequency generation for two primary reasons, i) the high frequency resolution of the laser source, and ii) the broad frequency coverage provided by difference

frequency mixing in LiNbO_3 . Both attributes have been instrumental in completing the experiments described in this thesis, and are discussed in more detail below.

The high frequency resolution ($\Delta\nu \approx 2\text{--}3$ MHz) of our laser source is essential for extracting both structural and dynamical information about weakly bound complexes. This is especially true for complexes with three or more constituents, where resolving the individual rovibrational transitions becomes much more difficult as the moments of inertia about the intermolecular axes increase. Additionally, the absorption profile of the transitions can be recorded with great accuracy. This allows information about the lifetimes of the complexes in the vibrationally excited state to be inferred from an analysis homogeneous broadening in the lineshapes.

Given that an infrared laser is of central importance to meet our experimental goals, the benefits of difference frequency generation must be compared to those of other, more widespread sources such as F-center and diode lasers. In this regard, the much greater spectral coverage of the difference frequency laser offers profound advantages. As shown in Figure 2.1, the *entire* region between $1.2\text{--}4.2$ μm can be accessed with our difference frequency laser, which is a region over which no other IR laser sources are presently capable of covering completely.

This frequency region encompasses the fundamental vibrations of most species containing C-H, N-H, and O-H moieties as well as the hydrogen halides HF, DF, and HCl. In addition, first and (for some) second overtone transitions can be accessed as well. Furthermore, the complete coverage over this region ensures that in addition to excitation of intramolecular vibrations of a species within a complex, *intermolecular* vibrations can be accessed as well, the analysis of which provides significant information about the interaction potential of the complex.

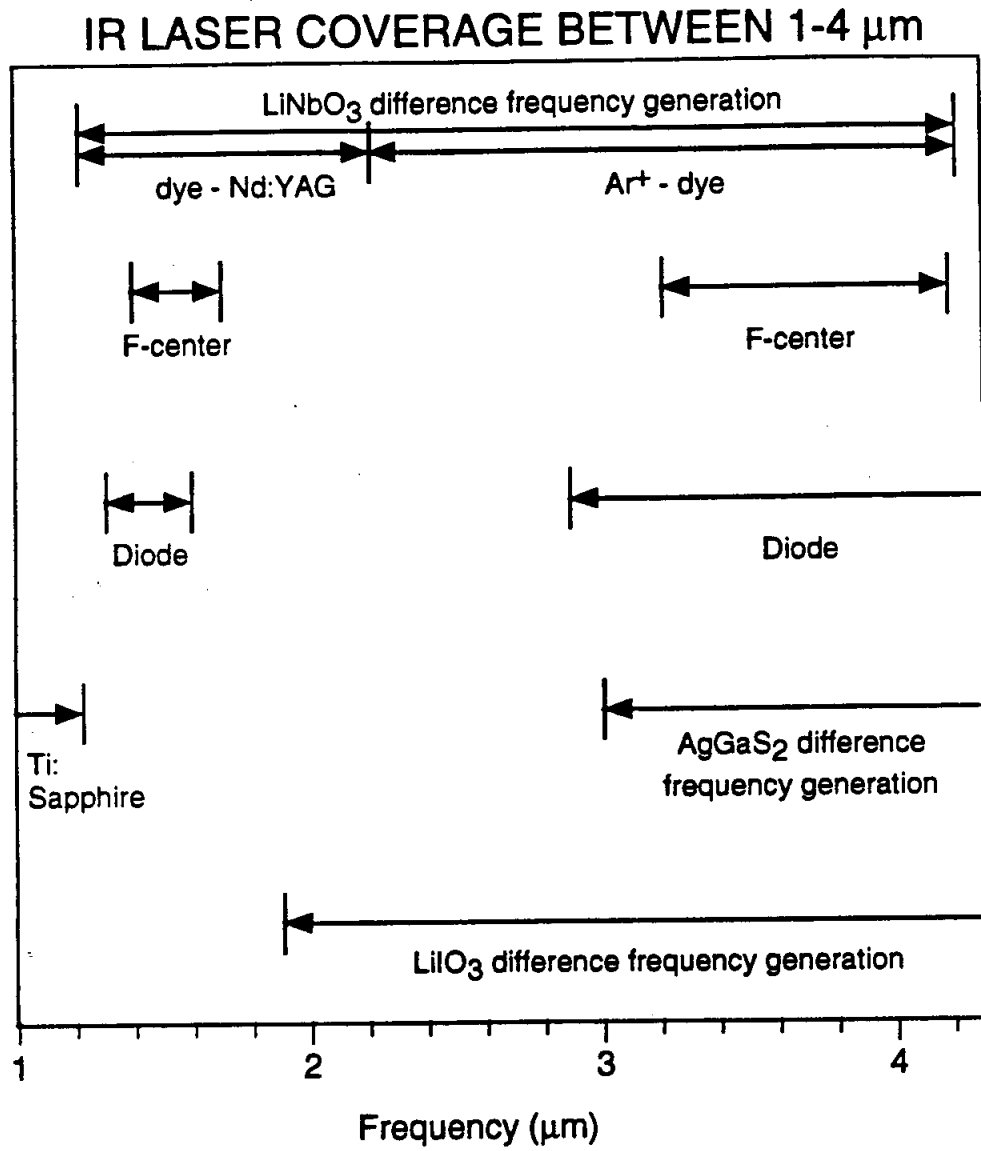


Figure 2.1: Frequency coverage provided by cw infrared lasers in the 1-4 μm region.

The rest of the chapter is organized as follows. First, a brief description of difference frequency generation is provided, followed by a discussion of the experimental apparatus. More detailed descriptions are then provided of the HeNe stabilized marker cavity and Ar⁺ locking electronics. The modifications required to convert from the 2.2–4.2 μm region to the 1.2–2.2 μm region are then discussed. Appendices are included at the end of the chapter containing circuit diagrams and operating guidelines for the dye laser stabilization servo, the HeNe-stabilized marker cavity, and the Ar⁺ stabilization electronics.

2.2 Overview of difference frequency generation

The following description of the difference frequency generation process is geared towards providing a physical picture for this nonlinear process; more detailed expositions are available in References [62, 47]. The propagation of a monochromatic light wave through a transparent, dielectric medium induces oscillatory motion of the electrons and ion cores of the medium. By virtue of the opposite charges of the electrons and ion cores, the displacements are in opposite directions. If the electric field is weak relative to the field that binds the electrons and ions ($\approx 3 \times 10^{10}$ V/m), the oscillating polarization induced in the medium is linearly proportional to the field strength. This can be expressed as

$$P_i = \epsilon_0 \sum_j \chi_{ij} E_j \quad (2.1)$$

where P_i is the polarization (i.e., induced dipole per unit volume of the dielectric), ϵ_0 is the permittivity of free space, and χ_{ij} is a dimensionless second rank tensor denoted the

linear susceptibility. χ_{ij} describes the electrodynamic properties of the electron/ion dipoles, and is closely related to the molecular polarizability α .¹ In the linear limit described by Eq. 2.1, the oscillating polarizability creates a second electromagnetic wave that oscillates at the same frequency as the original light wave.

However, if the electric field of the input wave is sufficiently large, the dipoles of the dielectric medium no longer respond linearly. The polarization can then be expressed as a Taylor series expansion of Eq. 2.1,

$$P_i = \epsilon_0 \sum_j \chi_{ij} E_j + \epsilon_0 \sum_{jk} \chi_{ijk} E_j E_k + \epsilon_0 \sum_{jkl} \chi_{ijkl} E_j E_k E_l + \dots \quad (2.3)$$

where χ_{ijk} is the second order nonlinear susceptibility (related to the molecular hyperpolarizability), χ_{ijkl} is the third order susceptibility, etc. The second term in the sum describes the nonlinear phenomenon of difference frequency generation, as well as the closely related phenomena of sum frequency generation, second harmonic generation, optical rectification, optical parametric amplification, and optical parametric oscillation [173]. The dependence of the polarization on the electric field demonstrated in Eq. 2.3 illustrates how the polarization can generate new frequency components not present in the incident radiation field. For example, the product of two sinusoidal electric fields at frequencies ω_1 and ω_2 is $\propto [\cos(\omega_1 - \omega_2) + \cos(\omega_1 + \omega_2)]$, which gives rise to second harmonic generation and optical rectification² when $\omega_1 = \omega_2$, and sum and difference frequency generation when $\omega_1 \neq \omega_2$. The second order susceptibility is

¹More specifically, Eq. 2.1 describes the bulk limit of polarization in an electric field. At the molecular level, the polarization is described by the field-dependent molecular dipole moment expansion [110],

$$\mu = \mu_0 + \sum_j \alpha_{ij} E_j \quad (2.2)$$

²The term "optical rectification" describes the generation of a static electric field within the nonlinear crystal [47].

strongly linked to the symmetry of the medium. Specifically, $\chi_{ijk} = 0$ if the medium contains an inversion center, and consequently a noncentrosymmetric material (e.g. LiNbO_3) is necessary for difference frequency generation.

The difference frequency process utilized in our laboratory (for IR in the 2.2-4.2 μm region) consists of generating light at the frequency difference between an Ar^+ laser at ω_1 and dye laser at ω_2 , i.e.,

$$\omega_3 = \omega_1 - \omega_2 \quad (2.4)$$

where ω_3 is the infrared frequency. Physically, the creation of an infrared photon is accompanied by the destruction of an Ar^+ photon. Conservation of energy thus requires the simultaneous generation of a photon at the dye laser color.³

The efficiency of difference frequency generation is significantly enhanced through a process denoted "phase matching" (see Ref. [47]). Phase matching describes the conditions necessary for the difference frequency wave to maintain a fixed phase relationship with respect to the incident waves. One requirement of phase matching is that the photon momenta $n_i\omega_i$ must be conserved, i.e.,

$$n_3\omega_3 = n_1\omega_1 - n_2\omega_2 \quad (2.5)$$

where $n_i = k_i c / \omega_i$ is the index of refraction sampled by ω_i in the medium. Expressed in terms of the wave vectors k_i , perfect phase matching is given by

$$\Delta k = k_1 + k_2 - k_3 = 0 \quad (2.6)$$

When perfect phase matching is not fulfilled, the efficiency of difference frequency generation decreases dramatically. This can be seen through the expression for the

³The process just described is fundamentally the same as optical parametric amplification (OPA). In OPA applications, however, the quantity of interest is the amplified input signal and the difference frequency light is often discarded. This is different than difference frequency generation, where the latter is the desired quantity.

intensity of the difference frequency light [47],

$$I_3 \propto \frac{I_1 I_2}{\lambda_3^2} L^2 \text{sinc}^2(\Delta k L / 2) \quad (2.7)$$

where I_i is the intensity of the electric fields, λ_3 is the wavelength of the difference frequency light, and L is the interaction length. For well-defined frequencies ω_1, ω_2 , and ω_3 , phase matching is achieved by varying the indices of refraction of the nonlinear medium.

The two methods commonly used for tuning the indices of refraction of a birefringent material such as LiNbO_3 are angle tuning and temperature tuning. Figure 2.2 shows how angle tuning, i.e., changing the angle θ of the Poynting vector of the incident beams with respect to the optic (extraordinary, or z) axis changes the effective index of refraction n_{eff} sampled by the incident radiation. One serious drawback of angle tuning is that the input beams do not propagate along one of the crystal axes, and consequently the beams are refracted as they propagate through the medium. As shown in Eq. 2.7, the conversion efficiency scales as the product of the input power and the square of the interaction length. Because angle tuning leads to relatively small interaction lengths, significant IR power is only realized for very large input power (e.g. from pulsed lasers).⁴

Temperature tuning takes advantage of the different rates at which the index of refraction of the extraordinary and ordinary axes tune with temperature. LiNbO_3 is particularly well suited for this type of phase matching. In addition, temperature tuning at $\theta = 0^\circ$ or 90° allows for a much longer interaction length than angle tuning,

⁴ LiIO_3 is a nonlinear medium for which angle tuning is used to achieve phase matching for difference frequency generation (see Figure 2.1). The corresponding cw power levels of $\approx 0.5 \mu\text{W}$ [374] are approximately two orders of magnitude lower than realized through temperature tuning of LiNbO_3 as is discussed below.

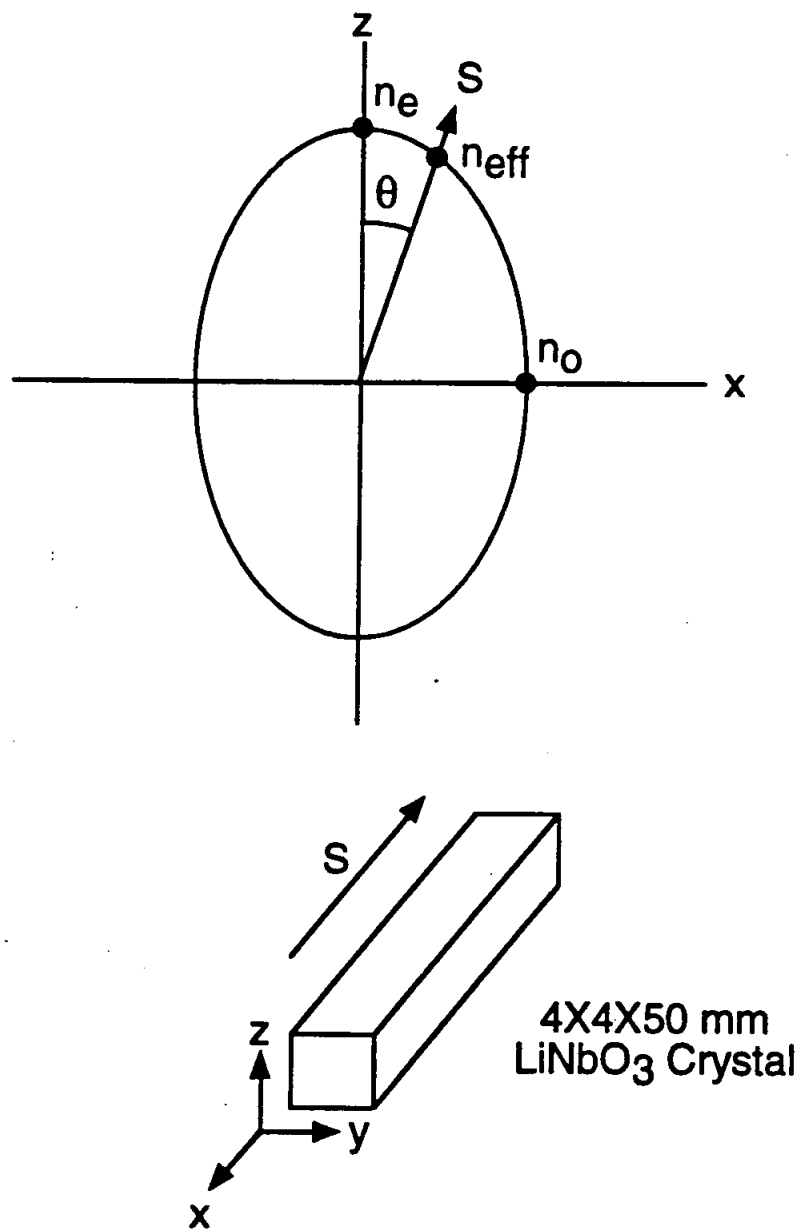


Figure 2.2: The index ellipsoid for a birefringent material demonstrating the varying index of refraction as a function of θ , the angle between the Poynting vector S and the optic (extraordinary) axis.

since in theory S for both incident beams remains collinear. This allows difference frequency conversion with relatively low power (≤ 500 mW) cw lasers to be feasible. In the literature, the type of phase matching utilized in our lab is designated as noncritical, 90° , Type I phase matching. Noncritical refers to temperature tuning as opposed to angle tuning (which is designated critical). 90° refers to the value of θ , as shown in Figure 2.2. Midwinter and Warner [271] have elucidated that in principle, two types of phase matching are possible for three wave mixing in birefringent crystals. For a negative uniaxial crystal (i.e., $n_e < n_o$) such as LiNbO_3 , Type I phase matching refers to cases where the two lowest frequency beams (i.e., the dye and IR in the generation of 2.2–4.2 μm IR) are polarized parallel to each other. Conversely, Type II phase matching refers to cases where they are polarized perpendicular to each other.

2.2.1 Generation of difference frequency light

The difference frequency generation technique utilized in our labs is based on the method developed by Pine [296], and is shown schematically in Figure 2.3. Although this figure relates specifically to the generation of 2.2–4.2 μm light, it is qualitatively similar to the experimental setup for 1.2–2.2 μm generation; the relatively minor modifications are described in a separate section below. 0.2–0.5 W of tunable visible light is provided by a Spectra Physics 380 ring dye laser (Rhodamine 6G is used for all experiments described in this thesis) pumped by 4–5 W from a Spectra Physics 2020 Ar^+ laser (not shown in the figure). The original stainless steel dye jet has been replaced by a sapphire nozzle, which provides a much more stable and uniform dye jet. The laser is housed in a flow hood equipped with a blower module (Laminaire

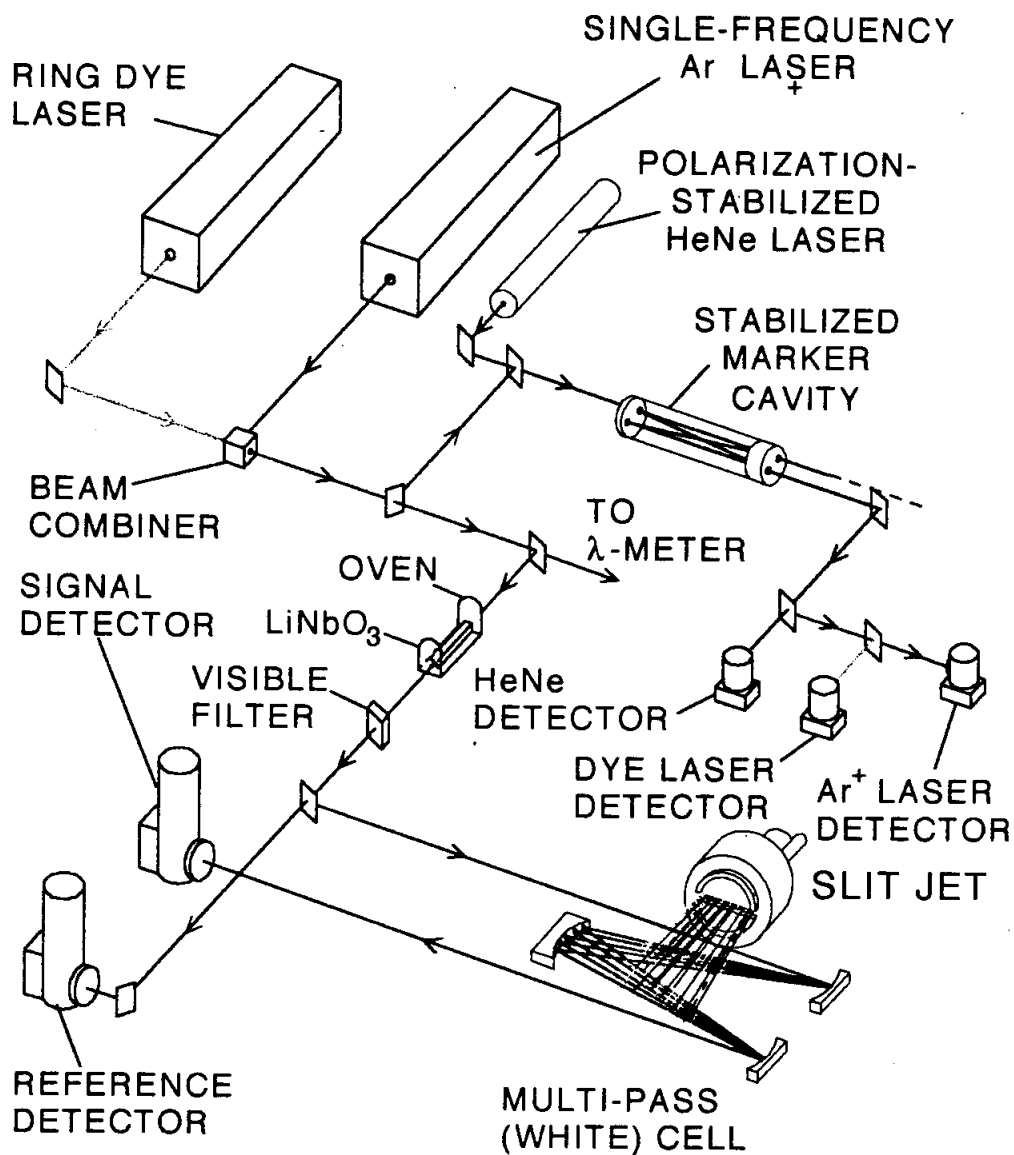


Figure 2.3: Schematic of the experimental apparatus used for the difference frequency generation of 2.2–4.2 μm infrared light.

model LP-24) which delivers a continuous flow of filtered air through the laser cavity. This serves to reduce the deposition of particulates on the intracavity optics and significantly decreases the frequency with which the optics need to be cleaned.

2.2.2 Dye laser servo control

The frequency stability of the infrared light ($\Delta\nu_{\text{IR}}$) is determined by the uncorrelated sum of the frequency noise of the two input lasers through

$$\Delta\nu_{\text{IR}}^2 = \Delta\nu_{\text{dye}}^2 + \Delta\nu_{\text{Ar}^+}^2 \quad (2.8)$$

Consequently, a means for actively stabilizing the frequency of the dye laser is a necessary component for achieving highly stable infrared light. This is of course true for the Ar^+ laser as well, and the method for its stabilization is discussed in a following section. The requirements of the dye laser locking electronics are actually twofold. First, the magnitude of the frequency excursions are to be minimized in order to increase the frequency resolution of the IR. Second, there must be a means to scan the dye laser incrementally, as this is the mechanism by which the IR is tuned. A simplified representation of the dye laser locking scheme is presented in Figure 2.4. A small part of the dye laser is picked off prior to combination with the Ar^+ laser and split equally into a power ("Power") and reference ("Ref") beam. Visible detectors (see Figure 2.5) monitor the light levels of both the "Power" and "Ref" beams; the latter is first directed through a 10 cm Fabry-Perot cavity that contains an intracavity galvo as a tuning element. The signal used to lock the laser is the "Ref" voltage electronically divided by the "Power" voltage. This division prevents amplitude fluctuations in the

Dye Laser Locking Scheme

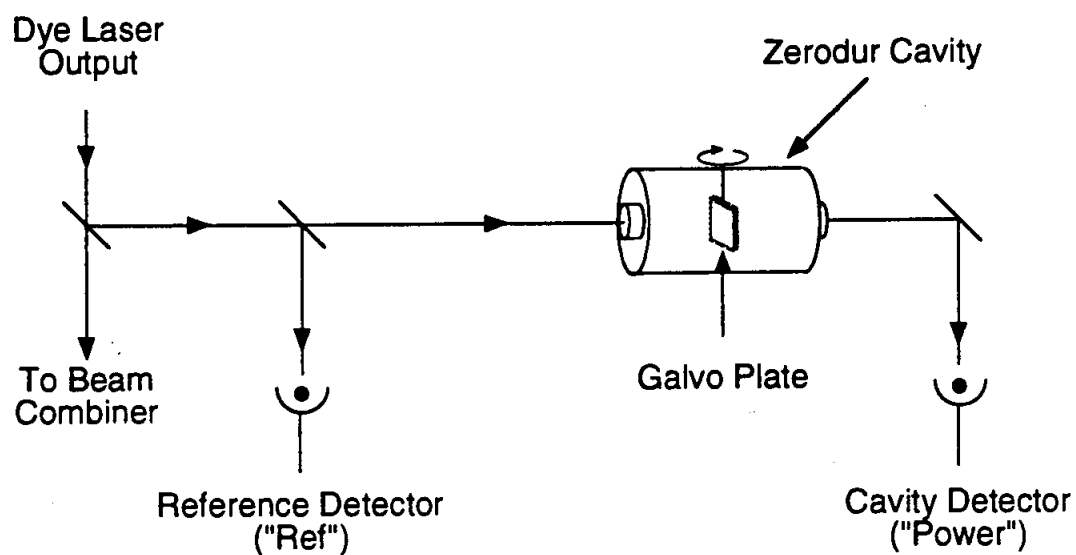


Figure 2.4: Simplified representation of the dye laser locking scheme.

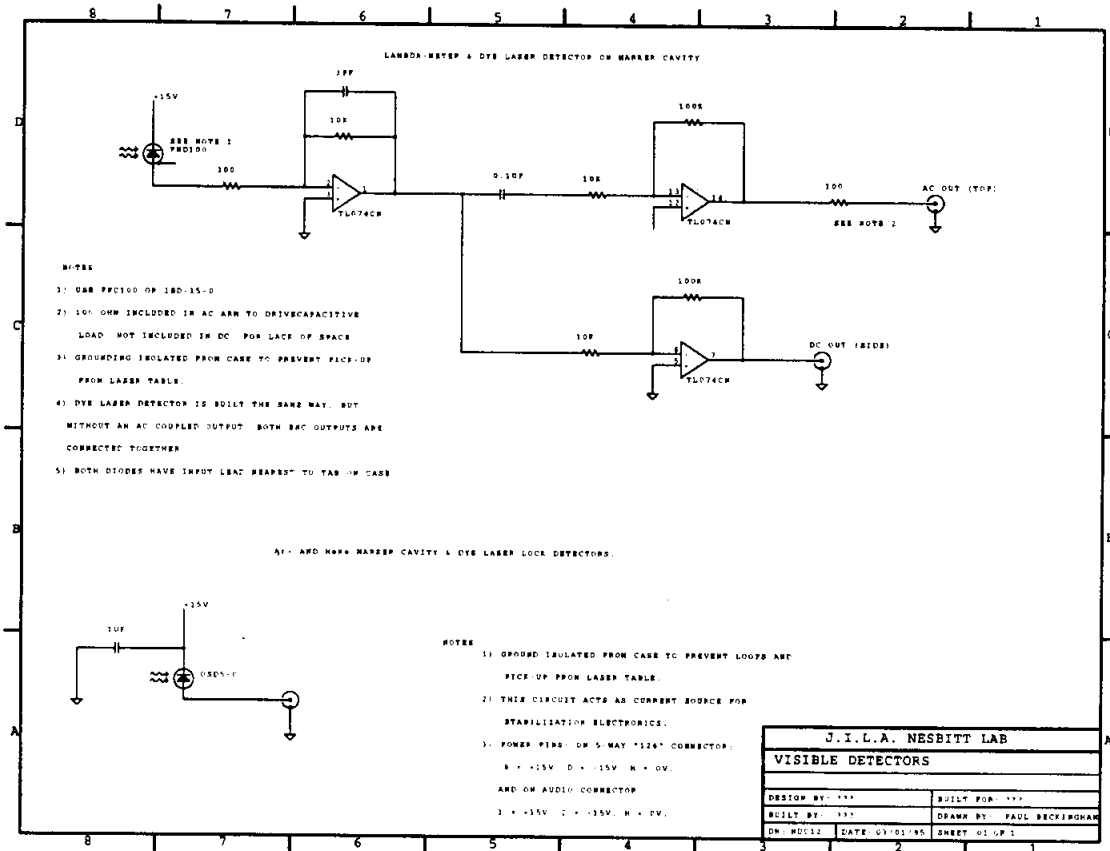


Figure 2.5: Circuit diagrams for visible detectors.

dye laser from being converted into frequency noise. This divided signal is summed with a small (negative) offset voltage that is adjusted to give a zero volt signal along the steep rising edge of the transmission fringe i.e., it is a side lock technique. When the lock switch is thrown, the voltage to the intracavity galvo driver (a driver developed for the JILA ring dye laser) is incremented until the zero crossing is detected. At this point, the voltage to the galvo driver is transferred to a digital sample-and-hold circuit for the duration of the scan.⁵

Scanning the laser is achieved by summing a computer generated voltage onto the galvo driver voltage. The computer generates a 0-5 V ramp over the course of 4096 steps. If this voltage is used unattenuated, the galvo driver (Model G108, General Scanning) increments the intracavity element 5×10^{-4} degrees/step, with a corresponding dye laser (and of course IR) frequency step of ≈ 18 MHz. For most scanning applications (especially when one is scanning for accurate rovibrational line-shapes) smaller frequency steps are desired, and the computer voltage is divided down in a separate stage prior to summing with the sample-and-hold voltage. As the voltage to the galvo driver is stepped during a scan, a feed forward signal is sent to the dye laser galvo driver and intracavity etalon to "track" the scanning. In addition, a proportional error signal is fed back to the piezoelectric transducer (PZT) on mirror 2 of the dye laser, and an integral error signal is sent to the galvos. The rms frequency noise of the dye laser is routinely ≈ 2 MHz on the ms or faster timescale as measured by frequency excursions on a Spectra Physics Model 450 spectrum analyzer.

This spectrum analyzer is also used during the course of the dye laser scan

⁵The use of digital vs analog sample-and-hold circuitry reduces the problem of drift on the locking voltage, which can be especially problematic with analog circuits. This drift would introduce nonlinearities in the scan, which would become more pronounced as the scan duration increases (e.g. due to increased averaging).

to verify mode-hop-free operation. This is accomplished by sending the photodiode output from the spectrum analyzer to a time-to-amplitude converter (TAC). The piezoelectric transducer (PZT) which supports the back mirror of the spectrum analyzer is continuously scanned with an amplified sawtooth voltage, which typically scans the cavity through three or four cavity modes (FSR=10 GHz). The TAC converts the time from the start of the sawtooth wave to when a preset photodiode voltage has been reached (typically corresponding to $\approx 3/4$ the height of a transmission fringe) to a voltage. As the dye laser scans, the arrival time of the fringe changes with respect to the start of the sawtooth, which leads to a slowly incrementing voltage ramp. This is demonstrated in Figure 2.6, which shows the data from a typical scan. At each laser step, the infrared absorbance, TAC signal, and etalon fringes are saved (as will be described in more detail below). The TAC signal, which resets every 10 GHz, not only indicates whether a mode hop has occurred, but more importantly facilitates file concatenation.

The circuit diagram and operational notes for the dye laser locking electronics are included in an appendix at the end of this chapter.

2.2.3 LiNbO₃ thermal control

The single frequency Ar⁺ light (0.4–0.5 W) is provided by a second Spectra Physics Model 2020 Ar⁺ laser equipped with an intracavity prism and etalon. In general, 488.0 nm (20486.8 cm⁻¹) light is used for 2.2–3.2 μ m IR generation and 514.5 nm (19429.8 cm⁻¹) for 3.2–4.2 μ m, as this allows the dye laser to operate in the frequency region near the peak of the Rhodamine 6G gain curve. The Ar⁺ output

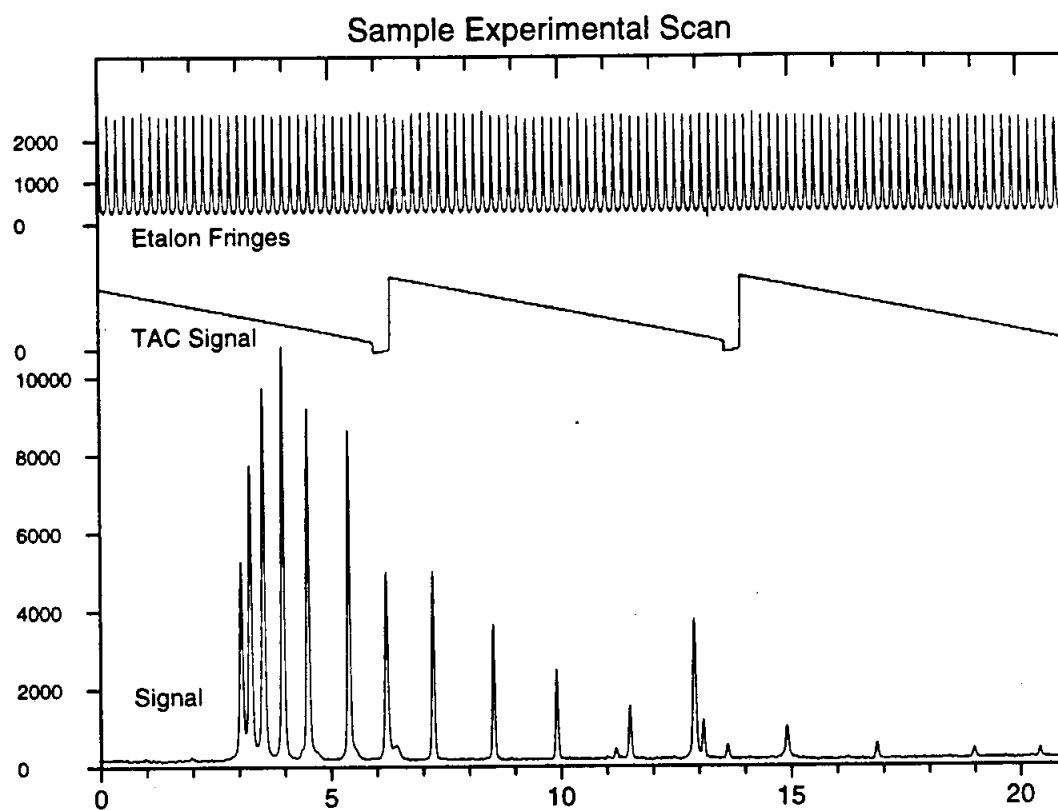


Figure 2.6: Typical experimental scan showing the TAC signal, the etalon fringes, and the IR signal.

is rendered collinear with the dye laser output via a polarization beamsplitter that is coated to reflect the vertically polarized Ar^+ light and transmit the horizontally polarized dye light. A pair of irises facilitates the overlapping of the beams, which are then focussed by an achromatic doublet into a $4 \times 4 \times 50$ mm LiNbO_3 crystal housed in a temperature controlled oven. The crystal is oriented such that the Ar^+ (dye) laser is oriented parallel to the extraordinary (ordinary) axes of the crystal. Because of the much lower peak power of cw vs pulsed operation, MgO doping of the crystal in order to increase the damage threshold [50] is not necessary. Additionally, antireflection coatings are not applied to the faces of the crystal, since coatings that can withstand the high temperature, oxygen rich environment are not presently available. A slow flow of O_2 is delivered to the oven core and faceplates, providing the high oxygen concentration necessary to counter the thermally driven reduction of LiNbO_3 .⁶

The oven core was constructed in the JILA shops, and is based on a commercial design (Chromatix CMX-4/IR). It consists of a copper core coated with either nickel or (currently) gold to prevent oxidation of the copper in the high temperature, oxygen-rich environment. The oven stabilization circuit is an adaptation of a previous design [266], which itself was based on a commercial (Chromatix) controller. The circuit diagram for the oven controller is given in Figure 2.7. For the experiments described in this thesis, the temperature stability of the crystal must be better

⁶A fairly recent failure of the oven servo allowed the oven to reach temperatures of > 600 °C for 6–8 hours. The LiNbO_3 turned from colorless to orange, and could not be used to generate difference frequency light due to excessive scatter of the Ar^+ light. The discoloration is consistent with the brown color realized upon reduction *in vacuo*, which is attributed to deoxygenation [12]. Exposure to a high O_2 flow for 48 hours lessened the discoloration but did not eliminate it. Because the discoloration appears to be localized at the surface, the faces are presently being polished in the hopes that the interior of the crystal is unaffected. However it should be noted that even in addition to discoloration, the high temperature may have generated localized defects in the crystal interior as a result of phase transitions. Adequate precautions should thus be taken when the crystal is returned to ensure proper performance.

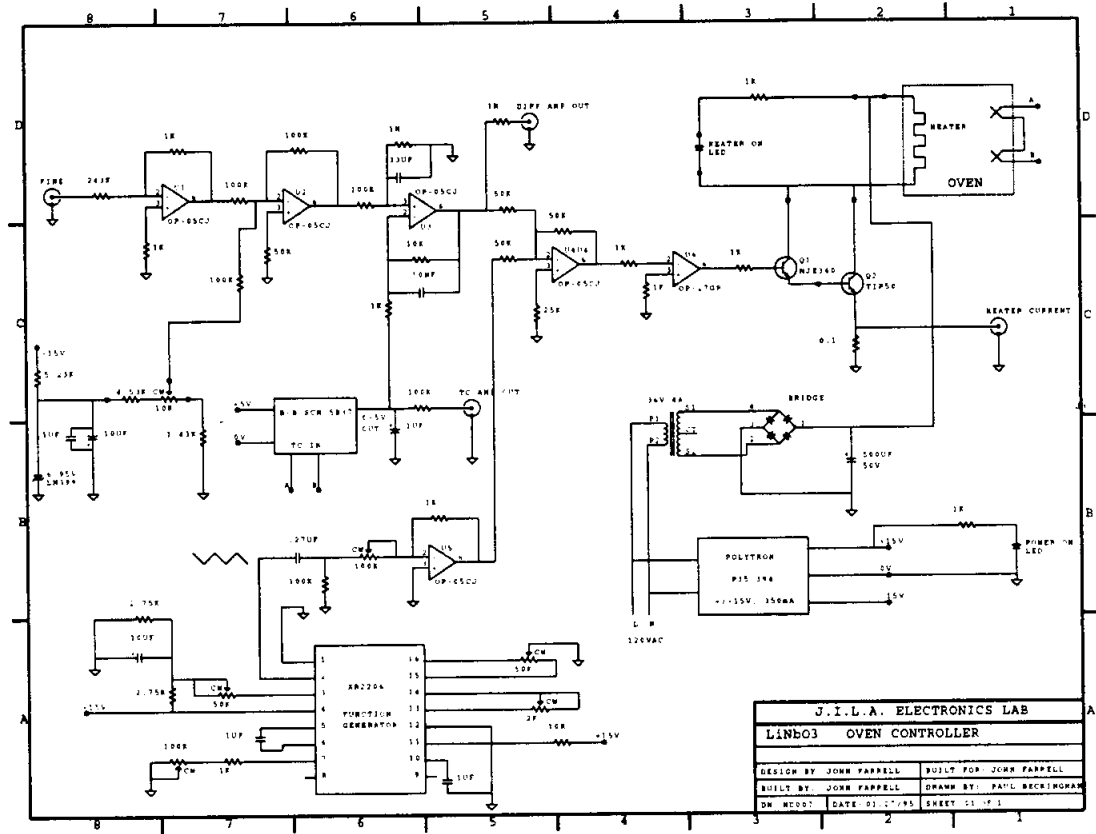


Figure 2.7: LiNbO₃ oven controller circuit

than $\approx \pm 0.05^\circ \text{C}$ in order to stay on the peak of the difference frequency generation curve. This level of control would not present a large problem if there weren't the additional requirement that the oven scan between 200–500 $^\circ\text{C}$, i.e., the temperature range required for 2.2–4.2 μm generation (see Figure 2.6 of Reference [266]). Consequently, the demands on the stabilization circuitry are that the temperature stability be approximately 1 part in 10^4 .

The temperature of the core is measured by a pair of iron-constantin thermocouples connected in series, the output from which is conditioned and converted to an analog output voltage in a chopper-stabilized isolated thermocouple input module (Burr-Brown Model SCM5B). This module is cold-junction compensated to correct for parasitic thermocouples formed by the thermocouple wire and screw terminals. The output voltage is compared to the request voltage, and the resulting error signal is summed with a small ($\approx 150 \text{ mV}$) triangle wave and then sent to a comparator which drives the heating circuitry. When the difference between the request and amplified thermocouple voltages is $> 15 \text{ mV}$ ($\approx 2^\circ\text{C}$), the comparator turns the heating either full on or full off. As the error signal becomes smaller (i.e., the system is approaching lock), the triangle wave begins to modulate the duty cycle of the heating, after which the lock is quickly established. The tightness of the lock is controlled by the amplitude of the triangle wave. The 150 mV amplitude mentioned above is the smallest that will acquire the lock in the temperature region of $\approx 400^\circ\text{C}$; the amplitude of the triangle wave could be reduced at cooler operating temperatures, although the stability of the lock is sufficiently high that this is not necessary.

The stability is demonstrated explicitly in Figure 2.8 which shows the stability of the infrared power (which provides an accurate "thermometer") over the course

of 20 minutes. The corresponding temperature stability is $\approx \pm 0.02^\circ\text{C}$. One limitation of the present circuit is that one must manually change the oven voltage to find the maximum of the gain curve. This can be especially inconvenient when the system begins to drift, since the direction of the correction is not always obvious. More seriously, if the IR light level begins to drop because the laser is scanning into an unanticipated atmospheric absorption, the operator infers this as being due to oven drift and changes the oven voltage in a futile attempt to "recover" infrared. An attractive alternative to manually tracking the oven to preserve phase matching has been demonstrated by Stephen Ashworth while he was a postdoc in our lab, which when implemented will eliminate the remaining "human servo" element of the experimental apparatus.

This method takes advantage of the fact that in addition to temperature, electric fields can be used to change the indices of refraction of a birefringent material (through the "electro-optic effect"). Steve placed 4×80 mm gold-coated mica electrodes adjacent to two faces of the LiNbO_3 crystal and applied a 10 V p-p sinusoidal field. This induced an $\approx 1.5\%$ modulation on the IR light, whose phase relationship with respect to the driving signal changes from in-phase to 180° out-of-phase depending on which side of the gain curve one is tuned to. It should be relatively straightforward to incorporate phase sensitive detection to lock the oven to the peak of the difference frequency generation curve. In fact, the circuitry developed for the HeNe stabilized marker cavity described below is quite similar in principle to what is required for this oven stabilization scheme. Implementation of this technique would relegate manual control of phase matching to the dustbin of history, never to be missed.

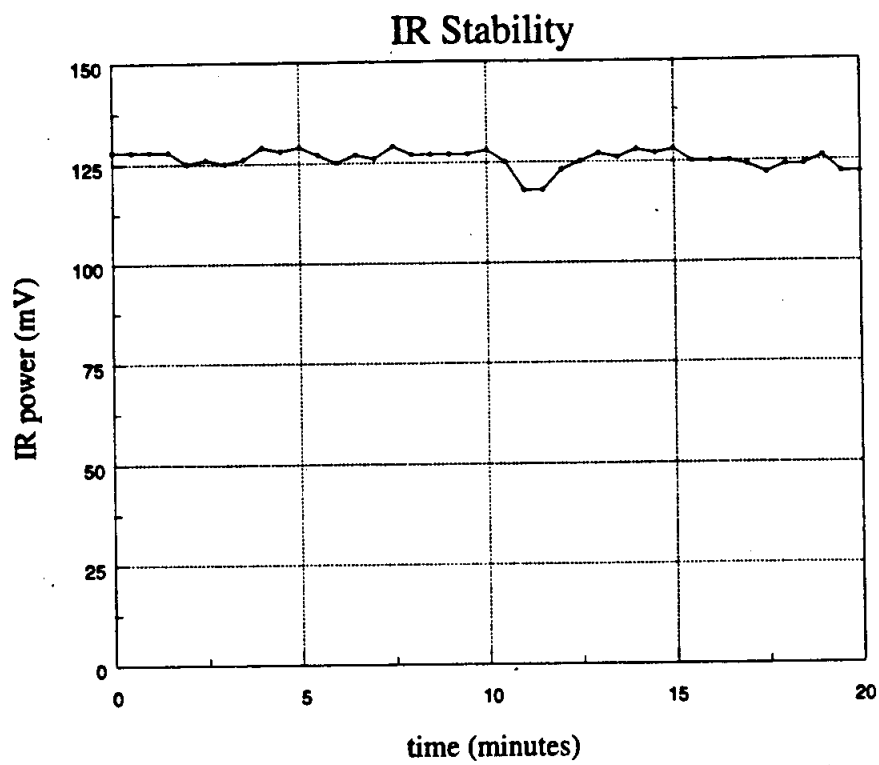


Figure 2.8: IR power as a function of time, demonstrating temperature stability of the oven of $\approx \pm 0.02^\circ\text{C}$ over 20 minutes.

2.2.4 Formation of weakly bound complexes in a slit supersonic expansion

Following the oven, visible filters are used to reject the visible beams and pass the infrared. The IR light is split into a signal and reference beam, with the former probing the long axis of the slit supersonic expansion (see Figure 2.9). The circuit for the electronics that provide the current pulses that open the valve is shown in Figure 2.10. Multipass (White cell [375]) optics are used to pass the infrared 12–20 times through the expansion for a total pathlength of 0.48–0.80 m. A detailed description of the pulsed slit jet can be found in reference [254]. The width of the 4 cm long slit can be varied through use of different “jaws” [254]. For most of the experiments described in this thesis, a 190 μm slit width was used, which is somewhat larger than the more typical values of 60–120 μm , but was chosen by virtue of the greater clustering achieved with the wider slits and the preference for large cluster formation in the experiments described herein. The vacuum chamber is evacuated by a rotary pump and Roots blower with a combined pumping speed of 540 ℓ/s ; the pressure in the vacuum chamber is typically between 50–100 mTorr for backing pressures \leq 700 Torr and 19 Hz pulse rate.

The gas is delivered to the pulsed valve via the gas handling system shown in Figure 2.11. Two mixing tanks (\approx 40 ℓ) are available for making “premixes,” and can be safely pressurized to \approx 2500 Torr. Premixes represent the most convenient and flexible method of generating the expansion gas mixture. Under routine operating conditions (Ar carrier gas, 300–500 Torr backing pressure, 19 Hz pulse rate, 600–800 μs pulse widths), the mix from a single tank will provide \approx 3–5 hours of operating time. Higher backing pressures and lighter carrier gases will decrease the run time,

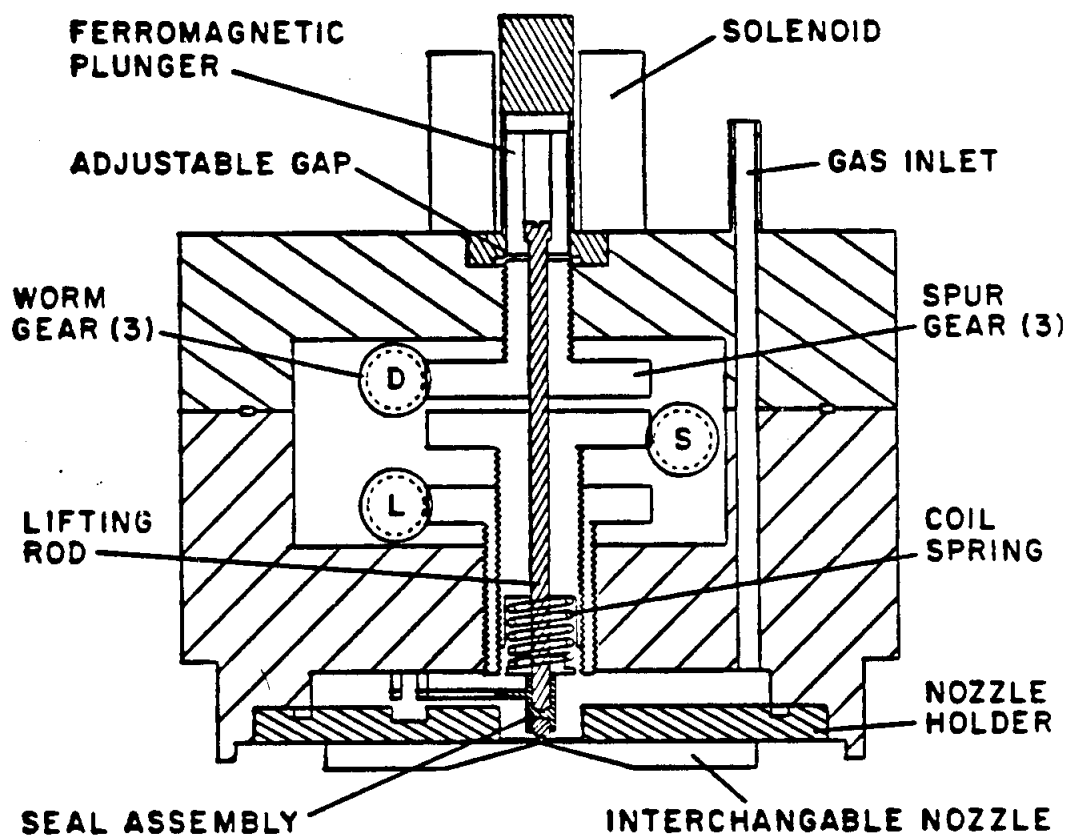


Figure 2.9: The pulsed slit valve used to generate the weakly bound complexes (from Reference [254])

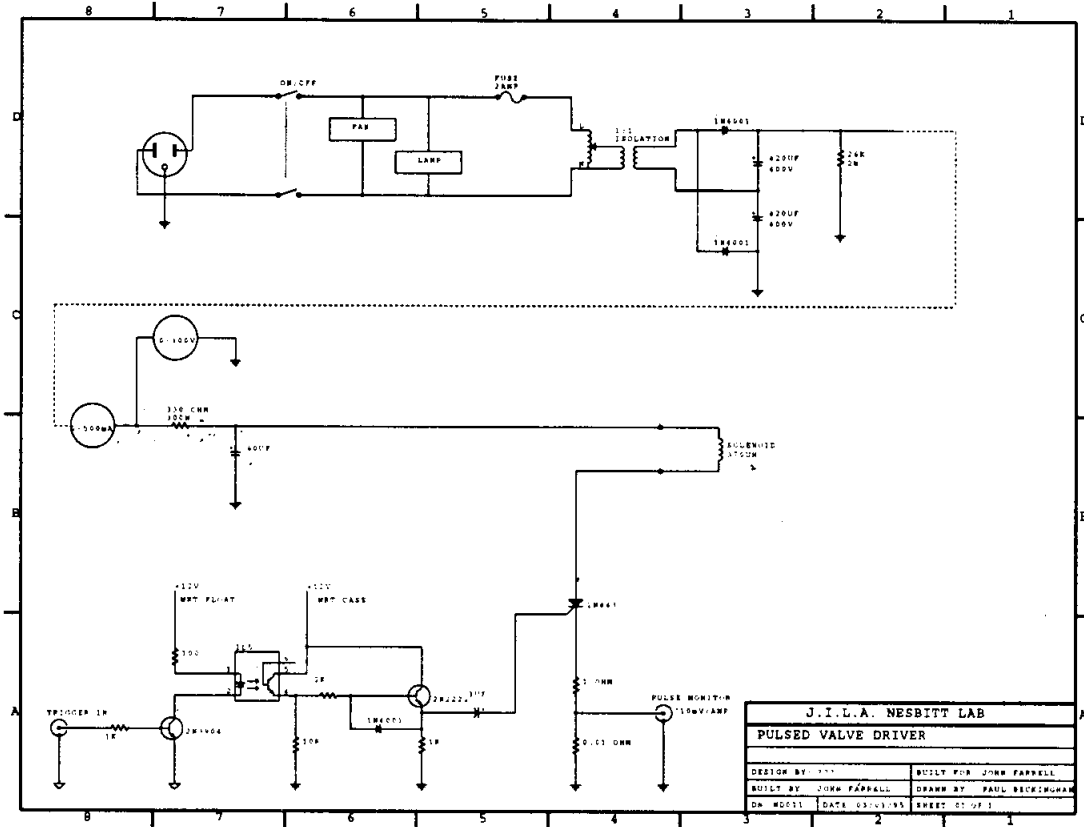


Figure 2.10: Circuit for pulsed valve driver.

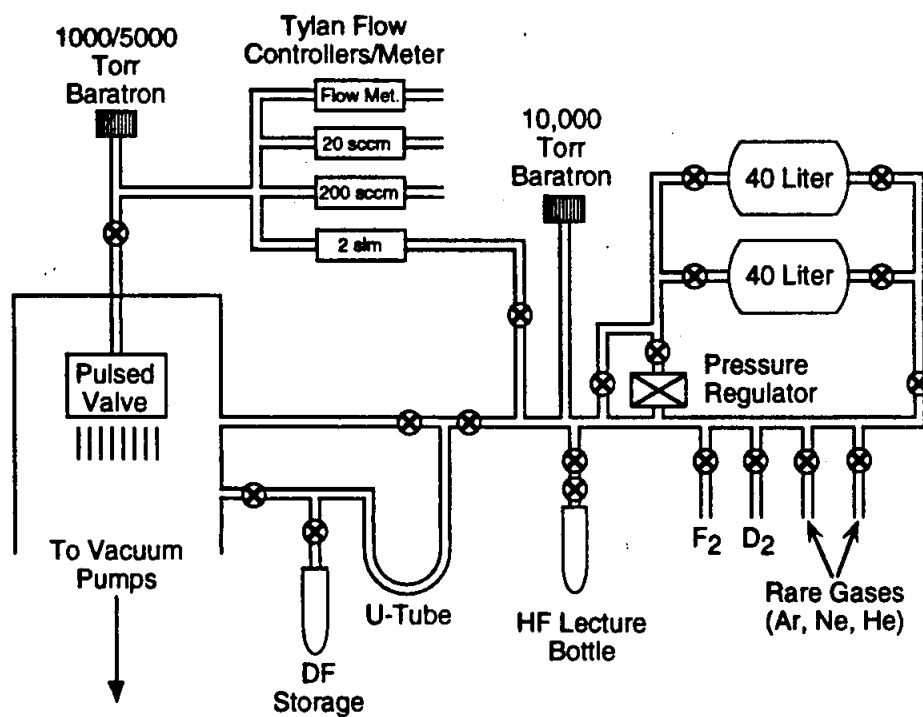


Figure 2.11: Schematic of the gas handling system for the pulsed slit jet spectrometer.

although this can be alleviated somewhat by using both mixing tanks simultaneously. In addition, commercially prepared mixtures can be obtained in 1A cylinders at much higher pressures than can be safely accommodated in the premix tanks, providing up to several days of uninterrupted operation.

The gas mixtures can be metered to the pulsed valve by (in decreasing order of convenience and versatility) flow controllers, flow meters, or manually adjusted leak or needle valves. The use of flow controllers (Tylan Model FC280S) provides the greatest control of the expansion gas, allowing the flow to be "dialed in" via a control knob. Three controllers with maximum rates of 2 slm, 200 sccm, and 20 sccm are available and can be used simultaneously to meter three separate gas mixes. Flow meters (Tylan Model FM380) and adjustable needle or leak valves may also be used, in particular when the desired flow rate is larger than can be accommodated with the largest (2 slm) flow meter. Larger flow meters are of course available, but operation at very high flow rates is not needed often enough at the present time to justify the expense of their purchase.

The backing (stagnation) pressure behind the pulsed valve is one of the primary variables that controls the size distribution of the clusters generated in the pulsed supersonic expansion. This is demonstrated in Figure 2.12, which shows temporal pulse profiles for ArDF as a function of backing pressure (0.3% DF in Ar). At low pressures ($P_0 \leq 400$ Torr), the ArDF absorbance is relatively constant during the 700 μ s duration that the pulsed valve is open. At higher backing pressures, the absorbance starts to decrease during the time that the valve is fully open; the nonuniform pulse profile arises because of the uneven gas flow during the opening and closing of the valve. The depletion upon full valve opening is nearly complete at a backing

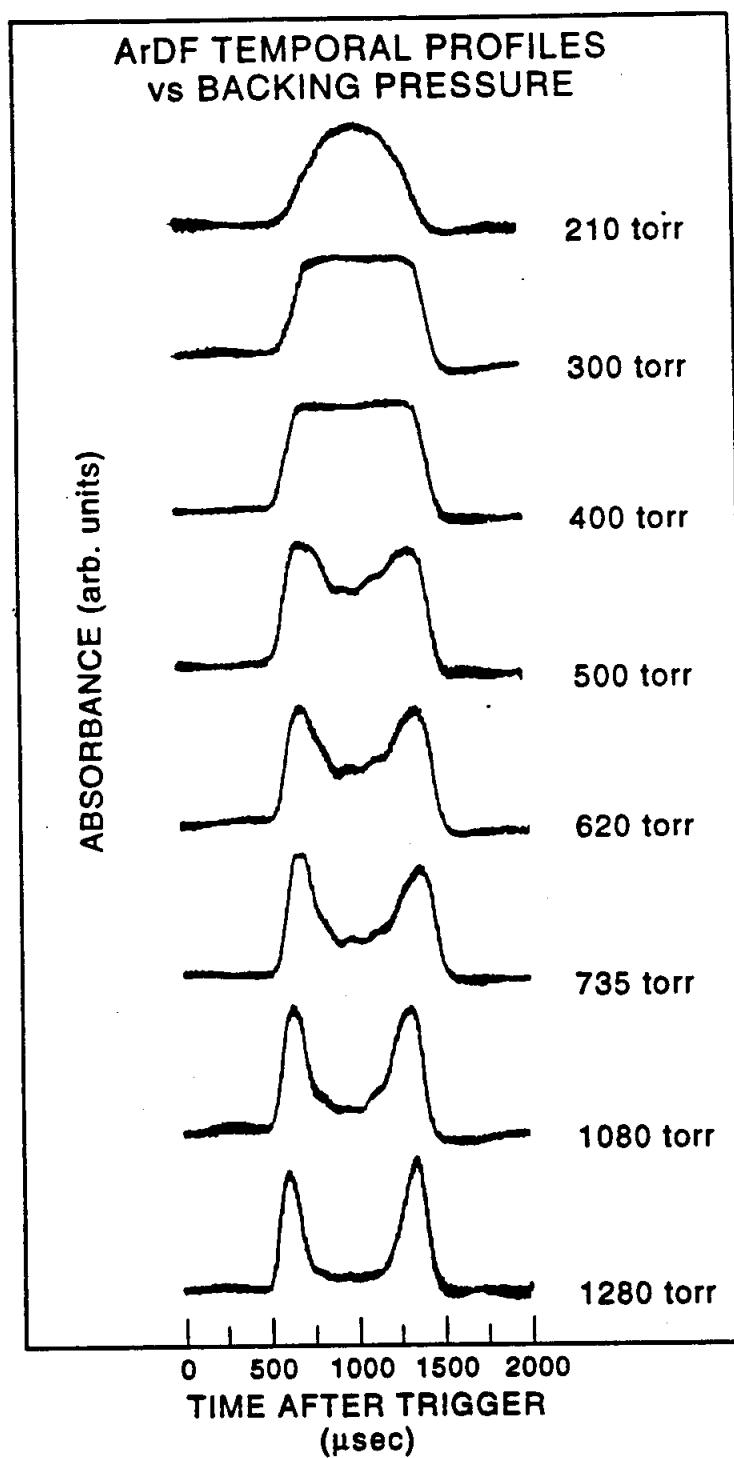


Figure 2.12: Temporal profiles of ArDF absorbance vs backing pressure.

pressure of 1300 Torr, where presumably the ArDF has been completely converted to larger Ar_mDF_n ($m, n \geq 2$) complexes. Figure 2.13 shows the absorbance vs backing pressure for ArDF, Ar_2DF , and Ar_3DF under the same conditions as in Figure 2.12. Under the conditions employed, the optimum backing pressures differ by only ≈ 100 Torr for ArDF vs Ar_3DF . This indicates that the transition to very large complexes is accomplished at relatively low pressures (≤ 1 atm) in the slit jet. This is in distinct contrast to pinhole expansions, where much higher (2-3 atm) backing pressures are typically employed for formation of the relatively small dimers and trimers.

Variations in the stoichiometry of the expansion gas mixture can also be utilized to modify the distribution of cluster size in the expansion. In particular, the addition of the lighter and less polarizable rare gases Ne and He leads to less clustering in the expansion. This arises from the reduced number of inelastic (cooling) collisions. Indeed, for experiments performed in the slit jet where clustering is undesirable (such as the study of IVR in small hydrocarbons [266]) the expansions are typically performed exclusively in He. Of course He and Ne must be present when complexes containing these atoms are desired, but the addition of small amounts of Ne and/or He can be used to enhance the signal of Ar complexes. This is especially true for Ar-containing dimers and trimers, where the reduced clustering at low pressures increases the optimum backing pressure for formation of a given complex.

An additional effect of the lighter rare gases is a modification of the expansion temperature. This is observed in pinhole expansions as well, with the heavier rare gases providing colder expansions. The opposite effect is generally observed in the slit jet, however, with *warmer* expansions realized with the heavier rare gases. This is because the much larger number of collisions in the slit vs pinhole jets gives rise to more

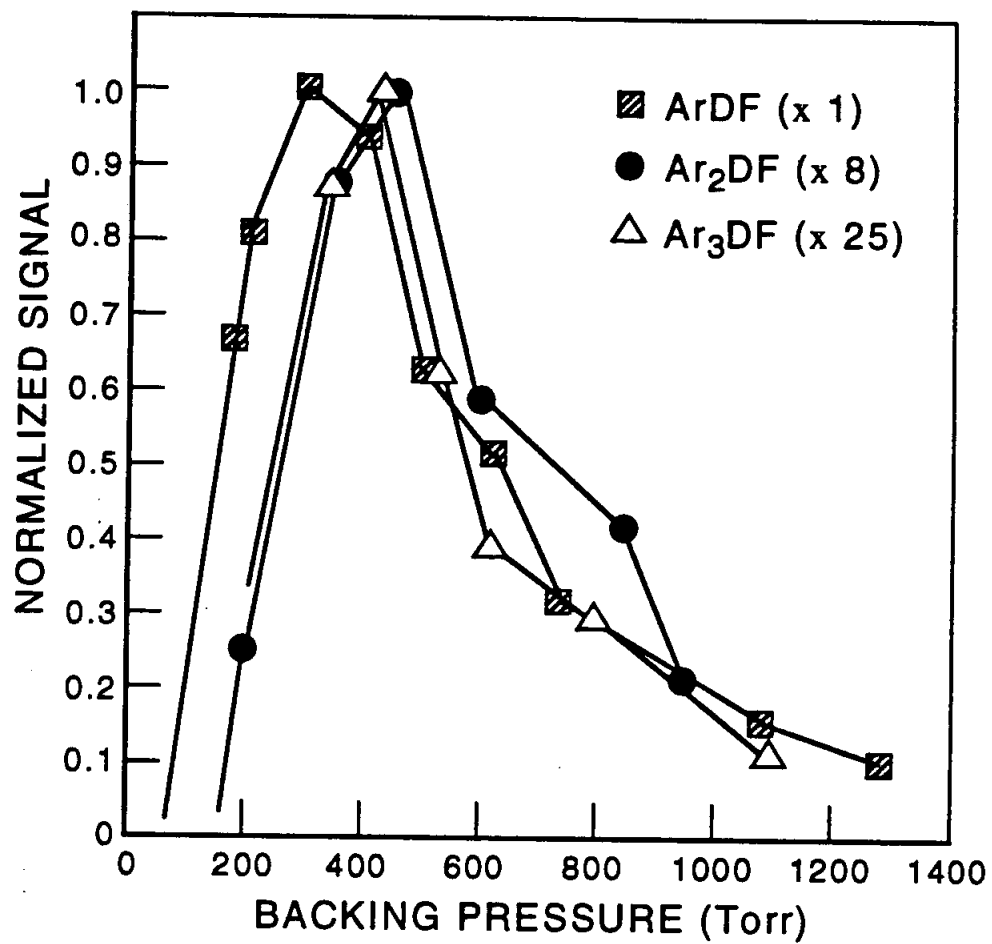


Figure 2.13: Absorbance vs backing pressure for ArDF, Ar₂DF, and Ar₃DF.

clustering, and the associated energy release warms the expansion. Consequently, both the backing pressure and expansion gas composition can be varied to "fine-tune" the characteristics of the expansion and correspondingly maximize the population of a given complex.

The slit jet also differs from the pinhole jet in the degree of equilibration between vibrational, rotational, and translational degrees of freedom. Previous experiments from our group have shown that the low frequency vibrations of OCO-HF are populated according to Boltzmann statistics, and that the corresponding vibrational temperature is the same within experimental error as the rotational temperature inferred from a Boltzmann plot of the rovibrational intensities [284]. Figure 2.14 shows such a plot for Ar₂DF; the linearity of the plot for a large range of J' ($J'=1-19$ in the figure) indicates that the rotational levels are indeed equilibrated.

The rovibrational lineshapes of nonpredissociating species in the slit jet allow an experimental line profile to be determined. There are both inhomogeneous and homogeneous broadening mechanisms which will affect the experimental profile. The former category includes contributions from non-uniform velocities of the expanding species, which are expected to be most prominent at the slit edges. Consequently, the effect may be significant for monomers but is expected to be less so for complexes since the relatively low densities in this region are not conducive to cluster synthesis. In addition, Doppler broadening arising from the dispersion of velocities projected along the optical axis will contribute to the inhomogeneous broadening. Nonorthogonal laser crossings inherent to the White cell optics constitute a third source of inhomogeneous broadening. As can be seen from Fig. 2.3, the laser intersects the expansion at slightly different angles each pass, giving rise to a Doppler shift proportional to $\cos(\theta)$ (see

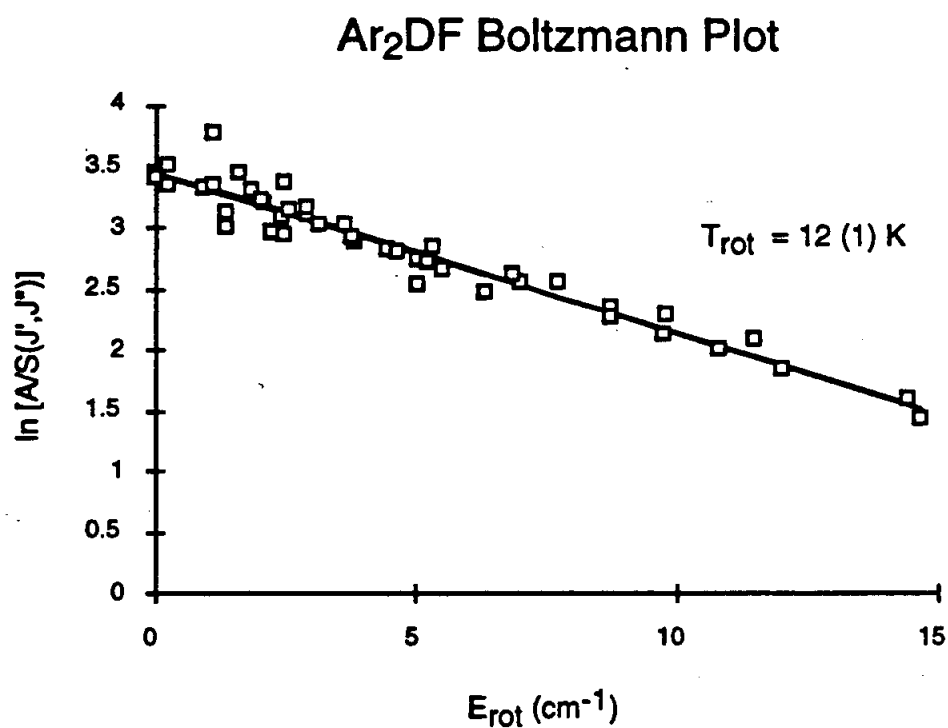


Figure 2.14: Boltzmann plot for Ar₂DF (encompassing $J'=1-19$), demonstrating the high degree of rotational equilibration. Experimental conditions: 0.8% DF in a 60:40 mixture of Ar:first run Ne at 500 Torr backing pressure.

Ref. [254]).

There are a number of sources of homogeneous broadening which could in principle contribute to the experimental line profile, e.g. power (saturation), pressure, and transit time broadening. These contribution of these effects is only ≤ 1 MHz [254], and hence do not contribute significantly. Laser jitter constitutes an additional source of homogeneous broadening. Based on typical rms values for the jitter of the Ar⁺ (1 MHz) and dye (2 MHz) lasers, Eq.2.8 indicates that the rms noise on the IR is < 3 MHz.

Because inhomogeneous and homogeneous broadening typically give rise to Gaussian and Lorentzian profiles, the lineshapes are conveniently expressed as a Voigt profile, i.e., the convolution of a Gaussian and Lorentzian. Because the Lorentzian profile contributes much more to the "wings" of the absorption than the Gaussian, least-squares fitting to a Voigt profile often provides results with a high degree of linear independence. Results for HF in an Ar expansion indicate a 58 MHz Gaussian component and a 2 MHz Lorentzian, indicating that the former dominates the experimental profile. It should be mentioned that ascribing physical meaning to the Lorentzian component of the experimental line profile should be attempted with caution. Although the broadening at the wings of the profile are typically attributable to homogeneous broadening, it could also reflect the contribution of a broad Gaussian, as would be expected for edge effects.⁷

Once an experimental profile is defined, the contributions of lifetime broad-

⁷In fact, fitting the absorption profiles for non-predissociating species to a sum of two Gaussians (with the second Gaussian having a reduced peak intensity and larger width to approximate the wing broadening) reproduces the observed lineshapes as well as the Voigt profile as determined through a comparison of the fit residuals. A high degree of parameter correlation is often present, however, in particular between the baseline offset of the taller Gaussian and the width of the shorter, reducing the desirability of this functional form.

ening can be assessed. The convolution of the experimental Voigt profile with the Lorentzian that results from homogeneous lifetime broadening is itself a Voigt, with the Lorentzian equal to the sum of the experimental and lifetime contributions. Consequently, the lifetime broadening is obtained by subtracting the experimental Lorentzian contribution from the measured Lorentzian.

Since the energy deposited by mid or near-IR excitation is greater than the binding energy of the complex, the vibrationally excited complex is metastable and lifetime broadening can comprise a significant source of broadening. When the energy localized in the high frequency intramolecular coordinate channels into the intermolecular coordinates, the complex predissociates.⁸ The lifetime of the excited complex is related via a Fourier transform to the homogeneous width of the lineshape through $\tau = 1/2\pi\Delta\nu_{\text{homogeneous}}$. When the lifetimes are longer than 10 ns, the associated homogeneous broadening of < 1 MHz is too small to extract from the typical 20–60 MHz experimental profile. Conversely, when the lifetime is very short (less than ≈ 10 ps) the homogeneous broadening can preclude rotational resolution. Although this is a relatively narrow time window, lifetimes for a large number of vibrationally excited complexes have been inferred via analysis of homogeneous broadening of the transitions.

⁸The unimolecular decay of the excited state is denoted predissociation because the complex dissociates before it can decay to the ground state by emission of a photon [327]. It is distinct from direct dissociation in that a curve crossing or energy transfer into another mode is involved (Chapter 12 of Ref. [327] contains an excellent discussion of predissociation of van der Waals molecules).

2.2.5 Data acquisition and storage

After passing through the expansion, the signal beam is detected with a liquid N₂-cooled InSb photovoltaic detector (active area = 0.049 mm²). The reference beam is monitored on a similar detector with the components chosen to match the frequency response of the two detectors. The photocurrents are converted to voltages in transimpedance amplifiers with a gain of 10⁵ Ω. The two signals are subtracted in homebuilt differential amplifier [266], which eliminates variations in the detected signal level arising from amplitude noise on the infrared light to $\approx 1-2 \times 10^{-4}$ of the incident light level. In the 10 kHz detection bandwidth, this corresponds to an absorption sensitivity on the order of 10⁻⁶/√Hz. The subtracted signal is amplified and low-pass filtered before being sent to an 8-bit transient digitizer (DSP model 2001 S, 1 μs/point) housed in a CAMAC crate (DSP Model Optima 860), which also contains a signal averaging module (DSP Model 4100). Additionally, the signal is high-pass filtered and sent to an oscilloscope for real time viewing of the signal. The digitized and averaged signal is passed as an integer array to the computer where it is decomposed into two 256 μs long baseline gates and a 512 μs long signal gate as shown in Figure 2.15. The temporal positions of the gates are set from the menu of the scanning program [330]. Typically, one of the baseline gates is set before and one after the signal gate, to correct for baseline offset. The signal is then [266]

$$\text{signal} = - \int_{t_1}^{t_2} g_{a1} e_{\text{baseline1}} dt + \int_{t_3}^{t_4} g_{\text{signal}} dt - \int_{t_5}^{t_6} g_{\text{baseline2}} dt \quad (2.9)$$

This signal is stored as a function of laser frequency to yield the spectrum.

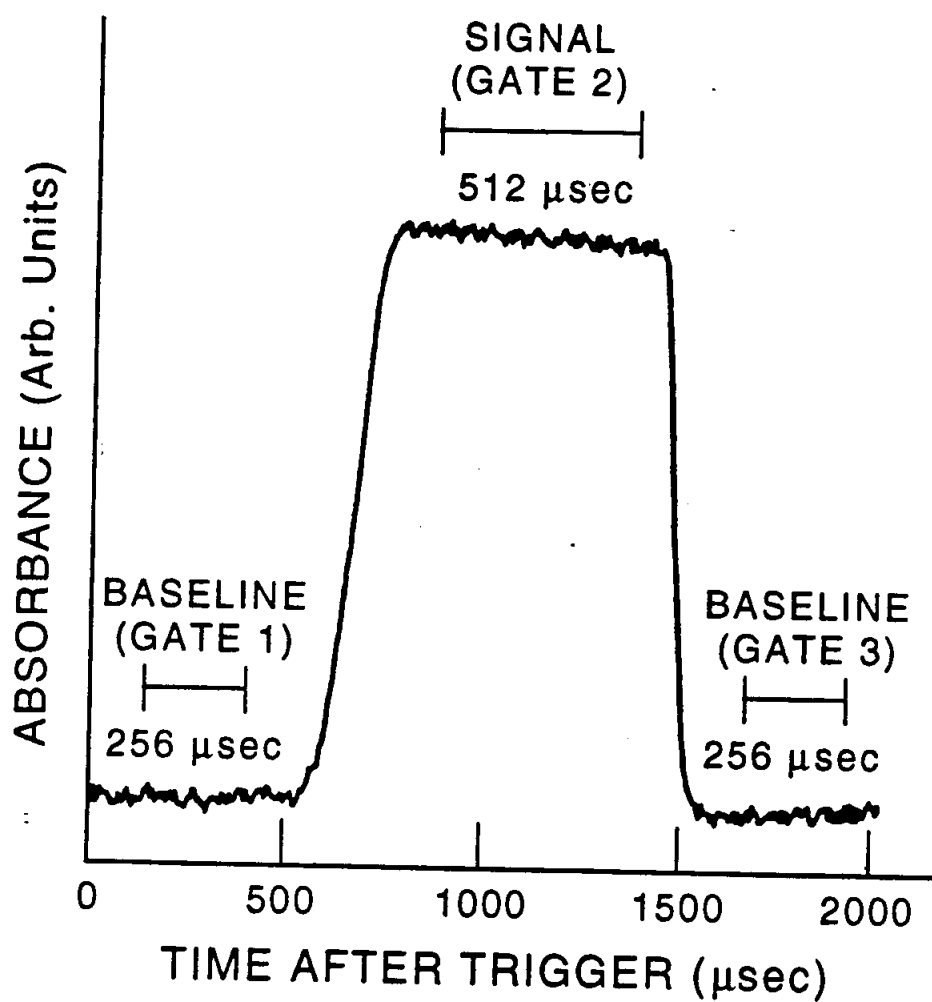


Figure 2.15: A time trace of a typical absorption signal from the difference frequency spectrometer. The first baseline gate is acquired before the valve begins to open at $\approx 600 \mu\text{sec}$. The signal gate is acquired after the valve has opened fully, and the second baseline gate is recorded after the valve has fully closed.

2.2.6 Frequency measurements

Prior to entering the LiNbO₃ oven, a small part of the (collinear) dye and Ar⁺ beams are directed to a traveling Michelson interferometer commonly referred to as the "lambda-meter" [159]. The lambda-meter is shown schematically in Figure 2.16 and a full description of its incorporation into the difference frequency system is given in Refs. [254, 266]. The Ar⁺ and dye laser beams are rendered collinear with the output of a polarization-stabilized HeNe laser, and the three beams are split by a beamsplitter and sent to a retroreflecting corner cube traveling on an airbearing cart. The cart travel introduces a Doppler shift,

$$\frac{\Delta\nu}{\nu_{\text{laser}}} = \frac{v_{\text{cart}}}{c} \quad (2.10)$$

either to higher or lower frequency depending on whether the light is propagating in the opposite or same direction as the cart, respectively. The beams are recombined on the same beamsplitter, separated by interference filters, and monitored by individual photodetectors. Because each recombined beam consists of two frequencies differing by $2\Delta\nu$, the detected signals carry a beat note. The frequency of the beat depends not only on the frequency of the light, but on the cart speed as well. Rather than measuring the cart speed, however, it is more convenient to compare the number of interference fringes detected for the dye and Ar⁺ laser with the number counted for the HeNe laser. Although the fringe frequency the HeNe, dye, and Ar⁺ lasers depends on the cart speed, their ratio does not. Consequently, the number of fringes counted the dye and Ar⁺ laser after a preselected number of fringes ($\approx 10^5$ - 10^6) have been

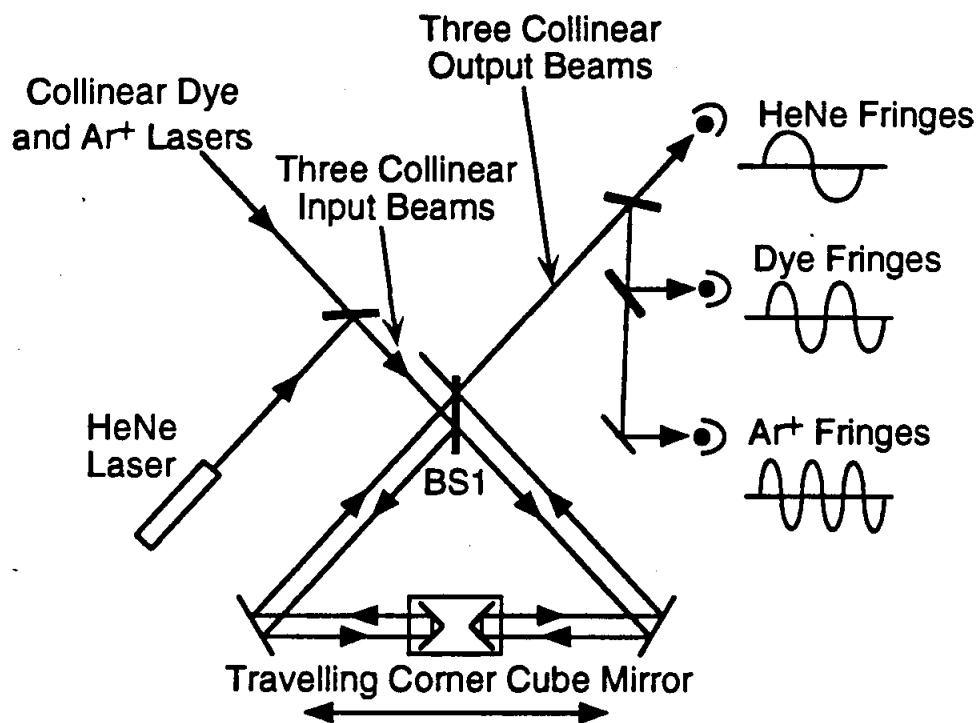


Figure 2.16: Schematic of the “lambda-meter,” i.e., the traveling Michelson interferometer used to measure the frequencies of the dye and Ar⁺ lasers.

counted for the HeNe allows their frequency to be determined through

$$\frac{\nu_{\text{dye,Ar}^+}}{N_{\text{dye,Ar}^+}} = \frac{\nu_{\text{HeNe}}}{N_{\text{HeNe}}} \quad (2.11)$$

The number of HeNe fringes counted is chosen so that the number of fringes counted for the dye and Ar⁺ laser is equal to their frequency in wavenumbers (cm⁻¹). The counting is effected by sending the fringes through a discriminator and detecting the number of zero-crossings. Since the Ar⁺ and dye lasers are likely to be between zero crossings when the last HeNe fringe is counted, an error of ± 1 fringe is introduced to the total number of dye/Ar⁺ fringes. An uncertainty of 1 fringe out of $\approx 10^6$ corresponds to an error of 0.02 cm⁻¹ for a single reading. The precision is increased by multiplying the dye and Ar⁺ laser fringes in a $\times 16$ phase-locked multiplier prior to counting. Following multiplication, the dye and Ar⁺ counting error of ± 1 fringe corresponds to ≈ 0.001 cm⁻¹. This uncertainty can be further reduced by averaging multiple readings; if the measurement errors are random, N readings will lead to a \sqrt{N} reduction.

Although the precision of such measurements is quite high, the accuracy is limited to ≈ 0.05 cm⁻¹ by i) frequency dependent errors arising from dispersion effects in air, and ii) differing pathlengths for the lasers through the interferometer path. These problems are circumvented by measuring the frequency of a molecular absorber and comparing to the accurately known value. The ratio of the observed to true frequency provides a correction factor which can be applied uniformly to other species, as long as the frequency of the reference absorption is not too far (≈ 50 cm⁻¹) away.

The frequency measurements of each rovibrational transition in an infrared

band by the procedure described above becomes prohibitively difficult and time consuming as the number of transitions increases. Rather than measure each line individually, it is desirable to determine the *absolute* frequency for one transition in the band, and convert the relative frequency differences between the other transitions to absolute frequencies. This procedure requires a method for determining precisely the frequency differences between individual transitions. The standard procedure for doing this is to use an optical cavity to record transmission fringes from the scanning (e.g. dye) laser, and interpolate between the fringes to determine the relative separations between transitions. The uniform implementation of this scheme requires that the spacing between the fringes does not change during the course of a scan, which typically requires some sort of active or passive stabilization of the cavity. Without such a technique, combatting the effects of drifts in the effective free spectral range of the cavity and the fixed frequency laser requires calibrating the free spectral range of each individual scan. This usually involves determining the frequency of the first and last transition in a scan via multiple readings of the lambda-meter, and using this frequency to calibrate the spacing of the etalon fringes. This was the method employed for the experiments described in Chapters 3, 6, and 9, and consequently the frequency precision of the data in these chapters is somewhat poorer (by \approx a factor of 3-4) than the data in the other chapters which utilized the stabilized marker cavity described below.

2.3 HeNe-stabilized transfer cavity and stabilization of Ar⁺ laser

In a sub-Doppler molecular spectrometer such as our difference frequency spectrometer, full use of the high resolution ($\Delta\nu \approx 2$ MHz) requires that a suitable calibration scheme is implemented. Since the scanning of the spectrum typically takes hours, excellent long term stability of the system is necessary. One way to obtain the proper calibration is by comparison to a precisely known reference spectrum. For example, the iodine absorption spectrum [145] provides a convenient reference in the frequency region from 14,800 to 20,000 cm^{-1} . The (center of mass) line positions are given to an absolute accuracy of ± 30 to ± 45 MHz throughout this region. However, such spectra are often not available in all regions of interest and can be difficult to record simultaneously. A second way to obtain precise spectral information for various molecular lines is by direct measurement of the wavelength or frequency in a wavemeter, e.g. the lambda-meter. It has been shown that this is possible with high precision but, as mentioned above, is prohibitively time consuming for most systems.

The most frequently used calibration method is therefore by interpolation of the molecular spectrum with the transmission spectrum of a suitable Fabry-Perot cavity. No absolute calibration is normally attained in this way, but for most applications, the easily obtained relative calibration is quite sufficient. The absolute accuracy can also be quite high if the optical spacing of the mirrors can be held constant. This is typically done by using a low thermal expansion spacer like Zerodur ceramic (a mixture of amorphous and crystalline quartz) and high quality temperature control. In addition the cavity has to be evacuated to avoid any drift of the transmission fringes due to change in the refractive index in the cavity caused by ambient pressure changes.

As an alternative to passive stabilization, we have chosen to actively lock an open cavity to a polarization stabilized HeNe laser. The stability of this HeNe laser has been determined to be < 0.1 MHz/hr through optical mode beating with an iodine-stabilized HeNe laser, and consequently the cavity has excellent *absolute* stability. However, in order for the recorded fringes to correspond to absolute frequency markers in the infrared, the residual drift in the fixed frequency laser must be eliminated. This is accomplished by locking the Ar^+ laser to a transmission fringe of the same cavity. In addition, this cavity is used to record marker fringes from the scanning of the dye laser, which therefore provides accurate frequency markers in the infrared. The design of the system is described below, and the magnitude of possible drifts due to dispersion of air is discussed. A comparison of successive frequency measurements of a molecular spectrum is then presented to demonstrate the successful performance of the apparatus.

2.3.1 Basic Considerations

The conventional approach to the construction of a highly stable calibration setup for optical spectrometers is the use of a suitable Fabry-Perot interferometer (FPI). A fixed frequency laser can either be locked to one of the cavity modes of the FPI or it can be used for calibration of a tunable scan. To reduce the influence of ambient temperature and pressure changes, a spacer for the mirrors with very low expansion coefficient is preferred and the whole optical cavity is typically placed in a sealed tank [168, 176]. The tank is often evacuated and always needs to be kept at as constant a temperature as possible.

To understand the necessary demands on the temperature stability of such a system and the tolerable pressure changes, we start from the well known condition for the frequency ν of a given longitudinal mode of a confocal FPI

$$\nu = \frac{Nc_o}{4nd} \quad (2.12)$$

with d the spacing between the mirrors, c_o the speed of light in vacuum, the refractive index n of the medium between the mirrors, and N the integral mode number. For the 632.8 nm (4.74×10^{14} Hz) output wavelength of a HeNe laser, the refractive index of air under standard conditions of 760 Torr (1 Torr = 0.13332 Pa) pressure, p_o , and 288 K temperature, T_o , is approximately $n=1 + 2.7593 \times 10^{-4}$, where the quantity $(n-1)$ is linearly proportional to the density of the gas medium [111]. A change δp in pressure at constant temperature will lead to a change in the density of the air in the cavity, and consequently to a new frequency, $\nu + \delta\nu$, of the desired mode given by

$$\nu + \delta\nu = \frac{Nc_o}{4 \left(n + (n-1) \frac{\delta p}{p_o} \right) d} \approx \frac{Nc_o}{4nd} \left(1 - \frac{n-1}{n} \frac{\delta p}{p_o} \right) \quad (2.13)$$

From Eqs. 2.12 and 2.13 it follows that

$$\delta\nu \approx -\frac{n-1}{n} \frac{\delta p}{p_o} \nu \approx -(n-1) \frac{\delta p}{p_o} \nu \quad (2.14)$$

For the HeNe laser frequency at near ambient pressures this amounts to a $\delta\nu$ of -172 MHz/Torr. Therefore, the pressure of the air between the mirrors has to be controlled to better than 0.01 Torr if a stability of the FPI on the order of 1 MHz is to be achieved.

The influence of a temperature change on an open cavity is twofold. One the one hand, it will change the density of the air in the FPI and influence the frequency of the cavity mode in a similar fashion to a pressure change, and on the other hand the

physical spacing of the mirrors will be changed by thermal expansion of the spacer. The former effect will be considered first.

At a constant pressure, a temperature change δT leads to a density change of the air between the mirrors which in turn leads to a frequency change of the cavity mode of

$$\delta\nu \approx (n - 1) \frac{\delta T}{T_0} \nu \quad (2.15)$$

where n is the index at temperature T_0 . As an example, for the HeNe laser at atmospheric pressure this already amounts to 455 MHz/K. Hence at ambient pressure, even small temperature changes would cause significant drifts. Again, keeping the FPI in an evacuated tank can eliminate this dependence of the mode frequency on the temperature.

The more commonly treated temperature influence on the frequency of a given FPI cavity mode is the thermal expansion of the spacer used to separate the mirrors. For a thermal expansion coefficient α of the spacer this influence can be seen to be

$$\nu + \delta\nu = \frac{Nc_0}{4nd(1 + \alpha\delta T)} \approx \frac{Nc_0}{4nd}(1 - \alpha\delta T) \quad (2.16)$$

or

$$\delta\nu \approx -\alpha\delta T\nu \quad (2.17)$$

For Zerodur ceramic $\alpha = -0.3 \times 10^{-7}/\text{K}$ and $\delta\nu = 14 \text{ MHz/K}$, while for fused silica $\alpha = 5.5 \times 10^{-7}/\text{K}$ and $\delta\nu = 260 \text{ MHz/K}$. This means that even with the extremely low expansion Zerodur as a spacer, the temperature of the FPI must be controlled to better than 0.1 K to ensure a frequency stability on the order of 1 MHz.

2.3.2 The FPI as a transfer cavity

The reasons discussed above commonly lead to the use of a temperature controlled FPI with a low expansion spacer placed in a vacuum tank if high pressure calibration of optical spectra is needed. However, such a system is fairly complicated to build, and potentially more seriously, not very convenient to align. The alternative we consider is an open cavity (at ambient pressure) which is not passively stabilized but instead, locked to a simple reference laser with a highly stable output frequency. Such a reference laser is indeed readily available in the polarization stabilized HeNe laser [290]. What remains to be investigated is the locking scheme and how well such a transfer cavity system performs over ranges of frequencies far from the HeNe laser output.

The system we have devised both i) to stabilize the frequency of the Ar⁺ laser and ii) to calibrate the scan of the dye laser used for the near IR cw difference frequency generation in our spectrometer is shown schematically in Figure 2.17. In the interest of simplicity, only the optical components are depicted.

The heart of the system is a 30 cm length FPI with very broadband mirrors ($T=6\pm 2\%$ for 400 to 780 nm). The measured finesse of this cavity is 20, i.e., it has a fringe width of 14 MHz at the 250 MHz free spectral range (FSR). The cavity is locked onto the frequency of a polarization stabilized HeNe laser whose absolute frequency stability was measured to be on the order of 0.1 MHz/hour by optical mode beating against an iodine stabilized laser from the Hall labs. Slow control of the cavity length is performed by heating the middle section of the confocal mirror spacer, while fast control is obtained using a PZT-supported end mirror. The Ar⁺ laser frequency is

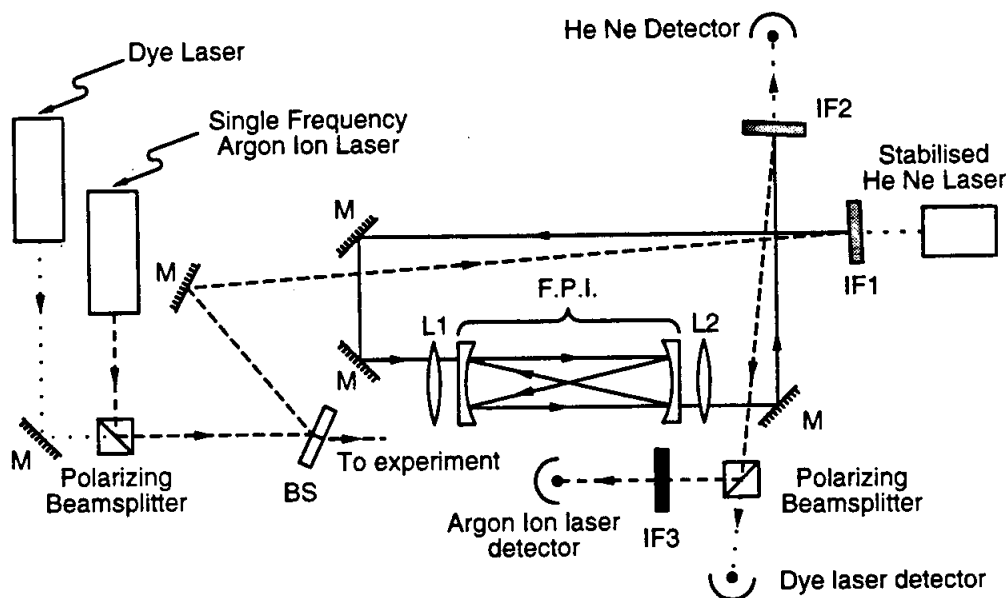


Figure 2.17: Schematic diagram of the optical setup used for stabilization of a difference frequency spectrometer. The transfer cavity (FPI) is locked onto a polarization stabilized HeNe laser. The single frequency Ar^+ laser, in turn, is locked to the cavity. Finally the scan of the dye laser is calibrated by recording the transmission fringes of the stabilized transfer cavity. A number of mirrors (M) are used to steer the beams, interference filters (IF) and polarizing beamsplitters are employed to combine the various laser beams collinearly or separate them after passing through the cavity. Two planoconvex lenses (L1 and L2) with $f=500$ mm are used to compensate for the refractive power of the cavity mirrors. All three beams are monitored on separate detectors. A beamsplitter (BS) is used to select the required amount of dye laser and Ar^+ laser radiation out of the main beam going to the experiment.

then locked to a suitable cavity mode of the FPI. Finally, the transmission pattern of the FPI is recorded for calibration as the dye laser is scanned. All three laser beams are suitably attenuated and combined collinearly with a polarizing beam splitter and/or interference filter before they are coupled into the transfer cavity. The transmitted light is similarly split into its three components and each color detected on a separate detector.

The design of the FPI is shown in somewhat more detail in Figure 2.18. Starting from the right, the spacer consists of a 12 cm long section of 2.5 cm diameter pyrex tubing, two stainless steel-to-pyrex graded seals welded together with their stainless steel sides, a second 8 cm long section of pyrex, and finally a 2.5 cm long tubular piezoceramic transducer (PZT). Most of the stainless steel part of the spacer is wrapped with heating tape to allow active control of the cavity length.

The numerical example given in the preceding section (HeNe laser frequency) shows that a 1 Torr increase in pressure (at constant temperature) of the air in the cavity would lead to a frequency shift of the cavity mode of -172 MHz. If the whole length of the spacer were heated for thermal control of the cavity length and fused silica used for a spacer, a drop by 0.7 K would compensate for this pressure change. However, heating the whole length is not very practical, instead only a fifth can typically be heated. For a fused silica cavity, the temperature of this shorter section must now be changed by 3.5 K. For a small pressure this scaling might just be acceptable, for larger variations it turns out to be prohibitive. Hence the choice of a 6 cm long stainless steel section as the heated part of the spacer, i.e., a material with a much higher thermal expansion coefficient. With $\alpha = 187 \times 10^{-7}/\text{K}$ for stainless steel, a drop in temperature of only 0.1 K suffices to compensate for the 1 Torr pressure rise.

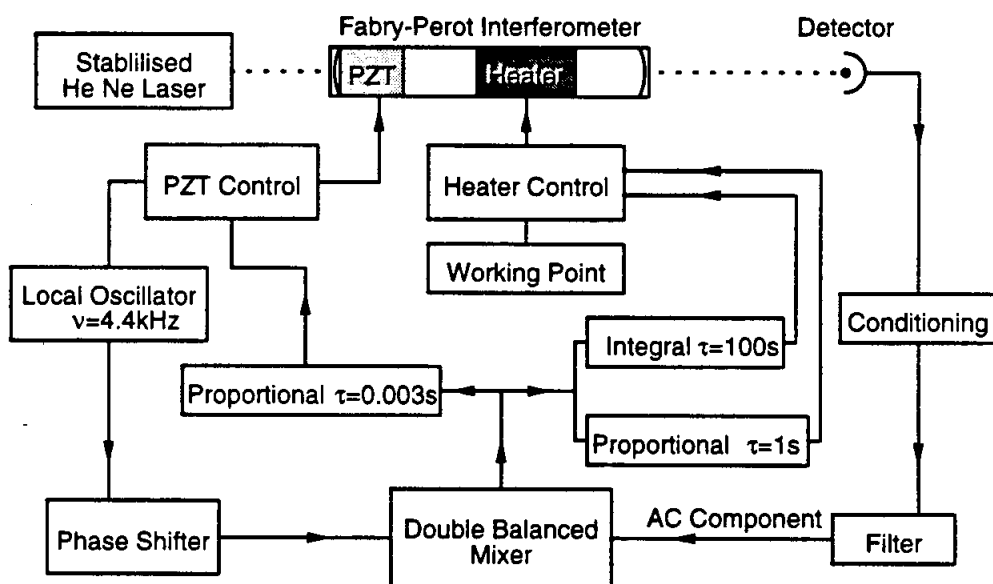


Figure 2.18: Schematic diagram of the electronic scheme used to stabilize the transfer cavity onto the stabilized HeNe laser. See text for details.

This allows moderate initial heating (about 20 K above room temperature) to access a wide dynamic range. In addition, the effect of heating the air inside the spacer (e.g. see Eq. 2.15) is minimized. Once the stainless steel part of the spacer has been chosen for the described reasons, pyrex glass with a 5-fold smaller expansion coefficient, $\alpha = 32 \times 10^{-7}/\text{K}$, is a natural and convenient choice for the remaining sections of the spacer. In particular, graded seals of stainless steel and pyrex are readily available and the ratio between the two expansion coefficients can nearly perfectly compensate for the ratio in length. A 1 K change in temperature of the pyrex (e.g. by a change in the lab temperature) can therefore be compensated by an equal but opposite change of the temperature of the stainless steel. These opposing effects help minimize the influence of ambient temperature changes on the average temperature of the air inside the FPI and the associated frequency shifts from changes in air density.

2.3.3 Possible limitations of performance for the HeNe-stabilized cavity

The system described in the preceding section transfers the stability of the reference HeNe laser to both the Ar^+ laser and the dye laser fringes through the use of an open transfer cavity. For this purpose, the length of the cavity is controlled so as to compensate for any changes in ambient pressure and temperature. However, the associated shift in frequency of any cavity mode depends on the refractive index of the medium between the mirrors at the corresponding wavelength. Since the refractive index of air depends upon wavelength, there will still be a small residual error in the system due to this dispersion that eventually limits the performance of the system. This section addresses at what level of precision this will happen. For simplicity, we

consider only the pressure dependence (at constant temperature) but by comparisons of Eqs. 2.14 and 2.15, the temperature dependence can be obtained by simple scaling.

To lock a cavity mode of the FPI (with mode number N_{HeNe}) to the frequency (ν_{HeNe}) of the stabilized HeNe laser at ambient pressure (p), the length (d) of the confocal cavity has to be

$$d = \frac{N_{\text{HeNe}}c_0}{4\nu_{\text{HeNe}}} \frac{1}{1 + (n_{\text{HeNe}} - 1)\frac{p}{p_0}} \approx \frac{N_{\text{HeNe}}c_0}{4\nu_{\text{HeNe}}} \left(1 - (n_{\text{HeNe}} - 1)\frac{p}{p_0}\right) \quad (2.18)$$

To compensate for a change δp in pressure, the mirror spacing must be adjusted to $d + \delta d$, where

$$\frac{\delta d}{\delta p} \approx \frac{-N_{\text{HeNe}}c_0}{4\nu_{\text{HeNe}}} (n_{\text{HeNe}} - 1) \frac{1}{p} \quad (2.19)$$

or

$$\delta d \approx -d(n_{\text{HeNe}} - 1) \frac{\delta p}{p_0} \quad (2.20)$$

In Eq. 2.20, the refractive index was set equal to 1 since we consider only linear terms in δd , i.e., first order changes in the cavity length.

A second mode of the transfer cavity (with mode number N_{laser}) with a frequency close to either the Ar^+ laser or the dye laser will, by analogy with Eq. 2.18, have a frequency ν_{laser} at the initial pressure of

$$\nu_{\text{laser}} \approx \frac{N_{\text{laser}}c_0}{4d} \left(1 - (n_{\text{laser}} - 1)\frac{p}{p_0}\right) \quad (2.21)$$

With the pressure changed by δp and the accompanying change in length δd to keep the cavity locked to the HeNe, the frequency for the mode will be changed by $\delta\nu_{\text{laser}}$ according to

$$\begin{aligned} \nu_{\text{laser}} + \delta\nu_{\text{laser}} &= \frac{N_{\text{laser}}c_0}{4(d + \delta d)} \frac{1}{1 + (n_{\text{laser}} - 1)\frac{p + \delta p}{p_0}} \\ &\approx \frac{N_{\text{laser}}c_0}{4d} \left(1 - \frac{\delta d}{d}\right) \left(1 - (n_{\text{laser}} - 1)\frac{p + \delta p}{p_0}\right) \end{aligned} \quad (2.22)$$

Substituting Eq. 2.20 and taking only linear terms in the changes and rearranging, one obtains

$$\begin{aligned}
 \nu_{\text{laser}} + \delta\nu_{\text{laser}} &\approx \frac{N_{\text{laser}}c_o}{4d} \left(1 + (n_{\text{laser}} - 1) \frac{\delta p}{p_o} \right) \left(1 - (n_{\text{laser}} - 1) \frac{p + \delta p}{p_o} \right) \\
 &\approx \frac{N_{\text{laser}}c_o}{4d} \left(1 + (n_{\text{laser}} - 1) \frac{\delta p}{p_o} - (n_{\text{laser}} - 1) \frac{p + \delta p}{p_o} \right) \\
 &\approx \frac{N_{\text{laser}}c_o}{4d} \left(\left[1 - (n_{\text{laser}} - 1) \frac{p}{p_o} \right] + [n_{\text{HeNe}} - n_{\text{laser}}] \frac{\delta p}{p_o} \right) \quad (2.23)
 \end{aligned}$$

Comparison to Eq. 2.21 finally yields

$$\delta\nu_{\text{laser}} \approx \frac{N_{\text{laser}}c_o}{4d} \frac{\delta p}{p_o} (n_{\text{HeNe}} - n_{\text{laser}}) \approx \nu_{\text{laser}} \frac{\delta p}{p_o} (n_{\text{HeNe}} - n_{\text{laser}}) \quad (2.24)$$

Eq. 2.23 shows that the residual error from the dispersion of the refractive index of air is proportional to the difference between the refractive index at the wavelength of the HeNe laser to which the cavity is locked and that of the second laser. Hence, the closer the two wavelengths can be chosen, the lower the residual error from the use of an open transfer cavity will be.

In our experiment the cavity is locked to the 632.8 nm line of the HeNe, and 3963 cm^{-1} IR light is generated by difference frequency mixing the 488.0 nm Ar^+ line (20486 cm^{-1}) and the 605.0 nm output (16523 cm^{-1}) of the dye laser. The refractive index of air (under standard temperature and pressure conditions) at these two wavelengths is $1 + 2.7843 \times 10^{-4}$ and 2.7626×10^{-4} , respectively[111]. With $n_{\text{HeNe}} = 1 + 2.7593 \times 10^{-4}$ this results in residual errors of $\delta\nu_{\text{dye}} = -0.22 \text{ MHz/Torr}$ and $\delta\nu_{\text{Ar}} = -2.02 \text{ MHz/Torr}$. For the resulting IR light, the drift is -1.8 MHz/Torr . One can see that, for the small pressure changes encountered in a typical laboratory environment, a stability on the order of $< 5 \text{ MHz}$ can be expected. The described transfer cavity scheme reduces the drift in calibration caused by pressure changes by about two orders of magnitude from the value expected for a simple marker cavity.

As a final point, it should be mentioned that even though there will be a considerable change in the length of the transfer cavity if the pressure changes a few Torr, the stabilization of the cavity to the HeNe laser ensures that the FSR changes by only an extremely small amount (on the order of 1 part in 10^8). Therefore, the FSR has to be calibrated only once to obtain the proper scaling of the dye laser calibration fringes. A new calibration is only required if a sufficiently different mode of the transfer cavity is locked onto the HeNe laser.

Implementation

In this section we explain in more detail how the cavity is actually locked to the stabilized HeNe laser and the Ar^+ laser in turn to the cavity. The recording of the transmission fringes with scanning the dye laser is standard and will not be detailed.

2.3.4 Locking of the transfer cavity to the HeNe laser

The scheme of locking the transfer cavity to the HeNe laser is shown in Figure 2.18. There are two ranges of frequency control needed: a fast response to correct for the small amplitude, predominantly acoustic fluctuations and a slow but large amplitude response to correct for the changes in average pressure and temperature in the laboratory.

For determining the direction and magnitude of the servo loop correction, a derivative shaped "discriminator" signal is required. An elegant optical method to this

end has been reported [163]; it does, however, require additional optical components not compatible with the triple laser setup used in this work. Instead, to obtain an error signal, the following scheme is used. The PZT is driven by a small sinusoidal voltage ($V_{pp} \approx 0.125$ V) derived from a local oscillator running at a frequency of $\nu_{mod} = 4.4$ KHz. The PZT changes the transmission frequency of the FPI by one FSR every 35 V. This small dither voltage therefore introduces a cavity modulation of < 1 MHz (i.e., less than 10% of the transmission width of a fringe) which is detected as amplitude modulation of the transmitted light at the frequency ν_{mod} . The phase of this amplitude modulation changes by 180° from one side of a fringe to the other and vanishes at the top of each fringe. To convert the phase behavior of the modulation into a derivative shaped discriminator signal, the ac component of the detector signal is demodulated in a double balanced mixer whose local oscillator input is an appropriately phase shifted and amplified version of the 4.4 KHz PZT dither voltage.

The discriminator signal is used with proportional/integral feedback to the PZT to control the length of the transfer cavity such that the frequency of the HeNe laser corresponds exactly to the center of the chosen transmission fringe. The 3 dB cutoff frequency of the servo loop is $f_c = 1/2\pi\tau = 50$ Hz with a unity gain frequency of 1.0 KHz. The maximum dc correction voltage that can be applied to the PZT is purposely limited to ± 11 V and yet is easily sufficient to lock the cavity. Hence the electronics can all be derived from conventional ± 15 V operational amplifiers and there is no need for a high voltage power supply. The ± 11 V limit translates into less than $1/3$ FSR change of the transmission frequency of the FPI in either direction, and thus the fast PZT control can never cause a jump to another longitudinal mode of the transfer cavity.

To monitor the proper locking of the FPI two checks are performed. The first one is to determine whether the residual error signal is within a predetermined range around 0 V, and monitored continuously via a front panel green/red LED. More importantly, the dc part of the photodetector signal monitoring the transmitted light is compared to a level of about 1/3 of its possible maximum at the top of a cavity fringe. If it drops below this limit, flip-flop circuitry is triggered which activates a red warning LED. The flip-flop can only be reset manually; hence the experimenter is alerted if the lock has ever been lost, and thus can have the assurance of complete lock integrity over an arbitrarily long series of spectral scans.

To counteract the effects of slow variations of the air pressure and temperature in the laboratory, the central stainless steel part of the cavity spacer is heated. The heater correction is derived from the integral and proportional feedback of the discriminator signal, and added onto a constant dc current (the working point) to ensure an average temperature of about 20 K above ambient room temperature. This initial offset places the lock point more than 100 FSR away from that of a room temperature cavity, and hence yields both large dynamic range and adequate speed for the heater control. The time constant of the proportional branch of the feedback is 1 sec to separate it cleanly from the 50 Hz knee in the PZT control bandwidth. The corresponding integral part of the heater servo just serves to zero the proportional corrections (i.e., to the PZT and heater), and for which a relatively long time constant of 100 sec proves entirely sufficient. Furthermore, this time constant prevents rapid heating or cooling of the cavity during momentary interruptions of the lock (i.e., due to blockage of the HeNe laser beam) which could cause an undesired relocking to a different longitudinal mode of the transfer cavity.

2.3.5 Frequency control of the Ar⁺ laser

For the frequency control of the single mode Ar⁺ laser, the rear mirror is PZT mounted, with a voltage requirement of 435 V per FSR (136 MHz) of the 110 cm laser cavity. The servo controller which stabilizes the output frequency of the Ar⁺ laser, therefore, has to supply at least this range of travel so a cavity mode can always be found to match the desired frequency determined by one of the modes of the transfer cavity. Here we implicitly assume that the center frequency of the transmission bandpass of the Ar⁺ intracavity etalon and the transfer cavity modes are separated by less than half the Ar⁺ FSR. On the other hand, too great a dynamic range of the PZT could allow the frequency of a particular longitudinal mode of the Ar⁺ laser to tune by more than the 250 MHz FSR of the transfer cavity. This would possibly lead to a situation where the servo loop controller could accidentally relock the Ar⁺ laser to an adjacent mode of the FPI. A change of the Ar⁺ laser frequency by exactly one FSR of the transfer cavity would result, and therefore a loss of the absolute frequency calibration of the setup. To prevent this, the controller is purposefully allowed less than 800 V travel, i.e., less than 2 FSR of the Ar⁺ laser.

With these ideas in mind, an integral feedback with a time constant adjustable around 50 msec is used. It consists of a low voltage part followed by a high voltage amplifier ($\times 100$). Since the transfer cavity is already dithered by the PZT, the necessary discriminator signal is derived from the Ar⁺ light transmitted through the FPI in an analogous way to the HeNe laser. As the unavoidable thermal expansion or contraction of the Ar⁺ laser cavity will eventually drive the controller into its upper

or lower limit, provisions for an automatic reset are implemented, as described below. These also allow for the automatic startup of the system and initial locking to the transfer cavity.

As long as the light power transmitted through the FPI (dc part of the detector signal) is below a preset limit, a small constant voltage is fed to the integrator, inducing a slow search for the proper lock point. As the transfer cavity fringe is approached, the detector signal rises, the discriminator signal is electronically switched to the integrator and the constant voltage disconnected, thereby quickly achieving a tight lock. The lock status is also indicated by a green/red LED on the front panel for operator convenience. If the PZT control voltage reaches either of the preset upper or lower limits, whose difference corresponds to roughly 1.5 FSR of the Ar^+ laser cavity (typically 650 V), the integrator is reset to a suitable starting point, and the next adjacent lock point is acquired after a short automated ramp search as described above. It should be emphasized that by this procedure a *neighboring* longitudinal mode ($N \rightarrow N \pm 1$) of the Ar^+ laser is locked to the *same* mode of the transfer cavity and therefore the frequency of this laser is kept constant throughout an arbitrary number of resets due to thermal expansion/contraction of the Ar^+ cavity length.

Test of the HeNe-stablized cavity performance

2.3.6 Optical and electronic tests

The first performance test of the stabilization system comprised measurements of the residual error signals and of the HeNe and Ar⁺ output frequencies. The residual error signal of the cavity lock onto the HeNe laser scales to an rms frequency error of less than 200 KHz between the HeNe laser and the cavity mode. In an independent experiment the beat note between the HeNe laser output and an I₂ stabilized HeNe laser was measured, and demonstrated a stability on the order of 100 KHz/hour over several hours, i.e., well within the published range [290].⁹ Therefore, the combined error due to the HeNe and the quality of the lock is believed to be well below 1 MHz and should not contribute noticeably to the overall system performance. In the absence of any serious external perturbations (such as accidental interruption of the beam or a visit from the Chinooks), the same mode of the cavity stays easily locked to the HeNe for periods on the order of a week.

Locking the Ar⁺ laser to the transfer cavity has a twofold effect. First, the long term frequency excursions clearly evident in the unstabilized laser are reduced dramatically and are indeed limited by the long term stability of the transfer cavity. We did not find a simple way to measure this independently, but spectral scans of the IR difference frequency system over molecular transitions reported below suffice to indicate an absolute stability of the Ar⁺ laser of better than a few MHz. Second, the linewidth of the laser is decreased considerably. This can both be measured from the residual error signal and independently (and more reliably) by observing the frequency distribution of the laser output with an additional scanning FPI. The latter

⁹It is worth mentioning that Niebauer *et al.* [290] have demonstrated a frequency stability of ≤ 20 MHz/year for polarization-stabilized HeNe lasers on which our design is based.

test was performed with a confocal cavity of 2 GHz FSR and a finesse of about 200. Both measurements show that the linewidth of the laser is indeed reduced from the free running value of about 10 MHz to typically 1 MHz. Since the best sub-Doppler linewidths we presently observe in the slit supersonic expansions are on the order of 30 MHz (at 4000 cm^{-1} for Ar carrier gas), this frequency stability should both increase the resolution and lead to more reliable line shape measurements.

2.3.7 Spectroscopic measurements

As a test of the overall performance of the stabilization and calibration setup described in this chapter, we have obtained repeated measurements of fixed molecular transitions of $(\text{HF})_2$ in the near IR. These spectra can be measured with sub-Doppler resolution and high signal-to-noise in the difference frequency spectrometer.

Shown in Figure 2.19 are repeated scans over the ${}^{\tau}Q_0^-$ branch of the $\nu_{\text{acc}} = 1 \leftarrow 0$ transition in $(\text{HF})_2$ (i.e., excitation of the "free" HF stretch) taken over the course of more than six hours. The wall clock time (p.m.) of data acquisition is shown for each spectrum. The top trace is the transmission spectrum of the transfer cavity as the dye laser is scanned and which permits successive scans over the IR transitions to be compared quantitatively. At the level of spectral resolution, there is no noticeable shift between the spectra over the course of 6 hours, attesting to the long term frequency stability of the transfer cavity lock design. A more exacting test of this frequency performance is described below.

For each of the experimental spectra a precise frequency scale is constructed in the following way: First, the positions of all the cavity fringes are determined

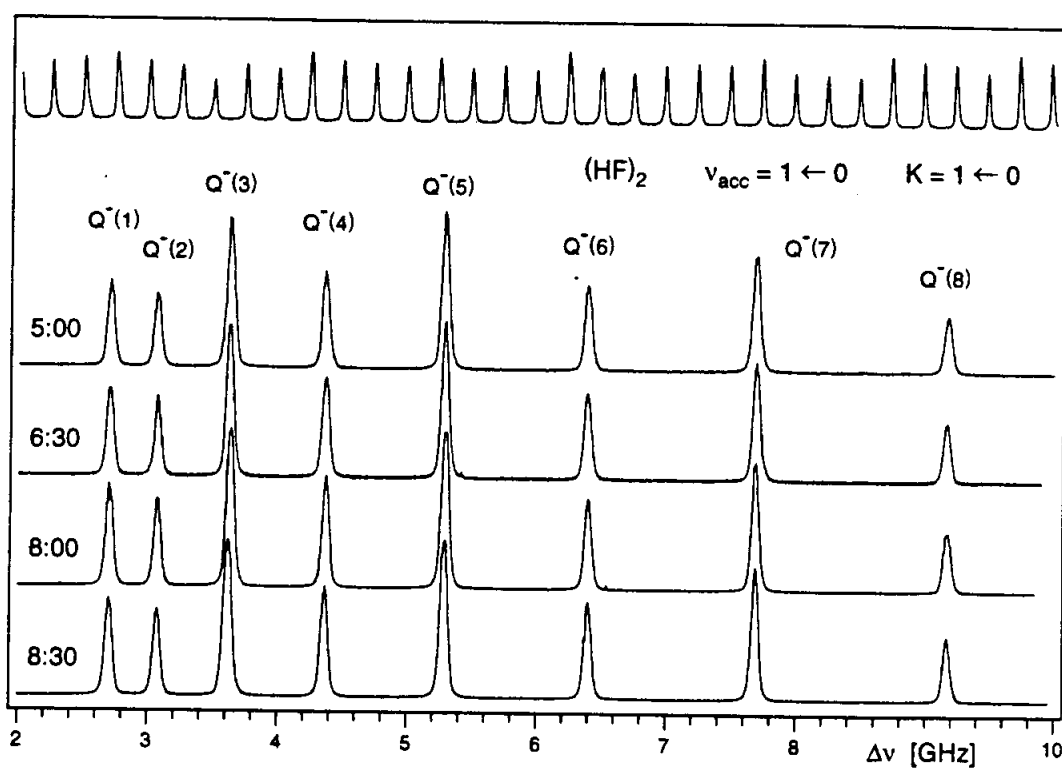


Figure 2.19: Part of the RQ_0^- branch of the HF dimer free hydrogen stretch fundamental (ν_{acc}) at 3893 cm^{-1} recorded at sub-Doppler resolution. The upper trace is the simultaneously recorded transmission fringes of the transfer cavity. The molecular spectrum was recorded at various times (i.e., from 3:00 to 8:30 PM) to test the long term stability of the calibration scheme described in this work.

with a fast computer algorithm [342]. Then frequencies are assigned to each of the fringes, and also to each data point by interpolation under the assumption of a linear scan between the fringes. With this preliminary scale the position of the lines in the molecular spectrum are determined, and compared to the positions of the spectrum taken at 5:00 pm (i.e., arbitrarily chosen as the reference spectrum). Since the relative numbering of the cavity fringes can differ initially from scan to scan, each scan is shifted laterally by an integral number of fringes to get the minimum deviation for a given reference peak. This procedure introduces no error since any drift of the overall system from scan to scan is certainly less than 1 FSR. No adjustment is made for any drift of the Ar^+ laser, i.e., it is locked solidly on the HeNe stabilized transfer cavity and assumed to be constant.

The measured drifts over the series of $(\text{HF})_2$ spectra are plotted as a function of the data acquisition time in Figure 2.20; no significant drift of the system over more than 6 hours is apparent. We have made similar measurements under improved frequency control of the dye laser and have confirmed that this system exhibits a comparable degree of frequency stability even over the course of a full week (see Figure 2.21). This indicates that an open transfer cavity locked to a stable reference laser is sufficient to calibrate sub-Doppler optical and IR molecular spectra with an accuracy on the order of a few MHz or better in routine, day to day applications.

2.4 Conversion to 1.2–2.2 μm region

The dye/ Ar^+ laser combination described earlier for the generation of 2.2–4.2 μm IR light cannot be extended to wavelengths shorter than 2.2 μm because the

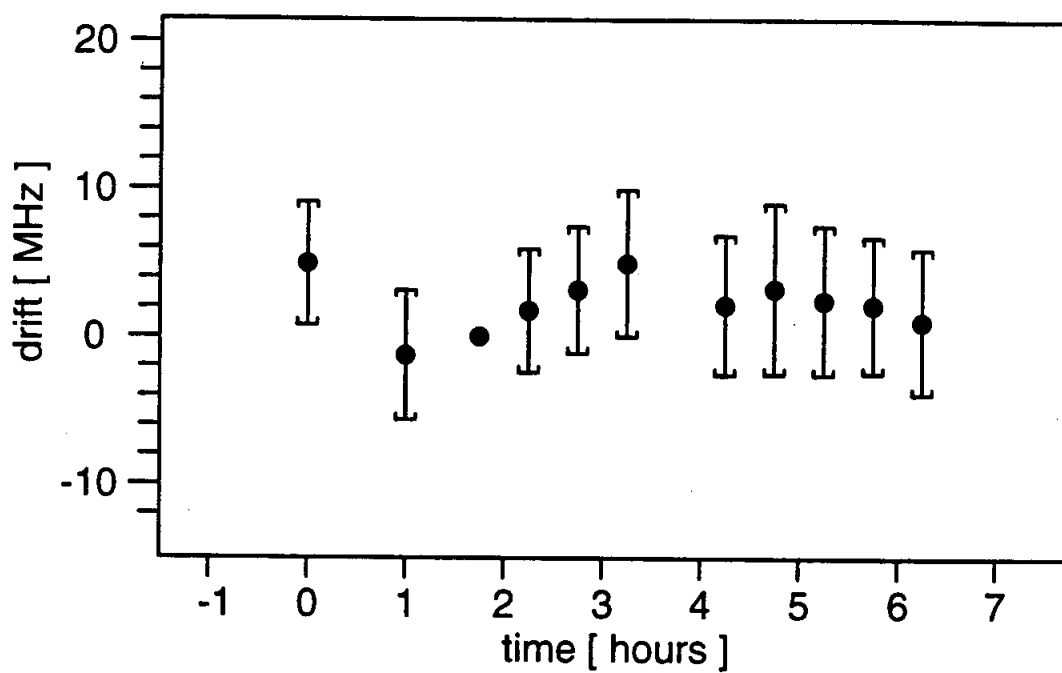


Figure 2.20: Frequency drift of the difference frequency spectrometer as a function of relative time. The error bars represent ± 1 standard deviation. The data scan taken at + 1.8 hr is used as a reference. See text for details.

Long-term Frequency Stability of Infrared Spectrometer

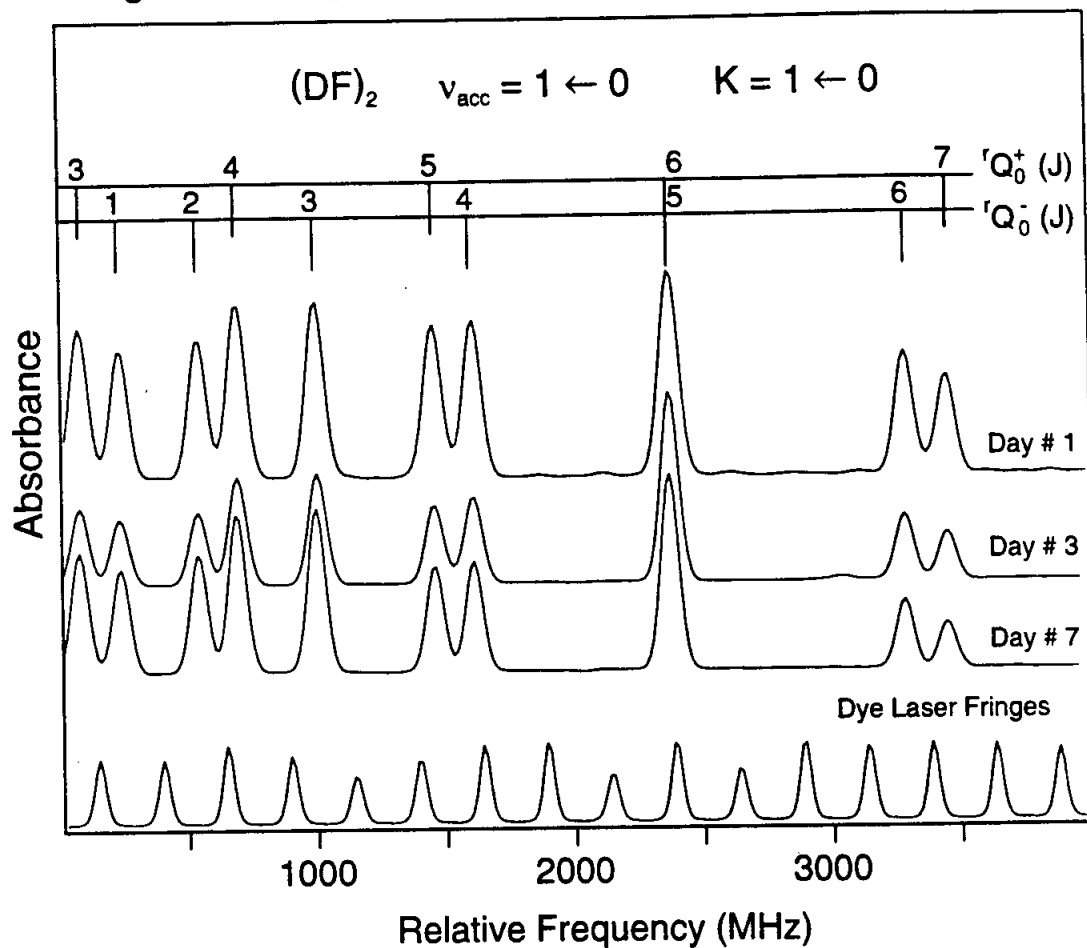


Figure 2.21: Series of scans over part of the ν_1 , $K = 1 \leftarrow 0$ Q branches of $(DF)_2$, taken over the course of one week. The spectra are aligned by overlapping the transmission fringes from a stabilized Fabry-Perot transfer cavity (displayed at the bottom of the figure) as described in the text. The long term drift of the frequency measurement technique is ≤ 5 MHz.

phase matching temperature drops below 200°C. This temperature must be maintained in order for the LiNbO₃ to self-anneal the index of refraction damage induced by absorption of the Ar⁺ laser light.¹⁰ Fortunately, only minor changes are required to convert the 2.2–4.2 μm spectrometer to 1.2–2.2 μm use. The necessary modifications are described in Refs. [264, 266] and the experimental setup is shown schematically in Figure 2.22. The dye laser is retained as the source of tunable light, and a 300 mW, cw Nd:YAG laser (Lightwave Electronics Model 122-1064-300F) takes the place of the Ar⁺ laser as the fixed frequency light source. Fortunately, the temperature range required for Type I, 90° phase matching in LiNbO₃ crystal for 1.2–2.2 μm difference frequency generation is quite similar as for 2.2–4.2 μm generation. This is shown in Figure 2.23 below and more completely in Figure 2.6 of Reference [266]. The same LiNbO₃ crystal can be used as in the 2.2–4.2 μm experiments, but must be rotated 90° to exchange to extraordinary and ordinary axes (since the horizontally polarized dye laser is now the higher frequency laser). Due to the ν^2 power dependence of the difference frequency process, higher power is generated in the 1.2–2.2 μm region than in the 2.2–4.2 μm region (see Eq. 2.7), with power levels of $\approx 50 \mu\text{W}$ routinely achieved with this scheme for input powers of $\approx 400 \text{ mW}$ (dye) and 300 mW (Nd:YAG). This represents a 5–10 fold enhancement over the power obtained in the 2.2–4.2 μm region with comparable input power levels.

The liquid N₂ cooled InSb detectors used to detect the 2.2–4.2 μm light do not have sufficient detectivity in the 1.2–2.2 μm region, and instead intrinsic germanium detectors are substituted. The photocurrents are converted to voltages with 10⁵ Ω transimpedance amplifiers and conditioned as described above for the 2.2–4.2 μm

¹⁰Extension to wavelengths longer than 4.2 μm is not feasible in LiNbO₃, as its phonon absorption region extends from 4.2–60 μm [296].

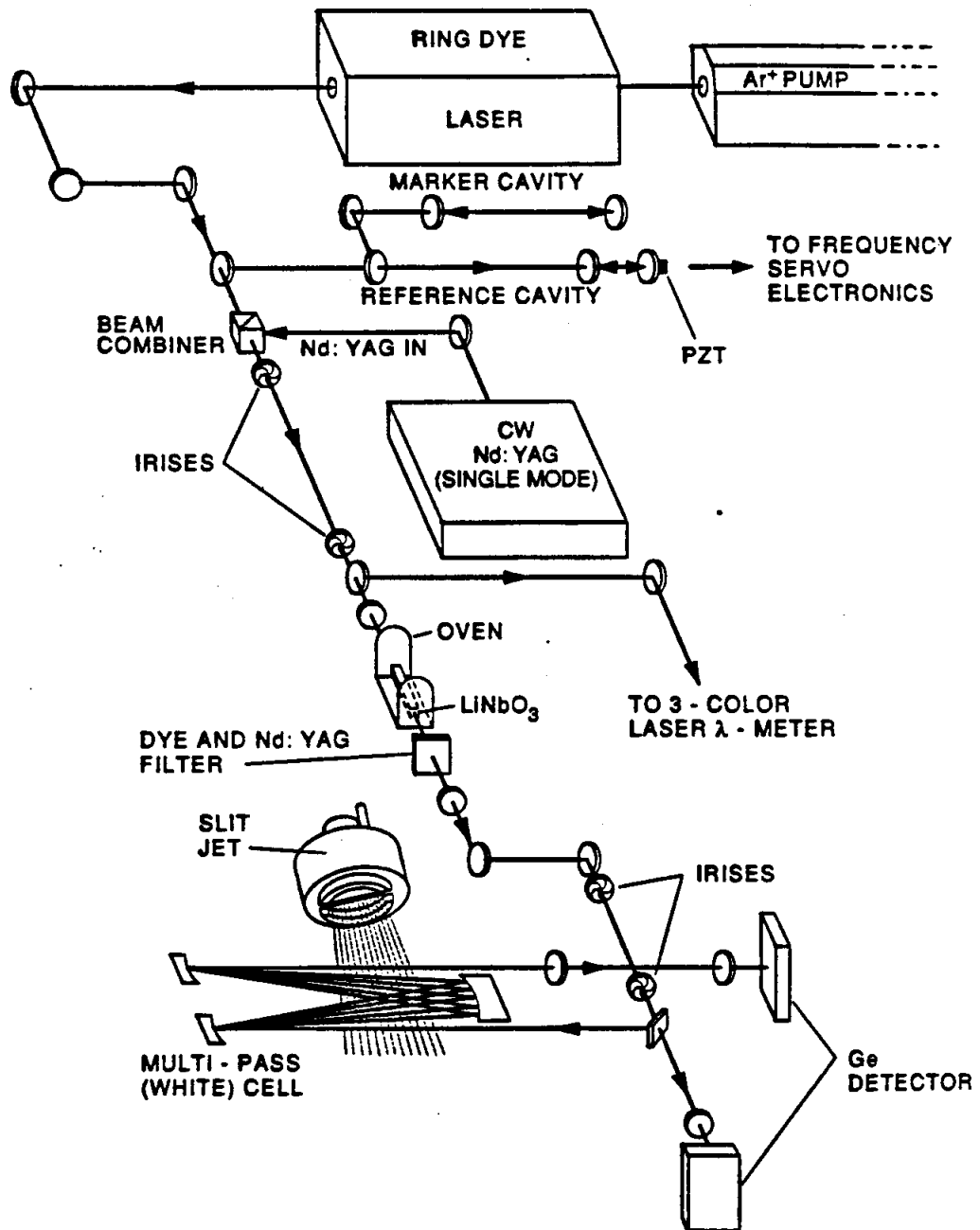


Figure 2.22: Experimental schematic for 1.2–2.2 μm difference frequency generation.

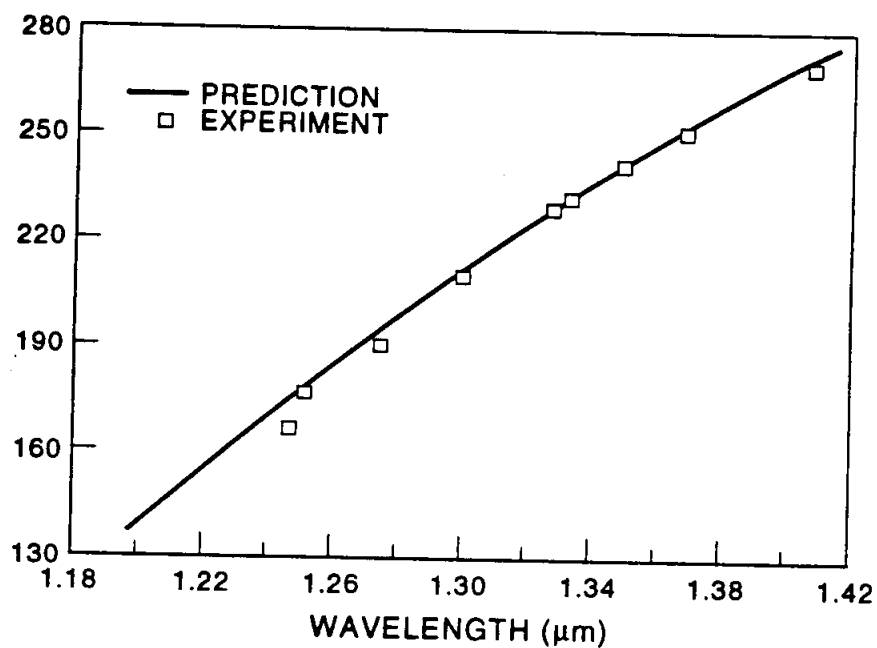


Figure 2.23: The temperature of the LiNbO_3 crystal necessary for 90° , type I phase matching vs the difference frequency obtained from the subtraction of the $1.06 \mu\text{m}$ radiation of a cw Nd:YAG from the tunable output of a ring dye laser operating on Rhodamine 6G (R6G). Tuning out to $1.6 \mu\text{m}$ is possible with R6G, and the region from 1.6 – $2.2 \mu\text{m}$ can be accessed via the use of redder dyes or by substituting a Ti:sapphire laser for the dye laser.

experiments. Additionally, a small number of optical elements must also be substituted, e.g. a polarization beamsplitter which combines the dye and Nd:YAG laser, the beam splitter that splits the 1.2–2.2 μm IR into signal and reference beams, the beam splitter used in the lambda-meter, and the optical element used to separate the dye and fixed frequency laser at the detection leg of the lambda-meter. Because of the \approx 2-fold lower frequency of the Nd:YAG laser vs the Ar^+ laser, the lambda-meter fringe frequency differs by approximately a factor of two. The phase-lock loop circuitry used to multiply the Ar^+ fringes does not have sufficient bandwidth (capture range = 190–740 kHz) to count the Nd:YAG fringes accurately, and consequently a circuit dedicated to the Nd:YAG (capture range = 130–540 kHz) has been constructed.

The dielectric coatings of the optics in the HeNe stabilized marker cavity described above do not have sufficient reflectivity to permit the active stabilization of the Nd:YAG laser. Although the Nd:YAG laser is intrinsically quite stable (specifications: $< 0.1\%$ amplitude noise, line width < 5 kHz over 1ms, long term drift < 50 MHz) such a scheme is highly desirable. As shown in Figure 2.24, the drift of the Nd:YAG laser (and hence IR) can be quite dramatic on the timescale required for recording a spectrum. Unfortunately, a single coating with sufficient reflectivity at the Ar^+ , dye, HeNe, and Nd:YAG colors, which would permit the use of a single transfer cavity for both 1.2–2.2 and 2.2–4.2 μm difference frequency generation, is not currently available. Consequently, incorporation of the stabilization scheme described above requires that a separate cavity dedicated to the 1.2–2.2 μm region be constructed.

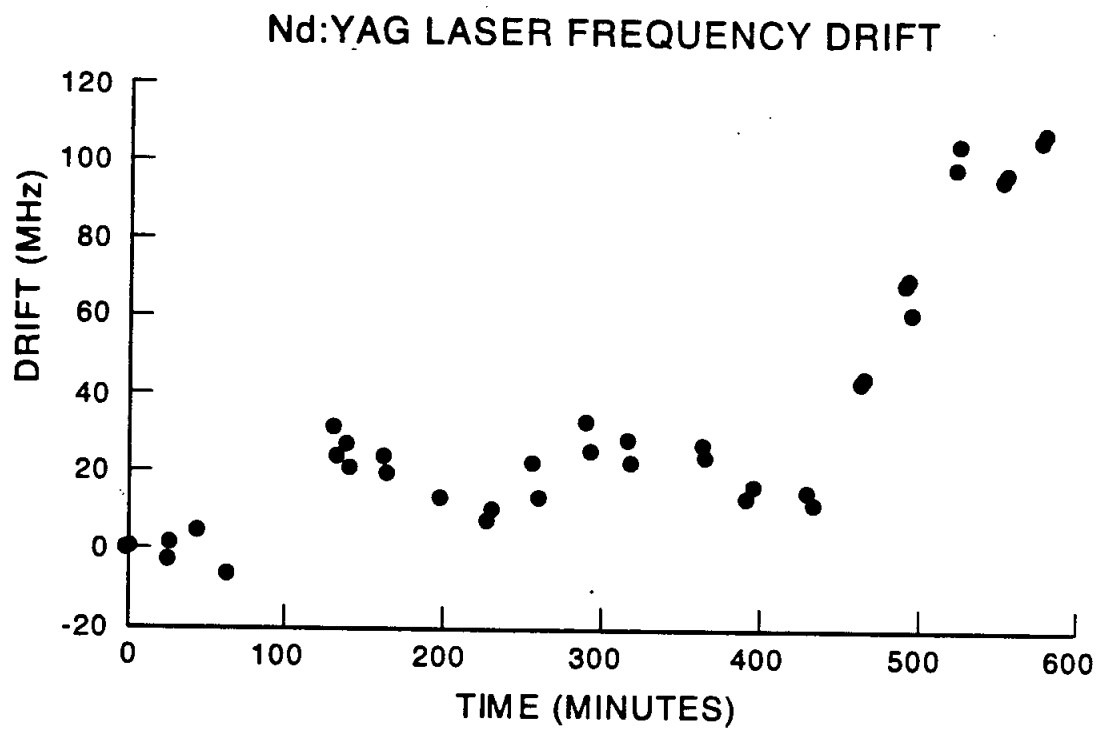


Figure 2.24: Frequency drift of the Nd:YAG laser as a function of time.

2.5 Appendices

2.5.1 Dye laser lock

General description

The dye laser locking circuitry is designed to lock the Spectra Physics dye laser to a galvo-driven external cavity. The active elements in the laser are a pair of galvo plates (laser Galvo's) and a PZT mounted mirror (PZT). The external cavity is aligned so that cavity modes are matched in order to give greater fringe contrast.

The principle of the lock is as follows. When the lock is acquired the reference cavity galvo is scanned until the first zero crossing is detected. At that point the voltage to the reference galvo driver is transferred to a digital sample and hold circuit (see circuit diagram in Figure 2.25). The voltage generated by the computer (to scan the laser) is then summed onto this voltage during a scan. In addition the ramp generated in the computer is fed forward onto the laser galvos.

When the zero crossing is detected the laser lock is turned on. This prevents the problem of high gain circuitry being active when the transmitted fringe in the reference cavity is its zero transmission (+0.4V) value. The "RAMP/OFFSET" switch determines a signal fed to the reference galvo. The amplitude of each is controlled by the "Coarse" and "Fine" pots. The ramp is also available — with no amplitude variation — on the "Synch" output. This can be used to drive the x-axis of a scope

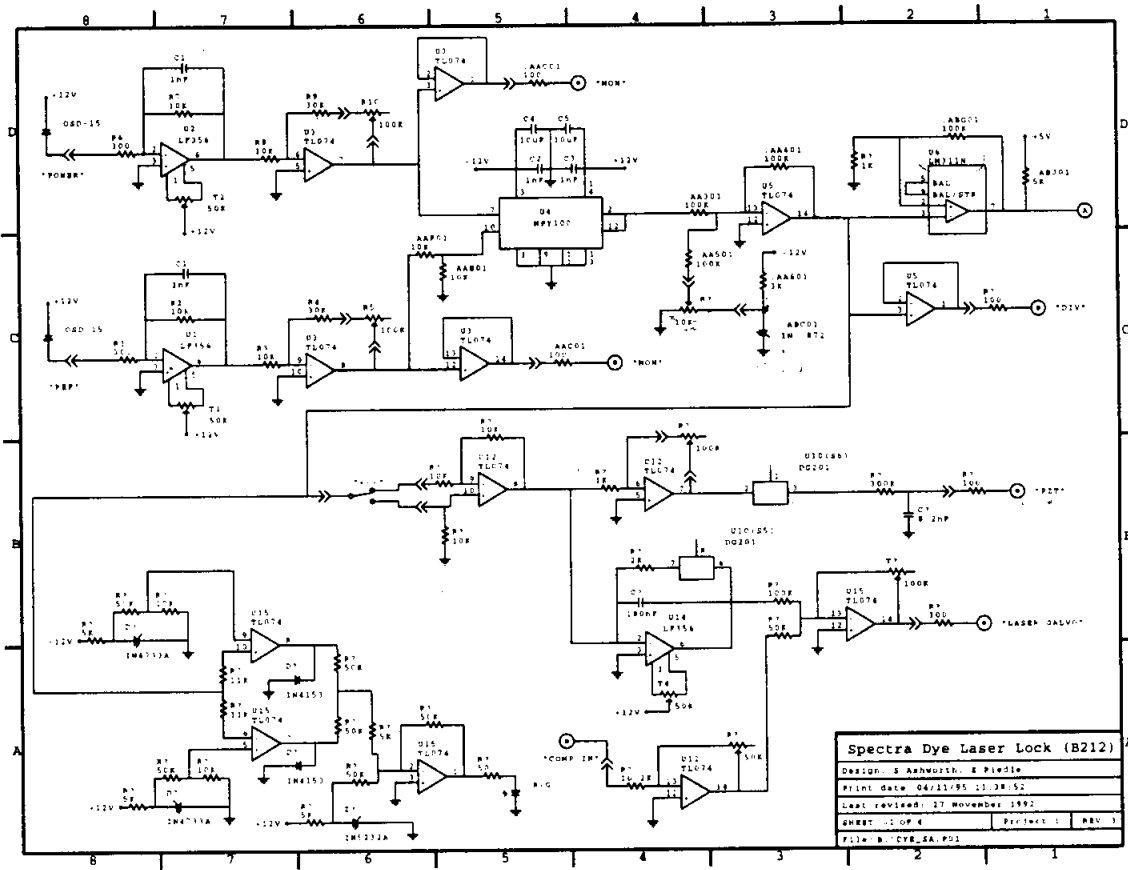


Figure 2.25: Circuit diagram for servo for locking the dye laser.

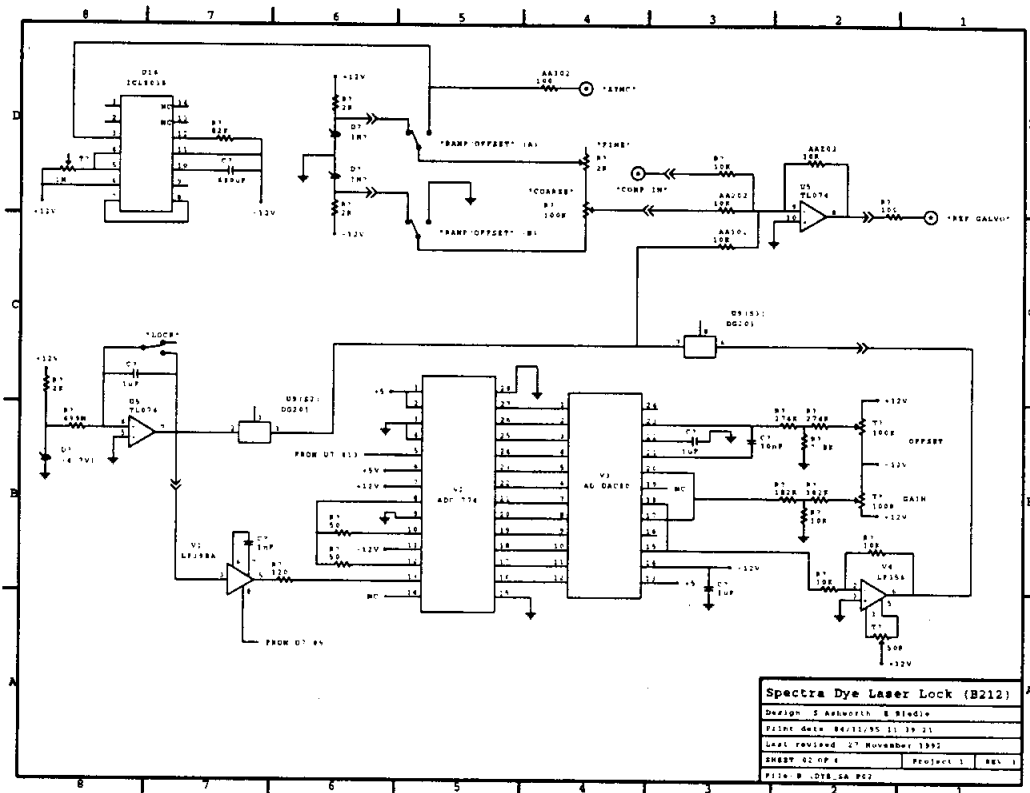


Figure 2.26: Page 2 of circuit diagram for servo for locking the dye laser.

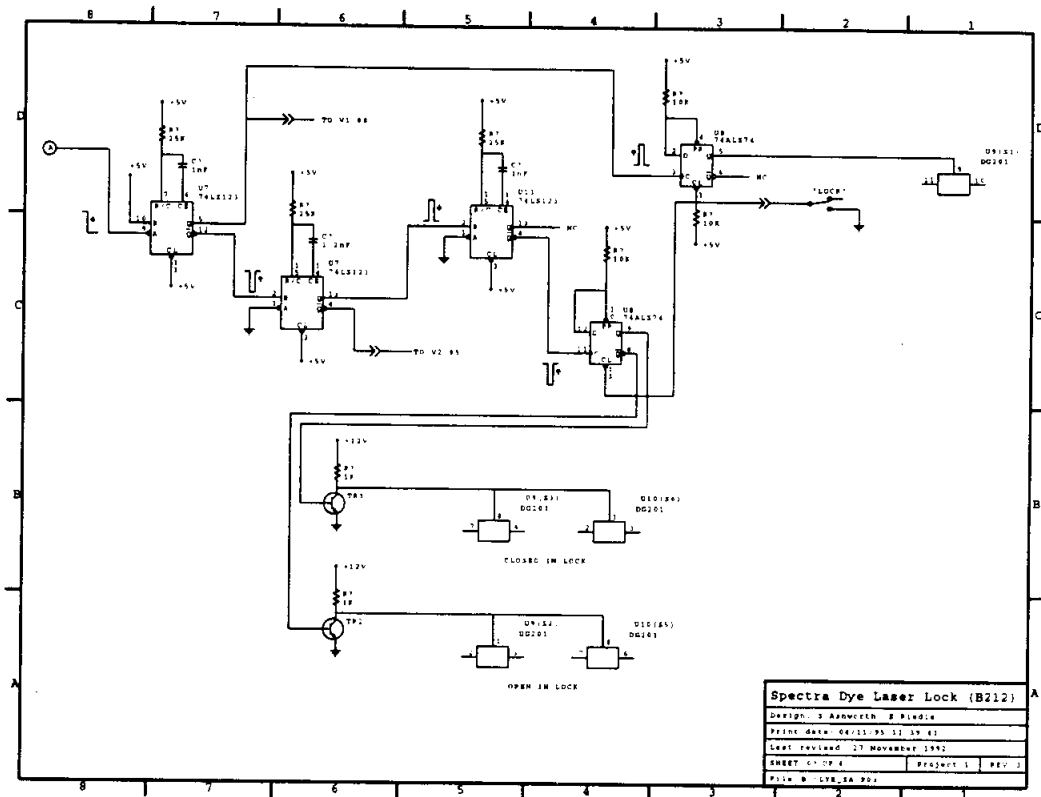


Figure 2.27: Page 3 of circuit diagram for servo for locking the dye laser.

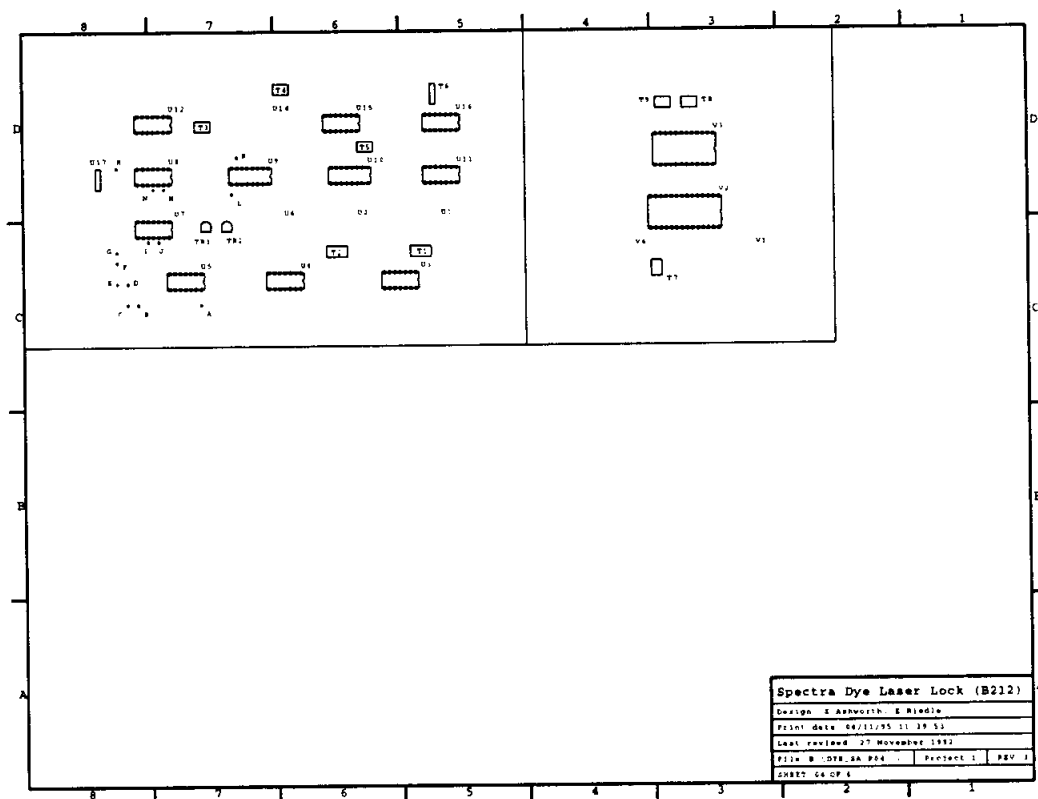


Figure 2.28: Page 4 of circuit diagram for servo for locking the dye laser.

when the ramp is being used.

The "+/-" switch inverts the signal to the lock circuitry and determines to which side of a fringe one locks. The LED is designed to go red when the "Div" signal is $> \pm 100$ mV from zero. Currently, the right-hand PZT gain pot is inactive. A PZT driver has been adapted for standard NIM use. Use this (two slot wide) rather than the older 3 slot versions for PZT control. The former has a 10 kHz roll-off frequency where the former has a 300 Hz roll-off!

A. INITIAL SET-UP

1. With no light falling on "Power" and "Ref" detectors (best to switch off room lights) use twin pots T1 and T2 to trim both "Mon" signals to zero.
2. With light on the detectors use "Ramp" switch to scan "Ref Galvo." Use "Synch" output to sweep x-axis of scope and align reference cavity.
3. Monitor "Div" signal (still ramping); adjust the power and reference gain until the fringe magnitude is $\approx 0.8V$, and adjust the offset so that the fringe crosses zero at approximately half-maximum.
4. With the laser PZT and Laser Galvo disconnected, set RAMP/OFFSET to OFF-SET, and throw the "Lock" switch; monitor "Div" signal (i.e., the error signal) and verify that it moves to approximately zero. Use T8 (offset) and T9 (gain) to adjust this, throwing system out-of-lock occasionally to reset everything. If T8 and T9 do not have sufficient dynamic range, use T7 carefully. [Beware: this step changes the digital sample and hold circuit characteristics.]
5. Connect BNC from laser galvos to the front panel mount labeled "Laser Galvo." Monitor spots reflected from galvos and "Div" signal. Adjust T5 until i) galvo spots do not move significantly when the lock is acquired, and ii) the galvo does not oscillate.

6. Connect BNC from laser PZT to the front panel mount labeled "PZT." Adjust PZT gain so that it is high but does not drive the PZT to oscillation.
7. Use scope probe to monitor the integrator output to galvos (from U14/356). Scan the computer. Adjust T3 (feed forward gain) until the computer scan causes less than 4V travel of integrator from initial position when locked.
8. Monitor the transmission fringe through the HeNe-stabilized marker cavity. Adjust the Ref Gain, Offset and PZT gain so that variations in transmitted signal are a minimum (i.e., try to achieve the tightest lock). Try both + and - positions to see which provides the better transmitted signal. (To reduce the very high frequency noise, use low pass filter to monitor the transmitted fringe.)

The system should now be in "initial" state.

B. DAY TO DAY SET-UP

1. Align cavity with the "Synch" output driving the x-axis of the oscilloscope.
2. Adjust gain and offsets to produce a 0.8V fringe on the "Div" signal.
3. Adjust "Offset" until fringe on "Div" channel is $\pm 0.4V$.
4. Switch from "Ramp" to "Offset" and throw lock switch.

C. NOTES

1. Chip bias tends to drift with temperature. Ensure chips are warm before trimming.
2. U14/356 has a constant offset of about 10 mV which cannot be trimmed out; be aware of this. To check this ground an input somewhere e.g. the input to U12 (#8,9).

D. TROUBLESHOOTING

1. Does not lock:
 - check offset on "Div" signal.

- check for multimode laser operation
- check reference galvo scanning (INITIAL SET-UP #4)
- check galvo offset in laser
- check BRF position

2. Does not scan:

- Reset computer to start of scan, reacquire lock
- check laser Galvo and BRF position
- verify that the computer ramp is connected
- check for multimode laser operation
- If galvo spots move when lock is acquired, adjust "Ref Gain" down and "PZT Gain" up until lock improves and galvo spots no longer move significantly when lock is acquired.

E. MEASURING REFERENCE CAVITY FSR

1. Acquire lock.
2. While monitoring the dye laser light transmitted through the HeNe-stabilized marker cavity, adjust the frequency offset so that the transmitted light is at a maximum (i.e., tune laser to top of a transmission fringe).
3. Read lambda-meter - average 10 times.
4. Using most recent value of FSR, calculate the frequency of a new fringe, a few FSR's away.
5. Go out of lock, move laser to calculated position, reacquire lock.

6. Read lambda-meter – average 10 times.
7. Calculate the number of fringes moved – round to the nearest integer. Calculate new FSR.
8. Break the lock, and reacquire after changing the dye laser frequency by $\approx 10\text{-}20\text{ cm}^{-1}$. Read lambda-meter – average 10 times. The most recent FSR should allow the exact number of fringes moved since the last iteration to be determined to within \pm two-tenths of a fringe. Adjust to nearest integer and recalculate FSR.
9. Repeat this cycle, increasing the frequency step each time, until the calculated FSR converges.

Note: If the number of fringes calculated after an iteration is more than 0.3 from an integer value, be suspicious and verify the readings and calculations.

2.5.2 Marker Cavity

General Description

The marker cavity is a 30 cm confocal Fabry-Perot cavity designed to be actively stabilized to the peak of the transmission of a polarization stabilized He-Ne laser. The cavity is constructed of two pyrex tubes separated by a stainless steel portion. One mirror is mounted directly onto the pyrex, the other to an inch long PZT which in turn is mounted onto the pyrex. Heater tape is wrapped around the SS portion and the PZT can be electrically driven.

The circuitry has an internal oscillator which is used to dither the PZT at

4.4 kHz. The resulting modulated transmission signal is detected with a photodiode and, after some signal conditioning and monitoring the AC part is mixed with the local oscillator signal in a double balanced mixer (DBM) to produce a demodulation (DEMOM) signal which is used in the feedback loop. The mechanical and electronic properties of the system are such that a phase shift is introduced between the local oscillator and the modulated transmission signal. The phase of the local oscillator signal to the DBM is therefore adjustable and is set such that the DEMOM signal has the correct phase and optimum amplitude.

Heating and cooling the central stainless steel portion of the tube is designed to be the primary source of stabilization. To this end there are proportional and integral parts to the heater control. The heater is set to some working point 6-8 V and the feedback is used to fine tune this value (see the circuit diagram in Figure 2.29). The integral part is designed to act slowly so that it is insensitive to the fast 0.1 Hz fluctuations in the DEMOM signal. The proportional part oscillates at about 1 Hz when the gain is too high. These alone are sufficient to lock with only 150 mV rms excursions on the DEMOM signal. A small proportional part with high gain has also been added as a DC offset to the PZT dither. This increases the lock's tightness by an order of magnitude. It is important to note that this DC offset is not sufficient to allow the PZT to jump to another fringe.

The two LED lights provide important diagnostic information. One is driven by the DEMOM signal ("LOCK") and turns red when the DEMOM signal is out of the range ± 90 mV. The other, which is green after lock has been established, turns red when the DC signal drops below 1 V. This indicates that a fringe has been lost completely and thus that the cavity may have changed length. This situation would

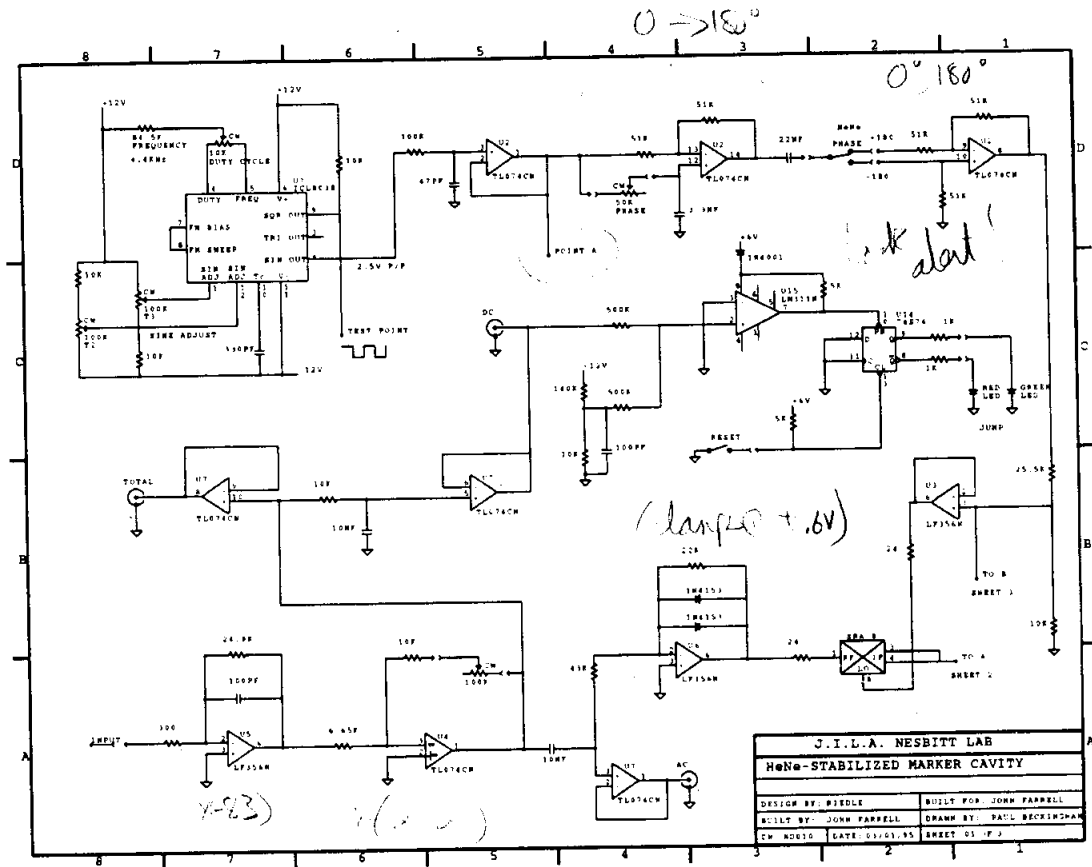


Figure 2.29: Circuit diagram for servo for locking the marker cavity.

2nd ⇒ gen

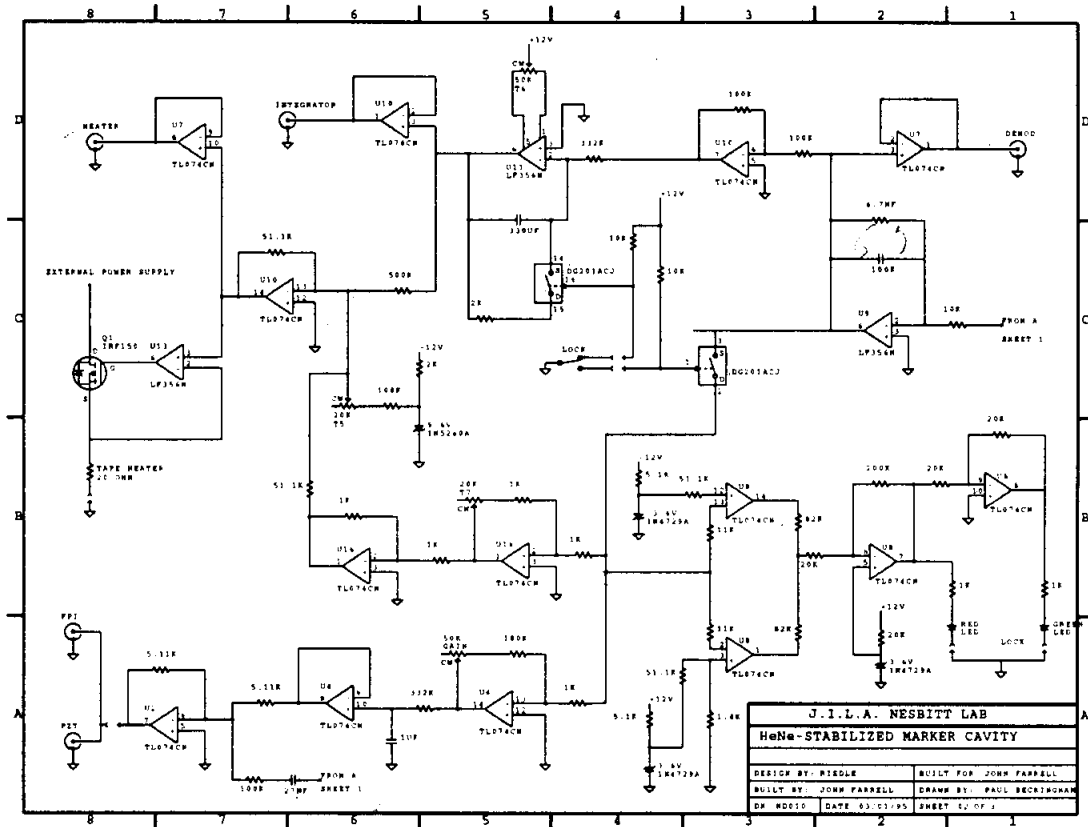


Figure 2.30: Page 2 of circuit diagram for servo for locking the marker cavity.

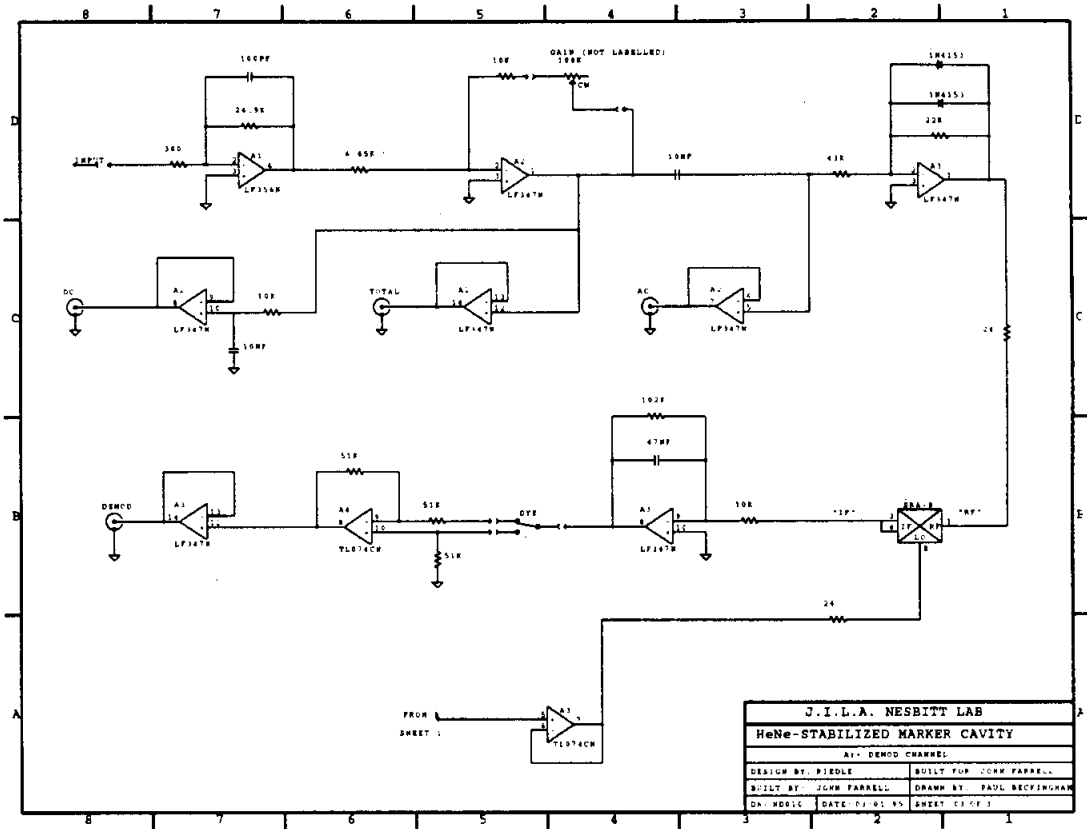


Figure 2.31: Page 3 of circuit diagram for servo for locking the marker cavity.

occur, for example, if the lab warms up (or cools down) more than the integrator can compensate for. However, a momentary disruption of the beam will turn this LED light red, although the system may still reacquire lock on the same HeNe fringe.

A. TO LOCK:

1. Align cavity optically. This may be done with the FPI controller alone. If one uses the FPI controller merely to ramp the PZT and take the "FPI" output from the cavity stabilizer to the FPI back panel, input one must be aware of two things:

i). There is no blanking on flyback so the scan may look a little different from a pure FPI scan.

ii). The FPI controller introduces a phase shift in the modulation, so if the phase of the "DEMODO" signal has been set using the FPI controller it will need to be adjusted during warm-up.

2. Connect PZT, heater and diode signal to front panel. (The diode signal should be connected to the upper "INPUT" BNC.) Connect external (12 V) power supply to rear panel. "LOCK" LED will be green and "JUMP" LED red.

3. Monitor DEMODO output. Check that a first derivative signal is being observed. Adjust phase with pot (phase) and switch (HeNe) so that phase DEMODO signal goes negative then positive during warm up and has optimum amplitude (peak-peak).

4. Adjust amplitude with top pot so that DEMODO signal is about 1.5 V peak to peak. TOTAL signal should be around 3-4 V.

5. Allow system to warm up. Twenty minutes to half an hour is probably sufficient, although more than 1 hr is better.

6. Switch to "LOCK" (Lock switch up). "LOCK" LED should turn red changing

to green when lock established. "JUMP" LED can be reset by briefly depressing the "RESET" button. Both lights should be green in normal operation. "JUMP" LED turns red to indicate a fringe has been lost if the DC signal drops below 1 V. Once this LED has turned red, it must be reset manually upon reestablishing lock. The "LOCK" LED changes when the DEMOD signal is $> \pm 90$ mV from ground (i.e. approx. 6% of total DEMOD travel).

7. DEMOD signal should now be centered at zero and with an rms deviation of approximately 10 mV.

B. NOTES

1. Ensure external power supply is connected to back panel before powering supply from mains. This will avoid shorts.
2. Chip bias tends to drift with temperature. It is best to adjust the unit when it is good and warm.
3. The "LOCK" LED is green when the discriminator is within ± 90 mV of ground. The "JUMP" LED changes state when the DC level of a fringe is greater than 1 V from ground.
4. The DEMOD signal shows an offset when the heater power supply is turned on. Do not try to trim this to zero without the heater connected and running.
5. The system will lock (DEMOD: ± 200 mV) without a PZT offset. To check heater function and proportional gain, ground pin 9 of chip 4 (TL074). This will mean that no DC offset is added to the PZT dither.
6. All of the front panel connections from the pins on the board are established from the reverse of the board via the 50 way ribbon cable, with the exceptions of the two input BNC leads (I,J and AK, AL) and the front panel "GROUND" connections.

There are three other connections to be made (other than the power pins PA-PD): these are from the IRF 150 mounted on the heat sink on the back panel, namely U, V and W.

7. The PZT gain needs to be set such that the system doesn't oscillate. The maximum gain is currently 200 and the system remains stable.

8. A 1 M Ω resistor to ground is installed at the marker cavity BNC. It has been found that after the FPI controller was used, the charge on the PZT was destroying the final PZT control chip in circuit. The resistor drains this charge in a few seconds.

C. TROUBLESHOOTING

1. No DEMOD signal:

- Check input connected
- Check PZT connected
- Check heater plugged in and external supply on
- Check monitoring correct BNC output

2. Does not lock:

- Check lock switch position
- Check HeNe lock
- Allow to heat up some more

3. Locks for a while then jumps:

- Leave to heat up - integrator has not enough range to pull it in.

4. DEMOD signal not at zero:

- Set up box so that there is access to the trimpots. With cavity in lock slowly and carefully adjust T6 until DEMOD centered at zero.

5. TOTAL signal asymmetric when in lock:

- Set box with access to trimpots. Adjust T4 until TOTAL signal as even possible. May have to now adjust T6 again to set DEMOD at zero. Monitor TOTAL signal at 20 mV per division - AC coupled for this adjustment.

2.5.3 Ar⁺ laser stabilization circuit

General Description

This circuit has been designed for active frequency stabilization of a single frequency Ar⁺ ion laser. The circuitry is designed to maintain the frequency of the Ar⁺ ion laser such that it corresponds to a fixed transmission maximum of the HeNe stabilized marker cavity. The transmission signal from the ion laser is detected with a photodiode and is conditioned (in the "Marker Cavity" controller) to produce a discriminator error signal which is used in the feedback loop (the signal comes out of the front panel BNC labeled "DEMOD" and goes into the input "DISC In." The circuit locks to the zero point of the error signal, corresponding to the maximum of the transmission fringe. Frequency drifts arising from changes in the length of the Ar⁺ laser cavity are counteracted by moving the back mirror of the laser with a piezoelectric transducer (PZT). This stabilized light source allows the transmission fringes from

scanning the dye laser to be used as absolute frequency markers in the infrared, greatly simplifying the task of measuring the frequencies of molecular transitions.

Details of circuit performance

A. Acquiring lock

If, when the "ACQUIRE" switch is thrown, the frequency of the Ar^+ ion laser does not correspond to a transmission maximum of the marker cavity, the photodiode signal is below the threshold value set by the "REF POWER" potentiometer on the front panel. This turns the output of the comparator (311 # 1) high, which causes the following to happen:

1. The LED lock light on the front panel glows red.
2. The incoming discriminator signal is blocked.
3. A voltage ramp to the integrator is activated.

The circuit schematic is shown in Figure 2.32. This voltage ramp, controlled by the "RAMP" potentiometer on the front panel, can either be positive or negative in order to scan the PZT up or down in voltage (more details are provided below). The output of this circuit is limited to a maximum of 8.2 volts so that the following amplification stage (x100) does not provide excessive voltage to the PZT. As the PZT voltage changes, the frequency of the Ar^+ laser will change until it corresponds to a transmission maximum of the marker cavity. At this point, the output of the lock comparator goes low, which :

1. turns the LED lock light green,
2. allows the discriminator signal through,
3. turns off the voltage ramp.

grd = 0
high = closed

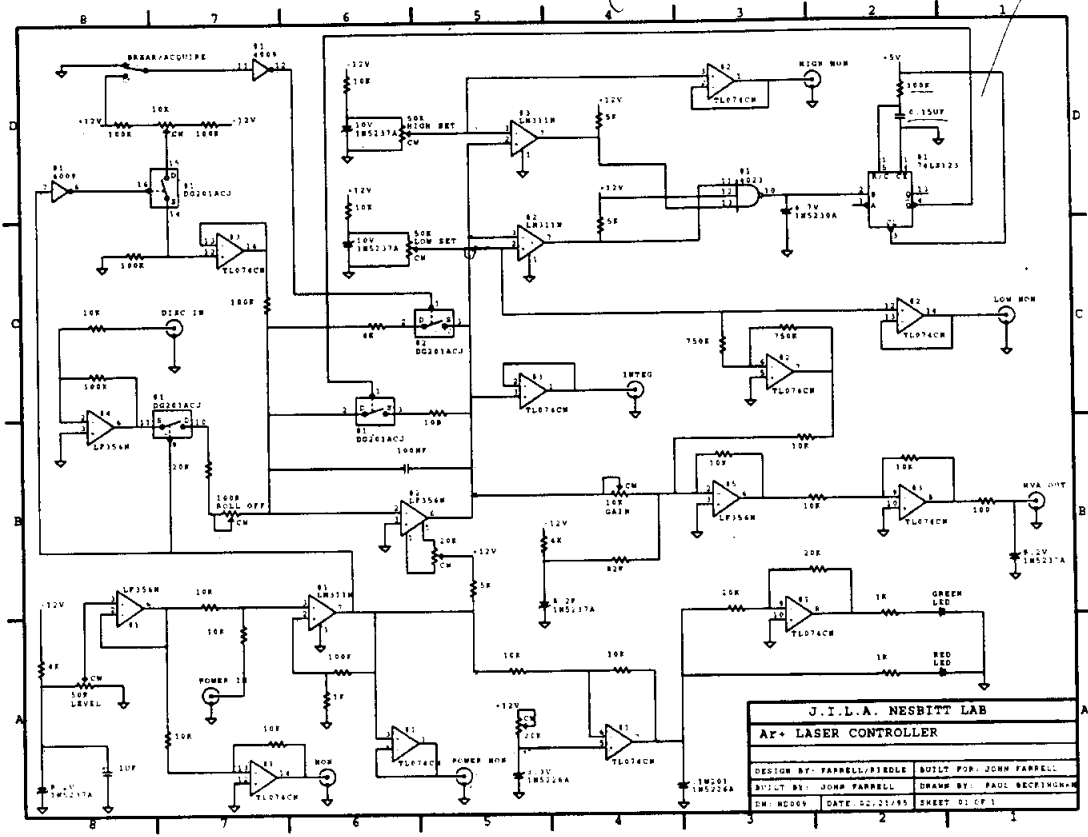


Figure 2.32: Ar+ laser stabilization circuit diagram.

B. In lock

Once the Ar^+ laser frequency corresponds to a transmission maximum of the marker cavity, the circuit locks to the zero point of the incoming discriminator signal. Fluctuations in frequency are corrected by an integral stage. Due to the intrinsic mechanical stability of the Ar^+ laser, there is no need for a proportional stage to correct for fast frequency excursions; in fact, there was a proportional stage included in the initial incarnation of this circuit, but it was found not only to be unnecessary, but actually detrimental to the overall performance.

Two potentiometers on the front panel marked "LOW Set" and "HIGH Set" determine the voltages (after amplification of 100 in the following stage) at which the PZT has reached its maximum desired travel. Once this point has been reached, the system resets itself.

C. System Reset

In order to achieve single frequency operation, the circuit must maintain a single marker cavity mode from the ion laser. In other words, upon resetting the system, the PZT should not change the frequency of the laser by more than the FSR of the marker cavity (250 MHz). The frequency of the Ar^+ laser changes 310 MHz when the PZT is ramped from 0 to 1 KV, and hence the total voltage ramp upon reset should not exceed 800 V to ensure that the same marker cavity mode is acquired.

As the integrator reaches either the upper or lower voltage limit, resetting the PZT so that the adjacent laser cavity mode is accessed will allow the same marker cavity mode to be maintained. The laser cavity modes are separated by 136 MHz, and thus after resetting the PZT must be more than 435 V either higher or lower to catch the next laser cavity mode. By setting the upper voltage limit to 500 V, a lower

limit of 100 V, and providing a positive voltage ramp upon reset, the system should quickly reacquire the proper cavity mode in both of the following situations:

1. System approaches upper voltage limit

If the integrator is approaching the upper limit of 500 V, the PZT is trying to counter the effects of an expanding laser cavity. Upon reset, the integrator will be cleared to 0 V and will scan upwards until it finds the next laser cavity mode which yields a transmission maximum of the marker cavity. Since the laser cavity modes are separated by 136 MHz (435 V) this will be accomplished after a ramp of approximately 60V. Assuming the laser cavity continues to expand, there will then be sufficient dynamic range (440 V) of the PZT left to offset this change. If the cavity soon starts to contract, there is again enough travel (160V) left in the PZT to keep the laser frequency at the maximum.

2. System approaches lower voltage limit

If the PZT reaches the lower voltage limit of -100 V, the laser cavity is in the process of contracting. Upon reset, the integrator starts from 0 V and ramps upward until it reaches the next laser cavity fringe at $(-100 \text{ V} + 435 \text{ V} = 335 \text{ V})$. At this point, there is again sufficient dynamic range left in the PZT to account for either a further contraction or subsequent expansion of the laser cavity.

In the above example, the maximum voltage to the PZT from the integral stage is 600 V (500 V from the upper voltage limit plus the inverted -100 V fed into the final amplification stage). Accounting for the 1 V offset for the proportional loop and its maximum positive excursion of 1 V, the maximum voltage which could be sent to the PZT is 800 V. Since the output of this circuit is amplified by a factor of 100, the maximum voltage which can leave the circuit box is 8 V. Currently there is

a a 8.2 V Zener diode which clamps the output voltage and prevents a larger voltage from being fed to the high voltage amplifier. It is possible to operate with a larger integrator voltage window by clipping this output Zener, but voltages greater than 10 V are not recommended due to possible saturation of the final amplifier.

Operational guidelines

The locking circuit obtains its discriminator power level signals from the device which locks the marker cavity. It has been empirically determined that the optimum "POWER In" voltage is ≈ 1.5 V. This level can be adjusted by changing the "DEMODO" potentiometer value on the "Marker Cavity" controller, but must also be accompanied by attenuation of the Ar^+ laser light reaching the detector. Typically attenuation by factors of 20-50 via neutral density filter combinations are necessary.

Once the proper power level has been obtained, the output from the "DISC Mon" BNC should be monitored. The "INT ROLLOFF" and "INT GAIN" potentiometers are then adjusted in order to minimize the discriminator signal (i.e. tighten the lock).

D. Notes

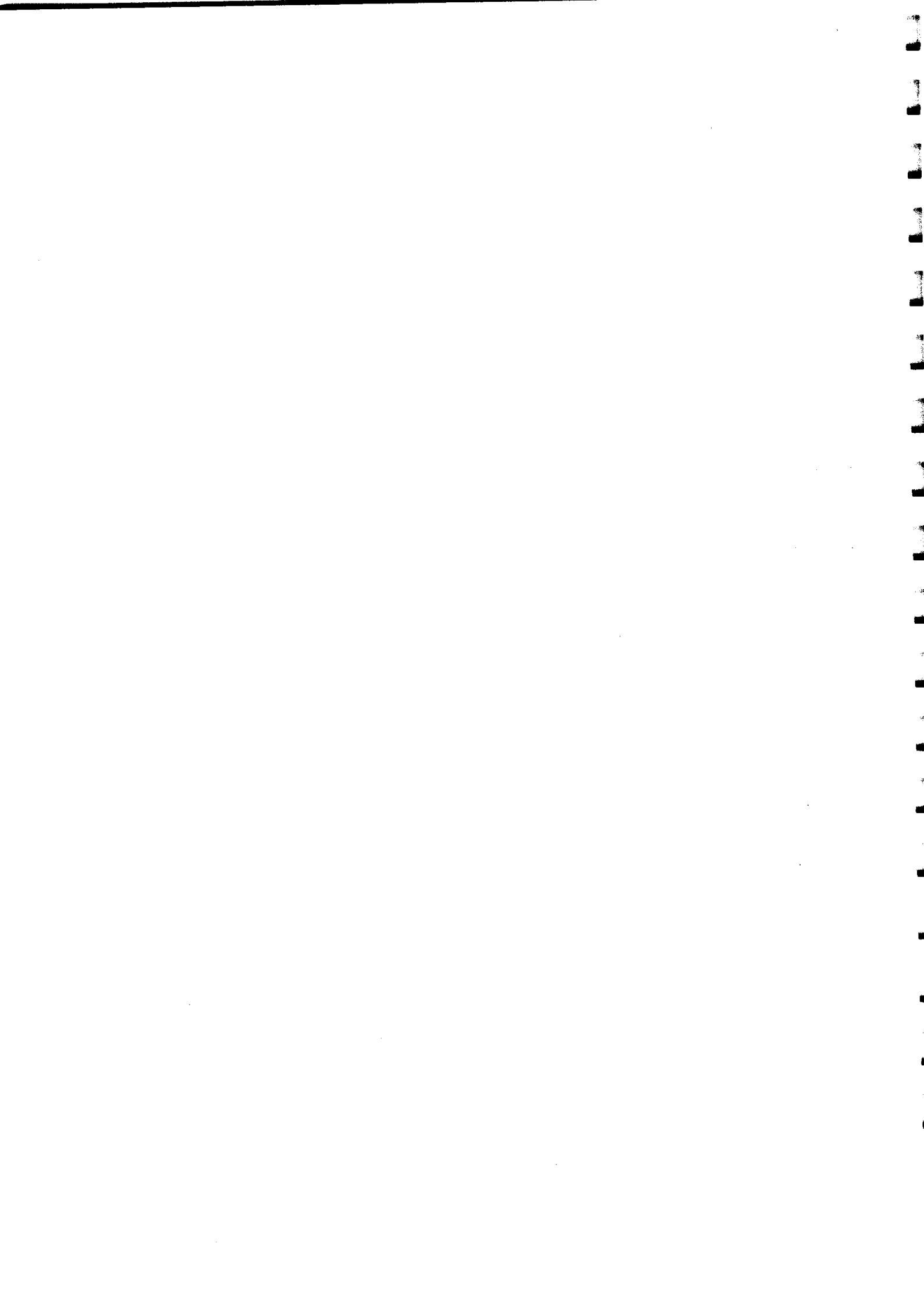
- i) Too much N_2 purging the laser will cause instabilities (i.e. oscillations).
- ii) Experience has shown that a relatively slow ramp (approx. 10 ms for the full ramp) allows the greatest ease in catching the fringe.

iii) "Typical" potentiometer settings:

Int Rolloff: 0 \rightarrow 2

Int Gain: 7 \rightarrow 10

Ref Power: 0.5 \rightarrow 2



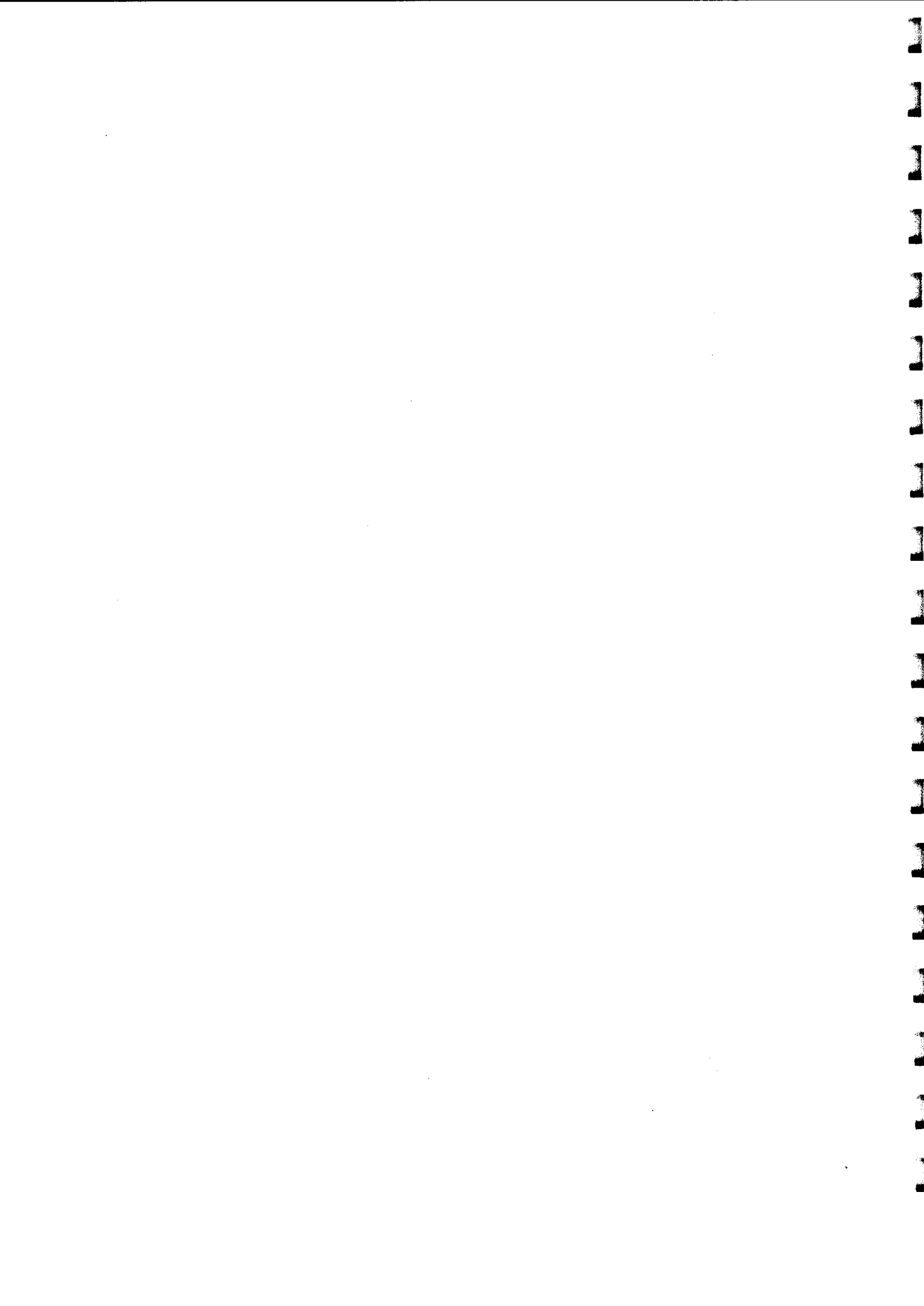
CHAPTER III

High-resolution infrared overtone spectroscopy of ArHF

3.1 Introduction

During the past few decades, weakly bound van der Waals and hydrogen-bonded clusters have been the focus of intense experimental and theoretical interest [281, 189, 158]. In particular, these complexes have proven extremely useful prototypes for studying the weak, intermolecular forces present between atoms and molecules during collisions [54]. One long standing goal of these efforts has been the construction of accurate potential-energy surfaces which include the dependence of all degrees of freedom of the complex, since such a potential provides the essential starting point for understanding a variety of dynamical phenomena such as state-to-state rotational energy transfer, vibrational predissociation, pressure broadening and shifting of spectral lines, and collisional alignment.

By virtue of their simplicity, the rare-gas hydrogen halide (RG-HX) dimers have served as particularly useful prototypes of such weak bonding phenomena. For example, direct observation of low-frequency intermolecular van der Waals modes, both in the far [107, 61] and near [251, 248, 329] IR, has provided considerable infor-



mation on the angular and radial parts of the intermolecular potential. Intramolecular degrees of freedom have also been probed by near-IR studies of vibrationally excited HX states of the complex [250, 248, 329, 181, 282, 252]. Most importantly, the relatively small number of degrees of freedom for such triatomic systems allows detailed quantum calculations on a trial potential-energy surface to be performed and thereby facilitate detailed comparison between theory and experiment.

The complete determination of a potential-energy surface for RG-HX complexes requires a knowledge of $V(R, r, \theta)$, where R is the radial separation of the RG and HX centers of mass, r is the displacement of the HX bond, and θ is the angle between R and r (see Figure 3.1). A particularly accurate description of the coupling between each of these three degrees of freedom is essential for predicting the vibrational energy transfer dynamics of these clusters. As one provocative example, the $V \rightarrow T$ predissociation from intramolecular vibrationally excited states has proven to be extremely slow for most¹ RG-HX complexes [250, 248, 329, 181, 282, 252], with the rate limited by the transfer of energy between the intramolecular (r) and intermolecular (R, θ) coordinates. Hence, any potential which attempts to model the transfer of energy from the diatom to the van der Waals bond must accurately reflect this intermolecular/intramolecular coupling.

However, despite recent near- and far-IR spectroscopic advances which have allowed experimental examination of the intermolecular vibrations in detail, full potentials even for such simple van der Waals clusters have not been available. To date, the potentials developed have primarily considered only the dependence upon the radial (R) and angular (θ) internal coordinates, but have necessarily averaged over the

¹A notable exception is ArDF, for which a vibrational predissociation lifetime of ≈ 100 ns has been determined recently [96].

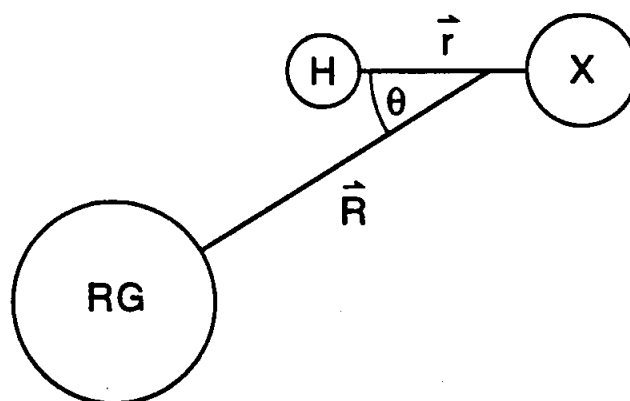


Figure 3.1: Coordinates used for defining the intermolecular potential of a rare-gas hydrogen halide van der Waals complex. R is the center-of-mass separation of the atom and diatom, θ is the angle between the rare-gas and HX bond axis, and r is the HX bond distance.

high-frequency stretching coordinate (τ) of the HX [186, 187, 282]. This so-called “adiabatic” separation of high-frequency intramolecular and low-frequency intermolecular coordinates has nonetheless been extremely useful in the analysis of van der Waals spectra and in the prediction of internal rotor ($R \rightarrow T$) predissociation dynamics [282]. The difficulty of obtaining a complete potential-energy surface is primarily due to the limited sampling of HX stretch coordinate available in the ground ($v_{HF}=0$) and first excited ($v_{HF}=1$) states probed. This difficulty has partly been addressed via studies of isotopically substituted masses for intramolecular vibrational motion, which sample slightly different regions of the r -dependent potential surface.

A far more direct alternative exists through accessing higher-energy intramolecular HX vibrations within the cluster. Although the ground ($v_{HF}=0$) and first ($v_{HF}=1$) vibrational levels of ArHF have been characterized extensively via tunable far-[107] and near-infrared [250] techniques respectively, there have been no corresponding studies

reported for clusters excited to higher vibrational levels of the HF. The results presented in this chapter represent the first rotationally resolved study of a triatomic van der Waals complex excited to an overtone stretching level of the HX subunit.

The two major difficulties encountered in accessing these overtone regions concern issues of both instrumental sensitivity and the availability of tunable, narrow band light in the regions of interest. Specifically, the absorption cross sections are typically much lower for overtone than for fundamental transitions and, consequently, the methods used to probe and detect these clusters must be up to several orders of magnitude more sensitive than required in the fundamental region. Furthermore, the necessary source of high resolution, broadly tunable infrared radiation to access the hydrogen stretching overtone region has not been available.

Of the two most common sources of narrow band tunable near IR light, i.e., color center and diode lasers, neither has proven sufficiently tunable to access the entire overtone region. Scoles and co-workers have obtained the rotationally resolved spectrum near $1.5 \mu\text{m}$ for the doubly-excited "free" H-C stretch in $(\text{HCN})_2$ (Ref. [268]) and HCN-HF (Ref. [211]) using an F_2^+ color center laser, although extension to other systems has been limited by the tuning range of the crystal. Diode lasers are also now available which, in principle, provide single-mode coverage between $1.3\text{-}1.6 \mu\text{m}$, although no van der Waals overtone studies have yet been reported with these sources.

Alternatively, cw difference frequency generation (DFG) methods have been developed which provide continuously tunable, near-IR light over a very broad range, limited primarily by the phase matching constraints of the nonlinear medium. The cw DFG scheme initially developed by Pine [296] utilizes both the relatively high nonlinear susceptibility and high thermo-optic coefficients of LiNbO_3 to subtract the

absorption of HF monomer at $7788.8562 \text{ cm}^{-1}$ [148]. Raw absorption strengths listed

tunable output of a cw dye laser from that of a single frequency Ar⁺ laser. By choice

3.3.2 ArHF internal rotor states from $j_{\text{HF}} = 1$: (2100) \leftarrow (0000) Σ bend and (2110) \leftarrow (0000) Π bend

In addition to transitions to the (2000) pure HF overtone stretching level, there is sufficient sensitivity to observe combination band transitions built upon this state in which the HF is simultaneously excited with one quantum of hindered internal HF rotation. Figure 3.3 shows a band centered at $\approx 7794 \text{ cm}^{-1}$ that is fivefold weaker than the pure overtone band, and also has the simple P/R branch structure characteristic of a $\Sigma \leftarrow \Sigma$ transition. Ground-state combination differences again unambiguously determine that this band originates in the (0000) ground state of ArHF. By analogy with the ArHF ($\nu_{\text{HF}} = 1 \leftarrow 0$ spectrum [251]), the upper state is identified as the (2100) Σ bend, which corresponds adiabatically with in-plane rotation of the HF within the complex with no projection of angular momentum along the internuclear axis. The integrated absorption intensity for this band is only 17(3)% that of the (2100) \leftarrow (0000) transition, where the number in parentheses represents 95% confidence limits. As shall be treated in Sec. 3.4, the relative intensities in these internal rotor combination bands provide useful information on the degree of hindering of the HF rotor in the ArHF complex.

In addition to the $K=0$ Σ bend, one would also expect two other projection components for a $b=1$ internal rotor level. These correspond to $K=1$ and form the doubly degenerate (2110) Π bend. Indeed we observe a third band centered near 7806 cm^{-1} with prominent P , Q , and R branches (see Figure 3.4). The presence of a Q branch and lack of a $P(1)$ line identifies this as a $\Pi \leftarrow \Sigma$ transition. Combination differences unambiguously identify the lower state as the (0000) state of ArHF; again by analogy to the ArHF ($\nu_{\text{HF}} = 1 \leftarrow 0$ spectrum, we assign this band to the

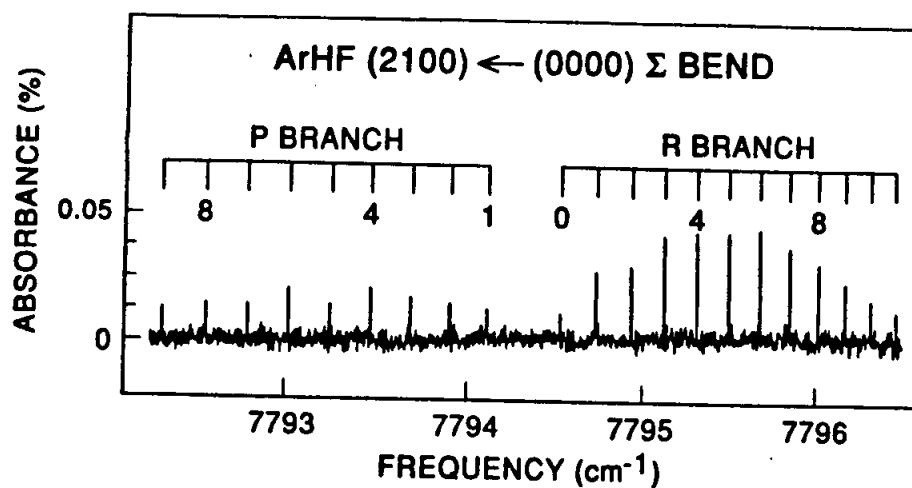


Figure 3.3: Spectrum of the ArHF (2100)←(0000) Σ bend. The integrated band intensity is 17(3)% of the (2000)←(0000) intensity. The conditions are as in Figure 3.2. The enhancement of *R* branch vs *P* branch intensity is a result of rotationally mediated Coriolis mixing of the Σ and Π bend vibrational wave functions, and is discussed in the text.

between the e parity Σ ($K=0$) and Π ($K=1$) bend internal rotor components, which has off-diagonal elements for the interaction which grow as $\sqrt{J(J+1)}$. For large diagonal separation of the Σ and Π bend vibrational origins, this translates into a systematic separation of the Σ^e and Π^e rotational levels by an amount proportional to $J(J+1)$, i.e. a shift in effective rotational constant. Since the Σ bend is at lower energy than the Π bend and the f parity levels remain unaffected, this second example of Coriolis mixing in ArHF (and indeed in all complexes of H(D)F and H(D)Cl with He, Ne, and Ar observed thus far) is most prominently demonstrated by a negative l doubling, i.e., $B(\Pi^f) - B(\Pi^e) < 0$. If the pair of internal rotor components are sufficiently close in energy, Coriolis mixing can also result in the anomalous intensities observed in the P and R branches of the various bands. This effect is quite evident in the present study, where the R branch is enhanced with respect to the P branch by much more than would be predicted for a $\Sigma \leftarrow \Sigma$ transition based on Hönl-London factors alone. A more detailed analysis of these intensity perturbations will be presented in Sec. 3.4.

In order to deperturb the spectra, it is necessary to account for both these Coriolis perturbations simultaneously. This involves construction of a 4×4 Hamiltonian matrix of the following form:

$$H = \begin{pmatrix} H_{11} & 0 & H_{13} & 0 \\ 0 & H_{22} & H_{23} & 0 \\ H_{31} & H_{32} & H_{33} & 0 \\ 0 & 0 & 0 & H_{44} \end{pmatrix} \quad (3.2)$$

where

$$H_{11} = \nu_{2100} + B_{2100}J(J+1) - D_{2100}[J(J+1)]^2,$$

$$H_{22} = \nu_{2002} + B_{2002}J(J+1) - D_{2002}[J(J+1)]^2,$$

$$H_{33} = \nu_{2110} + B_{211^e0}[J(J+1) - K^2] - D_{211^e0}[J(J+1) - K^2]^2,$$

$$H_{44} = \nu_{2110} + B_{211^f0}[J(J+1) - K^2] - D_{211^f0}[J(J+1) - K^2]^2,$$

$$H_{13} = H_{31} = \beta_{2100/211^e0} \sqrt{J(J+1)},$$

$$H_{23} = H_{32} = \beta_{2002/211^e0} \sqrt{J(J+1)}.$$

The diagonal elements correspond to the unperturbed energies of the Σ bend, van der Waals stretch overtone, and the e and f parity components of the Π bend. Off-diagonal elements proportional to $\sqrt{J(J+1)}$ couple the Π^e level with both the Σ bend and $n=2$ van der Waals stretch with fitted coefficients $\beta_{2100/211^e0}$ and $\beta_{2002/211^e0}$, respectively.

In the aforementioned analysis the Π^f state is assumed to be unperturbed since the nearest state of f parity is the (2111) Π bend plus van der Waals stretch predicted more than 30 cm^{-1} to higher energy. Hence, the Π^f and the deperturbed Π^e levels are constrained in the fit to share a common vibrational origin and rotational constant. Matrix diagonalization and least-squares fitting of the resulting eigenvalues yield the band origins and molecular constants shown in Table 3.3. The residual standard deviation of the fit, 0.00025 cm^{-1} , is comparable to the uncertainty of the measurements and signifies that the above four-level analysis sufficiently accounts for the observed interactions.

The deperturbed band origins for the Σ band and Π bend are 64.45 and 76.23 cm^{-1} above the (2000) origin, i.e., approximately 10% greater than the corresponding vibrations in the $\text{ArHF } v_{\text{HF}}=1$ manifold. These values are considerable higher than the $2B \approx 40 \text{ cm}^{-1}$ expected in the $j_{\text{HF}} = 1$ free rotor limit and reflect the magnitude of the angular anisotropy introduced by the Ar atom. The vibrational frequency of the $n=2$ van der Waals stretch is 77.20 cm^{-1} , again approximately 10% greater than in $\text{ArHF } v_{\text{HF}} = 1$, indicating an increase in the radial binding energy of the potential with HF excitation. In addition the rotational constants for these intermolecular bands are greater than for the corresponding vibrations in $\text{ArHF } v_{\text{HF}} = 1$, continuing the same trend noted for the (2000) level. As mentioned earlier, these results can be related to changes in the potential upon HF vibrational excitation as will be more fully addressed in Sec. 3.4.

We note that an alternate analysis which does not explicitly include this Coriolis coupling between all levels requires compensatory higher-order terms in centrifugal distortion to achieve the same quality of fit. However, an independent set of least-squares fits, in which Σ and Π bend Coriolis coupling is neglected and the Π^e and Π^f rotational constants are not constrained to be equal, yields an effective l -doubling constant of $q_l = -73.8(4)$ MHz. This can be simply related to the aforementioned matrix analysis from first-order perturbation theory [243], i.e.,

$$q_l = \frac{\beta^2}{E(\Sigma) - E(\Pi)} \quad (3.3)$$

From the results in Table 3.3, the coupling of the Σ and Π bend of $\beta=0.17 \text{ cm}^{-1}$ predicts the Σ bend to lie 11.7 cm^{-1} below the Π bend, in excellent agreement with the 11.8 cm^{-1} value observed experimentally.

3.4 Discussion

3.4.1 Overtone vibrational red shifts in ArHF

It is well known from matrix isolation studies that the environment surrounding an infrared chromophore can modify its vibrational energy level spacings [23]. Similarly, for van der Waals complexes, the single rare-gas atom "environment" can influence the intramolecular vibrational frequencies of the chromophore, and shift the transitions from those of the free monomer. For ArHF $\nu_{\text{HF}} = 1$, this shift is 9.65 cm^{-1} to the red, which increases nearly linearly to 20.91 cm^{-1} for overtone $\nu_{\text{HF}} = 2$ excitation. A similar behavior is also observed in N_2HF (Ref [129]), $(\text{HF})_2$ (Ref [346]), and $(\text{HCN})_2$ (Ref [268]) complexes, i.e., the redshift scales nearly linearly with the quanta of vibrational excitation. This behavior is qualitatively consistent with the simple physical picture of an oscillator with a shifted vibrational frequency and, hence, producing shifts in the transition frequency that scale linearly with the number of quanta.

More quantitatively, these redshifts signal a corresponding increase in dissociation energy upon vibrational excitation, and consequently the observed dependence indicates a nearly linear increase in D_0 for ArHF with ν_{HF} . Therefore, it should be possible to account for this linear redshift behavior by considering changes in the ArHF binding energy upon vibrational excitation using simple electrostatic arguments.

As determined by redshift calculations by Liu and Dykstra [238, 240] and recently extended to include large amplitude vibrational averaging by Hutson [190], the dominant dependence upon ν_{HF} excitation arises from changes in the induction energy, i.e.,

$$V_{\text{ind}} = -\frac{1}{2}\alpha_{\text{Ar}}|F|^2, \quad (3.4)$$

where α_{Ar} is the polarizability of the Ar and F is the electrical field induced at the Ar atom by the HF. In lowest order, changes in the induction term are dominated by the change in HF monomer dipole moment, which is known experimentally to increase near linearly with ν_{HF} . This in turn induces a dipole in the Ar atom,

$$\mu_{\nu_{\text{HF}}}^{\text{ind}} = \mu_0^{\text{ind}} + \xi \cdot \nu_{\text{HF}} = \alpha_{\text{Ar}} F \quad (3.5)$$

which also increases with ν_{HF} with proportionality constant ξ . Rearranging Eqs (3) and (4), one obtains

$$V_{\text{ind}} = -\frac{1}{2} \frac{(\mu_{\text{ind}}^2)}{\alpha_{\text{Ar}}} \approx -\frac{1}{2} \alpha_{\text{Ar}} [(\mu_{\text{ind}}^2) + 2\mu_0^{\text{ind}} \cdot \xi \cdot \nu_{\text{HF}}], \quad (3.6)$$

where terms of order ξ^2 and higher have been neglected. This simple treatment recovers the anticipated linear dependence of redshift on ν_{HF} .

Finally it should be noted that these redshift effects all scale with the projection of the HF dipole along the intermolecular axis and are further sensitive to averaging of the HF bend vibrational motion. This may begin to explain the slightly greater than linear increase in redshift with ν_{HF} , since the angular anisotropy of the ArHF potential also increases with ν_{HF} . This would tend to enhance the alignment of the HF along the intermolecular axis, effectively increasing the dipole-induced dipole effects even further.

3.4.2 Angular and radial potential-energy surface dependence on ν_{HF}

From the previous discussion of vibrational redshifts, one concludes that the dissociation energy of the complex increases with ν_{HF} . The question arises how this is apportioned between the angular and radial degrees of freedom.

The most direct probe of these effects is in the intermolecular vibrational frequencies, for which data now exist from $\nu_{\text{HF}} = 0, 1, \text{ and } 2$. The energies of the $(\nu_{\text{HF}}100)$ Σ bend, $(\nu_{\text{HF}}110)$ Π bend, and $(\nu_{\text{HF}}002)$ van der Waals stretch are displayed as a function of HF vibrational excitation in Figure 3.5. The strong increase in bend frequency with ν_{HF} , approximately $5\text{--}7\text{ cm}^{-1}$ per HF stretching quantum for both the Σ and Π bend levels, signals an increase in the angular anisotropy of the potential. There is also a similar rate of increase, roughly $5\text{--}6\text{ cm}^{-1}$ per quantum, in the $n=2$ van der Waals stretch energy with ν_{HF} .

The observed linear rate of increase with ν_{HF} for the bend and stretch vibrational frequencies follows from simple arguments, as presented earlier. Simply stated, if the vibrationally induced shifts in the intermolecular potential are small, then the leading term in the frequency shifts will in general be approximately linear in the perturbation. If the dominant ν_{HF} dependent perturbation of the potential is due to linear shifts in the electrostatic properties of HF with ν_{HF} , this would cleanly explain the experimental trends.

In addition to changes in intermolecular vibrational frequencies, information concerning the ν_{HF} dependence of the potential-energy surface can be obtained by examining the rotational constants of the various states. Figure 3.6 show a plot of how the rotational constants for the $(\nu_{\text{HF}}000)$, $(\nu_{\text{HF}}100)$ Σ bend, $(\nu_{\text{HF}}110)$ Π bend, and

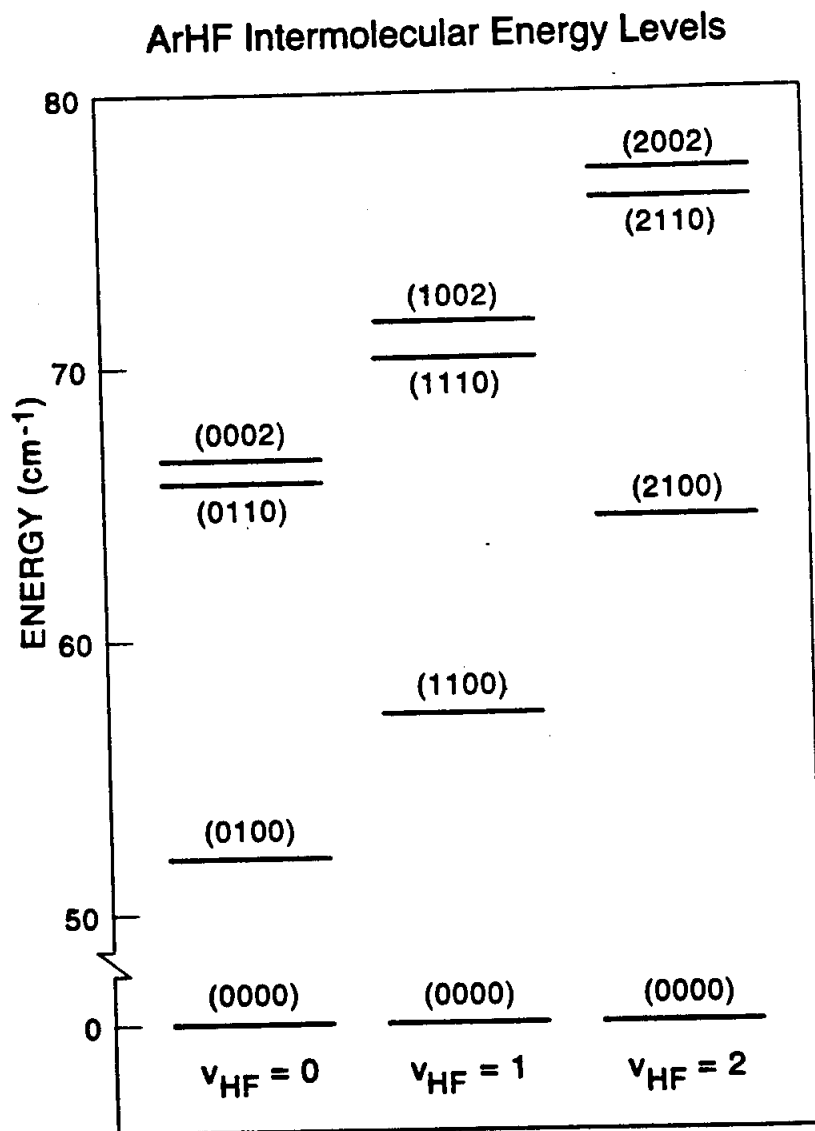


Figure 3.5: Energies of the ArHF Σ bend, Π bend, and doubly-excited van der Waals stretch vs quanta of stretch excitation in the HF. The increase in the bend/stretch energies with increasing ν_{HF} is a result of the increasing angular anisotropy and radial binding of the potential-energy surface.

($v_{\text{HF}}002$) van der Waals stretch scale with HF excitation. In each case B increases near linearly as a function of v_{HF} . Since the corresponding centrifugal distortion constants decrease with increasing v_{HF} , there is consistent evidence for a contraction of the complex and a deepening of the potential upon HF excitation.

However, closer examination of Figure 3.6 shows that the rate of increase for the rotational constants is not the same for all levels. For example, the rotational constant for the $n=2$ van der Waals stretch increases substantially faster than the ($v_{\text{HF}}000$) level. This behavior can be rationalized by the Dunham expression [356] $B_v = B_e(v_{vdW} + 1/2)$, in terms of which the slope in Figure 3.6 would be given by

$$\Delta B_v / \Delta v_{\text{HF}} = \Delta B_0 / \Delta v_{\text{HF}} - (\Delta \alpha_e / \Delta v_{\text{HF}})(v_{vdW}). \quad (3.7)$$

In Equation 3.7, the first term on the right-hand side reflects the contribution from the ($v_{\text{HF}}000$) level and the second term reflects the explicit contribution due to the $n=2$ van der Waals stretch excitation. From the Dunham expansion, $\alpha_e \approx B^2/\omega_e$, where ω_e is the equilibrium vibrational frequency. Since ω_e increases with v_{HF} , we expect α_e to decrease with v_{HF} . Consequently,

$$\Delta \alpha_e / \Delta v_{\text{HF}} < 0 \quad (3.8)$$

and the predicted slope in Equation 3.7 should be *greater* than that of the ($v_{\text{HF}}000$) level, in agreement with observation.

From a more quantitative perspective, these data can be incorporated into a fit of the potential surface which includes all intermolecular and intramolecular degrees of freedom. Hutson [190] has recently constructed such a potential by fitting all the data available for ArHF ($v_{\text{HF}} = 0, 1, \text{ and } 2$) and ArDF ($v_{\text{DF}} = 0 \text{ and } 1$) which accurately reproduces all the important spectroscopic features of these systems.

the Coriolis interaction. The eigenfunctions for the Σ and Π bends can be described in terms of the unperturbed states as

$$\begin{aligned}\psi_{\Sigma} &= a(J)\psi_{\Sigma^0} + b(J)\psi_{\Pi^0} \\ \psi_{\Pi} &= -b(J)\psi_{\Sigma^0} + a(J)\psi_{\Pi^0}\end{aligned}\tag{3.9}$$

with standard analytical expressions available in the two-state model for the J -dependent coefficients [170]. This mixing of the zero-order wave functions additionally mixes the transition dipole amplitudes for the R and P branches which, by quantum interference, can either enhance or diminish the observed rotational line strengths (for a detailed discussion, see Chapter 5 of reference [254]).

Since the rotational constants for the Σ bend, Π bend, and (2000) state are all very similar (< 3% difference), it is tempting to model these Coriolis effects on the transition intensities using an “internal” rotor analysis at fixed R . We note that these intensity anomalies are also well predicted in full three-dimensional (3D) quantum calculations for angular and radial intermolecular motion, which include the full angular-radial coupling explicitly. For the present discussion, however, we choose to forgo the 3D quantum calculations since a 2D angular analysis is much simpler, and already captures the essential physics of the Coriolis interaction.

Consistent with this, we calculate transition intensities with a Hamiltonian incorporating only angular terms, i.e.,

$$H = b_1 j^2 + b_2 l^2 + V(\theta)\tag{3.10}$$

Here b_1 and b_2 refer to the rotational constants for the diatom and complex, respectively, j^2 is the angular momentum for HF internal rotation, and l^2 is the end-over-end

angular momentum of the complex. Wave functions are determined in the $|JM_Jjl\rangle$ basis. The effective angular potential, $V(\theta)$, is represented as a Legendre expansion in $\cos(\theta)$, i.e.,

$$V(\theta) = \sum_n V_n P_n(\cos \Theta) \quad (3.11)$$

which greatly simplifies evaluation of the matrix elements. In the interest of simplicity, only terms up to V_2 are included. For $V_1 = -45 \text{ cm}^{-1}$ and $V_2 = -68 \text{ cm}^{-1}$, the Σ and Π bend frequencies are predicted to be 64.5 cm^{-1} and 76.2 cm^{-1} respectively, in excellent agreement with the experimentally determined values of 64.5 and 76.3 cm^{-1} . Diagonalization of this Hamiltonian matrix yields eigenvalues $E(v, J)$ and space fixed eigenvectors $\Psi = \sum_j C_{jl}^i |JM_Jjl\rangle$ for the (2000) and intermolecular bend states.

Transition intensities for the states are then calculated assuming laser polarization in the (space-fixed) z direction and a transition moment fixed collinear with the HF axis, i.e.,

$$I \propto |\langle J'M'_j j' l' | \mu_0 \cos(\theta) | JM_J j l \rangle|^2 \quad (3.12)$$

The calculated intensities are then weighted by Boltzmann factors consistent with the experimental temperature. The results of this calculation are presented in the Boltzmann plots shown in Figure 3.8. For the (2000) level, for which there are no significant Coriolis interactions, the corrected P and R branch intensities lie along lines of identical slope, indicating neither enhancement nor depletion of branch intensity over that predicted by population and standard Hönl-London factors. The calculated intensities, shown as solid lines in Figure 3.8, also have identical slopes and, therefore, are in very good agreement with experiment.

For the Σ and Π bend, however, the intensities of the P and R transitions lie along lines of different slopes. For the Π bend, the P branch curve lies below the

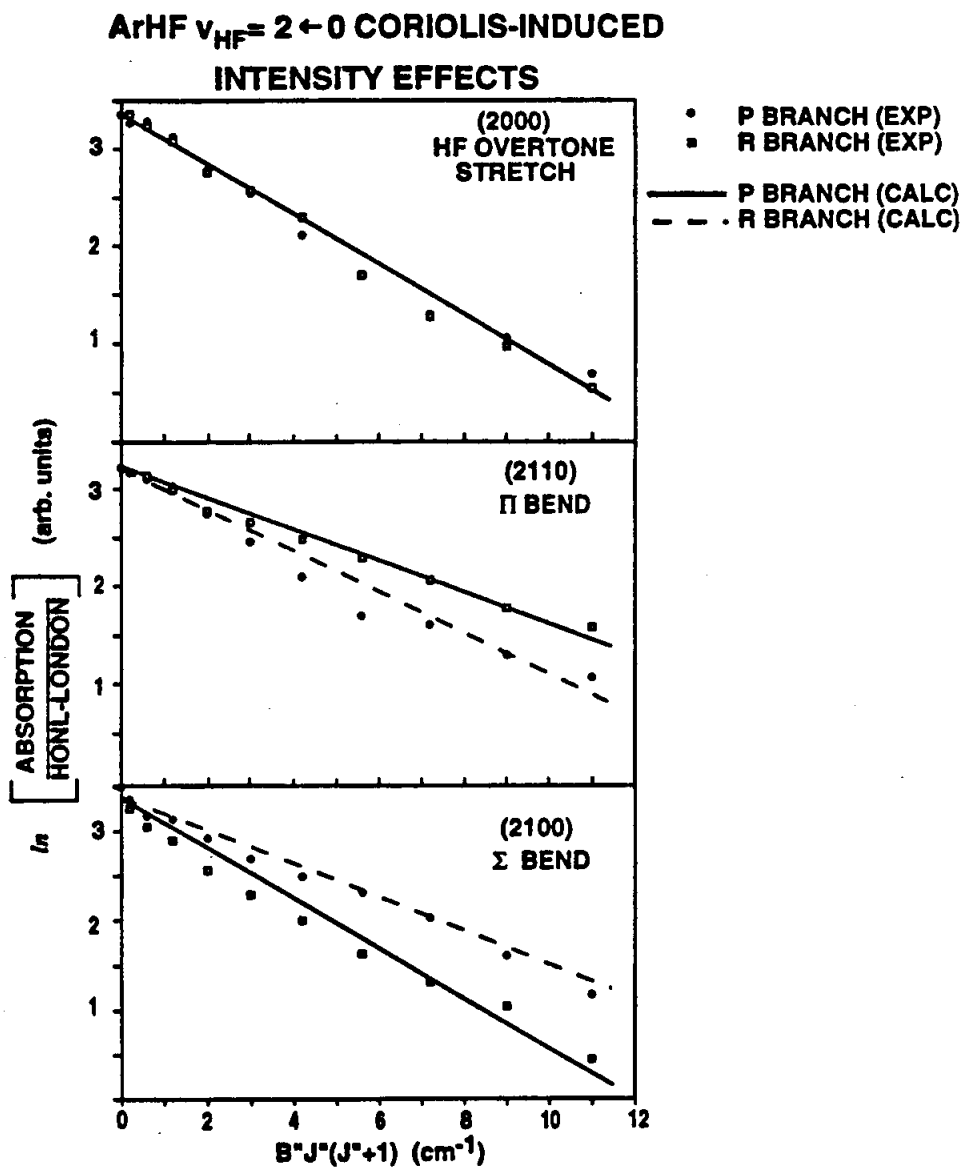


Figure 3.8: Boltzmann plots of the *P* and *R* branch intensities for the (2000) level, (2110) Π bend, and (2100) Σ bend. For the (2000) state, the normalized experimental data lie along lines of identical slope indicating no significant intensity perturbations. For the Π bend and Σ bend, however, a decreased slope is observed for the *P* and *R* branch, respectively, indicating that these branches have acquired additional intensity. In each case, however, a 2D Coriolis calculation described in the text (in solid lines) yield good agreement with observed intensities.

R branch, while for the Σ bend it is the *R* branch which is enhanced. However, these Coriolis mediated intensity effects in both Π and Σ bend transitions are accurately reproduced by the calculated intensities (solid lines in Figure 3.8), indicating that a 2D angular calculation is sufficient to interpret the observed intensity perturbation quantitatively.

3.4.4 Predissociation lifetimes in the ArHF ($v_{\text{HF}} = 2$) level

The existence of rotationally resolved overtone spectra for ArHF requires that the energy of overtone excitation of the HF (7800 cm^{-1}) remain localized in the intramolecular coordinate for a minimum of several hundred thousand vibrational periods before channeling into and rupturing the weak [$D_0 = 130 \text{ cm}^{-1}$ to form Ar + HF ($v = 2$)] intermolecular bond. An upper limit to these vibrational predissociation lifetimes can be assessed via analysis of the absorption line shapes from high-resolution scans over individual transitions. The resulting profiles are then fit to a Voigt profile in order to deconvolve the line shape into Gaussian and Lorentzian contributions. The Gaussian component arises from residual Doppler broadening from the expansion due to transverse velocity components along the optical axis. Saturation broadening of the overtone transitions are negligible at the $\leq 50 \mu\text{W}$ IR power levels used in these experiments, as is pressure broadening in the low-density expansion. Hence, any measurable Lorentzian component to the line shape can be ascribed to a predissociation broadening of the complex.

The results of the Voigt analysis of the pure overtone and combination band transitions reveal that the line shapes have a 79 (11) MHz Gaussian component with

only a statistically insignificant [0 (2) MHz] Lorentzian contribution. For a $\Delta\nu_{prediss} < 2$ MHz upper limit on the Lorentzian component, one can infer a strict 80 ns lower limit to the predissociation lifetime, although the actual predissociation lifetime may be orders of magnitude longer still.² It is worth emphasizing that the linewidths are the same for transitions to the (2000) level as for the intermolecular bend and $n = 2$ van der Waals stretch states, where an additional 55–70% of the necessary energy (i.e., 65–80 cm^{-1}), has already been deposited into the intermolecular dissociation coordinates.

This highly nonstatistical localization of intramolecular vibrational energy is not entirely surprising and was also observed for ArHF excited to $v_{\text{HF}} = 1$, as well as for all RG-HX complexes studied to date (see footnote 1, however). For ArHF $v_{\text{HF}} = 1$, the upper limit for the predissociation lifetime has been extended to > 600 μs [140], corresponding to several hundred million vibrations of the HF. The reasons for this extreme longevity have been discussed previously [275] and attributed to the difficulty of dissipating the excess energy into rotation and translation of the recoiling Ar and HF subunits.

Excitation to the overtone $v_{\text{HF}} = 2$ vibrational level in ArHF provides two vibrational predissociation channels energetically open, i.e., the HF can leave with either 0 or 1 quantum of vibrational excitation. The most resonant J rotational level energetically accessible to an outgoing HF ($v_{\text{HF}} = 1$) would be $J=13$ at 7495 cm^{-1} ,

²Block and Miller [35] have recently reported results from an IR-IR double resonance study of ArHF in $v_{\text{HF}}=2$. The bolometer signals for excitation to the (2000) level are *negative*, indicating that the predissociation lifetime is less than the molecular flight time (0.3 ms). The signals for excitation of the Σ and Π bends are positive, however, indicating that the lifetimes of these levels are > 0.3 ms. This interesting observation of longer lifetimes upon excitation of intermolecular vibrations is consistent with *ab initio* calculations by Tao and Klemperer [353] which predict a much greater coupling between the inter- and intramolecular coordinates at $\theta=0$ (i.e., the equilibrium orientation for the van der Waals ground state) than for nonlinear orientations (where the Σ and Π bend angular wavefunctions are peaked).

which would leave $\approx 100 \text{ cm}^{-1}$ for center-of-mass translation of the Ar and HF. Due to vibrational anharmonicity, the corresponding HF($v_{\text{HF}} = 0$) $J=13$ channel available to $v_{\text{HF}} = 1$ excited complexes is slightly more exothermic (150 cm^{-1}), which could, in principle, lead to a slightly faster dissociation rate for the $v_{\text{HF}} = 2$ complex. Similarly, the most resonant J rotational state available for HF($v = 0$) lies at 7515 cm^{-1} ($J = 19$), although given the vibrational longevity of $v_{\text{HF}} = 1$ complexes, relaxation resulting in a loss of two quanta of HF vibration would appear extremely unlikely. In all these scenarios, the large amount of angular momentum of the exiting HF must be balanced by orbital angular momentum of the outgoing pair, and requires high-order anisotropies in the intermolecular potential that are not physically reasonable at van der Waals separations.

It is instructive to compare these results to the predissociation dynamics of other weakly bound cluster excited to the first overtone of one of the subunits. The $2\nu_1$ "free" CH stretch spectra of $(\text{HCN})_2$ observed by Scoles and coworkers [268] also exhibit apparatus limited line shapes, and have been used to establish an upper limit of $90 \mu\text{s}$ for the predissociation lifetime of the complex. However, similar to the $v_{\text{HF}} = 1$ and $v_{\text{HF}} = 2$ excited ArHF complexes, predissociation line broadening was also undetectable in the corresponding ν_1 fundamental and, hence, comparison of the fundamental and overtone rates is not possible.

The only other complexes for which rotationally resolved spectra have been observed in the HF stretch overtone region are $(\text{HF})_2$ (Ref [346]) and N_2HF (Ref [129]) and for both complexes predissociation broadening has been detected which is approximately an order of magnitude greater than observed upon fundamental excitation. The fact that both complexes are formed from a diatom/diatom rather than

atom/diatom pair may facilitate the dissociation event due to the much greater density of open vibrational and rotational channels in the outgoing products. However, recent measurements of the CH stretch overtone of HCN-HF (Ref [211]) by Scoles and coworkers indicate only a twofold increase in predissociation lifetime for $2\nu_1$ vs ν_1 . This distribution of results emerging for different overtone excited species is quite intriguing and already suggests that mode specific vibrational dynamics play a key role in the predissociation event. Further studies on a variety of overtone excited systems will be clearly necessary to elucidate the underlying physics.

A natural extension of these studies would be to examine the predissociation dynamics of ArHF excited to even higher overtones of the HF. Although these transitions would be correspondingly weaker than those to the first overtone, the excitation energies for $\nu_{\text{HF}} = 3 \leftarrow 1$ and $\nu_{\text{HF}} = 4 \leftarrow 1$ begin to access the Ti:sapphire and dye laser regions of the spectrum and, hence, raise the possibility of even more sensitive detection schemes. Based on the present overtone studies of ArHF, we leave it as interesting speculation whether measurable predissociation would occur in these higher vibrational levels, or whether, as the $\nu_{\text{HF}} = 1$ and $\nu_{\text{HF}} = 2$ levels, they would remain extremely long lived Feshbach resonances.³

3.5 Summary

Direct infrared absorption has been used to record the spectra of ArHF excited to the first overtone of the HF stretch. In addition to the pure overtone

³Chang and Klemperer have indeed extended the study of ArHF to the $\nu_{\text{HF}} = 3$ manifold [69, 71] using LIF detection following excitation by a Ti:sapphire laser. No predissociation broadening has yet been observed, although dispersed fluorescence and two-photon techniques are planned to investigate the predissociation dynamics further.

(2000) \leftarrow (0000) band, three combination bands built upon the (2000) state are observed which provide new information on the radial and angular part of the Ar + HF ($v=2$) potential far from the equilibrium geometry. The large body of data which now available for the ArHF/DF complex has allowed the construction of an accurate potential which explicitly includes the dependence of both intermolecular and intramolecular degrees of freedom for the complex. The changes in the potential energy surface with HF vibrational excitation are discussed and several spectroscopic manifestations of an increased anisotropy and dissociation energy in the potential are noted. *R* and *P* branch intensity anomalies in the Σ and Π bends are observed and quantitatively attributed to rotationally mediated Coriolis interactions. Analysis of line shapes for $v=2$ transitions indicates apparatus limited Gaussian profiles with negligible predissociation broadening, which allows a lower limit of 80 ns to be assigned to the upper state lifetime.

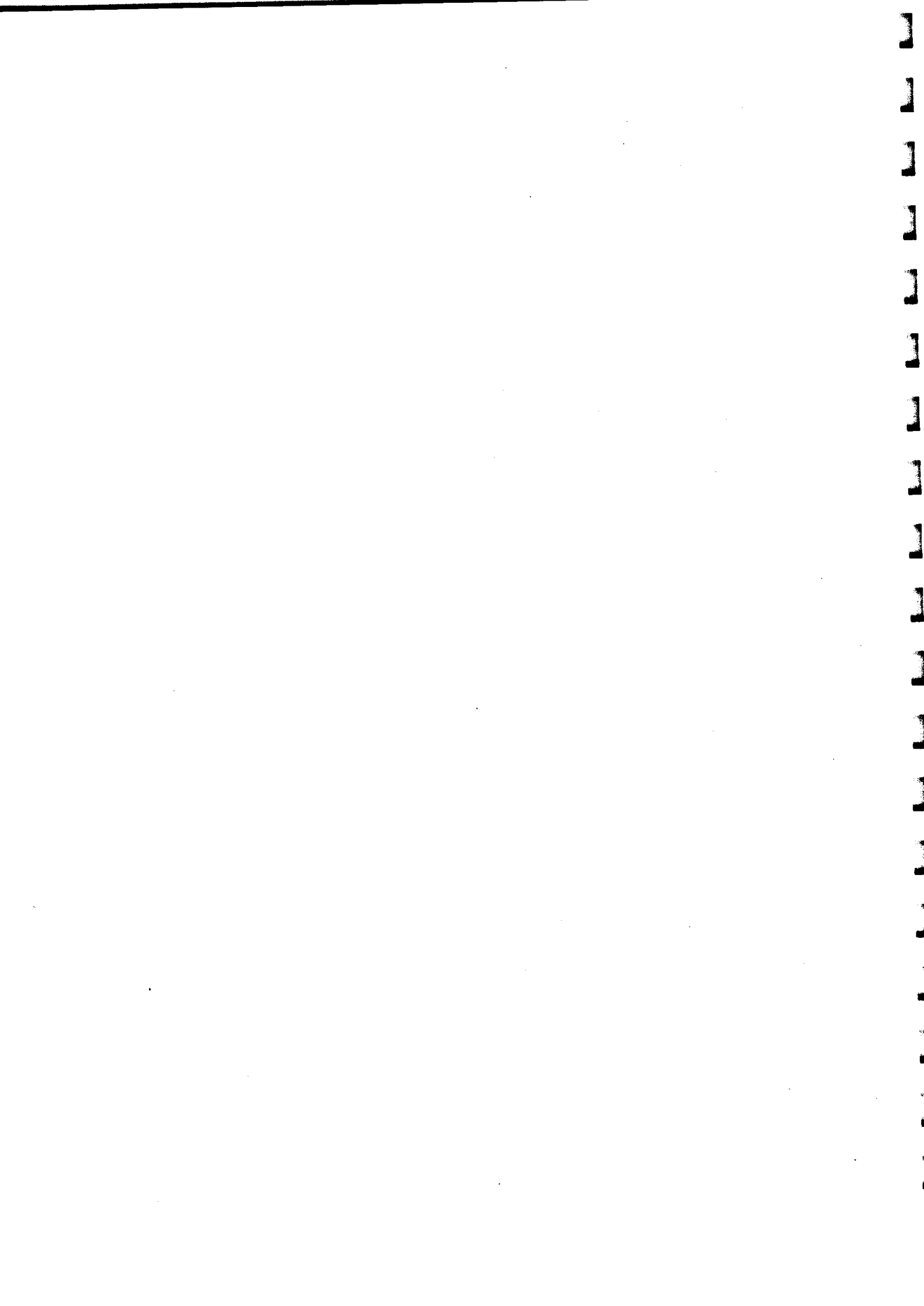


CHAPTER IV

Pairwise and nonpairwise additive forces in weakly bound complexes: High resolution infrared spectroscopy of Ar_nDF ($n = 1,2,3$)

4.1 Introduction

Although the kinetics and thermodynamics of solvation at the macroscopic level are reasonably well characterized, a more microscopic understanding at the quantum state level of detail has remained elusive. At the most basic level, potential energy surfaces capable of reproducing solute-solvent and solvent-solvent interactions to spectroscopic accuracy are extremely difficult to obtain. Secondly, even with such pair potentials, there is an incomplete knowledge about the importance and magnitude of nonpairwise additive (i.e. many body) terms in the full potentials. Finally, there are fundamental computational limitations for solving the full multidimensional dynamics even for a simple diatom solute with a few solvent molecules/atoms which renders most problems intractable. Attacking the problem of solvation and associated pairwise and nonpairwise additive terms by building up sequentially from smaller clusters of weakly bound species offers obvious advantages, though it is still a considerable theoretical challenge to pursue at the quantum state level for systems with even a few solvent species.



For weakly bound systems in which the requisite experimental data is available, semi-empirical methods have been quite successful at generating highly accurate potential surfaces. Traditionally, results from crossed molecular beam studies are used for modeling the repulsive wall, and bulk measurements such as virial coefficients, viscosity, thermal conductivity, and pressure broadening coefficients [260] have been used for the attractive region. Unfortunately, the bulk properties often involve substantial thermal averaging over quantum states, collision angles, and collision energies, which precludes a quantum state specific modeling of the interaction. Furthermore, nonpairwise additive contributions are often inextricably folded into the pair potentials extracted from these measurements. Although the use of these temperature and density dependent "effective" pair potentials greatly reduces the computational demands for liquid simulations, relatively little insight is gained from their form, and the numerical values cannot be extended easily even to closely related systems.

During the past decade, high resolution spectroscopy of weakly bound clusters has emerged as powerful alternative method for extracting information on the intermolecular potential, especially in the bound region ($E < D_0$). For a number of prototypical systems it has been possible to characterize a significant portion of the potential through the rotationally resolved study of intermolecular bending and stretching states. In addition, by exploiting the low temperatures and densities of supersonic expansions for cluster formation, these complexes can be formed and studied in an environment nearly free from external perturbations. During the past decade, the study of binary complexes has been an area of particularly active interest, both experimentally and theoretically. This is appropriate, since a detailed understanding of these dimer interactions is a necessary prerequisite before proceeding to larger

oligomers. The fruits of these numerous experimental and theoretical studies are potential energy surfaces for prototypical systems such as HF dimer [311], and complexes of rare gases with HF [190], HCl [188, 191], H₂ [229], H₂O [85] and NH₃ [328], which are sufficiently accurate for rigorous theoretical modeling of the structure and dynamics of larger complexes.

Investigations of van der Waals trimers and larger oligomers at rotational resolution are now possible as a result of impressive increases in experimental sensitivity in the microwave [150, 149, 152, 153, 154, 323, 155, 382], far-IR [112, 113, 114, 306], near-IR [265, 347, 136, 206], and visible [210, 232, 104, 156, 325] regions of the spectrum. For complexes in which the corresponding pair potentials are known accurately, properties such as rotational constants and vibrational frequencies can be compared to predictions based on calculations for pairwise additive potential energy surfaces, as first demonstrated on Ar₂HCl clusters by Saykally, Hutson and coworkers [112, 113, 114, 88]. Deviations between the observed and calculated values then highlight contributions due to nonpairwise additive, or three-body interactions. Although the study of three-body terms has a long history for atomic systems (see Ref.[115] for a recent review), little experimental data exists on the precise form or magnitude of these terms for molecular systems. Consequently, these studies provide the first quantitative probe of these nonpairwise additive terms, a crucial step towards describing larger solute-solvent interactions. Even though the corresponding theoretical analysis methods are quite demanding due to the number of internal degrees of freedom that must be treated self-consistently, there has recently been significant progress in this area [88, 117, 233].

Among the numerous weakly bound dimers that have been characterized experimentally, the rare gas-hydrogen halide complexes have arguably been studied in the

most detail. For example, complexes of the rare gases He-Xe with HF/DF, HCl/DCl, and HBr/DBr have been studied in the microwave [291, 164, 208, 18, 63, 209], far-IR [321, 107], and near-IR [178, 135, 252]. Within this group, ArHF/DF has emerged as the system about which the most spectroscopic information is available. The experimental data [164, 209, 107, 135, 103, 181, 243, 251, 128, 255, 69, 256] sample a significant region of the full three-dimensional potential energy surface for the lowest four HF vibrational levels of the ground electronic state. Hutson has constructed a potential energy surface [190] from the ArHF/DF data that is a function of all three internal degrees of freedom, i.e., the intermolecular bending and radial coordinates and the intramolecular vibrational coordinate (through the diatom mass reduced vibrational quantum number $\eta = (v + \frac{1}{2})/\sqrt{\mu_{\text{HF/DF}}}$). This potential, designated the H6(4,3,2), reproduces the data to near spectroscopic accuracy [190], as well as properties such as line shape parameters [147] for HF in a bath of Ar and rotationally inelastic scattering cross sections [74]. Additionally, the potential energy curve (1-D) for Ar-Ar is well known from extensive crossed beam and UV spectroscopic studies [14]. Thus, all contributions to the full potential energy surface are readily available for describing Ar_nHF clusters at the pairwise additive level.

With the pair potentials well determined, Ar_nHF/DF provides a particularly good system for studying the transformation to a more fully solvated complex. Additionally, rotationally resolved spectra for Ar_nHF/DF ($n \leq 4$) have already been reported in Fourier transform microwave studies by Gutowsky and coworkers [149, 150, 152, 153, 154], and infrared results have been reported for Ar_nHF ($n \leq 4$) by McLroy *et al.* [265] The present infrared study of Ar_nDF ($n=1-3$), therefore, allows comparison with the Ar_nHF complexes, probing the effects of isotopic substitution on

the structure and dynamics. Due to large amplitude motion, the changes induced by deuteration can have dramatic effects on the intermolecular dynamics. For instance, the zero-point librational motion of the hindered rotor is less in DF vs HF complexes, as indirectly evidenced by the vibrationally averaged angles of 32° and 41° between the diatom and van der Waals radial vectors for ArDF and ArHF, respectively [209]. The reduced zero point bending motion in the DF complexes leads to a stronger interaction (D_0 is $\approx 10\%$ larger for ArDF vs ArHF), and potentially greater coupling between the inter- and intramolecular degrees of freedom. Additionally, comparisons between theory and experiment for the equilibrium geometries of the complexes (shown for $n=1-3$ in Figure 4.1) and vibrational redshifts [267, 117, 233] provide critical tests of theoretical potentials. Furthermore, the spectroscopic data implicitly include the effects of nonpairwise interactions, and comparison with theoretical calculations using accurate pairwise potentials permits the *quantitative* determination of their sign and magnitude. Finally, near-IR excitation provides sufficient energy to rupture the intermolecular bonds; analysis of the rovibrational lineshapes can probe vibrational predissociation rates, and thereby provide dynamical information on coupling between the intermolecular and intramolecular degrees of freedom.

4.2 Experimental

Tunable 2–4 μm infrared light is generated via the difference frequency technique developed by Pine [296]. The output of a tunable ring dye laser (Rhodamine 6G) and a single frequency Ar^+ laser (514.5 nm) are rendered collinear, and focused into a $4 \times 4 \times 50$ mm LiNbO_3 crystal. The LiNbO_3 is housed in a temperature controlled

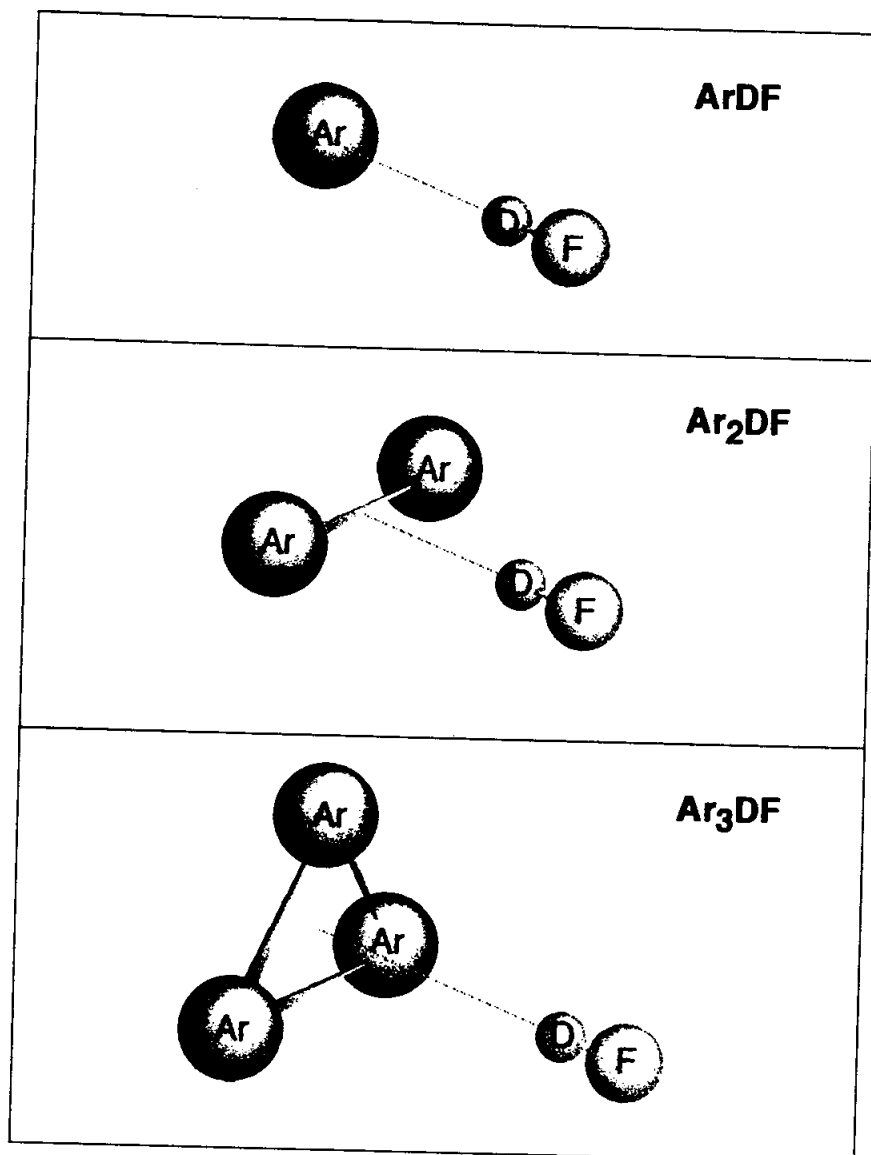
Ar_nDF EQUILIBRIUM GEOMETRIES

Figure 4.1: Pictorial representation of the equilibrium geometries for Ar_nDF , $n=1-3$.

oven, whose temperature is incremented synchronously with the scanning of the dye laser to preserve 90° , noncritical phase matching conditions. Upon exiting the oven, the infrared light is transmitted through a series of bandpass filters that reject the visible beams. The infrared light is split into a signal and reference beam, with the former probing the long axis of a supersonic expansion generated by a $4 \text{ cm} \times 190 \text{ }\mu\text{m}$ nozzle [247]. Ar_nDF complexes are formed by adiabatically expanding mixtures of DF (0.8% for ArDF and Ar_2DF , 0.5% for Ar_3DF) in a He/Ne/Ar buffer gas mixture, respectively, at a backing pressure of 600 torr. The buffer gas composition found to optimize the formation of the Ar_nDF complexes is a 50:50 mixture of Ar and "first-run" Ne (70% Ne, 30% He). Under these conditions, the relative populations (to within 20%) of $\text{ArDF}:\text{Ar}_2\text{DF}:\text{Ar}_3\text{DF}$ are 25:8:1 (for 0.8%DF) and 13:8:1 (0.5% DF). White cell optics are used to multipass the signal beam 20 times through the expansion for a total pathlength of 80 cm. Both the signal and reference beams are monitored with liquid N_2 cooled InSb photovoltaic detectors. The photocurrents from the detectors are amplified, filtered, and subtracted to eliminate common mode amplitude noise of the infrared light. The transient imbalance due to differential absorption is digitized, signal averaged, and stored as a function of laser frequency to yield the spectrum. Relative transition frequencies are referenced to P(15) of ArDF at $2895.0193 \text{ cm}^{-1}$ (Ref. [256]).

4.3 Results and Analysis

4.3.1 ArDF

A complete analysis of the ArDF $v_{DF}=1 \leftarrow 0$ fundamental spectrum, including 10 intermolecular bending and stretching states built upon $v_{DF}=1$, will be reported elsewhere [256], and only the results relevant to the current study will be described here. The spectrum of the $v_{DF} = 1 \leftarrow 0$ fundamental consists of a simple P/R branch structure characteristic of a $\Sigma \leftarrow \Sigma$ transition of a vibrationally averaged, linear molecule. This is consistent with the microwave results [209], from which a linear equilibrium geometry was inferred (see Figure 4.1). A section of the $v_{DF}=1 \leftarrow 0$ spectrum that includes the ArDF P branch is shown in Figure 4.2. The band origin is at $2897.6593(2) \text{ cm}^{-1}$ (Ref. [256]), i.e., 8.9656 cm^{-1} below the DF monomer rotationless origin of $2906.6609 \text{ cm}^{-1}$ (Ref. [254]). This redshift represents a 0.30% decrease in stretching energy of the DF, and is fractionally larger than the 9.6541 cm^{-1} ($\Delta\nu_{\text{redshift}}/\nu_0=0.24\%$) redshift reported for ArHF [251]. The magnitude of the redshift correlates with the change in binding energy of the complex upon DF vibrational excitation [179], and signifies a strengthening of the van der Waals intermolecular bond. Further evidence for a stronger intermolecular bond in the vibrationally excited state is provided by the fitted B rotational constant, which increases $+0.29\%$ upon vibrational excitation, signifying a decrease in the vibrationally averaged Ar-DF center of mass separation. The ArDF data have been incorporated with the extensive body of data collected for ArHF in the construction of Hutson's H6(4,3,2) semi-empirical potential energy surface for ArDF/HF [190], which has been used in calculations of the structure and dynamics of the larger $\text{Ar}_n\text{DF}/\text{HF}$ complexes as discussed in more detail below.

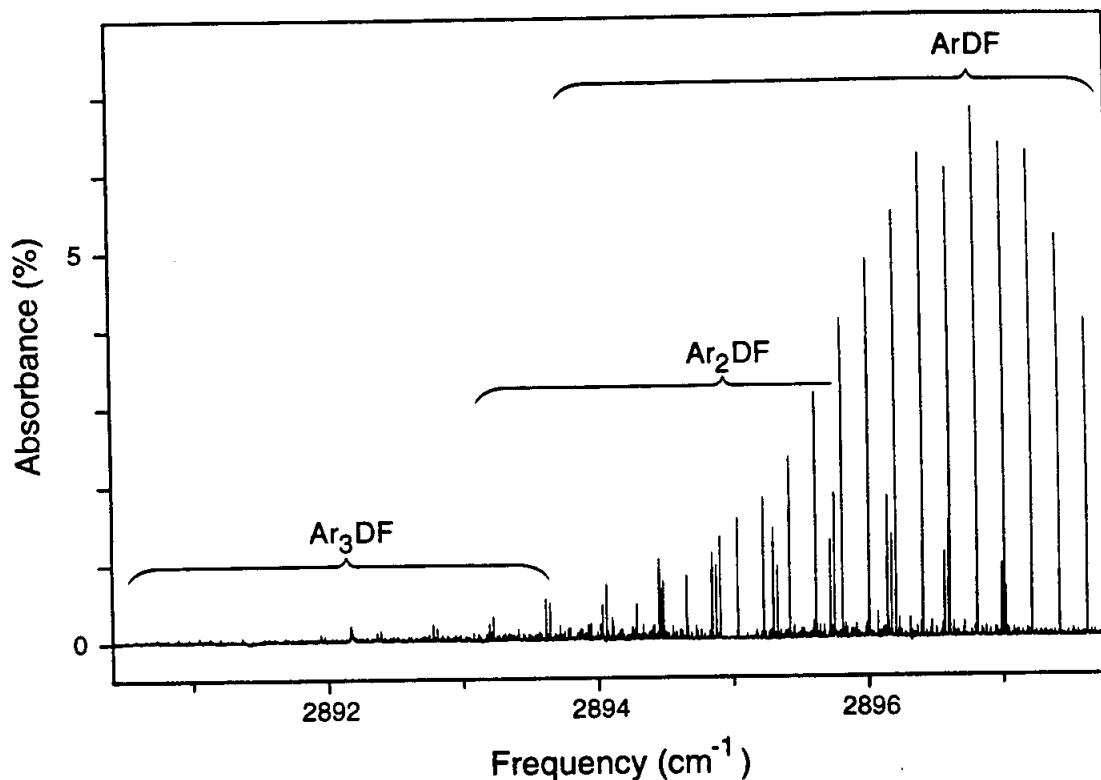
Ar_nDF ($n=1-3$) $\nu_{\text{DF}} = 1 \leftarrow 0$ Overview Spectrum


Figure 4.2: Overview scan of the region to the red of the ArDF origin near 2898 cm^{-1} . The strong regular progression is the P branch of ArDF, while the regular doublet progression with approximately one-third the ArDF intensity is due to ν_1 , $K = 1 \leftarrow 0$ P branch transitions of $(\text{DF})_2$. The weak spectral structure centered near 2895 cm^{-1} is due to P and R branch transitions of Ar₂DF. The DF lies along the intermediate (B) principle axis of the complex, and for the b -type transition observed there is no central Q branch; this is apparent as a null gap near 2895 cm^{-1} . The feature near 2892.2 cm^{-1} is the Q branch of Ar₃DF, whose P branch transitions can be seen readily in the figure extending towards lower frequency.

4.3.2 Ar₂DF

As with our observation of Ar_nHF complexes [265], the larger clusters of Ar with DF were first observed as "contaminants" in the spectrum of the ArHF/DF dimer. This is evident in Figure 4.2 as excess spectral structure between 2893–2897 cm⁻¹. Figure 4.3 shows an expanded region around P(18) of ArDF; the shaded peaks are due to $\nu_{DF} = 1 \leftarrow 0$ transitions of ArDF and $\nu_1, K = 1 \leftarrow 0$ transitions of (DF)₂ [299], and have been suppressed for clarity. The observation of spectroscopic transitions with expansion gas mixtures containing only DF and rare gas diluent implies that this structure is due to transitions of Ar_n(DF)_m ($n, m \geq 2$) complexes. The dense rotational structure evident in Figure 4.3 is consistent with a vibrationally averaged, asymmetric top, qualitatively similar in appearance to the $\nu_{HF} = 1 \leftarrow 0$ transition of Ar₂HF [265]. From a previous analysis by Gutwosky and coworkers [153], the equilibrium geometry of the complex is inferred to be *T*-shaped, with the DF lying along a C₂ symmetry axis (see Figure 4.1). Assignment of the observed near-IR transitions to $\nu_{DF} = 1 \leftarrow 0$ of Ar₂DF is readily verified using combination differences incorporating the previously determined ground state constants [153].

The equilibrium location of the DF lies along the intermediate (B) principle axis of Ar₂DF, and thus the rovibrational spectrum contains *b* - type transitions (i.e., $\Delta K_a, \Delta K_c = \pm 1, \pm 3$, etc.). The presence of two equivalent Ar atoms with spin $I = 0$ constrains the available quantum states by Bose-Einstein statistics, i.e., the overall wavefunction must be symmetric with respect to exchange of the identical nuclei. By virtue of this constraint and the symmetry properties of the full Hamiltonian [146],

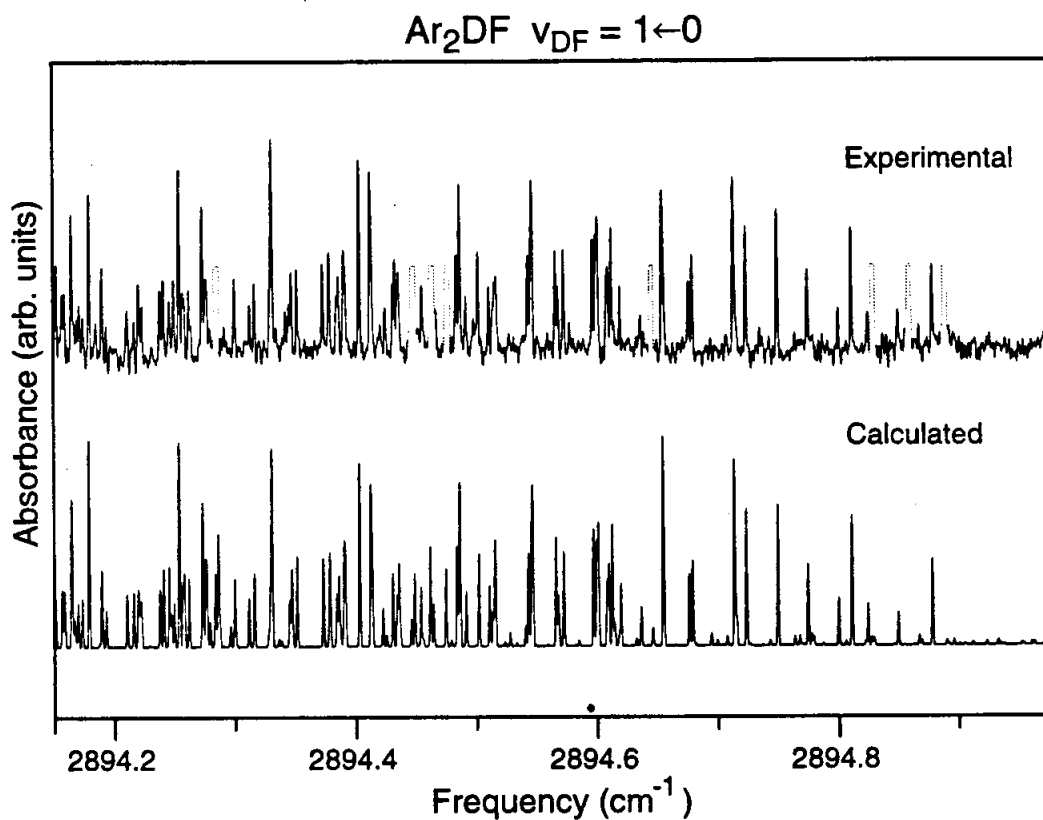


Figure 4.3: Experimental and calculated spectra for Ar_2DF near the band origin. The latter is generated using the constants listed in Table 4.2, obtained from a least squares fit of the experimental data. The shaded peaks in the experimental spectrum are transitions of ArDF and $(\text{DF})_2$, and have been suppressed for clarity.

only $K_a K_c = ee$ or oo states have non-zero statistical weights in the ground vibrational state. The observed transition frequencies are listed in Table 4.1. The infrared data are combined with the microwave data of Gutowsky *et al.* [153], weighted by the inverse square of the measurement uncertainty, and fit simultaneously to a Watson A-reduction Hamiltonian using the I' representation [369]. The quality of the fit is maximized by constraining the diagonal sextic distortion terms Φ_{JK} , Φ_{KJ} , and Φ_K to be the same for both the ground and vibrationally excited state. As was observed in the microwave analysis [153], inclusion of the sextic distortion term diagonal in J (i.e., Φ_J in the A-reduction Hamiltonian) decreases the quality of the fit, and consequently is omitted. The results from the fit are included in Table 4.2. A comparison of the experimental data with a simulated spectrum generated using the constants from the fit is shown in Figure 4.3, corroborating the assignment and demonstrating the excellent numerical agreement achieved. It is worth stressing, however, that a good spectral fit to a perturbatively corrected asymmetric rotor Hamiltonian is simply a very useful zeroth order characterization of rotational energy level patterns and does not in itself imply rigidity of the molecular framework.

The band origin is $2894.98439(3) \text{ cm}^{-1}$, i.e., redshifted 11.677 cm^{-1} from the uncomplexed DF origin. This is only 25% larger than the 8.696 cm^{-1} redshift for the first Ar atom in ArDF, indicating a highly nonlinear dependence of the redshift on n . The rotational constants increase slightly ($\approx 0.15\%$) upon vibrational excitation, consistent with a slight contraction in the vibrationally averaged geometry upon intramolecular excitation. These effects are quite similar to the behavior observed for Ar_2HF (Ref [265]), as well as ArDF/HF (Ref [256, 251]).

Table 4.1: Observed transition frequencies for the $\nu_{DF} = 1 \leftarrow 0$ transition in Ar_2DF .

$J'_{K'_a, K'_c}$	\leftarrow	J_{K_a, K_c}	Energy	$J'_{K'_a, K'_c}$	\leftarrow	J_{K_a, K_c}	Energy
0 _{0,0}	\leftarrow	1 _{1,1}	2894.8291(4)	5 _{4,2}	\leftarrow	4 _{3,1}	2895.9507(2)
1 _{1,1}	\leftarrow	0 _{0,0}	2895.1403(3)	5 _{4,2}	\leftarrow	5 _{3,3}	2895.4616(0)
1 _{1,1}	\leftarrow	2 _{0,2}	2894.8542(2)	5 _{4,2}	\leftarrow	6 _{5,1}	2893.7901(0)
1 _{1,1}	\leftarrow	2 _{2,0}	2894.5715(2)	5 _{5,1}	\leftarrow	4 _{4,0}	2896.0892(-1)
2 _{0,2}	\leftarrow	1 _{1,1}	2895.1152(1)	6 _{0,6}	\leftarrow	5 _{1,5}	2895.4840(1)
2 _{0,2}	\leftarrow	2 _{1,1}	2894.8826(1)	6 _{1,5}	\leftarrow	5 _{2,4}	2895.4968(0)
2 _{0,2}	\leftarrow	3 _{1,3}	2894.6832(2)	6 _{1,5}	\leftarrow	6 _{0,6}	2895.3631(2)
2 _{1,1}	\leftarrow	2 _{0,2}	2895.0870(0)	6 _{1,5}	\leftarrow	6 _{2,4}	2894.7537(0)
2 _{1,1}	\leftarrow	2 _{2,0}	2894.8046(3)	6 _{2,4}	\leftarrow	6 _{1,5}	2895.2219(0)
2 _{1,1}	\leftarrow	3 _{2,2}	2894.5185(1)	6 _{2,4}	\leftarrow	6 _{3,3}	2894.7277(2)
2 _{2,0}	\leftarrow	2 _{1,1}	2895.1657(1)	6 _{2,4}	\leftarrow	7 _{3,5}	2894.0804(-2)
2 _{2,0}	\leftarrow	3 _{3,1}	2894.3541(2)	6 _{3,3}	\leftarrow	6 _{2,4}	2895.2488(0)
3 _{1,3}	\leftarrow	2 _{0,2}	2895.2868(1)	6 _{3,3}	\leftarrow	7 _{4,4}	2893.8573(2)
3 _{1,3}	\leftarrow	4 _{0,4}	2894.6584(-5)	6 _{4,2}	\leftarrow	5 _{3,3}	2896.0585(1)
3 _{2,2}	\leftarrow	2 _{1,1}	2895.4522(2)	6 _{4,2}	\leftarrow	6 _{3,3}	2895.4289(3)
3 _{2,2}	\leftarrow	4 _{3,1}	2894.2428(-1)	6 _{4,2}	\leftarrow	6 _{5,1}	2894.3870(1)
3 _{3,1}	\leftarrow	2 _{2,0}	2895.6170(-2)	6 _{4,2}	\leftarrow	7 _{5,3}	2893.6960(1)
3 _{3,1}	\leftarrow	4 _{4,0}	2894.1190(3)	6 _{5,1}	\leftarrow	5 _{4,2}	2896.1881(0)
4 _{0,4}	\leftarrow	3 _{1,3}	2895.3119(1)	6 _{5,1}	\leftarrow	7 _{6,2}	2893.5596(0)
4 _{0,4}	\leftarrow	4 _{1,3}	2894.7789(1)	6 _{6,0}	\leftarrow	5 _{5,1}	2896.3241(0)
4 _{0,4}	\leftarrow	5 _{1,5}	2894.5499(-1)	6 _{6,0}	\leftarrow	7 _{7,1}	2893.4261(-2)
4 _{1,3}	\leftarrow	3 _{2,2}	2895.2524(5)	7 _{1,7}	\leftarrow	6 _{0,6}	2895.5693(3)
4 _{1,3}	\leftarrow	4 _{0,4}	2895.1931(4)	7 _{1,7}	\leftarrow	7 _{2,6}	2894.4947(2)
4 _{1,3}	\leftarrow	4 _{2,2}	2894.8154(1)	7 _{1,7}	\leftarrow	8 _{0,8}	2894.3333(1)
4 _{1,3}	\leftarrow	5 _{2,4}	2894.3945(3)	7 _{2,6}	\leftarrow	6 _{1,5}	2895.6880(2)
4 _{2,2}	\leftarrow	4 _{1,3}	2895.1568(0)	7 _{2,6}	\leftarrow	7 _{3,5}	2894.5465(0)
4 _{2,2}	\leftarrow	4 _{3,1}	2894.6803(1)	7 _{2,6}	\leftarrow	8 _{1,7}	2894.2754(-2)
4 _{2,2}	\leftarrow	5 _{3,3}	2894.1915(1)	7 _{3,5}	\leftarrow	6 _{2,4}	2895.8968(1)
4 _{4,0}	\leftarrow	3 _{3,1}	2895.8550(3)	7 _{3,5}	\leftarrow	7 _{2,6}	2895.4316(1)
4 _{4,0}	\leftarrow	4 _{3,1}	2895.4574(1)	7 _{3,5}	\leftarrow	7 _{4,4}	2894.5050(0)
4 _{4,0}	\leftarrow	5 _{5,1}	2893.8872(-1)	7 _{3,5}	\leftarrow	8 _{4,4}	2893.6841(-1)
5 _{1,5}	\leftarrow	4 _{0,4}	2895.4219(0)	7 _{4,4}	\leftarrow	6 _{3,3}	2896.1212(-2)
5 _{1,5}	\leftarrow	5 _{2,4}	2894.6231(-2)	7 _{4,4}	\leftarrow	7 _{3,5}	2895.4743(-1)
5 _{1,5}	\leftarrow	6 _{0,6}	2894.4897(3)	7 _{4,4}	\leftarrow	7 _{5,3}	2894.3886(-1)
5 _{2,4}	\leftarrow	4 _{1,3}	2895.5784(-1)	7 _{4,4}	\leftarrow	8 _{5,3}	2893.5941(-2)
5 _{2,4}	\leftarrow	5 _{1,5}	2895.3499(1)	7 _{5,3}	\leftarrow	6 _{4,2}	2896.2843(0)
5 _{2,4}	\leftarrow	5 _{3,3}	2894.6127(-4)	7 _{5,3}	\leftarrow	8 _{6,2}	2893.4635(2)
5 _{2,4}	\leftarrow	6 _{3,3}	2893.9838(5)	7 _{6,2}	\leftarrow	6 _{5,1}	2896.4227(0)
5 _{3,3}	\leftarrow	4 _{2,2}	2895.7821(-1)	7 _{6,2}	\leftarrow	7 _{5,3}	2895.7317(-1)
5 _{3,3}	\leftarrow	5 _{2,4}	2895.3612(0)	7 _{6,2}	\leftarrow	8 _{7,1}	2893.3298(-1)
5 _{3,3}	\leftarrow	5 _{4,2}	2894.5139(-1)	7 _{7,1}	\leftarrow	8 _{8,0}	2893.1973(-1)
5 _{3,3}	\leftarrow	6 _{4,2}	2893.9179(-2)	8 _{0,8}	\leftarrow	7 _{1,7}	2895.6439(2)

$J'_{K'_a, K'_c}$	\leftarrow	J_{K_a, K_c}	Energy	$J'_{K'_a, K'_c}$	\leftarrow	J_{K_a, K_c}	Energy
8 _{0,8}	\leftarrow	9 _{1,9}	2894.2561(1)	10 _{1,9}	\leftarrow	10 _{2,8}	2894.4154(3)
8 _{1,7}	\leftarrow	7 _{2,6}	2895.7030(1)	10 _{1,9}	\leftarrow	11 _{2,10}	2894.0246(-1)
8 _{1,7}	\leftarrow	8 _{0,8}	2895.5415(0)	10 _{1,9}	\leftarrow	9 _{2,8}	2895.8758(1)
8 _{1,7}	\leftarrow	8 _{2,6}	2894.6031(0)	10 _{2,8}	\leftarrow	10 _{3,7}	2894.6046(0)
8 _{1,7}	\leftarrow	9 _{2,8}	2894.1663(1)	10 _{2,8}	\leftarrow	11 _{3,9}	2893.9113(1)
8 _{2,6}	\leftarrow	7 _{3,5}	2895.6485(6)	10 _{2,8}	\leftarrow	9 _{3,7}	2895.9014(-1)
8 _{2,6}	\leftarrow	8 _{1,7}	2895.3769(-1)	10 _{3,7}	\leftarrow	10 _{2,8}	2895.3822(0)
8 _{2,6}	\leftarrow	8 _{3,5}	2894.7175(1)	10 _{3,7}	\leftarrow	11 _{4,8}	2893.6866(-1)
8 _{2,6}	\leftarrow	9 _{3,7}	2894.0006(-5)	10 _{3,7}	\leftarrow	9 _{4,6}	2895.7632(-2)
8 _{3,5}	\leftarrow	8 _{2,6}	2895.2635(-1)	10 _{4,6}	\leftarrow	10 _{3,7}	2895.3297(0)
8 _{3,5}	\leftarrow	8 _{4,4}	2894.6161(0)	10 _{4,6}	\leftarrow	11 _{5,7}	2893.4025(-2)
8 _{3,5}	\leftarrow	9 _{4,6}	2893.7472(0)	10 _{4,6}	\leftarrow	9 _{3,7}	2896.6267(1)
8 _{4,4}	\leftarrow	7 _{3,5}	2896.2965(0)	10 _{5,5}	\leftarrow	10 _{4,6}	2895.5025(-1)
8 _{4,4}	\leftarrow	8 _{3,5}	2895.3659(0)	10 _{5,5}	\leftarrow	11 _{6,6}	2893.1921(0)
8 _{4,4}	\leftarrow	9 _{5,5}	2893.5230(1)	10 _{5,5}	\leftarrow	9 _{4,6}	2896.6079(1)
8 _{5,3}	\leftarrow	7 _{4,4}	2896.3882(0)	10 _{6,4}	\leftarrow	11 _{7,5}	2893.0448(-1)
8 _{5,3}	\leftarrow	9 _{6,4}	2893.3691(-2)	10 _{7,3}	\leftarrow	11 _{8,4}	2892.9104(0)
8 _{6,2}	\leftarrow	9 _{7,3}	2893.2338(-1)	10 _{7,3}	\leftarrow	9 _{6,4}	2896.8541(-2)
8 _{7,1}	\leftarrow	7 _{6,2}	2896.6576(1)	10 _{8,2}	\leftarrow	11 _{9,3}	2892.7784(0)
8 _{7,1}	\leftarrow	9 _{8,2}	2893.1013(1)	10 _{8,2}	\leftarrow	9 _{7,3}	2896.9905(-1)
8 _{8,0}	\leftarrow	7 _{7,1}	2896.7930(-1)	10 _{9,1}	\leftarrow	11 _{10,2}	2892.6478(1)
8 _{8,0}	\leftarrow	9 _{9,1}	2892.9695(-1)	10 _{9,1}	\leftarrow	9 _{8,2}	2897.1260(0)
9 _{1,9}	\leftarrow	10 _{0,10}	2894.1809(1)	10 _{10,0}	\leftarrow	11 _{11,1}	2892.5181(0)
9 _{2,8}	\leftarrow	8 _{1,7}	2895.8146(0)	10 _{10,0}	\leftarrow	9 _{9,1}	2897.2608(0)
9 _{2,8}	\leftarrow	9 _{1,9}	2895.6335(1)	11 _{1,11}	\leftarrow	10 _{0,10}	2895.8792(0)
9 _{3,7}	\leftarrow	8 _{2,6}	2895.9810(0)	11 _{1,11}	\leftarrow	12 _{0,12}	2894.0296(-1)
9 _{3,7}	\leftarrow	9 _{2,8}	2895.5442(1)	11 _{2,10}	\leftarrow	10 _{1,9}	2895.9615(0)
9 _{3,7}	\leftarrow	9 _{4,6}	2894.4648(1)	11 _{2,10}	\leftarrow	11 _{3,9}	2894.3022(0)
9 _{4,6}	\leftarrow	10 _{5,5}	2893.3798(-3)	11 _{3,9}	\leftarrow	10 _{2,8}	2896.0769(1)
9 _{4,6}	\leftarrow	8 _{3,5}	2896.2361(0)	11 _{3,9}	\leftarrow	11 _{4,8}	2894.3810(-3)
9 _{4,6}	\leftarrow	9 _{3,7}	2895.5199(1)	11 _{3,9}	\leftarrow	12 _{2,10}	2893.8909(6)
9 _{5,5}	\leftarrow	10 _{6,4}	2893.2709(-4)	11 _{4,8}	\leftarrow	10 _{3,7}	2896.3027(1)
9 _{5,5}	\leftarrow	8 _{4,4}	2896.4623(2)	11 _{4,8}	\leftarrow	11 _{3,9}	2895.6093(1)
9 _{6,4}	\leftarrow	10 _{7,3}	2893.1385(0)	11 _{4,8}	\leftarrow	11 _{5,7}	2894.3756(-1)
9 _{6,4}	\leftarrow	8 _{5,3}	2896.6178(-1)	11 _{4,8}	\leftarrow	12 _{5,7}	2893.0986(-1)
9 _{7,3}	\leftarrow	10 _{8,2}	2893.0053(-2)	11 _{6,6}	\leftarrow	10 _{5,5}	2896.8010(-1)
9 _{8,2}	\leftarrow	10 _{9,1}	2892.8736(-2)	11 _{6,6}	\leftarrow	12 _{7,5}	2892.9497(2)
9 _{8,2}	\leftarrow	8 _{7,1}	2896.8920(1)	11 _{7,5}	\leftarrow	10 _{6,4}	2896.9510(-1)
9 _{9,1}	\leftarrow	10 _{10,0}	2892.7431(-1)	11 _{7,5}	\leftarrow	12 _{8,4}	2892.8159(0)
9 _{9,1}	\leftarrow	8 _{8,0}	2897.0271(0)	11 _{8,4}	\leftarrow	10 _{7,3}	2897.0887(-2)
10 _{0,10}	\leftarrow	9 _{1,9}	2895.8008(1)	11 _{8,4}	\leftarrow	12 _{9,3}	2892.6834(0)
10 _{0,10}	\leftarrow	11 _{1,11}	2894.1051(1)	11 _{9,3}	\leftarrow	10 _{8,2}	2897.2245(-2)

$J'_{K'_a, K'_c}$	\leftarrow	J_{K_a, K_c}	Energy	$J'_{K'_a, K'_c}$	\leftarrow	J_{K_a, K_c}	Energy
11 _{9,3}	\leftarrow	12 _{10,2}	2892.5525(-1)	14 _{2,12}	\leftarrow	15 _{3,13}	2893.6479(2)
11 _{11,1}	\leftarrow	10 _{10,0}	2897.4942(2)	14 _{3,11}	\leftarrow	13 _{4,10}	2896.3117(3)
11 _{11,1}	\leftarrow	12 _{12,0}	2892.2946(0)	14 _{6,8}	\leftarrow	13 _{5,9}	2897.1778(4)
12 _{0,12}	\leftarrow	11 _{1,11}	2895.9574(0)	14 _{7,7}	\leftarrow	13 _{6,8}	2897.2489(1)
12 _{1,11}	\leftarrow	11 _{2,10}	2896.0360(-1)	14 _{7,7}	\leftarrow	14 _{6,8}	2895.7965(1)
12 _{1,11}	\leftarrow	13 _{2,12}	2893.8767(0)	14 _{7,7}	\leftarrow	15 _{8,8}	2892.5427(1)
12 _{2,10}	\leftarrow	11 _{3,9}	2896.1010(1)	14 _{8,6}	\leftarrow	15 _{9,7}	2892.4034(2)
12 _{2,10}	\leftarrow	12 _{1,11}	2895.7520(1)	14 _{9,5}	\leftarrow	13 _{8,6}	2897.5187(-2)
12 _{3,9}	\leftarrow	12 _{4,8}	2894.6005(0)	14 _{9,5}	\leftarrow	15 _{10,6}	2892.2709(4)
12 _{3,9}	\leftarrow	13 _{4,10}	2893.6322(-1)	14 _{10,4}	\leftarrow	13 _{9,5}	2897.6550(-1)
12 _{5,7}	\leftarrow	12 _{6,6}	2894.3495(0)	14 _{12,2}	\leftarrow	13 _{11,3}	2897.9240(-2)
12 _{6,6}	\leftarrow	11 _{5,7}	2896.9259(1)	15 _{1,15}	\leftarrow	14 _{0,14}	2896.1932(2)
12 _{6,6}	\leftarrow	13 _{7,7}	2892.8654(0)	15 _{1,15}	\leftarrow	16 _{0,16}	2893.7294(-5)
12 _{7,5}	\leftarrow	11 _{6,6}	2897.0498(-1)	15 _{2,14}	\leftarrow	16 _{1,15}	2893.6534(2)
12 _{8,4}	\leftarrow	11 _{7,5}	2897.1867(-2)	15 _{3,13}	\leftarrow	14 _{2,12}	2896.3550(3)
12 _{8,4}	\leftarrow	13 _{9,5}	2892.5892(1)	15 _{3,13}	\leftarrow	16 _{2,14}	2893.5769(3)
12 _{9,3}	\leftarrow	13 _{10,4}	2892.4578(-2)	15 _{4,12}	\leftarrow	14 _{3,11}	2896.4623(-4)
12 _{9,3}	\leftarrow	11 _{8,4}	2897.3229(-3)	15 _{4,12}	\leftarrow	16 _{3,13}	2893.5091(4)
12 _{10,2}	\leftarrow	11 _{9,3}	2897.4583(-1)	15 _{6,10}	\leftarrow	14 _{5,9}	2897.0146(7)
12 _{10,2}	\leftarrow	13 _{11,3}	2892.3284(1)	15 _{8,8}	\leftarrow	14 _{7,7}	2897.4719(0)
12 _{11,1}	\leftarrow	11 _{10,2}	2897.5929(1)	15 _{9,7}	\leftarrow	14 _{8,6}	2897.6156(2)
12 _{11,1}	\leftarrow	13 _{12,2}	2892.2000(1)	15 _{12,4}	\leftarrow	14 _{11,3}	2898.0224(-3)
12 _{12,0}	\leftarrow	11 _{11,1}	2897.7269(2)	16 _{1,15}	\leftarrow	15 _{2,14}	2896.3506(-4)
12 _{12,0}	\leftarrow	13 _{13,1}	2892.0728(0)	16 _{1,15}	\leftarrow	17 _{2,16}	2893.5790(1)
13 _{1,13}	\leftarrow	12 _{0,12}	2896.0360(1)	16 _{2,14}	\leftarrow	17 _{3,15}	2893.5017(4)
13 _{1,13}	\leftarrow	14 _{0,14}	2893.8793(-1)	16 _{3,13}	\leftarrow	17 _{4,14}	2893.4164(8)
13 _{2,12}	\leftarrow	12 _{1,11}	2896.1159(0)	17 _{1,17}	\leftarrow	16 _{0,16}	2896.3506(1)
13 _{2,12}	\leftarrow	14 _{1,13}	2893.8026(1)	17 _{1,17}	\leftarrow	18 _{0,18}	2893.5809(-4)
13 _{3,11}	\leftarrow	12 _{2,10}	2896.2062(2)	17 _{2,16}	\leftarrow	16 _{1,15}	2896.4298(1)
13 _{3,11}	\leftarrow	14 _{2,12}	2893.7280(-2)	17 _{2,16}	\leftarrow	18 _{1,17}	2893.5051(3)
13 _{4,10}	\leftarrow	13 _{3,11}	2895.7376(2)	17 _{3,15}	\leftarrow	18 _{2,16}	2893.4285(4)
13 _{4,10}	\leftarrow	14 _{3,11}	2893.6890(1)	18 _{0,18}	\leftarrow	17 _{1,17}	2896.4298(4)
13 _{5,9}	\leftarrow	13 _{4,10}	2895.6814(3)	18 _{0,18}	\leftarrow	19 _{1,19}	2893.5067(-6)
13 _{7,7}	\leftarrow	14 _{8,6}	2892.6295(2)	18 _{1,17}	\leftarrow	17 _{2,16}	2896.5080(-4)
13 _{8,6}	\leftarrow	12 _{7,5}	2897.2834(-2)	18 _{1,17}	\leftarrow	19 _{2,18}	2893.4311(2)
13 _{8,6}	\leftarrow	14 _{9,5}	2892.4954(-2)	18 _{2,16}	\leftarrow	17 _{3,15}	2896.5877(1)
13 _{9,5}	\leftarrow	12 _{8,4}	2897.4211(-2)	19 _{1,19}	\leftarrow	18 _{0,18}	2896.5080(-4)
13 _{10,4}	\leftarrow	14 _{11,3}	2892.2344(4)	19 _{2,18}	\leftarrow	18 _{1,17}	2896.5877(4)
13 _{11,3}	\leftarrow	12 _{10,2}	2897.6914(-2)				
13 _{11,3}	\leftarrow	14 _{12,2}	2892.1060(4)				
14 _{0,14}	\leftarrow	13 _{1,13}	2896.1144(0)				
14 _{0,14}	\leftarrow	15 _{1,15}	2893.8043(-3)				

Table 4.2: Spectroscopic constants (in cm^{-1}) derived from a simultaneous least-squares fit of the Ar_2DF data in Table 4.2 and the microwave data from Ref. [153]. The data were fit to an A-reduction Watson Hamiltonian using the I' representation. Uncertainties represent one standard deviation.

	$\nu_{\text{DF}} = 0$	$\nu_{\text{DF}} = 1$
A	0.11697288 (3)	0.1171458 (11)
B	0.05817716 (2)	0.0582606 (11)
C	0.03854372 (2)	0.0386020 (6)
$\Delta_J \times 10^7$	5.4742 (32)	5.450 (38)
$\Delta_{JK} \times 10^7$	1.240 (23)	0.592(159)
$\Delta_K \times 10^7$	34.516 (26)	33.75 (15)
$\delta_J \times 10^7$	1.9433 (17)	1.970 (21)
$\delta_K \times 10^7$	12.696 (26)	12.57 (20)
$\Phi_{JK} \times 10^{10} \text{ }^a$	3.24 (82)	3.24 (82)
$\Phi_{KJ} \times 10^{10} \text{ }^a$	-1.94 (26)	-1.94 (26)
$\Phi_K \times 10^{10} \text{ }^a$	1.74 (21)	1.74 (21)
ν_0		2894.98439 (3)

^a The diagonal sextic distortion coefficients for the vibrational ground state were floated in the least squares fit with the infrared data constrained to be equal. Inclusion of the diagonal sextic distortion term Φ_J and the off-diagonal sextic distortion terms reduces the quality of the fit and were thus omitted.

4.3.3 Ar₃DF

Among the high- J transitions of the Ar₂DF P branch, an additional rotationally resolved spectrum is observed near 2892.2 cm⁻¹ (see Figure 4.2) which is ascribed to the Ar₃DF by analogy with the Ar₃HF results [265]. The rotational structure is characteristic of a vibrationally averaged symmetric top, with a strong (only partially resolved) Q branch, and well resolved P/R branches which can be readily assigned out to $J' \geq 20$. Substructure in the P/R branch due to centrifugally induced K splittings are not resolved, further corroborating a vibrationally averaged symmetric top geometry. Combination differences calculated with the $\nu_{DF}=0$ constants confirm the assignment to Ar₃DF, which was previously observed in the microwave by Gutowsky and coworkers [149, 152]. The near-IR transition frequencies are listed in Table 4.3. The spectra are consistent with a vibrationally averaged, C_{3v} ground state structure (shown in Figure 4.1) with the Ar atoms arranged as an equilateral triangle and the DF lying along an axis perpendicular to plane of Ar atoms. The transition moment for excitation of the DF stretch is parallel to the symmetry axis, and thus the infrared spectrum exhibits structure characteristic of a parallel transition of an oblate, symmetric top.

As mentioned above, the transitions to individual K sublevels are not resolved in either the Q or P/R branch, and consequently the data are fit to a simplified form of a symmetric top Hamiltonian:

$$H = BJ(J + 1) - D_J [J(J + 1)]^2 \quad (4.1)$$

The results of the fit are listed in Table 4.4. The vibrational origin is 2892.20652 (11) cm⁻¹, which is redshifted 2.78 cm⁻¹ from the Ar₂DF origin, i.e., only 24% of the influ-

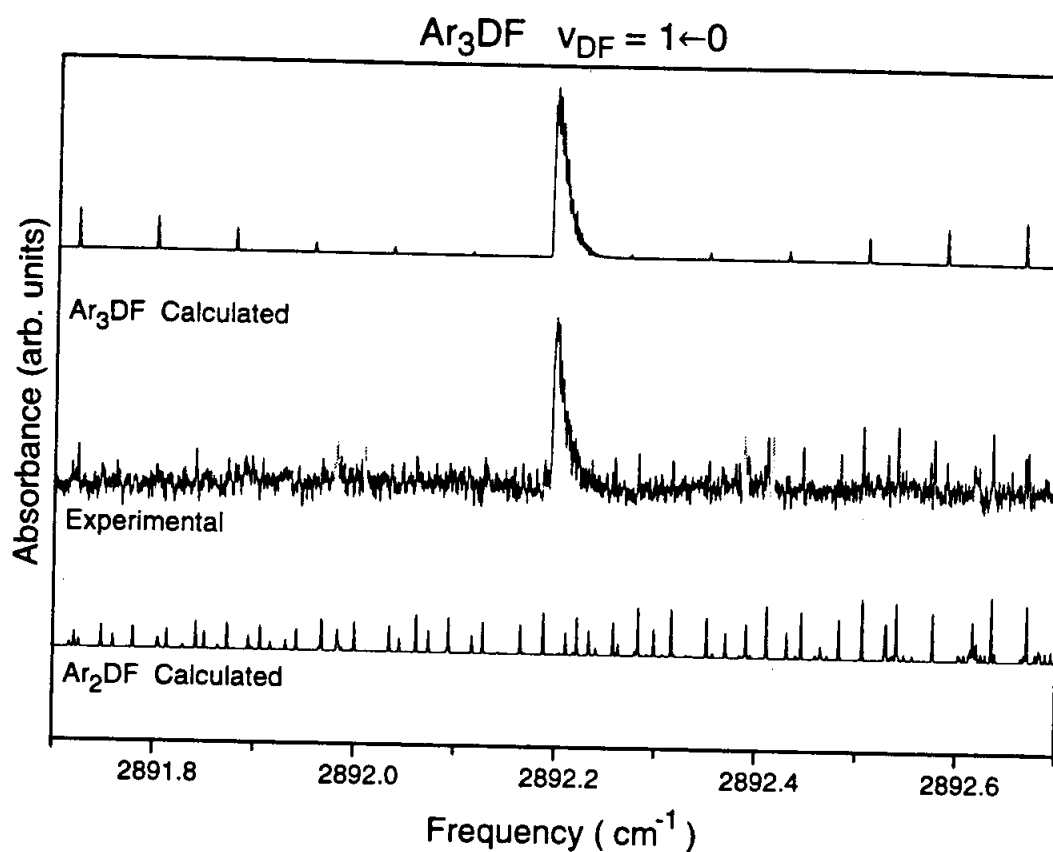


Figure 4.4: Experimental spectrum near the $\text{Ar}_3\text{DF } \nu_{\text{DF}} = 1 \leftarrow 0$ origin, and spectral simulations of Ar_2DF and Ar_3DF calculated at a rotational temperature of 8.5 K. The shaded peaks that appear as doublets in the experimental spectrum at 2892.6 and 2892.2 cm^{-1} are $P(13)$ and $P(14)$, respectively, of the $\nu_1, K = 1 \leftarrow 0$ transition of $(\text{DF})_2$. All the structure can be attributed to transitions of either Ar_3DF , Ar_2DF , or $(\text{DF})_2$, and there is no evidence for transitions attributable to Ar_nDF complexes with $n \geq 4$.

Table 4.3: Transition frequencies for the $\nu_{DF} = 1 \leftarrow 0$ transition in Ar_3DF .

J'	\leftarrow	J''	Energy (o-c)	J'	\leftarrow	J''	Energy (o-c)
20	\leftarrow	19	^a	4	\leftarrow	5	^a
19	\leftarrow	18	2893.7110 (1)	5	\leftarrow	6	2891.7353 (0)
18	\leftarrow	17	^a	6	\leftarrow	7	2891.6572 (1)
17	\leftarrow	16	2893.5524 (1)	7	\leftarrow	8	2891.5791 (0)
16	\leftarrow	15	2893.4731 (1)	8	\leftarrow	9	2891.5008 (-3)
15	\leftarrow	14	2893.3938 (1)	9	\leftarrow	10	2891.4232 (0)
14	\leftarrow	13	2893.3143 (0)	10	\leftarrow	11	2891.3455 (0)
13	\leftarrow	12	^a	11	\leftarrow	12	2891.2678 (-2)
12	\leftarrow	11	2893.1558 (1)	12	\leftarrow	13	2891.1906 (1)
11	\leftarrow	10	2893.0765 (1)	13	\leftarrow	14	2891.1130 (-2)
10	\leftarrow	9	2892.9973 (1)	14	\leftarrow	15	2891.0360 (-1)
9	\leftarrow	8	2892.9181 (2)	15	\leftarrow	16	2890.9589 (-2)
8	\leftarrow	7	^a	16	\leftarrow	17	2890.8823 (1)
7	\leftarrow	6	2892.7591 (-4)				
6	\leftarrow	5	2892.6805 (1)				
5	\leftarrow	4	2892.6017 (5)				

^a Peaks are blended with Ar_2DF transitions, and are not used in the least squares fit.

Table 4.4: Spectroscopic constants (in cm^{-1}) derived from a least-squares fit of the microwave (Ref. [153]) and infrared Ar_3DF data from Table 4.3. Uncertainties represent one standard deviation.

	$\nu_{\text{DF}} = 0$	$\nu_{\text{DF}} = 1$
ν_0	0.0	2892.20652 (11)
B	0.039373192 (10)	0.0394100 (23)
$\Delta C \times 10^4$		1.96 (10) ^a
$D_J \times 10^7$	2.1907 (14)	2.178 (50)
$D_{JK} \times 10^7$	-1.9200 (10) ^b	-1.6 (24) ^a

^a Determined from an analysis of line-broadening arising from K -splitting of the rovibrational lines and shading of the Q branch as described in the text. ^b Value reported in work of Gutowsky *et al.* [153] based on observed K -splitting in the molecular transitions.

ence of the first Ar atom, but nearly equivalent to the second Ar atom. Comparison of the B rotational constant for the ground and vibrationally excited state shows a slight ($\approx 0.09\%$) increase in the latter. This again is consistent with a subtle contraction of vibrationally averaged distances in the complex upon intramolecular excitation, and similar to the behavior observed for ArDF and Ar_2DF .

Information in addition to B' and D'_J is available from an analysis of other features of the spectrum, e.g. line broadening in the P/R branch transitions, the shading of the Q branch, and the intensity ratio of the Q branch vs P/R branch. Although the splittings of the P/R branch lines from the different K -sublevels are not resolved, a comparison of high- J P and R branch transitions shows that there is a systematic broadening of lines in the P branch that is not detected in the R branch. This broadening arises predominantly from the change in D_{JK} upon vibrational excitation; since D''_{JK} was determined in the microwave analysis of Gutowsky and coworkers, the analysis of this broadening permits a determination of D'_{JK} , which is shown in Table 4.4.

The blue shading of the Q branch indicates that $(C-B)$ increases upon vibrational excitation. Since both B' and B'' are known accurately from the least squares fit of the transition frequencies, an analysis of this shading provides an estimate for ΔC . ΔC can be determined by fitting the experimental Q branch contour to a simulation in which ΔC and the rotational temperature T are adjusted until the residual sum of squares is minimized, keeping the ground state and upper state constants (B, D_J , and D_{JK}) fixed at the values already determined from P/R branch analysis. The value for ΔC determined in this manner is listed in Table 4.4; a simulation incorporating all the fitted constants reproduces the experimental spectrum reasonably well, as is shown in Figure 4.4. The increase in C is again consistent with slight contraction of the vibrationally averaged Ar_3 ring upon $\nu_{DF}=1$ excitation, though this could also arise from greater tilting of the Ar_3 plane away from the symmetry axis due to large amplitude rocking motions.

Although the above analysis only provides information about ΔC , the absolute magnitude of C'' and C' can be approximated from the relative intensities of the P/R vs Q branch. As elucidated by Herzberg [170], the Hönl-London factors for Q branch transitions of a symmetric top are largest for high- K levels, while low- K states contribute more intensity to P/R branch transitions. Furthermore, since the energy difference between high and low K levels in an oblate top is determined in lowest order by $(C-B)$, a small C'' contributes a larger Boltzmann weighting for high K states, and thus a larger integrated Q vs P/R branch intensity. The experimental ratio of integrated Q vs P/R branch intensity is 1.43(15):1, which predicts a value for C'' (or equivalently C') of $0.025(5) \text{ cm}^{-1}$. Within uncertainty, this is in agreement with the equilibrium value of $C'' = 0.0304 \text{ cm}^{-1}$ calculated classically by McIlroy and Nesbitt

for Ar_3HF using a pairwise additive surface, as well as the variationally more rigorous value of $C'' = 0.0291$ calculated for Ar_3 by Cooper *et al.* [87]

4.4 Discussion

Near-infrared excitation of the Ar_nDF complexes subtly alters the vibrationally averaged geometries, and the magnitude of these changes can be assessed by comparing the rotational constants in each vibrational manifold. This information can then be related to the dependence of the interaction potential on the high frequency stretching coordinate. The coupling between the intramolecular and intermolecular coordinates is also reflected in the magnitude of the vibrational redshifts and vibrational predissociation lifetimes. These parameters can be highly sensitive to small changes in the interaction potential, and consequently provide rigorous tests of both the potentials and computational methodology. It is worth noting that while the present data are sensitive primarily to the high frequency intramolecular coordinate, analysis of intermolecular bending states (which can be accessed as combination bands in the near infrared spectrum) provide additional information on the angular dependence of the potential. We have observed 4 such van der Waals intermolecular vibrations (the in-plane and out-of-plane bends for both Ar_2DF and Ar_2HF) recently in our laboratories [131], which are described in Chapter 5.

4.4.1 Ar_nDF Vibrationally Averaged Geometries and Nonpairwise Additive Effects

The effect of DF excitation on the Ar_nDF vibrationally averaged geometries can be ascertained through a comparison of the rotational constants in each vibrational manifold. In ArDF , vibrational excitation increases the B rotational constant and decreases the centrifugal distortion constant D . Both changes are consistent with a decrease in the vibrationally averaged center of mass separation, and a strengthening of the intermolecular bond. Within a pseudodiatom approximation, the +0.29% change in B corresponds to a -0.15% change in the vibrationally averaged center of mass separation. The increased attraction suggests an increase in the binding energy D_0 , the magnitude of which can be determined from the vibrational redshift as discussed below.

The microwave and infrared data for Ar_2DF are consistent with a planar, T -shaped structure. Unfortunately, an inertial analysis that includes the contributions from large amplitude motion requires information not contained in the near-IR rotational constants. Consequently, we invoke a simplified treatment, [153] in which contributions from these coordinates are ignored, and the rotational constants A , B , and C are used to determine the vibrationally averaged center of mass separations between Ar-Ar and $\text{Ar}_2\text{-DF}$. Since the high frequency DF stretching coordinate is coupled only weakly to the much lower frequency intermolecular modes, such an approximation should not be drastic for the purposes of comparing structural changes upon DF excitation. The observed increase in A , B , and C upon vibrational excitation reflects small decreases in the vibrationally averaged Ar-Ar and $\text{Ar}_2\text{-DF}$ center of mass separations. The Ar-Ar separation decreases from 3.820 Å to 3.817 Å upon

DF excitation, and the Ar-DF separation from 3.510 Å to 3.507 Å. These changes are consistent with the decrease in vibrationally averaged separation for ArDF, and corresponding stronger attraction in the vibrationally excited state.

For a rigid, planar molecule, the inertial defect ($\Delta_0 = 1/C - 1/B - 1/A$) is zero [370], while for non-rigid molecules the presence of in-plane (out-of-plane) motion is manifested as a positive (negative) inertial defect. In both the $\nu_{DF} = 0$ and 1 vibrational manifolds of Ar₂DF, the inertial defect is large and positive (3.484 and 3.452 amu Å², respectively), indicating the presence of predominantly in-plane, large amplitude motion. If the bulk of the large amplitude motion can be attributed to motion of the light deuterium atom, the positive inertial defect suggests that motion of the DF in the molecular plane has a smaller restoring force than out-of-plane motion. This is supported by the hyperfine analysis of Gutowsky [152], in which the vibrationally averaged angle for in-plane bending is approximately 10% greater than for out-of-plane bending. These results also imply that excitation of the in-plane bend should occur at lower frequency than the out-of-plane bend, a conjecture verified by the experimental frequencies of 45.2 and 72.1 cm⁻¹, respectively, in the $\nu_{DF} = 1$ manifold [131].

For the $K = 0 \leftarrow 0$ Ar₃DF transitions, there are a limited number of spectroscopic parameters from which to determine structural data. Even if contributions from the low frequency intermolecular coordinates are neglected, there are still too few spectroscopic constants to determine a vibrationally averaged geometry. We note, however, that B increases upon vibrational excitation, consistent with the behavior observed for ArDF and Ar₂DF, indicating a contraction of the complex upon DF excitation. Furthermore, C also increases upon vibrational excitation. In Ar₃DF/HF, the magnitude of C is largely dominated by the moment of inertia of the three Ar

atoms about the intermolecular axis. The positive ΔC could thus be interpreted as a decrease in the vibrationally averaged Ar-Ar separation in the Ar_3 ring, although a decrease in the tilt of the Ar_3 plane with respect to the intermolecular axis would also lead to such a change.

The ground state energies and vibrationally averaged structures for $\text{Ar}_n\text{HF}/\text{DF}$ ($n \leq 4$) have been calculated using diffusion quantum Monte Carlo (DQMC) techniques [233], incorporating the H6(4,3,2) ArDF/HF potential and the HFD-B and HFD-C Ar-Ar potentials. [14] Within the pairwise additive approximation, the lowest energy isomers calculated for Ar_nDF and Ar_nHF ($n=1-4$) agree with experiment, suggesting that this approximation is valid for calculating energetic ordering of isomers. The DQMC calculations have also addressed the effects of a three-body dispersion term on the ground state energies. This term is analogous to the isotropic Axilrod-Teller triple dipole (DDD) dispersion term [13], and has been invoked frequently in the study of many body interactions in atomic systems. It arises from a third-order perturbation theory modeling of the triple-dipole dispersion energy between three polarizable species. This term is attractive at linear configurations, where the induced dipoles can be oriented most favorably on all three atoms, and is repulsive when the atoms are arranged as a triangle. It is worth emphasizing, however, that even with a repulsive DDD energy for a particular equilibrium geometry, the overall dispersion energy is still attractive — it is just less than the sum of three pairwise interactions.

The triangular equilibrium geometry of $\text{Ar}_2\text{DF}/\text{HF}$ contributes a repulsive DDD term. Similarly, the argon atoms in $\text{Ar}_3\text{DF}/\text{HF}$ are oriented as an equilateral triangle, which also gives rise to another repulsive DDD term. However, inclusion of these DDD terms raises the total energy of these isomers by only $3-11 \text{ cm}^{-1}$ [233],

and the next closest minima on the multidimensional potential surfaces are sufficiently high that the ordering of the lowest energy isomers does not change. This is not the case for $\text{Ar}_4\text{DF}/\text{HF}$, however. At the pairwise additive level, the lowest energy isomer for both isotopomers has C_{3v} symmetry, with the D/H end of the diatom pointing towards the face of an Ar_4 tetrahedron. More precisely, the DF/HF occupies a site that corresponds to an axial argon in the trigonal bipyramidal Ar_5 (Ref. [233]), as illustrated in Figure 4.5. Slightly higher in energy ($\approx 2.2 \text{ cm}^{-1}$ for Ar_4HF , 3.7 cm^{-1} for Ar_4DF) is an isomer with C_{2v} symmetry, in which the diatom is substituted for an equatorial argon in the Ar_5 trigonal bipyramid. Upon inclusion of the DDD term, the energy difference between the C_{2v} and C_{3v} isomers drops to 1.3 and 1.7 cm^{-1} for Ar_4HF and Ar_4DF , i.e., they are isoenergetic within the error limits of the calculation. In fact, in the $\nu_{\text{DF}} = 1$ manifold of Ar_4DF the C_{2v} isomer is *lower* in energy than the C_{3v} . It is likely that inclusion of additional three-body terms may further alter the ordering of the isomers, and calculations are in progress to determine these effects [234].

The detection of the C_{3v} isomer of Ar_4HF and Ar_4DF in the microwave [154] suggests that near-IR transitions might also be observable. Indeed, the infrared spectrum of this isomer has been characterized for Ar_4HF [265]. The integrated Q branch intensity ratio for $\text{Ar}_3\text{HF}:\text{Ar}_4\text{HF}$ is $\approx 7:1$; if a similar scaling applies for the DF complexes, the Ar_4DF Q branch should have sufficient intensity to detect. However, no evidence for Ar_4DF transitions have been identified in the present study, despite an extensive search. Based on the signal to noise of the Ar_3DF Q branch under expansion conditions similar to those which maximize Ar_4HF formation, we estimate that the Ar_4DF Q branch must be ≥ 10 -fold weaker than Ar_3DF (assuming a similar

Ar₄HF/DF Lowest Energy Isomers

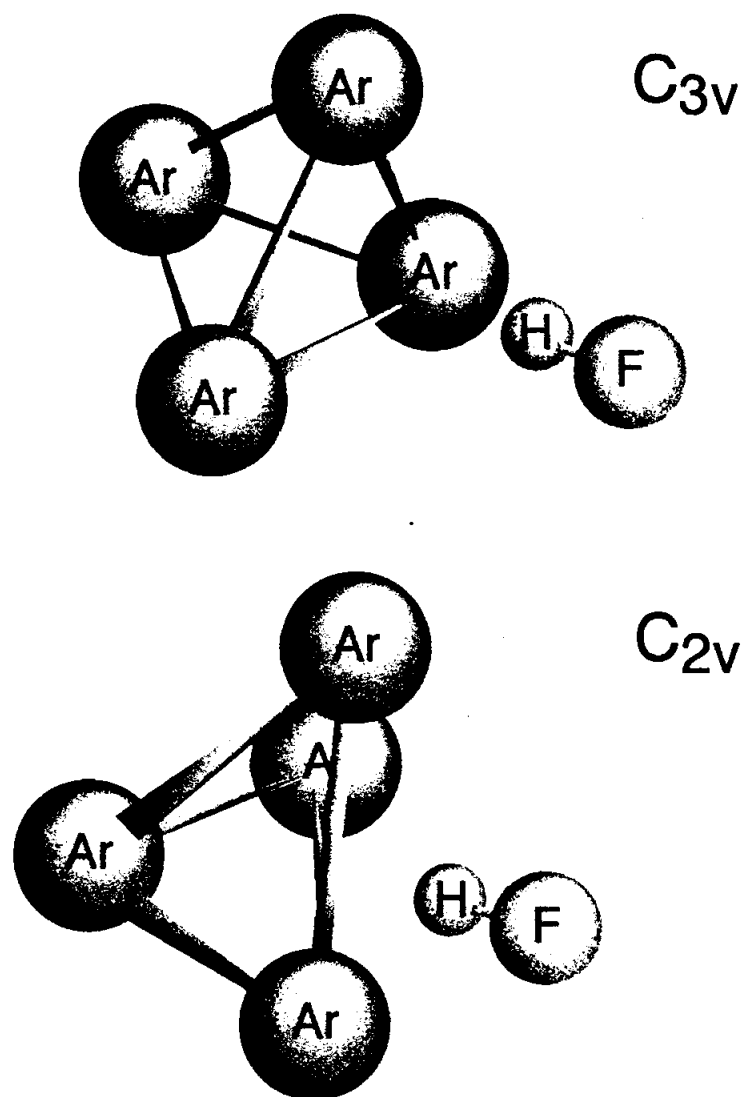


Figure 4.5: Pictorial representations of the two lowest energy isomers for Ar₄HF/DF.

Q branch shading as observed for Ar_nHF). The absence of an observed Q branch for Ar_4DF indicates that the scaling of peak intensity is less for the DF complexes. This could be attributed to a larger ΔC for Ar_4DF vs Ar_4HF upon vibrational excitation, which would increase the shading and reduce the peak intensity of the Q branch. However, such a change would not be expected to be dramatic, based on the Ar_nHF results and the $> 5 \text{ \AA}$ separation between the fourth argon atom and the DF. An alternative explanation is that the actual energy difference between the C_{2v} and C_{3v} isomers is smaller for Ar_4DF than Ar_4HF . The corresponding decrease in population for the Ar_4DF C_{3v} isomer would therefore translate into a reduced peak intensity of the Q branch. The resulting increase in population of the C_{2v} isomer, on the other hand, would not be manifested experimentally, since the peak intensity of this isomer's asymmetric top spectrum would be more than an order of magnitude weaker than that of the C_{3v} symmetric top, and would not be observable at our present S/N.

Close coupling calculations have also been presented for the $\text{Ar}_n\text{HF/DF}$ system. Although these calculations are more precise than the Monte Carlo calculations, size limitations not applicable to Monte Carlo methods presently restrict the close coupling calculations to clusters with $n \leq 2$. However, the calculations are not restricted to the lowest vibrational state of a given symmetry, as is the case with the Monte Carlo techniques, and thus a larger number of excited states can be calculated. This is particularly important for comparison with experimental data that samples excited intermolecular vibrations of the complexes [131].

Ernesti and Hutson [117, 118] have presented calculations for $\text{Ar}_2\text{HF/DF}$ in which the five low frequency intermolecular degrees of freedom are treated explicitly. The rotational constants calculated at the pairwise-additive level of approximation are

Table 4.5: Comparison of the Ar_2HF and Ar_2DF rotational constants with those predicted by Ernesti and Hutson (Ref. [117, 118]). The numbers in parentheses are the errors between the calculated and experimental constants.

	Experiment	Pairwise	+ 3-body
ArHF			
B''	0.10226	0.10228 (+0.02%)	—
B'	0.10262	0.10262 (+0.00%)	—
Ar₂HF			
A''	0.11929	0.11993 (+0.5%)	0.11987 (+0.5%)
B''	0.05801	0.05889 (+1.5%)	0.05801 (+0.0%)
C''	0.03873	0.03911 (+1.0%)	0.03870 (-0.1%)
A'	0.11937	0.11988 (+0.4%)	0.11987 (+0.4%)
B'	0.05812	0.05910 (+1.7%)	0.05813 (+0.0%)
C'	0.03879	0.03921 (+1.1%)	0.03876 (-0.1%)
ArDF			
B''	0.10140	0.10122 (-0.18%)	—
B'	0.10169	0.10150 (-0.19%)	—
Ar₂DF			
A''	0.11697	0.11805 (+0.92%)	0.11798 (+0.86%)
B''	0.05818	0.05941 (+2.11%)	0.05824 (+0.10%)
C''	0.03854	0.03913 (+1.53%)	0.03636 (-5.66%)

in good agreement with the experimental values (see Table 4.5), but are consistently larger, indicating that the pairwise additive approximation leads to an interaction energy that is too attractive. The pair potentials reproduce the rotational constants of the respective dimers to better than 0.1%, suggesting that the disagreement in the $\text{Ar}_2\text{HF}/\text{DF}$ rotational constants is not attributable to deficiencies in the pair potentials.

These results indicate that three-body terms that are repulsive at the equilibrium geometry must be included to bring the calculated rotational constants in line

with experiment. Hutson and coworkers [88, 117, 118] have investigated the effect of several three-body terms on reducing the discrepancies with experiment. Specifically, the inclusion of terms accounting for i) the anisotropic DDD interaction, and ii) the interaction between the dipole moments induced on the argon atoms by the permanent dipole moment of the HF/DF, does not change the predicted constants significantly. However, Hutson has identified a third term which, when coupled with the above two terms, does change the constants in the direction necessary to improve agreement with experiment. This term arises from the interaction of the permanent dipole moment of the DF/HF with the quadrupole formed on the Ar_2 due to overlap distortion effects [88, 118]. This interaction, when included with the DDD and induced dipole-induced dipole terms, improves the agreement between the calculated and experimental rotational constants as shown in Table 4.5.

The identification of a three-body term that is directly linked to the presence of a molecular species, and thus has no counterpart in atomic systems, provides intriguing new insight as such terms are expected to be important for all related molecular systems. As can be seen from Table 4.5, however, the agreement is still relatively poor for the A constant of Ar_2HF and Ar_2DF , and for C of Ar_2DF , signifying that refinements to the three-body terms are still necessary. Since the present data sample limited regions of the intermolecular potentials of the complexes, efforts to refine the form of these three-body terms are best done in conjunction with data from the intermolecular bending states of Ar_2DF and Ar_2HF [131], and which sample a more substantial region of the potential surface. Further theoretical efforts to extract a detailed three-body "surface" from this high resolution cluster data, both for intermolecular vibrations and rotational constants, are currently underway [121].

4.4.2 Vibrational Redshifts

The complexation-induced frequency shifts for $\text{Ar}_n\text{DF}/\text{HF}$ allow the characterization of the small shifts in monomer vibrational energy upon the incremental addition of "solvent" atoms. For large values of n , the shifts might be expected to approach asymptotically the values observed in condensed phase environments. The Monte Carlo calculations of Lewerenz [233] indicate that the wavefunctions for the Ar atoms in the complexes are highly localized, with the complexes best described as a DF/HF pointing towards an argon "microcrystal". Consequently, a natural point of comparison for the vibrational frequency shifts is the corresponding shift observed in an Ar matrix. The incremental perturbations to the monomer stretching potential can be expected to decrease as successive solvation shells are filled, and thus should be most dramatic for the first solvation shell, i.e., precisely the region sampled by the Ar_nDF complexes.

The vibrational origins of Ar_nDF and Ar_nHF complexes are listed in Table 4.6, along with the shifts observed in an Ar matrix. The redshift of 8.696 cm^{-1} for ArDF reflects a 0.30% decrease in the DF stretching frequency. While this change is small compared to the DF vibrational frequency, it correlates with a 7.5% increase in binding energy D_0 [179]. For Ar_2DF , the second Ar leads to an incremental redshift of 2.981 cm^{-1} , i.e., only $\approx 1/3$ the shift induced by the first atom. This behavior suggests a strong orientation dependence to the shifts, and can be contrasted with the vibrational redshifts for Ar_nCO_2 ($n=1,2$) and the electronic blueshifts for I_2 -(rare gas) $_n$ ($n=1-6$) complexes, for which the shifts are approximately linear with n . For

T-shaped complexes of CO₂ and I₂, however, the potential energy surface has multiple equivalent minima in which the rare gas atoms can reside, and the shifts upon sequential atom addition are approximately the same until all the equivalent minima are filled. For DF/HF, there is only one (collinear) minimum corresponding to the lowest energy orientation. Hence with two or more solvent atoms, each must compete for the optimal location with respect to the molecular axis, which reduces the overall redshift interaction per atom.

The Ar₃DF origin is 2.777 cm⁻¹ below that of Ar₂DF, leading to a total redshift of 14.454 cm⁻¹. The 2.777 cm⁻¹ incremental redshift for Ar₃DF is very nearly equal to the 2.981 cm⁻¹ incremental shift for Ar₂DF. This nonlinear but monotonic increase in frequency shifts for the Ar_{*n*}DF/HF complexes is illustrated in Figure 4.6. Interestingly, the redshifts for Ar₃DF and Ar₃HF are almost halfway to the values observed in Ar matrices. Furthermore, as suggested by the minor incremental redshift observed between the C_{3v} Ar₃HF and Ar₄HF structures (which differ nominally by an Ar in the second shell), the frequency shifts appear to be dominated by the first solvation shell [265, 242]. Thus, the frequency shifts which accompany the addition of the remaining nine argon atoms (predominantly around the F atom) to complete the first solvation shell must be of the same magnitude as the first three, further emphasizing the strong angular anisotropy and positional dependence of the redshifts.

A comparison of the incremental redshifts for Ar_{*n*}DF and Ar_{*n*}HF for a given *n* requires that the isotopic dependence of solvation induced frequency shifts be taken into account. Buckingham [51] has presented a model based on first- and second-order perturbation theory which predicts that $\Delta\nu_{\text{redshift}}/\nu_{\text{monomer}}$ is independent of isotopic

Table 4.6: Experimental vibrational redshifts for DF (this work) and HF (Ref [265]) with sequential addition of argon "solvent" atoms. Also shown are redshifts calculated using diffusion quantum Monte Carlo techniques from Ref. [233] and bound state variational calculations by Ernesti and Hutson from Refs. ([117, 118]). The two columns reflect the values calculated within the approximation of pairwise additivity, and including corrective three-body terms as described more fully in the text.

	Vibrational Origin	redshift cm^{-1}	incremental redshift, cm^{-1}	QDMC ^a		Variational ^b	
				Pairwise	+3-Body	Pairwise	+3-body
DF	2906.6609 ^c	—	—	—	—	—	—
ArDF	2897.9653 ^d	-8.696	-8.696	-9.3(3) (+6.9%)	—	-8.694 (-0.02%)	—
Ar ₂ DF	2894.9844	-11.677	-2.981	-13.1(4) (+12.2%)	-12.6(4) (+7.9%)	-12.06 (+3.3%)	-11.46 (-1.9%)
Ar ₃ DF	2892.2065	-14.454	-2.777	-14.9(6) (+3.1%)	-15.0(6) (+3.8%)	—	—
Ar Matrix	2876.87 ^e	-29.79	—	—	—	—	—
HF	3961.4229 ^f	—	—	—	—	—	—
ArHF	3951.7688 ^g	-9.654	-9.654	-9.8(4) (+1.5%)	—	-9.655 (+0.01%)	—
Ar ₂ HF	3946.5919 ^h	-14.827	-5.173	-15.6(4) (+5.2%)	-16.1(5) (+8.6%)	-15.354 (+3.6%)	-14.577 (-1.7%)
Ar ₃ HF	3942.1634 ^h	-19.260	-4.429	-22.3(6) (+15.8%)	-21.8(6) (+13.2%)	—	—
Ar ₄ HF	3941.7260 ^h	-19.697	-0.437	-20.6(8) (+4.6%)	-21.0(7) (+6.6%)	—	—
Ar Matrix	3920.05 ^e	-41.37	—	—	—	—	—

^aRef. 233

^bRef. 117, 118

^cRef. 254

^dRef. 256

^eRef. 6

^fRef. 148

^gRef. 251

^hRef. 265

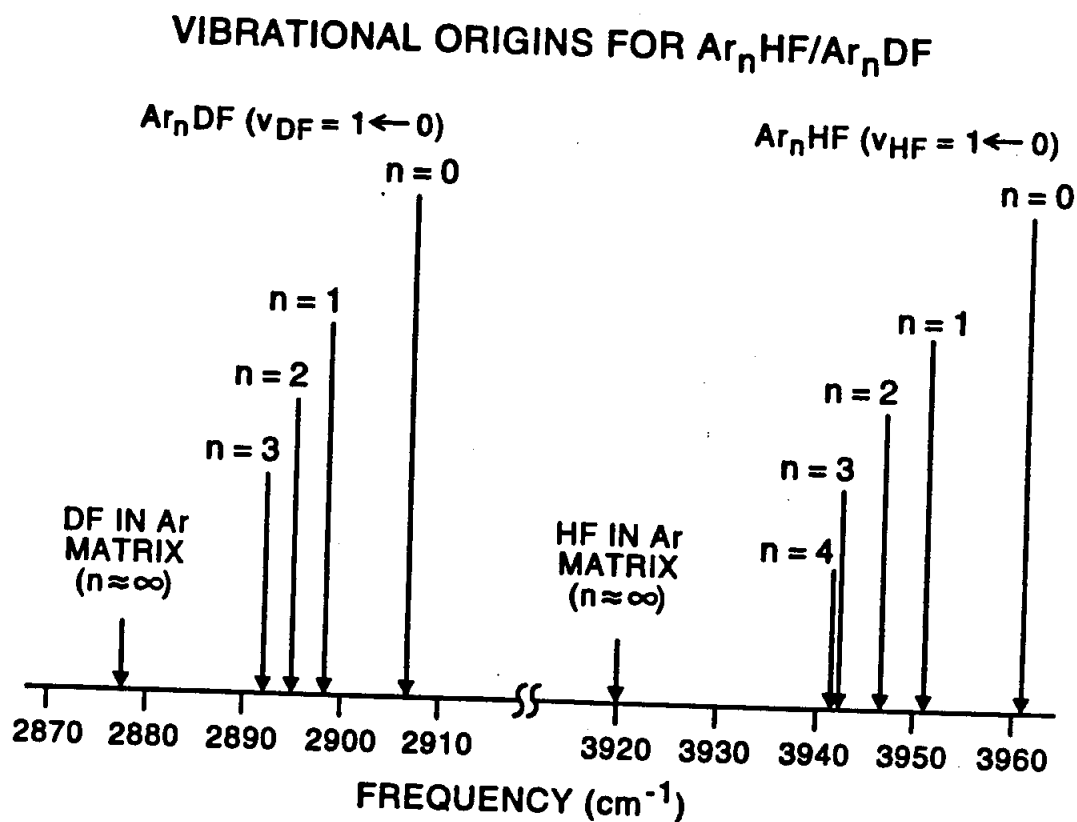


Figure 4.6: Vibrational origins for complexes of DF/HF and argon as a function of n , the number of Ar atoms in the complex. The corresponding vibrational origins of DF and HF observed in argon matrices are also shown.

composition. Thus for a given n , the model predicts:

$$\frac{\Delta\nu_{\text{Ar}_n\text{DF}}}{\nu_{\text{DF}}} = \frac{\Delta\nu_{\text{Ar}_n\text{HF}}}{\nu_{\text{HF}}} \quad (4.2)$$

Figure 4.7 shows a plot of $\Delta\nu_{\text{redshift}}/\nu_{\text{monomer}}$ vs n for Ar_nDF and Ar_nHF . The ratio $\Delta\nu_{\text{redshift}}/\nu_{\text{monomer}}$ is indeed nearly the same for both the HF and DF complexes, indicating that the isotopic dependence of the redshifts for these systems is well described by the above model. The slightly larger fractional shifts for the DF complexes most likely reflect the reduced zero-point bending motion of the DF complexes, which keeps the DF more localized about the intermolecular axis than the HF, leading to an enhanced redshift interaction. It is interesting to note that the fractional redshifts in the matrix limit are nearly 10% smaller for DF than HF; thus the approach to the matrix value with number of Ar atoms is indeed faster for the deuterated species.

Calculations of the vibrational redshifts for the $\text{Ar}_n\text{DF}/\text{HF}$ complexes have been reported by Lewerenz [233] for $\text{Ar}_n\text{DF}/\text{HF}$ ($n \leq 4$). Within the pairwise-additive approximation, the vibrational redshifts calculated for $\nu_{\text{DF}/\text{HF}} = 1$ of Ar_nDF and HF complexes (listed in Table 4.6) show good agreement with, but systematically overpredict, the experimental values. Since the redshifts correlate with the increase in binding energy upon vibrational excitation, it is apparent that the nonpairwise additive terms necessary to correct the predicted redshifts must lead to a binding energy smaller than predicted by pairwise-additivity. This is consistent with results from the preceding section, which identified the need for repulsive three-body terms in the interaction potential. Inclusion of the isotropic triple dipole term discussed above does not improve the agreement with experiment, as shown in Table 4.6. In fact, within the quoted error limits the values are largely unchanged, indicating that the

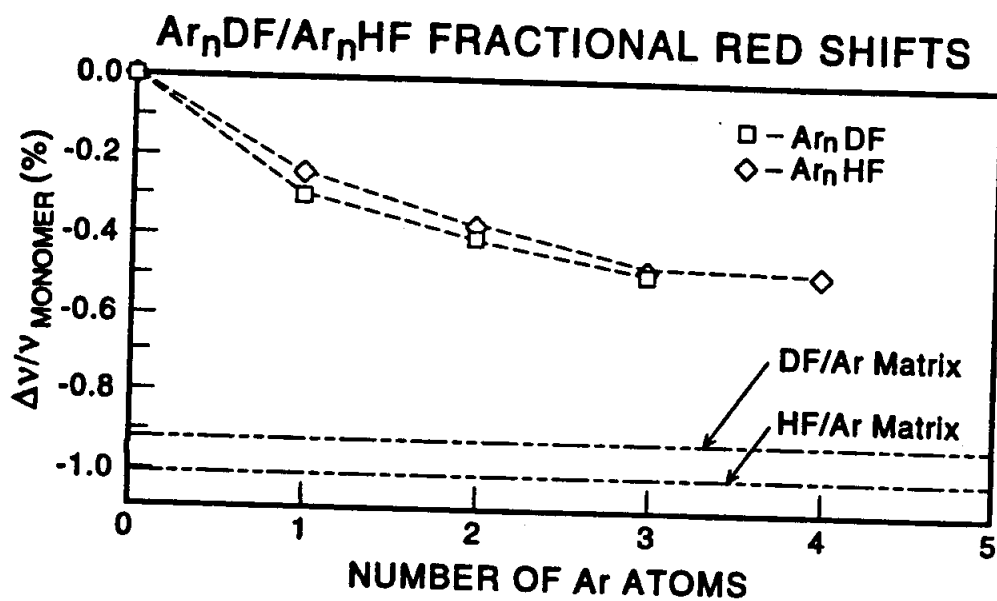


Figure 4.7: Fractional vibrational redshifts for Ar_nHF and Ar_nDF as a function of n. The redshifts for n=3 are nearly 50% the matrix values, in which the DF/HF is surrounded by 12 nearest neighbors in the first solvation shell.

DDD term does not have a significant effect on the vibrational redshift. Calculations that include the induced dipole-induced dipole and dipole-exchange quadrupole terms are currently underway [234].

The calculations of Ernesti and Hutson [117] allow an even more rigorous determination to be made of three-body effects on the vibrational redshifts of Ar_2DF and Ar_2HF . The redshifts predicted for Ar_2DF and Ar_2HF using pairwise additive surfaces are 12.06 cm^{-1} and 15.35 cm^{-1} , respectively, which are 0.38 cm^{-1} and 0.53 cm^{-1} larger than the experimental values. The sign of the discrepancy is again consistent with the neglect of repulsive, three-body terms. When the three-body terms discussed in the preceding section are included, the predicted (observed) values are 11.46 (11.68) cm^{-1} and 14.78 (14.83) cm^{-1} for Ar_2DF and Ar_2HF , respectively, reducing the discrepancy between the experimental results by approximately a factor of two. Refinement of this analysis should achieve improved agreement with experiment, and consequently a more detailed characterization of nonpairwise additive contributions to the full potential energy surface.

4.4.3 Vibrational Predissociation Lifetimes

Studies of vibrational predissociation in weakly bound complexes provide information on the timescale for coupling the inter- and intramolecular degrees of freedom. The coupling in rare gas-hydrogen halide complexes is particularly weak, and as a consequence vibrational predissociation lifetimes exceed ≈ 10 – 100 ns . This timescale corresponds to several hundred thousand monomer vibrations before the excitation energy channels into and ruptures the weak ($D_0 \approx 5$ – 10 cm^{-1} for He-HX

complexes [252], $\approx 180 \text{ cm}^{-1}$ for Xe-HX complexes [135]) intermolecular bond. Little is known about the effect sequential addition of solvent atoms has on the vibrational predissociation lifetimes of the complexes. In the near-IR studies of Ar_nHF ($n=2-4$) [265] and Ar_2CO_2 , [344] no evidence for predissociative broadening was detected, allowing lower limits of 10–20 ns to be assigned to the lifetimes.

For the analysis of the Ar_nDF rovibrational lineshapes, multiple scans were recorded at 1.4 MHz laser steps, with 16 averages at each step to reduce statistical uncertainties. A mixture of 0.5% DF in Ar was used at a backing pressure of 350 torr, with Ar chosen as the carrier gas to minimize residual Doppler broadening in the expansion. As shown previously [244], the sub-Doppler apparatus limited lineshape is dominated by thermal broadening of the sample at the translational temperature in the slit jet, with low intensity wings due to angular spread of the molecules at both edges of the slit. Consequently the lineshapes are nearly purely Gaussian, and can be quantitatively modeled via lineshape analysis of the corresponding DF monomer. As a conservative upper limit, the cluster lineshapes can be fit simply to a Voigt deconvolution, with the resulting Lorentzian component ascribed to predissociation broadening. Factors such as power and pressure broadening that could contribute an additional Lorentzian component to the lineshapes are negligible at the microwatt power levels and molecular densities in the slit supersonic expansion. Because the signal to noise of the transitions is quite high ($\approx 30:1$ for Ar_2DF), both the homogeneous and heterogeneous components are determined as unconstrained parameters in the least squares fit.

The inferred Lorentzian broadening for Ar_2DF transitions is 2.3 (21) MHz, i.e. zero within 95% experimental confidence limits (see Figure 4.8). It is more diffi-

cult to extract quantitative information from the Ar_3DF lineshapes, due to the lower S/N, unresolved Q branch structure, and the possibility of K -broadening in the P/R branches. For transitions in which the K -broadening is minimized, however, the lineshapes acquired under optimum expansion conditions (described in Section II) yield Lorentzian components on the order of 1.2(32) MHz, i.e. indistinguishable from zero within experimental uncertainty. In summary, the data show no compelling evidence for predissociation broadening in the $v = 1$ level of Ar_2DF and Ar_3DF , though we can not exclude the possibility of predissociation on the > 70 ns time scale. In fact, detailed lineshape analysis of the much higher S/N ArDF dimer suggests that predissociative broadening may indeed be present, and furthermore may depend on the intermolecular vibrational mode excited. However, extraction of this predissociative component requires a more quantitative modeling of the apparatus lineshapes in the slit jet, and will be described elsewhere.

4.5 Summary

High resolution, rotationally resolved spectra of the $\nu_{\text{DF}} = 1 \leftarrow 0$ stretch in Ar_nDF ($n=1-3$) have been recorded using a slit-jet infrared spectrometer. The Ar atoms are distributed symmetrically about the DF axis, concentrated at the D end of the DF. The vibrational frequency shifts are 8.696, 11.677, and 14.461 cm^{-1} for $n=1-3$, respectively. The nonlinear but monotonic dependence of the redshift on n reflects a competition for collinear complexation with the DF subunit. This nonlinear redshift behavior differs qualitatively from chromophores such as CO_2 and I_2 , where complexation can occur at many equivalent sites around the central plane

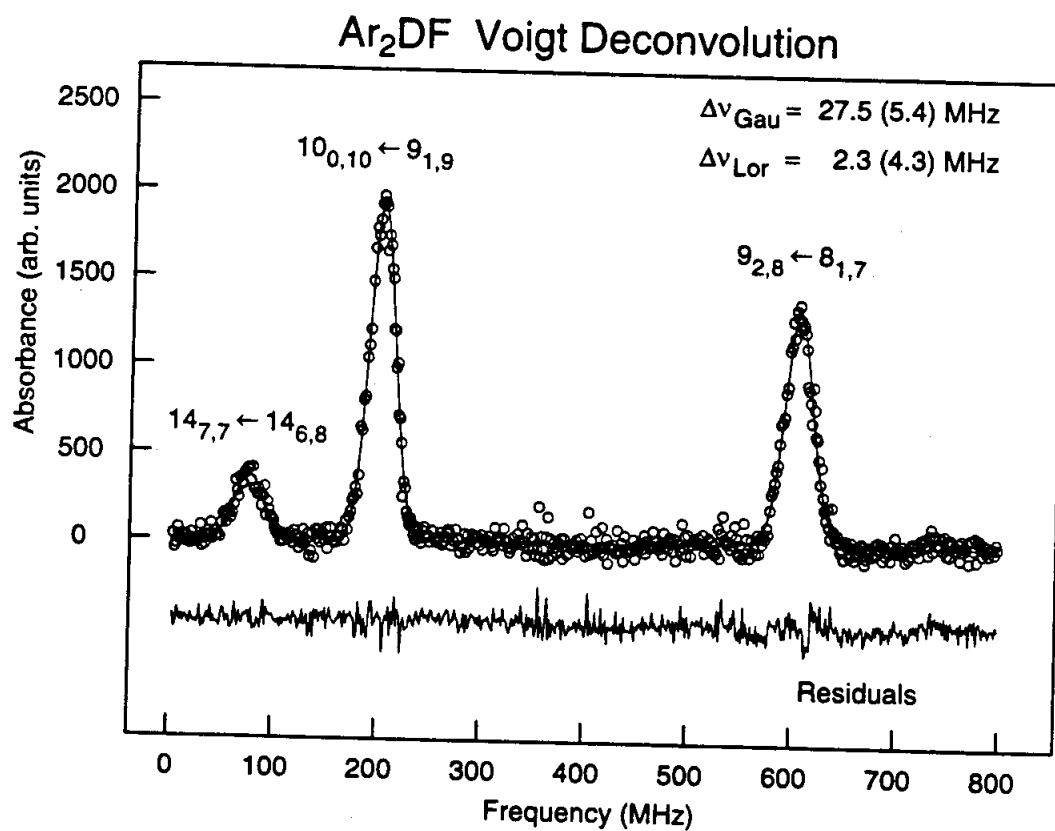


Figure 4.8: Representative Voigt lineshape deconvolutions for $v = 1 \leftarrow 0$ transitions of Ar₂DF.

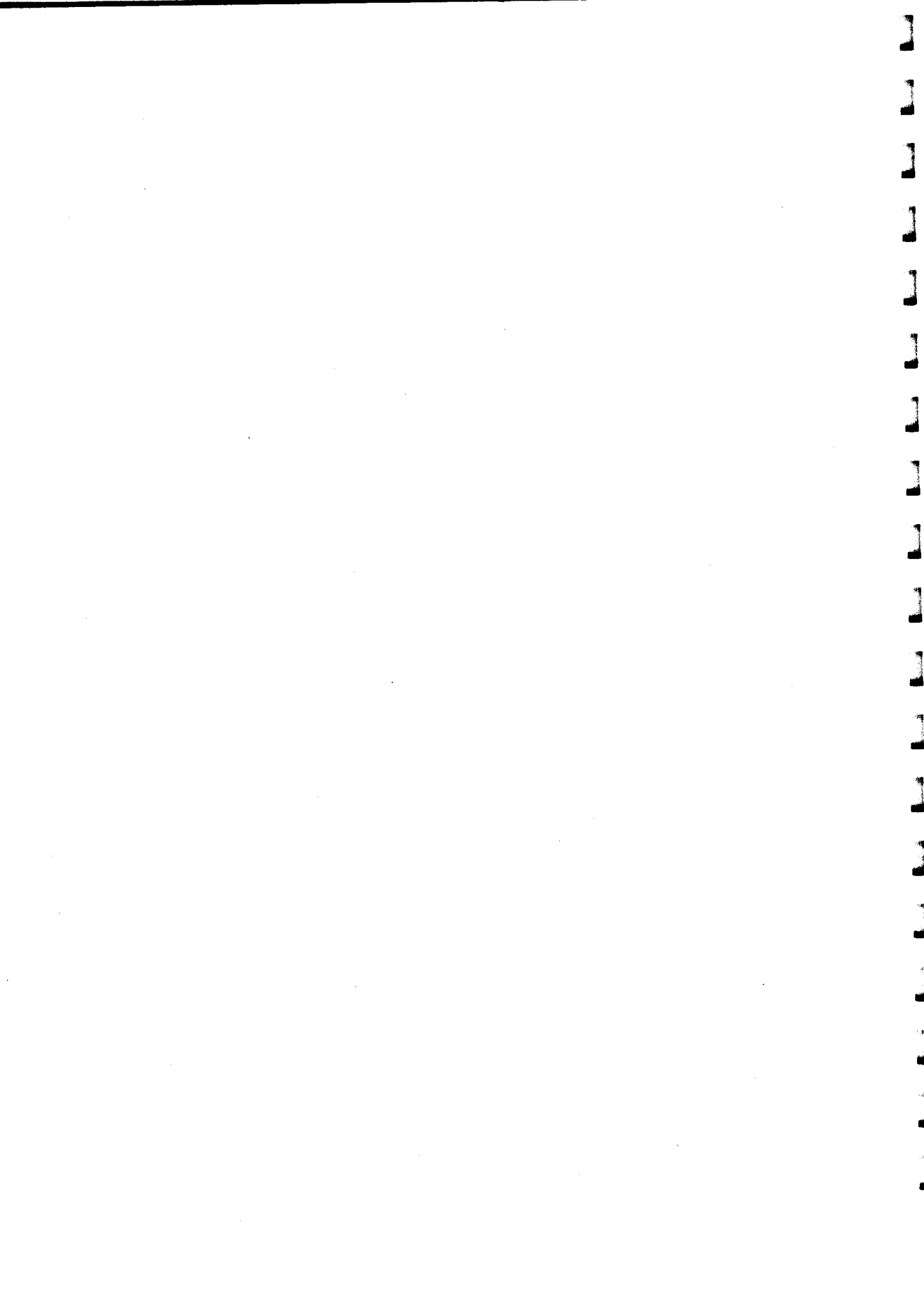
of symmetry. As observed for Ar_3HF , the redshift for Ar_3DF is already nearly half the shift observed in an argon matrix, even though the first solvation shell is only 25% full. This underscores the very strong radial and angular dependence to the red shift effects, and offers hope for experimentally probing the transition between gas and condensed phase behavior with only a very modest number of "solvent" atoms.

The lowest energy structural isomers are predicted reliably by Quantum Monte Carlo calculations using pairwise additive Ar-Ar and Ar-DF/HF potentials. Similarly, the predicted redshifts agree qualitatively with the experimental shifts, although they are systematically larger. Close coupling calculations have also been performed for $\text{Ar}_2\text{DF}/\text{HF}$; the predicted rotational constants again consistently over-predict the experimental values. The discrepancies are larger than the errors for the dimers calculated on their respective pair potentials, signifying the need for corrective nonpairwise additive (three-body) terms in the calculations.

Three such terms have been investigated in these calculations, which account for: i) triple dipole dispersion, ii) induced dipole-induced dipole interactions between the two argon atoms, and iii) the interaction of the permanent dipole moment of the DF/HF with the exchange quadrupole on the Ar_2 . The inclusion of an isotropic triple dipole dispersion term in the Monte Carlo calculations does not improve agreement with experiment within the uncertainty of the calculations, suggesting that this is not the dominant three-body interaction in this molecular system. Close coupling calculations for $\text{Ar}_2\text{DF}/\text{HF}$ have also been performed which include the three terms listed above, and verify that the triple dipole dispersion has relatively little effect on the calculated frequencies or rotational constants. This is also true for the induced dipole-induced dipole term, whereas the effects of the exchange quadrupole are quite

pronounced. Although inclusion of these terms improves the accuracy of the calculations, the vibrational redshifts and rotational constants are still not reproduced to spectroscopic precision, signifying that further work is necessary to fully characterize the nonpairwise additivity of the potential.

One natural extension of this work is the rotationally resolved study of intermolecular bending states for $\text{Ar}_n\text{DF}/\text{HF}$. Such states have recently been observed for $\text{Ar}_2\text{DF}/\text{HF}$, and should help assess how valid the three-body terms discussed above are for regions of the potential significantly away from the equilibrium geometry. Similarly, the study of related trimer complexes should be quite useful for further characterizing nonpairwise additive forces. For example, a high resolution near-IR study of Ar_2HCl would complement nicely the far-IR work of Elrod *et al.* [112, 113, 114]. Additionally, the study of hydrogen halide complexes with two different rare gas atoms (e.g. ArNeHF) should help elucidate the applicability of the terms investigated for $\text{Ar}_2\text{HF}/\text{DF}/\text{HCl}/\text{DCI}$. These systems also hold promise for furthering our understanding of the role of exchange multipole terms, since the mixed rare gas complexes give rise to an additional exchange dipole interaction with the permanent dipole moment of the DF/HF .

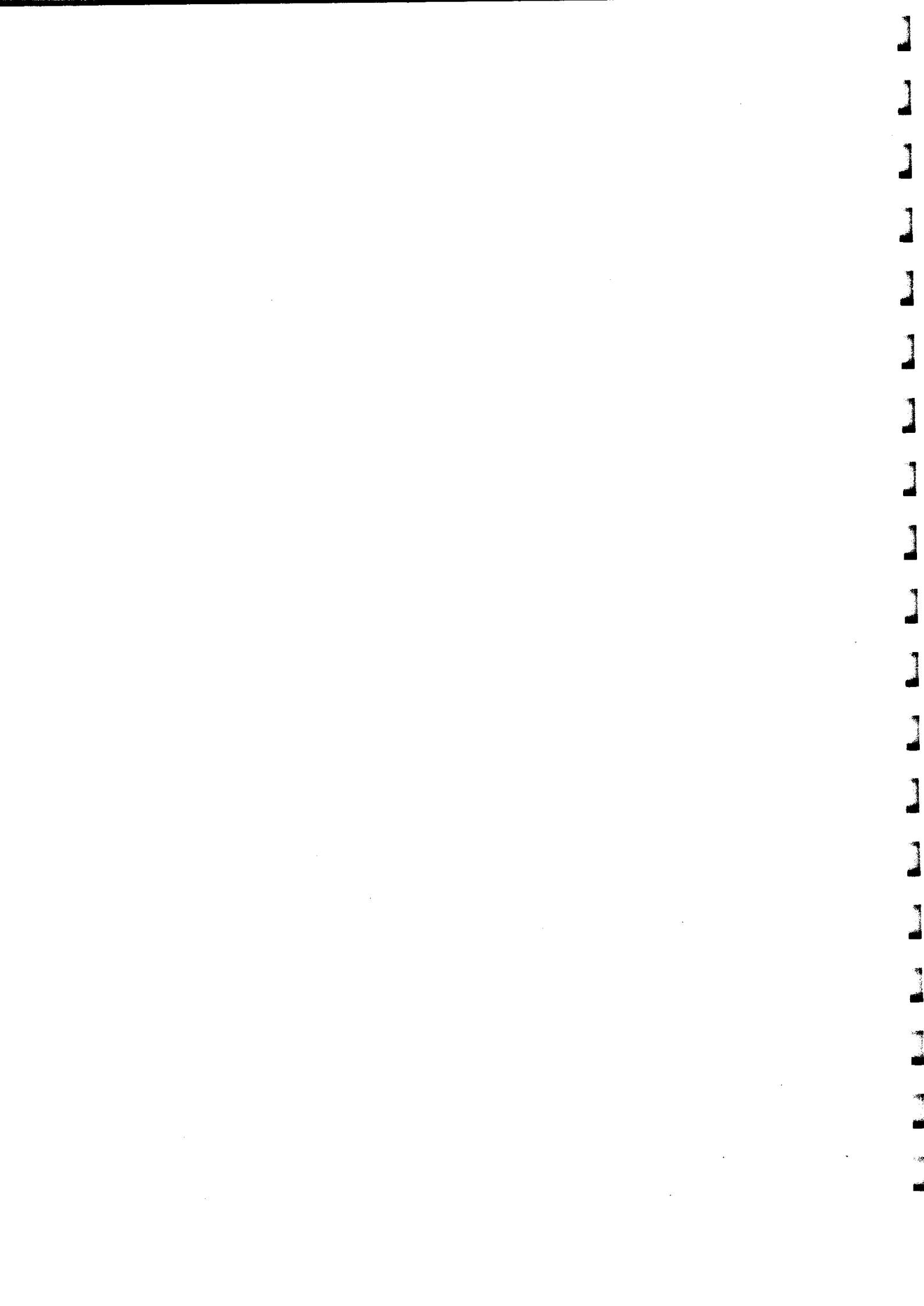


CHAPTER V

Near-IR spectroscopy of Ar_2HF and Ar_2DF intermolecular van der Waals modes:
Detailed probes of nonadditive intermolecular forces.

5.1 Introduction

The intense experimental and theoretical interest devoted to weakly bound van der Waals and hydrogen bonded complexes has been fueled by their demonstrated ability in elucidating detailed information about intermolecular forces. Dramatic progress has been realized for prototypical binary systems such as Ar-HF , Ar-HCl , $\text{Ar-H}_2\text{O}$, and Ar-NH_3 , for which accurate potential energy surfaces have been constructed from inversion of rotationally resolved spectroscopic data. The accuracy of these potentials in the bound region is a consequence of the large portion of the potential probed via excitation of intermolecular bending and stretching states. The availability of accurate pair potentials is essential prior to launching a meaningful theoretical assault on larger oligomers. Although the respective pair potentials may reproduce the experimental data on the dimers such as vibrational frequencies and binding energies to high accuracy, the "pairwise additive" potential constructed from



the sum of pair potentials, e.g.,

$$V = \sum_{i>j}^N V_2(r_i, r_j) \quad (5.1)$$

may predict properties for larger oligomers that are significantly different than observed experimentally. This is because the true interaction potential also includes three- and higher n -body terms,

$$V = \sum_{i>j}^N V_2(r_i, r_j) + \sum_{i>j>k}^N V_3(r_i, r_j, r_k) + \sum_{i>j>k>l}^N V_4(r_i, r_j, r_k, r_l) + \dots \quad (5.2)$$

The importance of higher order terms has been well documented for rare gas systems. As a well known example, the binding energies for rare gas solids calculated on pairwise additive potentials are ≈ 4 –10% larger than observed experimentally [115]. The discrepancies are larger than the associated uncertainties of the pair potentials, and arise from the neglect of multibody, or nonadditive terms. The study of nonadditivity in atomic systems, initiated more than 50 years ago by Axilrod and Teller [13] and Muto [280], has progressed to a high level of understanding. The effects of numerous nonadditive terms on reducing the discrepancies with experiment have been studied for rare gas systems. Much less is known, however, about nonadditive terms in the potentials of systems with *molecular* constituents.

The dearth of knowledge about molecular nonadditive terms reflects the difficulties, both experimental and theoretical, of isolating their contributions. Because nonadditivity typically constitutes a small correction to the pairwise additive interaction, sensitive experimental techniques are required to extract accurate data. The theoretical challenge is correspondingly difficult, for it is necessary to determine the pairwise interactions contributions before those from nonadditive terms can be deduced. For systems where this criterion is met, the problem of ascribing a functional

form to the nonadditive terms must be addressed. While intuition can serve as a valuable guide, useful insight can also be provided by *ab initio* calculations of nonadditive effects. In particular, Chałasiński, Szczęśniak, and coworkers [352, 94] have presented calculations for a number of weakly bound systems which decompose the nonadditivity into physically meaningful components due to dispersion, induction, and exchange. It is not entirely clear yet how accurate the nonadditive terms determined from such *ab initio* techniques are, however, due to the limited systems for which the requisite experimental data is available.

A logical starting point for understanding nonadditive intermolecular forces is trimers, for which the nonadditive contributions to the interaction potential consist solely of "three-body" terms. The trimer systems that currently hold the most promise for both spectroscopic characterization and theoretical modelling are the complexes formed between a hydrogen halide and rare gas (in particular Ar) atoms. The simplest of these are the tetratomic complexes $\text{Ar}_2\text{HF}/\text{DF}$ and $\text{Ar}_2\text{HCl}/\text{DCl}$. The Ar-Ar potential is known accurately from crossed beam scattering and UV spectroscopic studies, and reproduces vibrational frequencies, rotational constants, scattering cross sections, and second virial coefficients to within experimental error. Furthermore, the Ar-HF and Ar-HCl potential energy surfaces are known to high accuracy, not only as a function of the low frequency van der Waals stretching and bending coordinates, but also the high frequency intramolecular stretch as well. This dependence is built in parametrically through the mass reduced quantum number $\eta = (v + \frac{1}{2})/\sqrt{\mu_{\text{HX}}/D_{\text{X}}}$ ($\text{X}=\text{F},\text{Cl}$), and permits calculations of the intermolecular potential energy surface in vibrationally excited levels for both the hydrogen and deuterium isotopomers. The global accuracy of the ArHF potential over the bound region is estimated to be \leq

0.3%, which is roughly one part in 1000 of the well depth [192]. The ArHF potential has been tested against, and found capable of reproducing, new van der Waals spectroscopic data [255, 71], lineshape parameters for HF in a bath of Ar[147], and rotationally inelastic cross sections for Ar + HF scattering [74].

Important experimental results have already been reported for Ar₂HF/DF and Ar₂HCl/DCl, initiated by the microwave experiments of Gutowsky and coworkers [152, 214]. These studies established the equilibrium geometries of the complexes as T-shaped, with C_{2v} symmetry (as indicated in Figure 5.1), and identified substantial large amplitude motion even in the ground state. For example, the vibrationally averaged angles for Ar₂HF are $\langle\theta\rangle = 32.8^\circ$, $\langle\phi\rangle = 27.7^\circ$, and $\langle\chi\rangle \approx 7^\circ$. Elrod *et al.* [112, 113, 114, 115] have observed and analyzed three intermolecular bending states for Ar₂HCl and one for Ar₂DCl in the far-IR, which sample substantially larger regions of the angular potential. In addition, the van der Waals ground states of Ar₂HF [265] and Ar₂DF[130] have been studied in the mid-IR, via excitation of the $v=1$ HF/DF stretch.

The first calculations of nonadditive effects in these complexes were performed by Hutson *et al.* [187], who compared spectroscopic parameters for Ar₂HCl with the microwave data of Klots *et al.*[214] Even within the rather drastic (but at that time necessary) dynamical restrictions employed, nonadditivity was manifested at levels that were significant with respect to the uncertainty in the pair potentials. Specifically, the predicted rotational constants were too large, and the anisotropy of the HCl bending motion was underpredicted. Little quantitative information could be extracted, however, because of the restrictions of the calculations and the limited region of the potential sampled by the microwave data. Cooper and Hutson [88] have

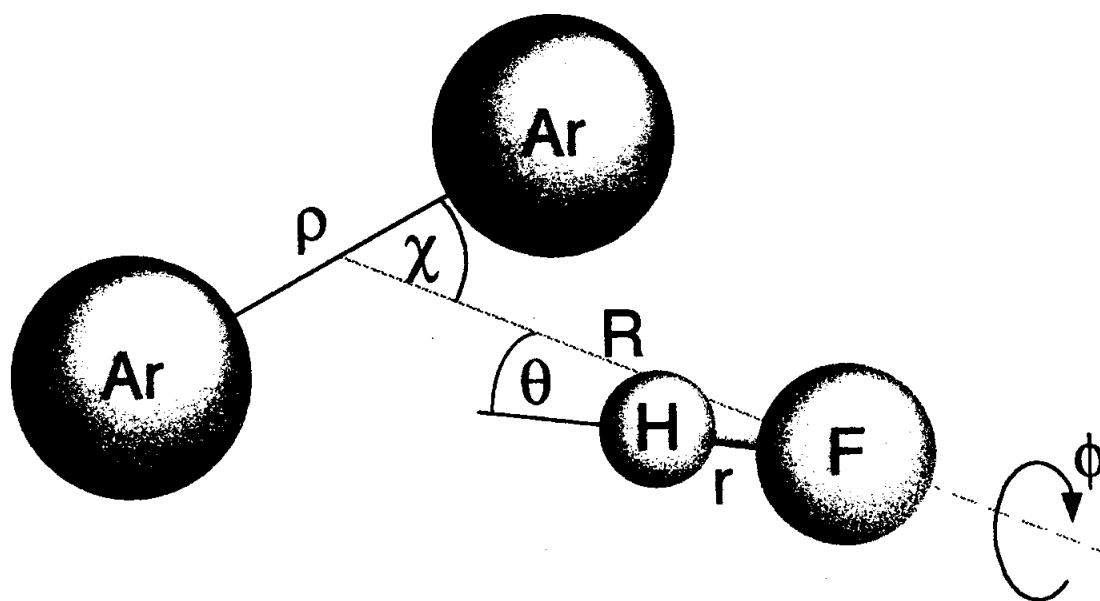


Figure 5.1: $\text{Ar}_2\text{HF}/\text{DF}$ intermolecular degrees of freedom expressed in Jacobi (scattering) coordinates.

recently performed improved close coupling calculations, including explicitly the dependence of all five intermolecular degrees of freedom. The rotational constants and vibrational frequencies were compared to the microwave and far-IR values of Elrod *et al.* [114] These calculations are sufficiently accurate to identify significant discrepancies between the experimental results and the values predicted within the assumption of pairwise additivity. Cooper and Hutson examined the effect of a number of non-additive terms on reducing the discrepancy with experiment, and found that several terms accounting for dispersion, induction, and exchange interactions are necessary to bring the calculated results in line with experiment. However, it is not clear how general the terms deemed important for $\text{Ar}_2\text{HCl}/\text{DCl}$ are for other molecular systems. This is hard to predict even for the closely related system $\text{Ar}_2\text{HF}/\text{DF}$, because the ArHF potential is much more anisotropic than the ArHCl potential. Consequently, the relative importance of specific nonadditive terms may be appreciably different.

Some insight into this issue has been obtained from the calculations of Ernesti and Hutson on the rotational constants and vibrational redshifts for Ar_2HF [118] in the van der Waals ground state. However, the applicability of the results is difficult to determine due to the rather limited region of the intermolecular potential sampled. In the present study, states are accessed that correspond to hindered librational motion of the HF/DF and thus sample a much larger region of the potential. Additionally, Ernesti and Hutson have recently extended their five dimensional calculations of $\text{Ar}_2\text{HF}/\text{DF}$ [118, 121] to include intermolecular excitation. Consequently, the experimental data and theoretical calculations are at a stage where the effects of nonadditivity in $\text{Ar}_2\text{HF}/\text{DF}$ can be assessed in detail, making a comparison with the $\text{Ar}_2\text{HCl}/\text{DCl}$ results more straightforward and meaningful. Finally, Cybulski *et*

al. [94] have recently presented *ab initio* calculations of nonadditive forces for the Ar_2HF system, which provides one of the systems where *ab initio* nonadditivity can be compared quantitatively with experiment.

The rest of the chapter is organized as follows. Section 5.2 provides a brief explanation of the experimental apparatus and conditions. Analysis of the spectroscopic data is presented in Section 5.3, as well as a discussion of the Coriolis and/or anharmonic perturbations identified in the Ar_2HF spectra. Section 5.4 presents results of two-dimensional angular calculations, which are found capable of reproducing the intermolecular vibrational frequencies semiquantitatively. Comparison of the experimental data with full five-dimensional calculations are also provided, which allow an assessment of the magnitude and physical origin of nonadditive effects for these trimers. The effects of several nonadditive terms are discussed and compared to predictions from *ab initio* calculations.

5.2 Experimental

$\text{Ar}_2\text{HF}/\text{DF}$ complexes are formed in a supersonic expansion generated by expanding 0.5% HF/DF in a 60:40 mix of Ar:Ne-70 (a 70/30 mixture of Ne/He from the first distillation cut of Ne) through a $4 \text{ cm} \times 190 \mu\text{m}$ pulsed slit jet [247]. The complexes are detected via time-gated, dual beam direct absorption detection of infrared light. The IR is generated via nonlinear mixing of a fixed frequency Ar^+ laser (488.0 nm for studying Ar_2HF and 514.5 nm for Ar_2DF) and a tunable ring dye laser (Rhodamine 6G pumped by 4 W from a second Ar^+ laser). Multipass optics are used to pass the infrared light 20 times through the expansion for a total absorption

pathlength of 80 cm.

The single frequency Ar^+ laser is frequency stabilized to a transfer cavity that is actively locked to a polarization stabilized HeNe laser, providing both short term [320] and long term [130] stability of ≤ 5 MHz. Transmission fringes obtained by scanning the dye laser are also recorded with this cavity, and provide accurate infrared frequency markers. The transition frequencies of the intermolecular bands are measured with a traveling Michelson interferometer, and are referenced to nearby monomer transitions. The in-plane and out-of-plane bends of Ar_2HF are referenced to $R(1)$ of HF at $4038.9625 \text{ cm}^{-1}$ (Ref. [148]), and the in-plane and out-of-plane bends of Ar_2DF to $R(1)$ and $R(2)$ of DF, at $2948.3057 \text{ cm}^{-1}$ and $2968.2050 \text{ cm}^{-1}$, respectively (Ref. [254]).

5.3 Results and Analysis

The intermolecular vibrations of $\text{Ar}_2\text{HF/DF}$ can be separated into two types, depending on whether the hindered internal rotation of the diatom is excited. The vibrational states in which the rotor is unexcited ($j_{\text{HF/DF}}=0$) closely resemble the fundamental vibrations of the isoelectronic species Ar_2Ne . These "heavy atom" vibrations consist of only in-plane motion (see Ref. [88] for a more detailed description). The three lowest states in which the HF/DF is librationaly excited correlate adiabatically with $j_{\text{HF/DF}}=1$. If the $\text{Ar}_2\text{HF/DF}$ potential were anisotropic with respect to HF/DF angular motion, these three states would be degenerate and would correlate with $|k|=1$ (Π) and $k=0$ (Σ) states. The angular anisotropy of the $\text{Ar}_2\text{HF/DF}$ potential completely lifts the $j = 1$ rotor's three-fold spatial degeneracy, giving rise

to states characterized by k , the (approximately conserved) projection of j along the intermolecular axis. The two states with $|k| = 1$ correlate to in-plane and out-of-plane vibrations, and are the states characterized in this study. The state with $k=0$ has been designated the Σ (Ref. [88]) or parallel (Ref. [112]) bend, and in the rigid molecule limit correlates with the overtone of the lowest $|k| = 1$ bending vibration. Although k is explicitly not a good quantum number for $\text{Ar}_2\text{HF/DF}$, we will denote the state correlating with $k=0$ the Σ bend for consistency with Hutson and coworkers, whose calculations we will be comparing to our experimental data.

The equilibrium geometry of $\text{Ar}_2\text{HF/DF}$ has been inferred to be T -shaped, with the HF/DF lying along a C_2 symmetry axis. In Figure 5.1, this corresponds to $\theta = 0^\circ$ and $\chi = 90^\circ$ (ϕ is cyclic at $\theta = 0^\circ$). The presence of two equivalent Ar atoms with nuclear spin $I = 0$ constrains the available quantum states by Bose-Einstein statistics, i.e., the overall wave function must be symmetric with respect to exchange of the equivalent nuclei. By virtue of this constraint, and the symmetry properties of the full Hamiltonian, only $K_a K_c = ee$ or oo states have non-zero statistical weights in the ground vibrational state.

5.3.1 Ar_2DF in-plane bend

The transition moment for the in-plane bend is along the a inertial axis, and the resulting A type band should consist of asymmetric top structure with a prominent central Q branch. A band that fulfills these criteria is observed $\approx 45 \text{ cm}^{-1}$ above the Ar_2DF ($\nu_{\text{DF}} = 1$) vibrational origin (see Figure 5.2). Combination differences utilizing the accurately known microwave constants confirm that the transitions originate from

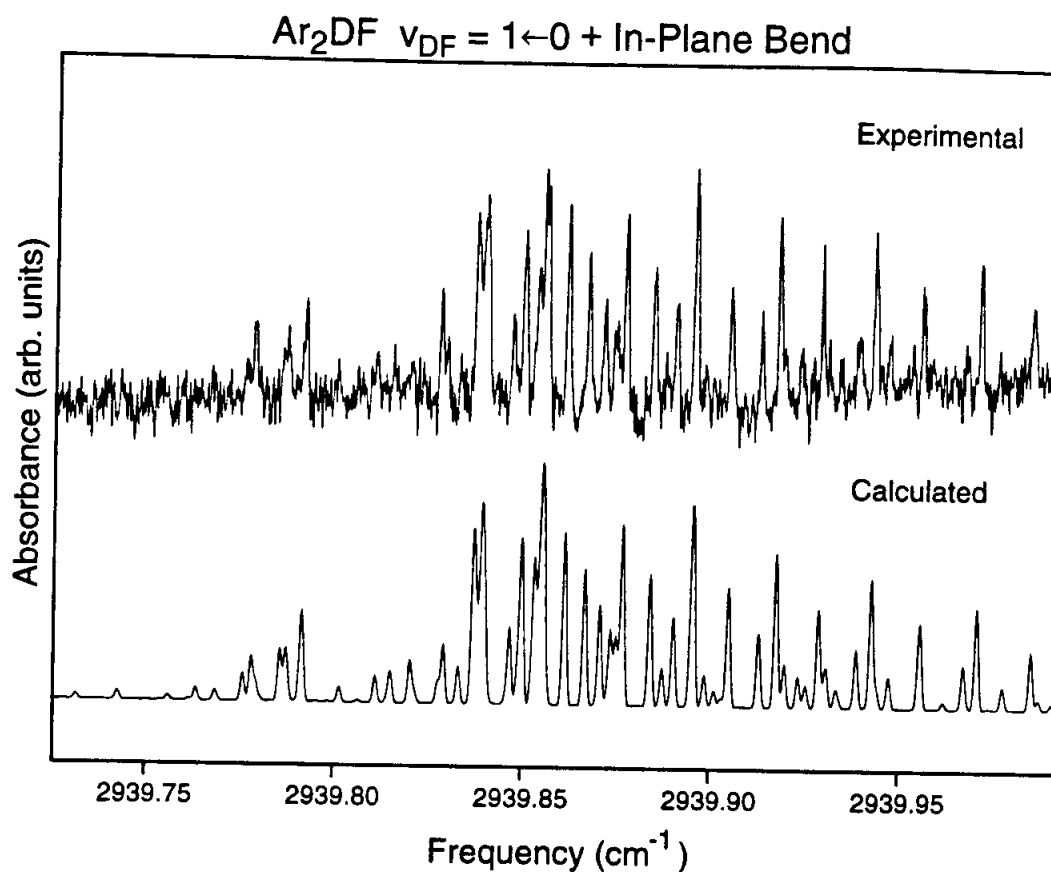


Figure 5.2: Sample experimental and calculated spectra for the Q branch region of the Ar_2DF in-plane bend. The latter is generated using the constants listed in Table 5.2, which are obtained from a least squares fit of the experimental data to a Watson A Hamiltonian. The excellent agreement signifies that no significant rotational perturbations are present in the spectrum.

the Ar₂DF ground state. Infrared selection rules identify this as an *A* type band ($\Delta K_a = 0, \pm 2, \dots, \Delta K_c = \pm 1, \pm 3, \dots$), and consequently it is assigned to the in-plane bend of Ar₂DF. The transition frequencies, shown in Table 5.1, are well fit to a Watson *A*-type Hamiltonian in the *I'* representation, i.e.,

$$\begin{aligned} \hat{H} = & \frac{1}{2}(B + C)\hat{J}^2 + \left[A - \frac{1}{2}(B + C) \right] \hat{J}_a^2 + \frac{1}{2}(B - C) \{ [\hat{J}_b - \hat{J}_c]^2 \} \\ & - \Delta_J \hat{J}^4 - \Delta_{JK} \hat{J}^2 \hat{J}_a^2 - \Delta_K \hat{J}_a^4 \\ & - 2\delta_J \hat{J}^2 (\hat{J}_b^2 - \hat{J}_c^2) - \delta_K \left[\hat{J}_a^2 (\hat{J}_b^2 - \hat{J}_c^2) + (\hat{J}_b^2 - \hat{J}_c^2) \hat{J}_a^2 \right] \end{aligned} \quad (5.3)$$

The results of the fit are shown in Table 5.2. Although the integrated intensity of the in-plane bend is approximately 4 times less than the intermolecular ground state, a sufficient number of transitions (150) are assigned to determine all five quartic distortion constants. The residual standard deviation of the fit is 0.00016 cm⁻¹ (4.8 MHz), which is comparable to the experimental precision. The quality of the fit is corroborated in Figure 5.2, which shows a comparison of the experimental *Q* branch with a simulation generated using the constants in Table 5.2. It is of course quite possible that perturbations by nominally "dark" intermolecular vibrations are being absorbed by the fit constants. For example, if the perturbing states interact via a Coriolis mechanism, the perturbation increases quadratically with *J* [170]. Consequently, if the energy difference between the states is large enough (so that there are no rotational level crossings), the rotational constants *A*, *B*, and *C* obtained from the fit will differ from the unperturbed values. However, the centrifugal distortion constants depend on \hat{J}^4 , are thus much more sensitive to such perturbations. Indeed, the value of Δ_{JK} for the in-plane bend is opposite in sign and 10-fold larger than the value for the intermolecular ground state, suggesting that such interactions may in

Table 5.1: Observed transition frequencies for the $\nu_{DF} = 1 \leftarrow 0 +$ in-plane bend transition in Ar_2DF . The numbers in parentheses represent (observed-calculated) values using the constants listed in Table 5.2.

$J'_{K'_a, K'_c}$	\leftarrow	J_{K_a, K_c}	Energy	$J'_{K'_a, K'_c}$	\leftarrow	J_{K_a, K_c}	Energy
1 _{0,1}	\leftarrow	2 _{0,2}	2939.64485(-7)	6 _{4,3}	\leftarrow	7 _{4,4}	2939.14868(2)
2 _{1,2}	\leftarrow	1 _{1,1}	2940.00890(20)	6 _{5,2}	\leftarrow	6 _{5,1}	2939.86718(10)
2 _{1,2}	\leftarrow	3 _{1,3}	2939.57649(-9)	6 _{5,2}	\leftarrow	7 _{5,3}	2939.17590(-22)
2 _{2,1}	\leftarrow	3 _{2,2}	2939.55132(-14)	6 _{6,1}	\leftarrow	6 _{6,0}	2939.89567(-21)
3 _{0,3}	\leftarrow	2 _{0,2}	2940.10317(-9)	7 _{0,7}	\leftarrow	6 _{0,6}	2940.39135(-5)
3 _{0,3}	\leftarrow	4 _{0,4}	2939.47549(3)	7 _{0,7}	\leftarrow	8 _{0,8}	2939.15544(-14)
3 _{1,2}	\leftarrow	2 _{1,1}	2940.14423(23)	7 _{1,6}	\leftarrow	6 _{1,5}	2940.47234(-10)
3 _{1,2}	\leftarrow	4 _{1,3}	2939.41172(15)	7 _{2,5}	\leftarrow	8 _{2,6}	2938.96517(17)
3 _{2,1}	\leftarrow	2 _{2,0}	2940.14089(20)	7 _{3,4}	\leftarrow	6 _{3,3}	2940.53460(-8)
3 _{2,1}	\leftarrow	4 _{2,2}	2939.41840(28)	7 _{3,4}	\leftarrow	8 _{3,5}	2938.95737(16)
3 _{3,0}	\leftarrow	3 _{3,1}	2939.85017(-2)	7 _{4,3}	\leftarrow	8 _{4,4}	2939.01728(-12)
4 _{1,4}	\leftarrow	3 _{1,3}	2940.16871(19)	7 _{5,2}	\leftarrow	6 _{5,1}	2940.54630(-24)
4 _{1,4}	\leftarrow	5 _{1,5}	2939.40689(12)	7 _{5,2}	\leftarrow	7 _{5,3}	2939.85545(-13)
4 _{2,3}	\leftarrow	3 _{2,2}	2940.21504(13)	7 _{6,1}	\leftarrow	7 _{6,2}	2939.88468(15)
4 _{2,3}	\leftarrow	4 _{2,2}	2939.77852(23)	7 _{6,1}	\leftarrow	8 _{6,2}	2939.09582(-32)
4 _{2,3}	\leftarrow	5 _{2,4}	2939.35713(-9)	7 _{7,0}	\leftarrow	7 _{7,1}	2939.91786(-13)
4 _{3,2}	\leftarrow	3 _{3,1}	2940.23648(-24)	8 _{1,8}	\leftarrow	7 _{1,7}	2940.46072(-1)
4 _{3,2}	\leftarrow	5 _{3,3}	2939.35027(-18)	8 _{1,8}	\leftarrow	9 _{1,9}	2939.07287(-9)
4 _{4,1}	\leftarrow	4 _{4,0}	2939.86172(17)	8 _{2,7}	\leftarrow	9 _{2,8}	2938.99347(-3)
5 _{0,5}	\leftarrow	4 _{0,4}	2940.25040(6)	8 _{3,6}	\leftarrow	7 _{3,5}	2940.58213(-19)
5 _{0,5}	\leftarrow	6 _{0,6}	2939.31793(1)	8 _{3,6}	\leftarrow	9 _{3,7}	2938.93551(4)
5 _{1,4}	\leftarrow	4 _{1,3}	2940.32277(-17)	8 _{4,5}	\leftarrow	7 _{4,4}	2940.61229(-9)
5 _{1,4}	\leftarrow	6 _{1,5}	2939.22190(-13)	8 _{4,5}	\leftarrow	9 _{4,6}	2938.92270(1)
5 _{2,3}	\leftarrow	4 _{2,2}	2940.34475(-1)	8 _{5,4}	\leftarrow	7 _{5,3}	2940.63374(-33)
5 _{2,3}	\leftarrow	6 _{2,4}	2939.18059(3)	8 _{5,4}	\leftarrow	9 _{5,5}	2938.94641(10)
5 _{3,2}	\leftarrow	4 _{3,1}	2940.33606(16)	8 _{6,3}	\leftarrow	7 _{6,2}	2940.65957(2)
5 _{3,2}	\leftarrow	5 _{3,3}	2939.84720(16)	8 _{6,3}	\leftarrow	8 _{6,2}	2939.87143(27)
5 _{3,2}	\leftarrow	6 _{3,3}	2939.21717(-7)	8 _{6,3}	\leftarrow	9 _{6,4}	2938.98166(6)
5 _{4,1}	\leftarrow	5 _{4,2}	2939.85385(15)	8 _{7,2}	\leftarrow	8 _{7,1}	2939.90508(-16)
5 _{4,1}	\leftarrow	6 _{4,2}	2939.25798(17)	8 _{8,1}	\leftarrow	8 _{8,0}	2939.94323(2)
5 _{5,0}	\leftarrow	5 _{5,1}	2939.87712(7)	9 _{0,9}	\leftarrow	10 _{0,10}	2938.98822(5)
6 _{1,6}	\leftarrow	5 _{1,5}	2940.31782(-21)	9 _{1,8}	\leftarrow	8 _{1,7}	2940.60644(-28)
6 _{1,6}	\leftarrow	7 _{1,7}	2939.24007(-8)	9 _{1,8}	\leftarrow	10 _{1,9}	2938.89974(-6)
6 _{2,5}	\leftarrow	5 _{2,4}	2940.37923(-26)	9 _{2,7}	\leftarrow	8 _{2,6}	2940.68554(13)
6 _{2,5}	\leftarrow	7 _{2,6}	2939.17113(-1)	9 _{2,7}	\leftarrow	10 _{2,8}	2938.78792(4)
6 _{3,4}	\leftarrow	5 _{3,3}	2940.41607(16)	9 _{3,6}	\leftarrow	10 _{3,7}	2938.71061(4)
6 _{3,4}	\leftarrow	7 _{3,5}	2939.13903(-15)	9 _{5,4}	\leftarrow	9 _{5,5}	2939.82969(30)
6 _{4,3}	\leftarrow	5 _{4,2}	2940.43608(-17)	9 _{6,3}	\leftarrow	10 _{6,4}	2938.86306(-17)

fact be present. It will be shown below that such perturbations are not only present in the Ar₂HF spectra, but are quite pronounced.

5.3.2 Ar₂DF out-of-plane bend

The transition moment for the out-of-plane bend is along the *c* inertial axis, and the resulting *C* type band also give rises to a prominent central *Q* branch. Figure 5.3 shows the region near the origin of a band centered $\approx 72 \text{ cm}^{-1}$ above the $\nu_{\text{DF}}=1$ origin. Combination differences verify that the transitions originate from the Ar₂DF ground state, and the selection rules indicate that the band is *C* type ($\Delta K_a = \pm 1, \pm 3, \dots$, $\Delta K_c = 0, \pm 2, \dots$). Consequently, this band is assigned the out-of-plane bend.

The transitions to this band, listed in Table 5.3, are also well fit to the Hamiltonian in Eq. 5.3. The fit results, listed in Table 5.2, indicate that this band is fit to experimental precision. The Ar₂DF out-of-plane bend is the weakest of the four bands observed in this study, and has $\approx 1/8$ the integrated intensity of the transition to the intermolecular ground state. The corresponding fewer number of observed transitions limits the number of distortion constants that can be determined with statistical significance. Nevertheless, the excellent agreement between the experimental spectrum and that calculated using the constants in Table 5.2 (shown in Figure 5.3), together with the good fit quality indicates that there are no significant perturbations to this band.

For a rigid planar molecule, the inertial defect is zero, while positive (negative) values reflect large amplitude in-plane (out-of-plane) motion. The van der Waals

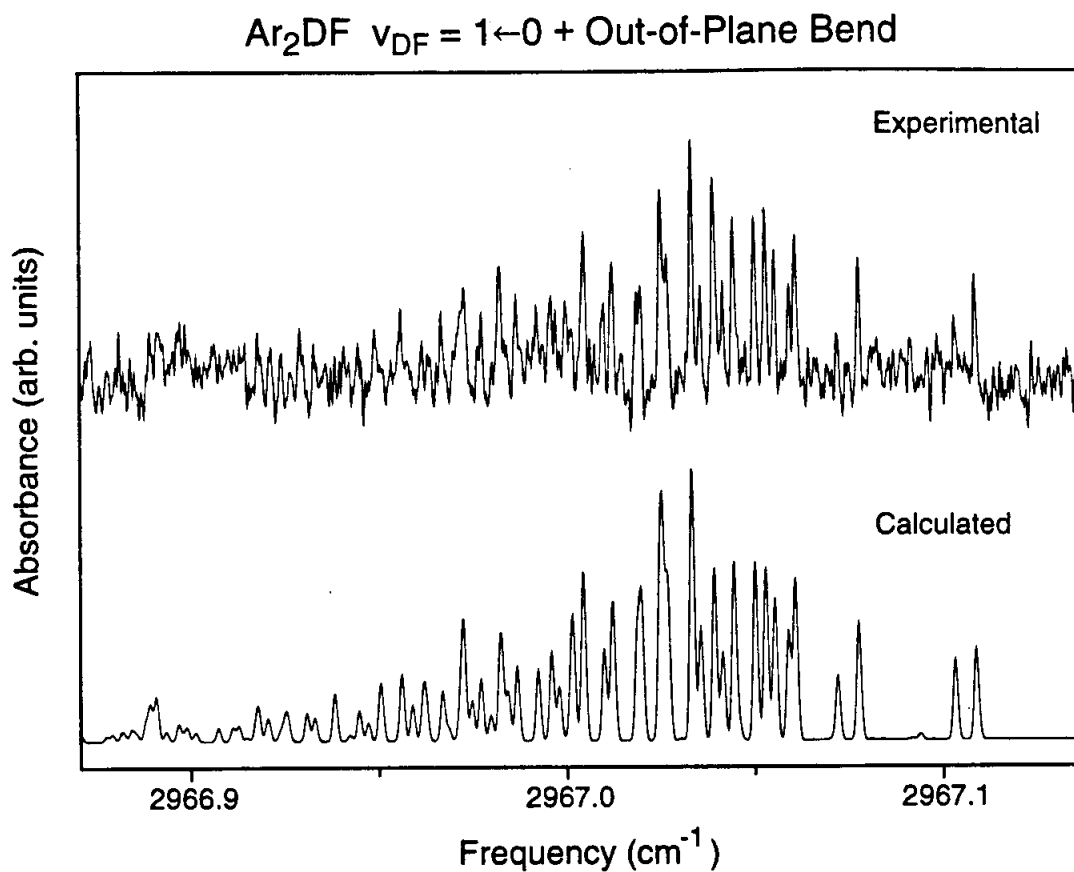


Figure 5.3: Sample experimental and calculated spectra for the Q branch region of the out-of-plane bend of Ar_2DF . The latter is generated using the constants listed in Table 5.2, which are obtained from a least squares fit of the experimental data to a Watson A Hamiltonian. As is observed for the Ar_2DF in-plane bend, the agreement is excellent, indicating that neither bending state has significant rotational perturbations present.

Table 5.3: Observed transition frequencies for the $\nu_{DF} = 1 \leftarrow 0 +$ out-of-plane bend transition in Ar_2DF . The numbers in parentheses represent (observed-calculated) values using the constants listed in Table 5.2.

$J'_{K'_a, K'_c}$	\leftarrow	J_{K_a, K_c}	Energy	$J'_{K'_a, K'_c}$	\leftarrow	J_{K_a, K_c}	Energy
2 _{2,1}	\leftarrow	1 _{1,1}	2967.49264(1)	7 _{1,6}	\leftarrow	8 _{2,6}	2965.95555(24)
2 _{2,1}	\leftarrow	3 _{3,1}	2966.44858(27)	7 _{3,4}	\leftarrow	6 _{2,4}	2968.06988(35)
3 _{0,3}	\leftarrow	3 _{1,3}	2967.07156(10)	7 _{3,4}	\leftarrow	8 _{4,4}	2965.85720(19)
3 _{1,2}	\leftarrow	3 _{2,2}	2966.94765(-2)	7 _{4,3}	\leftarrow	6 _{3,3}	2968.18147(-19)
3 _{2,1}	\leftarrow	2 _{1,1}	2967.57184(-5)	7 _{4,3}	\leftarrow	8 _{5,3}	2965.65468(15)
3 _{2,1}	\leftarrow	4 _{3,1}	2966.36255(-28)	7 _{6,1}	\leftarrow	6 _{5,1}	2968.38136(-14)
4 _{1,4}	\leftarrow	4 _{0,4}	2967.10749(1)	7 _{6,1}	\leftarrow	8 _{7,1}	2965.28884(29)
4 _{2,3}	\leftarrow	3 _{1,3}	2967.73386(-2)	8 _{1,8}	\leftarrow	8 _{0,8}	2967.07992(-5)
4 _{2,3}	\leftarrow	5 _{3,3}	2966.23517(-25)	8 _{2,7}	\leftarrow	8 _{1,7}	2967.08912(43)
4 _{3,2}	\leftarrow	3 _{2,2}	2967.80229(-8)	8 _{5,4}	\leftarrow	7 _{4,4}	2968.39590(7)
4 _{3,2}	\leftarrow	5 _{4,2}	2966.09731(-14)	8 _{5,4}	\leftarrow	9 _{6,4}	2965.37728(40)
5 _{0,5}	\leftarrow	5 _{1,5}	2967.08523(-1)	8 _{6,3}	\leftarrow	7 _{5,3}	2968.48099(-9)
5 _{1,4}	\leftarrow	4 _{0,4}	2967.81076(28)	8 _{6,3}	\leftarrow	9 _{7,3}	2965.19372(20)
5 _{1,4}	\leftarrow	5 _{2,4}	2967.01206(12)	9 _{0,9}	\leftarrow	9 _{1,9}	2967.07430(-9)
5 _{1,4}	\leftarrow	6 _{2,4}	2966.26895(14)	9 _{4,5}	\leftarrow	8 _{3,5}	2968.35785(-32)
5 _{3,2}	\leftarrow	4 _{2,2}	2967.87651(-20)	9 _{4,5}	\leftarrow	10 _{5,5}	2965.50147(-51)
5 _{3,2}	\leftarrow	6 _{4,2}	2966.01238(-13)	10 _{1,10}	\leftarrow	10 _{0,10}	2967.06907(-12)
5 _{4,1}	\leftarrow	4 _{3,1}	2967.99743(-26)	10 _{2,9}	\leftarrow	10 _{1,9}	2967.06558(4)
5 _{4,1}	\leftarrow	6 _{5,1}	2965.83707(-20)	10 _{3,8}	\leftarrow	10 _{2,8}	2967.10182(-4)
5 _{5,0}	\leftarrow	4 _{4,0}	2968.09557(-18)	11 _{0,11}	\leftarrow	11 _{1,11}	2967.06325(11)
5 _{5,0}	\leftarrow	6 _{6,0}	2965.66263(-12)	11 _{2,9}	\leftarrow	11 _{3,9}	2967.03450(12)
6 _{1,6}	\leftarrow	6 _{0,6}	2967.09072(8)	12 _{1,12}	\leftarrow	12 _{0,12}	2967.05660(-11)
6 _{2,5}	\leftarrow	6 _{1,5}	2967.13314(-5)	12 _{2,11}	\leftarrow	12 _{1,11}	2967.04864(4)
6 _{3,4}	\leftarrow	5 _{2,4}	2968.02942(12)	13 _{0,13}	\leftarrow	13 _{1,13}	2967.04961(-11)
6 _{3,4}	\leftarrow	7 _{4,4}	2965.89444(-2)	13 _{1,12}	\leftarrow	13 _{2,12}	2967.03965(-16)
6 _{4,3}	\leftarrow	5 _{3,3}	2968.10289(-5)	14 _{1,14}	\leftarrow	14 _{0,14}	2967.04204(-19)
6 _{4,3}	\leftarrow	7 _{5,3}	2965.74043(4)	15 _{0,15}	\leftarrow	15 _{1,15}	2967.03450(30)
6 _{6,1}	\leftarrow	5 _{5,1}	2968.28243(21)	16 _{1,16}	\leftarrow	16 _{0,16}	2967.02562(-2)
6 _{6,1}	\leftarrow	7 _{7,1}	2965.38426(-14)	17 _{0,17}	\leftarrow	17 _{1,17}	2967.01642(-13)
7 _{0,7}	\leftarrow	7 _{1,7}	2967.08284(-1)	18 _{1,18}	\leftarrow	18 _{0,18}	2967.00721(30)
7 _{1,6}	\leftarrow	6 _{0,6}	2968.12959(1)	19 _{0,19}	\leftarrow	19 _{1,19}	2966.99655(-17)

ground states for both $v_{DF}=0$ and 1 have inertial defects which are large and positive, indicating that the bulk of the large amplitude motion is in the molecular plane. Excitation of the in-plane bend increases the inertial defect as would be expected, while out-of-plane excitation leads to a decrease. Interestingly, however, the inertial defect for the out-of-plane bend is still quite positive. This indicates that residual in-plane DF motion and zero-point motion from the low frequency "heavy atom" vibrations still contribute strongly to the large amplitude motion of the complex.

5.3.3 Ar₂HF in-plane bend

As for Ar₂DF, the Ar₂HF in-plane bend gives rise to an *A* type band, with a prominent central *Q* branch. Figure 5.4 shows part of a band that is located ≈ 62 cm⁻¹ above the Ar₂HF $v_{HF}=1$ origin, with approximately 1/4 the integrated intensity of the intermolecular ground state. Combination differences verify that the transitions originate from the ground state of Ar₂HF. The assigned transition frequencies, listed in Table 5.4, are poorly fit to Eq. 5.3, in contrast to the good fits realized for the Ar₂DF in-plane and out-of-plane bends. The residual standard deviation of the fit is approximately 70 times larger than the experimental precision. The results of the fit are shown in Table 5.5. Although most of the low *J* lines can be confidently assigned, the assignment of transitions accessing higher *J* and *K_a* becomes ambiguous as the discrepancies between the calculated frequencies and the assignments allowed by combination differences grow increasingly large. It is worth emphasizing that by virtue of the high frequency stability of the spectrometer, agreement with combination differences provides a rigorous criterion for assignment. For example, the average

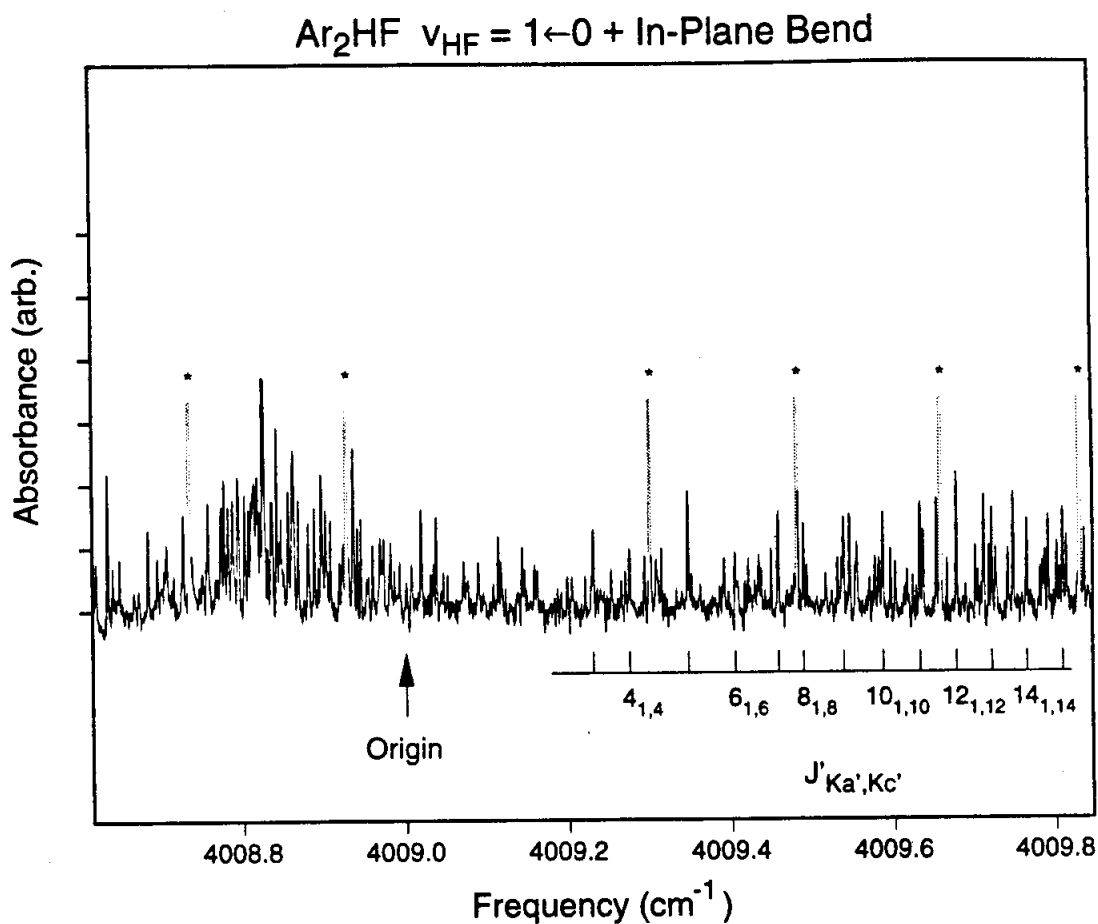


Figure 5.4: Region near the origin of the Ar_2HF in-plane bend. The shaded peaks marked by an asterisk are $P(2)$ through $R(3)$ of the $\text{ArHF } \Sigma$ bend. The band appears to be perturbed by multiple states, which precludes an unambiguous assignment of all observed transitions. Evidence for one perturbation is shown in the figure, which labels the transitions to the lowest K_a level for each J ($J_{K_a K_c} = J_{1J}/J_{0J}$ for J even/odd). The spacing appears irregular near $J \approx 5-8$, suggesting a crossing of rotational manifolds with a background state. This interpretation is corroborated by the fit residuals, which are large and positive for $J \leq 6$, and negative for $J \geq 7$, suggesting that the crossing is localized near these J values.

Table 5.4: Observed transition frequencies for the $\nu_{\text{HF}} = 1 \leftarrow 0 +$ in-plane bend transition in Ar_2HF . The numbers in parentheses represent (observed-calculated) values using the constants listed in Table 5.5.

$J'_{K'_a, K'_c} \leftarrow J_{K_a, K_c}$	Energy	$J'_{K'_a, K'_c} \leftarrow J_{K_a, K_c}$	Energy
2 _{1,2} \leftarrow 1 _{1,1}	4009.1285(0)	7 _{1,6} \leftarrow 8 _{1,7}	4008.1386(3)
2 _{1,2} \leftarrow 3 _{1,3}	4008.6955(0)	7 _{2,5} \leftarrow 6 _{2,4}	4009.6672(22)
2 _{2,1} \leftarrow 3 _{2,2}	4008.6472(-2)	7 _{2,5} \leftarrow 7 _{2,6}	4009.1932(22)
3 _{0,3} \leftarrow 2 _{0,2}	4009.2279(-1)	7 _{2,5} \leftarrow 8 _{2,6}	4008.1006(22)
3 _{0,3} \leftarrow 4 _{0,4}	4008.5973(-1)	7 _{3,4} \leftarrow 6 _{3,3}	4009.6028(-28)
3 _{1,2} \leftarrow 2 _{1,1}	4009.2704(-1)	7 _{3,4} \leftarrow 8 _{3,5}	4008.0320(-28)
3 _{1,2} \leftarrow 4 _{1,3}	4008.5379(-1)	7 _{4,3} \leftarrow 6 _{4,2}	4009.5529(-7)
3 _{2,1} \leftarrow 2 _{2,0}	4009.2519(7)	7 _{4,3} \leftarrow 8 _{4,4}	4008.0458(-7)
3 _{2,1} \leftarrow 4 _{2,2}	4008.5315(7)	7 _{5,2} \leftarrow 6 _{5,1}	4009.5118(3)
4 _{1,4} \leftarrow 3 _{1,3}	4009.2762(-1)	7 _{5,2} \leftarrow 7 _{5,3}	4008.8217(2)
4 _{1,4} \leftarrow 5 _{1,5}	4008.5117(-1)	7 _{5,2} \leftarrow 8 _{5,3}	4008.0292(3)
4 _{2,3} \leftarrow 3 _{2,2}	4009.3115(0)	8 _{1,8} \leftarrow 7 _{1,7}	4009.5075(-9)
4 _{2,3} \leftarrow 4 _{2,2}	4008.8775(0)	8 _{1,8} \leftarrow 9 _{1,9}	4008.1133(-9)
4 _{2,3} \leftarrow 5 _{2,4}	4008.4528(0)	8 _{2,7} \leftarrow 7 _{2,6}	4009.5689(-2)
4 _{3,2} \leftarrow 3 _{3,1}	4009.2960(-3)	8 _{2,7} \leftarrow 9 _{2,8}	4008.0265(-2)
4 _{3,2} \leftarrow 5 _{3,3}	4008.4105(-3)	8 _{3,6} \leftarrow 7 _{3,5}	4009.6235(1)
5 _{0,5} \leftarrow 4 _{0,4}	4009.3538(-1)	8 _{3,6} \leftarrow 8 _{3,5}	4008.7033(1)
5 _{0,5} \leftarrow 6 _{0,6}	4008.4167(-1)	8 _{3,6} \leftarrow 9 _{3,7}	4007.9743(1)
5 _{1,4} \leftarrow 4 _{1,3}	4009.4480(4)	8 _{4,5} \leftarrow 7 _{4,4}	4009.6300(-1)
5 _{1,4} \leftarrow 6 _{1,5}	4008.3437(4)	8 _{4,5} \leftarrow 9 _{4,6}	4007.9417(-1)
5 _{2,3} \leftarrow 4 _{2,2}	4009.4647(2)	8 _{5,4} \leftarrow 7 _{5,3}	4009.6028(0)
5 _{2,3} \leftarrow 6 _{2,4}	4008.3031(2)	8 _{5,4} \leftarrow 8 _{5,3}	4008.8097(0)
5 _{3,2} \leftarrow 4 _{3,1}	4009.4019(-6)	8 _{5,4} \leftarrow 9 _{5,5}	4007.9174(0)
5 _{3,2} \leftarrow 5 _{3,3}	4008.9134(-6)	8 _{6,3} \leftarrow 7 _{6,2}	4009.5768(15)
5 _{3,2} \leftarrow 6 _{3,3}	4008.2874(-6)	8 _{6,3} \leftarrow 8 _{6,2}	4008.7891(15)
5 _{4,1} \leftarrow 4 _{4,0}	4009.3585(0)	8 _{6,3} \leftarrow 9 _{6,4}	4007.9007(15)
5 _{4,1} \leftarrow 6 _{4,2}	4008.2717(0)	8 _{7,2} \leftarrow 7 _{7,1}	4009.4954(-14)
6 _{1,6} \leftarrow 5 _{1,5}	4009.4163(11)	8 _{7,2} \leftarrow 9 _{7,3}	4007.8259(-14)
6 _{1,6} \leftarrow 7 _{1,7}	4008.3336(11)	9 _{0,9} \leftarrow 8 _{0,8}	4009.5609(-7)
6 _{2,5} \leftarrow 5 _{2,4}	4009.4563(-4)	9 _{0,9} \leftarrow 10 _{0,10}	4008.0114(-7)
6 _{2,5} \leftarrow 7 _{2,6}	4008.2452(-3)	9 _{2,7} \leftarrow 8 _{2,6}	4009.7486(-1)
6 _{3,4} \leftarrow 7 _{3,5}	4008.1961(-5)	9 _{2,7} \leftarrow 10 _{2,8}	4007.8416(-1)
6 _{4,3} \leftarrow 5 _{4,2}	4009.4513(-3)	9 _{5,4} \leftarrow 8 _{5,3}	4009.6993(-3)
6 _{4,3} \leftarrow 6 _{4,2}	4008.8561(-3)	9 _{5,4} \leftarrow 10 _{5,5}	4007.7985(-3)
6 _{4,3} \leftarrow 7 _{4,4}	4008.1649(-3)	10 _{1,10} \leftarrow 9 _{1,9}	4009.6135(-4)
7 _{0,7} \leftarrow 6 _{0,6}	4009.4740(9)	10 _{1,10} \leftarrow 11 _{1,11}	4007.9100(-4)
7 _{0,7} \leftarrow 8 _{0,8}	4008.2323(9)	10 _{2,9} \leftarrow 9 _{2,8}	4009.6458(2)
7 _{1,6} \leftarrow 6 _{1,5}	4009.5582(2)	10 _{2,9} \leftarrow 11 _{2,10}	4007.7871(2)

Table 5.4 (Cont.)

$J'_{K'_a, K'_c}$	\leftarrow	J_{K_a, K_c}	Energy	$J'_{K'_a, K'_c}$	\leftarrow	J_{K_a, K_c}	Energy
10 _{4,7}	\leftarrow	9 _{4,6}	4009.7643(0)	13 _{0,13}	\leftarrow	14 _{0,14}	4007.5927(1)
10 _{4,7}	\leftarrow	11 _{4,8}	4007.6869(0)	14 _{1,14}	\leftarrow	13 _{1,13}	4009.8064(1)
10 _{6,5}	\leftarrow	9 _{6,4}	4009.7555(8)	14 _{1,14}	\leftarrow	15 _{1,15}	4007.4860(2)
10 _{6,5}	\leftarrow	11 _{6,6}	4007.6724(8)	15 _{0,15}	\leftarrow	14 _{0,14}	4009.8544(2)
11 _{0,11}	\leftarrow	10 _{0,10}	4009.6631(-2)	15 _{0,15}	\leftarrow	16 _{0,16}	4007.3800(3)
11 _{0,11}	\leftarrow	12 _{0,12}	4007.8051(-2)	16 _{1,16}	\leftarrow	15 _{1,15}	4009.9025(3)
11 _{2,9}	\leftarrow	10 _{2,8}	4009.7643(-5)	16 _{1,16}	\leftarrow	17 _{1,17}	4007.2747(3)
11 _{2,9}	\leftarrow	12 _{2,10}	4007.5644(-5)	17 _{0,17}	\leftarrow	16 _{0,16}	4009.9474(-1)
11 _{3,8}	\leftarrow	10 _{3,7}	4009.9395(10)	17 _{0,17}	\leftarrow	18 _{0,18}	4007.1655(-1)
11 _{3,8}	\leftarrow	12 _{3,9}	4007.5523(10)	18 _{1,18}	\leftarrow	17 _{1,17}	4009.9953(-2)
11 _{4,7}	\leftarrow	10 _{4,6}	4009.9692(-10)	18 _{1,18}	\leftarrow	19 _{1,19}	4007.0599(-2)
11 _{4,7}	\leftarrow	12 _{4,8}	4007.5378(-10)	19 _{0,19}	\leftarrow	18 _{0,18}	4010.0433(-2)
12 _{1,12}	\leftarrow	11 _{1,11}	4009.7118(0)	19 _{0,19}	\leftarrow	20 _{0,20}	4006.9547(-2)
12 _{1,12}	\leftarrow	13 _{1,13}	4007.6993(0)	20 _{1,20}	\leftarrow	19 _{1,19}	4010.0911(1)
13 _{0,13}	\leftarrow	12 _{0,12}	4009.7593(1)	20 _{1,20}	\leftarrow	21 _{1,21}	4006.8492(2)

deviation between the observed and calculated combination difference for the Ar₂DF in-plane and out-of-plane bends is 5.6 ± 3.6 MHz (100 transitions) and 5.2 ± 3.4 MHz (37 transitions) respectively. The agreement for the 104 Ar₂HF in-plane bend transitions verified by combination differences is 5.5 ± 4.5 MHz, in good agreement with the Ar₂DF bands. This level of agreement sets well defined limits for the deviation between the observed and calculated combination differences that will be tolerated prior to assigning a pair of transitions. Indeed, for an unperturbed asymmetric top spectrum, this tight rein on the allowed discrepancies permits rapid assignment and iterative refinement of the molecular constants.

For a highly perturbed band, however, the predicted frequency for a transition may differ sufficiently from an assignment allowed by combination differences that unambiguous assignment is not always possible. This is especially true for a relatively congested spectrum. The transitions listed in Table 5.4 represent $\approx 3/5$ of the total

Table 5.5: Spectroscopic constants (in cm^{-1}) derived from least-squares fitting of the Ar_2HF data to an A-reduction Watson Hamiltonian using the I' representation. The $\nu_{\text{HF}}=0$ and $\nu_{\text{HF}}=1$ constants are derived from a simultaneous fit of the microwave (Ref. [152]) and IR data (Ref. [265]). The constants for the intermolecular bending states are obtained from fits to the infrared data, holding the ground state constants fixed at the values shown in column 1. Uncertainties represent one standard deviation.

	$\nu_{\text{HF}} = 0$	$\nu_{\text{HF}} = 1$	$\nu_{\text{HF}} = 1 +$ in-plane bend	$\nu_{\text{HF}} = 1 +$ out-of-plane bend
A	0.11929837 (17)	0.119358 (28)	0.11277 (28)	0.123492 (47)
B	0.05801327 (8)	0.0581314 (65)	0.05782 (18)	0.058521 (48)
C	0.03872452 (6)	0.0387889 (13)	0.037375 (34)	0.038507 (61)
$\Delta_J \times 10^7$	5.682 (11)	7.50 (48)	-9.1 (67)	7.3 (18)
$\Delta_{JK} \times 10^7$	^a	-49.7 (52)	^b	^b
$\Delta_K \times 10^7$	39.03 (26)	173.8 (40)	-173 (68)	79.9 (53)
$\delta_J \times 10^7$	1.9959 (49)	3.01 (24)	14.2 (32)	2.8 (23)
$\delta_K \times 10^7$	12.789 (48)	^b	-885 (34)	^b
$\Phi_J \times 10^{10}$	0.099 (42)	^b	^b	^b
$\Phi_{JK} \times 10^{10}$	3.8 (13)	^b	^b	^b
$\Phi_{KJ} \times 10^{10}$	-21.3 (50)	^b	^b	^b
$\Phi_K \times 10^{10}$	25.5 (119)	^b	^b	^b
RMS error	.00070 ^c	.00070 ^c	0.00754	.00325
Δ_0 ($\text{u}\text{\AA}^2$)	3.433	3.372	10.00	13.06
ν_0	0.0	3946.59205 (13)	4008.9669 (24)	4035.17483 (86)

^a Parameter is constrained to 0.0 in the fit.

^b The experimental data were insufficient to determine these parameters with statistical significance, and were constrained in the fit to the values reported in column 1 for $\nu_{\text{HF}} = 0$.

^c The reported value is for the simultaneous fit of the $\nu_{\text{HF}} = 0$ and 1 data.

5.4 Discussion

Although both the in-plane and out-of-plane bends of $\text{Ar}_2\text{HF}/\text{DF}$ correlate adiabatically with $j = 1$ motion of the diatom, the bending frequencies are appreciably larger than the energy required for exciting the uncomplexed monomer (see Figure 5.7). Specifically, the 62 and 88 cm^{-1} bending energies for the in-plane and out-of-plane bends of Ar_2HF are ≈ 1.5 –2 times the 40 cm^{-1} required for $j = 1$ rotation of HF. The difference is even more pronounced for Ar_2DF , where the in-plane and out-of-plane bending energies of 45 and 72 cm^{-1} , respectively, are 2–4 times the 20 cm^{-1} required for DF $j = 1$ rotation. The bending frequencies are larger in the complexes due to the hindering effect of the potential anisotropy. This is also reflected in the bending frequencies for ArHF/DF , which are also depicted in Figure 5.7. The degeneracy of the $|k|=1$ ArHF/DF Π bend is lifted by addition of a second argon, with the in-plane (out-of-plane) bend decreasing (increasing) in energy. The reduced energy for the $\text{Ar}_2\text{HF}/\text{DF}$ in-plane bend vs the ArHF/DF Π bend can be qualitatively understood by considering that the HF/DF bending motion in $\text{Ar}_2\text{HF}/\text{DF}$ keeps the H/D in closer proximity to an Ar atom throughout its librational motion. Conversely, the out-of-plane excitation moves the H/D away from both argons, a path along which the potential's restoring force is greater.

The present $\text{Ar}_2\text{HF}/\text{DF}$ intermolecular bending state data and previous near-IR [265, 130] and microwave [152] data on the van der Waals ground states collectively sample a large region of the intermolecular potential corresponding to motion of the HF/DF. Together with the availability of highly accurate potentials for the corresponding Ar-Ar and Ar-HF/DF dimers, this permits us to address a key question:

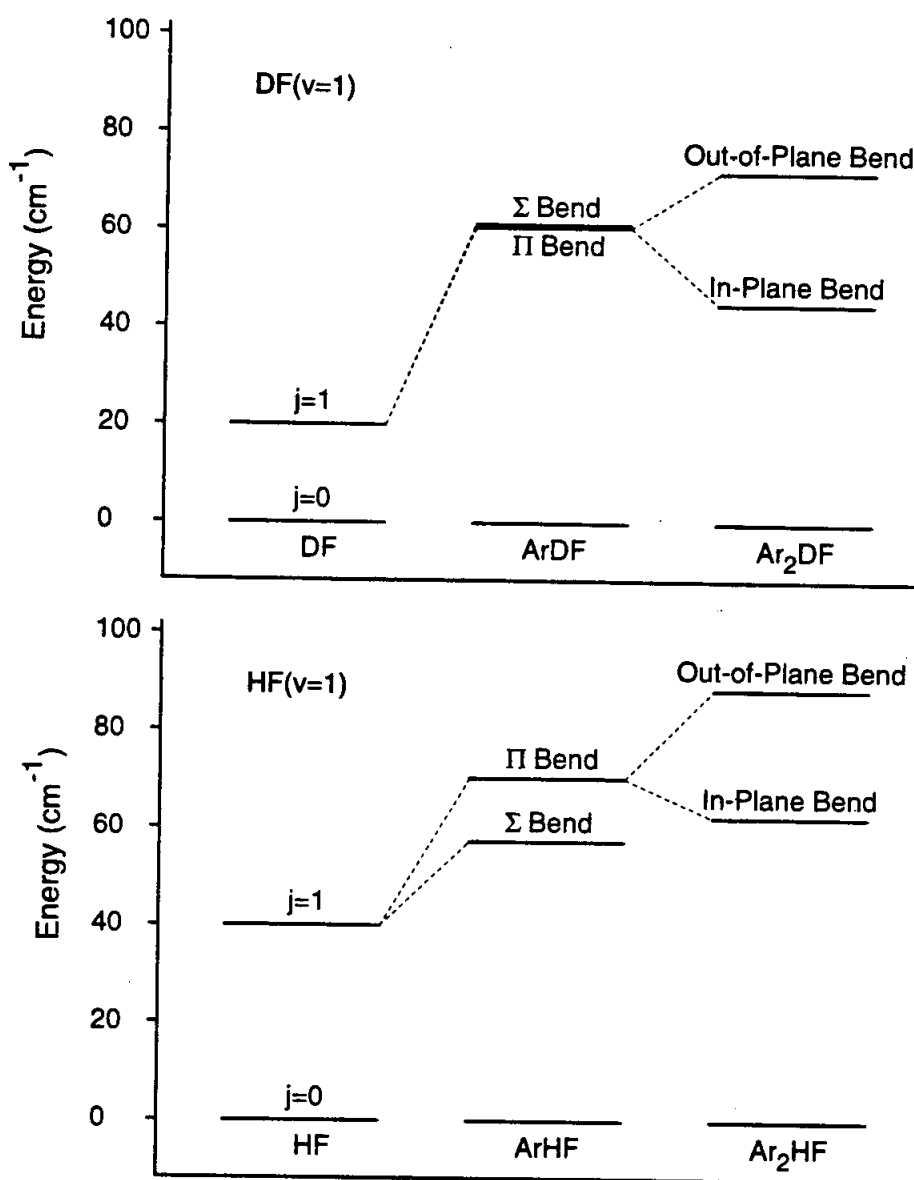


Figure 5.7: States correlating to $j_{\text{HF/DF}}=1$ for HF/DF, ArHF/DF, and Ar₂HF/DF. The potential anisotropy of the complexes hinders the rotational motion of the diatom, increasing the energy with respect to the uncomplexed monomer. The effects are more prominent in the DF complexes due to the smaller rotational constant of DF vs HF. The (degenerate) Π bend of ArHF/DF correlates with $|k|=1$, where k is the (approximately conserved) projection of j on the intermolecular axis. The states correlating asymptotically with $|k|=1$ in Ar₂HF/DF are the in-plane and out-of-plane bends. The librational motion for in-plane bending keeps the HF/DF in closer proximity to the Ar atoms, and consequently is lower in energy than the out-of-plane bend, which samples regions of the intermolecular potential away from both argons.

how well do calculations on a pairwise additive potential reproduce the spectroscopic data? This question is first addressed at a simple level, through comparison with experiment of in-plane and out-of-plane bending frequencies predicted from 2-D angular calculations. Although these calculations cannot be used to extract information on nonadditive forces in the potential, they do provide insight into the level of agreement that can be anticipated for calculations of bending frequencies for larger $\text{Ar}_n\text{HF}/\text{DF}$ complexes which have not yet been observed. Next, the results of full 5-D calculations by Ernesti and Hutson [118] are presented, which are capable of elucidating the effects of nonadditivity. Indeed, discrepancies in bending frequencies are observed that are significantly larger than the estimated $\pm 0.05 \text{ cm}^{-1}$ accuracy of the calculations (reflecting uncertainties in both the calculations and dimer potentials [118]). Ernesti and Hutson have also presented calculations that assess the relative importance of three nonadditive terms in reducing the discrepancy with experiment. The results from these calculations are compared to those from recent *ab initio* calculations. Because the *ab initio* calculations can be done at comparable levels of theory for a wide range of systems, they provide an attractive method for calculating nonadditive forces. The results for $\text{Ar}_2\text{HF}/\text{DF}$ present one of the few cases where the calculated nonadditivity can be compared directly with experiment.

5.4.1 Comparison with 2-D angular calculations

Two dimensional calculations that treat only the angular motion of the HF/DF rotor are the simplest that generate eigenstates corresponding to the in-plane and out-of-plane bends of $\text{Ar}_2\text{HF}/\text{DF}$. Although much more sophisticated 5-D calcula-

tions have been performed for this system (and are discussed in the following section), it is worth comparing calculated vibrational frequencies to experiment at the 2-D level, to assess how useful similar calculations might be for larger $\text{Ar}_n\text{HF/DF}$ ($n \geq 3$) systems where full dimensional calculations are not yet feasible. Because these calculations explicitly neglect contributions from the Ar-Ar stretching and bending motion and the $\text{Ar}_2\text{-HF/DF}$ stretch, (or equivalently coupling with the HF/DF angular coordinates ρ , χ , and R) any significant coupling between these vibrations and the angular HF/DF motion will be reflected in the level of agreement with experiment.

The angular coordinate system used in the calculations is shown in Figure 5.1, where θ and ϕ are the azimuthal and equatorial angles, respectively, of the HF/DF about the intermolecular axis. The radial distances between the Ar atoms and the HF/DF are fixed at their vibrationally averaged values, as determined from an inertial analysis of the rotational constants in the $\nu_{\text{HF/DF}}=1$ manifold. End-over-end rotation of the complex is also neglected, and as a result Coriolis interactions between the bending states will not be accounted for. However, this is not a serious approximation for the purpose of comparing vibrational frequencies at a semiquantitative level. The resulting effective Hamiltonian is

$$\hat{H} = b\hat{j}^2 + V(\theta, \phi) \quad (5.5)$$

where b is the HF/DF rotational constant and \hat{j}^2 is the body fixed angular momentum operator for HF/DF rotation. $V(\theta, \phi)$ is the intermolecular potential, and can be written simply as the sum of two ArHF/DF potential terms and an Ar-Ar term. However, since rotation of the HF/DF does not change the Ar-Ar interaction within the pairwise additive approximation, its (isotropic) contribution does not affect the

HF/DF bending frequencies and it has been omitted in these calculations. The potential constructed from the sum of two H6(4,3,2) ArHF/DF terms is expanded in spherical harmonics for computational simplicity:

$$V(\theta, \phi) = \sum_{lm} C_{lm} Y_{lm}(\theta, \phi) \quad (5.6)$$

The expansion coefficients including terms up to $l=5$ are listed in Table 5.7. A polar plot of the potential for Ar₂HF ($v_{\text{HF}}=1$) is shown in Figure 5.8; the potential for Ar₂DF ($v_{\text{DF}}=1$) is qualitatively similar. It is clear from the figure that the restoring force for in-plane motion is less than for out-of-plane motion, which is consistent with the observed ordering of excitation energies.

The angular wave functions of the complex are expanded in a complete basis of body fixed spherical harmonics Y_{jk} centered on the rotor:

$$\Psi_i(\theta, \phi) = \sum_{jk} a_{ijk} Y_{jk}(\theta, \phi) \quad (5.7)$$

The matrix elements of $V(\theta, \phi)$ can be evaluated analytically to be

$$\begin{aligned} \langle \Psi_i | V(\theta, \phi) | \Psi_{i'} \rangle &= \sum_{lm} C_{lm} \sum_{jj'kk'} a_{ijk} a_{i'j'k'} \sqrt{\frac{(2j+1)(2l+1)(2j'+1)}{4\pi}} \\ &\times \begin{pmatrix} j & l & j' \\ 0 & 0 & 0 \end{pmatrix} \begin{pmatrix} j & l & j' \\ k & m & k' \end{pmatrix} \end{aligned} \quad (5.8)$$

The eigenvalues are found explicitly by matrix diagonalization; the angular energies for the bending states investigated here are converged to $< 0.002 \text{ cm}^{-1}$ with $l=5$ and $j, k \leq 9$.

Figure 5.9 shows polar plots of $|\Psi(\theta, \phi)|^2$ for the four lowest eigenstates from the 2-D calculations of Ar₂HF and Ar₂DF. These states are the intermolecular ground state and the three intermolecular bending states that correlate asymptotically with

Table 5.7: Spherical harmonic expansion coefficients (in cm^{-1}) for the intermolecular potentials used in the 2-D $\text{Ar}_n\text{HF/DF}$ calculations.

l	m	ArHF	ArDF	Ar_2HF	Ar_2DF	Ar_3HF	Ar_3DF	Ar_4HF	Ar_4DF
0	0	-371.383	-365.915	-729.828	-726.905	-1103.635	-1085.523	-1121.562	-1101.135
1	0	-84.459	-80.303	-139.263	-130.209	-194.707	-178.524	-197.083	-181.345
2	0	-81.261	-77.525	-85.799	-83.003	-94.960	-89.776	-96.673	-91.448
2	± 2			-27.276	-27.085				
3	0	-34.770	-29.276	-15.637	-12.686	-0.825	-0.781	-0.840	-1.121
3	± 2			-23.115	-19.816				
3	± 3					± 14.453	± 12.109	± 14.715	± 12.229
4	0	-17.428	-16.931	2.900	3.203	14.975	14.342	15.169	14.373
4	± 2			-15.285	-15.171				
4	± 3					± 14.597	± 13.996	± 14.913	± 14.188
4	± 4			-1.491	-1.514				
5	0	-0.223	0.255	0.073	-0.214	0.184	-0.448	0.228	-0.412
5	± 2			-0.117	0.334				
5	± 3					± 0.180	∓ 0.439	± 0.211	∓ 0.421
5	± 4			-0.026	0.077				
6	0		0.136			-0.153	-0.169	-0.129	-0.157
6	± 3					∓ 0.198	∓ 0.218	∓ 0.180	∓ 0.213
6	± 6					0.013	0.014	0.012	0.014

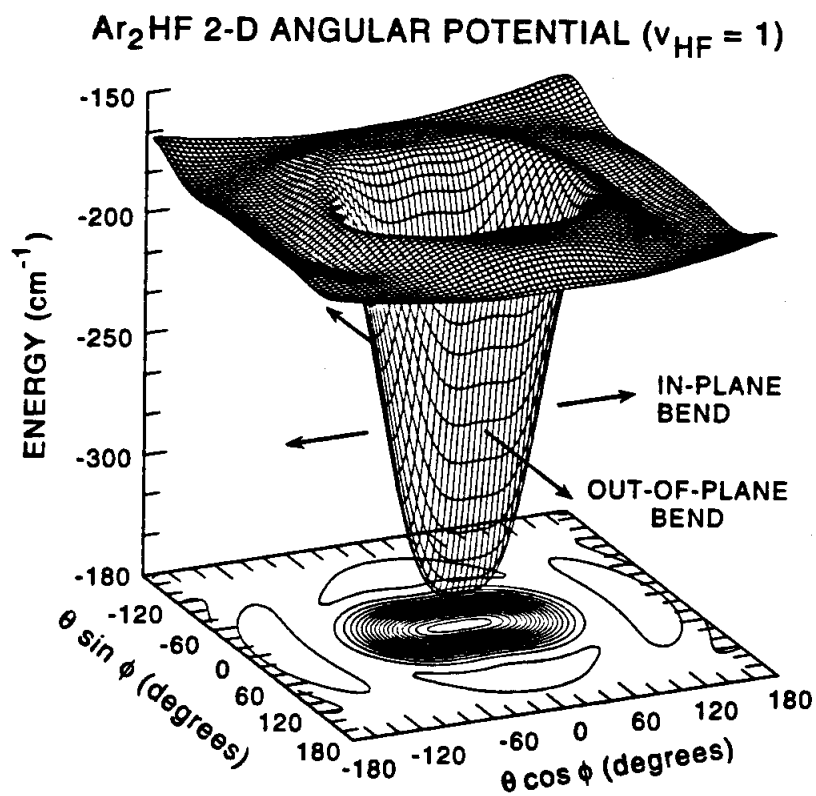


Figure 5.8: Polar plot of the Ar₂HF ($v_{\text{HF}}=1$) potential obtained from expanding the sum of two pairwise ArHF potentials in spherical harmonics. The isotropic Ar-Ar contribution is not included. The potential shown is based on fixed radial distances of $\rho=3.825 \text{ \AA}$, $R = 2.980 \text{ \AA}$, and with $\chi=90^\circ$. The lower restoring force for in-plane vs out-of-plane motion is apparent.

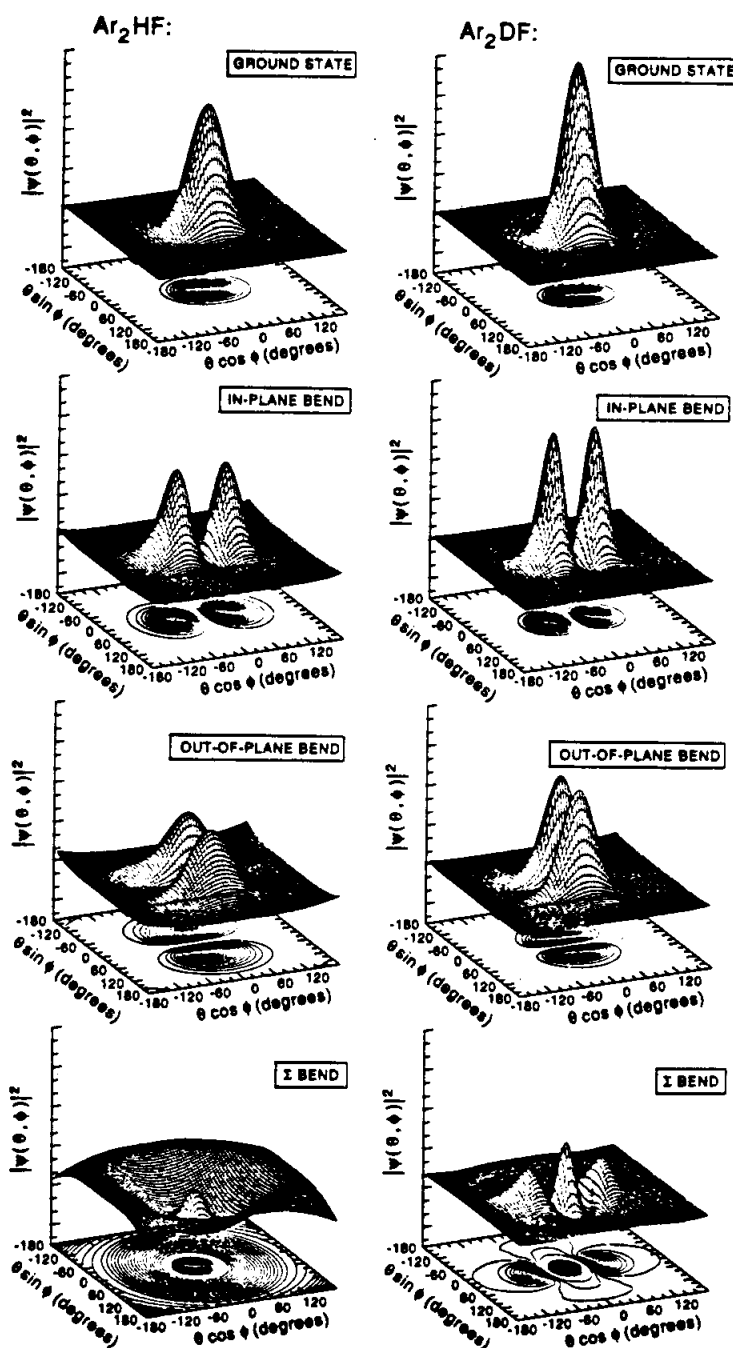


Figure 5.9: Two dimensional (radially averaged) wave functions for the lowest four vibrational states of Ar_2HF and Ar_2DF . The ground state refers to the van der Waals ground state, while the in-plane, out-of-plane, and Σ bends correlate adiabatically with $j_{\text{HF/DF}}=1$. The wave functions for the ground state, in-plane bend, and out-of-plane bend are qualitatively similar both the HF and DF complex, although the greater delocalization for Ar_2HF is evident. The wave functions for the Σ bend are dramatically different, however. The Σ bend wave function for Ar_2DF resembles the first overtone of the in-plane bend, with which it correlates in the rigid molecule limit, whereas the Ar_2HF Σ bend wave function is peaked at the inverted $\text{Ar}_2\text{-FH}$ geometry. This distinct difference clearly demonstrates the differences in the bending dynamics of the two isotopomers.

$j_{\text{HF/DF}}=1$, i.e., the in-plane, out-of-plane, and Σ bends. The wave functions for the ground state, in-plane, and out-of-plane bends are readily assigned based on their nodal patterns. It is clear from the wave functions that the intermolecular bending states sample a much larger region of the angular potential than the intermolecular ground state, which is essential for accurately modelling the anisotropy of nonpairwise additive terms in the potential as discussed in the next section. Comparison of the Ar_2HF vs Ar_2DF wave functions for these states illustrates that they are qualitatively similar, but are more localized for the DF complex, reflecting the reduced librational zero-point motion of the heavier isotopomer.

This is even more evident in a comparison of the Σ bend wave functions. As mentioned earlier, in the rigid molecule limit the Σ bend correlates to the overtone of the lowest bending fundamental, i.e., the in-plane bend for the present system. Indeed, $|\Psi(\theta, \phi)|^2$ for the Ar_2DF Σ bend closely resembles the overtone of the in-plane bend. Interestingly, this is clearly *not* the case for the Ar_2HF Σ bend. The wave function for the latter is peaked at $\theta=180^\circ$, corresponding to the inverted $\text{Ar}_2\text{-FH}$ geometry. In addition only one node is visible, and in this regard closely resembles the the Σ bend wave function for ArHF (which is also peaked at the inverted (Ar-FH) geometry). The dramatic difference between the Σ bend wave function for the HF and DF complex reflects the transition from a nearly free rotor to a near-rigid molecule behavior mediated by isotopic substitution. This behavior clearly demonstrates the caution that must be applied in attributing normal mode labels to higher intermolecular vibrations of weakly bound complexes.

The predicted $\text{Ar}_2\text{HF/DF}$ intermolecular bending frequencies are presented in Table 5.8. The 2-D calculations not only predict the correct ordering of the inter-

Table 5.8: Vibrational energies (cm^{-1}) of $\text{Ar}_n\text{HF/DF}$ ($n=1-4$) intermolecular rotor states in the $\nu_{\text{HF/DF}} = 1$ manifold. The 2-D angular calculations are performed on a pairwise additive potential, with the radial separations held fixed at their vibrationally averaged values.

	Experimental	2-D calc
<u>ArHF</u>		
Σ /parallel bend	57.334 ^a	62.117 (+8.3%)
Π /perpendicular bend	70.337 ^a	74.406 (+5.8%)
<u>ArDF</u>		
Σ /parallel bend	61.013 ^b	66.612 (+9.2%)
Π /perpendicular bend	60.741 ^b	64.110 (+5.5%)
<u>Ar₂HF</u>		
in-plane bend	62.375	69.242 (+11.0%)
out-of-plane bend	88.584	96.562 (+9.0%)
Σ /parallel bend	-	92.513
<u>Ar₂DF</u>		
in-plane bend	44.851	48.056 (+7.1%)
out-of-plane bend	72.116	77.225 (+7.1%)
Σ /parallel bend	-	88.328
<u>Ar₃HF</u>		
Σ /parallel bend	-	120.3
Π /perpendicular bend	-	86.1
<u>Ar₃DF</u>		
Σ /parallel bend	-	105.3
Π /perpendicular bend	-	61.7
<u>Ar₄HF</u>		
Σ /parallel bend	-	121.9
Π /perpendicular bend	-	86.8
<u>Ar₄DF</u>		
Σ /parallel bend	-	106.8
Π /perpendicular bend	-	62.4

^a Reference [251]

^b Reference [256]

molecular bending states, but also give semiquantitative agreement with experiment. This contradicts previous calculations from this laboratory in which the in-plane and out-of-plane bends of Ar_2HF were predicted to be nearly degenerate [267]. The source of this discrepancy has been traced to an error in the computer code used in the earlier calculations. The level of agreement for the $\text{Ar}_2\text{HF}/\text{DF}$ intermolecular bending frequencies is comparable to that realized for ArHF/DF (also shown in Table 5.8). Since angular-radial coupling has been shown to be very small for ArHF/DF , the similar level of agreement for $\text{Ar}_2\text{HF}/\text{DF}$ suggests that the same might be true for the trimer potential. However, such an assessment can only be quantified from full dimensional calculations, which are presented below.

The qualitative success of the 2-D calculations in predicting the bending frequencies of $\text{Ar}_2\text{HF}/\text{DF}$ suggests that similar calculations may be useful for $\text{Ar}_n\text{HF}/\text{DF}$ ($n \geq 3$). Multidimensional quantum mechanical calculations that treat all the degrees of freedom for these complexes are not feasible at present, and consequently the 2-D calculations may prove helpful in assisting experimental searches for the HF/DF bending states. With this as motivation, results of 2-D angular calculations for $\text{Ar}_3\text{HF}/\text{DF}$ and $\text{Ar}_4\text{HF}/\text{DF}$ are presented in Table 5.8, using the potential expansion coefficients listed in Table 5.7. The predicted bending frequencies are quite similar for the Ar_3 and Ar_4 complexes, indicating that the contribution of the fourth argon atom to the bending dynamics is quite small. This is not surprising, since the fourth argon atom resides behind the other three (forming an Ar_4 tetrahedron) in what correlates to the second solvation shell of HF/DF. The small increase in bending frequencies for $\text{Ar}_4\text{HF}/\text{DF}$ vs $\text{Ar}_3\text{HF}/\text{DF}$ suggests that the intermolecular potential is slightly more attractive for the pentamers, which is consistent with the very small incremental redshift observed

between $n=3$ and 4 in the near-IR spectra of Ar_nHF [265].

5.4.2 Comparison with 5-D calculations

Hutson and coworkers have recently performed quantum close coupling calculations for $\text{Ar}_2\text{HX}/\text{DX}$ complexes ($X=\text{F},\text{Cl}$) which include all five intermolecular degrees of freedom. The dependence on the intramolecular stretching coordinate can also be investigated in these calculations, since the ArHX potentials depend parametrically on the HX coordinate through the mass reduced quantum number $\eta = (v + \frac{1}{2})/\sqrt{\mu_{\text{HX}/\text{DX}}}$ (where $\mu_{\text{HX}/\text{DX}}$ is the reduced mass of the diatom). Although the coupling between the intramolecular and intermolecular coordinates is expected to be small due to the large difference in excitation frequencies (10's of cm^{-1} vs 3000–4000 cm^{-1}), accurately accounting for the $v_{\text{HF}/\text{DF}}$ dependence is essential for extracting vibrational redshifts as well as accurately modelling rotational constants and intermolecular vibrational frequencies.

The calculations performed on a pairwise additive $\text{Ar}_2\text{HF}/\text{DF}$ potential incorporate the $\text{H6}(4,3,2)$ ArHF/DF potential [190] and the HFDID1 $\text{Ar}-\text{Ar}$ potential [15]. Both potentials have been constructed by fitting to high resolution spectroscopic data, and reproduce vibrational energy levels and rotational constants to near-spectroscopic accuracy. By virtue of the high accuracy of these potentials, comparison of calculated vs experimental $\text{Ar}_2\text{HF}/\text{DF}$ vibrational frequencies and rotational constants allows the validity of the pairwise additive approximation to be assessed. Significant discrepancies (i.e., those that are larger than can be attributed to residual errors in the potentials or to uncertainties in the calculations) allow one to assess the

Table 5.9: Frequencies (in cm^{-1}) for the in-plane and out-of-plane internal rotor states of Ar_2DF and Ar_2HF . Also listed are the values predicted from five dimensional calculations, both on a pairwise additive potential, and including nonadditive terms (from Ref. [121] and Ref. [118] for Ar_2DF and Ar_2HF , respectively).

	Experimental	Pairwise-Additive	+Nonadditive ^a
Ar_2DF in-plane bend	44.851	49.66 (+10.7%)	45.58 (+1.6%)
out-of-plane bend	72.116	75.40 (+4.6%)	71.59 (-0.7%)
Ar_2HF in-plane bend	62.375	66.348 (+6.4%)	62.000 (-0.6%)
out-of-plane bend	88.584	91.703 (+3.5%)	87.575 (-1.4%)

^a The nonadditive terms account for anisotropic triple-dipole dispersion, induced dipole-induced dipole, and exchange quadrupole-HF/DF multipole interactions as described in the text.

nonadditive contributions to the potential.

The $\text{Ar}_2\text{HF}/\text{DF}$ intermolecular bending frequencies calculated on the pairwise additive potential are shown in Table 5.9. The calculated frequencies agree qualitatively with experiment, but are consistently larger (by ≈ 4 –10%). Interestingly, the calculated values are within 2–5% of those predicted by the 2-D calculations described in the preceding section. This indicates that inclusion of the other three intermolecular coordinates, which sample predominantly the low frequency heavy atom vibrations, does not yield significant improvement in the predicted vibrational frequencies. This suggests that in-plane and out-of-plane angular motion of the HF/DF may be only weakly coupled to the other intermolecular coordinates, at least at the level required to predict vibrational frequencies.

More importantly, it is evident that full dimensional calculations on the pairwise additive surface are incapable of predicting the intermolecular vibrational frequencies to spectroscopic accuracy. The discrepancies of 2.1–4.8 cm^{-1} (4–10%) are

significantly larger the $\pm 0.5 \text{ cm}^{-1}$ theoretical uncertainties in the calculated frequencies. It is important to note that the pairwise additive potential consistently predicts vibrational frequencies that are *too large*. This indicates that the restoring force for in-plane and out-of-plane motion is overpredicted, consistent with pairwise additive potential that is overly anisotropic in the diatom bending coordinate. Consequently, even though the level of agreement is qualitatively quite good, it is clear that the contributions of nonadditive forces to the intermolecular bending frequencies are present at a significant and readily determinable level.

Additional information about nonadditive terms in the intermolecular potential is available from an analysis of the $\text{Ar}_2\text{HF}/\text{DF}$ rotational constants. Ernesti and Hutson [120] have recently described a method for accurately calculating rotational constants of floppy triatomic systems that has been applied to $\text{Ar}_2\text{HF}/\text{DF}$ [118]. Because it is currently not possible to solve the full rovibrational problem for $J > 0$, the rotational constants are calculated from expectation values of the vibrational wave functions. The HF/DF is treated as a point mass in these calculations, and consequently Coriolis interactions with the HF/DF rotor states are not accounted for. In light of the significant perturbations to the Ar_2HF in-plane and out-of-plane bend, comparisons between the calculated and experimental constants may prove difficult to interpret, and therefore comparison of experiment vs theory may be more instructive for Ar_2DF where Coriolis interactions are not as pronounced.

Table 5.10 lists the experimental rotational constants and those calculated on the pairwise additive potential. The predicted rotational constants for the Ar_2DF in-plane and out-of-plane bends are in good agreement with experiment, but are systematically larger. The sign of the discrepancies indicates that the vibrationally av-

Table 5.10: Comparison of the experimental rotational constants for the in-plane and out-of-plane bends of Ar_2HF and Ar_2DF with those calculated by Ernesti and Hutson (Ref. [118, 121]) on a pairwise additive potential and including nonadditive terms as described in the text.

	Experiment	Pairwise Additive	+ Nonadditive
		<u>$\text{ArHF } v=1$</u>	
<i>B</i>	0.10262	0.10262 (+0.0%)	
		<u>$\text{Ar}_2\text{HF } v=1$</u>	
		in-plane bend	
<i>A</i>	0.11277	0.12115 (+7.4%)	0.12217 (+8.3%)
<i>B</i>	0.05782	0.05788 (+0.1%)	0.05723 (-1.0%)
<i>C</i>	0.03738	0.03868 (+3.5%)	0.03855 (+3.1%)
		out-of-plane bend	
<i>A</i>	0.12349	0.11847 (-4.1%)	0.11818 (-4.3%)
<i>B</i>	0.05852	0.05834 (-0.3%)	0.05793 (-1.0%)
<i>C</i>	0.03851	0.03867 (+0.4%)	0.03845 (-0.1%)
		<u>$\text{ArDF } v=1$</u>	
<i>B</i>	0.10169	0.10150 (-0.2%)	
		<u>$\text{Ar}_2\text{DF } v=1$</u>	
		in-plane bend	
<i>A</i>	0.11882	0.11935 (+0.4%)	0.11904 (+0.2%)
<i>B</i>	0.05706	0.05801 (+1.7%)	0.05738 (+0.6%)
<i>C</i>	0.03860	0.03859 (-0.0%)	0.03823 (-1.0%)
		out-of-plane bend	
<i>A</i>	0.11275	0.11655 (+3.4%)	0.11620 (+3.1%)
<i>B</i>	0.05846	0.05867 (+0.4%)	0.05799 (-0.8%)
<i>C</i>	0.03831	0.03863 (+0.8%)	0.03827 (-0.1%)

eraged geometries are predicted to be more compact than observed experimentally. The same trend is observed for the intermolecular ground states of Ar_2DF and Ar_2HF in both the $\nu_{\text{HF/DF}}=0$ and 1 manifolds, where the effects of Coriolis interactions are expected to be negligible [130]. These results imply that the pairwise potential is too attractive, and that it must be augmented by repulsive nonadditive terms.

As anticipated, the agreement between the calculated and experimental rotational constants is relatively poor for Ar_2HF , and it is quite difficult to establish an overall trend in the discrepancies. Interestingly, the large difference between the predicted and observed A constant of the Ar_2HF out-of-plane bend is consistent in sign and magnitude with the discrepancy discussed in Section III.B, which is based on extrapolating the fractional change in A from the Ar_2DF out-of-plane bend. This supports the assertion that the A constant is absorbing the effects of the Coriolis perturbation, the effects of which are not accounted for in the theoretical calculations.

The need for repulsive nonadditive terms identified above is supported by calculations of the HF/DF vibrational redshifts in the $\text{Ar}_n\text{HF/DF}$ complexes ($n=1-4$) [130]. The redshifts calculated on pairwise additive potentials systematically overpredict the magnitudes of the shifts. Since the redshift correlates to the change in binding energy of the complex upon vibrational excitation [179], these results support the assertion that the pairwise potential is too attractive. Summarizing, the intermolecular bending frequencies, rotational constants, and vibrational redshifts calculated on the pairwise additive potential all signify the need for nonadditive terms that correct the overly attractive and anisotropic pairwise potential.

It is important to note that the same qualitative trend is observed for the analogous $\text{Ar}_2\text{HCl/DCl}$ system [114, 88]. Specifically, the errors in the rotational

constants and intermolecular bending frequencies calculated on a pairwise additive potential are ≈ 5 times larger than can be attributed to errors in the pair potentials or to computational inaccuracy. Additionally, the calculated frequencies and rotational constants are consistently larger than observed experimentally. It is thus clear that nonadditivity is a small but important component of the intermolecular potential for $\text{Ar}_2\text{HX/DX}$ trimers, and furthermore that the nonadditivity is destabilizing at the equilibrium geometry, i.e., it decreases the attractiveness and anisotropy of the potential.

Hutson and coworkers have investigated the effects of several nonadditive terms on improving the agreement with experiment for both $\text{Ar}_2\text{HCl/DCl}$ [88, 116] and $\text{Ar}_2\text{HF/DF}$ [118, 121]. Four terms have been included in the calculations, accounting for both long range (induction and dispersion based) and short range (exchange based) interactions. Two of these terms, i.e., the Axilrod-Teller triple dipole dispersion (long range) and exchange overlap (short range), do not require the presence of a permanent multipole moment in the substituents. Both of these have been well studied in connection with nonadditivity of rare gas systems. The remaining two terms account for induction and exchange quadrupole-dipole interactions, and depend explicitly on the presence of a dipolar molecular species. Consequently, the relative importance of these molecular nonadditive terms has not been investigated in as much detail as those present in rare gas systems.

The most familiar of the terms described above is the Axilrod-Teller triple dipole dispersion term (DDD) [13], which arises from the change in the mutual polarization of two atoms by the presence of a third (see Figure 5.10a). The evaluation of this term for molecular systems is more complicated than for atomic systems due

Three-Body Terms for $\text{Ar}_2\text{HF/DF}$

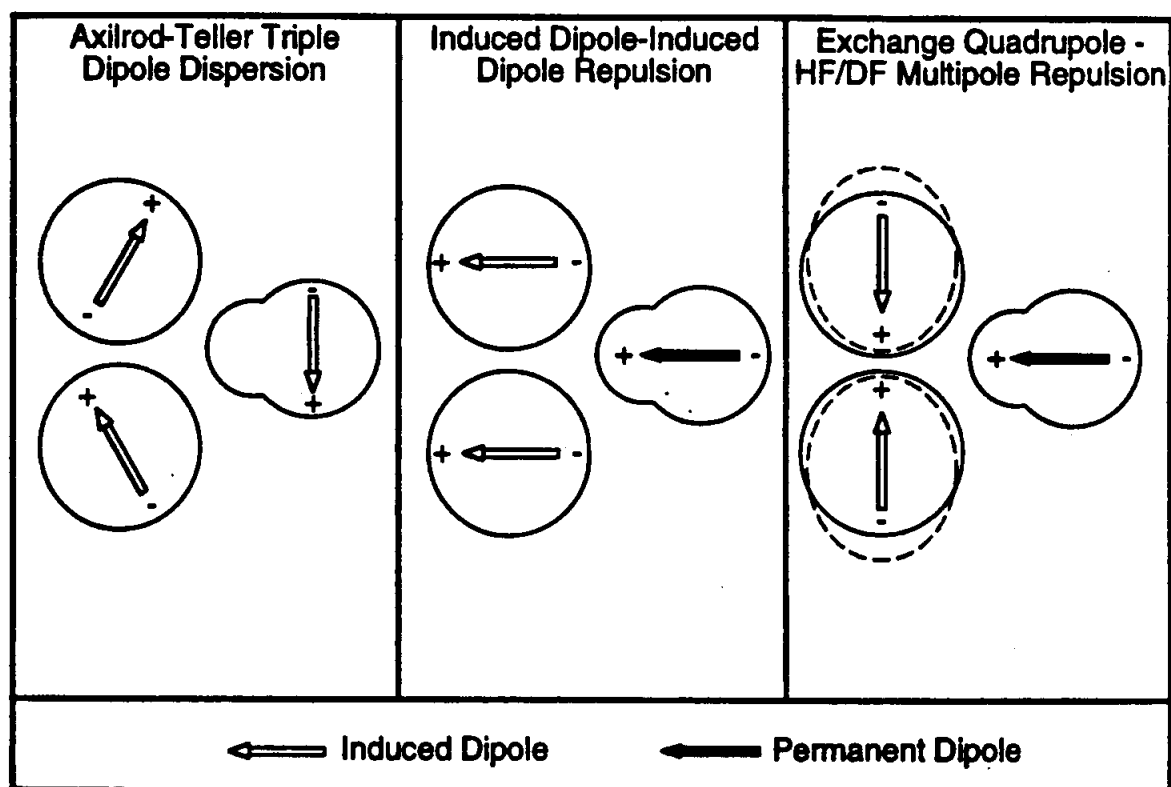


Figure 5.10: Pictorial representation of the nonadditive terms used in the calculations by Ernesti and Hutson that are found to be necessary for reproducing spectroscopic data on $\text{Ar}_2\text{HF/DF}$.

to the anisotropy of the molecule's polarizability, although for HF and HCl the modelling of this anisotropy is rather straightforward. Because the DDD contribution is repulsive and properly anisotropic at the triangular $\text{Ar}_2\text{HF}/\text{DF}$ equilibrium geometry (i.e., it decreases the total energy of the system), it should correct the predicted rotational constants and vibrational frequencies in the right direction. This is indeed what the calculations show, although the magnitude of the correction is relatively small, and is insufficient to account for the bulk of the nonadditive interaction. More specifically, the DDD term only provides $\approx 10\%$ of the necessary correction to the intermolecular vibrational frequencies. The effects of the exchange overlap term have not been investigated for $\text{Ar}_2\text{HF}/\text{DF}$, since it was found to be relatively insignificant in correcting the rotational constants and vibrational frequencies for $\text{Ar}_2\text{HCl}/\text{DCl}$ [88]. The relative unimportance of the DDD and exchange overlap terms in the calculations for $\text{Ar}_2\text{HF}/\text{DF}$ and Ar_2HCl makes it clear that the nonadditive terms important for atomic systems do not constitute the majority of the nonadditivity for even a simple, dipolar molecular system such as Ar_2HF .

The contributions from induction and the exchange quadrupole-dipole interaction have a more pronounced affect on the calculated properties. the spectroscopic properties. The induced dipole-induced dipole interaction, illustrated in Figure 5.10b, is the lowest order term accounting for the interaction of the multipoles on the Ar atoms induced by the permanent multipoles of the HF/DF. Similarly, the exchange quadrupole-dipole interaction investigated by Ernesti and Hutson is the lowest order term describing the interaction of the HF/DF multipole moments with the exchange quadrupole of the Ar_2 (see Figure 5.10c). The exchange quadrupole forms due to the redistribution of electron density in the region between the nuclei in order

to reduce overlap repulsion. Both the induced dipole-induced dipole and exchange quadrupole-dipole interactions are repulsive at the equilibrium geometry, and are highly anisotropic. The intermolecular bending frequencies predicted from calculations that include these two contributions (as well as their cross terms), together with triple dipole dispersion exhibit appreciably improved agreement with experiment. This is demonstrated in Figure 5.11, where the discrepancy decreases from 4-11% at the pairwise additive level to $< 2\%$ upon inclusion of the nonadditive terms (i.e., close to the estimated $\pm 0.5 \text{ cm}^{-1}$ accuracy of the calculation).

The agreement for the Ar_2DF rotational constants, however, does not improve dramatically when the nonadditive terms are included. Ostensibly, the residual disagreement could reflect the manifestations of Coriolis interactions not accounted for in the calculated values but absorbed by the Watson Hamiltonian. This is supported by the better agreement observed for the intermolecular ground states [130, 118], where Coriolis effects are expected to be less prominent. It is also worth mentioning that improved agreement is seen for the vibrational redshifts of $\text{Ar}_2\text{HF/DF}$ upon inclusion of the nonadditive contributions, with the discrepancy decreasing from 3-4% (pairwise additive) to $< 2\%$ (+nonadditive).

These findings closely parallel those for $\text{Ar}_2\text{HCl/DCl}$, where the best agreement with experiment requires calculations incorporating the combined effects of all the nonadditive terms described above. Furthermore, the relative importance of the individual terms is quite similar, with the exchange quadrupole-dipole and induced dipole-induced dipole contributions being much more important than the DDD contribution in correcting the vibrational frequencies and rotational constants. The similarity in form and magnitude of the nonadditive terms investigated for $\text{Ar}_2\text{HF/DF}$

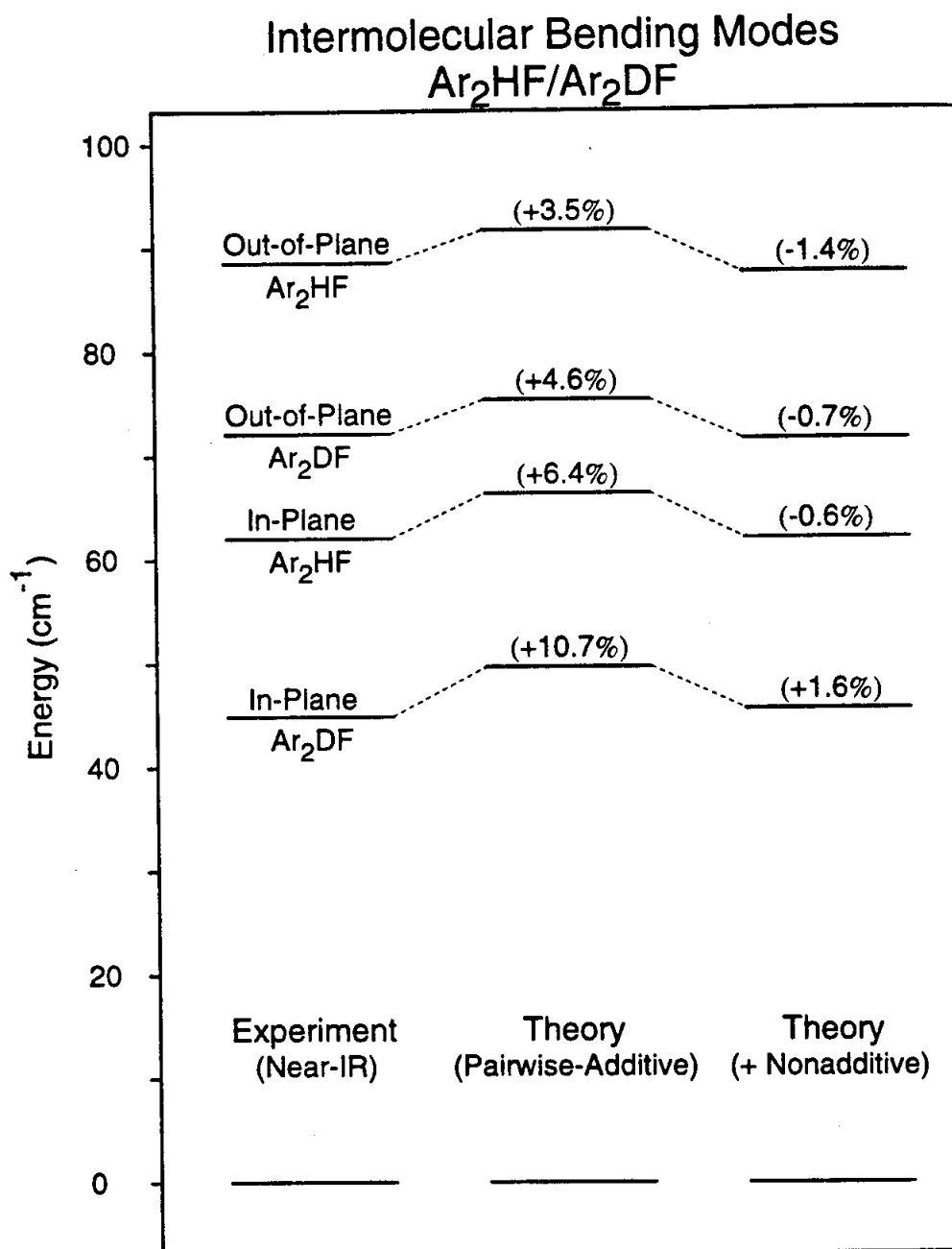


Figure 5.11: Comparison of experimental and calculated vibrational energies for the in-plane and out-of-plane bends for Ar₂HF and Ar₂DF. The values predicted assuming pairwise additivity are consistently larger than the experimental, signifying that the anisotropy of the HF/DF bending motion is overpredicted. The inclusion of the nonadditive terms discussed in the text reduces significantly the discrepancy with experiment.

and Ar_2HCl is perhaps not surprising based on the great similarity of the systems. However, it is an important result because it establishes that the form of nonadditive terms for molecular systems may be rather general, and that extension to less closely related systems may be relatively straightforward.

5.4.3 Assessment of Ar_2HF nonadditivity from *ab initio* calculations

It is instructive to compare the above results for Ar_2HF with the nonadditive energy from the *ab initio* calculations of Cybulski, Szczęśniak, and Chałasiński [352, 94], as this is one of the few systems where *ab initio* nonadditivity can be compared to experiment. The nonadditivity is calculated using the supermolecular Møller-Plesset perturbation theory in conjunction with the perturbation theory of intermolecular forces (a detailed review of this approach has been given in Ref. [68]). This approach uses the uncomplexed monomers as the zero-order basis, and treats the van der Waals interactions at successive levels of perturbation theory. The advantage of this approach is that the total interaction can be decomposed into physically meaningful contributions due to exchange, dispersion, and induction.

The calculations are carried out to third order perturbation theory, which is sufficient to account for terms analogous to the DDD, induced dipole-induced dipole, and exchange quadrupole-dipole terms discussed above. Whereas Ernesti and Hutson have calculated the nonadditivity over the full range of θ and ϕ , however, the *ab initio* calculations have only investigated the θ dependence at $\phi=0^\circ$ and 90° . At the equilibrium geometry ($\theta = 0$), the total nonadditive energy is $+15 \text{ cm}^{-1}$, in almost exact agreement with the value calculated by Ernesti and Hutson. In addition, the θ

dependence of the total nonadditivity is qualitatively similar, reaching a minimum of $\approx 0 \text{ cm}^{-1}$ at $(\theta, \phi) \approx (80^\circ, 0^\circ)$ along the in-plane path and $\approx 2\text{--}3 \text{ cm}^{-1}$ at $(\theta, \phi) \approx (100^\circ, 90^\circ)$ along the out-of-plane path.

The individual components of the total *ab initio* nonadditivity have been decomposed into terms analogous to those investigated by Ernesti and Hutson, and it is thus possible to compare the relative magnitudes of the individual terms. The most important component of the total nonadditivity predicted by the *ab initio* calculations arises from the "exchange nonadditivity". This can be decomposed into an electrostatic term, analogous to the exchange quadrupole-HF multipole interaction, and an exchange term, analogous to the short-range exchange overlap term included in the Ar_2HCl (but not Ar_2HF) calculations. The electrostatic energy is repulsive ($\approx +10 \text{ cm}^{-1}$) at $\theta = 0$, in good agreement with the $\approx +9 \text{ cm}^{-1}$ calculated for the exchange quadrupole-HF multipole interaction by Ernesti and Hutson. In addition, the angular dependence of the interaction is quite similar. The agreement in magnitude and anisotropy is also quite good for terms accounting for the induced dipole-induced dipole and DDD interactions. These results signify that the *ab initio* calculations reproduce nearly quantitatively not only the *total* nonadditivity found to be important by Ernesti and Hutson in correcting the experimental data, but the individual components as well. Consequently, similar calculations for systems where experimental data and/or accurate potentials are not yet available should be quite useful in elucidating the nature of the nonadditive interactions in weakly bound systems.

5.5 Summary

The in-plane and out-of-plane intermolecular bends of Ar_2HF and Ar_2DF have been characterized via direct IR absorption in a slit supersonic expansion. The Ar_2HF in-plane and out-of-plane bending frequencies are 62.375 cm^{-1} and 88.584 cm^{-1} , respectively. For Ar_2DF , the in-plane and out-of-plane frequencies are 44.851 cm^{-1} and 72.116 cm^{-1} , respectively. These vibrational frequencies are qualitatively reproduced by two dimensional calculations on a pairwise additive potential, but are between 7–11% too high. Full five dimensional calculations exhibit somewhat better agreement, although the predicted values are again consistently too large (by 4–11%).

The comparison of calculated rotational constants with experiment is complicated for Ar_2HF by extensive perturbations in the spectrum that are not accounted for in the calculations. These perturbations are attributed to Coriolis and/or anharmonic interactions with background states corresponding predominantly to heavy atom vibrations. Such perturbations are not as evident in the Ar_2DF in-plane and out-of-plane bends, which can be fit to experimental precision using conventional asymmetric top formalism. The Ar_2DF rotational constants calculated on the pairwise additive potential are systematically larger than the experimental values. This is consistent with the discrepancies identified for the intermolecular ground states of $\text{Ar}_2\text{HF}/\text{DF}$, and indicate that the pairwise additive potential predicts vibrationally averaged geometries that are more compact than observed experimentally.

The above experimental data indicate that the pairwise additive potential is too anisotropic and attractive. This highlights the need for nonadditive terms, and is consistent with the conclusion reached from an analysis of the vibrational redshifts

in $\text{Ar}_n\text{HF/DF}$ [130], as well as from far-IR results of the closely related $\text{Ar}_2\text{HCl/DCI}$ system [114, 115]. Three nonadditive terms have been investigated for $\text{Ar}_2\text{HF/DF}$ by Ernesti and Hutson, closely related to the terms included in previous calculations for Ar_2HCl [88]. The combined effects of terms accounting for anisotropic dispersion, induced dipole-induced dipole interactions of the Ar atoms, and the exchange quadrupole-HF/DF multipole interactions are capable of significantly improving the agreement with experiment. However, the remaining discrepancies are still larger than can be accounted for based on inaccuracies in the calculations and pair potentials, signifying that further experimental and theoretical efforts are necessary to fully account for the nonadditive interactions.

The experimental and theoretical results for $\text{Ar}_2\text{HF/DF}$ and $\text{Ar}_2\text{HCl/DCI}$ suggest that the majority of the nonadditivity in the intermolecular potentials can be accounted for by the inclusion of a small number of terms. It is of course essential that additional experimental and theoretical efforts be directed toward isolating nonadditive effects in other weakly bound systems as well, in order to further our understanding of these fundamentally important interactions. The growing body of high resolution spectroscopic data on trimers and larger oligomers, coupled with the concomitant increase in the number of accurate pair potentials, portends rapid growth in our understanding of nonpairwise additive intermolecular forces. Furthermore, nonadditive terms calculated by *ab initio* methods should also prove quite useful for extending our understanding to less closely related systems.

CHAPTER VI

High resolution 1.3 μm overtone spectroscopy of HF dimer in a slit jet: $K_a = 0 \leftarrow 0$
and $K_a = 1 \leftarrow 0$ subbands of $\nu_{\text{acc}} = 2 \leftarrow 0$

6.1 Introduction

The hydrogen fluoride dimer, $(\text{HF})_2$, has long served as an important prototype weakly bound molecule, revealing many aspects of the detailed inter- and intramolecular vibrational dynamics of hydrogen bonding. Early studies of this species utilizing low resolution IR absorption in HF gas cells attributed excess absorption between the strong monomer lines to weakly associated $(\text{HF})_n$ clusters in the gas phase. The first rotationally resolved spectroscopy of HF dimer was performed in a series of molecular beam electric resonance (MBER) studies in the microwave region by Klemperer and coworkers. These studies were the first to elucidate the relatively facile tunneling between the two indistinguishable HF configurations as hydrogen "donor" and "acceptor" subunits, with a frequency of 0.66 cm^{-1} for the $K_a=0$ vibrational ground state tunneling levels.

Extension of spectroscopic studies of HF dimer into the near IR HF stretching region proved feasible via direct absorption in cooled cells with the development of narrow band tunable 2-4 μm laser sources by Pine *et al.* [298, 299]. However,

due to the high internal energy (3900 cm^{-1} in the vibrationally excited upper state, predissociation channels to form two HF monomer species become energetically open. Since both detection sensitivity and prospects for rotationally resolved structure rely on relatively slow predissociation from the upper state, the utility of such near IR absorption methods for high resolution spectroscopic investigation of weakly bound complexes was far from obvious. Hence, the initial observation by Pine and coworkers of extensive rovibrational structure in the HF dimer fundamental region was quite surprising, and indicated predissociation lifetimes vastly longer than the fundamental vibrational period. This observation of long lived metastable vibrational states in complexes has since opened the way for high resolution IR studies of a wide variety of molecular species [281]. Due to its relevance to hydrogen bonding, simple molecular structure, small number of electrons, and demonstrated richness of intramolecular tunneling and predissociation dynamics, $(\text{HF})_2$ has continued to be a primary target for increasingly sophisticated experimental [100] and theoretical investigations [278].

A major focus of these studies has been the elucidation of the intriguing and nonstatistical vibrational mode dependence of tunneling and predissociation phenomena in this coupled oscillator pair. These results for $(\text{HF})_2$ excited to the 3900 cm^{-1} fundamental region can be summarized as follows [299, 302]. 1) Though predissociation lifetimes are surprisingly long (as long as 20–30 ns), a strong mode specificity in the predissociation lifetimes is observed, with rates for the $\nu_1=\nu_{\text{acc}}=1$ (hydrogen bond acceptor) and $\nu_2=\nu_{\text{don}}=1$ (hydrogen bond donor) vibrational manifolds differing by up to 50 fold [302]. 2) There is a significant decrease in the tunneling splittings for HF dimer from 0.66 cm^{-1} to 0.22 cm^{-1} upon vibrational excitation of either the ν_{acc} or ν_{don} components for the $v=1$ dyad [298, 299]. This has been interpreted in terms of

an increase in the effective barrier separating the two indistinguishable conformers in which the HF donor and HF acceptor roles are interchanged, since this also requires simultaneous exchange of the HF ($v=1$) vibrational quantum.

Theoretical efforts to reproduce these observations have demonstrated a high sensitivity to small changes in the potential energy surface, and in particular, to the number of degrees of freedom included in the calculations. One of the serious challenges in such calculations is the enormous dynamic range of time scales that needs to be treated self consistently, ranging from intramolecular HF vibrational frequencies of 4000 cm^{-1} , to tunneling splittings of 0.22 cm^{-1} , to predissociation linewidths of 0.0002 cm^{-1} . These challenges are further augmented by the number of low frequency intermolecular vibrational modes, and both *ab initio* and experimental evidence [363, 311, 261] for a highly anisotropic and long range intermolecular potential surface with unusually strong angular-angular and angular-radial coupling.

Despite these considerable challenges, there has been some success in using simplified models with restricted numbers of degrees of freedom to describe the K_a rotational, vibrational, and isotopic dependence of the tunneling splittings [299, 364, 278, 138, 58, 119, 162]. These calculations also make predictions for the behavior in other excited states, and hence provide an opportunity for experimental tests of the ability of such reduced dimensional calculations to reproduce the essential tunneling dynamics. It would be extremely useful, therefore, to have high resolution information on a wider range of intramolecular and intermolecular vibrational states in HF dimer. Through the use of slit jet direct absorption methods in the $3\text{ }\mu\text{m}$ region accessed by conventional cw difference frequency generation methods [247], work in our laboratories has been directed toward mapping out the low frequency, *intermolecular* "van

der Waals" modes in the HF dimer and DF dimer complexes, built on the excitation of one quantum of HF/DF stretch (i.e., the $v=1$ dyad) [5, 95]. Of parallel interest would be to probe higher *intramolecular* vibrational quanta of HF stretch excitation, for which there would be a variety of nearly isoenergetic vibrational levels (i.e., the $v=2,3,\dots$ polyads) associated with multiple arrangements of the quanta among the H-accepting and H-donating HF oscillator pair. As there is a clear vibrational state dependence to both the predissociation and tunneling behavior, extension into these higher overtone vibrational levels can provide crucial tests of the dynamical models developed from the lower vibrational levels.

In this chapter, slit jet direct absorption methods are applied to the overtone spectrum of HF dimer (i.e., the $v=2$ triad). More specifically, we present detailed measurements of vibrational frequencies, tunneling splittings, and predissociation linewidths for $2\nu_{acc}$ in both the $K'_a = 0$ and 1 levels. The results are in qualitative accord with several theoretical predictions, but reveal important discrepancies that indicate a more complex behavior in the tunneling and vibrational predissociation dynamics than suggested by reduced dimensional treatments.

Important limits on the overtone behavior of HF dimer have already been set by a static long path cell FTIR study of the $(HF)_2$ overtone region by von Puttkamer and Quack [362, 365]. Although residual pressure broadening prevents J -rotational resolution and narrow lifetime estimates in that study, the analysis of band contours yields plausible K_a -rotational and vibrational assignments for the first overtone triad components of various (HF,DF) isotopomers in addition to upper limits for lifetime broadening. High resolution supersonic jet spectroscopy in the overtone region can provide complementary and much more detailed information about the $(HF)_2$ overtone

triad. While supersonic jet direct absorption spectroscopy preferentially accesses low J and K states and its sensitivity relies on relatively long predissociation lifetimes, the low translational and rotational temperatures yield significantly reduced Doppler widths and spectral congestion. Furthermore, due to the low jet temperatures and the large B rotational constant for the monomer, all but the $R(0)$ HF absorptions are essentially eliminated and do not interfere with the dimer spectrum.

One issue that will prove of particular relevance to the analysis and interpretation of the present work is the exchange symmetry assignment of the $(\text{HF})_2$ stretching modes in the $v=2$ triad. Using the notation of Quack and coworkers [363, 307], and restricting ourselves to in-plane (even parity) vibrational motions, any vibrational state of $(\text{HF})_2$ is either symmetric ($\Gamma_{\text{totvib}}=A^+$) or antisymmetric ($\Gamma_{\text{totvib}}=B^+$) in the molecular symmetry group M_{S_4} with respect to an exchange of the HF subunits. The rotationally resolved spectra discussed in this chapter allow an unambiguous identification of this *total* vibrational symmetry of the upper state via ground state combination differences, nuclear spin statistics, and the now very well established “trans” or disrotatory tunneling path predominance in $(\text{HF})_2$ which results in the rigorous Γ_{totvib} selection rule $A^+ \leftrightarrow B^+$ for even parity vibrational states.

In a simplified (2+1)-D picture of the HF stretching polyads, i.e., two anharmonic oscillators coupled by an effective one-dimensional exchange path, one is tempted to split this vibrational symmetry further into a 2-D stretching Γ_{stretch} and a 1-D tunneling Γ_{tun} contribution, with $\Gamma_{\text{totvib}} = \Gamma_{\text{stretch}} \times \Gamma_{\text{tun}}$. Of course, the resulting state labels of Γ_{tun} and Γ_{stretch} are necessarily less rigorous than the overall vibrational classification, Γ_{totvib} . Nonetheless, these approximate symmetry labels have been used frequently in connection with the above (2+1)-D model to predict the symmetries of

the upper and lower tunneling states, based on the plausible picture that there is an additional node across the tunneling coordinate in the $\Gamma_{\text{tun}}=B^+$ state which makes it higher in energy than the parenting $\Gamma_{\text{tun}}=A^+$ state. However, with the introduction of other degrees of freedom (and possibly state mixing within the HF stretching polyad itself, such a clean separation may break down due to anharmonic resonances. This chapter provides experimental evidence for such resonances in the first overtone triad and therefore points out clear limits of even adiabatic 2-D and (2+1)-D dynamical calculations in this model complex. The results also emphasize that the detailed interpretation of dynamical quantities such as the tunneling splittings and predissociation lifetimes in HF dimer may have to go substantially beyond the bright states in which the effects are experimentally observed.

6.2 Experimental

A mixture of 2% HF in Ar at a total pressure of 300 Torr is expanded through the slit nozzle. Pulses of 840 μs width are used with a repetition rate of 19 Hz and the center 512 μs part of the pulse profile is used for signal averaging. Under these expansion conditions, the $R(0)$ line of $v = 2 \leftarrow 0$ in HF monomer appears as a 95% absorption close to the nozzle and shows evidence for only marginal clustering ($\leq 5\%$) in the temporal pulse profile. Such conditions yield the maximum $(\text{HF})_2$ concentrations. As noted in previous studies [246] of N_2OHF complexes under the present pulsed valve stagnation pressure and HF concentrations, small amounts of N_2O (0.2–0.5%) in the mixture can be used to promote $(\text{HF})_2$ formation in Ar expansions on the order of 20–50%.

Frequency calibrations are made with respect to the $P(1)$ (7709.6839 cm^{-1}) lines of monomeric HF, $v = 2 \leftarrow 0$ [148]. Due to the two-fold larger residual Doppler widths in the overtone region ($\Delta\nu_D \approx 75\text{ MHz}$ for $v = 2 \leftarrow 0$ in ArHF), the accuracy of the calibration procedure is somewhat less than typically achieved in the $2\text{--}4\text{ }\mu\text{m}$ range, but still better than 0.0008 cm^{-1} . The monomer overtone absorption cross sections are reduced from corresponding fundamental absorption cross sections by \approx a factor of 30, and coupled with much larger Doppler and predissociation broadening (as will be discussed below) leads to a direct absorption detection sensitivity for $(\text{HF})_2$ that is approximately two orders of magnitude lower than for excitations to the $v = 2 \leftarrow 0$ manifold. Nonetheless, the 48 cm path length, suppression of Doppler broadening, and the $1/r$ drop off in molecular density characteristic of the slit expansion geometry still permit detection of $(\text{HF})_2$ in the $v = 2 \leftarrow 0$ overtone region with S/N in excess of 50:1.

6.3 Spectroscopic results and analysis

Two tunneling-split K subbands characteristic of $(\text{HF})_2$ are found in the region from 7670 to 7720 cm^{-1} . Ground state combination differences, free jet population arguments and spin-statistics unambiguously prove that they originate in the $K=0$ vibrational ground state ($\Gamma_{\text{vib}}=A^+$) and first excited tunneling ($\Gamma_{\text{vib}}=B^+$) levels of $(\text{HF})_2$. From here on we suppress the K_a notation and use the conventional $K \equiv K_a$ labelling appropriate for a prolate, near symmetric top. The lower frequency band system near 7682.8 cm^{-1} is of parallel type ($K = 0 \leftarrow 0$) with P and R branches which can be followed out to about $J''=12$. The upper band system near 7711.4 cm^{-1}

has two prominent Q branches (shown in Figure 6.1) in addition to P and R branch lines. This perpendicular character, the lack of $P(1)$ and appearance of $Q(1)$ and $R(0)$ identifies it as a $K = 1 \leftarrow 0$ band. From local anharmonic mode predictions based on the $(\text{HF})_2 v = 1$ dyad, the observed bands are consistent with a vibrational assignment to the $\nu_{\text{acc}} = 2 \leftarrow 0$ of the $v = 2$ triad, i.e., the stretch overtone ($2\nu_{\text{acc}}$) of the free or hydrogen bond acceptor HF molecule, as will be discussed in much more detail in the following sections. The 28.6 cm^{-1} spacing between the $K = 1 \leftarrow 0$ perpendicular and $K = 0 \leftarrow 0$ parallel subbands is formally equivalent to the A rotational constant in the vibrationally excited state. Though such rigid rotor concepts have limited physical meaning in such a floppy molecule [299], this is at least consistent with the observed trend for the $\nu_{\text{acc}}=0$ ($A=35.4 \text{ cm}^{-1}$) and $\nu_{\text{acc}}=1$ ($A=32.0 \text{ cm}^{-1}$) vibrational levels [299], producing further support for the vibrational assignment.

All measured transitions are summarized in Table 6.1. The observed data are least-squares fit the the usual [222, 364, 310] expansion in $J(J+1)$,

$$E_{JK} = \nu_K + [\bar{B}_K \pm \delta_{K1} b_K] J(J+1) - D_K J^2(J+1)^2 + H_K J^3(J+1)^3 \quad (6.1)$$

In equation #, ν_K is the subband center for a vibrational level Γ ($\equiv \Gamma_{\text{vib}}$), and a function only of the rotational quantum number K (extrapolated to $J=0$ for fixed K).

Furthermore, $\bar{B}_K [\equiv 1/2(B_K + C_K)]$, D_K , and H_K are K -dependent rotational and centrifugal distortion constants in symmetric top notation [222], while the Kronecker δ_{K1} brings in an asymmetry splitting term due to $b_K = (B_K - C_K)$ which is relevant only for $K=1$. In the fit, the ground state constants are held fixed at the values from the most comprehensive fit to microwave, MBER, and FIR transitions as well as IR combination differences (a total of 1171 transitions) [311]. Both fixed and fitted

(HF)₂ OVERTONE SPECTRA
 $2\nu_{acc}$, $K = 1 \leftarrow 0$ ORIGIN

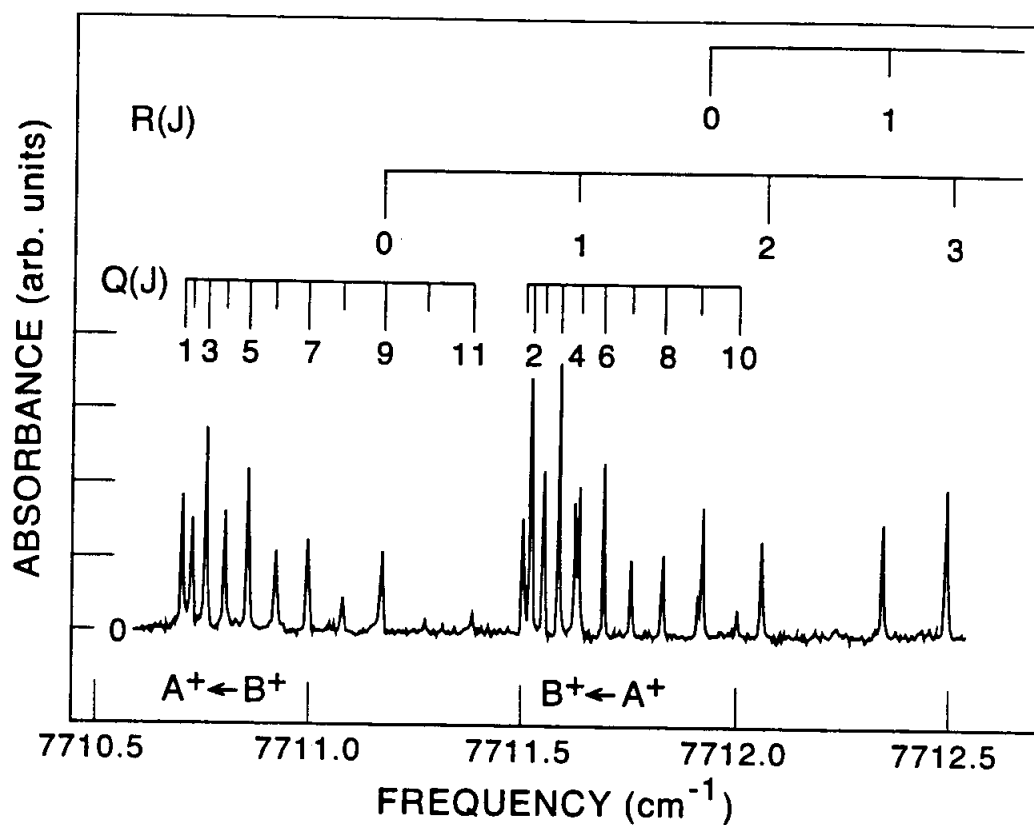


Figure 6.1: Q branches of the $K = 1 \leftarrow 0$ subbands of $2\nu_{acc}$ ($T_{rot} = 11 \pm 1$ K). The A^+ and B^+ symmetry labels refer to Γ_{vib} , the overall vibrational symmetry. Note the 10:6 spin statistical alteration and the slightly higher peak absorbances of the upper frequency component, which are due to differences in Boltzmann population as well as lower predissociation rates.

Table 6.1: The observed and fitted transitions of the $K = 0 \leftarrow 0$ and $K = 1 \leftarrow 0$ subbands of $(\text{HF})_2$. The transitions are further categorized by their total vibrational symmetry, $\Gamma'_{\text{vib}} \leftarrow \Gamma''_{\text{vib}}$. The numbers in parentheses represent their deviations from a weighted least-squares fit (observed-calculated) and a_{est} is an estimate of their relative accuracy. The inverse square of a_{est} are used as weights in the fit, whose rms is 0.0004 cm^{-1} . The standard deviation for a unit weight is 0.40, thus indicating that the estimated accuracies a_{est} define confidence intervals of about 99%.

$K = 0 \leftarrow 0$ (parallel band)				
$A^+ \leftarrow B^+$				
$J'_{K'_a K'_c} \leftarrow J_{K_a K_c}$	ν (cm^{-1})	$a_{\text{est}} (\times 10^4 \text{ cm}^{-1})$	ν (cm^{-1})	$a_{\text{est}} (\times 10^4 \text{ cm}^{-1})$
$9_{0,9} \leftarrow 10_{0,10}$	a		7678.9878(-1)	10
$8_{0,8} \leftarrow 9_{0,9}$	a		a	
$7_{0,7} \leftarrow 8_{0,8}$	a		7679.7461(4)	10
$6_{0,6} \leftarrow 7_{0,7}$	7679.2700(-4)	50	7680.1333(-9)	10
$5_{0,5} \leftarrow 6_{0,6}$	7679.6650(11)	50	7680.5296(2)	10
$4_{0,4} \leftarrow 5_{0,5}$	7680.0635(-4)	20	7680.9310(1)	10
$3_{0,3} \leftarrow 4_{0,4}$	7680.4711(3)	20	7681.3388(-1)	10
$2_{0,2} \leftarrow 3_{0,3}$	7680.8847(4)	20	7681.7527(-6)	10
$1_{0,1} \leftarrow 2_{0,2}$	a		7682.1746(4)	10
$0_{0,0} \leftarrow 1_{0,1}$	a		7682.6017(4)	10
$1_{0,1} \leftarrow 0_{0,0}$	a		7683.4740(-3)	10
$2_{0,2} \leftarrow 1_{0,1}$	7683.0493(-4)	20	7683.9200(-1)	10
$3_{0,3} \leftarrow 2_{0,2}$	7683.5020(0)	20	7684.3725(3)	10
$4_{0,4} \leftarrow 3_{0,3}$	7683.9598(-9)	20	7684.8301(0)	10
$5_{0,5} \leftarrow 4_{0,4}$	7684.4270(13)	20	7685.2940(-1)	10
$6_{0,6} \leftarrow 5_{0,5}$	7684.8967(-1)	20	7685.7642(0)	10
$7_{0,7} \leftarrow 6_{0,6}$	7685.3740(-1)	50	7686.2399(0)	10
$8_{0,8} \leftarrow 7_{0,7}$	7685.8574(0)	20	7686.7218(2)	10
$9_{0,9} \leftarrow 8_{0,8}$	7685.3460(-8)	50	7687.2091(3)	10
$10_{0,10} \leftarrow 9_{0,9}$	a		7687.7014(-2)	10
$11_{0,11} \leftarrow 10_{0,10}$	a		a	
$12_{0,12} \leftarrow 11_{0,11}$	7687.8510(2)	50	a	
$K = 1 \leftarrow 0$ (perpendicular band)				
$A^+ \leftarrow B^+$				
$J'_{K'_a K'_c} \leftarrow J_{K_a K_c}$	ν (cm^{-1})	$a_{\text{est}} (\times 10^4 \text{ cm}^{-1})$	ν (cm^{-1})	$a_{\text{est}} (\times 10^4 \text{ cm}^{-1})$
$6_{1,6} \leftarrow 7_{0,7}$	a		7708.5713(6)	10
$5_{1,5} \leftarrow 6_{0,6}$	7708.2205(6)	10	7708.9669(2)	10
$4_{1,4} \leftarrow 5_{0,5}$	7708.6210(4)	10	7709.3685(-6)	10
$3_{1,3} \leftarrow 4_{0,4}$	7709.0276(-2)	10	7709.7770(-8)	10
$2_{1,2} \leftarrow 3_{0,3}$	7709.4411(-5)	10	a	
$1_{1,1} \leftarrow 2_{0,2}$	a		a	
$1_{1,0} \leftarrow 1_{0,0}$	7710.7312(-4)	10	7711.4837 ^b	10

Table 6.1 cont.

 $K = 0 \leftarrow 0$ (parallel band)

$J'_{K'_a K'_c} \leftarrow J_{K_a K_c}$	$A^+ \leftarrow B^+$		$B^+ \leftarrow A^+$	
	ν (cm ⁻¹)	$a_{\text{est}} (\times 10^4 \text{ cm}^{-1})$	ν (cm ⁻¹)	$a_{\text{est}} (\times 10^4 \text{ cm}^{-1})$
2 _{1,1} \leftarrow 2 _{0,1}	7710.7513(0)	10	7711.5034(1)	10
3 _{1,2} \leftarrow 3 _{0,2}	7710.7809(0)	10	7711.5320(1)	10
4 _{1,3} \leftarrow 4 _{0,3}	7710.8198(-2)	10	7711.5700(1)	10
5 _{1,4} \leftarrow 5 _{0,4}	7710.8692(0)	10	7711.6175(1)	10
6 _{1,5} \leftarrow 6 _{0,5}	7710.9278(-3)	10	7711.6748(2)	10
7 _{1,6} \leftarrow 7 _{0,6}	7710.9969(0)	10	7711.7416(4)	10
8 _{1,7} \leftarrow 8 _{0,7}	7711.0752(-3)	10	7711.8174(0)	10
9 _{1,8} \leftarrow 9 _{0,8}	7711.1637 ^c	10	7711.9033(0)	10
10 _{1,9} \leftarrow 10 _{0,10}	7711.2628(6)	10	7711.9987(0)	10
11 _{1,10} \leftarrow 11 _{0,11}	7711.3700(-2)	10	7712.1028(-9)	10
12 _{1,11} \leftarrow 12 _{0,12}	7711.4837 ^b	10	7712.2186(0)	10
13 _{1,12} \leftarrow 13 _{0,13}	a		7712.3433(3)	10
1 _{0,1} \leftarrow 0 _{0,0}	7711.1637 ^b	10	7711.9139(-3)	10
2 _{0,2} \leftarrow 1 _{0,1}	7711.6074(2)	10	7712.3601(4)	10
3 _{0,3} \leftarrow 2 _{0,2}	7712.0598(6)	10	7712.8110(0)	10
4 _{0,4} \leftarrow 3 _{0,3}	7712.5173(0)	10	7713.2686(2)	10
5 _{0,5} \leftarrow 4 _{0,4}	7712.9823(5)	10	7713.7313(-2)	10
6 _{0,6} \leftarrow 5 _{0,5}	7713.4520(-2)	10	7714.2006(0)	10
7 _{0,7} \leftarrow 6 _{0,6}	7713.9289(1)	10	7714.6751(-2)	10
8 _{0,8} \leftarrow 7 _{0,7}	7714.4106(-6)	10	a	

^a Too weak to be observed^b Coincident with 12_{1,11} \leftarrow 12_{0,12} of $A^+ \leftarrow B^+$.^c Coincident with 1_{1,0} \leftarrow 0_{0,0} of $A^+ \leftarrow B^+$.^d Coincident with 1_{1,0} \leftarrow 1_{0,1} of $B^+ \leftarrow A^+$.^e Coincident with 9_{1,8} \leftarrow 9_{0,9} of $A^+ \leftarrow B^+$.

constants are shown in Table 6.2.

It is instructive to compare the two band centers with predictions from previous FTIR band head analysis. Neither of the two bands had been observed before in the low resolution FTIR studies due to monomer overlap ($K = 1$) and lack of prominent Q branches ($K = 0$), but the upper states have been accessed independently by $\Delta K = -1$ transitions [365]. Apart from a systematic offset ($\approx 0.3 \text{ cm}^{-1}$) in the FTIR data [365] resulting from the evaluation of Q branch maxima rather than origins, the agreement is good. The quality of the agreement is even higher for the tunneling splittings, where these offsets should cancel to first order.

The \bar{B} rotational constants continue the trend toward larger values already observed in the fundamental, i.e., $\Delta B/B = 1.4\text{--}1.5\%$ for $\nu_{\text{acc}} = 2 \leftarrow 0$ vs $\Delta B/B = 0.5\text{--}0.6\%$ for $\nu_{\text{acc}} = 1 \leftarrow 0$ [298, 365]. This, together with the reduction in the formal A rotational constant from 35.4 cm^{-1} in the $\nu_{\text{acc}} = 0$ ground state down to 32.0 cm^{-1} in $\nu_{\text{acc}} = 1$ and further down to 28.6 cm^{-1} in $\nu_{\text{acc}} = 2$, suggests an ongoing tightening and bending of the dimer structure with HF stretching excitation as previously discussed [365]. We find further support for this distortion in the asymmetry parameter $b_1 \equiv B_{K=1} - C_{K=1}$, which shows a systematic increase for $K=1$ from the ground state ($b_1^{A^+} = 3.17594(2) \times 10^{-3} \text{ cm}^{-1}$, $b_1^{B^+} = 3.04153(3) \times 10^{-3} \text{ cm}^{-1}$) [311], to $\nu_{\text{acc}}=1$ ($b_1^{A^+} = 3.3003(4) \times 10^{-3} \text{ cm}^{-1}$, $b_1^{B^+} = 3.2620(4) \times 10^{-3} \text{ cm}^{-1}$) [298], to $\nu_{\text{acc}}=2$ ($b_1^{A^+} = 3.48(1) \times 10^{-3} \text{ cm}^{-1}$, $b_1^{B^+} = 3.46(1) \times 10^{-3} \text{ cm}^{-1}$). Withing tunneling pairs for overtone levels, the difference in \bar{B} and b_1 values is small and of marginal statistical significance due to the limited range of J values probed. For the purpose of clarity, the symmetry labels here always refer to the total vibrational symmetry, Γ_{vib} , which is equal to the product of HF stretching (Γ_{stretch}) and HF exchange tunneling (Γ_{tun})

Table 6.2: Spectroscopic constants (in cm^{-1} except as noted) from a weighted least squares fit to the $(\text{HF})_2$ transition frequencies in Table 6.1. Values for the ground state $K=0$ levels are known to higher precision and thus are held fixed in the fitting procedure. Lorentzian line width components (FWHM) are obtained from Voigt fits to the observed transitions and averaged over all upper state J (see the text for details of the fit). The numbers in parentheses give one standard deviation in units of the last digit.

State	Constant	$\Gamma_{\text{vib}} = A^+$	$\Gamma_{\text{vib}} = B^+$	FTIR ^a	<i>ab initio</i> ^b
Ground state	$\nu_{K=0}^{gs}$	0	0.6586901(7)		
$K = 0$	$\Delta\nu_T$	0.6586901(7) ^c			
(Refs [310],	\bar{B}_0	0.2167132(2)	0.2165755(2)		
[311])	$D_0 \times 10^6$	2.0604(4)	2.0422(5)		
	$H_0 \times 10^{12}$	-44.4(2)	-45.6(3)		
$2\nu_{\text{acc}}$	$\nu_{K=0}^{2\nu_{\text{acc}}}$	7682.8228(5)	7683.0347(5)	7683.1	7675.1
$K = 0$	$\Delta\nu_T$	0.2119(5) ^c		0.2	-1.0
	\bar{B}_0	0.21981(2)	0.21983(1)		
	$D_0 \times 10^6$	2.1(2)	2.3(1)		
	$\Delta\nu_{\text{PD}}$	175(25) MHz	56(20) MHz	≤ 3200 MHz	
$2\nu_{\text{acc}}$	$\nu_{K=1}^{2\nu_{\text{acc}}}$	7711.3805(2)	7711.4747(3)	7711.8	7704.3
$K = 1$	$\Delta\nu_T$	0.0942(3) ^c		0.0	-1.4
	\bar{B}_1	0.220618(9)	0.220599(6)		
	$b_1 \times 10^3$	3.48(1)	3.46(1)		
	$D_1 \times 10^6$	2.05(8)	1.97(4)		
	$\Delta\nu_{\text{PD}}$	114(11) MHz	67(8) MHz	≤ 3200 MHz	

^a Reference [365]

^b Reference [196]

^c Based on the definition of $\Delta\nu_T$, only the absolute value can be determined from the present overtone spectra in the absence of further Γ_{stretch} and Γ_{turn} symmetry information (see Table 6.4).

symmetries. To avoid any potential confusion, if either (Γ_{stretch}) or (Γ_{tun}) is used, it is explicitly labeled as such.

An important result of the present work is the energetic sequence of the tunneling pairs. Note that if we define a tunneling splitting as the *signed* energy

$$\Delta\nu_T = \nu_K^{\Gamma_{\text{tun}}=B^+} - \nu_K^{\Gamma_{\text{tun}}=A^+} \quad (6.2)$$

its sign remains undefined in the spectra as long as Γ_{stretch} is unknown or ill-defined. Only the product $\Gamma_{\text{vib}} = \Gamma_{\text{stretch}} \times \Gamma_{\text{tun}}$ can be inferred directly and unambiguously from the spectra, and is given in Table 6.2 as well as Figure 6.1. For both observed K states, we find that the energetically lower member of the tunneling doublets has $\Gamma_{\text{vib}} = A^+$, as has been assumed somewhat ad hoc in the earlier FTIR work [365]. The observed *decrease* in the magnitude of the tunneling with *increasing* K quantum number is in contrast to all previous results on $(\text{HF})_2$ and to qualitative [299, 364, 138] and quantitative [58, 59, 311] models derived from them. This breakdown of the simple dynamical tunneling picture will be discussed below.

6.4 Vibrational predissociation measurements

The observed linewidths of the overtone transitions contain important information concerning the stretching dynamics in $(\text{HF})_2$. In transitions observed in the present study the line shape can be approximated well by a Voigt profile, i.e., a convolution of a Lorentzian and a Gaussian contribution. Furthermore, the line shape is consistent with only a *single* broadened transition, and thus there is no indication for the onset of additional tunneling splitting due to hydrogen exchange between the

two HF monomers. The Gaussian contribution in the slit jet results from the residual Doppler broadening from thermally distributed velocity components of the expanding molecules perpendicular to the expansion axis and parallel to the optical axis of the White cell arrangement. In principle, the complex multipass ray geometry could also contribute to asymmetric non-Gaussian profiles. However, $2\nu_1$ transitions of ArHF, where the upper vibrational level is extremely long lived and hence Doppler broadening clearly dominates, do not show any significant asymmetry under identical expansion conditions, and can be fit to a Gaussian profile to very good approximation. Power levels ($\leq 50\mu\text{W}$) are orders of magnitude below those required to induce measurable saturation broadening. Collisional rates in the low density expansion contribute a negligible pressure broadening component to the linewidth as do transit time effects due to a finite beam size. The Lorentzian contribution from such a Voigt fit can therefore be interpreted as lifetime broadening due to predissociation. Possible mechanisms of such a predissociation process in the overtone levels of $(\text{HF})_2$ have been discussed in detail [365, 274]. In order to isolate this Lorentzian contribution from the observed spectra, the experimental Doppler broadening has been determined in three independent ways:

i) For selected strong Q branch lines of the $K = 1 \leftarrow 0$ band, an unconstrained fit of a Voigt profile is possible and yields the intrinsic Gaussian and predissociative Lorentzian widths. By this method, one obtains a Gaussian component of 100 ± 50 MHz.

ii) The same Voigt deconvolution procedure can be applied to ArHF $2\nu_1$ transitions also observed under identical expansion conditions. Here, the profile is very close to Gaussian due to the long lifetime of this van der Waals complex. From an analysis of several R branch transitions one finds 79 ± 11 MHz and a statistically in-

significant Lorentzian component. From extensive previous studies of stable molecules in the slit jet, the observed residual Doppler widths can be well predicted from the common jet temperature for rotational and vibrational degrees of freedom. This reflects the more complete equilibration between translation, rotation, and vibration accessible in the slit expansion due to a slower $1/r$ density drop off with distance. It is important to note that this broadening is a reflection of the transverse thermal distribution, and not a measure of the large non-zero average velocity of the longitudinal flow. This of course is based on (sufficiently) orthogonal alignment of the White cell with respect to the expansion axis, which then samples predominantly the thermal (and hence mass dependent) contributions to the Doppler width. Specifically, from the mass ratio between ArHF and $(\text{HF})_2$, one predicts 97 ± 14 MHz as the Gaussian component for $(\text{HF})_2$, in good agreement with the results from i).

iii) A purely thermodynamic prediction of the residual Doppler broadening component for $(\text{HF})_2$ can also be made based on the observed Boltzmann rotational distributions. A fit of the $K = 1 \leftarrow 0$ $(\text{HF})_2$ Q branch line intensities yields a rotational temperature of 11 ± 1 K for this complex under the expansion conditions stated. Assuming $T_{\text{rot}} \approx T_{\text{trans}}$, as has been demonstrated repeatedly for the slit nozzle expansion [244, 284], one obtains a prediction of 87 ± 7 MHz for the $(\text{HF})_2$ Doppler width, again in good agreement with estimates i) and ii).

For consistency, we therefore fit all lines to Voigt profiles with a fixed Gaussian contribution of 95 MHz to obtain the Lorentzian widths. Figure 6.2 shows a sample least-squares Voigt fits obtained in this way, with the results summarized in Table 6.3. Statistically significant J -dependences for the predissociation lifetimes are not observed (see Table 6.3a) in good agreement with previous studies [302] of the

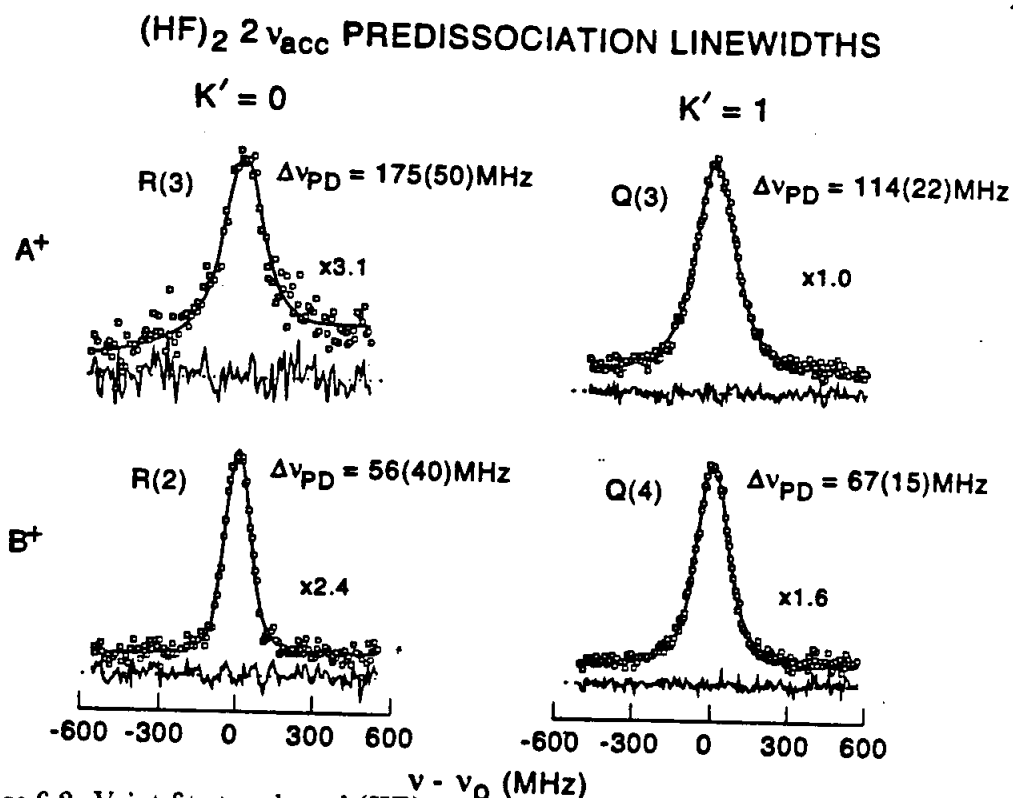


Figure 6.2: Voigt fits to selected (HF)₂ transitions showing the unusual K'_0 and tunneling symmetry dependence of the predissociation linewidths. The A⁺ and B⁺ symmetry labels refer to Γ_{vib} for the upper state.

fundamental HF dimer region. Hence the values reported in Table 6.3b represent averages over J' , for each K' and overall symmetry level (i.e., A⁺, B⁺).

We note briefly that the range of predissociation rates (50 to 175 MHz) observed for $2\nu_{\text{acc}}$ is much broader than the corresponding range of predissociation rates (6.4 to 11.8 MHz) in the fundamental ν_{acc} region [302]. This provides further evidence for the assignment of the overtone vibration in (HF)₂ to $2\nu_{\text{acc}}$, since it would be unlikely that either of the two other triad members, $\nu_{\text{acc}} + \nu_{\text{don}}$ or $2\nu_{\text{don}}$, would exhibit a decreased predissociation rate below the 330(30) MHz values observed for the ν_{don} fundamental. For comparison, a similar order of magnitude increase in vibrational predissociation rates is observed in hydrogen bonded dimer systems such as HF overtone excited N₂HF [129], i.e., where there is no possible ambiguity about the nature

Table 6.3: (a) Predissociation linewidths (in MHz) measured for upper states of transitions in HF dimer, $\nu_{\text{acc}} = 2 \leftarrow 0$. (b) Predissociation linewidths in fundamental^b and overtone excited (HF)₂.

a		Transition		$\Delta\nu_{\text{PD}}^a$	
$\Gamma_{\text{vib}} = A^+$ $K = 0 \leftarrow 0$	$R(3)$	178(28)	$\Gamma_{\text{vib}} = A^+$ $K = 1 \leftarrow 0$	$Q(3)$	116(8)
	$R(4)$	173(23)		$Q(4)$	111(28)
	Average	175(25)		$Q(5)$	123(16)
				$R(3)$	116(13)
			Average	114(11)	
$\Gamma_{\text{vib}} = B^+$ $K = 0 \leftarrow 0$	$R(1)$	58(25)	$\Gamma_{\text{vib}} = B^+$ $K = 1 \leftarrow 0$	$Q(3)$	64(5)
	$R(2)$	52(18)		$Q(4)$	70(10)
	Average	56(20)		$R(3)$	68(9)
				Average	67(8)
b		$\Delta\nu_{\text{PD}}^{\Gamma_{\text{vib}}=A^+}$		$\Delta\nu_{\text{PD}}^{\Gamma_{\text{vib}}=B^+}$	
	$K = 0$	$K = 1$	$K = 0$	$K = 1$	
ν_{acc}^c	9.5(5)	11.8(5)	6.4(5)	10.2(5)	
$2\nu_{\text{acc}}$	175(25)	114(11)	56(20)	67(8)	
ν_{don}	330(30)	—	330(30)	—	

^a Uncertainty represents 1σ estimates.

^b Reference [302]

^c The symmetries A^+ and B^+ refer to $\Gamma_{\text{vib}} = \Gamma_{\text{stretch}} \times \Gamma_{\text{tun}}$. In Ref. [302], the symmetries are labeled by Γ_{tun} only, which due to the $\Gamma_{\text{stretch}} = B^+$ symmetry of the ν_{acc} vibration, reverses the symmetry designations. For $2\nu_{\text{acc}}$, however, neither Γ_{tun} nor Γ_{stretch} is determined from the spectra, and hence for consistency we consider only the Γ_{vib} symmetry label for both ν_{acc} and $2\nu_{\text{acc}}$.

of the $\nu_{\text{HF}} = 2 \leftarrow 0$ excitation.

From the above discussion it is quite likely that both the $\nu_{\text{don}} + \nu_{\text{acc}}$ and $2\nu_{\text{don}}$ levels are strongly predissociated. The corresponding loss of peak absorption sensitivity and spectral resolution due to excessive line broadening may explain why preliminary searches for these other bands have not proven successful, though an exhaustive search has not yet been completed. It is worth noting that structure ($\Delta\nu \leq 3200$ MHz) in the cooled cell FTIR spectra has been observed near 7555 cm^{-1} [365], tentatively assigned to $2\nu_{\text{don}}$. Spectroscopic detection of the other members of the triad by high resolution methods should facilitate a more comprehensive understanding of these intriguing predissociation dynamics. In any event, the present results refine the previous lower bounds of the predissociation lifetimes for $2\nu_{\text{acc}}$ from FTIR studies [365] by almost two orders of magnitude.

Finally, as illustrated in Figure 6.3a and Table 6.3, there is a relatively strong K and tunneling symmetry dependence to the predissociation linewidths. The K dependence of the $2\nu_{\text{acc}}$ linewidths for the $\Gamma_{\text{vib}} = \text{B}^+$ tunneling symmetry component (i.e., 56(20) MHz and 67(8) MHz for $K=0$ and 1, respectively) closely parallels the behavior noted by Pine and Fraser [302] for the ν_{acc} fundamental (i.e., 6.4(5) and 10.2(5) MHz for $\Gamma_{\text{vib}} = \text{B}^+$, $K=0$ and 1, respectively) with the rates scaled upward by roughly by a factor of 6–9 for the additional quantum of excitation. Again, this is consistent with the 10-fold increase in linewidths observed between the N_2HF fundamental and overtone spectra. We note for later discussion that the corresponding behavior for the $\Gamma_{\text{vib}} = \text{A}^+$ tunneling symmetry component (i.e., 175(25) and 114(11) MHz for $K=0$ and 1) does not scale as simply with the ν_{acc} fundamental data [302] [9.5(5) and 11.8(5) MHz for $K=0$ and 1], but rather is in accord with a simple coupling model proposed in

Table 6.4: Tunneling splittings $\Delta\nu_T \equiv \nu_K^{\Gamma_{\text{tun}}=B^+} - \nu_K^{\Gamma_{\text{tun}}=A^+}$ in ground state, fundamental, and overtone excited (HF)₂.

	$K = 0$	$K = 1$
0	19.74703(2) GHz	31.91104(1) GHz
ν_{acc}	6.4616981) GHz	10.4888(27) GHz
$2\nu_{\text{acc}}$	6.353(15) GHz ^b	2.824(9) GHz ^b

^a Reference [299]

^b The *sign* of the tunneling splitting in Eq. (6.2) is not known until the Γ_{stretch} and Γ_{tun} symmetries of the levels can be unambiguously determined.

Ref. [301] and later abandoned [302] in view of the ν_{acc} fundamental results. There are also similar K dependent anomalies exhibited in the tunneling splitting and transition intensities as well (see Table 6.4). This suggests a perturbative “mixing” with other near resonant inter- or intramolecular vibrations of the same total symmetry, as will be considered in more detail in the following section.

6.5 Discussion

6.5.1 Vibrational overtone assignment in the $v=2$ triad

Let us first turn to the vibrational assignment of the observed bands. Within a 2D local mode picture of (HF)₂, experimental data [365] as well as *ab initio* results [238, 216] suggest a rather well separated energetic triad structure. Upon complexation, the harmonic force constants for the local HF stretching modes are somewhat softened with respect to free HF ($\omega_e = 4138.3 \text{ cm}^{-1}$) [184], resulting in red shifts of

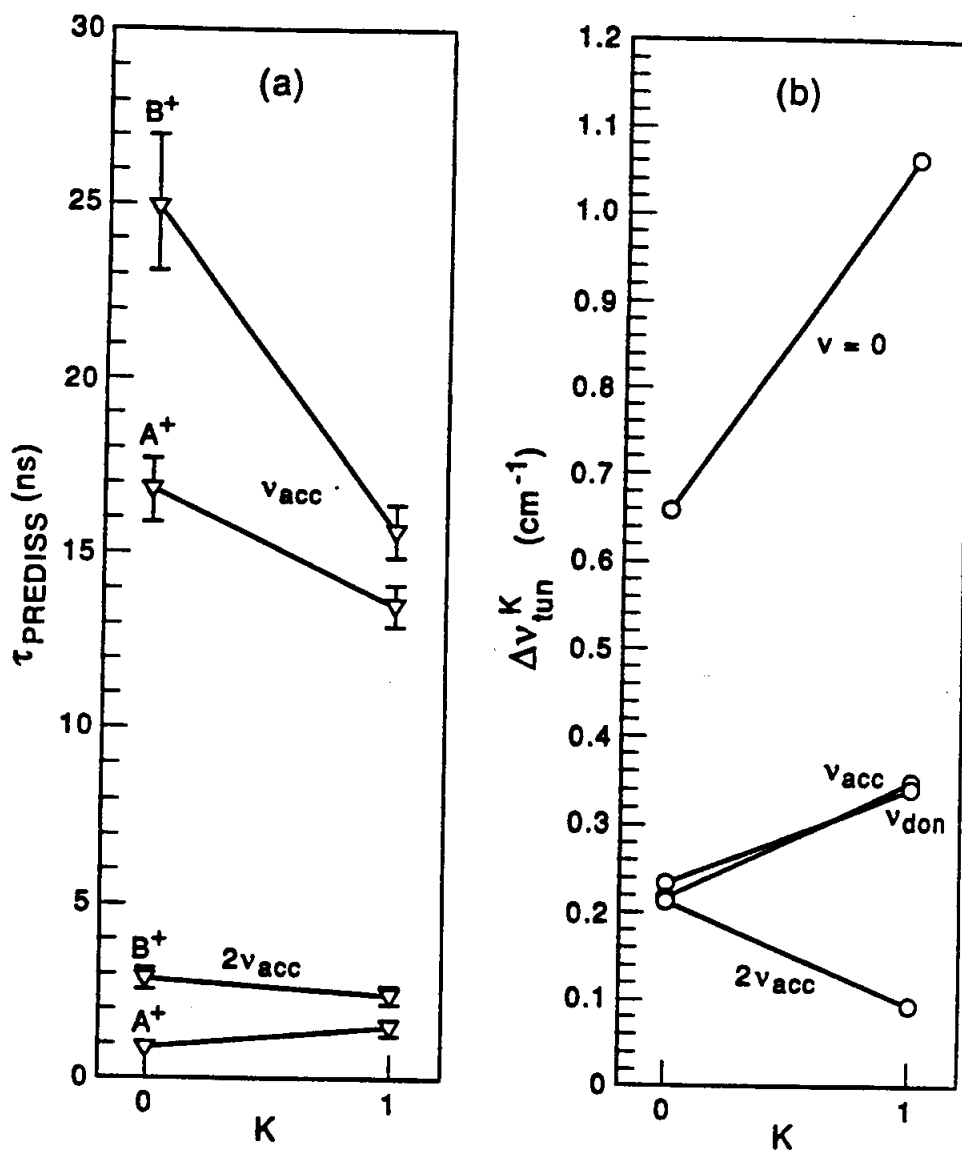


Figure 6.3: a) Predissociation lifetimes τ obtained from Lorentzian linewidths $\Delta\nu_{\text{PD}}$ (FWHM, dimension of frequency) according to $\tau = 1/(2\pi\Delta\nu_{\text{PD}})$ for $\Gamma_{\text{vib}} = \text{A}^+, \text{B}^+$ levels of ν_{acc} , ν_{don} , and $2\nu_{\text{acc}}$ (this work) as a function of K quantum number. b) Tunneling splittings $\Delta\nu_{\text{T}}$ (in cm^{-1}) = $\nu_K^{\Gamma_{\text{vib}}=\text{B}^+} - \nu_K^{\Gamma_{\text{vib}}=\text{A}^+}$ as a function of the K quantum number for $v=0$ ν_{acc} , ν_{don} , and $2\nu_{\text{acc}}$ (this work). Due to lack of explicit knowledge of the $\Gamma_{\text{tun}} = \text{A}^+, \text{B}^+$ symmetry label ordering for $2\nu_{\text{acc}}$, only the magnitude, $|\Delta\nu_{\text{T}}|$, can be determined unambiguously. Error bars represent one standard deviation.

$\Delta\omega_e \approx -30 \text{ cm}^{-1}$ and -90 cm^{-1} for ν_{acc} and ν_{don} stretches, respectively. According to high level *ab initio* results [216], there is only a relatively small off-diagonal anharmonicity coupling ($< 10\text{--}20 \text{ cm}^{-1}$) between the two modes. The diagonal anharmonicity of the underlying free HF oscillator ($\omega_e x_e = 89.9 \text{ cm}^{-1}$) appears to be only moderately affected by the shifts in harmonic frequencies induced by hydrogen bond formation [238, 216]. This simplified scheme leads to an overtone sequence $2\nu_{\text{don}} < 2\nu_{\text{acc}} < \nu_{\text{don}} + \nu_{\text{acc}}$, with separations of about 120 cm^{-1} between each of the neighboring pairs (as illustrated in Figure 6.4), in contrast to the $2\omega_{\text{don}} < \omega_{\text{don}} + \omega_{\text{acc}} < 2\omega_{\text{acc}}$ ordering expected in the harmonic limit [365]. Even though vibrational resonances are expected to lead to some mixing, it is plausible to expect that the magnitude of the potential coupling is not sufficient to scramble this local mode structure beyond recognition.

It is therefore reasonable to make a local mode assignment of the observed vibrational state based on its energy, and confirm with other spectroscopic properties. Assignment to $2\nu_{\text{don}}$ would imply a highly unrealistic anharmonicity constant $\omega_e x_e$ of 27 cm^{-1} , three fold smaller than the monomer value. A $2\nu_{\text{acc}}$ interpretation leads to the much more reasonable value of 89.5 cm^{-1} , which is in close agreement with the monomer result of 89.9 cm^{-1} [184], or 86 cm^{-1} , if for consistency the HF monomer anharmonicity analysis is restricted to the fundamental and first overtone only. In order to assign the observed bands to the local mode combination band $\nu_{\text{don}} + \nu_{\text{acc}}$, one would have to invoke a negative off-diagonal anharmonicity contribution in excess of 100 cm^{-1} , which seems quite unlikely in this zero order picture. Hence, the nearly quantitative agreement between anharmonic, local mode predictions and the observed vibrational band origin provides strong support for the $2\nu_{\text{acc}}$ assignment, as indicated

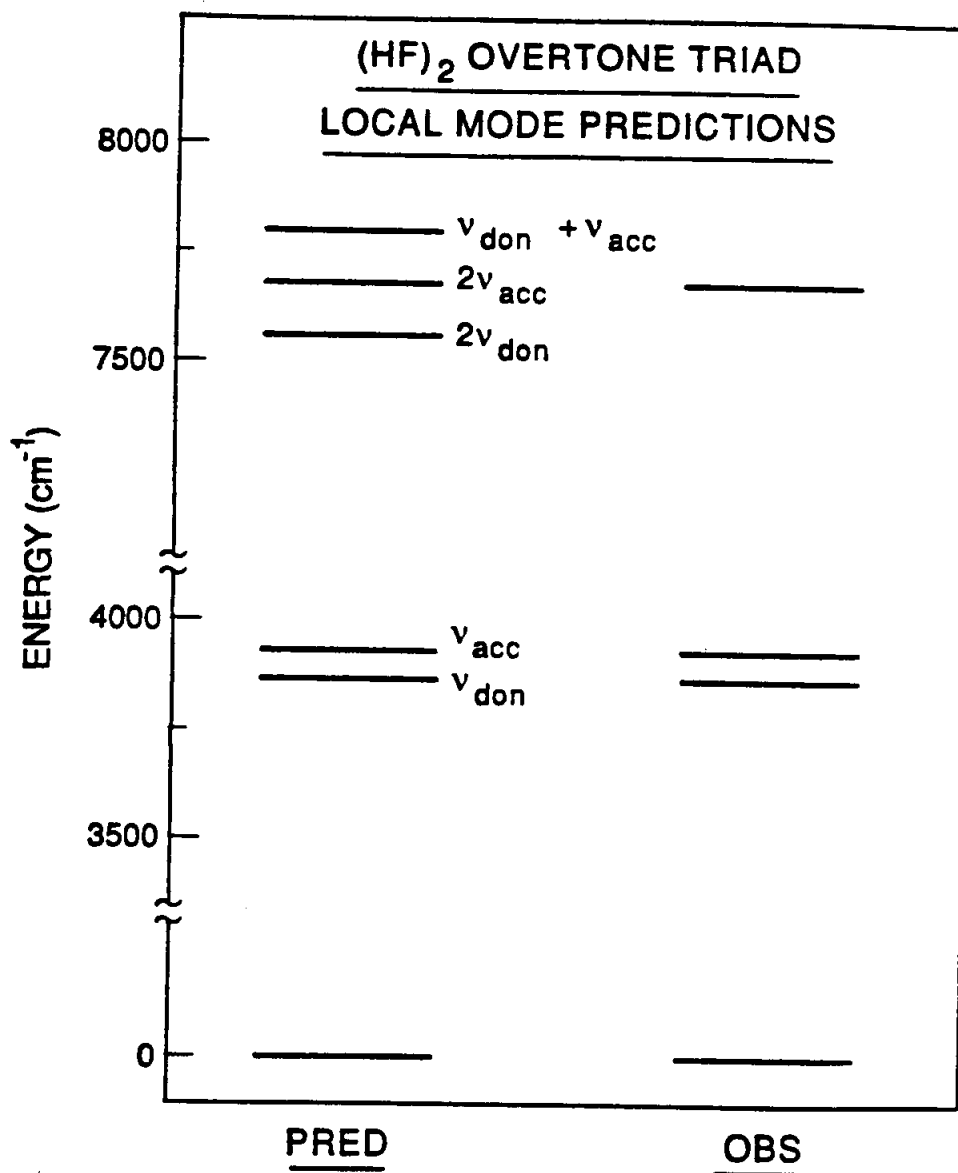


Figure 6.4: Energy level dyad and triad for (HF)₂ fundamental and overtone transitions. Left hand side: predictions from a local mode model, including HF anharmonicity ($\omega_e x_e = 89.9 \text{ cm}^{-1}$) and donor/acceptor red shifts ($\Delta\omega_e^{\text{don}} \approx 90 \text{ cm}^{-1}$, $\Delta\omega_e^{\text{acc}} \approx 30 \text{ cm}^{-1}$), obtained from the fundamental transitions. Right hand side: observed overtone band from this work, in excellent agreement with the predicted $2\nu_{\text{acc}}$ transition frequency.

in Figure 6.4.

Analysis of the tunneling splittings provides further spectroscopic support for this assignment. Excitation of the ν_{acc} or ν_{don} fundamental in HF dimer decreases the tunneling splitting three-fold from 0.66 to 0.22 cm^{-1} [298, 365]. This reduction has been analyzed in terms of an effective 1D dynamical model of the tunneling event [138], whereby exchange of the HF vibrational quantum leads to an increase in an effective 1D tunneling barrier. Withing this model, one would expect the tunneling splittings for the $v=2$ triad to behave quite differently than for the $v=1$ dyad. For example, in either the $v_{\text{acc}}=2$ or $v_{\text{don}}=2$ levels, two quanta of HF vibration must be exchanged, and one would anticipate a further increase in effective barrier and corresponding decrease in tunneling splitting. Indeed, for the $K=1$ symmetry levels the observed tunneling splittings are three-fold smaller than in the $v_{\text{acc}}=1$ or $v_{\text{don}}=1$. In contrast, one might expect that the tunneling splittings for the $\nu_{\text{acc}} + \nu_{\text{don}}$ level, where no quanta of HF vibration need to be exchanged, would be comparable to the 0.66 cm^{-1} splitting of the ground state, i.e., 5-10 fold larger than observed experimentally. Of course, such a splitting argument only rules out the $\nu_{\text{acc}} + \nu_{\text{don}}$ level. However, the assignment of the observed spectra as arising from $2\nu_{\text{don}}$ appears quite unlikely based on the anharmonicity and predissociation predictions described below.

Nonetheless, it is worth noting that some subtle difficulties remain with the observed overtone bands to $v_{\text{acc}} = 2 \leftarrow 0$. The results obtained in the fundamental region [298, 299, 365] suggest that $2\nu_{\text{acc}}$ should be $\Delta K = \pm 1$. Indeed, this is supported by the smooth trend in A between the ground state ($A = 35.4 \text{ cm}^{-1}$), ν_{acc} ($A = 32 \text{ cm}^{-1}$), and $2\nu_{\text{acc}}$ ($A = 28.6 \text{ cm}^{-1}$) values. This trend indicates that the HF oscillator is bent progressively away from the intermolecular axis, smoothly approaching the

limiting case of a perpendicular $(\text{HF})_2$ geometry for which A would be approximately $B_{\text{HF}} \approx 20 \text{ cm}^{-1}$ [299]. Though this geometric interpretation is quite consistent with the observed perpendicular $K = 1 \leftarrow 0$ band (see Figure 6.1), it is in contrast to the observation of a *comparably* strong, parallel $K = 0 \leftarrow 0$ transition. Based on the relative intensities of the two bands (and normal Hönl-London factors for a rigid near symmetric top), one finds a formal ratio of the vibrational transition dipole moments of $\mu_{\parallel}/\mu_{\perp} = 1.2 \pm 0.2$. Since the $\nu_{\text{don}} = 1 \leftarrow 0$ band carries predominantly parallel oscillator strength, such a ratio might suggest a $\nu_{\text{acc}} + \nu_{\text{don}}$ assignment, though this is a less likely scenario by tunneling, predissociation, and energetics arguments discussed above.

Two further explanations for the intensity anomaly should be mentioned for completeness, although they appear to be very unlikely due to absolute intensity considerations: i) What we observe might itself not be a pure triad member but rather a combination band of, say, $2\nu_{\text{don}}$ and an intermolecular vibration to make up for the $2\nu_{\text{acc}} = 2\nu_{\text{don}}$ anharmonic energy difference. However, such a combination band would be much weaker than the simple overtone excitation, and furthermore, would be expected to exhibit linewidths in excess of $\nu_{\text{don}} = 1$, in contrast to the significantly narrower linewidths observed. ii) It could be imagined that the observed perpendicular band is due to $2\nu_{\text{acc}}$, while the parallel band is not, thus rendering all K -correlations discussed here artificial. This would necessitate the unlikely occurrence of a strong parallel subband of another vibration which accidentally appears within a fraction of 1 cm^{-1} at the location where we predict the parallel subband of $2\nu_{\text{acc}}$. The possibility of such an accidental coincidence could be further tested by a J -resolved measurement of the subband system near 7646.3 and 7647.6 cm^{-1} , which is probably

due to $K = 0 \leftarrow 1$ transitions of $2\nu_{\text{acc}}$ [365]. Attempts to see this band at much higher resolution at the slit jet temperatures have as yet proven unsuccessful. However, since the lower state is thermally excited by 35 cm^{-1} , this is not surprising under typical expansion temperatures, and will require further investigation under much warmer jet conditions.

Hence, we have the situation that the tunneling splitting, energetics, and vibrational predissociation behavior strongly support the assignment of the bands to $\nu_{\text{acc}} = 2 \leftarrow 0$, and yet the strong $\Delta K=0$ intensity indicates the presence of another vibrational state nearby. If there is indeed strong vibrational mixing with other zero order states, one could reasonably argue that a detailed labeling of the observed state is irrelevant. However, we prefer to keep the $2\nu_{\text{acc}}$ label based on the likely origin of the initial oscillator strength and the above quantitative arguments. Hence, we must explore the possibility of a resonance with a nearby bright state carrying predominantly parallel character, but before doing so, we must consider the influence of exchange symmetry on these interactions.

6.5.2 Tunneling splittings and exchange symmetries

The discussion thus far has centered around an *energetic* local mode assignment, but there is further information in the spectra to be obtained from symmetry considerations. In order to take indistinguishability of the two HF units into account, we have to classify the states in terms of the exchange symmetry ($\Gamma_{\text{vib}}=A^+, B^+$), i.e., we have to consider correctly symmetrized or antisymmetrized modes to describe the spectroscopic eigenstates. The high barrier between equivalent conformers leads

to closely neighbored pairs of states with opposite exchange symmetry. Specific resonances can influence the energy ordering in such pairs of levels and thus complicate the symmetry picture without affecting the local mode stretching character appreciably. Note that the tunneling splittings between the two symmetry components ($\approx 0.1 \text{ cm}^{-1}$) are 2–3 orders of magnitude *smaller* than the anticipated span of triad energies. Hence in a relative sense, the observed states are already quite close to the limit of an infinitely high exchange barrier. Therefore, any stretching or tunneling symmetry classification is likely to be more fragile than the simple energetic statements based on the anharmonicity of the oscillators and the hydrogen bonding shifts. In ν_{acc} and ν_{don} fundamental dyad of $(\text{HF})_2$, symmetry selective resonances seem to be insignificant, although justifying the size and equality of the observed tunneling splittings remains a quantitative challenge for theory.

An even more quantitative challenge in interpreting the fundamental and overtone data self consistently appears from a detailed analysis of the vibrational and tunneling symmetries. Based on the assumption of positive tunneling splittings and a trans- or disrotatory exchange path, the predominantly acceptor stretch ν_{acc} is assigned the $\Gamma_{\text{stretch}}=\text{B}^+$ stretching symmetry label and designated ν_1 while the eigenstate with predominantly donor stretch characteristics, ν_{don} , is symmetric with respect to HF exchange ($\Gamma_{\text{stretch}}=\text{A}^+$) and is given the normal mode label ν_2 . (We note, in the interest of clarity, that the ν_1 and ν_2 normal mode quantum labels of Mills and Robiette [279, 75] have alternatively been designated ν_a and ν_s by Hougen and Ohashi [175].) Formally, the overtones of these spectroscopic states, $2\nu_1$ and $2\nu_2$, have $\Gamma_{\text{stretch}}=\text{A}^+$ by definition, while the combination band $\nu_1 + \nu_2$ is antisymmetric, i.e., $\Gamma_{\text{stretch}}=\text{B}^+$.

However, the correlation between this symmetry assignment and the more physically transparent "local mode" triad labels is subtle, and depends upon the shape of the potential coupling as well as other factors. A recent 2D-stretching + 1D-tunneling analysis of a high level 6D *ab initio* potential surface yields the following correlation between overtone quanta distribution and Γ_{stretch} : $2\nu_{\text{don}} \equiv 2\nu_2$ ($\Gamma_{\text{stretch}}=A^+$), $2\nu_{\text{acc}} \equiv \nu_1 + \nu_2$ ($\Gamma_{\text{stretch}}=B^+$), $\nu_{\text{don}} + \nu_{\text{acc}} \equiv 2\nu_1$ ($\Gamma_{\text{stretch}}=A^+$) and positive tunneling splittings [196] as defined by Equation 2. We note that such a result is also obtained with high generality by simple model calculations for harmonically coupled Morse oscillators connected by a disrotatory tunneling path [279, 75], while rather dramatic coupling strengths are needed to break the correlation. On the other hand, the present experimental data prove unambiguously that the lower of the two tunneling levels of the observed state has $\Gamma_{\text{vib}}=A^+$ vibrational symmetry for $K=1$ and 1, consistent with $\Gamma_{\text{stretch}}=A^+$ and positive tunneling splittings (i.e., $\nu_K^{\Gamma_{\text{tun}}=B^+} > \nu_K^{\Gamma_{\text{tun}}=A^+}$) or $\Gamma_{\text{stretch}}=B^+$ and negative tunneling splittings (i.e., $\nu_K^{\Gamma_{\text{tun}}=B^+} < \nu_K^{\Gamma_{\text{tun}}=A^+}$). Several plausible explanations of this apparent discrepancy can be considered.

i) The observed stretching state is not $2\nu_{\text{acc}}$ but either $2\nu_{\text{don}}$ or $\nu_{\text{don}} + \nu_{\text{acc}}$, which are predicted at 7570 and 7798 cm^{-1} by *ab initio* calculations [196], i.e., more than 100 cm^{-1} to higher and lower energies from the experimental value. This possibility has been discussed before [311] and, considering also the approximations implicit in the dynamical model, would not be unusual for a system of this size. However, it is unlikely in light of the success realized in the description of symmetry and energetics of the fundamental dyad ($\nu_{\text{acc}}, \nu_{\text{don}}$) by essentially the same potential surface [59] and model approximations.

ii) The observed stretching state is indeed $2\nu_{\text{acc}}$, but restriction of the dy-

namical dynamical treatment to $2 + 1$ adiabatically separated degrees of freedom out of six coupled vibrations neglects small but crucial effects on shifts of the tunneling levels, which could reverse the tunneling sequence without significantly influencing the coarse stretching level structure of the triad.

iii) Inaccuracies in the 6D *ab initio* surfaces are responsible for the discrepancies, and even a full 6D quantum mechanical calculation with the present surfaces would yield the same quantitative results predicted in the 2D stretching and 1D tunneling analysis. One or both of the two latter effects are likely, although none of the rationalizations can be completely dismissed at the current state of experiment and theory.

6.5.3 Symmetry and K -state dependent perturbations

In order to elucidate possible explanations for the discrepancy, we discuss the observed irregularities in the $2\nu_{\text{acc}}$ band in more detail. This necessarily involves arguments of a speculative nature, which have to be checked and revised by future investigations of the triad.

The simplest picture for $2\nu_{\text{acc}}$ seems to require a local resonance to explain K and tunneling state dependent anomalies in the spectra. A reasonable starting point is provided by the assumption that the $K=1$ levels are not affected very much by the local resonance. Here, predissociation lifetimes, tunneling splittings, and rotational constants behave more or less as expected. The tunneling splitting of 0.094 cm^{-1} is qualitatively in line with earlier vibrational exchange [138] or effective barrier [364, 365, 278] arguments. We find a fourfold decrease of tunneling in $2\nu_{\text{acc}}$ (0.094 cm^{-1})

relative to ν_{acc} (0.35 cm^{-1}), similar to the threefold decrease between ν_{acc} (0.35 cm^{-1}) and the ground state (1.06 cm^{-1}). The relative size of the B_1 , D_1 , and b_1 rotational constants for the $\Gamma_{\text{stretch}}=A^+$ and $\Gamma_{\text{stretch}}=B^+$ levels is also consistent with findings for other $K=1$ (stretching) states [298], although here the statistical significance is sometimes marginal. Predissociation line widths appear to be a particularly sensitive probe of level interactions in the present case. For $K=1$, they lie in a reasonable range with respect to the fundamental ν_{acc} results, although there is a somewhat larger Γ_{vib} symmetry dependence ($\Delta\nu_{\text{PD}}^{\Gamma_{\text{vib}}=A^+} \approx 1.7 \Delta\nu_{\text{PD}}^{\Gamma_{\text{vib}}=B^+}$), at variance with the comparable linewidths observed in ν_{acc} and possibly indicating some residual mixing of the $2\nu_{\text{acc}}$ zero order $\Gamma_{\text{vib}}=A^+$ level with a more rapidly predissociative dark state.

On the other hand, for $K=0$ of $2\nu_{\text{acc}}$ there is a strong indication for mixing with another vibrational state, about which we can speculate. The $K=0$ tunneling splitting of 0.212 cm^{-1} appears to be "too large", relative to the 0.094 cm^{-1} $K=1$ value, and certainly in light of the proposed physical picture of centrifugal assistance over the tunneling barrier with K excitation [299]. In addition, the $K=0$ splittings are nearly the same magnitude in $2\nu_{\text{acc}}$ (0.212 cm^{-1}) as in ν_{acc} (0.216 cm^{-1}), which goes against the interpretation of an *increased* dynamical barrier [138] to tunneling with the requirement of vibrational exchange of the HF quanta. The effect is too dramatic to be explained by the change in vibrationally averaged geometry present in $2\nu_{\text{acc}}$. More likely, it is due to a selective perturbation of one of the tunneling components and therefore indicates either a large tunneling splitting in the perturbing state or a very local resonance. Indeed, the $\Gamma_{\text{vib}}=A^+$ predissociation lifetime is significantly shorter than the longer lived $\Gamma_{\text{vib}}=B^+$ state. There could thus be a specific route for predissociation available to $K=0$, $\Gamma_{\text{vib}}=A^+$ (and perhaps also weakly present in $K=1$,

$\Gamma_{\text{vib}}=A^+$), which is not accessible to the corresponding $\Gamma_{\text{vib}}=B^+$ states.

In principle, such symmetry and rotation effects in the predissociation rate can be caused by the selection rules governing the dissociation process [311, 307]. Indeed, in systems such as rare gas-hydrogen halides [79, 282, 252, 253, 255] and ArH_2O [223, 285] there can be quite dramatic effects due to an energetically open channel accessible to only one e or f parity component. However, these situations typically result from quite specific energy resonances with little translational and no rotation in the outgoing products. In contrast, $(\text{HF})_2$ excited to the $2\nu_{\text{acc}}$ level at 7683 cm^{-1} must dispose of at least 2660 cm^{-1} into rotation and translation of the $\text{HF}(v=1) + \text{HF}(v=0)$ [we note, however, that $\text{HF}(v=0, J=9) + \text{HF}(v=1, J=6)$ is almost a perfectly resonant product channel with essentially no excess energy for translation [98, 273] and another 3961 cm^{-1} to access the $\text{HF}(v=0) + \text{HF}(v=0)$ channel. For the present case of $(\text{HF})_2$ therefore, where the number of accessible dissociation channels is relatively large, it appears more reasonable to invoke a specific vibrational coincidence within the quasibound manifold of $(\text{HF})_2$ levels of $\Gamma_{\text{vib}}=A^+$ symmetry.

Let us pursue this hypothesis further. In the absence of knowledge about the perturbing state, we cannot decide whether we observe weak mixing with a very short lived state or stronger mixing with a state of intermediate lifetime. However, the K and tunneling selectivity of the phenomenon indicates that the two interacting states are only a few cm^{-1} apart, possibly much closer. Since it is only the $\Gamma_{\text{vib}}=A^+$ symmetry levels which appear significantly perturbed, one can conclude that the perturbing level is *above* $2\nu_{\text{acc}}$, thereby shifting the $\Gamma_{\text{vib}}=A^+$ levels to the lower energy and hence resulting in the anomalously large tunneling splittings observed for $K=0$. An interesting question in this context is whether this local resonance could possibly

invert the tunneling pair sequence in $2\nu_{\text{acc}}$ and thus recover in zero order the *ab initio* prediction [196] of $\Gamma_{\text{stretch}}=B^+$ for both $K=0$ and 1. This of course would require a downward shift in the $\Gamma_{\text{vib}}=A^+$ levels by $\geq 0.22 \text{ cm}^{-1}$ for $K=0$ and $\geq 0.1 \text{ cm}^{-1}$ for $K=1$, which would be sufficiently large to dominate the small and weakly K dependent tunneling splittings anticipated in the unperturbed levels. Indeed, there is some support from FTIR spectroscopy [365] for such a reverse ordering of the tunneling levels, but unfortunately, it is largely masked by the large pressure broadening in the cooled cells. Observation of rotationally resolved $K=2,3$ levels [365] of $2\nu_{\text{acc}}$ would shed some light on this problem. In particular, it would immediately provide helpful information on the global vs local nature of the perturbation. It merits mentioning again that the magnitude of such perturbative shifts responsible for a possible shift in the tunneling symmetry would be quite small with respect to the much larger separations for the $v=2$ triad levels. Finally, we note that if such perturbations in the $\Gamma_{\text{vib}}=A^+$ manifold were responsible for the sign reversal of the tunneling splittings, the relative magnitude of the shifts would require a greater mixing with dark state(s) for the $K=0$ vs $K=1$ levels, and which would also be consistent with the larger $K=0$ vs $K=1$ predissociative linewidths experimentally observed.

One can think about possible candidates for the observed perturbation and one them, namely $2\nu_{\text{don}} + \nu_4$, seems particularly likely. This combination band between the lowest member of the two-quantum stretching triad and the lowest intermolecular mode is predicted to fall in the region of interest. The dimer stretch ν_4 has been located at $125 \pm 5 \text{ cm}^{-1}$ through indirect FIR spectroscopic evidence [310, 311, 261]. From the redshift of the observed $2\nu_{\text{don}}$ band [365] by about $-200 \pm 15 \text{ cm}^{-1}$ relative to the monomer, one infers an increase of the hydrogen bond energy ($D_0=1062 \text{ cm}^{-1}$)

[300, 98, 273] by roughly 20% in $2\nu_{\text{don}}$. This should give rise to a comparable increase in the dimer stretching frequency, leading to a predicted $50 \pm 20 \text{ cm}^{-1}$ red shift of $2\nu_{\text{don}} + \nu_4$ in $(\text{HF})_2$ relative to $v=2$ of HF monomer. Additionally, one would expect strong coupling between these two inter- and intramolecular stretching modes, since both involve motion of the hydrogen bridge atom in the same direction. Such stretch-stretch coupling might lead to enough oscillator strength for direct observation as a combination band in the overtone IR region. Furthermore, this coupling would tend to increase the red shift of this predominantly parallel band into closer resonance with the $2\nu_{\text{acc}}$ overtone band observed in the present studies (i.e., red shifted by 68 cm^{-1} from $v=2$ of HF monomer), while any other combination of $2\nu_{\text{don}}$ with intermolecular modes would be higher in frequency. One cannot strictly exclude $2\nu_{\text{don}} + \nu_5$ at the moment, with ν_5 being the disrotatory, in-plane bending fundamental near 160 cm^{-1} [310, 58, 311, 261, 3]. This would yield an attractive rationalization of the tunneling selectivity of the perturbation, but it is less likely from an energetic point of view.

The question then naturally arises why similar $K=0$ perturbations are not observed in the $v=1$ dyad of $(\text{HF})_2$. A simple answer is that all intermolecular vibrational frequencies to which such couplings could exist exceed the energy difference at the $v=1$ level between the ν_{acc} and ν_{don} components. Hence, the only coupling energetically feasible additionally requires $\Delta K \neq 0$ to establish a near resonance. Indeed, perturbations [299, 365] in the $K=2$ manifold of ν_{acc} are observed, quite possibly due to a $\Delta K = -1$ resonance with a slightly higher $\nu_{\text{don}} + \nu_4$ combination state with $K=1$. Further support for this explanation could be obtained by near-IR observation of such $(\text{HF})_2$ combination bands in the fundamental and overtone regions.

One final aspect of the experimental spectra remains to be discussed: the

comparable intensity of the $K = 0 \leftarrow 0$ parallel transitions relative to the $K = 1 \leftarrow 0$ perpendicular bands. As previously mentioned, the roughly equal perpendicular and parallel band intensities are at variance with the zeroth order expectation based on a nearly perpendicular orientation of the ν_{acc} HF bond with respect to the ν_{don} HF subunit. In light of the resonant perturbation of the $2\nu_{\text{acc}}$, $\Gamma_{\text{vib}}=A^+$, $K'=0$ manifold discussed above, it would be natural to suspect this also as a mechanism for enhancing the $K = 0 \leftarrow 0$ band. However, no unassigned lines were found in this band region and there is also no pronounced tunneling level dependence of the integrated $K = 0 \leftarrow 0$ intensity that would indicate a different extent of level interaction observed for the $\Gamma_{\text{vib}}=A^+, B^+$ sublevels. Hence the resonant perturbation of the $\Gamma_{\text{vib}}=A^+$ manifold discussed above cannot account for this strong intensity. The only bright zero order states that can give rise to such a uniform intensity enhancement seem to be $2\nu_{\text{don}}$ and $\nu_{\text{don}} + \nu_{\text{acc}}$. The current (HF)₂ potentials [216, 196, 311] do not support extensive intratriad mixing [59, 197, 279] as illustrated quite clearly by the pronounced local mode pattern for the dipole transition moments calculated by Jensen *et al.* [196] and which predict a much weaker parallel $K = 0 \leftarrow 0$ parallel band than observed experimentally. However, it is worth noting that the corresponding $K = 0 \leftarrow 0$ parallel band in the *fundamental* $\nu_{\text{acc}} = 1 \leftarrow 0$ region of the spectrum is only twofold weaker than the $K = 1 \leftarrow 0$ perpendicular band, i.e., already stronger than expected from a geometric interpretation of the free HF dipole transition moment. Within the context of a local mode assignment, this suggests that current models may underestimate intrapolyad mixing via anharmonic couplings at both the fundamental and overtone level.

Finally, one may turn the preceding discussion around and ask whether $v=2$

intrapolyad mixing alone may be able to rationalize the tunneling and lifetime anomalies beyond the explanation of the intensity anomaly, without having to postulate a local resonance at all. For example, the $\nu_{\text{don}} + \nu_{\text{acc}}$ state is expected to have the required large tunneling splittings [138] as well as a short predissociation lifetime [365]. Assuming preferential $K=0$ coupling of this state to $2\nu_{\text{acc}}$, one could thus provide a plausible explanation for the tunneling, lifetime, and intensity anomalies in the observed bands simultaneously. However, the magnitude and K -selectivity of the effects can only be rationalized by the assumption of a rather small energy spacing between the two zero order states. Though this is not impossible, it appears to be quite unlikely in the anharmonic local mode picture upon which our $2\nu_{\text{acc}}$ assignment is based, as shown in Figure 6.4.

6.5.4 Vibrational predissociation and H-atom exchange dynamics

If the interpretation of the observed dynamic anomalies on the $\Gamma_{\text{vib}}=A^+$ band system are correct, one can infer an "intrinsic" lower limit to the predissociation lifetime for the zero order $2\nu_{\text{acc}}$ stretching overtone state from the $\Gamma_{\text{vib}}=B^+$ manifold to be ≥ 3 ns. Since it may prove necessary to invoke substantial intratriad mixing in order to explain the relative parallel/perpendicular intensities, this 3 ns lifetime should be treated only as a lower limit. Note that in contrast to the fundamental excitation of $(\text{HF})_2$ [302], the predissociation process in $2\nu_{\text{acc}}$ is not restricted to pure $V \rightarrow R, T$ energy transfer ($V, R, T =$ vibration, rotation, translation), but can also involve a $V \rightarrow V$ component in the sense that the second vibrational quantum supplies the energy needed to keep one vibrational quantum in one of the HF's upon dissociation

of the dimer. In fact, it is quite plausible that most of the fragment pairs will still contain one HF stretching quantum, which as mentioned previously would leave only $\approx 2660 \text{ cm}^{-1}$ (for $K=0$ excitation) to be dissipated into rotational and translational energy of the monomer products.

Theoretical estimates for predissociation rates in the $(\text{HF})_2$ complex have yielded an amazing range of results that depend sensitively on the potential surface employed (e.g. see references cited in reference [365]). Ironically, the most numerically "successful" predictions [157] for predissociation from $\nu_{\text{don}}=1$ are obtained from semiempirical potentials partly based on liquid HF simulations [92]. This is almost certainly fortuitous, however, since these potentials contain effective many-body contributions not present in the dimer, and exhibit particularly poor agreement with hydrogen bond dissociation energies [350] well known from gas phase studies [300, 98]. High level dynamical calculations on more reliable gas phase potential energy surfaces [310, 59, 311], where agreement with available $(\text{HF})_2$ experimental data for the low frequency vibrations [366, 310] is well established [311], still remain to be performed.

An interesting question concerns the possible onset of *H atom exchange*, a phenomenon which is very common in extensively hydrogen bonded networks (e.g. isotopic scrambling in $\text{H}_2\text{O}/\text{D}_2\text{O}$ and HF/DF mixtures). While the *HF exchange* process in $(\text{HF})_2$ leaves the HF units intact and occurs over an effective C_{2h} barrier of about 300 cm^{-1} [310, 58, 311], the corresponding *H atom exchange* process requires breaking the HF units in a concerted transition state of D_{2h} symmetry, whose energy has been estimated by *ab initio* methods to be $14500\text{--}20300 \text{ cm}^{-1}$ [144, 207, 167]. Since lower values for this barrier cannot be excluded and quantum tunneling of the involved protons may be appreciable at even lower energies, the lack of spectral evidence for

hydrogen exchange in the overtone spectra near 7700 cm^{-1} is not surprising but worth mentioning. As discussed in the previous section, there is no evidence for additional tunneling spectral structure down to the homogeneous limit of approximately 50 MHz, indicating that the bond breaking hydrogen exchange process in $2\nu_{\text{acc}}$ occurs at least on a timescale longer than the timescale for simple predissociation, i.e., $\geq 3\text{ ns}$. It would be interesting, however, to extend these studies to yet higher numbers of vibrational quanta in an attempt to probe the energetic barrier to unimolecular chemical rearrangement in the $(\text{HF})_2$ complex [60].

6.6 Conclusions

The spectroscopic results presented in this paper provide detailed insight into some of the stretch overtone dynamics of the $(\text{HF})_2$ molecule. They greatly extend previous lower resolution work in static cells, while they also point out limitations of existing dynamical calculations in high level 6D *ab initio* potential surfaces.

The observed band system centered at 7682.823 cm^{-1} correlates well energetically with $2\nu_{\text{acc}}$, the overtone of the acceptor HF stretching motion in $(\text{HF})_2$. Among the relevant findings are: i) There exists strong tunneling and K -rotational dependence of the predissociation linewidths, with predissociation lifetimes as long as 3 ns even at excitation energies seven times higher than the dissociation limit. ii) Tunneling splittings in $2\nu_{\text{acc}}$ excited $(\text{HF})_2$ due to exchange of the identical HF subunits is observed and analyzed. In agreement with expectations based on intramolecular energy transfer of the two quanta of HF stretch during the tunneling event, the observed splittings in $2\nu_{\text{acc}}$ are smaller than those in either ν_{acc} , ν_{don} , or the ground vibrational

state. However, the K -dependence of these splittings contradicts the simple and physically reasonable pattern established in studies of the fundamental excitations. iii) A surprisingly intense parallel component of the transition moment is observed, in contrast to geometrical and more elaborate dynamical predictions for a pure acceptor stretching state.

One interpretation consistent with these findings involves global as well as resonant interactions on $2\nu_{\text{acc}}$ with other vibrational states. The detailed nature and mechanism of such interactions will become apparent with the accumulation of additional spectroscopic data for the overtone triad of $(\text{HF})_2$.

CHAPTER VII

High resolution infrared spectroscopy of DF-DF, HF-DF, and DF-HF: Near-resonant intermolecular energy transfer dynamics

7.1 Introduction

Although it has been more than two decades since the first rotationally resolved spectra were recorded for HF dimer [108], experimental and theoretical interest in this prototypical hydrogen bonded system remains strong. A large part of this interest is attributable to the rich dynamics exhibited by this relatively simple complex. In particular, HF dimer has emerged as a valuable system for studying molecular energy transfer, due to i) the highly nonstatistical and mode-specific energy transfer processes, ii) the availability of accurate, full dimensional potential energy surfaces, and iii) recent theoretical advances which permit quantum calculations that treat all degrees of freedom.

The first evidence of mode specific energy transfer in HF-HF was presented in the cooled cell infrared study of Pine *et al.* [298, 299]. This specificity reflects the structural inequivalence of the HF molecules, as shown in Figure 7.1. The HF in which the H participates directly in the hydrogen bond is referred to as the "bound" HF (or hydrogen bond donor) while the other is labeled the "free" HF (or hydrogen bond

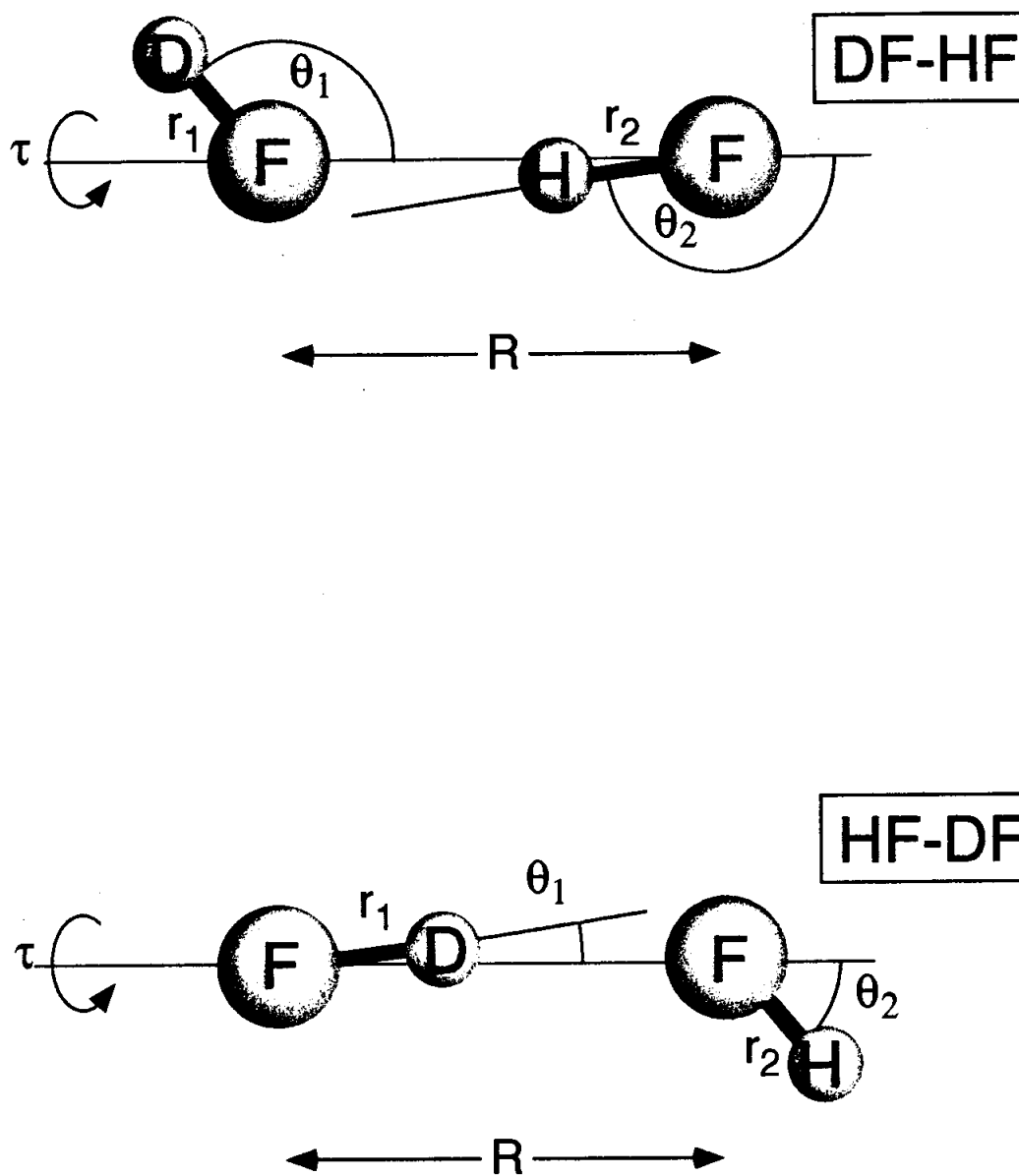


Figure 7.1: Ground state geometries and Jacobi coordinates for DF/HF dimers. R describes the radial separation of the diatom centers of mass, θ_1 and θ_2 are the in-plane angles of the diatoms, r_1 and r_2 are the intramolecular stretching coordinates, and τ is the out-of-plane torsional coordinate.

acceptor). Because of the different roles in the hydrogen bond, excitation of the HF stretch occurs at well separated energies, and it is possible to selectively excite either the bound or free HF. Pine *et al.* [298, 299] observed that while the linewidths for free HF transitions were consistent with the expected Doppler and pressure broadening, the bound HF transitions were considerably broader. This difference was attributed to increased lifetime broadening for bound HF excitation. In later experiments, Pine and Fraser [302] utilized a supersonic expansion to reduce the experimental Doppler and pressure broadening. This permitted the difference in the lifetime broadening to be quantified, and indicated a 35-fold faster predissociation rate for bound vs free HF. In addition, the predissociation rate was found to increase with K excitation of the free HF, and furthermore depends on the tunneling symmetry of the vibrational level.

In recent years, the mode specificity, K -dependence, and tunneling symmetry dependence of the predissociation lifetimes has also been observed in overtone stretching levels of HF and upon excitation of van der Waals vibrations. Suhm *et al.* [346] obtained rotationally resolved spectra for excitation of 2 quanta of the free HF stretch in HF-HF, and found that the vibrational predissociation lifetimes are approximately an order of magnitude larger than for the fundamental. The tunneling and K -dependence is even more pronounced in the $\nu_{\text{HF}}=2$ manifold, which has been rationalized in terms of a dynamical coupling with the other members of the $\nu_{\text{HF}}=2$ triad. Chang and Klemperer [70, 72] have observed all four members of the $\nu_{\text{HF}}=3$ tetrad of HF-HF. The predissociation lifetimes for states with three quanta in the bound HF stretch are 100-fold shorter when three quanta of the free HF are excited. Recently, Anderson *et al.* have observed all four *intermolecular* vibrations in the $\nu_{\text{HF}}=1$ man-

partner.

ifold of HF-HF, which are accessed as combination bands build upon either the free and bound HF stretch. Excitation of intermolecular (van der Waals) vibrations built on the free HF stretch decreases the predissociation lifetimes, although the lifetimes

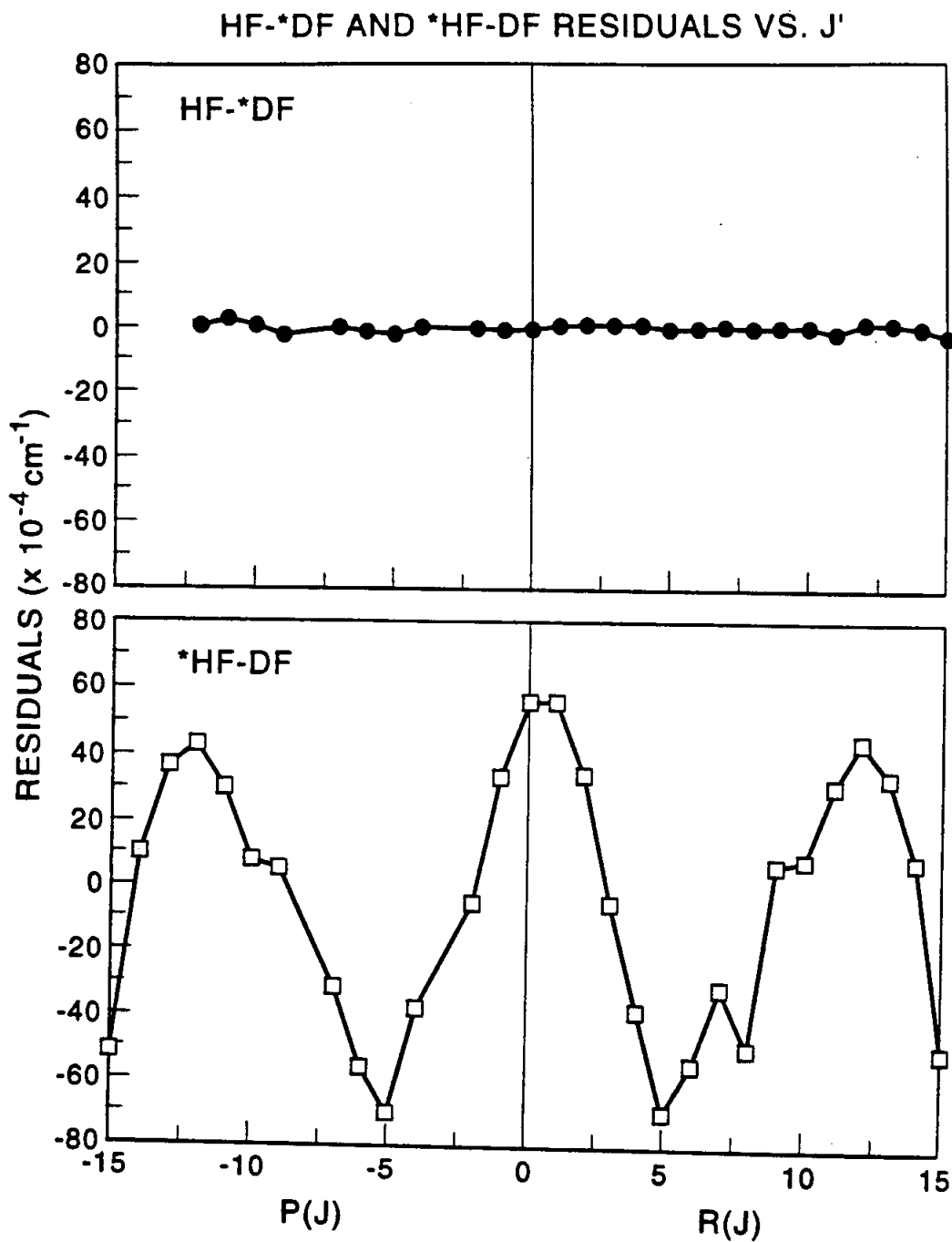


Figure 7.9: Residuals from the fit of the $K = 0 \leftarrow 0$ transitions of HF-*DF and $K = 1 \leftarrow 0$ of *HF-DF.

held fixed to the HF-DF values have an rms error an order of magnitude smaller than when the constants are constrained to the DF-HF values. While these results suggest that the band originates from $K'' = 0$ of HF-DF, a $K'' = 2$ origin also represents a plausible assignment for this perpendicular band. However, a $K = 1 \leftarrow 2$ transition of DF-*HF would be expected at lower frequency than the DF-*HF origin, while the present band is $\approx 90 \text{ cm}^{-1}$ higher. On the basis of this evidence, the ground state of this band is attributed to $K'' = 0$ of HF-DF.

The rms error from a least squares fit of the transition frequencies of this band is 0.0023 cm^{-1} , which is more than an order of magnitude larger than the experimental precision and suggests that this band is also perturbed. Given that both this band and $K = 1 \leftarrow 0$ of *HF-DF are perturbed, it is logical to determine whether the perturbations can be accounted for via a two state coupling between these levels. Since $K'=1$ for both states, a parallel Coriolis interaction is investigated, in which the states are coupled via a J -independent matrix element $\beta K \delta_{K_1, K_2}$. The corresponding 2×2 effective Hamiltonian matrix describing the excited states is

$$H = \begin{pmatrix} H_{11} & \beta_{12} \\ \beta_{21} & H_{22} \end{pmatrix} \quad (7.3)$$

where H_{11} and H_{22} are the unperturbed energies of $K = 1 \leftarrow 0$ of *HF-DF and the additional band, respectively, and $\beta_{12} = \beta_{21}^*$ is the off-diagonal coupling element. Least squares fitting the transition frequencies to this Hamiltonian yields the constants shown in Table 7.7. The rms error decreases 3-fold upon inclusion of the coupling, indicating that a two state analysis is capable of accounting the interaction. However, although much improved, the rms error of the fit is still 10 times larger than the experimental precision, indicating that there are additional interactions that cannot

be accounted for solely via a two state model.

Even though there is evidence for a large number of additional state mixing interactions in $K' = 1$ of $^*HF-DF$, no transitions attributable to "dark" states have been identified. This is also true for $K' = 0$ of $^*HF-DF$ and $DF-^*HF$. Although a number of weak peaks are visible in the $K' = 0$ $^*HF-DF$ spectrum shown in Figure 7.7, all these peaks can be accounted for as either due to $K = 1 \leftarrow 1$ of $^*HF-DF$ or $K = 0 \leftarrow 0 / K = 1 \leftarrow 1$ of $HF-HF$. Consequently, it appears that the nature of the interaction between the "resonance band" and $K' = 1$ of $^*HF-DF$ is different than the other interactions with the HF -excited dimers. In fact, as we will show below in the discussion section, this band arises from an interaction $K' = 1$ of $DF-^*HF$, the analysis of which permits the difference between the binding energies of $HF-DF$ and $DF-HF$ to be determined spectroscopically.

7.4 Tests of potential energy surfaces

In this section, an assessment of theoretical potentials is made on the basis of comparisons between experimental and calculated properties. The intramolecular HF and DF stretching frequencies in the dimers are discussed first, followed by the vibrational predissociation lifetimes.

Table 7.8: Experimental and calculated vibrational redshifts (in cm^{-1}) for $K = 0 \leftarrow 0$ transitions in HF-HF, DF-DF, HF-DF, and DF-HF.

	Vibrational Origin	red shift cm^{-1}	Theoretical Predictions		
			6-D Variational ^a	<i>ab initio</i> ^b	Monte Carlo ^c
HF	3961.4229 ^d	—	—	—	—
*HF-HF	3930.9030 ^e	30.5199	20.8 (+31.8%)	36.7 (-20.3%)	35 (-15%)
*HF-DF	3927.4615	33.9615	—	38.2 (-12.5%)	29 (+15%)
HF-*HF	3868.3127 ^e	93.1102	65.0 (+30.2%)	87.0 (+6.6%)	112 (-20%)
DF-*HF	3867.7190	93.7039	—	86.4 (+7.8%)	—
DF	2906.6609 ^f	—	—	—	—
*DF-DF	2882.6939	23.9670	—	27.8 (-16.0%)	27 (-13%)
*DF-HF	2882.0658	24.5951	—	29.4 (-19.5%)	—
DF-*DF	2834.6190 ^e	72.0419	—	63.8 (+11.4%)	108 (-50%)
HF-*DF	2838.0477	68.6132	—	61.2 (+10.8%)	156 (-129%)

^a Reference [381]

^b Reference [196]

^c Reference [350]

^d Reference [148]

^e Reference [299]

^f Reference [254]

7.4.1 Isotopic frequency shifts

It is well known from solution-phase studies that hydrogen bond formation shifts the vibrational frequency of the monomer with respect to the gas phase value, with stretching vibrations typically lowered in frequency [318]. The vibrational frequencies for the dimers are therefore expected to be lower than for the uncomplexed monomers. Indeed, the HF vibrational frequencies in HF-HF are redshifted 30.5 and 93.1 cm^{-1} for *HF-HF and HF-*HF, respectively (see Table 7.8). These shifts represent decreases of the HF stretching energy of 0.8% and 2.4% respectively. For DF-DF, the redshifts are 24.0 and 72.0 cm^{-1} for *DF-DF and DF-*DF. The corresponding

0.8% and 2.5% fractional changes in the uncomplexed DF stretching energy are in essentially complete agreement with the HF-HF results, which indicates a simple isotopic scaling of the redshifts as has been observed for other weakly bound complexes [130].

The larger redshift bound vs free excitation reflects the greater participation in the hydrogen bond by the bound diatom. As has been demonstrated in theoretical simulations of HF clusters, HF complex formation is accompanied by bond elongation, which can increase the bond length by up to 3% [351]. The greater participation in the hydrogen bond for the bound HF thus leads to a more significant weakening of the intramolecular bond and a corresponding larger frequency shift. Accurate estimates of the frequency shifts for a given HF complex thus requires that the corresponding changes in the harmonic and anharmonic frequencies of the HF be determined.

The vibrational redshifts for HF-DF and DF-HF are listed in Table 7.8. It is evident that isotopic substitution of the unexcited HF/DF leads to a very small frequency shift ($0.6\text{--}3.4\text{ cm}^{-1}$). While this is a small fraction of the HF/DF stretching frequency ($\leq 0.1\%$), it corresponds to fractional changes in the redshifts of up to 11%. The vibrational origins for HF-HF and its isotopomers are illustrated in Figure 7.10 for both $K' = 0$ and 1. Isotopic substitution of HF-HF leads to a decrease in the vibrational origin, i.e., $\nu_0(*\text{HF-DF}) < \nu_0(*\text{HF-HF})$ and $\nu_0(\text{DF-*HF}) < \nu_0(\text{HF-*HF})$. Since HF-DF and DF-HF are more strongly bound than HF-HF (by $20\text{--}100\text{ cm}^{-1}$), larger frequency shifts would be expected for the HF/DF dimers, in agreement with the observed energetic ordering. If isotopic substitution of DF-DF were to follow this same trend, the mixed dimers would have higher vibrational frequencies. This is indeed the case for HF-*DF and DF-*DF, where ν_0 for the former is 3.4 cm^{-1} higher

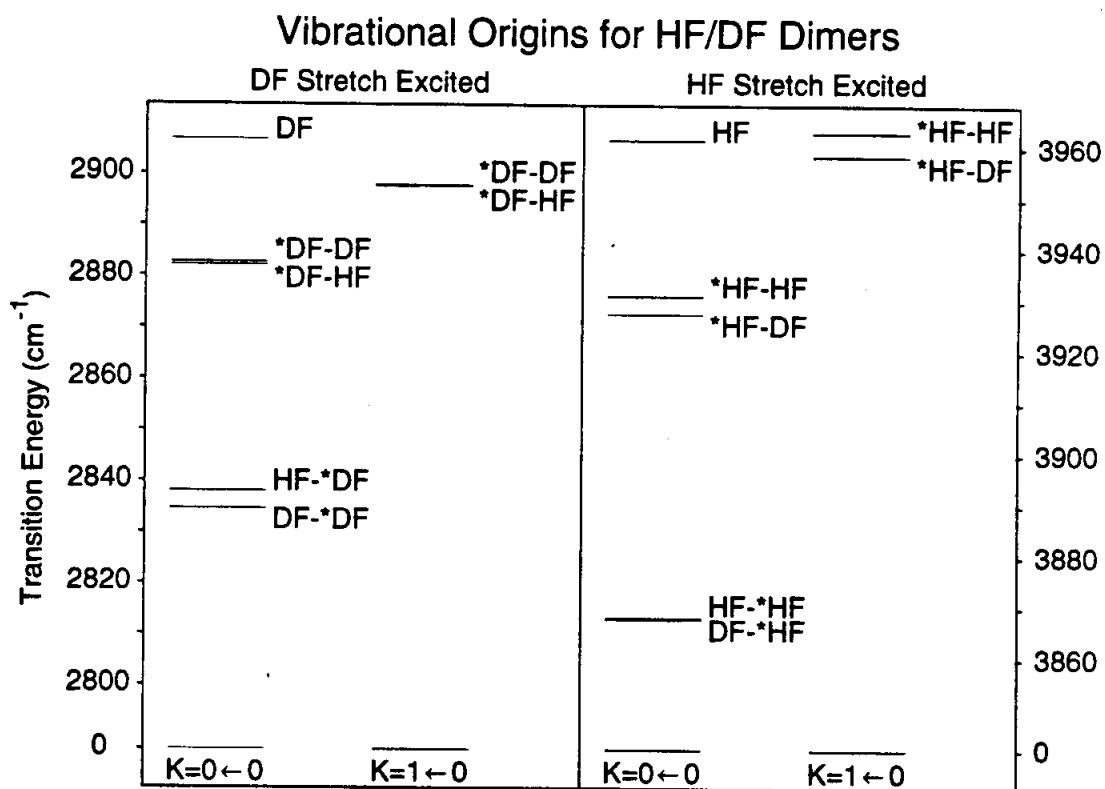


Figure 7.10: Vibrational origins for $K' = 0$ and 1 of HF-HF, DF-DF, HF-DF, and DF-HF in both the HF and DF stretching regions.

than the latter. This trend does not hold for *DF-DF in both $K' = 0$ and 1, where the *DF-HF origins are lower in energy.

Relatively few theoretical calculations have been presented for the intramolecular stretching frequencies of the HF/DF dimers. Zhang and coworkers [381] have recently presented 6-D calculations of the HF-*HF and *HF-HF stretching energies, which employ the SQSBDE potential of Quack and Suhm [311]. These calculated vibrational frequencies are converged to $\approx 0.1 \text{ cm}^{-1}$, and thus provide stringent tests of the theoretical potentials. The results, shown in Table 7.8, indicate that the intramolecular stretching frequencies are qualitatively reproduced, but the redshifts are in rather poor agreement with experiment. Unfortunately, these calculations have not yet been extended to the DF isotopomers, which would provide important information on a region of the potential for which relatively few *ab initio* points have been calculated.

It is worth mentioning that vibrational frequencies have been calculated for HF-HF and its isotopomers on several potentials by Sun and Watts [350] using diffusion Monte Carlo techniques. The calculations which give the best agreement with experiment are listed in Table 7.8. The agreement is relatively good except for *DF-HF and DF-*DF, where the redshifts are dramatically overpredicted. However, these calculations did not incorporate a 6-D potential energy surface for the complexes, but rather utilized separate monomer and intermolecular potentials coupled by a mean field local method. Consequently the level of agreement reflects the quality of the potentials and the dynamical restrictions that were imposed.

In addition, Jensen *et al.* [196], have calculated HF/DF stretching energies on the BKLK potential [57]. The results, listed in Table 7.8, exhibit somewhat better

agreement with experiment than the calculations of Sun and Watts. The energetic ordering of the origins for the isotopomers are qualitatively reproduced, except in the case of HF-^{*}HF/DF-^{*}HF. The quantitative accuracy of the frequency shifts is $\approx 20\%$, which is much larger than the relative differences between the isotopomers. Because these calculations also impose dynamical restrictions (specifically, the intramolecular stretching motion was adiabatically separated from the lower frequency stretching and torsional coordinates), it is difficult to determine what fraction of the discrepancies are due to the potential.

The comparison of the intramolecular stretching energies of the deuterium isotopomers of HF-HF with values predicted from converged full dimensional calculations would provide important information on the current potentials. Furthermore, the large body of experimental data that has been amassed for intramolecular vibrational energy levels for HF-HF and its isotopomers will hopefully permit a more accurate modeling of the intramolecular coordinates in the potential.

7.4.2 Vibrational predissociation

The vibrational predissociation of HF-HF represents one of the more intriguing dynamical aspects of the dimer, and has been studied extensively both theoretically [157, 387, 386, 361] and experimentally [237, 358, 298, 100, 299, 182, 302, 138, 98, 36, 346, 70, 39, 72]. The more than 30-fold decrease in lifetime for HF-^{*}HF vs ^{*}HF-HF [302] and the bimodal j distribution of the HF fragments [36] reflect the highly non-statistical nature of the predissociation event. These effects are highly sensitive to subtle details of the intermolecular potential and thus constitute stringent tests on

the potential energy surfaces.

The results of the lineshape analysis are presented in Table 7.9. For each of the complexes, excitation of the bound HF/DF stretch leads to a shorter lifetime than free excitation. This is evident in Figure 7.11, which shows representative lineshapes for both bound and free excitations of the dimers. The four broadest lineshapes are observed for bound excitation, while excitation of the free HF/DF gives the smallest lifetime broadening. The ≈ 10 – 20 fold decrease in lifetimes for bound vs free excitation in DF-DF and the mixed dimers is in qualitative agreement with the ≈ 30 fold difference for HF-HF. It is worth noting that the trend for shorter lifetimes upon bound excitation is quite general, and has been observed for other hydrogen halide systems such as the HCl/DCl dimers [331, 332], as well as HCN-HCN [205].

The ordering of the lifetimes for $K' = 0$ of the isotopomers is

$$\tau_{\bullet\text{DF-DF}} > \tau_{\bullet\text{HF-HF}} > \tau_{\bullet\text{DF-HF}} > \tau_{\bullet\text{HF-DF}} > \tau_{\text{DF-}\bullet\text{DF}} > \tau_{\text{HF-}\bullet\text{DF}} > \tau_{\text{DF-}\bullet\text{HF}} > \tau_{\text{HF-}\bullet\text{HF}}$$

The lifetimes for all isotopomers decrease upon K excitation. The magnitude of the decrease is difficult to establish by virtue of pronounced J dependences observed for a number of the bands. This is demonstrated in Fig. 7.12 for $K' = 0$ and 1 of $\bullet\text{HF-DF}$. However, the J' values most affected by the perturbations are readily identified, as is discussed further below. The broadening of the less perturbed transitions can then be used as an estimate of the zero-order lifetime broadening of the bands. With this approximation, the corresponding decrease in lifetimes upon K excitation is ≈ 10 – 50% , which implies that this intermolecular motion leads to a more efficient coupling with the dissociation coordinate.

Zhang, Bačić, and coworkers have presented calculations of the vibrational

Table 7.9: Mode and isomer specific predissociation linewidths for the mixed HF/DF dimers. Uncertainties represent 1σ .

Species	K'	$\Delta\nu_{\text{prediss}}$ (MHz)	τ_{prediss} (nsec)	$\tau_{\text{prediss}}^{\text{Theory}}$ (nsec)
*DF-DF	0	3.2 (17)	50 (27)	
	1	2-7 ^a	23-80	
DF-*DF	0	56.2 (2.4)	2.83 (13)	
	1	65 (7)	2.4 (3)	
*DF-HF	0	29.0 (13)	5.5 (3)	19 ^d
	1	29-32 ^a	5.0-5.5	
HF-*DF	0	122 (3)	1.30 (4)	7.6 ^d
	1	141 (14)	1.13 (12)	
DF-*HF	0	280 (35)	0.57 (8)	4.0 ^d
*HF-DF	0	2-33 ^a	4.8-80	160 ^d
	1	10-45 ^a	3.5-16	
Resonance band	1	227 (5)	0.70 (2)	
*HF-HF ^b	0	6.4 (0.5) (A ⁺) ^c	24.9 (21)	32.3 ^e
		9.5 (0.5) (B ⁺) ^c	16.8 (9)	39.0 ^e
	1	10.2 (0.5) (A ⁺) ^c	15.6 (8)	
		11.8 (0.5) (B ⁺) ^c	13.5 (6)	
HF-*HF ^b	0	330 (30)	0.48 (6)	3.30/3.12 ^{e,f}

^a A J' dependence is observed for these transitions. See the text for more details.

^b From reference [302].

^c The predissociation lifetimes for *HF-HF exhibited a statistically significant dependence on the tunneling level out of which the transition originated, which are included following the values.

^d From Ref. [388].

^e From Ref. [361].

^f The results are for the A⁺/B⁺ levels, respectively, for which no significant difference could be determined experimentally.

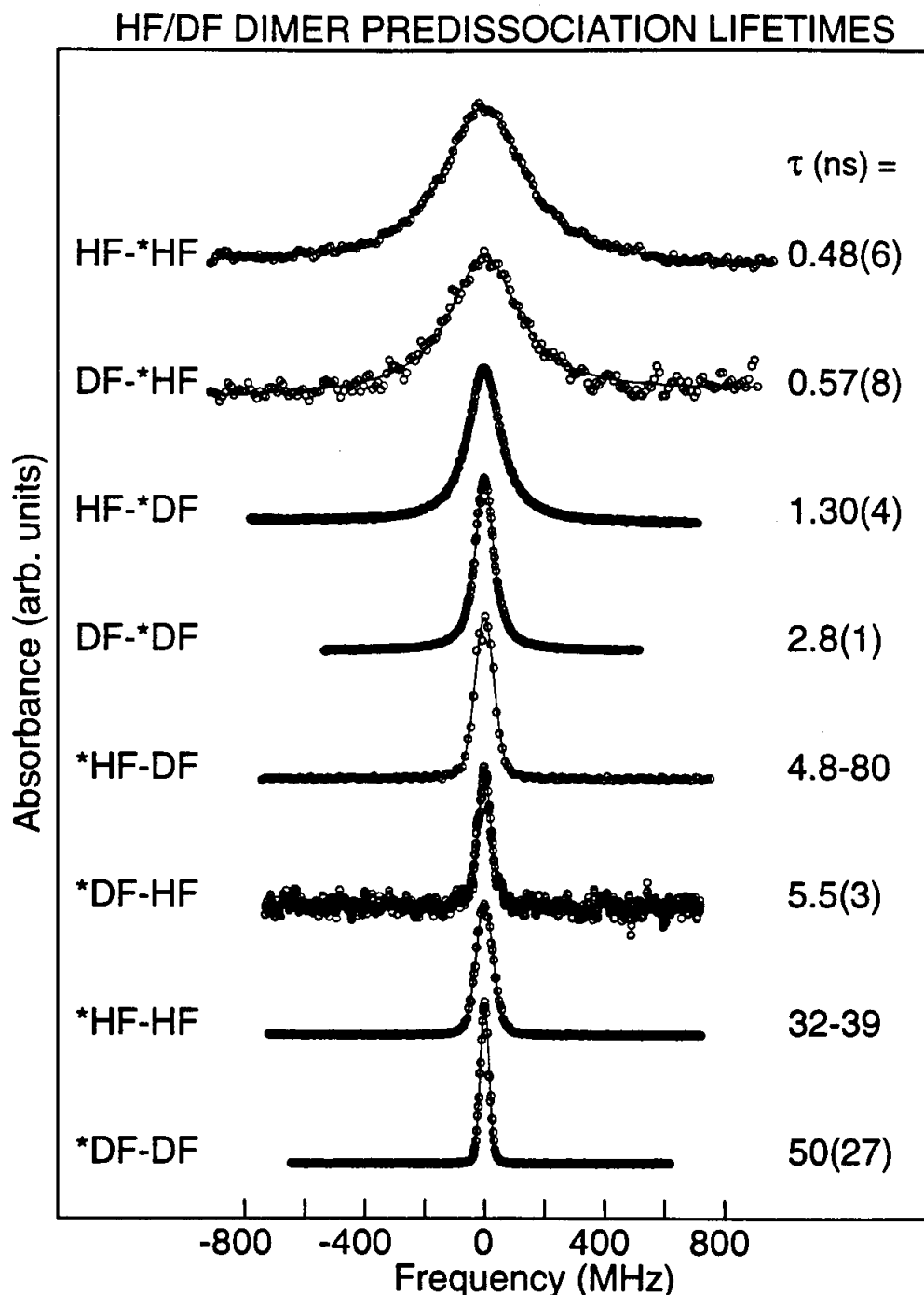


Figure 7.11: Representative rovibrational lineshapes for $K = 0 \leftarrow 0$ transitions of the HF/DF dimers. The circles represent experimental data, and the lines are the simulated Voigt profiles which deconvolve the inhomogeneous and homogeneous (lifetime) broadening. The broadening is inversely proportional to the lifetime of the excited state. The transitions for which a range of broadening is reported identify bands in which either a J' dependence (*HF-DF) or a tunneling symmetry dependence (*HF-HF) is observed (see text for details).

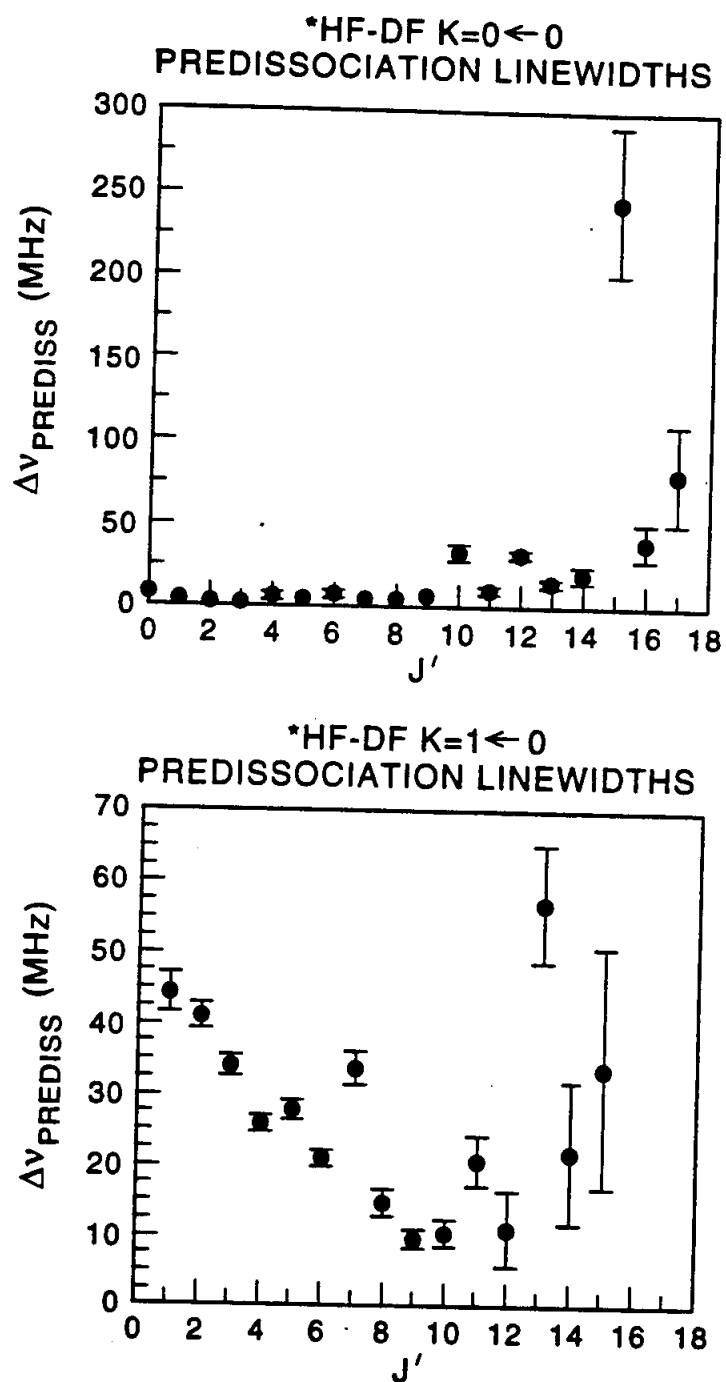


Figure 7.12: Predissociation linewidths for $K = 0 \leftarrow 0$ and $K = 1 \leftarrow 0$ of *HF-DF, demonstrating the pronounced J' dependence of these bands. The highly localized broadening is attributed to interactions with DF-excited dimer vibrations as described in the text.

predissociation lifetimes for HF-HF [361], HF-DF [388], and DF-HF [388]. Both the BKLK potential of Bunker *et al.* [57] and the SQSBDE potential of Quack and Suhm [311] were included in the calculations. The results are shown in Table 7.9 for calculation on the SQSBDE potential of Quack and Suhm [311], which provides the better agreement with experiment. The qualitative agreement between the experiment and theory is quite good, with the calculated values exhibiting shorter lifetimes for bound vs free excitation. In addition, the longer lifetime observed for DF-*HF vs HF-*HF is reproduced. The qualitatively wrong lifetime ordering is predicted for *HF-DF vs *HF-HF, however, where the former is predicted to fall apart faster, in disagreement with experiment. In addition to the good qualitative agreement demonstrated, the quantitative accuracy is also reasonably good. The calculated values are systematically too large, typically exceeding the experimental lifetime by a factor of 2–10. Because these calculations provide information on the accuracy of the potentials, in particular the anisotropy of the repulsive wall, vibrational predissociation calculations for DF-DF would be invaluable in identifying how accurate this potential is for the fully deuterated isotopomer. This would be especially helpful in light of the deficiencies identified for the calculated intermolecular (van der Waals) vibrational frequencies for DF-DF [95].

7.5 Further tests of potential energy surfaces: The difference in binding energy for HF-DF and DF-HF

The identity of the state shown in Figure 7.8 that interacts with $K' = 1$ of *HF-DF merits further discussion, as it is the only perturbing state for which rotational

structure is observed. There are a number of interesting features of the "resonance band" spectrum which differ markedly from the $K = 1 \leftarrow 0$ spectrum of $^*\text{HF-DF}$, which are useful in elucidating the identity of the upper state. First, the rovibrational lines are considerably broader than the $K = 1 \leftarrow 0$ transitions of $^*\text{HF-DF}$. The measured predissociation broadening is ≈ 225 MHz, which is an order of magnitude larger than the broadening of the $^*\text{HF-DF}$ $K = 1 \leftarrow 0$ transitions. Additionally, the strong redshading of the Q branch indicates a large decrease in \bar{B} upon vibrational excitation, whereas a blue shading is observed for $K = 1 \leftarrow 0$ of $^*\text{HF-DF}$.

Because the extensive state mixing identified in the HF-excited dimers can be attributed to interactions with intermolecular vibrations built on the DF-excited dimers (as will be discussed below), this resonance state could ostensibly be a highly excited intermolecular vibration that is deriving intensity from $K = 1 \leftarrow 0$ of $^*\text{HF-DF}$. Excitation of intermolecular vibrations decreases the rotational constants for HF-HF [5] and DF-DF [95], and therefore would give rise to a red-shaded Q branch as is observed. In addition, the results from HF-HF and DF-DF indicate that the lifetime of a highly excited intermolecular state can be expected to be shorter than the bright state, which would be consistent with the observed broader lineshapes.

However, an intriguing alternative explanation appears possible. As shown in Figure 7.13, $K' = 1$ of DF- $^*\text{HF}$ is estimated to be nearly isoenergetic with $K' = 1$ of $^*\text{HF-DF}$. Even though the transition energies for the bound and free HF stretches are very different, this mismatch is largely made up by the difference in D_0 for the two isomers. Although no transitions to $K' = 1$ of DF- $^*\text{HF}$ have yet been observed, it can be readily estimated to be ≈ 15 cm^{-1} higher than $K' = 0$ based on K for $^*\text{DF-HF}$ (see Table 7.4). An assignment of this state to $K' = 1$ of DF- $^*\text{HF}$ requires the difference

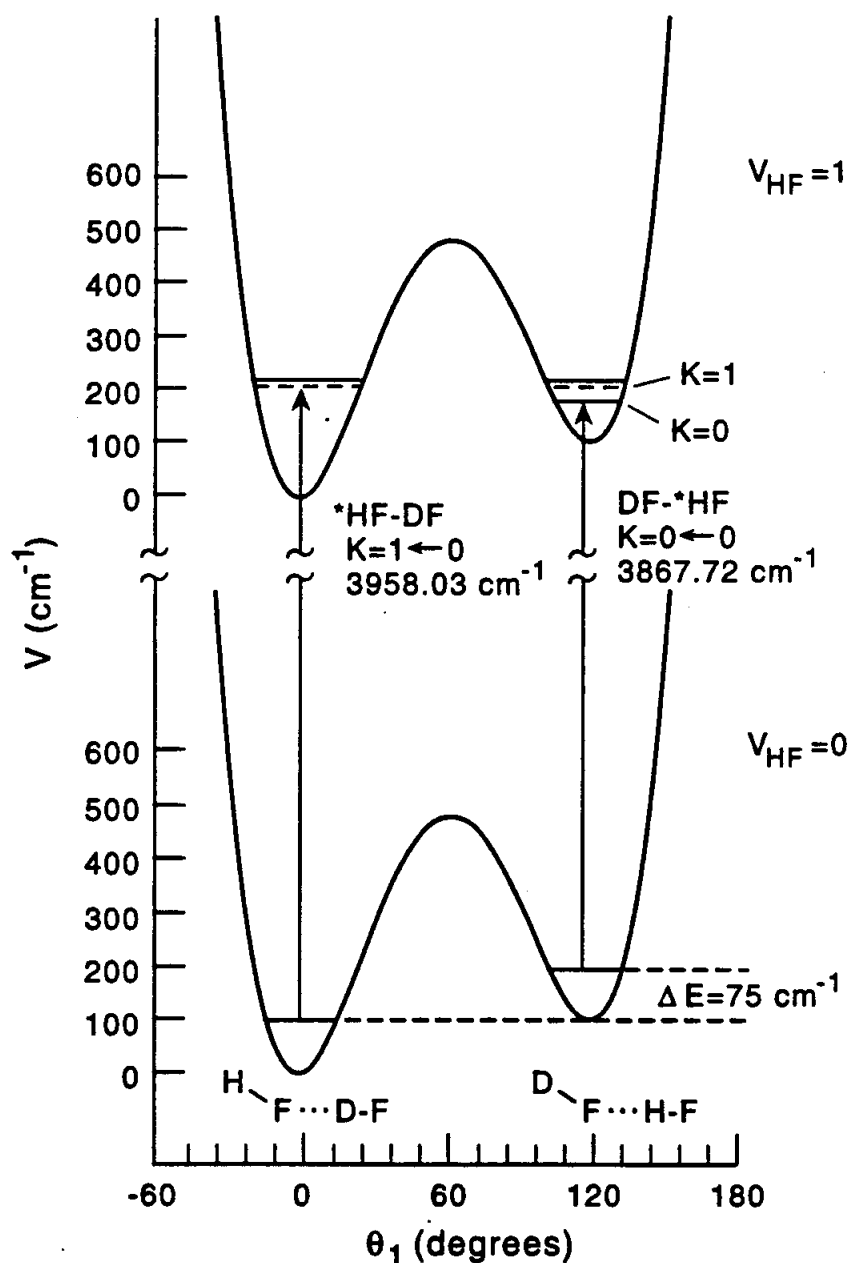
$K'=1$ PERTURBATIONS OF $^*HF-DF$ AND $DF-^*HF$


Figure 7.13: Energy diagram showing a possible origin of the "resonance state" which perturbs and gains intensity from $K = 1 \leftarrow 0$ of $^*HF-DF$. The perturbing state is tentatively identified as $K' = 1$ of $DF-^*HF$. The excitation energy of $K = 1 \leftarrow 0$ of $^*HF-DF$ is equal to the frequency of $K = 1 \leftarrow 0$ of $DF-^*HF$ and the energy difference between the two isomers, if the latter is estimated to be 75 cm^{-1} . This is in good agreement with the 65 cm^{-1} predicted by calculations the SQSBDE potential of Quack and Suhm [311], but is 10 cm^{-1} smaller than the recently reported difference by Bemish *et al.* [25] determined by photofragment spectroscopy.

in D_0 to be 75 cm^{-1} , however, which is 10 cm^{-1} lower than the value determined by Bemish *et al.* [25].

It is important, therefore, to list the evidence supporting this assignment. The Coriolis mixing of the two zero-order states is given by an effective rotation in Hilbert space,

$$\begin{aligned}\Psi_{\text{HF-DF}} &= \cos(\theta)\Psi_{\text{HF-DF}}^0 + \sin(\theta)\Psi_{\text{ResonanceBand}}^0 \\ \Psi_{\text{ResonanceBand}} &= \cos(\theta)\Psi_{\text{ResonanceBand}}^0 - \sin(\theta)\Psi_{\text{HF-DF}}^0\end{aligned}\quad (7.4)$$

where the angle of rotation is given by

$$\tan(2\theta) = \frac{2\beta}{\Delta E} \quad (7.5)$$

and β is the coupling matrix element from Eq. 7.3 that describes the degree of Coriolis mixing. Both β and ΔE have been determined from the least-squares analysis and are given in Table 7.7. Consequently, Eq. 7.5 predicts $\theta = 25^\circ$. The fractional parentage of each eigenstate is proportional to the square modulus of the coefficient for the zero order wavefunction, i.e., $\cos^2(\theta)$, which indicates that each state contain an $\approx 20\%$ admixture of the other.

The lifetime broadening of the pure resonance band can thus be inferred to be $\approx 280 \text{ MHz}$, and the zero order rotational constant is $\approx 0.209 \text{ cm}^{-1}$, obtained by scaling the observed values. These values are almost identical to those observed for $K' = 0$ of DF-*HF (see Tables 7.4 and 7.9), and expected for $K' = 1$ of DF-*HF. Although it is possible that a highly excited intermolecular vibrational state of *DF-HF or HF-*DF would have a predissociation rate and rotational constant essentially the same as expected for $K' = 1$ of HF-*DF, this appears unlikely. An assignment of the perturbing state to $K' = 1$ of DF-*HF gives an energy difference between the two

isomers (i.e., difference in D_0) of $74.8(5) \text{ cm}^{-1}$. The error bars reflect the uncertainty in K , which has been estimated at 15.6 cm^{-1} based on the *DF-HF data in Table 7.4.

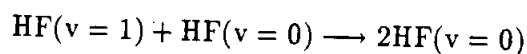
The coupling between the resonance band and $K' = 1$ of *HF-DF could also explain the discrepancies between the energy difference between HF-DF and DF-HF inferred in this study and the value reported by Bemish *et al.* [25]. In the previous studies of HF-DF by Bemish *et al.* and Fraser and Pine [138], no mention of the resonance band is made, and it is therefore safe to conclude that the photofragment distribution determined following $K = 1 \leftarrow 0$ excitation of *HF-DF did not take into account the possibility of a 20% admixture of the DF-HF isomer. Because of the pronounced difference in bound vs free distribution, the discrepancies may reflect the effects of "contamination" by the second isomer.

7.6 Energy transfer in the mixed HF/DF dimers

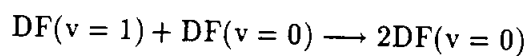
7.6.1 Comparison of full and half-collision dynamics

The study of vibrational predissociation in weakly bound complexes provides an opportunity to examine energy transfer dynamics from a "half-collision" perspective. The advantages of using weakly bound complexes include i), the relatively high degree of orientation between the constituents, ii) a highly restricted set of impact parameters, iii) the state selectivity afforded by high resolution lasers which allows precise control of energy deposition.

The results shown in Table 7.9 indicate that the lifetimes for DF-DF following free and bound DF excitation are longer than observed for the corresponding excitation of HF-HF. More specifically, the lifetime for $K'=0$ of *DF-DF is \approx two times longer than for $K' = 0$ of *HF-HF, while the difference between $K' = 0$ of DF-*DF and HF-*HF is approximately a factor of five. The faster vibrational predissociation for HF-HF vs DF-DF is consistent with the difference in rates for self relaxation of HF and DF in thermal cells. For example, the rate constant for the process



is four times faster [322] than for



Consequently, the two-fold (five-fold) greater lifetime for free (bound) excitation of DF-DF vs HF-HF agree nearly quantitatively with the ratio of self relaxation rates. Interestingly, the $V \rightarrow R, T$ rates for relaxation of DF by HF [257] are intermediate between the rates for HF-HF and DF-DF, in agreement with the ordering of vibrational predissociation lifetimes observed for the mixed dimers. These results support the role of complex formation as a precursor to vibrational relaxation as inferred from the negative temperature dependence of the HF/DF relaxation rates [257].

The vibrational relaxation rates determined from static gas cell experiments are useful in explaining qualitative trends in the vibrational predissociation lifetimes of the HF/DF dimers. The lifetimes for both HF-DF and DF-HF listed in Table 7.9 indicate that isotopic substitution of the unexcited HF/DF does not alter the predissociation dynamics dramatically. It is clear, however, that a definite trend does exist. For example, the predissociation lifetimes of *HF-DF and HF-*DF are *longer* than

*HF-HF and HF-*HF, indicating that substitution of a DF for HF increases the lifetime of the upper state. Similarly, the *DF-DF and DF-*DF lifetimes are *longer* than the *DF-HF and HF-*DF lifetimes. Simply stated, the upper state lifetimes decrease when an HF is substituted for a DF, and increase when DF is substituted for HF. This is in accord with the results from vibrational relaxation studies, in which HF is found to be more efficient than DF in $V \rightarrow R, T$ relaxation of DF. This can be attributed to the larger rotational constant of HF, and the fewer rotational quanta required to carry of a given amount of energy.

One might be tempted to invoke a momentum gap perspective as a means of interpreting the lifetime differences between DF-DF and HF-HF. Within this framework, the lifetime scales exponentially with the translational energy imparted to the dissociation fragments. Correspondingly, the product channels with the largest energy in vibration and rotation will be those that provide the most efficient path for predissociation. However, the state-resolved photodissociation experiments of Miller and coworkers [98, 38] have demonstrated that HF-HF predissociation is poorly explained using the momentum gap framework. For example, the HF rotational levels populated upon vibrational predissociation are distributed bimodally, with one HF highly excited and the other relatively unexcited. Consequently, even though the fragment channel with $(j_1, j_2) = (5, 10)$ is the most resonant channel for predissociation of *HF-HF ($\Delta E_{\text{trans}} = 51 \text{ cm}^{-1}$), the probability of populating the next closest $(j_1, j_2) = (1, 11)$ channel ($\Delta E_{\text{trans}} = 184 \text{ cm}^{-1}$), is nearly 6 fold larger. Furthermore, the product channel with the greatest probability of being populated is $(j_1, j_2) = (3, 10)$, for which $\Delta E_{\text{trans}} = 419 \text{ cm}^{-1}$. As a further illustration of the complexity of the predissociation dynamics, the product state distribution differs based on the symmetry of

the tunneling level in the upper state, reflecting the high sensitivity to subtle details of the potential surface. It is thus clear (and perhaps not entirely surprising) that the predissociation dynamics of HF-HF and its isotopomers are much more intricate than can be accounted for by simple scaling relationships.

7.6.2 Near-resonant state mixing between HF- and DF-excited mixed dimers

The inability to fit the rovibrational transitions of the HF-excited mixed dimers to experimental precision is evidence for near-resonant mixing with background states. These interactions cannot be attributed to the ground vibrational state, since i) similar interactions have not been observed in microwave experiments on HF-DF or DF-HF, and ii) the DF-excited mixed dimers, which come out of the same ground state as the HF-excited dimers, do not exhibit similar effects. Consequently the perturbations must be in the upper vibrational state. The prospect of interactions with near-resonant background states may seem surprising at first, since HF is in its lowest vibrational state and the DF stretch is more than 1000 cm^{-1} lower in energy. However, the binding energies of HF-DF (1165 cm^{-1}) [25] and DF-HF (1080 cm^{-1}) [25] exceed the energy difference between the HF and DF stretch, and therefore the asymptotic channel corresponding to HF ($v=0$) + DF ($v=1$) is *closed*. Consequently, there is a manifold of *bound* vibrational states built on the DF ($v=1$) stretch of the mixed dimers that can interact with *HF-DF and DF-*HF.

It is worth mentioning that similar effects have been observed in the near-IR spectra of ArCO₂ [137], KrCO₂ [137], and (CO₂)₂ [204]. In these complexes,

transitions to the lower component of the $\nu_1 + \nu_3/2\nu_2^0 + \nu_3$ Fermi diad of CO_2 are well fit to an asymmetric top Hamiltonian, while transitions to the upper component are not. The energy difference between the Fermi diad members (102 cm^{-1}) is less than the binding energies of the complexes, and the difficulty in fitting the transitions has been attributed to perturbations with van der Waals stretching and/or bending states built on the lower Fermi component. A similar effect has also been observed in the near-IR spectra of ArH_2O , where transitions to the asymmetric stretch are shifted and broadened by an internal rotor state built on the lower lying symmetric stretch [285].

In order to establish the statistical plausibility of attributing the observed perturbations to highly excited van der Waals modes, an estimate of the density of states at the energies of the HF-excited dimers is needed. There are four intermolecular vibrational modes in the HF and DF dimers, which are typically referred to as the "F-F stretch," "symmetric bend," "antisymmetric bend," and "out-of-plane bend" [311]. The fundamental energies of the F-F stretch, symmetric bend, and out-of-plane bend have been calculated for HF-DF and DF-HF by Zhang *et al.* [389]. The energies of the antisymmetric bend can be estimated roughly based on the values observed for HF-HF [5] and DF-DF [95]. Figure 7.14 shows an approximation to the density of states near $\approx 3900 \text{ cm}^{-1}$ for combinations of van der Waals modes built on the DF-excited dimers. The calculated state density at 3950 cm^{-1} is $\rho_{K=0} \approx 0.6/\text{cm}^{-1}$. The true density of states is expected to be larger than shown in the figure, since anharmonicity has been neglected. The increase due to anharmonicity can be approximated with the harmonic frequencies from Quack and Suhm [311] and the assumption of a 5% anharmonicity in each of the intermolecular modes. The resulting state density is $\approx 1.5/\text{cm}^{-1}$. Because

Near-Resonant Interactions Between
HF-Excited Mixed HF/DF Dimers and Intermolecular
States built upon DF-Excited Mixed HF/DF Dimers

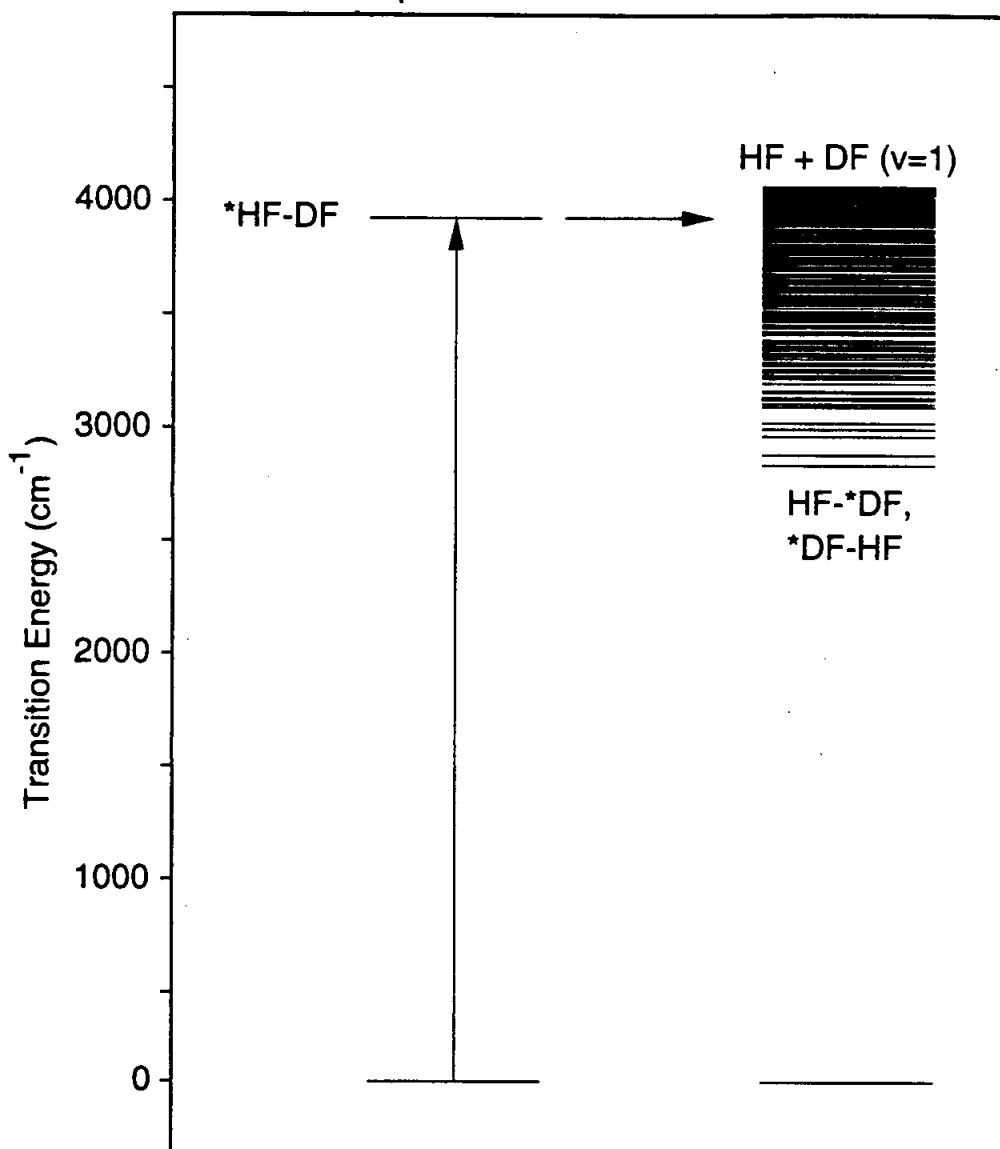


Figure 7.14: An energy level diagram showing the predicted intermolecular bending and stretching levels built on DF-excited HF-DF and DF-HF. Only $K=0$ levels are shown, based on harmonic intermolecular frequencies. The density of states near 3900 cm^{-1} is estimated to be \approx two-fold higher when anharmonicity is taken into account. Perturbations to the spectra of *HF-DF and DF-*HF are attributed to interactions with this dense manifold of vibrational states.

the values are expected to be similar for each $K' > 0$, the state density range is estimated to be $\rho_K \approx 0.6\text{--}1.5$ states/cm⁻¹.

We now seek to determine whether this state density is consistent with number required to account for the observed interactions. Figure 7.15 shows the (observed-calculated) energy values in the upper vibrational state for $K' = 0$ of *HF-DF. It is clear that the rotational progression is well modeled until $J' = 9$, after which a number of very localized deviations are apparent. In particular, $J' = 10, 12, 13$, and 15 are markedly shifted. Interestingly, the lifetime broadening of the rovibrational line-shapes is noticeably larger for $J' = 10, 12$, and 15 than for $J \leq 9$ (see Figure 7.12), which provides corroborating evidence for a localized coupling of these states to nominally "dark" states. The highly localized perturbations imply a rapid crossing of rotational levels, corresponding to a large difference in B for *HF-DF and the background states. This appears reasonable, since the rotational constants for the lowest intermolecular states of HF-HF and DF-DF are up to 5% smaller than the fundamental.

If the interactions are indeed highly localized for a given J' , then at least three separate states are needed to account for the observed shifts. Consequently we investigate whether the observed deviations can be modeled by a four state interaction. The effective Hamiltonian matrix employed to describe the excited states is

$$H = \begin{pmatrix} H_{11} & H_{12} & H_{13} & H_{14} \\ H_{21} & H_{22} & 0 & 0 \\ H_{31} & 0 & H_{33} & 0 \\ H_{41} & 0 & 0 & H_{44} \end{pmatrix} \quad (7.6)$$

where $H_{11} = \nu_{\text{*HF-DF}} + B_{\text{*HF-DF}}J(J+1)$ is the energy of the bright state, and $H_{22}, H_{3,3}, H_{4,4} = \nu_{ii} + B_{ii}J(J+1)$ are the unperturbed energies of the dark states.

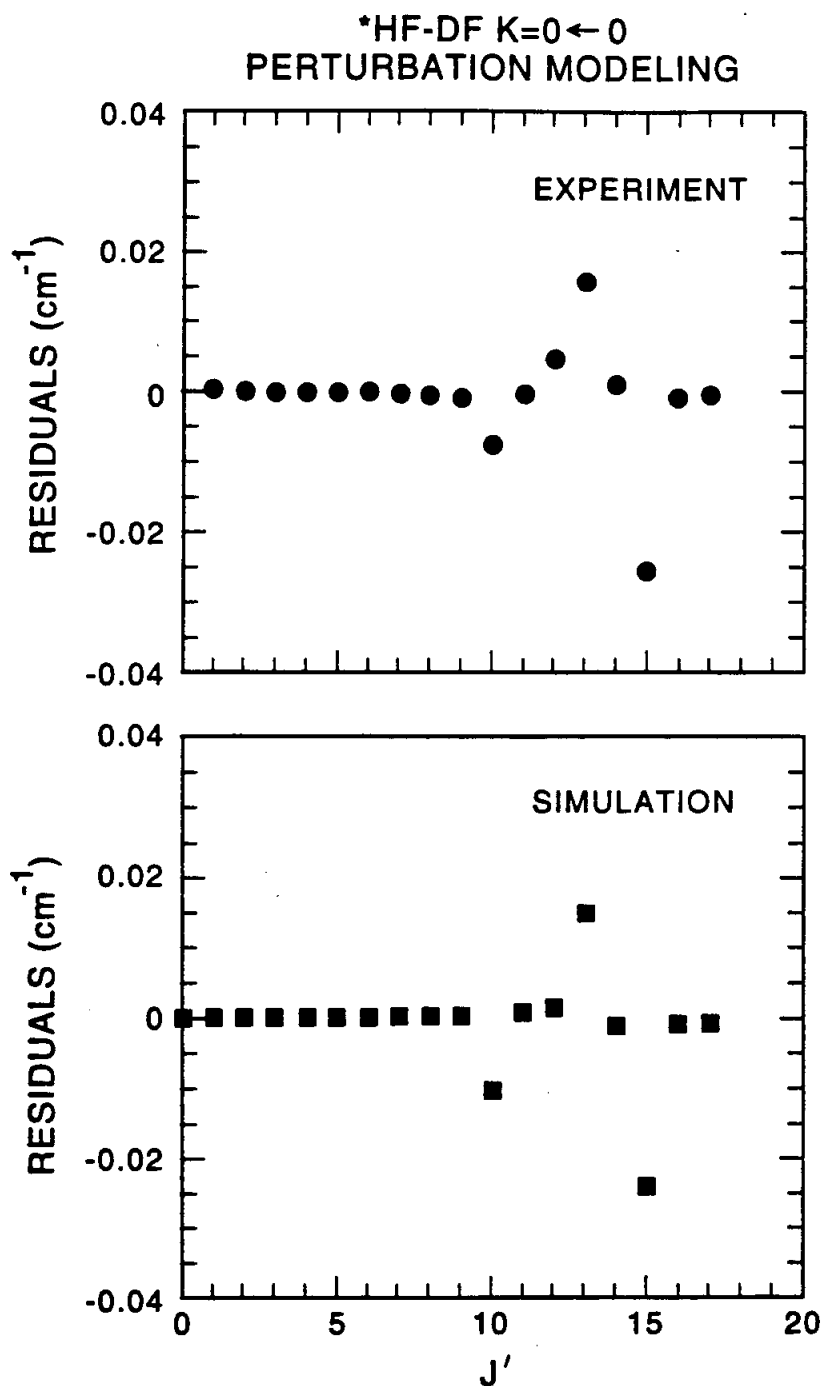


Figure 7.15: a.) Residuals (observed - calculated) deviations for *HF-DF $K = 0 \leftarrow 0$ transitions. The highly localized frequency perturbations at $J'=10, 13,$ and 15 are modeled using a four state model as described in the text. b.) The results of this modeling, demonstrating that such an interaction is capable of reproducing the observed frequency perturbations.

Table 7.10: Vibrational origin and rotational constants (in cm^{-1}) used in modeling the perturbations to the rovibrational frequencies of *HF-DF $K = 0 \leftarrow 0$. The constants chosen for each state were chosen to perturb a specific J' of the bright state, which is listed in the second column. The constants chosen for the dark state are not obtained from a least squares fit, and consequently do not represent unique solutions to the perturbations. Rather, they are representative of multiple state interactions that explain the observed perturbations and corroborate the interpretation of the identity of the background states as discussed in the text.

State	Crossing J'	ν_0	B	β
*HF-DF $K = 0 \leftarrow 0$		3927.46	0.21821	
#1	10	3929.47	0.2	0.010
#2	13	3930.77	0.2	0.015
#3	15	3931.84	0.2	0.020

Because the spectrum contains no information about the rotational constants or vibrational origins, the rotational constants are arbitrarily set equal to 0.2 cm^{-1} . This value represents a 5% reduction of the DF-HF rotational constant, which is based on the changes in B observed for the HF-HF and DF-DF intermolecular bends. The origins are chosen so that a near resonance is established at either $J' = 10, 13,$ or 15 . The off-diagonal matrix elements $H_{1i} = H_{i1}$ are set equal to β , i.e., appropriate for anharmonic or parallel Coriolis interactions (although perpendicular Coriolis interactions have been found to give rise to comparable effects in the present limit of a highly localized interaction). Figure 7.15b shows the results of the simulation, using the molecular constants listed in Table 7.10. It is evident that multiple, localized interactions are capable of reproducing the observed spectral perturbations. The values of β are approximately an order of magnitude smaller than the coefficient that couples the resonance band and $K' = 1$ of *HF-DF, which reflects the higher order coupling terms in the potential required to connect multiply excited intermolecular states with *HF-DF. The state density required in the above analysis is $\rho \approx 1 \text{ state/cm}^{-1}$. A sim-

ilar analysis for the $K' = 0$ of DF-*HF and $K' = 1$ of *HF-DF indicates that a similar state density of $\rho \approx 1-2$ states/cm⁻¹ can qualitatively reproduce the observed perturbations. These values of ρ for the HF-excited dimers are within the range estimated above for the intermolecular state density and therefore corroborates the assignment of the background states to intermolecular vibrations of DF-excited HF-DF and DF-HF.

7.7 Summary

The high resolution IR spectra of DF-DF, HF-DF, and DF-HF have been recorded using a slit jet infrared spectrometer. Results are presented for both HF and DF stretch excitation of the complexes. The rovibrational spectra for the DF-excited complexes are well modeled by standard energy level expressions, while the HF-excited complexes are not. Highly localized frequency shifts and enhanced lifetime broadening indicate the presence of multiple perturbations to each band. Intramolecular stretching frequencies and predissociation lifetimes are reproduced with semiquantitative accuracy by theoretical calculations which incorporate six dimensional potential energy surfaces. Transitions to a state that derives oscillator strength from $K = 1 \leftarrow 0$ of *HF-DF are attributed to $K' = 1$ of DF-*HF, and permit the difference between D_0 for DF-HF and HF-DF to be estimated at 74.8 (5) cm⁻¹. The predissociation lifetimes of the HF/DF dimers are interpreted in terms of a half-collision process. The ratios of the dimer lifetimes are consistent with the ratios of self relaxation rates for HF/DF mixtures in static gas cells. The perturbations to the HF-excited mixed dimers are modeled with multi-state interactions. The density of states required to reproduce the observed perturbations is comparable to the state density estimated at the energies of

the HF-excited mixed dimers, which indicates that the interactions can be attributed to intermolecular vibrations built on the DF-excited mixed dimers.

CHAPTER VIII

High-resolution slit jet spectroscopy and vibrational dynamics of the degenerate DF stretching fundamental ν_5 in $(DF)_3$

Hydrogen bonded networks are among the most important oligomers and most intriguing building blocks of nature [295], for which $(HF)_n$ represents a realistic prototype. HF dimer and its isotopomers have played a key role in the development of our understanding of the pairwise additive aspects of the hydrogen bond dynamics [281, 273, 311, 84]. Furthermore, nonpairwise additive interactions in hydrogen bonded networks [30] are thought to be of central importance for the HF trimer [65] and larger oligomers, providing additional impetus for a detailed experimental study of these systems. In another context, the sequence of $(HF)_n$ oligomers ($n=1,2,3,\dots$) provides an appropriate coordinate along which the transition from small molecule dynamics to large molecule dynamics [308, 274] in a moderately strong coupling environment can be investigated.

Unfortunately, available experimental data on the hydrogen fluoride trimer species beyond vapour phase property deconvolutions [345, 134] and matrix spectra [11] are very limited. The majority of the previous work has been based on mass-spectroscopic, pulsed-infrared (IR) laser predissociation studies [237, 218], combined with isotopic substitution investigations in order to distinguish between fragmentation from higher clusters in the electron bombardment ionizer [237, 270]. There are

also some unpublished data at much higher spectral resolution on HF oligomers obtained with cw IR lasers in cooled cell [304] and bolometric [277] measurements, but no rotational structure has been observed in the HF stretching region. In total, with the exception of a CO₂ laser line tuning study of some hydrogen bond combination band transitions [218], no rotationally resolved spectra have been obtained for any isotopomer of (HF)₃.

In this chapter, high resolution, IR laser absorption spectra are presented for (DF)₃ formed in a slit supersonic expansion. In contrast to the near IR studies of (HF)₃, the data reveal clear rotational structure characteristic of a cyclic, 6-membered "ring," and therefore provide the first accurate experimental evidence for the equilibrium geometry for any hydrogen fluoride oligomer beyond the well-studied dimer. Furthermore, the spectra clearly display homogeneous rotational fine structure in 2-3 orders of magnitude excess of what could be anticipated from a single vibrational band. This homogeneous structure signals strong intramolecular vibrational coupling of the DF stretch "bright" state to a dense manifold of "dark" vibrational levels. The high number of coupled states evident in the (DF)₃ spectrum suggests predominant state density contributions from *open chain*, DF-DF-DF structures, with an average homogeneous coupling width of 0.133 cm⁻¹. Hence, the (DF)₃ spectra experimentally elucidate a novel intramolecular vibrational coupling (IVR) mechanism which involves single hydrogen bond cleavage, and consequent opening of the (DF)₃ ring on the 40 ps timescale (see Figure 8.1).

From a theoretical perspective, a large number of studies of (HF)₃ have been published (see [65, 207, 351, 219] and references cited therein) and have now reached a satisfactory level of convergence in terms of the minimum geometry. (HF)₃ is calcu-

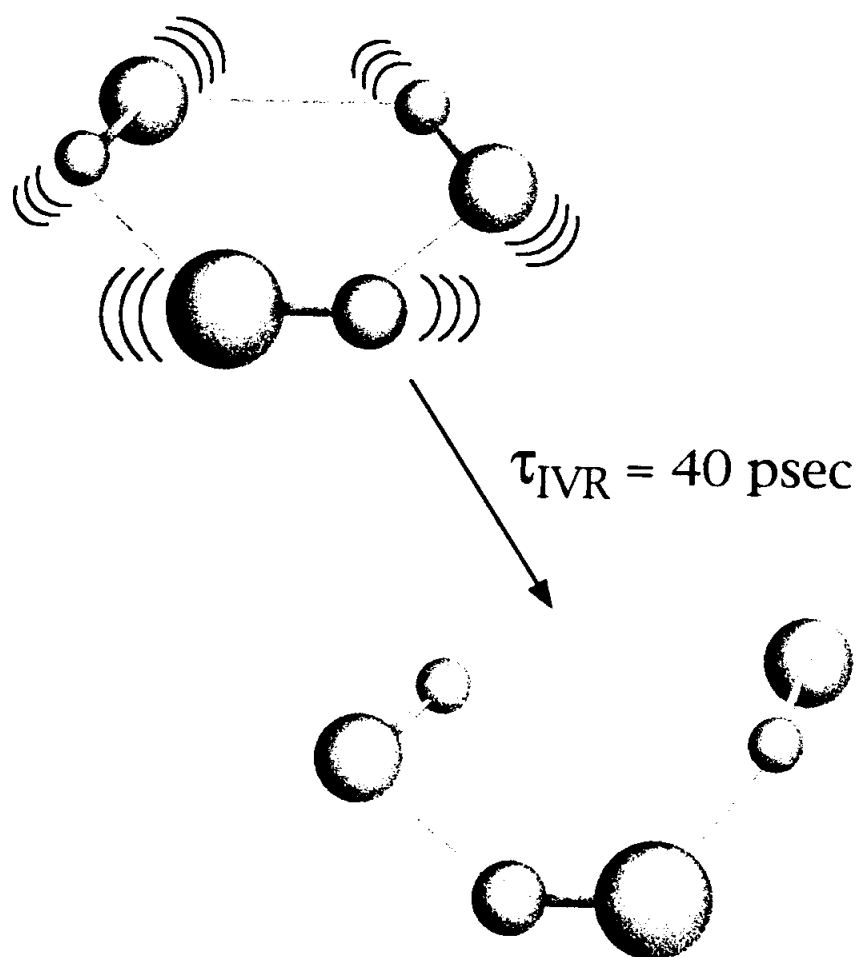


Figure 8.1: Pictorial representation of the IR induced unimolecular opening of the $(DF)_3$ ring.

vestigation of $(DF)_n$ oligomers, using direct absorption of tunable IR laser light in a slit supersonic expansion. The DF was synthesized by reacting D_2 with F_2 and does not contain significant amounts of HF as estimated by the ratio between DF stretch fundamental transitions for the HFDF and DFDF dimer species [298, 138]. The optimum expansion conditions are found to be 0.8% DF in a 1:1 mixture of Ar and first run Ne at a total backing pressure of approximately 700 torr (1 torr = 133 Pa). Under such conditions the strongest absorptions of $(DF)_3$ amounted to approximately 0.5% in a 12-pass White cell arrangement (48cm absorption path).

The degenerate DF stretching fundamental ν_5 is predicted near 2733 cm^{-1} [313] by theory and assigned at 2717 cm^{-1} (2720 cm^{-1}) in an Ar (Ne) matrix [11]. Low resolution vibrational predissociation studies of HF/DF oligomers also indicate a band at 2720 cm^{-1} , which by isotopic analysis could be ascribed to either $(DF)_3$ or $HF(DF)_2$ [270]. With this information to narrow the spectral search, the ν_5 DF stretch band was quickly located. Figure 8.2 shows a survey over this perpendicular band found at 2724.6 cm^{-1} . The negative absorptions are due to ν_1 transitions of HDO formed in the vacuum chamber during the first hours of scanning, and are used for the calibration [293].

The $(DF)_3 \nu_5$ band consists of a typical planar oblate top perpendicular band envelope ($A = B \approx 2C$), but with far more spectral congestion than anticipated for such a simple top spectrum. Our preliminary approach to the congested structure is twofold. First, the spectrum is treated in a coarse-grained manner (i.e., resolution $\geq 0.01\text{ cm}^{-1}$) by assuming a homogeneous Lorentzian broadening, Γ_L , of each of the predicted rovibrational lines. Such an analysis would be consistent, for example, with predissociation broadening on each of the rotational transitions. As we shall show

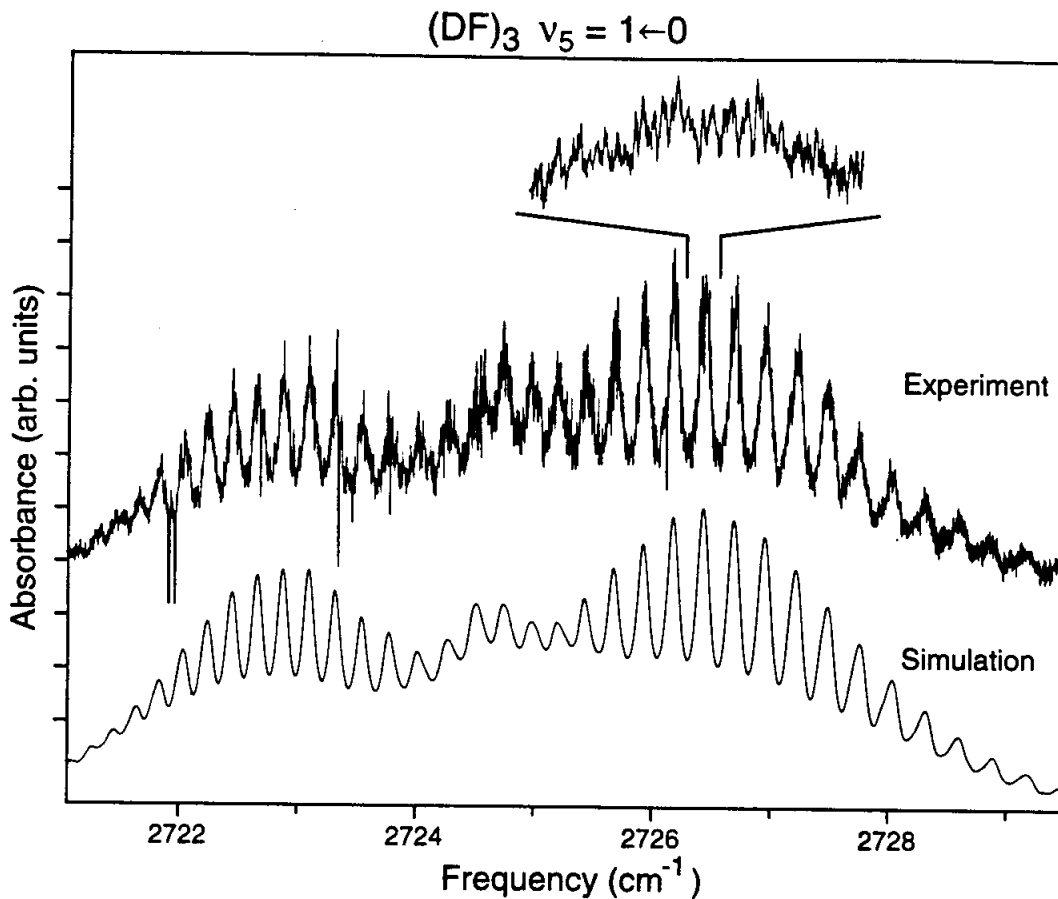


Figure 8.2: Survey spectrum over ν_5 of $(DF)_3$, displaying a clear perpendicular band characteristic of a planar oblate symmetric top. The scratchiness in the experimental spectrum does not reflect noise, but rather “fine” spectral structure as shown in the inset. The inverted absorption signals are due to HDO traces in the vacuum chamber, and are used for calibration. The lower trace is a simulation of the $(DF)_3$ band based on an oblate symmetric top model at 10.3 K using the best fit constants in Table 8.1, with each transition broadened by a uniform Lorentzian linewidth (FWHM) of $\Gamma_L = 0.133 \text{ cm}^{-1}$.

later, however, the broadening is, in fact, *not* due to predissociation, but rather to intramolecular vibrational mode coupling to long-lived, discrete levels in the (DF)₃.

We therefore initially fit the band contour to a C_{3h} symmetric top spectrum allowing for (i) inertial defects in both states; (ii) rigid molecule nuclear spin statistics (C_{3h} , $g_I = 38$ for $K = 3n$, $g_I = 35$ otherwise); (iii) variable temperature, and, (iv) a variable but uniform (i.e., J independent) Lorentzian profile. The fit is obtained in a repeated sequence of Monte Carlo search in parameter space and simplex root-mean-square minimization [305] with frequent parameter scrambling to avoid trapping in secondary minima. The preliminary results are summarized in Figure 8.2 and in Table 8.1. The fitted rotational temperature of 10.3 K is in good agreement with $T_{rot} = 11.5 \pm 1$ K determined from the ν_1 spectra of (DF)₂ recorded under identical expansion conditions. The inertial defect is found to be very small in the lower state, consistent with a planar ring geometry. In the upper state, the inertial defect is significantly different from zero; this is consistent with large amplitude motion of an in plane vibration ($B' > 2C'$). The sign of the change in C ($\Delta = C' - C'' = +0.0007$ cm^{-1}) is consistent with the expected shortening of the hydrogen bond upon DF excitation. A more quantitative comparison between theory and experiment requires the evaluation of 12-dimensional centrifugal effects; the result of such a quantum Monte Carlo calculation within the "clamped coordinate" approximation [311] yields $C'' = 0.121$ cm^{-1} with a 2σ uncertainty of 0.001 cm^{-1} for the analytical potential [313]. This is already in excellent agreement with the experimental value of 0.11992 cm^{-1} obtained from the present study.

Next, the origin of the *fine-grained* congestion (i.e., resolution ≤ 0.01 cm^{-1}) in the experimental spectrum is addressed. At first glance, the inferred homogeneous

Table 8.1: Spectroscopic constants obtained in the band shape fit, quoted with about one more digit than considered significant. The root-mean-square deviation, which is dominated by the pronounced fine structure (down to at least 40 MHz FWHM), amounts to $\approx 4\%$ of the full band amplitude. D_0 refers to the dissociation energy into a monomer and a dimer fragment inferred from the existence of narrow line structure. Also shown are theoretical predictions based on an analytical non-additive potential energy surface.

Constant	Expt. value	Prediction (Ref. [313])
ν_5/cm^{-1}	2724.595	2733
C''/cm^{-1}	0.11992	0.121 ± 0.001
C'/cm^{-1}	0.12062	
$B''/2\text{cm}^{-1}$	0.11989	
$B'/2\text{cm}^{-1}$	0.12214	
$\zeta_5 C/\text{cm}^{-1}$	-0.0001	
Γ_L/GHz	4.00	
T_{rot}/K	10.3	
D_0/cm^{-1}	>2724.6	2768 ± 5

line widths $\Gamma_L = 0.133 \text{ cm}^{-1}$) and the loss of fully resolved rotational structure in the trimer spectrum might be attributed simply to predissociation broadening in the upper vibrational level. However, in sharp contrast with this interpretation, there is residual spectral structure apparent in the spectrum which is quite real and reproducible. This is evidenced in Figure 8.3a, which shows a typical high resolution part of the spectrum in the low frequency 7Q branch wing. The reproducibility of this fine structure is shown in Figure 8.4. Note the up to 40% fine structure modulation on top of the coarse Q -branch intensity oscillations with estimated linewidths of ≤ 40 MHz. Due to the spectral congestion, it is not possible to deconvolute Gaussian and Lorentzian contributions for these lines. However, based on measured Gaussian components of ArDF (37 ± 2 MHz) and $(\text{DF})_2$ (39 ± 4 MHz) transitions under the same expansion conditions, the predicted Doppler width is already 35 MHz. Hence, it is unlikely that the observed linewidths are essentially dominated by reduced Doppler

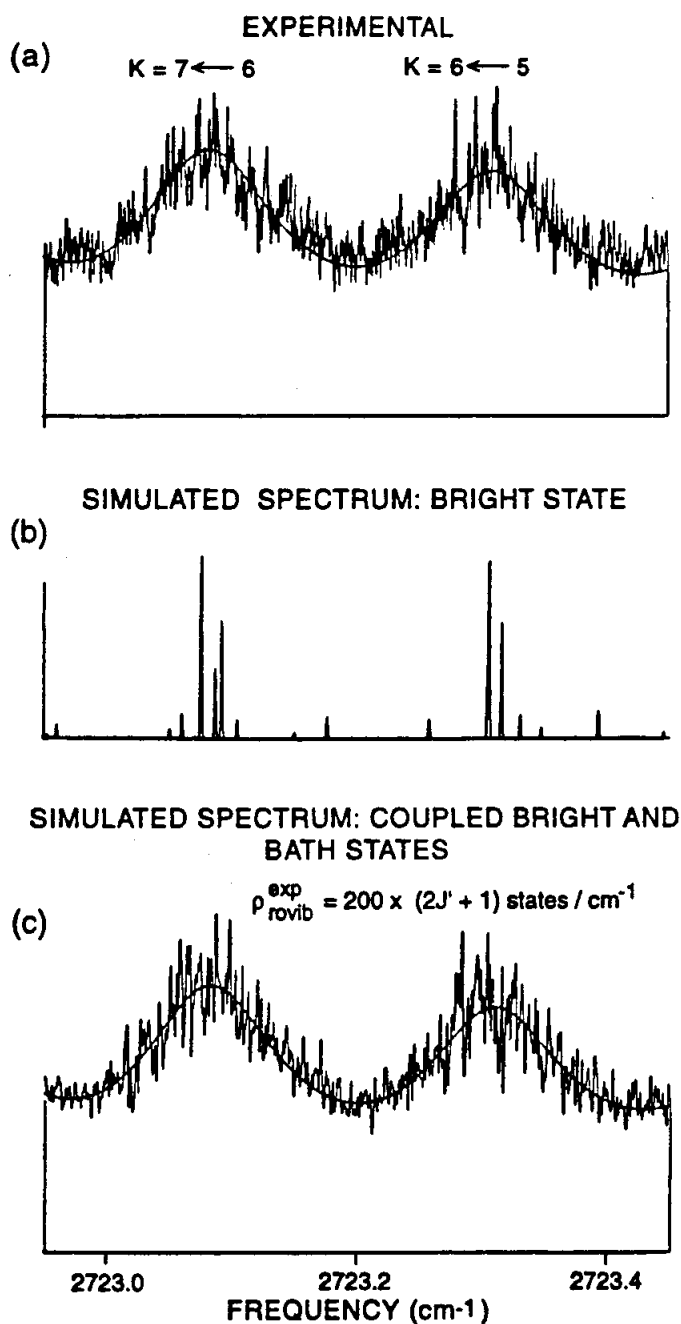


Figure 8.3: a) A blow up region of two rQ -branches (assigned to be $K = 7 \leftarrow 6$ and $6 \leftarrow 5$) superimposed on the band shape simulation of Fig.2. The S/N ratio for the strongest sharp lines in this unsmoothed spectrum is approximately 10. b) Simulated $10.3 \text{ K } \nu_5$ spectrum using the constants given in Table 8.1 with a Gaussian line profile of 40 MHz FWHM, demonstrating the sparse and completely resolved spectra anticipated of $(DF)_3$ in the absence of IVR coupling to a high density of bath states. c) Synthetic spectrum which is generated by splitting each bright rovibrational 40 MHz FWHM state from b) into a Wigner distributed random pattern of $\rho_{\text{rovib}}^{\text{exp}} = 200 \times (2J' + 1)$ states per cm^{-1} with a Lorentzian intensity distribution profile. Again, the simulation of fig. 1 is superimposed.

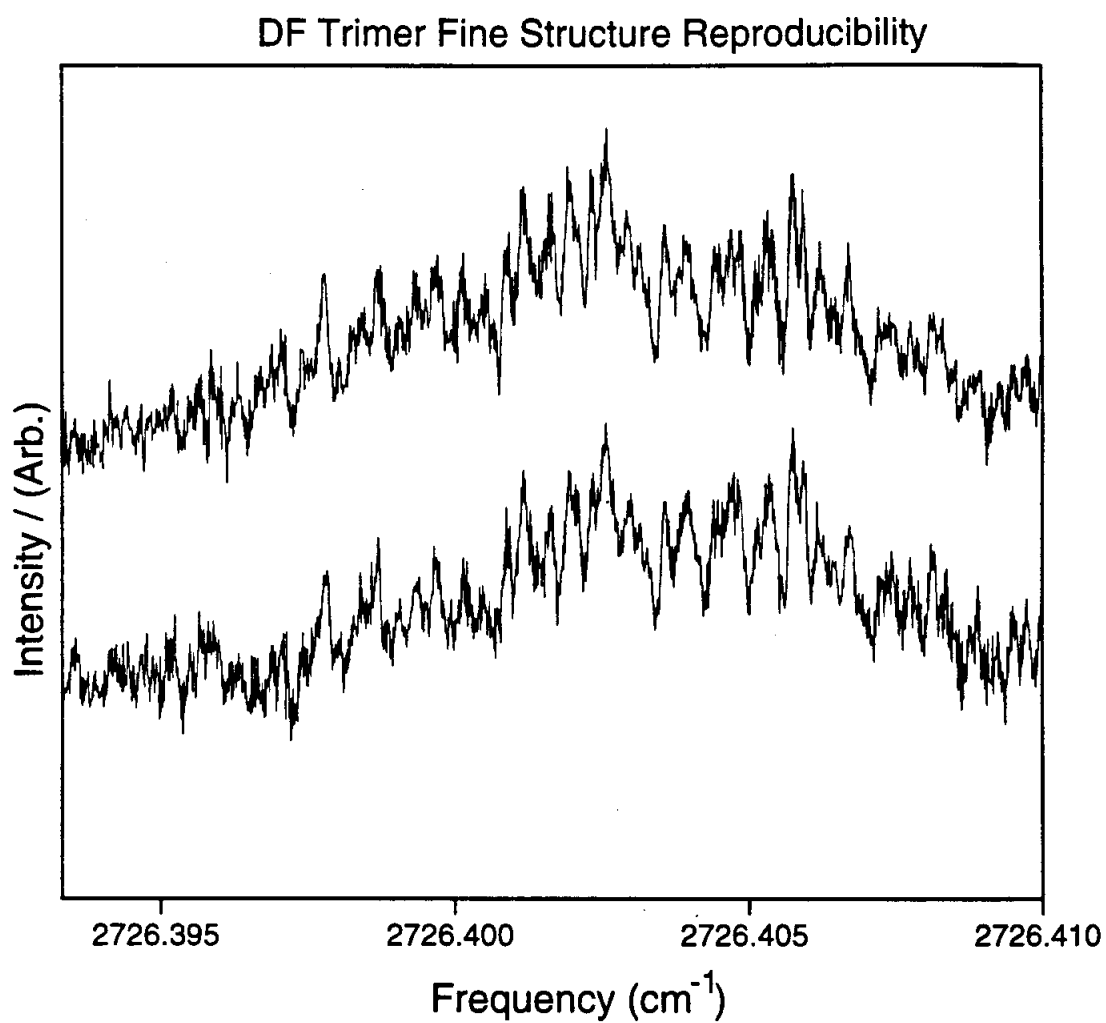


Figure 8.4: Two scans over the ν_Q (assigned to be $K = 7 \leftarrow 6$) demonstrating the reproducibility of the fine spectral structure

broadening in the slit jet. Nevertheless, 40 MHz certainly represents a rigorous *upper* bound for any lifetime broadening in these lines. This would be in agreement with the theoretical prediction of an upper $(DF)_3$ stretching state which is stable with respect to predissociation into $DF + (DF)_2$ (see Table 8.1 and Figure 8.5). Note that this prediction relies on anharmonic effects in the zero-point energy and three-body effects in the potential. Neglect of any of these effects leads to the prediction of a predissociative upper state. This provides strong support for the accuracy of the analytical potential proposed for $(HF)_3$ [313]. Of course, the experimental data would not be strictly inconsistent with a **finite** predissociation lifetime well above 4 ns. However, this would be unlikely, since if the dissociation channel were indeed energetically open, it would certainly be close to perfectly resonant, with minimal energy release into translation and expected rapid predissociation [281]. The 4 ns lower bound for the predissociation lifetime should be contrasted to the 2.5-21 ps lifetime of the ν_5 vibration in the hydrogen isotopomer [270], which can predissociate (see Figure 8.6), also according to the recent theoretical predictions [313].

We are thus left with the need to account for the extensive spectral fine structure in the jet cooled $(DF)_3$ spectrum. This clearly can not be attributed to symmetric top predictions for a single DF stretch 'bright' state, as shown in Figure 8.3c. Inhomogeneous (hot) spectral contributions can be safely excluded based on the lowest frequency vibration in $(DF)_3$ ($\approx 150 \text{ cm}^{-1}$) (Ref. [313]) and general experience on vibrational cooling in slit jet expansions. The coincidence of two vibrational bands with different predissociation lifetimes is ruled out by (i) symmetry, since only one infrared active DF stretching vibration is predicted for a C_{3h} structure of $(DF)_3$; (ii) the good agreement with *ab initio* structural predictions for a single band; (iii) the

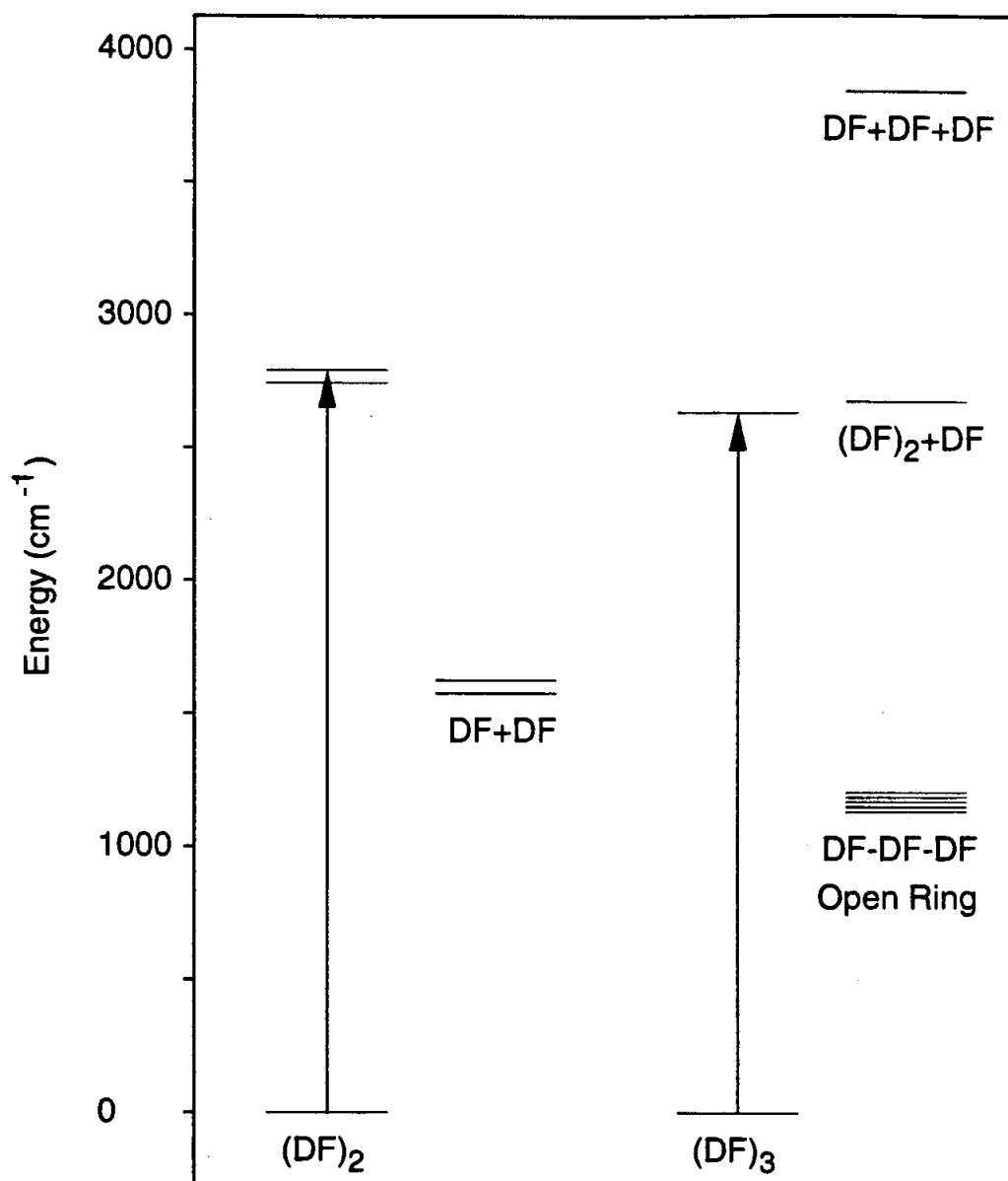
$(DF)_2/(DF)_3$ Dissociation Energetics

Figure 8.5: The dissociation energetics for $(DF)_2$ and $(DF)_3$. Upon IR excitation, $(DF)_2$ has sufficient energy to fragment into two DF molecules. In contrast, the experimental data and theoretical calculations [313] suggest that $(DF)_3$ is energetically forbidden to fragment into a dimer and monomer. The complex does have sufficient energy however to break on hydrogen bond, accessing the DF-DF-DF open chain structure.

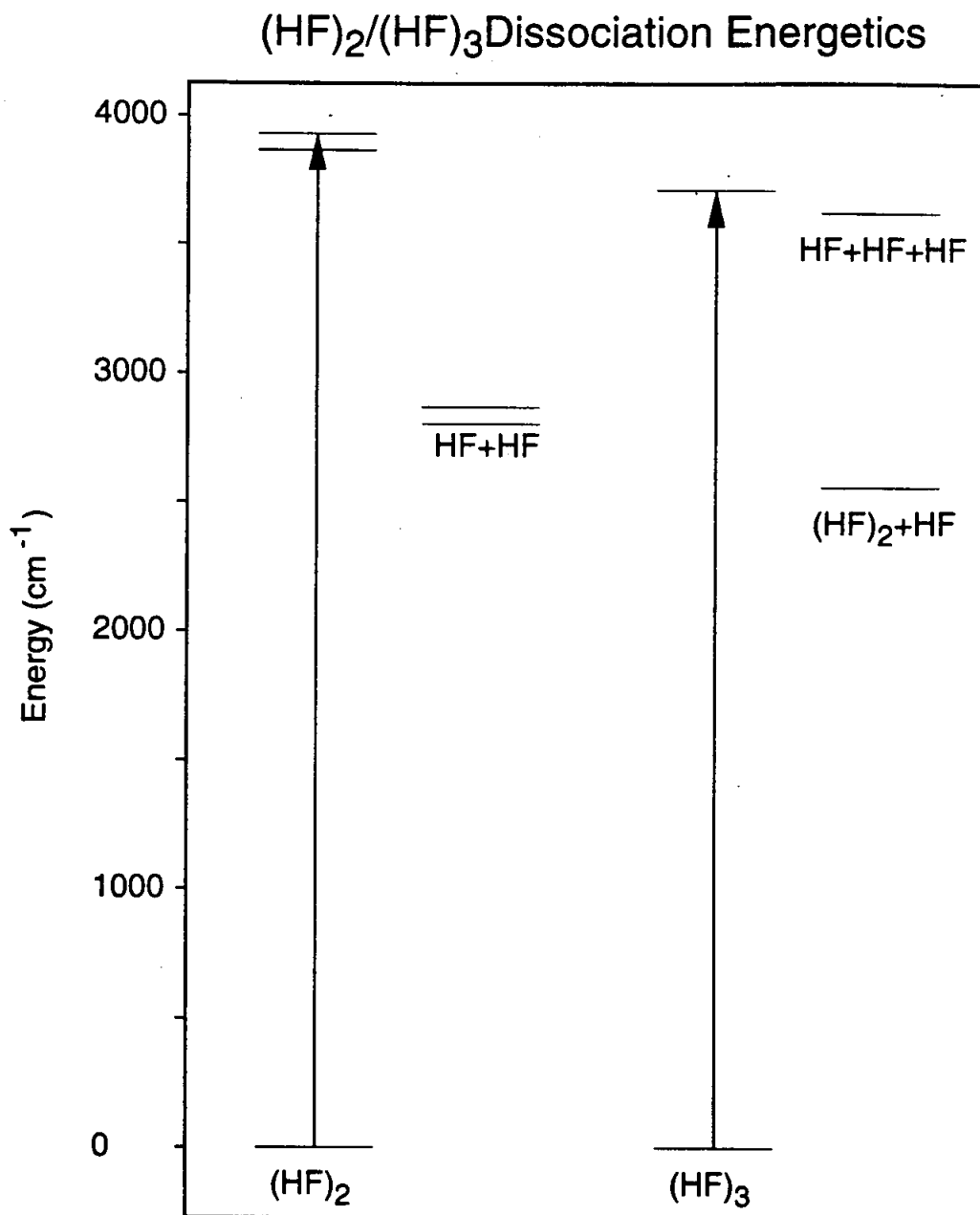


Figure 8.6: The dissociation energetics for $(\text{HF})_2$ and $(\text{HF})_3$. In contrast to the DF trimer, both $(\text{HF})_2$ and $(\text{HF})_3$ have sufficient energy to fragment following IR excitation of an intramolecular stretch. This process is thought to be very rapid for $(\text{HF})_3$, precluding the recording its rotationally resolved spectrum.

Table 8.2: Harmonic vibrational frequencies for DF trimer based on the quantum Monte Carlo calculations discussed in the text.

Mode	ω_e	Symmetry	Description
ν_1	2798	A'	DF stretch
ν_2	612	A'	In-plane bend
ν_3	174	A'	Symmetric (F-F) stretch
ν_4	450	A'	Out-of-plane (H) symmetric bend
ν_5	2836	E'	IR active stretch
ν_6	366	E'	In-plane bend
ν_7	178	E'	Degenerate stretch
ν_8	303	E'	Degenerate out-of plane bend

2–3 orders of magnitude excess density of the sharp spectral features; and (iv) the high DF isotopic purity of the gas sample, which precludes the possibility of HFDFDF or HFHFDF contamination. However, the data are consistent with an alternate interpretation which considers coupling of the bright DF stretch state to a dense but discrete ensemble of background states, i.e., intramolecular vibrational redistribution (IVR) into the intermolecular ring modes comprising the hydrogen bonded network.

In order to investigate this situation more quantitatively, we have estimated the vibrational density of states for $(DF)_3$ near 2725cm^{-1} . Our method utilizes a direct state count based on the available analytical potential and quantum Monte Carlo calculations [313], counting E states as single states [309]. The harmonic vibrational frequencies for the eight fundamental vibrations of $(DF)_3$ are listed in Table 8.2. As expected for such anharmonic systems, the vibrational state density is strongly dependent on the level of sophistication of the model, ranging from $\rho_{\text{vib}} \approx 70$ states/ cm^{-1} in a simple harmonic model up to nearly $\rho_{\text{vib}} \approx 500$ states/ cm^{-1} when anharmonic fundamentals and coupling estimates are included [311, 313]. Allowing for parity (factor 1/2) and nuclear spin (factor 1/2) conservation, the density of vibrational states

which can couple to the bright stretching state is estimated to be on the order of $\rho_{\text{vib}} \approx 100/\text{cm}^{-1}$. If we allow for rovibrational couplings that conserve only J' (i.e., complete loss of K as a good quantum number), the state density for a given bright J' upper state could then increase $\rho_{\text{rovib}}^{\text{tot}} \approx (2J' + 1) \times 100/\text{cm}^{-1}$.

Experimentally, we can estimate the density of states coupling to the DF stretching state by replacing the Lorentzian convolution (Figure 8.3a) by a random distribution of coupled states $\rho_{\text{rovib}}^{\text{exp}}$, and then by varying $\rho_{\text{rovib}}^{\text{exp}}$ to reproduce the appropriate contrast in the experimentally observed fine structure (Figure 8.3c). First of all, the requisite line density is significantly greater than $125 \text{ states}/\text{cm}^{-1}$. Hence, the spectra are inconsistent with any model that *only* considers coupling between anharmonic vibrational states, and neglects the additional $(2J + 1)$ contributions from rotational state mixing. Secondly, the results of this simulation are surprisingly sensitive to the level spacing statistics and vary over an order of magnitude from Bixon-Jortner [31] (i.e., equal spacing) to Poisson (i.e., random spacing). A physically justifiable choice of the level statistics in this dense coupling environment is given by the Wigner distribution function [378], for which Figure 8.3c demonstrates good qualitative agreement using $\rho_{\text{rovib}}^{\text{exp}} = 200 \times (2J + 1) \text{ coupling states}/\text{cm}^{-1}$.

This experimental estimate should be compared with, and is already slightly in excess of, the theoretical estimates of the total rovibrational state density from a direct anharmonic state count of $\rho_{\text{rovib}}^{\text{tot}} \approx 125 \times (2J + 1) \text{ states}/\text{cm}^{-1}$ described above. Hence, one must invoke coupling to essentially all available rovibrational states allowed by nuclear spin symmetry, parity and J' -conservation. The observed spectrum is therefore consistent with nearly complete IVR of the DF stretching excitation energy into the full phase space energetically available through the manifold of hydrogen bond

modes [308]. Furthermore, the timescale for such an IVR process can be estimated from the $\Gamma_L \approx 0.133 \text{ cm}^{-1}$ homogeneous widths determined in the spectral fit to be roughly 40 ps. The contrast to $(\text{HF})_2$ and its isotopomers, where IVR is extremely incomplete even on the nanosecond timescale of IR predissociation [300, 138, 365], is particularly noteworthy.

At this point, we can speculate on the nature of these excited "bath" states near 2725cm^{-1} . These states are well above the energy required [313] for ring opening ($\approx 1000\text{-}1500\text{cm}^{-1}$) in a regime where floppy, chainlike conformations dominate the rovibrational partition function due to their higher entropy. By considering the energy carried in ring opening vibrations, more than 90% of the states at 2725cm^{-1} may be conservatively classified as "open chains" (i.e., with *one* hydrogen bond broken) in the vibrational state counts. On the other hand, the nearly Doppler limited fine structure in the observed spectrum suggests insufficient energy for chain dissociation into a monomer and a dimer fragment, i.e., $(\text{DF})_3$ excited to one quantum of DF stretch appears to be in an energetic range which allows breaking of *one*, but not *two* hydrogen bonds. Thus, the IVR fine structure in the spectrum predominantly reflects a spectroscopic window into the complex pattern of eigenstates associated with a highly vibrationally excited, *open* ring structure. While three-body forces certainly enhance coupling of the monomer stretch manifold to the hydrogen bond coordinates in the trimer, it appears that the density of states is the decisive factor in this contrasting behaviour. Stated from a time domain perspective, a coherent, pulsed excitation of these eigenstates would therefore lead to a time dependent relaxation on a 40 ps time scale, corresponding to an IR induced unimolecular opening of the $(\text{DF})_3$ ring.

lated to be cyclic with C_{3h} symmetry and with a FF distance of about 260 pm. This is considerably shorter than for $(HF)_2$ (275pm [311]) but still a long way from the "zig zag," open chain structures with vibrationally averaged FF distances near 250pm observed in condensed phase (see [207]) and in the gas phase under large cluster conditions [195]. Theoretical well depth data for the trimer are in somewhat less agreement, due to correlation and basis set superposition effects, and fundamental frequencies are only predicted at the harmonic level. On the other hand, any prospects for comparison with experimentally accessible quantities are vibrationally averaged rotational constants, anharmonic frequencies, and binding energies corrected for zero point effects. Indeed, detailed investigations for the HF dimer [311, 261] have clearly shown that experimentally reliable predictions must include such anharmonic quantum effects for many and very often for all nuclear degrees of freedom. This is a formidable task for a 12-dimensional system such as $(HF)_3$ but has been recently achieved [313] using quantum Monte Carlo calculations in a nonpairwise additive full-dimensional analytical potential. Details of the determination of the pairwise and nonpairwise additive terms in the $(HF)_n$ potential surface can be found elsewhere [313]; we focus here only on key results of these studies of relevance to the trimer. In particular, theory predicts that upon vibrational excitation in the IR active degenerate DF stretch fundamental, the fully deuterated trimer should be energetically *bound* for low rotational angular momentum, whereas the corresponding HF trimer can energetically *predissociate* into a monomer and a dimer upon HF stretching excitation [313]. Hence, the high resolution, near-IR spectrum of $(DF)_3$ could yield structural rotational and dynamical information which has proven so elusive for the $(HF)_3$ system.

With this as our theoretical stimulus, we have initiated a spectroscopic in-

CHAPTER IX

High resolution infrared overtone spectroscopy of N_2 -HF: Vibrational redshifts and predissociation rates as a function of HF stretching quanta.

9.1 Introduction

By virtue of the isolated nature of the reagents, photochemistry and spectroscopy of weakly bound binary complexes have served as valuable tools for probing unimolecular dynamics [158, 371]. The field of molecular energy transfer has been an area of particularly active research, and our understanding of phenomena such as vibrational predissociation and intramolecular vibrational redistribution has improved dramatically as a result of studies incorporating these small molecular systems [158]. Recently, significant progress has been made in our ability to monitor state-to-state dissociation rates as well as the effects of intermolecular orientation on the rates of these processes. These studies have greatly furthered our understanding of intermolecular forces, and complement investigations ranging from the characterization of many-body forces in rare-gas hydrogen halide systems [112, 114], to the examination of phase transitions in larger clusters still too small to assume the properties of the associated bulk matter [215, 235].

There are a number of factors that make van der Waals complexes well suited

for energy transfer studies. First, the coupling between the constituents is often sufficiently weak that the nature of electronic and vibrational excitations is very similar to that of the isolated molecule. This allows the selective preparation of initial states that can be well described in terms of the quantum labels of the monomer. Second, the intermolecular bond is typically much weaker than a "true" chemical bond, which allows relatively small amounts of energy to access states metastable with respect to dissociation. For example, there have been a large number of vibrational predissociation studies [185, 281] carried out in the near-IR with excitation energies between 1000 and 4000 cm^{-1} in systems with dissociation energies ranging from 1000 cm^{-1} down to a few cm^{-1} . Third, these complexes are readily formed in the cold environments of supersonic expansions, conditions that thermodynamically favor cluster formation through the absence of thermally dissociative collisions. The complexes formed under these conditions typically have little or no excitation in the internal degrees of freedom, and this often leads to a relatively high degree of orientation of the subunits. This can significantly reduce the regions of phase space accessible to the metastable, vibrationally excited complex, thereby potentially reducing the number of degrees of freedom required to model the relevant dynamics. An additional benefit derived from the supersonic sources is the low temperature routinely obtained, which significantly reduces spectral congestion and considerably simplifies the interpretation of the spectrum.

Vibrational predissociation dynamics in complexes formed between rare gas (RG) atoms and halogens, interhalogens, and radical diatoms, have been extensively studied using LIF techniques [232, 338, 122, 80, 81, 367, 166]. In these experiments, the complexes are promoted to an electronically excited state with well defined vibra-

tional quanta in the diatom, and the lifetimes and products of the vibrational predissociation process are monitored. The observation of interesting dynamical effects such as rotational rainbows [368] and interference structures [80] have helped elucidate the mechanism of the predissociation event. Additionally, these studies have allowed the determination of accurate potential energy surfaces and dissociation energies for a number of complexes [80, 81]. Theoretical approaches ranging from classical to 3D full quantum calculations have been used to model results for complexes of Ne with ICl and Cl₂ [236, 359, 81], and have demonstrated good agreement with the experimental data.

One potential limitation of electronic state preparation is the presence of nonadiabatic relaxation pathways which may complicate the analysis of the ensuing dynamics. These processes are nonexistent in the ground electronic state, and consequently infrared-based techniques can offer distinct advantages over electronic studies for some systems. Indeed, complexes of many of the simplest molecular species, such as H₂O, CH₄, HF, HCl, etc., cannot be studied via LIF techniques but are quite amenable to investigation in the IR. The number of systems that have been studied using IR techniques is now quite large [281, 83], and the predissociation dynamics observed in mid-infrared experiments have been shown to be quite complex for even the relatively simple binary systems [33, 284, 252, 249, 97, 205]. As one classic example of mode-specific behavior, excitation of the "bound" vs the "free" HF in (HF)₂ leads to vibrational predissociation rates that differ by more than a factor of 30 [302]. Furthermore, these rates can vary dramatically upon isotopic substitution, as has been demonstrated recently for (HF)₂/(DF)₂ (ref [299]), (HCl)₂/(DCl)₂ (refs [331] and [332]), and the mixed dimers of HF/DF [132] and HCl/DCl [333]. The faster vibrational predisso-

ciation rate for HCl-DCl upon HCl vs DCl excitation has been rationalized in terms of intermolecular $V \rightarrow V$ transfer from the excited HCl to the DCl concomitant with the predissociation event, a channel not available upon excitation of the lower frequency DCl stretch. Similar differences in vibrational predissociation rates have also been explained in terms of near resonant $V \rightarrow V$ transfer for the mixed dimers of HF/HCl [139], as well as D_2/H_2 -HF [245, 249], N_2HF/DF [287], and C_2H_2 -HCl/DCl [99].

Several theoretical models have been developed to rationalize the wide range of predissociation rates for these weakly bound systems. Early progress in this area led to the momentum gap law [29] and subsequent refinements thereof [123, 124, 125, 126]. Additionally, a correlation law has been developed by Miller [272] based on a Golden Rule treatment of the predissociation rate and a perturbative treatment of the coupling between the monomer and complex vibrational potentials. These methods have provided a semiquantitative understanding of the predissociation dynamics, but the development of more quantitative models has been hampered by the lack of detailed potential energy surfaces which explicitly account for the intermode coupling, i.e., the coupling between the high frequency intramolecular and the low frequency intermolecular (van der Waals) modes. Construction of such multidimensional potentials has in general not been possible due to the lack of experimental data which probes sufficient regions of the potential surface sensitive to this coupling.

Two approaches have recently been introduced that provide the experimental data necessary to bridge this gap. Techniques that access *overtone* vibrations in the chromophores have recently been developed [264, 268, 69], providing information on how the intermode coupling *changes* as a function of the high frequency stretching coordinate. The complexes that have been studied in this manner include Ar-HF

[128, 69], (HF)₂ [346, 70], (HCN)₂ [268], and HCN-HF [211]. In addition, King and coworkers [336] and Miller and coworkers [98, 262] have developed techniques that resolve the final state distributions of the vibrational predissociation products. Since vibrational predissociation of weakly bound complexes is analogous to a half-collision event, the analysis of product states accessed from a well characterized initial state provides information about the anisotropy in the potential as well as the geometry of the transition state. Both of these experimental approaches provide complementary information, and indeed establish rigorous tests of theoretical models designed to model dynamics sensitive to this intermode coupling.

In this paper we present data for N₂-HF excited to the first overtone stretching level of the HF. The results from the present study can be compared with those reported from mid-IR and microwave experiments to help elucidate the effect of HF stretch excitation on the vibrationally averaged structure and vibrational predissociation dynamics of the complex. The spectroscopic observables that provide this information are the redshift (i.e., the frequency shift of the chromophore upon complexation), the changes in rotational and centrifugal distortion constants as a function of ν_{HF} , and vibrational predissociation rate. The approach used to understand the changes in the vibrational redshift with increasing ν_{HF} incorporates a perturbative treatment of the coupling between the intermolecular and intramolecular coordinates. The particular model employed is based on electrostatics, correlating the changes in the potential with changes of the monomer's electrical properties upon vibrational excitation. The correlation between the changes in the rotational and centrifugal distortion constants with ν_{HF} and the intermolecular potential is established through the use of rotational-RKR techniques [77, 286], which allow the generation of one

dimensional (i.e., collinear) potentials for the interaction between the N_2 and HF in a given vibrational level. Additionally, the faster vibrational predissociation rate for N_2 -HF excited to $2\nu_1$ vs ν_1 is examined. The possibility of near-resonant $N_2(v) + HF$ continuum states accelerating the predissociation of $2\nu_1$ is discussed, as is the role increased coupling between the intramolecular and intermolecular coordinates could play in enhancing $V \rightarrow V$ energy transfer channels.

9.2 Experimental

The slit jet difference frequency infrared spectrometer used in these studies [247] and the modifications that allow access to the first overtone stretching region of HF [264] have been described in detail previously. The high resolution, tunable $1.3 \mu\text{m}$ light is generated via a variation of the difference frequency generation technique developed by Pine [296]. The single frequency output of a cw Nd:YAG laser and tunable ring dye laser are rendered collinear and focused into a $4 \times 4 \times 50 \text{ mm}$ LiNbO_3 crystal. The crystal is housed in a temperature controlled oven, whose temperature is ramped synchronously with the scanning of the dye laser to preserve 90° non-critical phase matching conditions. This scheme can typically generate approximately $50 \mu\text{W}$ of infrared light with 2–3 MHz linewidths for 300 and 400 mW of Nd:YAG and dye laser radiation, respectively. After exiting the oven, the difference frequency light is transmitted through a series of bandpass filters that reflect the dye and Nd:YAG beams. The infrared light is then recollimated and split into signal and reference beams, with the former directed along the long axis of a supersonic expansion generated by a $4 \text{ cm} \times 130 \mu\text{m}$ pulsed slit jet.

The N_2 -HF clusters are formed via the adiabatic expansion of an HF/ N_2 /rare gas mixture through the pulsed slit valve. The gas mixture found to maximize N_2 -HF cluster formation consists of 1.5% HF in a 60:40 mix of N_2 with "first-run" Ne (i.e., a 70:30 Ne:He mixture from the first distillation of Ne) at a total backing pressure of 600–800 torr. Multipass optics are used to obtain 16 passes through the expansion which provides a 64 cm absorption pathlength. Both the signal and reference beams are monitored with room temperature intrinsic germanium photovoltaic detectors, the photocurrents from which are subtracted in order to eliminate common mode amplitude noise on the laser light. The transient imbalance due to differential absorption is digitized, signal averaged, and stored as a function of laser frequency to yield the spectrum. Transition frequencies are measured with a traveling Michelson interferometer referenced to a polarization-stabilized HeNe laser [159], with the $P(1)$, $\nu_{HF} = 2 \leftarrow 0$ absorption of HF monomer at $7709.6839 \text{ cm}^{-1}$ [148] serving as an absolute frequency standard.

Line-shape analysis is performed by taking small (5–8 MHz) incremental laser steps over each rovibrational transition. To improve the signal-to-noise ratios, 16 averages are recorded at each laser step, and multiple scans over each transition are performed to reduce the statistical uncertainties. The resulting line shapes are least-squares fit to a Voigt profile to deconvolve the Gaussian and Lorentzian components of each transition. The Gaussian component arises from residual Doppler broadening in the expansion and is determined as an unconstrained parameter in the Voigt fits. The results are in good agreement with the Gaussian component determined for $\nu_{HF} = 2 \leftarrow 0$ transitions in Ar-HF, for which there is no detectable vibrational predissociation broadening [128] at our $\leq 2\text{--}3$ MHz resolution. The Lorentzian component

provides a spectroscopic determination of the predissociative lifetime of the complex via $\tau = 1/2\pi\Delta\nu_{\text{prediss}}$.

9.3 Results and Analysis

Throughout the remainder of the paper, we will refer to the $\nu_{\text{HF}} = 2 \leftarrow 0$ and $\nu_{\text{HF}} = 1 \leftarrow 0$ transitions of $\text{N}_2\text{-HF}$ as $2\nu_1$ and ν_1 respectively, to avoid confusion with vibrational transitions of the HF monomer. Similarly, the levels accessed by the ν_1 and $2\nu_1$ transitions will be denoted $v = 1$ and $v = 2$, respectively, with the understanding that only the HF within the complex is undergoing excitation.

The initial search for the $2\nu_1$ origin was guided by the results from previous overtone studies of van der Waals clusters [268, 346, 128], for which the frequency shift upon complexation is approximately twice that observed upon fundamental excitation. Based on a 43 cm^{-1} redshift for ν_1 excitation [244], the $2\nu_1$ band is anticipated to be near 7660 cm^{-1} , i.e., approximately 90 cm^{-1} to the red of the the $\nu_{\text{HF}} = 2 \leftarrow 0$ origin of HF at 7750.8 cm^{-1} . Figure 9.1 shows a band centered at 7657 cm^{-1} , which exhibits simple *P/R* branch structure indicative of a $\Sigma \leftarrow \Sigma$ transition for a near-linear molecule. The spectrum is observed only when N_2 and HF are simultaneously present in the expansion. The location of the origin, band structure, and dependence upon expansion gas composition strongly indicate that $\text{N}_2\text{-HF}$ is the complex giving rise to this spectrum; this assignment is unambiguously confirmed by agreement ($\pm 0.0005 \text{ cm}^{-1}$) with ground state combination differences from previous microwave studies [343]. The observed transition frequencies for $\text{N}_2\text{-HF}$ are listed in Table 9.1.

The band shows no evidence of local perturbations, and consequently tran-

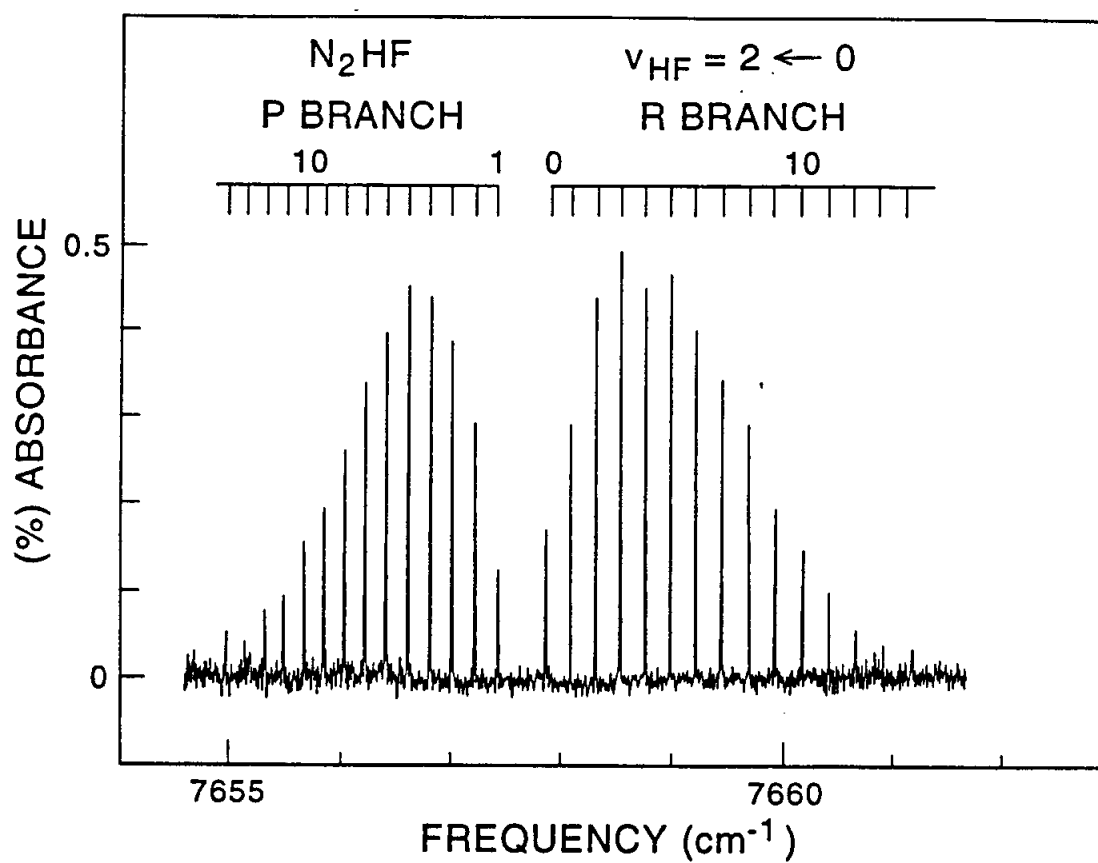


Figure 9.1: Spectrum of N_2 -HF excited to the first overtone stretching level of the HF. The spectrum was constructed by overlapping 1.5 cm^{-1} scans, averaging 15 pulses per 14 MHz frequency step.

Table 9.1: Observed transitions to the $2\nu_1$ level of N_2 -HF. Numbers in parentheses represent (observed - calculated) deviations, in units of the least significant digit. The residual standard deviation of the fit is $0.000\ 25\ \text{cm}^{-1}$.

J'	\leftarrow	J''	$\nu\ (\text{cm}^{-1})$
14	\leftarrow	15	7654.5210 (-5)
13	\leftarrow	14	7654.6920 (0)
12	\leftarrow	13	7654.8659 (1)
11	\leftarrow	12	7655.0426 (-1)
10	\leftarrow	11	7655.2232 (4)
9	\leftarrow	10	7655.4065 (3)
8	\leftarrow	9	7655.5923 (-3)
7	\leftarrow	8	7655.7823 (1)
6	\leftarrow	7	7655.9749 (2)
5	\leftarrow	6	7656.1705 (2)
4	\leftarrow	5	7656.3685 (-4)
3	\leftarrow	4	7656.5704 (0)
2	\leftarrow	3	7656.7749 (0)
1	\leftarrow	2	7656.9822 (-1)
0	\leftarrow	1	7657.1922 (-4)
1	\leftarrow	0	7657.6218 (0)
2	\leftarrow	1	7657.8408 (1)
3	\leftarrow	2	7658.0624 (0)
4	\leftarrow	3	7658.2869 (-1)
5	\leftarrow	4	7658.5147 (-3)
6	\leftarrow	5	7658.7449 (2)
7	\leftarrow	6	7658.9778 (0)
8	\leftarrow	7	7659.2138 (1)
9	\leftarrow	8	7659.4522 (-3)
10	\leftarrow	9	7659.6944 (3)
11	\leftarrow	10	7659.9386 (0)
12	\leftarrow	11	7660.1860 (0)
13	\leftarrow	12	7660.4364 (2)
14	\leftarrow	13	7660.6892 (-3)
15	\leftarrow	14	7660.9454 (-2)
16	\leftarrow	15	7661.2045 (-1)

Table 9.2: Molecular constants obtained from least-squares analysis of the N_2 -HF $2\nu_1$ transitions listed in Table I (in cm^{-1}). Uncertainties in parentheses represent 95% confidence limits. The experimental data from the ground [343] and first [244] vibrational HF levels are included in the fit, weighted by the inverse of the square of the measurement uncertainty.

	ground state	ν_1	$2\nu_1$
ν_0	0.0000	3918.24332(14)	7657.40573(33)
B_v	0.106 585 48(3)	0.107 1782(14)	0.108 0225(76)
$D_v \times 10^7$	5.673(41)	5.295(47)	4.84(30)
$H_v \times 10^{11}$	-1.38(27)	-1.33(30)	0.0 ^a

^a Parameter constrained to be 0.0.

sitions to this level are fit to the standard expansion in $J(J+1)$,

$$E = \nu_0 + B' J'(J'+1) - D'[J'(J'+1)]^2 + \dots - B'' J''(J''+1) + D''[J''(J''+1)]^2 + \dots \quad (9.1)$$

To enhance the quality of the fit, data from the microwave [343] and ν_1 studies [244] of N_2 -HF are also included in the analysis, weighted by the inverse square of the measurement uncertainty. Least-squares fitting of these data yields the band origins, rotational constants, and centrifugal distortion constants for each vibrational level of the complex; these values are listed in Table 9.2.

The origin of this band determined from the fit is $7657.4057(3) \text{ cm}^{-1}$, which is redshifted 93.39 cm^{-1} from the $\nu_{\text{HF}} = 2 \leftarrow 0$ origin of the HF monomer. This is slightly more than twice the 43.18 cm^{-1} redshift exhibited upon ν_1 excitation, and reflects a systematic deepening of the intermolecular potential as a function of HF vibrational excitation. The B rotational constant exhibits a similar trend, increasing monotonically from the ground vibrational state to $v = 1$ to $v = 2$ (see Table 9.2). This corresponds to a systematic decrease in the vibrationally averaged center-of-mass

separation between the N_2 and HF, and together with the redshift provides explicit information on *changes* in the intermolecular potential as a function of HF stretching quanta. These interactions are discussed in more detail in the discussion section.

The average Doppler and Lorentzian components of the individual rovibrational line shapes for $2\nu_1$ transitions are determined via a Voigt analysis. For transitions near the peak of the Boltzmann distribution, the signal-to-noise ratio is sufficient to float both the Doppler and Lorentzian widths, yielding an average Doppler width of 80 ± 10 MHz. This is approximately a factor of 2 larger than the 38 ± 6 MHz determined for ν_1 transitions of N_2 -HF under similar expansion conditions, which is quantitatively consistent with the two-fold higher infrared frequencies observed in the overtone region. For the peaks with lower signal to noise, the Doppler contributions are fixed at 80 MHz in order to reduce uncertainties in the Lorentzian components. Factors that could inhomogeneously broaden the rovibrational lineshapes, such as collisional and power broadening, are negligible in the low density environment of the free jet expansion and $\leq 50 \mu\text{W}$ difference frequency power levels. Consequently the Lorentzian component determined from the Voigt deconvolution described above can be directly related to the timescale for energy transfer from the excited HF to the intermolecular modes, which by analogy to the results for ν_1 [244] excitation is attributable to vibrational predissociation. The predissociation linewidths for $J'=1-11$ are listed in Table 9.3, and within the accuracy of the measurements do not reflect a J' dependence. The average Lorentzian component of 79 ± 11 MHz corresponds to a lifetime of 2.0 ± 0.3 ns, which translates into an 11-fold faster vibrational predissociation for $2\nu_1$ than for ν_1 excitation. These results are discussed in more detail below.

Table 9.3: Average predissociation linewidths for P and R branch transitions of $2\nu_1$ of N_2 -HF. The numbers in parentheses represent 1σ standard deviation. The variation in uncertainty reflects the increase in signal/noise near the peak of the Boltzmann distribution. The overall average is $\Delta\nu_{\text{prediss}} = 79 \pm 11$ MHz, corresponding to a predissociation lifetime of 2.0 ± 0.3 ns.

J'	Linewidth (MHz)
0	90(25)
1	90(30)
2	80(25)
3	65(30)
4	75(20)
5	85(10)
6	80(10)
7	90(20)
8	70(10)
9	80(20)
10	55(30)
11	85(30)

9.4 Discussion

9.4.1 Vibrational Redshifts

Figure 9.2 shows the vibrational redshifts vs. the number of vibrational quanta in the IR chromophore of all van der Waals complexes for which rotationally resolved overtone data have been reported. These values are also listed in Table 9.4. The small magnitude of the redshifts with respect to the monomer frequencies ($\Delta\nu_{\text{redshift}}/\nu_0 \leq 1\%$) suggests that a perturbative treatment of the interaction of the intermolecular and intramolecular bonds is justified. Liu and Dykstra have presented calculations [238, 239, 240] in which the change in the intramolecular stretching po-

Table 9.4: Vibrational redshifts (in cm^{-1}) of van der Waals complexes containing HF for which rotationally resolved overtone data have been reported. ν_1 refers to HF stretch excitation (for $(\text{HF})_2$ the data are for the "free" HF).

Complex	ν_1	ν_1/ν_1	$2\nu_1$	$2\nu_1/\nu_1$	$3\nu_1$	$3\nu_1/\nu_1$
$\text{N}_2\text{-HF}$	-43.180 ^a	1.000	-93.389 ^b	2.163	-152.557 ^c	3.533
$(\text{HF})_2$	-30.523 ^d	1.000	-67.972 ^e	2.227	-99.306 ^f	3.254
Ar-HF	-9.654 ^g	1.000	-20.912 ^h	2.166	-33.773 ⁱ	3.498

^a Reference [244]

^b This work

^c Reference [357]

^d Reference [298]

^e Reference [346]

^f Reference [70]

^g Reference [251]

^h Reference [128]

ⁱ Reference [69]

tential $V(r)$ upon hydrogen bond formation is represented by an interaction term, $V^{\text{int}}(r) = s \cdot r$, where s is the slope of the perturbing interaction potential as determined from *ab initio* calculations and r is the intramolecular stretching coordinate. The model is electrostatic in nature; the interaction of the molecule's polarizabilities and multipole moments with the electric field of a nearby molecule leads to changes in the intramolecular stretching potential of the molecule. This interaction has been found to be nearly linear with r for a large number of molecules, including HF [238]. The addition of a linear term to the anharmonic stretching potential changes the equilibrium curvature, and hence the potential force constant. As a consequence, the vibrational transition frequencies of the monomer within the complex are shifted with respect to that of the free molecule.

The redshift predicted by this model for ν_1 excitation of $\text{N}_2\text{-HF}$ is 34 cm^{-1} , in fair agreement with the experimental value of 43 cm^{-1} . While quantitative agree-

VIBRATIONAL REDSHIFT VS VIBRATIONAL STRETCHING QUANTA

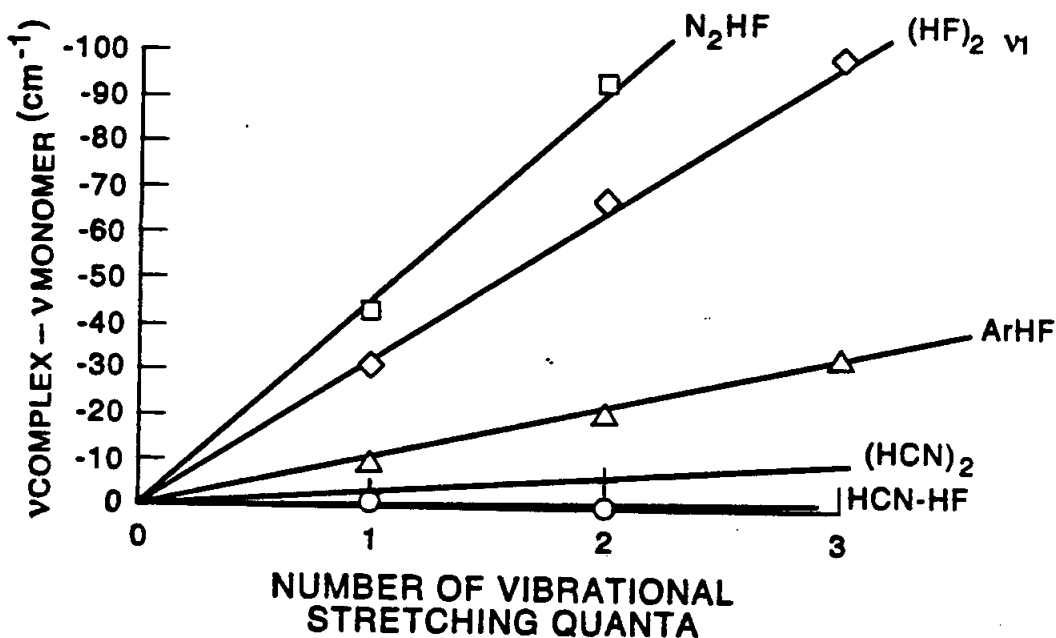


Figure 9.2: Vibrational redshifts vs the quanta of stretch excitation in the infrared chromophore of all complexes for which rotationally resolved data have been reported in an overtone level. The experimental data for N_2 -HF ($v=1$) are from reference [244] and for ($v=2$) from the present work; for $(HF)_2$ ($v=1, 2$, and 3) the data are from ref [298], [346], and [70], respectively; for Ar-HF ($v=1, 2$, and 3) the data are from ref [251], [128], and [69], respectively; for $(HCN)_2$ ($v=1$ and 2) the data are from ref [205] and [268]; and for HCN-HF ($v=1$ and 2), the data are from ref [97] and [211]. The linearity of the plot arises from a perturbative interaction between the intermolecular (van der Waals) bond and the high frequency intramolecular bond, as described in the text.

ment between the calculated and experimental redshifts requires that the slope s be accurately determined, the calculation of the redshift *ratios* do not. Consequently we can extend this formalism to determine the vibrational dependence of the redshifts. By modeling the anharmonic stretching potential of the HF as a Morse oscillator, one has

$$V(r) = D_e \left(1 - e^{-a(r-r_e)}\right)^2 \quad (9.2)$$

with associated harmonic force constant k_e , harmonic frequency ω_e , and anharmonicity $\omega_e x_e$. Addition of the interaction term yields $V'(r)$, the modified stretching potential

$$\begin{aligned} V'(r) &= V(r) + V^{\text{int}}(r) \\ &= D_e \left(1 - e^{-a(r-r_e)}\right)^2 + s \cdot r \end{aligned} \quad (9.3)$$

Evaluation of the curvature of this potential near the new equilibrium value of r allows k' , the modified harmonic force constant, to be determined from which it is possible to derive expressions for ω'_e and $\omega'_e x'_e$. Neglecting terms higher than first order in s , we calculate the *ratios* of the frequency shifts for $v = 2/v = 1$ and $v = 3/v = 1$ for HF containing complexes to be 2.01 and 3.03, respectively, and independent of the value of s . This is in reasonable agreement with the experimentally observed ratios listed in Table 9.4 for N₂-HF (2.16 and 3.53), Ar-HF (2.17 and 3.50), and (HF)₂ (2.23 and 3.25).

This simple one-dimensional model correctly reproduces the qualitative behavior of the vibrational dependence of the redshifts, but consistently underpredicts the experimentally observed ratios. This discrepancy can be attributed to the effects of angular interactions not accounted for in this one-dimensional treatment. Specifically, the increase in angular anisotropy of the intermolecular potential with increasing ν_{HF}

will tend to increase the alignment of the HF along the intermolecular axis, effectively further increasing both the strength of the hydrogen bond and the coupling with the intramolecular stretch. This effect has been experimentally observed from infrared Stark spectroscopy of Ar-HF [181], where the vibrationally averaged bend angle of the HF decreases from $\langle \theta^2 \rangle^{1/2} = 48^\circ$ in $\nu_{\text{HF}} = 0$ to 43° in $\nu_{\text{HF}} = 1$. Similar results have been reported from Stark spectroscopy of ν_1 of N₂-HF [201], although the decrease in the average HF bending angle could not be quantified.

The work of Liu and Dykstra on which the above calculation is based lends a plausible physical picture to the origin of the vibrational redshifts for weakly bound complexes. Further support for the role of electrostatic interactions as a primary contributor to the redshifts has been given by Hutson [190] for Ar-HF. It was found that the vibrationally averaged induction energy could explain approximately 80% of the redshift for both $v = 1$ and 2. This can be contrasted, however, by the recent high level *ab initio* calculations on Ar-HF by Tao and Klemperer [353] in which the increase in electrostatic interactions are apparently offset by terms such as the exchange repulsion, and the dominant factor contributing to the redshift is actually the dispersion energy. Whether this is also valid for more strongly interacting, hydrogen bonding systems such as N₂-HF is unclear. A detailed *ab initio* analysis of how and why intermolecular potentials for hydrogen bonding change with intramolecular vibrational excitation of the subunits clearly merits further theoretical attention.

9.4.2 Rotational Constants

Analysis of the rotational and centrifugal distortion constants as a function of HF stretching quanta provides information about the intermode coupling that is complementary to that obtained from the redshift analysis. In particular, the rotational constant provides the vibrationally averaged center-of-mass separation for a given HF vibrational level of the complex. Previous overtone studies of Ar-HF [128, 69] and (HF)₂ [346, 70] have shown that the B rotational constant increases with monomer vibrational level, reflecting a decrease in the vibrationally averaged center-of-mass separation. This is consistent with a contraction of the complex and strengthening of the intermolecular bond. Further supporting evidence lies in the behavior of the centrifugal distortion constant D , which *decreases* as a function of monomer vibrational level. These trends are present for N₂-HF as well, and are a manifestation of the same physical interactions responsible for the vibrational redshifts. This behavior is most simply rationalized by examining the changes in the electrical properties of the HF as a function of ν_{HF} . Since both the HF dipole moment and polarizability increase upon vibrational excitation, the dipole-induced dipole and dispersion interactions also increase. Regardless whether the dominant contribution to the redshift arises from induction or dispersion, the net result is an increase in the intermolecular bond strength and corresponding decrease in bond length.

Nesbitt and Child [286] have shown that it is possible to invert experimental rotational and centrifugal distortion constants of van der Waals complexes to obtain information about the potential energy surface for a given vibrational level of the monomer constituents. This "rotational-RKR" procedure is analogous to the RKR

inversion used for generating potential energy surfaces for diatomics from vibrational spectroscopic data, and similarly provides the classical inner and outer turning points of the *intermolecular* potential. The quantitative accuracy of this inversion procedure has been tested on rotational eigenvalues derived from model 1-D potentials [286], as well as through comparison of potential parameters determined for N₂-HF and its isotopomers in the ground and first vibrational levels of the HF stretch [287]. In the latter study, a high level of consistency is found between the predicted force constants and equilibrium well depths for the different ¹⁵N/¹⁴N isotopomers, as is expected within the Born-Oppenheimer approximation. Furthermore, this method is able to reproduce quantitatively the $v = 1$ vibrational redshifts for both the N₂-HF and N₂-DF complexes.

By incorporating the rotational and centrifugal distortion constants listed in Table 9.2 for $v = 2$ of N₂-HF it is possible to generate a similar one-dimensional radial potential for the complex excited to the first overtone stretching level of HF. It is worth emphasizing that these potential curves represent adiabatic averages over all other coordinates, i.e., the intramolecular HF and N₂ stretches and intermolecular bends. Figure 9.3 shows the one dimensional potential curves for the three lowest HF vibrational levels in N₂-HF, obtained from fitting the inner and outer turning points of the potential to a Lennard-Jones 6-12 functional form. The deepening of the potential with increasing quanta of HF stretch is clearly evident from the figure, and demonstrates that the changes in the intermolecular potential between different HF vibrational levels of the complex are qualitatively reproduced.

An assessment of the quantitative accuracy of these potential curves is available from a comparison of the predicted redshifts with those observed experimentally.

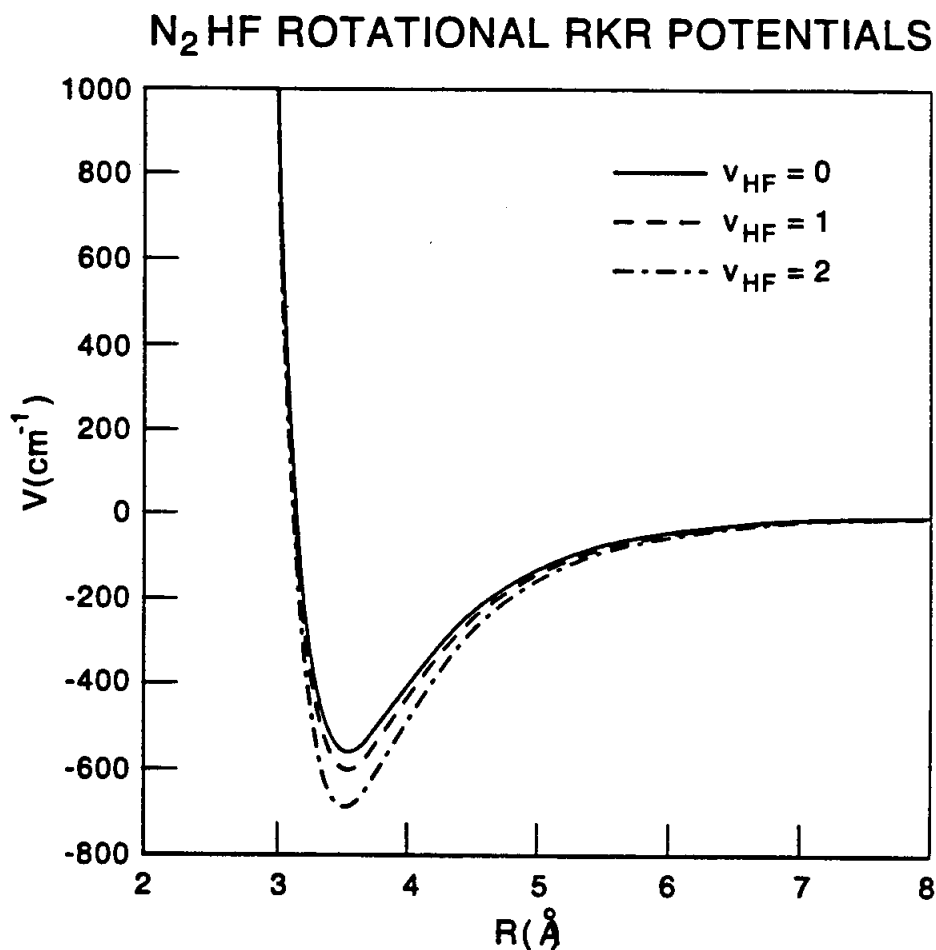


Figure 9.3: One-dimensional potential curves for N₂-HF generated by inversion of the rotational and centrifugal distortion constants using the rotational-RKR technique of Nesbitt and Child. [286]. The rotational-RKR procedure provides the inner and outer classical turning points of the intermolecular potential near the equilibrium position. The long range behavior of the potentials is approximated by electrostatic terms as discussed in ref [286]. The three curves are for the (HF) vibrational ground state, first, and second vibrationally excited states, and reflect the increasing well depth with increased stretch excitation of the monomer.

Since our spectroscopic data are most sensitive to the region near the potential minimum, fitting to any of several functional forms is sufficient to reproduce the harmonic and low-order anharmonic behavior of the potential. The calculated redshifts are obtained by subtracting the value of D_0 for the ground vibrational state from D_0 of ν_1 and $2\nu_1$. For ν_1 , the calculated redshift for $^{14}\text{N}_2\text{-HF}$ is $40 \pm 2 \text{ cm}^{-1}$, in excellent agreement with the experimentally observed value of 43 cm^{-1} . Likewise, good agreement is achieved for $2\nu_1$, where the predicted redshift is $106 \pm 20 \text{ cm}^{-1}$ vs the observed 93 cm^{-1} . The larger uncertainty for $2\nu_1$ simply reflects the smaller range of J 's observed and the correspondingly smaller precision of the higher order centrifugal constants determined from the spectral fit. However, even though the error bars bracket the experimental value for $2\nu_1$, the calculated redshift for $3\nu_1$ of $250 \pm 80 \text{ cm}^{-1}$ differs somewhat from the recently reported value of 153 cm^{-1} [357]. While the experimental trend of a near-linear redshift with ν_{HF} remains valid for higher vibrational excitation of the HF, the one-dimensional model appears to systematically overpredict the magnitude of the redshifts. It is worth restating, however, that the rotational-RKR method is most sensitive to the equilibrium region of the potential, and that reproducing the redshifts also requires a reliable characterization of the long range potential, where the 1-D collinear approximation eventually breaks down.

9.4.3 Vibrational Predissociation

The vibrational predissociation lifetime of $\text{N}_2\text{-HF}$ following $2\nu_1$ excitation is $2.0 \pm 0.3 \text{ ns}$, which is 11-fold faster than the $22 \pm 5 \text{ ns}$ reported for ν_1 [201]. The shorter lifetime for the $v = 2$ vs $v = 1$ level is in qualitative agreement with statistical

theories, which predict a monotonic increase in the vibrational predissociation rate with increasing internal energy. Additionally, this value agrees qualitatively with the ratio reported for vibrational relaxation of HF by N₂ in cell experiments at 295 K [42], in which N₂ relaxes HF ($v_{\text{HF}}=2$) 6 times faster than HF ($v_{\text{HF}}=1$). Given the extensive averaging over energy and orientation implicit in the bimolecular relaxation rate constants, it is difficult to extract any quantitative comparison with the vibrational predissociation rates. However, the similarity in the vibrational dependence of the unimolecular and bimolecular rates suggests the importance of complex formation in the collisional process. In fact, the rate constants from these cell studies do show an inverse temperature dependence below 400 K, supporting the role of complex formation in the bimolecular relaxation event.

It is interesting to speculate about the factors giving rise to the differences in the $v = 1$ vs $v = 2$ rates, since the predissociation dynamics in each case are governed by the *same* Born-Oppenheimer potential surface. From previous studies of weakly bound clusters it is known that one of the factors that can accelerate the rate of vibrational predissociation is a near-resonance with product vibrational and rotational continuum states, i.e., the rate increases when there is little translational energy imparted into the recoiling fragments. As an example, vibrational predissociation following ν_1 excitation of N₂-DF (i.e., $v_{\text{DF}} = 1 \leftarrow 0$) occurs more than an order of magnitude faster than observed following ν_1 excitation of N₂-HF [287]. This increase can be rationalized as arising from a near-resonant $V \rightarrow V$ channel to form N₂ ($v_{\text{N}_2}=1$) and DF ($v_{\text{DF}}=0$), which would serve to reduce dramatically the energy deposited as rotational and translational excitation of the products. Conversely, vibrational predissociation of N₂-HF via the same mechanism requires an additional $\approx 1000 \text{ cm}^{-1}$ to

be partitioned between rotational and translational energy of the fragments.

Bohac and Miller [39] have recently characterized the final state distribution of the N_2 and HF vibrational predissociation products following ν_1 excitation of N_2 -HF. Their results indicate nearly equal probability of populating $v_{N_2} = 1$ and $v_{N_2} = 0$, and population of the highest corresponding j_{HF} level accessible in each N_2 vibrational channel such as to minimize the relative translational energy of the products. Similar distributions have been observed by King and coworkers [336] following HF excitation of NO-HF, in which $v_{NO} = 1$ and $v_{NO} = 0$ are formed with equal probability. From analysis of the Doppler profiles of the NO, values for j_{HF} in each NO vibrational channel were determined again to be the highest energetically available, and minimize the translational center-of-mass energy of the product fragments.

In the gas-phase collisional relaxation studies of HF ($v_{HF} = 1-3$) by N_2 , the dominant relaxation channel proceeds via $\Delta v_{HF} = -1$ [42]. This is of course the pathway accessed for vibrational predissociation of N_2 -HF from $v = 1$, and if N_2 -HF excited to the $v = 2$ level follows this trend, similar quantum state distributions of the HF and N_2 might be expected. The dissociation energy of N_2 -HF has recently been determined to be $390 \pm 20 \text{ cm}^{-1}$ [276] and it is thus possible to determine whether a near-resonant product channel exists for $2\nu_1$ vs ν_1 which could accelerate the rate of predissociation. Table 9.5 shows the j_{HF} values observed [39] for both $v_{N_2} = 1$ and $v_{N_2} = 0$ following vibrational predissociation from $v = 1$ of N_2 -HF, and the remaining energy which must be partitioned as N_2 rotational energy and relative translational energy of the fragments. Also listed in Table 9.5 are the maximum j values for HF (denoted j_{max}^{HF}) energetically allowed for $v = 2$ for the $\Delta v_{HF} = -1$ pathway. As anticipated above, the ΔE values are quite similar for the $v = 1$ and

Table 9.5: Vibrational relaxation channels for vibrational predissociation following $v = 1$ and $v = 2$ excitation of N_2 -HF. v_{HF} and v_{N_2} refer to the final vibrational levels of the HF and N_2 products, j_{max}^{HF} to the largest values of HF rotation that can be accessed energetically, and ΔE to the remaining energy that must be partitioned between N_2 rotation and relative translational energy of the fragments. The values of HF j_{max}^{HF} and v_{N_2} for ν_1 excitation are from reference [39] and represent experimentally observed quantities, while the values for $2\nu_1$ are predictions based on a N_2 -HF binding energy of $D_0=390 \text{ cm}^{-1}$.

Excitation	Vibrational Predissociation Products			
	v_{HF}	v_{N_2}	j_{max}^{HF}	$\Delta E \text{ (cm}^{-1}\text{)}$
ν_1	0	0	12	374
	0	1	7	54
$2\nu_1$	1	0	12	107
	1	1	6	233
	0	0	18	489
	0	1	15	128
	0	2	10	401
	0	3	3	117

$v = 2$ initial states, suggesting that the a simple energetic near-resonant $\Delta v = -1$ channel cannot satisfactorily explain the 11-fold increased vibrational predissociation rate for $v = 2$.

It is possible, however, that vibrational predissociation of the complex following excitation to $v = 2$ proceeds via the $\Delta v_{HF} = -2$ channel, and access to this pathway might contribute to the increased rate. In this scenario there is sufficient energy available to populate up to $v_{N_2}=3$. Although such multiple-quantum changes in vibrational level are typically unfavorable in bimolecular relaxations, the highly oriented, collinear geometry of the N_2 and HF in the complex could potentially enhance such intermolecular $V \rightarrow V$ transfer. Listed in Table 9.5 are the N_2 vibrational and corresponding j_{max}^{HF} levels which could be populated if vibrational predissociation occurred via a $\Delta v_{HF} = -2$ pathway. The $v_{HF} = 0$, $v_{N_2} = 3$ channel is of particular

interest, since three quanta of N_2 vibration act as a sink for 6904 cm^{-1} , leaving only $\approx 370\text{ cm}^{-1}$ of energy to partition as rotational and translational energy of the products. With $j_{HF} = 3$, only 117 cm^{-1} would remain to be partitioned between N_2 rotation and product translation. While this near resonance and the low angular momentum of the diatom could explain the increased rate for $v = 2$ vibrational predissociation, the necessary five-quantum transfer of vibrational excitation would reflect a surprising, though intriguing, energy transfer event. It is worth mentioning that this reasoning implicitly assumes that the availability of resonant $V \rightarrow V$ channels accelerates predissociation, although the results of Bohac and Miller [39] show that predissociation of N_2 -HF following ν_1 excitation occurs as readily via the $V \rightarrow V$ channel as the $V \rightarrow R, T$ channel, even though the latter requires much more energy to be imparted as rotational and relative translational energy. Clearly, resolution of the HF and N_2 rovibrational distributions following vibrational predissociation of the complex excited to overtone vibrational levels would be invaluable in determining whether large multiple-quantum $V \rightarrow V$ channels constitute significant dissociation pathways.

The above treatment based on simple energetic grounds neglects the effects of HF excitation on the coupling between the intramolecular and intermolecular coordinates. This type of coupling is also responsible for the vibrational relaxation of molecules in solution, in which the coupling with bulk modes of the solvent determine the efficiency of vibrational relaxation [376, 377]. Consequently a knowledge of how this coupling varies as a function of monomer excitation is necessary to reproduce the observed predissociation rates. The theoretical framework for understanding the influence of intermode coupling on the vibrational predissociation rate of weakly bound complexes has been established by Beswick and Jortner [28, 29] and Ewing

[123, 124, 125, 126]. Recently Miller has proposed an empirical relationship discerned from a number of complexes studied in the near IR. This model incorporates a Golden Rule treatment of the vibrational predissociation and a perturbative treatment of the coupling between intramolecular and intermolecular potentials, and predicts that the vibrational predissociation rate should scale with the *square* of the redshift for different complexes containing the same chromophore. Comparison with experimental data for a series of HF-containing complexes excited to the $\nu_{\text{HF}} = 1$ manifold shows reasonable agreement with the experimentally observed rates. Scoles and coworkers [211] have recently extended this treatment to permit a comparison of vibrational predissociation rates for the *same* complex in different vibrational levels. Within their stated assumptions, i.e., i) the intermolecular wave functions are identical in the first overtone and fundamental levels of the monomer, ii) the monomer wave functions are negligibly affected by complexation, and iii) the intermode potential coupling function does not change with the monomer vibrational level, the ratio of predissociation rates between the fundamental and first overtone levels of the monomer for any complex is predicted to be $k_{\nu=2}/k_{\nu=1} \approx 2$. While this is in qualitative agreement with their results for HCN-HF [211] where the ratio is 1.8, the agreement is poor for the present N_2 -HF results where $k_{\nu=2}/k_{\nu=1} = 11$, and for ν_1 excitation of $(\text{HF})_2$, where $k_{\nu=2}/k_{\nu=1} = 10$ [346].

It is evident from these overtone studies that the predissociation dynamics of these simple systems are sufficiently complex that even qualitatively accurate models for predicting vibrational predissociation trends are difficult to formulate, and may depend on details of the potential energy surfaces that have proven hard to measure. However, with the increasing sensitivity of experimental methods, the spec-

troscopic data necessary to construct accurate potential energy surfaces for individual complexes are becoming available. Furthermore, concurrent advances in computational methodology are permitting the extraction of highly accurate potentials from spectroscopic data for increasingly larger systems, and the prospect of full quantum dynamical calculations on these potentials has improved dramatically. The sensitivity of the rotational-RKR inversion to the near-equilibrium region of the intermolecular potential suggests that these v dependent potentials may prove useful in theoretical predissociation models for linear hydrogen bonded complexes. Extension to other systems is quite feasible, and experimental results from isotope and overtone studies, as well as those that resolve the final product state distributions, will provide the necessary, rigorous tests of these theoretical models.

9.5 Summary

The high resolution spectrum of the first overtone HF stretching level of N_2 -HF has been recorded using direct absorption of tunable infrared light. The band origin, at 7657.4057 cm^{-1} , is redshifted 93.39 cm^{-1} from the $\nu_{\text{HF}} = 2 \leftarrow 0$ origin of free HF. This redshift is slightly more than twice that observed for ν_1 excitation of N_2 -HF, and can be rationalized in terms of electrostatic-based perturbations in the monomer vibrational potential induced by complex formation. The changes in the intermolecular/intramolecular coupling with monomer vibrational level manifested in the redshift are also evident in the rotational constants. The rotational and centrifugal distortion constants are used to generate a one-dimensional radial potential from rotational RKR inversion, as has been done for N_2 -HF in the ground and first HF

stretching level. These potentials are capable of reproducing the vibrational redshifts of the complexes within experimental error. Analysis of the homogeneous broadening of the rovibrational line shapes allows a vibrational predissociation lifetime of 2.0 ± 0.3 ns to be determined, which is more than an order of magnitude faster than observed upon $v = 1$ excitation. This magnitude of rate increase cannot be rationalized solely on the basis of a simple energetic resonance, and most likely reflects greater dynamical coupling between the intermolecular and intramolecular coordinates for $v = 2$ vs $v = 1$. In addition, near-resonant, multiple-quantum $V \rightarrow V$ channels not available for $v = 1$ may accelerate vibrational predissociation from $v = 2$. While theories developed to model vibrational predissociation trends cannot satisfactorily explain the observed rates, calculations on potentials constructed from spectroscopic data such as the RKR-based potentials described above are promising candidates for more quantitative studies.

BIBLIOGRAPHY

- [1] Harry C. Allen, Jr. and Paul C. Cross. *Molecular Vib-Rotors*. John Wiley and Sons, New York, 1963.
- [2] M. P. Allen and D. J. Tildesley. *Computer Simulation of Liquids*. Oxford University Press, New York, 1987.
- [3] S. C. Althorpe, D. C. Clary, and P. R. Bunker. Calculation of the far-infrared spectra for (HF)₂, (HCl)₂, and (HBr)₂. *Chem. Phys. Lett.*, 187:345-353, 1991.
- [4] David T. Anderson. *High resolution infrared spectroscopy and photolysis of solutes in cryogenic solids*. PhD thesis, Dartmouth College, 1993.
- [5] David T. Anderson, Scott Davis, and David J. Nesbitt. HF dimer intermolecular potential and quantum dynamics: A near-IR study of all four intermolecular modes. Manuscript in preparation.
- [6] D. T. Anderson and J. S. Winn. Matrix isolated HF: The high resolution infrared spectrum of cryogenically solvated hindered rotor. *Chem. Phys.*, 189:171-178, 1994.
- [7] David T. Anderson and David J. Nesbitt. Private communication.
- [8] Lester Andrews, Benue J. Kelsall, and Robert T. Arlinghaus. FTIR observation of the N₂-HF complex in solid argon. *J. Chem. Phys.*, 79:2488-2490, 1983.
- [9] Lester Andrews and Steven R. Davis. FTIR observation of N≡N stretching fundamentals in hydrogen-bonded complexes in solid argon. *J. Chem. Phys.*, 83:4983-4989, 1985.
- [10] Lester Andrews and Martin Moskovits, editors. *Chemistry and Physics of Matrix-Isolated Species*. North-Holland, 1989.
- [11] L. Andrews. Applications of FTIR spectroscopy. In Durig [106], pages 183-216.
- [12] A. Ashkin, G. D. Boyd, J. M. Dziedzic, R. G. Smith, A. A. Ballman, J. J. Levinstein, and K. Nassau. Optically-induced refractive index inhomogeneities in LiNbO₃ and LiTaO₃. *Appl. Phys. Lett.*, 9:72-74, 1966.
- [13] B. M. Axilrod and E. Teller. Interaction of the van der Waals type between three atoms. *J. Chem. Phys.*, 11:299-300, 1943.

- [14] R. A. Aziz. In Klein [212].
- [15] Ronald A. Aziz. A highly accurate interatomic potential for argon. *J. Chem. Phys.*, 99:4518-4525, 1993.
- [16] Z. Bačić, M. Kennedy-Mandziuk, J. W. Moskowitz, and K. E. Schmidt. He₂Cl₂ and He₃Cl₂ van der Waals clusters: A quantum Monte Carlo study. *J. Chem. Phys.*, 97:6472-6480, 1992.
- [17] Z. Bačić. Private communication.
- [18] F. A. Baiocchi, T. A. Dixon, C. H. Joyner, and W. Klemperer. Microwave and radio frequency spectra of Xe-HF. *J. Chem. Phys.*, 75:2041-2046, 1981.
- [19] A. J. Barnes. Vibrational spectroscopy of molecular complexes in low-temperature matrices. In Ratajczak and Orville-Thomas [316], pages 273-299.
- [20] Andrew E. Barton, David J. B. Howlett, and Brian J. Howard. The rotational spectrum and structure of van der Waals complexes: III. Neon-deuterium chloride. *Mol. Phys.*, 41:619-628, 1982.
- [21] Andrew E. Barton and Brian J. Howard. An intermolecular potential-energy surface for (HF)₂. *Faraday Discuss. Chem. Soc.*, 73:45-62, 1982.
- [22] Edwin D. Becker and George C. Pimentel. Spectroscopic studies of reactive molecules by the matrix isolation method. *J. Chem. Phys.*, 25:224-228, 1956.
- [23] Edwin D. Becker, George C. Pimentel, and Mathias Van Thiel. Matrix isolation studies: Infrared spectra of intermediate species in the photolysis of hydrazoic acid. *J. Chem. Phys.*, 26:145-150, 1956.
- [24] S. P. Belov, E. N. Karyakin, I. N. Kozin, A. F. Krupnov, O. L. Polyansky, M. Yu. Tretyakov, N. F. Zobov, R. D. Suenram, and W. J. Lafferty. Tunneling-rotation spectrum of the hydrogen fluoride dimer. *J. Mol. Spectrosc.*, 141:204-222, 1990.
- [25] R. J. Bemish, M. Wu, and R. E. Miller. Probing the dynamics of weakly bound complexes using high-resolution laser spectroscopy. *Faraday Disc. Chem. Soc.*, 97:57-68, 1994.
- [26] Mark A. Benzel and Clifford E. Dykstra. The nature of hydrogen bonding in the NN-HF, OC-HF, and HCN-HF complexes. *J. Chem. Phys.*, 78:4052-4062, 1983.
- [27] Mark A. Benzel and Clifford E. Dykstra. Erratum: The nature of hydrogen bonding in the NN-HF, OC-HF, and HCN-HF complexes [J. Chem. Phys. 78, 4052 (1983)]. *J. Chem. Phys.*, 80:3510-3511, 1984.
- [28] J. A. Beswick and Joshua Jortner. Model for vibrational predissociation of van der Waals molecules. *Chem. Phys. Lett.*, 49:13-18, 1977.
- [29] J. A. Beswick and Joshua Jortner. Intramolecular dynamics of van der Waals molecules. *Adv. Chem. Phys.*, 47:363-506, 1981.

- [30] A. Beyer, A. Karpfen, and P. Schuster. In Boschke [40], pages 1-40.
- [31] Mordechai Bixon and Joshua Jortner. Intramolecular radiationless transitions. *J. Chem. Phys.*, 48:715, 1968.
- [32] Joseph A. Blazy, Benjamin M. DeKoven, Timothy D. Russell, and Donald H. Levy. The binding energy of iodine-rare gas van der Waals molecules. *J. Chem. Phys.*, 72:2439-2444, 1980.
- [33] P. A. Block, K. W. Jucks, L. G. Pedersen, and R. E. Miller. The linear and T-shaped isomers of C_2H_2-HCN : Vibrational dynamics from infrared spectroscopy and ab initio theory. *Chem. Phys.*, 139:15-30, 1989.
- [34] P. A. Block, Mark D. Marshall, L. G. Pedersen, and R. E. Miller. Wide amplitude motion in the water-carbon dioxide and water-acetylene complexes. *J. Chem. Phys.*, 96:7321-7332, 1992.
- [35] P. A. Block and R. E. Miller. Infrared-infrared double resonance spectroscopy of Ar-HF. Intermolecular state dependence of the dipole moment and vibrational predissociation in $v_{HF}=2$. *Chem. Phys. Lett.*, 226:317-324, 1994.
- [36] E. J. Bohac, Mark D. Marshall, and R. E. Miller. Initial state effects in the vibrational predissociation of hydrogen fluoride dimer. *J. Chem. Phys.*, 96:6681-6695, 1992.
- [37] E. J. Bohac and R. E. Miller. State-to-state vibrational predissociation of H_2HF and D_2HF . Direct comparisons between theory and experiment. *J. Chem. Phys.*, 98:2604-2613, 1993.
- [38] E. J. Bohac and R. E. Miller. The trans-bending and F-F stretching vibrations of HF dimer in $v_{HF}=1$: The influence of intermolecular vibrational excitation on the predissociation dynamics. *J. Chem. Phys.*, 99:1537-1544, 1993.
- [39] E. J. Bohac and R. E. Miller. Intermolecular $V - V$ energy transfer in the photodissociation of weakly bound complexes: A new experimental approach. *Phys. Rev. Lett.*, 71:54-57, 1993.
- [40] F. L. Boschke, editor. *Topics in Current Chemistry*, volume 120. Springer, Berlin, 1984.
- [41] J. F. Bott and N. Cohen. Temperature dependence of V-V and V-R,T energy transfer measurements in mixtures containing HF. *J. Chem. Phys.*, 58:4539-4549, 1973.
- [42] J. F. Bott. Vibrational relaxation of HF($v=1, 2$, and 3) in H_2 , N_2 , and CO_2 . *J. Chem. Phys.*, 65:4239-4245, 1976.
- [43] J. F. Bott and R. F. Heidner. Vibrational relaxation of HF($v=1$ and 3) in H_2, N_2 , and D_2 at 200 and 295 K. *J. Chem. Phys.*, 72:3211-3215, 1980.

- [44] J. F. Bott. Vibrational relaxation of DF($v=1$ and 3) in H_2 , D_2 , N_2 , and HF at 200 K. *J. Chem. Phys.*, 74:2827-2831, 1981.
- [45] M. T. Bowers, G. I. Kerley, and W. H. Flygare. Vibration-rotation spectra of monomeric HF in the rare gas lattices: II. *J. Chem. Phys.*, 45:3399-3414, 1966.
- [46] Joel M. Bowman, editor. *Advances in Molecular Vibrations and Collision Dynamics*, volume 1A. JAI Press, Greenwich, CT, 1991.
- [47] Robert W. Boyd *Nonlinear Optics*. Academic Press, Boston, 1992.
- [48] S. Bratož and M. L. Martin. Infrared spectra of highly compressed gas mixtures of the type HCl + X. a theoretical study. *J. Chem. Phys.*, 42:1051-1062, 1965.
- [49] Margaret Bruehl and James T. Hynes. Vibrational relaxation times for a model hydrogen-bonded complex in a polar solvent. *Chem. Phys.*, 175:205-221, 1993.
- [50] D. A. Bryan, Robert Gerson, and H. E. Tomasche. Increased optical damage resistance in lithium niobate. *Appl. Phys. Lett.*, 44:847-849, 1984.
- [51] A. D. Buckingham. Solvent effects in vibrational spectroscopy. *Trans. Faraday Soc.*, 56:753-760, 1960.
- [52] A. D. Buckingham. Theory of long-range dispersion forces. *Disc. Far. Soc.*, 40:232-238, 1965.
- [53] A. D. Buckingham and P. W. Fowler. A model for the geometries of van der Waals complexes. *Can. J. Chem.*, 63:2018-2025, 1985.
- [54] A. D. Buckingham, P. W. Fowler, and Jeremy M. Hutson. Theoretical studies of van der Waals molecules and intermolecular forces. *Chem. Rev.*, 88:963-988, 1988.
- [55] S. Buelow, G. Radhakrishnan, and C. Wittig. The CO_2DBr precursor geometry limited reaction of deuterium with carbon dioxide. *J. Phys. Chem.*, 91:5409-5412, 1987.
- [56] Phillip R. Bunker. *Molecular Symmetry and Spectroscopy*. Academic Press, London, 1979.
- [57] P. R. Bunker, Manfred Kofranek, Hans Lischka, and Alfred Karpfen. An analytical six-dimensional potential energy surface for $(HF)_2$ from *ab initio* calculations. *J. Chem. Phys.*, 89:3002-3007, 1988.
- [58] P. R. Bunker, T. Carrington, Jr., P. C. Gomez, M. D. Marshall, M. Kofranek, H. Lischka, and A. Karpfen. *J. Chem. Phys.*, 91:5154, 1989.
- [59] P. R. Bunker, Per Jensen, Alfred Karpfen, Manfred Kofranek, and Hans Lischka. An *ab initio* calculation of the stretching energies for the HF dimer. *J. Chem. Phys.*, 92:7432-7440, 1990.

- [60] P. R. Bunker, Per Jensen, and A. Karpfen. The $v_1 + v_2 = 4$ stretching overtones of the hf dimer, and H-atom exchange. *J. Molec. Spec.*, 149:512-518, 1991.
- [61] K. C. Busarow, G. A. Blake, K. B. Laughlin, R. C. Cohen, Y. T. Lee, and R. J. Saykally. *J. Chem. Phys.*, 89:1268, 1988.
- [62] P. N. Butcher and D. Cotter *The Elements of Nonlinear Optics*. Cambridge University Press, Cambridge, 1990.
- [63] L. W. Buxton, E. J. Campbell, M. R. Keenan, T. J. Balle, and W. H. Flygare. The rotational spectrum, nuclear spin-spin coupling, nuclear quadrupole coupling, and molecular structure of KrHF. *Chem. Phys.*, 54:173-181, 1981.
- [64] Robert L. Byer. Diode laser-pumped solid-state lasers. *Science*, 239:742-747, 1988.
- [65] G. Chałasiński, S. M. Cybulski, M. M. Szcześniak, and S. Scheiner. Nonadditive effects in HF and HCl trimers. *J. Chem. Phys.*, 91:7048-7056, 1989.
- [66] G. Chałasiński, M. M. Szcześniak, and S. M. Cybulski. Calculations of non-additive effects by means of supermolecular Møller-Plesset perturbation theory approach: Ar₃ and Ar₄. *J. Chem. Phys.*, 92:2481-2487, 1990.
- [67] G. Chałasiński, M. M. Szcześniak, and B. Kukawska-Tarnawska. Ab initio study of intermolecular potential for ArHCl. *J. Chem. Phys.*, 94:6677-6685, 1991.
- [68] G. Chałasiński and M. M. Szcześniak. Origins of structure and energetics of van der Waals clusters from ab initio calculations. *Chem. Rev.*, 94:1723-1765, 1994.
- [69] Huan-C. Chang and William Klemperer. Observation of ArHF (3000) and its combination modes by laser-induced fluorescence. *J. Chem. Phys.*, 98:2497-2506, 1993.
- [70] Huan-C. Chang and William Klemperer. State-specific vibrational predissociation and interconversion tunneling quenching at $3\nu_1$ and $3\nu_2$ of (HF)₂. *J. Chem. Phys.*, 98:9266-9278, 1993.
- [71] Huan-C Chang, Fu-Ming Tao, William Klemperer, Catherine Healey, and Jeremy M. Hutson. The Ar-HF intermolecular potential: Overtone spectroscopy and ab initio calculations. *J. Chem. Phys.*, 99:9337-9349, 1993.
- [72] Huan-C. Chang and William Klemperer. The vibrational second overtones of HF dimer: A quartet. *J. Chem. Phys.*, 100:1-14, 1994.
- [73] Huan-C. Chang and William Klemperer. High-overtone spectroscopy and photodissociation of hydrogen fluoride complexes. *Faraday Discuss.*, 97:00-00, 1994.
- [74] William B. Chapman, Aram Schiffman, Zhong-Quan Zhao, and David J. Nesbitt. Rotationally inelastic scattering of Ar and HF. page manuscript in preparation, 1995.

- [75] M. S. Child and R. T. Lawton. Local and normal vibrational states: A harmonically coupled anharmonic-oscillator model. *Faraday Discuss. Chem. Soc.*, 71:273-285, 1981.
- [76] M. S. Child. Local mode overtone spectra. *Acc. Chem. Res.*, 18:45-50, 1985.
- [77] M. S. Child and D. J. Nesbitt. RKR-based inversion of rotational progressions. *Chem. Phys. Lett.*, 149:404-410, 1988.
- [78] Benjamin Chu. *Molecular Forces; Based on the Baker Lectures by Peter J. W. Debye*. Interscience Publishers, New York, 1967.
- [79] David C. Clary, Christopher M. Lovejoy, S.V. O'Neil, and David J. Nesbitt. Infrared spectrum of NeHF. *Phys. Rev. Lett.*, 61:1576-1579, 1988.
- [80] Joseph I. Cline, Brian P. Reid, Dwight D. Evard, N. Sivakumar, Nadine Halberstadt, and Kenneth C. Janda. State-to-state vibrational predissociation dynamics and spectroscopy of HeCl₂: Experiment and theory. *J. Chem. Phys.*, 89:3535-3552, 1988.
- [81] Joseph I. Cline, N. Sivakumar, Dwight D. Evard, Craig R. Bieler, Brian P. Reid, Nadine Halberstadt, Sally R. Hair, and Kenneth C. Janda. Product state distributions for the vibrational predissociation of NeCl₂. *J. Chem. Phys.*, 90:2605-2616, 1989.
- [82] R. C. Cohen, Kerry L. Busarow, Y. T. Lee, and R. J. Saykally. Tunable far infrared laser spectroscopy of van der Waals bonds: The intermolecular stretching vibration and effective radial potentials for Ar-H₂O. *J. Chem. Phys.*, 92:169-183, 1990.
- [83] Ronald C. Cohen and R. J. Saykally. Multidimensional intermolecular potential surfaces from vibration-rotation-tunneling (VRT) spectra of van der Waals complexes. *Annu. Rev. Phys. Chem.*, 42:369-392, 1991.
- [84] R. C. Cohen and R. J. Saykally. Vibration-rotation-tunneling spectroscopy of the van der Waals bond: A new look at intermolecular forces. *J. Phys. Chem.*, 96:1024-1040, 1992.
- [85] Ronald C. Cohen and R. J. Saykally. Determination of an improved intermolecular global potential energy surface for Ar-H₂O from vibration-rotation-tunneling spectroscopy. *J. Chem. Phys.*, 98:6007-6030, 1993.
- [86] E. A. Colbourn and A. E. Douglas. The spectrum and ground state potential curve of Ar₂. *J. Chem. Phys.*, 65:1741-1745, 1976.
- [87] Adam R. Cooper, S. Jain, and Jeremy M. Hutson. Methods for calculating the bound state energies of van der Waals trimers: Applications to Ar₃. *J. Chem. Phys.*, 98:2160-2169, 1992.

- [88] Adam Cooper and Jeremy Hutson. Nonadditive intermolecular forces from the spectroscopy of van der Waals trimers: Calculations on Ar_2HCl . *J. Chem. Phys.*, 98:5337-5351, 1993.
- [89] R. A. Copeland, D. J. Pearson, Jeanne M. Robinson, and F. F. Crim. Laser double resonance measurements of vibrational energy transfer rates and mechanisms in $\text{HF}(v=2)$. *J. Chem. Phys.*, 77:3974-3982, 1982.
- [90] R. A. Copeland, D. J. Pearson, Jeanne M. Robinson, and F. F. Crim. Erratum: Laser double resonance measurements of vibrational energy transfer rates and mechanisms in $\text{HF}(v=2)$ [J. Chem. Phys. 77, 3974 (1982)]. *J. Chem. Phys.*, 78:6344, 1983.
- [91] M. J. Coulombe and A. S. Pine. Linear scan control of tunable lasers using a scanning Fabry-Perot. *Appl. Opt.*, 18:1505-1512, 1979.
- [92] Michael E. Cournoyer and William L. Jorgensen. An improved intermolecular potential function for simulations of liquid hydrogen fluoride. *Mol. Phys.*, 51:119-132, 1984.
- [93] Thomas E. Creighton. The problem of how and why proteins adopt folded conformations. *J. Phys. Chem.*, 89:2452-2459, 1985.
- [94] S. M. Cybulski, M. M. Szczeniński, and G. Chałasiński. Ab initio study of nonadditive interactions in the Ar_2HF and Ar_2HCl clusters. II. Analysis of exchange and induction effects. *J. Chem. Phys.*, 101:10708-10716, 1994.
- [95] Scott Davis, David T. Anderson, and David J. Nesbitt. Isotopic substitution of a hydrogen bond: A near-IR study of all four intermolecular modes in DF dimer. Manuscript in preparation.
- [96] Scott Davis, John T. Farrell, Jr., David T. Anderson, and David J. Nesbitt, 10^4 -fold isotope effect: A study of vibrational predissociation in ArDF ($v_{\text{DF}}=1$). Manuscript in preparation.
- [97] D. C. Dayton and R. E. Miller. Mode-dependent vibrational predissociation in the HCN-HF binary complex. *Chem. Phys. Lett.*, 143:181-185, 1988.
- [98] D. C. Dayton, K. W. Jucks, and R. E. Miller. Photofragment angular distributions for HF dimer: Scalar $J - J$ correlations in state-to-state photodissociation. *J. Chem. Phys.*, 90:2631-2638, 1989.
- [99] D. C. Dayton, P. A. Block, and R. E. Miller. Spectroscopic evidence for near-resonant intermolecular energy transfer in the vibrational predissociation of $\text{C}_2\text{H}_2\text{-HX}$ and $\text{C}_2\text{H}_2\text{-DX}$ ($\text{X}=\text{Cl}, \text{Br}, \text{and I}$) complexes. *J. Phys. Chem.*, 95:2881-2888, 1991.
- [100] Robert L. DeLeon and J. S. Muentzer. Vibrational predissociation in the hydrogen fluoride dimer. *J. Chem. Phys.*, 80:6092-6094, 1984.

- [101] J. N. Demas. *Excited State Lifetime Measurements*. Academic Press, New York, 1983.
- [102] W. Demtröder. *Laser Spectroscopy*. Springer-Verlag, Berlin, 1988.
- [103] T. A. Dixon, C. H. Joyner, F. A. Baiocchi, and W. Klemperer. The rotational and hyperfine spectrum of ArHF. *J. Chem. Phys.*, 74:6539-6543, 1981.
- [104] Janet C. Drobits and Marsha I. Lester. Optical-optical double resonance of the ICl-Ne complex: Binding energies in the $E(0^+)$, $A(3\Pi_1)$, and $X(1\Sigma^+)$ states. *J. Chem. Phys.*, 86:1662-1669, 1987.
- [105] Stephen Drucker, Fu-Ming Tao, and William Klemperer. Bound States of He-HCN: Ab Initio Calculation and High-Resolution Spectroscopy. *J. Phys. Chem.*, 99:2646, 1995.
- [106] J. R. Durig, editor. *Vibrational Spectra and Structure*. Elsevier, New York, 1990.
- [107] M. A. Dvorak, S. W. Reeve, W. A. Burns, A. Grushow, and K. R. Leopold. Observation of three intermolecular vibrational states in ArHF. *Chem. Phys. Lett.*, 185:399-402, 1991.
- [108] Thomas R Dyke, Brian J. Howard, and William Klemperer. Radiofrequency and microwave spectrum of the hydrogen fluoride dimer; a nonrigid molecule. *J. Chem. Phys.*, 56:2442-2454, 1972.
- [109] Clifford E. Dykstra. Molecular mechanics for weakly interacting assemblies of rare gas atoms and small molecules. *J. Am. Chem. Soc.*, 111:6168-6174, 1989.
- [110] David F. Eaton Nonlinear Optical Materials. *Science*, 253:281-287, 1991.
- [111] Bengt Edlen. The refractive index of air. *Metrologia*, 2:71-80, 1966.
- [112] M. J. Elrod, D. W. Steyert, and R. J. Saykally. Tunable far infrared laser spectroscopy of a ternary van der Waals cluster Ar₂HCl: A sensitive probe of three-body forces. *J. Chem. Phys.*, 94:58-66, 1991.
- [113] M. J. Elrod, D. W. Steyert, and R. J. Saykally. An investigation of three-body effects in intermolecular forces. II. Far-infrared vibration-rotation-tunneling laser spectroscopy of Ar₂HCl. *J. Chem. Phys.*, 95:3182-3190, 1991.
- [114] M. J. Elrod, J. G. Loeser, and R. J. Saykally. An investigation of three-body effects in intermolecular forces. III. Far infrared laser vibration-rotation-tunneling spectroscopy of the lowest internal rotor states of Ar₂HCl. *J. Chem. Phys.*, 98:5352-5361, 1993.
- [115] M. J. Elrod and R. J. Saykally. Many body effects in intermolecular forces. *Chem. Rev.*, 94:1975-1997, 1994.

- [116] M. J. Elrod, R. J. Saykally, Adam R. Cooper, and Jeremy H. Hutson. Non-additive intermolecular forces from the spectroscopy of van der Waals trimers: far-infrared spectra and calculations on Ar_2DCl . *Mol. Phys.*, 81:579-598, 1994.
- [117] Andreas Ernesti and Jeremy M. Hutson. Non-additive intermolecular forces from the spectroscopy of van der Waals trimers: the effect of monomer vibrational excitation in Ar_2HF and Ar_2HCl . *Faraday Discuss. Chem. Soc.*, 97:119-129, 1994.
- [118] Andreas Ernesti and Jeremy M. Hutson. Non-additive intermolecular forces from the spectroscopy of van der Waals trimers: a theoretical study of Ar_2HF . *Phys. Rev. A*, 51:239-250, 1995.
- [119] V. C. Epa and P. R. Bunker. The Watson $U(\rho)$ term in the one-dimensional semirigid bender Hamiltonian for the HF dimer. *J. Mol. Spectrosc.*, 150:511-520, 1991.
- [120] Andreas Ernesti and Jeremy M. Hutson. On the rotational constants of floppy molecules. *Chem. Phys. Lett.*, 222:257-262, 1994.
- [121] Andreas Ernesti and Jeremy M. Hutson. Non-additive intermolecular forces from the spectroscopy of van der Waals trimers: a theoretical study of Ar_2DF . *J. Chem. Phys.*, work in progress.
- [122] Dwight D. Evard, Craig R. Bieler, Joseph I. Cline, N. Sivakumar, and Kenneth C. Janda. The vibrational predissociation dynamics of ArCl_2 : Intramolecular vibrational relaxation in a triatomic van der Waals molecule? *J. Chem. Phys.*, 89:2829-2838, 1988.
- [123] George E. Ewing. A guide to the lifetimes of vibrationally excited van der Waals molecules: The momentum gap. *J. Chem. Phys.*, 71:3143-3144, 1979.
- [124] George E. Ewing. Vibrational predissociation in hydrogen bonded clusters. *J. Chem. Phys.*, 72:2096-2106, 1980.
- [125] George E. Ewing. Curve crossing and vibrational predissociation of van der Waals molecules. *Chem. Phys.*, 63:411-418, 1981.
- [126] George E. Ewing. Relaxation channels of vibrationally excited van der Waals molecules. *Faraday Discuss. Chem. Soc.*, 73:324-338, 1982.
- [127] George E. Ewing. Selection rules for vibrational energy transfer: Vibrational predissociation of van der Waals molecules. *J. Phys. Chem.*, 91:4662-4671, 1987.
- [128] John T. Farrell, Jr., Ofer Sneh, Andrew McIlroy, Alan E. W. Knight, and David J. Nesbitt. High resolution infrared overtone spectroscopy of ArHF via Nd:YAG/dye laser difference frequency generation. *J. Chem. Phys.*, 97:7967-7978, 1992.

- [129] John T. Farrell, Jr., Ofer Sneh, and David J. Nesbitt. High resolution infrared overtone spectroscopy of N_2HF : Vibrational redshifts and predissociation rate as a function of HF stretching quanta. *J. Phys. Chem.*, 98:6068-6074, 1994.
- [130] John T. Farrell, Jr., Scott Davis, and David J. Nesbitt. Structural and dynamical manifestations of non-pairwise additive forces in weakly bound complexes: High resolution infrared spectroscopy on Ar_nDF , $n=1-3$. *J. Chem. Phys.*, in press.
- [131] John T. Farrell, Jr. and David J. Nesbitt. Near-IR spectroscopy of Ar_2HF and Ar_2DF intermolecular van der Waals modes: Detailed probes of nonadditive intermolecular forces. Manuscript in preparation.
- [132] John T. Farrell, Jr., Martin A. Suhm, and David J. Nesbitt. High resolution infrared spectroscopy of DF-DF, HF-DF, and DF-HF: Isotopic shifts, vibrational state mixing, and isotope-, mode-, and j - specific vibrational predissociation lifetimes. Manuscript in preparation.
- [133] J.-M. Flaud, C. Camy-Peyret, and R. A. Toth. *Water Vapour Line Parameters From Microwave To Medium Infrared*. Pergamon Press, Oxford, 1981.
- [134] E. U. Franck and F. Meyer. Fluorwasserstoff III: Spezifische wärme und assoziation im gas bei niedrigem druck. *Z. Elektrochem.*, 63:571-582, 1959.
- [135] G. T. Fraser and A. S. Pine. van der Waals potentials from the infrared spectra of rare gas-HF complexes. *J. Chem. Phys.*, 85:2502-2515, 1986.
- [136] G. T. Fraser, A. S. Pine, W. J. Lafferty, and R. E. Miller. Sub-Doppler infrared spectrum of the carbon dioxide trimer. *J. Chem. Phys.*, 87:1502-1508, 1987.
- [137] G. T. Fraser and A. S. Pine, and R. D. Suenram. Optothermal-infrared and pulsed-nozzle Fourier-transform microwave spectroscopy of rare gas- CO_2 complexes *J. Chem. Phys.*, 88:6157-6167, 1988.
- [138] G. T. Fraser and A. S. Pine. Vibrational predissociation in the HF stretching mode of HF-DF. *J. Chem. Phys.*, 91:633-636, 1989.
- [139] G. T. Fraser and A. S. Pine. Microwave and infrared electric-resonance optothermal spectroscopy of HF-HCl and HCl-HF. *J. Chem. Phys.*, 91:637-645, 1989.
- [140] G. T. Fraser and A. S. Pine. Infrared and microwave study of angular-radial coupling effects in Ar-HCN. *J. Chem. Phys.*, 91:3319-3326, 1989. Has revised estimate for lifetime of Ar-HF $v=1$ of $\tau > 600 \mu\text{sec}$.
- [141] G. T. Fraser. Vibrational exchange upon interconversion tunneling in $(HF)_2$ and $(HCCO)_2$. *J. Chem. Phys.*, 90:2097-2108, 1989.
- [142] H. Friedman and S. Kimel. Theory of shifts of vibration-rotation lines of diatomic molecules in noble-gas matrices. Intermolecular forces in crystals. *J. Chem. Phys.*, 43:3925, 1965.

- [143] Aaron W. Garrett and Timothy S. Zwier. Multiphoton ionization studies of clusters of immiscible liquids. II. $C_6H_6-(H_2O)_n$, $n=3-8$ and $(C_6H_6)_2-(H_2O)_{1,2}$. *J. Chem. Phys.*, 96:3402-3410, 1992.
- [144] Jeffrey F. Gaw, Yukio Yamaguchi, Mark A. Vincent, and Henry F. Schaeffer III. Vibrational frequency shifts in hydrogen-bonded systems: The hydrogen fluoride dimer and trimer. *J. Am. Chem. Soc.*, 106:3133-3138, 1984.
- [145] S. Gerstenkorn and P. Luc. *Atlas du spectroscopie d'absorption de la molecule d'iode*. CRNS, Paris, 1978.
- [146] Walter Gordy and Robert L. Cook. *Microwave Molecular Spectra*. Interscience Publishers, New York, 1970.
- [147] Sheldon Green and Jeremy Hutson. Spectral line shape parameters for HF in a bath of Ar are accurately predicted by a potential inferred from spectra of the van der Waals dimer. *J. Chem. Phys.*, 100:891-898, 1994.
- [148] G. Guelachvili. Absolute wavenumber measurements of 1-0, 2-0, HF and 2-0, $H^{35}Cl$, $H^{37}Cl$ absorption bands. *Opt. Comm.*, 19:150-154, 1976.
- [149] H. S. Gutowsky, T. D. Klots, Carl Chuang, John D. Keen, C. A. Schmuttenmaer, and Tryggvi Emilsson. Rotational spectra and structures of small clusters: Ar_3HF and Ar_3DF . *J. Am. Chem. Soc.*, 107:7174-7175, 1985.
- [150] H. S. Gutowsky, T. D. Klots, Carl Chuang, C. A. Schmuttenmaer, and Tryggvi Emilsson. Rotational spectrum and structure of the Ar_2HF trimer. *J. Chem. Phys.*, 83:4817-4818, 1985.
- [151] H. S. Gutowsky, Carl Chuang, John D. Keen, T. D. Klots, and Tryggvi Emilsson. Microwave rotational spectra, hyperfine interactions, and structure of the hydrogen fluoride dimers. *J. Chem. Phys.*, 83:2070-2077, 1985.
- [152] H. S. Gutowsky, T. D. Klots, Carl Chuang, C. A. Schmuttenmaer, and Tryggvi Emilsson. Rotational spectra and structures of the Ar_2-H/DF trimers. *J. Chem. Phys.*, 86:569-576, 1987.
- [153] H. S. Gutowsky, T. D. Klots, Carl Chuang, John D. Keen, C. A. Schmuttenmaer, and Tryggvi Emilsson. Rotational spectra and structures of the small clusters Ar_3HF and Ar_3DF . *J. Am. Chem. Soc.*, 109:5633-5638, 1987.
- [154] H. S. Gutowsky, Carl Chuang, T. D. Klots, Tryggvi Emilsson, R. S. Ruoff, and Karl R. Krause. Rotational spectra and structures of small clusters: The Ar_4-H/DF pentamers. *J. Chem. Phys.*, 88:2919-2924, 1988.
- [155] H. S. Gutowsky, T. D. Klots, and C. E. Dykstra. Rotational spectrum and potential surface for Ar_2-HCN : A T-shaped cluster with internal rotation. *J. Chem. Phys.*, 93:6216-6225, 1990.

- [156] Sally R. Hair, Joseph I. Cline, Craig R. Bieler, and Kenneth C. Janda. The structure and dissociation dynamics of the Ne_2Cl_2 van der Waals complex. *J. Chem. Phys.*, 90:2935-2943, 1989.
- [157] N. Halberstadt, Ph. Bréchnignac, J. A. Beswick, and M. Shapiro. Theory of mode specific vibrational predissociation: The HF dimer. *J. Chem. Phys.*, 84:170-175, 1986.
- [158] N. Halberstadt and K. C. Janda, editors. *Dynamics of Polyatomic van der Waals Complexes*, Vol. 227 of NATO Advanced Study Institute, Series B:Physics. Plenum, New York, 1990.
- [159] J. L. Hall and S. A. Lee. Interferometric real-time display of cw dye laser wavelength with sub-Doppler accuracy. *Appl. Phys. Lett.*, 29:367-369, 1976.
- [160] Jun Han, Zhongcheng Wang, Avery L. McIntosh, Robert R. Lucchese, and John W. Bevan. Investigation of the ground vibrational state structure of H^{35}Cl trimer based on the resolved K , J substructure of the ν_5 vibrational band. *J. Chem. Phys.*, 100:7101-7108, 1994.
- [161] Gene C. Hancock, Donald G. Truhlar, and Clifford E. Dykstra. An analytic representation of the six-dimensional potential energy surface of hydrogen fluoride dimer. *J. Chem. Phys.*, 88:1786-1796, 1988.
- [162] Gene C. Hancock and Donald G. Truhlar. Reaction-path analysis of the effect of monomer excitation on the tunneling splitting of the hydrogen fluoride dimer. *J. Chem. Phys.*, 90:3498-3505, 1989.
- [163] T. W. Hänsch and B. Couillaud. Laser frequency stabilization by polarization spectroscopy of a reflecting reference cavity. *Opt. Comm.*, 35:441-444, 1980.
- [164] Stephen J. Harris, Stewart E. Novick, and William Klemperer. Determination of the structure of ArHF . *J. Chem. Phys.*, 60:3208-3209, 1974.
- [165] Detlev Häusler, Jane Rice, and Curt Wittig. $\text{CO}(X^2\Pi)$ and $\text{SD}(X^2\Pi)$ from reactions of D atoms with OCS under bulk and precursor geometry limited conditions. *J. Phys. Chem.*, 91:5413-5415, 1987.
- [166] Michael C. Heaven. Spectroscopy and dynamics of open-shell van der Waals molecules. *Annu. Rev. Phys. Chem.*, 43:283-, 1992.
- [167] D. Heidrich, M. Rückert, D. Volkmann, and H.-J. Köhler. Zyklische H-transferstrukturen in der gasphase: Ab-initio-berechnungen an HF-dimeren und trimeren. *Z. Chem.*, 24:419-420, 1984.
- [168] J. Helmcke, J. J. Snyder, A. Morinaga, F. Mensing, and M. Gläser. *Appl. Phys. B*, 43:85, 1987.
- [169] P. R. Herman, P. E. LaRocque, and B. P. Stoicheff. Vacuum ultraviolet laser spectroscopy. V. Rovibronic spectra of Ar_2 and constants of hte ground and excited states. *J. Chem. Phys.*, 89:4535-4549, 1988.

- [170] G. Herzberg. *Infrared and Raman Spectra of Polyatomic Molecules*. Van Nostrand, New York, 1945. p 421.
- [171] G. Herzberg. *Molecular Spectra and Molecular Structure I. Spectra of Diatomic Molecules*. Van Nostrand Reinhold, New York, 1950.
- [172] Joanne R. Hetzler, Michael P. Casassa, and David S. King. Product energy correlations in the dissociation of overtone excited NO dimer. *J. Phys. Chem.*, 95:8086-8095, 1991.
- [173] Thomas V Higgins Nonlinear crystals: Where the colors of the rainbow begin. *Laser Focus World*, 28:125-133, 1992.
- [174] J. O. Hirschfelder, C. F. Curtiss, and R. B. Bird. *Molecular Theory of Gases and Liquids*. Wiley, New York, 1954.
- [175] Jon T. Hougen and Nobukimi Ohashi. Group theoretical treatment of the planar internal rotation problem in $(\text{HF})_2$. *J. Mol. Spec.*, 109:134-165, 1985.
- [176] J. Hough, D. Hills, M. D. Rayman, L.-S. Ma, L. Hollberg, and J. L. Hall. *Appl. Phys. B*, 33:179, 1984.
- [177] Brian J. Howard, Thomas R. Dyke, and William Klemperer. The molecular beam spectrum and the structure of the hydrogen fluoride dimer. *J. Chem. Phys.*, 81:5417, 1984.
- [178] B. J. Howard and A. S. Pine. Rotational predissociation and libration in the infrared spectrum of Ar-HCl. *Chem. Phys. Lett.*, 122:1-8, 1985.
- [179] B. J. Howard. High resolution infrared spectroscopy of van der Waals molecules. In Weber [371], pages 69-84.
- [180] Wu-Yi Hsiang. On the sphere packing problem and the proof of Kepler's conjecture. *Int. J. Math.*, 4:739-831, 1993.
- [181] Z. S. Huang, K. W. Jucks, and R. E. Miller. The argon-hydrogen fluoride binary complex: An example of a long lived metastable system. *J. Chem. Phys.*, 85:6905-6909, 1986.
- [182] Z. S. Huang, K. W. Jucks, and R. E. Miller. The vibrational predissociation lifetime of the HF dimer upon exciting the "free-H" stretching vibration. *J. Chem. Phys.*, 85:3338-3341, 1986.
- [183] Z. S. Huang and R. E. Miller. Sub-Doppler resolution infrared spectroscopy of water dimer. *J. Chem. Phys.*, 88:8008-8009, 1988.
- [184] K. P. Huber and G. Herzberg. *Constants of Diatomic Molecules*. Van Nostrand Reinhold, New York, 1979.
- [185] Friedrich Huisken. Infrared vibrational predissociation spectroscopy of small size-selected clusters. *Adv. Chem. Phys.*, 81:63-140, 1992.

- [186] Jeremy M. Hutson. The intermolecular potential of Ar-HCl: Determination from high-resolution spectroscopy. *J. Chem. Phys.*, 89:4550-4557, 1988.
- [187] Jeremy M. Hutson, J. Alberto Beswick, and Nadine Halberstadt. A theoretical study of the Ar₂HCl van der Waals cluster. *J. Chem. Phys.*, 90:1337-1344, 1989.
- [188] Jeremy M. Hutson. The intermolecular potential of Ne-HCl: Determination from high-resolution spectroscopy. *J. Chem. Phys.*, 91:4448-4454, 1989.
- [189] Jeremy M. Hutson. Atom-asymmetric top van der Waals complexes: Angular momentum coupling in Ar-H₂O. *J. Chem. Phys.*, 92:157-168, 1990.
- [190] Jeremy M. Hutson. Vibrational dependence of the anisotropic intermolecular potential of Ar-HF. *J. Chem. Phys.*, 96:6752-6767, 1992.
- [191] Jeremy M. Hutson. Vibrational dependence of the anisotropic intermolecular potential of ArHCl. *J. Phys. Chem.*, 96:4237-4247, 1992.
- [192] J. M. Hutson. Private communication.
- [193] Jacob N. Israelachvili. *Intermolecular and Surface Forces*. Academic Press, London, 1985.
- [194] H. A. Jahn. Note on Coriolis coupling terms in polyatomic molecules. *Phys. Rev.*, 56:680-683, 1939.
- [195] Jay Janzen and L. S. Bartell. Electron-diffraction structural study of polymeric gaseous hydrogen fluoride. *J. Chem. Phys.*, 50:3611-3618, 1969.
- [196] Per Jensen, P. R. Bunker, Alfred Karpfen, Manfred Kofranek, and Hans Lischka. An ab initio calculation of the intramolecular stretching spectra for the HF dimer and its D-substituted isotopic species. *J. Chem. Phys.*, 93:6266-6280, 1990.
- [197] Per Jensen, P. R. Bunker, and A. Karpfen. An ab initio calculation of the nonadiabatic effect of the tunneling splitting in vibrationally excited (HF)₂. *J. Mol. Spectrosc.*, 148:385-390, 1991.
- [198] Melvin D. Joesten and L. J. Schaad. *Hydrogen Bonding*. Marcel Dekker, Inc., New York, 1974.
- [199] William L. Jolly. *Modern Inorganic Chemistry*. McGraw-Hill, New York, 1984.
- [200] D. L. Joo, Dennis J. Clouthier, and A. J. Merer. Determination of the spectroscopic constants of a dark vibrational state: Fermi and Coriolis perturbations in the ν_2 band of formyl chloride. *J. Chem. Phys.*, 101:31-38, 1994.
- [201] K. W. Jucks, Z. S. Huang, and Roger E. Miller. The nitrogen-hydrogen fluoride dimer: Infrared spectroscopy and vibrational predissociation. *J. Chem. Phys.*, 86:1098-1103, 1987.

- [202] K. W. Jucks, Z. S. Huang, D. Dayton, R. E. Miller, and W. J. Lafferty. The structure of the carbon dioxide dimer from near infrared spectroscopy. *J. Chem. Phys.*, 86:4341-4346, 1987.
- [203] K. W. Jucks and R. E. Miller. The effect of vibrational state mixing on the predissociation lifetime of OC-HF. *J. Chem. Phys.*, 86:6637-6645, 1987.
- [204] K. W. Jucks, Z. S. Huang, R. E. Miller, G. T. Fraser, A. S. Pine, and W. J. Lafferty. Structure and vibrational dynamics of the CO₂ dimer from the sub-Doppler infrared spectrum of the 2.7 μm Fermi diad. *J. Chem. Phys.*, 88:2185-2195, 1988.
- [205] K. W. Jucks and R. E. Miller. Infrared spectroscopy of the hydrogen cyanide dimer. *J. Chem. Phys.*, 88:6059-6067, 1988.
- [206] K. W. Jucks and R. E. Miller. Near infrared spectroscopic observation of the linear and cyclic isomers of the hydrogen cyanide trimer. *J. Chem. Phys.*, 88:2196-2204, 1988.
- [207] Alfred Karpfen. Ab initio studies on hydrogen bonded clusters: Structure and vibrational spectra of cyclic (HF)_n complexes. *Int. J. Quantum Chem., Quantum Chem. Symp.*, 24:129-140, 1990.
- [208] M. R. Keenan, E. J. Campbell, T. J. Balle, L. W. Buxton, T. K. Minton, P. D. Soper, and W. H. Flygare. Rotational spectra and molecular structures of ArHBr and KrHBr. *J. Chem. Phys.*, 72:3070-3080, 1980.
- [209] M. R. Keenan, L. W. Buxton, E. J. Campbell, and W. H. Flygare. Molecular structure of ArDF: An analysis of the bending mode in the rare gas-hydrogen halides. *J. Chem. Phys.*, 74:2133-2137, 1981.
- [210] Jonathan E. Kenny, Kenneth E. Johnson, Wayne Sharfin, and Donald H. Levy. The photodissociation of van der Waals molecules: Complexes of iodine, neon, and helium. *J. Chem. Phys.*, 72:1109-1119, 1980.
- [211] E. R. Th. Kerstel, H. Meyer, K. K. Lehmann, and G. Scoles. The rotationally resolved 1.5 μm spectrum of the HCN-HF hydrogen-bonded complex. *J. Chem. Phys.*, 97:8896-8905, 1992.
- [212] M. L. Klein, editor. *Inert Gases*. Springer, Berlin, 1989.
- [213] William Klemperer. Comment during general discussion. *Faraday Disc. Chem. Soc.*, 96:363, 1994.
- [214] T. D. Klots, Carl Chuang, R. S. Ruoff, T. Emilsson, and H. S. Gutowsky. Rotational spectra and structures of the Ar₂H³⁵Cl/³⁷Cl trimers. *J. Chem. Phys.*, 86:5315-5322, 1987.
- [215] Mary Ann Kmetc and Robert J. LeRoy. Infrared signatures for isomerization and melting in inhomogeneous van der Waals clusters. *J. Chem. Phys.*, 95:6271-6283, 1991.

- [216] Manfred Kofranek, Hans Lischka, and Alfred Karpfen. Coupled pair functional study on the hydrogen fluoride dimer. 1. Energy surface and characterization of stationary points. *Chem. Phys.*, 121:137-153, 1988.
- [217] Kirk D. Kolenbrander and James M. Lisy. Vibrational predissociation spectroscopy of binary HF-base complexes. *J. Chem. Phys.*, 85:2463-2471, 1986.
- [218] Kirk D. Kolenbrander, Clifford E. Dykstra, and James M. Lisy. Torsional vibrational modes of (HF)₃: IR-IR double resonance spectroscopy and electrical interaction theory. *J. Chem. Phys.*, 88:5995-6012, 1988.
- [219] Andrew Komornicki, David A. Dixon, and Peter R. Taylor. Concerted hydrogen atom exchange between three HF molecules. *J. Chem. Phys.*, 96:2920-2925, 1992.
- [220] H. W. Kroto. *Molecular Rotation Spectra*. Dover, New York, 1992.
- [221] G. A. Kuipers. The spectrum of monomeric hydrogen fluoride: line shapes, intensities, and breadths. *J. Mol. Spectrosc.*, 2:75-98, 1958.
- [222] W. J. Lafferty, R. D. Suenram, and F. J. Lovas. Microwave spectra of (HF)₂, (DF)₂, HFDF, and DFHF hydrogen bonded complexes. *J. Mol. Spectroscopy*, 123:434-452, 1987.
- [223] Robert Lascola and David J. Nesbitt. Slit-jet near-infrared spectroscopy and internal rotor dynamics of the ArH₂O van der Waals complex: An angular potential-energy surface for internal H₂O rotation. *J. Chem. Phys.*, 95:7917-7932, 1991.
- [224] Curtis Laush, James M. Lisy, Friedrich Huisken, and Axel Kulcke. The experimental determination of vibrational transition moments for HF dimer. *J. Chem. Phys.*, 98:5982-5984, 1993.
- [225] A. C. Legon, P. D. Soper, and W. H. Flygare. The rotational spectrum, ¹⁴N-nuclear quadrupole coupling constants, and H,¹⁹F nuclear spin-nuclear spin coupling constant of the cyanogen-hydrogen fluoride dimer. *J. Chem. Phys.*, 74:4936-4943, 1981.
- [226] A. C. Legon and D. J. Millen. Determination of properties of hydrogen-bonded dimers by rotational spectroscopy and a classification of dimer geometries. *Faraday Discuss. Chem. Soc.*, 73:71-87, 1982. Pretty good description of assigning equilibrium geometries to weakly bound complexes.
- [227] K. R. Leopold, G. T. Fraser, S. E. Novick, and W. Klemperer. Current themes in microwave and infrared spectroscopy of weakly bound complexes. *Chem. Rev.*, 94:1807-1827, 1994.
- [228] Frédéric Le Quéré and Stephen K. Gray. Quantum dynamics of van der Waals clusters: Model results for He₂Cl₂ and Ne₂Cl₂ fragmentation. *J. Chem. Phys.*, 98:5396-5407, 1993.

- [229] Robert J. Le Roy and Jeremy M. Hutson. Ar-H₂ potential. *J. Chem. Phys.*, 86:837, 1987.
- [230] Robert J. Le Roy, Mark R. Davies, and Mimi E. Lam. Rate proportional to (frequency shift)² and other "all else being equal" correlations in vibrational predissociation. *J. Phys. Chem.*, 95:2167-2175, 1991.
- [231] Samuel Leutwyler and Jürg Bösiger. Microscopic solvation: The first solvent shell. *Faraday Discuss. Chem. Soc.*, 86:225-240, 1988.
- [232] Donald H. Levy. van der Waals molecules. *Adv. Chem. Phys.*, 47:323-362, 1981.
- [233] M. Lewerenz. Quantum Monte Carlo calculation of argon-HF clusters: Non-additive forces, isomerization, and HF frequency shifts. *J. Chem. Phys.*, in press.
- [234] M. Lewerenz. Private communication.
- [235] Xiuling Li, M. Y. Hahn, M. S. El-Shall, and Robert L. Whetten. Nonbulk convergence of solvent spectral shifts in doped molecular clusters. *J. Phys. Chem.*, 95:8524-8528, 1991.
- [236] Nurit Lipkin, Nimrod Moiseyev, and Claude Leforestier. A three dimensional study of necl predissociation resonances by the complex scaled discrete variable representation method. *J. Chem. Phys.*, 98:1888-1901, 1993.
- [237] James M. Lisy, Andrzej Tramer, Matthew F. Vernon, and Yuan T. Lee. Vibrational predissociation spectra of (HF)_n, n=2-6. *J. Chem. Phys.*, 75:4733-4734, 1981.
- [238] Shi-Yi Liu and Clifford E. Dykstra. A theory of vibrational transition frequency shifts due to hydrogen bonding. *J. Phys. Chem.*, 90:3097-3103, 1986.
- [239] Shi-Yi Liu, Clifford E. Dykstra, and David J. Malik. Electrical effects on the vibrational transitions of hydrogen fluoride due to hydrogen bonding and applied fields. *Chem. Phys. Lett.*, 130:403-409, 1986.
- [240] Shi-Yi Liu and Clifford E. Dykstra. Electrically caused vibrational frequency shifts and dipole moments in rare gas hydrogen bonded complexes. *Chem. Phys. Lett.*, 136:22-25, 1987.
- [241] Suyan Liu, Zlatko Bačić, Jules W. Moskowitz, and Kevin E. Schmidt. Equilibrium structures and approximate HF vibrational redshifts for Ar_nHF (n=1-14) van der Waals clusters. *J. Chem. Phys.*, 100:7166-7181, 1994.
- [242] Suyan Liu, Zlatko Bačić, Jules W. Moskowitz, and Kevin E. Schmidt. HF vibrational red shift for the icosahedral Ar₁₂HF van der Waals cluster is the same as in an Ar matrix: quantum five-dimensional bound state calculations. *J. Chem. Phys.*, page submitted, 1994.

- [243] Christopher M. Lovejoy, Michael D. Schuder, and David J. Nesbitt. High resolution IR laser spectroscopy of van der Waals complexes in slit supersonic jets: Observation and analysis of ν_1 , $\nu_1 + \nu_2$, and $\nu_1 + 2\nu_3$ in ArHF. *J. Chem. Phys.*, 85:4890-4902, 1986.
- [244] Christopher M. Lovejoy and David J. Nesbitt. High sensitivity, high-resolution IR laser spectroscopy in slit supersonic jets: Application to N₂HF ν_1 and $\nu_5 + \nu_1 - \nu_5$. *J. Chem. Phys.*, 86:3151-3165, 1987.
- [245] Christopher M. Lovejoy, Jr. David D. Nelson, and David J. Nesbitt. Hindered internal rotation in jet cooled H₂HF. *J. Chem. Phys.*, 87:5621-5628, 1987.
- [246] Christopher M. Lovejoy and David J. Nesbitt. The near-infrared spectrum of ONNHF — direct evidence for geometric isomerism in a hydrogen bonded cluster. *J. Chem. Phys.*, 87:1450-1451, 1987.
- [247] Christopher M. Lovejoy and David J. Nesbitt. Slit pulsed valve for generation of long-path-length supersonic expansions. *Rev. Sci. Instrum.*, 58:807-811, 1987.
- [248] Christopher M. Lovejoy and David J. Nesbitt. Infrared-active combination bands in ArHCl. *Chem. Phys. Lett.*, 146:582-588, 1988.
- [249] Christopher M. Lovejoy, David D. Nelson, Jr., and David J. Nesbitt. The infrared spectrum of D₂HF. *J. Chem. Phys.*, 89:7180-7188, 1988.
- [250] Christopher M. Lovejoy and David J. Nesbitt. The infrared spectrum of nitrous oxide-HF isomers. *J. Chem. Phys.*, 90:4671-4680, 1989.
- [251] Christopher M. Lovejoy and David J. Nesbitt. Intramolecular dynamics of van der Waals molecules: An extended infrared study of ArHF. *J. Chem. Phys.*, 91:2790-2807, 1989.
- [252] Christopher M. Lovejoy and David J. Nesbitt. Mode specific internal and direct rotational predissociation in HeHF, HeDF, and HeHCl: van der Waals complexes in the weak binding limit. *J. Chem. Phys.*, 93:5387-5407, 1990.
- [253] Christopher M. Lovejoy and David J. Nesbitt. Rotational predissociation, vibrational mixing, and van der Waals intermolecular potentials of NeDF. *J. Chem. Phys.*, 94:208-223, 1991.
- [254] Christopher M. Lovejoy. *Intramolecular dynamics of van der Waals complexes as elucidated by infrared spectroscopy in slit supersonic expansions*. PhD thesis, University of Colorado, 1991.
- [255] C. M. Lovejoy, J. H. Hutson, and D. J. Nesbitt. A spectroscopic puzzle in ArHF solved: The test of a new potential. *J. Chem. Phys.*, 97:8009-8018, 1992.
- [256] Christopher M. Lovejoy, Theodore G. Lindemann, and David J. Nesbitt. Rotation-induced mode mixing in ArDF. Manuscript in preparation.

- [257] Roy A. Lucht and Terrill A. Cool. Temperature dependence of vibrational relaxation in the HF-DF, HF-CO₂, and DF-CO₂ systems. II. *J. Chem. Phys.*, 63:3962-3970, 1975.
- [258] David Luckhaus and Martin Quack. The far infrared pure rotational spectrum and the Coriolis coupling between ν_3 and ν_8 in CH³⁵ClF₂. *Mol. Phys.*, 68:745-758, 1989.
- [259] David Luckhaus, Martin Quack, Ulrich Schmitt, and Martin A. Suhm. On FTIR spectroscopy in asynchronously pulsed supersonic free jet expansions and on the interpretation of stretching spectra of HF clusters. *Ber. Bunsenges. Phys. Chem.*, 99:457-468, 1995.
- [260] Geoffrey C. Maitland, Maurice Rigby, E. Brian Smith, and William Wakeham. *Intermolecular Forces*. Clarendon, Oxford, 1987.
- [261] Mark D. Marshall, Per Jensen, and P. R. Bunker. An ab initio close-coupling calculation of the lower vibrational energies of the HF dimer. *Chem. Phys. Lett.*, 176:255-260, 1991.
- [262] Mark D. Marshall, E. J. Bohac, and R. E. Miller. Vector correlations in the vibrational predissociation of hydrogen fluoride dimer. *J. Chem. Phys.*, 97:3307-3317, 1992.
- [263] M. G. Mason, W. G. Von Holle, and D. W. Robinson. Mid- and far-infrared spectra of HF and DF in rare-gas matrices. *J. Chem. Phys.*, 54:3491-3499, 1971.
- [264] Andrew McIlroy and David J. Nesbitt. Narrow band 1.2-2.2 μm light via cw Nd:YAG/dye laser difference frequency generation: Application to the overtone absorption spectrum of ArHF. *Chem. Phys. Lett.*, 187:215-219, 1991.
- [265] Andrew McIlroy, Robert Lascola, Christopher M. Lovejoy, and David J. Nesbitt. Structural dependence of HF vibrational red shifts in Ar_nHF, n=1-4, via high-resolution slit jet infrared spectroscopy. *J. Phys. Chem.*, 95:2636-2644, 1991.
- [266] Andrew McIlroy. *Intermolecular rovibrational dynamics of hydrocarbons and Ar_nHF van der Waals clusters via high resolution infrared spectroscopy*. PhD thesis, University of Colorado, 1991.
- [267] Andrew McIlroy and David J. Nesbitt. Intermolecular HF motion in Ar_nHF micromatrices (n=1,2,3,4): Classical and quantum calculations on a pairwise additive potential surface. *J. Chem. Phys.*, 97:6044-6056, 1992.
- [268] H. Meyer, E. R. Th. Kerstel, D. Zhuang, and G. Scoles. Sub-doppler rotationally resolved overtone spectroscopy of the HCN dimer. *J. Chem. Phys.*, 90:4623-4625, 1989.

- [269] Daniel W. Michael, Clifford E. Dykstra, and James M. Lisy. Changes in the electronic structure and vibrational potential of hydrogen fluoride upon dimerization: A well-correlated (HF_2 potential energy surface. *J. Chem. Phys.*, 81:5998-6006, 1984.
- [270] Daniel W. Michael and James M. Lisy. Vibrational predissociation spectroscopy of $(\text{HF})_3$. *J. Chem. Phys.*, 85:2528-2537, 1986.
- [271] J. E. Midwinter and J. Warner. The effects of phase matching method and of uniaxial crystal symmetry on the polar distribution of second-order non-linear optical polarization. *Brit. J. Appl. Phys.*, 16:1135-1142, 1965.
- [272] R. E. Miller. The vibrational spectroscopy and dynamics of weakly bound neutral complexes. *Science*, 240:447-453, 1988.
- [273] R. E. Miller. Vibrationally induced dynamics in hydrogen-bonded complexes. *Acc. Chem. Res.*, 23:10-16, 1990.
- [274] W. H. Miller. On the relation between absorption linewidths, intramolecular vibrational energy redistribution (IVR), and unimolecular decay rates. *Phys. Rep.*, 199:124-129, 1991.
- [275] R. E. Miller. Optothermal vibrational spectroscopy of molecular complexes. In Bowman [46], pages 83-108.
- [276] R. E. Miller. Private communication. 1993.
- [277] R. E. Miller. Private communication.
- [278] Ian M. Mills. Born-Oppenheimer failure in the separation of low-frequency molecular vibrations. *J. Phys. Chem.*, 88:532-536, 1984.
- [279] I. M. Mills and A. G. Robiette. On the relationship of normal modes to local modes in molecular vibrations. *Mol. Phys.*, 56:743-765, 1985.
- [280] Y. Muto. *Proc. Phys. Math. Soc. Japan*, 17:629, 1943.
- [281] David J. Nesbitt. High-resolution infrared spectroscopy of weakly bound molecular complexes. *Chem. Rev.*, 88:843-870, 1988.
- [282] D. J. Nesbitt, C. M. Lovejoy, S. V. O'Neil, and D. C. Clary. Slit jet infrared spectroscopy of NeHF complexes: Internal rotor and J -dependent predissociation dynamics. *J. Chem. Phys.*, 91:722-731, 1989.
- [283] David J. Nesbitt, Mark S. Child, and David C. Clary. Rydberg-Klein-Rees inversion of high resolution van der Waals infrared spectra: An intermolecular potential energy surface for $\text{Ar} + \text{HF}$ ($v=1$). *J. Chem. Phys.*, 90:4855-4864, 1989.
- [284] David J. Nesbitt and Christopher M. Lovejoy. Multiple intermolecular bend vibrational excitation of a hydrogen bond: An extended infrared study of OCOHF . *J. Chem. Phys.*, 93:7716-7730, 1990.

- [285] David J. Nesbitt and Robert Lascola. Vibration, rotation, and parity specific predissociation dynamics in asymmetric OH stretch excited ArH₂O: A half collision study of resonant V-V energy transfer in a weakly bound complex. *J. Chem. Phys.*, 97:8096-8110, 1992.
- [286] David J. Nesbitt and Mark S. Child. Rotational-RKR inversion of intermolecular stretching potentials: Extension to linear hydrogen bonded complexes. *J. Chem. Phys.*, 98:478-486, 1993.
- [287] David J. Nesbitt, Theodore J. Lindeman, John T. Farrell, Jr., and Chris M. Lovejoy. Slit jet IR spectroscopy of hydrogen bonded N₂HF isotopomers: Rotational RKR analysis and H/D dependent vibrational predissociation rates. *J. Chem. Phys.*, 100:775-785, 1994.
- [288] David J. Nesbitt. High-Resolution, direct infrared laser absorption spectroscopy in slit supersonic jets: Intermolecular forces and unimolecular dynamics in clusters. *Annu. Rev. Phys. Chem.*, 45:367-399, 1994.
- [289] Scott L. Nikolaisen, Harry E. Cartland, and Curt Wittig. CO internal excitation from the reaction: H+CO₂ → CO + OH. *J. Chem. Phys.*, 96:4378-4386, 1992.
- [290] T. M. Niebauer, James E. Faller, H. M. Godwin, John L. Hall, and R. L. Barger. Frequency stability measurements on polarization-stabilized HeNe lasers. *App. Opt.*, 27:1285-1289, 1988.
- [291] Stewart E. Novick, Paul Davies, Stephen J. Harris, and William Klemperer. Determination of the structure of ArHCl. *J. Chem. Phys.*, 59:2273-2279, 1973.
- [292] S. V. O'Neil, D. J. Nesbitt, P. Rosmus, H.-J. Werner, and D. C. Clary. Weakly bound NeHF. *J. Chem. Phys.*, 91:711-721, 1989.
- [293] N. Papineau, C. Camy-Peyret, and J.-M. Flaud. The 2ν₂ and ν₁ bands of HD¹⁶O. *J. Mol. Spectrosc.*, 92:451-468, 1982.
- [294] D. Papoušek and M. R. Aliev. *Molecular Vibrational-Rotational Spectra*. Elsevier Scientific Publishing Company, Amsterdam, 1982.
- [295] Linus Pauling. *The Nature of the Chemical Bond*. Cornell University Press, Ithaca, New York, 1940.
- [296] A. S. Pine. Doppler-limited molecular spectroscopy by difference-frequency mixing. *J. Opt. Soc. Am.*, 64:1683-1690, 1974.
- [297] A. S. Pine. Collisional narrowing of HF fundamental band spectral lines by neon and argon. *J. Mol. Spec.*, 82:435-448, 1980.
- [298] A. S. Pine and W. J. Lafferty. Rotational structure and vibrational predissociation in the HF stretching bands of the HF dimer. *J. Chem. Phys.*, 78:2154-2162, 1983.

- [299] A. S. Pine, W. J. Lafferty, and B. J. Howard. Vibrational predissociation, tunneling, and rotational saturation in the HF and DF dimers. *J. Chem. Phys.*, 81:2939-2950, 1984.
- [300] A. S. Pine and B. J. Howard. Hydrogen bond energies of the HF and HCl dimers from absolute infrared intensities. *J. Chem. Phys.*, 84:590-596, 1986.
- [301] A. S. Pine. Vibrational anomalies and dynamic coupling in hydrogen-bonded van der Waals molecules. In Weber [371], pages 93-105.
- [302] A. S. Pine and G. T. Fraser. Vibrational, rotational, and tunneling dependence of vibrational predissociation in the HF dimer. *J. Chem. Phys.*, 89:6636-6643, 1988.
- [303] A. S. Pine and G. T. Fraser. Vibrational predissociation in the CO₂ dimer and rare gas-CO₂ complexes. *J. Chem. Phys.*, 89:100-109, 1988.
- [304] A. S. Pine. Private communication.
- [305] William H. Press, Brian P. Flannery, Saul A. Teukolsky, and William T. Vetterling. *Numerical Recipes*. Cambridge University Press, Cambridge, 1986.
- [306] N. Pugliano and R. J. Saykally. Measurement of quantum tunneling between chiral isomers of the cyclic water trimer. *Science*, 257:1937-1940, 1992.
- [307] Martin Quack. Detailed symmetry selection rules for reactive collisions. *Mol. Phys.*, 34:477-504, 1977.
- [308] Martin Quack. Comment during general discussion. *Faraday Discuss. Chem. Soc.*, 71:359-364, 1981.
- [309] Martin Quack. On the densities and numbers of rovibronic states of a given symmetry species: rigid and nonrigid molecules, transition states, and scattering channels. *J. Chem. Phys.*, 82:3277-3283, 1985.
- [310] Martin Quack and Martin A. Suhm. Observation and assignment of the hydrogen bond exchange disrotatory in plane bending vibration ν_5 in (HF)₂. *Chem. Phys. Lett.*, 171:517, 1990.
- [311] Martin Quack and Martin A. Suhm. Potential energy surfaces, quasiadiabatic channels, rovibrational spectra, and intramolecular dynamics of (HF)₂ and its isotopomers from quantum Monte Carlo calculations. *J. Chem. Phys.*, 95:28-59, 1991.
- [312] Martin Quack and Martin A. Suhm. Quasiadiabatic channels and effective transition-state barriers for the disrotatory in-plane hydrogen-bond exchange motion in (HF)₂. *Chem. Phys. Lett.*, 183:187-194, 1991.
- [313] Martin Quack, Jürgen Stohner, and Martin A. Suhm. Vibrational dynamics of (HF)_n aggregates from an ab initio based analytical (1+2+3)-body potential. *J. Mol. Struct.*, 294:33-36, 1993.

- [314] Martin Quack, Ulrich Schmitt, and Martin A. Suhm. Evidence for the $(\text{HF})_5$ complex in the HF stretching FTIR absorption spectra of pulsed and continuous supersonic jet expansions of hydrogen fluoride. *Chem. Phys. Lett.*, 208:446-452, 1993.
- [315] Martin Quack and Martin A. Suhm. Accurate quantum Monte Carlo calculations of the tunneling splitting in $(\text{HF})_2$ on a six-dimensional potential hypersurface. *Chem. Phys. Lett.*, 234:71-76, 1995.
- [316] H. Ratajczak and W. J. Orville-Thomas, editors. *Molecular Interactions, Volume 1*. John Wiley and Sons, Chichester, 1980.
- [317] H. Ratajczak and W. J. Orville-Thomas, editors. *Molecular Interactions, Volume 3*. John Wiley and Sons, Chichester, 1982.
- [318] Christian Reichardt. *Solvents and solvent effects in organic chemistry*. VCH Verlagsgesellschaft, Weinheim, 1988.
- [319] Philip J. Reid, Stephen J. Doig, Steven D. Wickham, and Richard A. Mathies. Photochemical ring-opening reactions are complete in picoseconds: A time-resolved UV resonance Raman study of 1,3-Cyclohexadiene. *J. Am. Chem. Soc.*, 115:4754-4763, 1993.
- [320] Eberhard Riedle, Stephen H. Ashworth, John T. Farrell, Jr., and David J. Nesbitt. Stabilization and precise calibration of a cw difference frequency spectrometer by use of a simple transfer cavity. *Rev. Sci. Instrum.*, 65:42-48, 1994.
- [321] Ruth L. Robinson, Douglas Ray, Dz-Hung Gwo, and Richard J. Saykally. An extended study of the lowest Π bending vibration-rotation spectrum of Ar-HCl by intracavity far infrared laser/microwave double resonance spectroscopy. *J. Chem. Phys.*, 87:5149-5155, 1987.
- [322] J. M. Robinson, M. A. Muyskens, K. J. Rehnsberger, and F. F. Crim. State-to-state vibrational energy transfer in DF($v=1-3$). *J. Chem. Phys.*, 93:3207-3214, 1990.
- [323] R. S. Ruoff, T. Emilsson, T. D. Klots, C. Chuang, and H. S. Gutowsky. Rotational spectrum and structure of the linear HCN trimer. *J. Chem. Phys.*, 89:138-148, 1988.
- [324] R. S. Ruoff, T. D. Klots, T. Emilsson, and H. S. Gutowsky. Relaxation of conformers and isomers in seeded supersonic jets of inert gases. *J. Chem. Phys.*, 93:3142-3150, 1990.
- [325] William D. Sands, Craig R. Bieler, and Kenneth C. Janda. Spectroscopy and dynamics of He_2Cl_2 : A quantum liquid cluster? *J. Chem. Phys.*, 95:729-734, 1991.
- [326] Richard J. Saykally and Geoffrey A. Blake. Molecular interactions and hydrogen bond tunneling dynamics: Some new perspectives. *Science*, 259:1570-1575, 1993.

- [327] Reinhard Schinke *Photodissociation Dynamics*. Cambridge University Press, Cambridge, 1993.
- [328] C. A. Schmuttenmaer, R. C. Cohen, and R. J. Saykally. Spectroscopic determination of the intermolecular potential energy surface for Ar-NH₃. *J. Chem. Phys.*, 101:146, 1994.
- [329] Michael D. Schuder, Jr. David D. Nelson, and David J. Nesbitt. Investigation of internal rotor dynamics of NeDCl and ArDCl via infrared absorption spectroscopy. *J. Chem. Phys.*, 94:5796-5811, 1991.
- [330] Michael D. Schuder. *High resolution infrared spectroscopy of van der Waals and hydrogen bonded dimers in slit supersonic jets: Large amplitude angular motion in HCl- and DCl-containing weakly bound species*. PhD thesis, University of Colorado, 1991.
- [331] Michael D. Schuder, Christopher M. Lovejoy, Robert Lascola, and David J. Nesbitt. High resolution, jet-cooled infrared spectroscopy of (HCl)₂: Analysis of ν_1 and ν_2 HCl stretching fundamentals, interconversion tunneling, and mode-specific predissociation lifetimes. *J. Chem. Phys.*, 99:4346-4362, 1993.
- [332] Michael D. Schuder, David D. Nelson, Jr., and David J. Nesbitt. Slit-jet near-infrared diode laser spectroscopy of (DCl)₂: ν_1 , ν_2 DCl stretching fundamentals, tunneling dynamics, and the influence of large amplitude "geared" intermolecular rotation. *J. Chem. Phys.*, 99:5045-5060, 1993.
- [333] Michael D. Schuder and David J. Nesbitt. High resolution near-IR spectroscopy of HCl-DCl and DCl-HCl: Relative binding energies, isomer interconversion rates, and mode specific vibrational predissociation. *J. Chem. Phys.*, 100:7250-7267, 1994.
- [334] Wayne Sharfin, Kenneth E. Johnson, Lennard Wharton, and Donald H. Levy. Energy distribution in the photodissociation products of van der Waals molecules: Iodine-helium complexes. *J. Chem. Phys.*, 71:1292-1299, 1979.
- [335] Wayne Sharfin, Kenneth E. Johnson, Lennard Wharton, and Donald H. Levy. Erratum: Energy distribution in the photodissociation products of van der Waals molecules: Iodine-helium complexes [J. Chem. Phys 71, 1292, (1979)]. *J. Chem. Phys.*, 78:610, 1983.
- [336] Joanne H. Shorter, Michael P. Casassa, and David S. King. Fragment state correlations in the dissociation of NOHF($v=1$). *J. Chem. Phys.*, 97:1824-1831, 1992.
- [337] Edwin L. Sibert III. Corrections to the Born-Oppenheimer treatment of the tunneling splitting in the HF dimer. *J. Phys. Chem.*, 93:5022-5024, 1989.
- [338] John M. Skene, Janet C. Drobits, and Marsha I. Lester. Dynamical effects in the vibrational predissociation of ICl-rare gas complexes. *J. Chem. Phys.*, 85:2329-2331, 1986.

- [339] Richard E. Smalley, Lennard Wharton, and Donald H. Levy. The structure of the HeI_2 van der Waals molecule. *J. Chem. Phys.*, 68:671-674, 1978.
- [340] D. F. Smith. Hydrogen fluoride polymer spectrum, hexamer and tetramer. *J. Chem. Phys.*, 28:1040-1056, 1958.
- [341] D. F. Smith. The overlapping hydrogen fluoride monomer-dimer spectra. *J. Mol. Spectrosc.*, 3:473-485, 1959.
- [342] J. J. Snyder. Algorithm for fast digital analysis of interference fringes. *Appl. Opt.*, 19:1223-1225, 1980.
- [343] P. D. Soper, A. C. Legon, W. G. Read, and W. H. Flygare. The microwave rotational spectrum, molecular geometry, ^{14}N nuclear quadrupole coupling constants, and H, ^{19}F nuclear spin-nuclear spin coupling constant of the nitrogen-hydrogen fluoride dimer. *J. Chem. Phys.*, 76:292-300, 1982.
- [344] Jeanette M. Sperhac, Miles J. Weida, and David J. Nesbitt. High resolution diode laser spectroscopy of Ar_2CO_2 . Manuscript in preparation.
- [345] W. Strohmeier and G. Briegleb. Über den assoziationszustand des HF im Gaszustand. I und II. *Z. Elektrochem.*, 57:662-674, 1953.
- [346] Martin A. Suhm, John T. Farrell, Jr., Andrew McIlroy, and David J. Nesbitt. High resolution $1.3 \mu\text{m}$ overtone spectroscopy of HF dimer in a slit jet: $K_a = 0 \leftarrow 0$ and $K_a = 1 \leftarrow 0$ subbands of $v_{\text{acc}} = 2 \leftarrow 0$. *J. Chem. Phys.*, 97:5341-5354, 1992.
- [347] Martin A. Suhm, John T. Farrell, Jr., Stephen Ashworth, and David J. Nesbitt. High resolution IR spectroscopy of DF trimer: A cyclic ground state structure and DF stretch induced intramolecular vibrational coupling. *J. Chem. Phys.*, 98:5985-5989, 1993.
- [348] Martin A. Suhm. Reliable determination of multidimensional analytical fitting bias. *Chem. Phys. Lett.*, 223:474-480, 1994.
- [349] Martin A. Suhm and David J. Nesbitt. Infrared spectroscopy related to potential surfaces and dynamics of weakly bound trimers. *Chem. Soc. Rev.*, 24:45, 1995.
- [350] Huai Sun and R. O. Watts. Diffusion Monte Carlo simulations of hydrogen fluoride dimers. *J. Chem. Phys.*, 92:603-616, 1990.
- [351] Huai Sun, Robert O. Watts, and U. Buck. The infrared spectrum and structure of hydrogen fluoride clusters and the liquid: Semiclassical and classical studies. *J. Chem. Phys.*, 96:1810-1821, 1992.
- [352] M. M. Szczyński, G. Chałasiński, and P. Piecuch. The nonadditive interactions in the Ar_2HF and Ar_2HCl clusters: An *ab initio* study. *J. Chem. Phys.*, 99:6732-6741, 1993.

- [353] Fu-Ming Tao and William Klemperer. Accurate *ab initio* potential energy surfaces of Ar-HF, Ar-H₂O, and Ar-NH₃. *J. Chem. Phys.*, 101:1129–1145, 1994.
- [354] Alice E. Thornley and Jeremy M. Hutson. Bound-state wave functions from coupled channel calculations using log-derivative propagators: Application to spectroscopic intensities in Ar-HF. *J. Chem. Phys.*, 101:5578–5584, 1994.
- [355] K. G. Tokhadze and Z. Mielke. About origin of *Q* component on the vibration-rotation band of HF in simple solvents. *J. Chem. Phys.*, 99:5071–5077, 1993.
- [356] C. H. Townes and A. L. Schawlow. *Microwave Spectroscopy*. McGraw-Hill, New York, 1955.
- [357] Susy N. Tsang, Huan-C. Chang, and William Klemperer. Characterization of N₂HF at 3ν₁ stretch. *J. Phys. Chem.*, 98:7313–7318, 1994.
- [358] Matthew F. Vernon, James M. Lisy, Douglas J. Krajnovich, Andrzej Tramer, Hoi-Sing Kwok, and Yuan T. Lee. Vibrational predissociation spectra and dynamics of small molecular clusters of H₂O and HF. *Faraday Discuss. Chem. Soc.*, 73:387–397, 1982.
- [359] P. Villarreal, S. Miret-Artés, O. Roncero, G. Delgado-Barrio, J. A. Beswick, N. Halberstadt, and R. D. Coalson. A wave packet Golden Rule treatment of vibrational predissociation. *J. Chem. Phys.*, 94:4230–4233, 1991.
- [360] B. Vodar and H. Vu. *J. Quant. Spectrosc. Radiat. Transfer*, 3:397, 1963.
- [361] Michael von Dirke, Zlatko Bačić, Dong H. Zhang, and John Z. H. Zhang. Vibrational predissociation of HF dimer in ν_{HF}=1: influence of initially excited intermolecular vibrations on the fragmentation dynamics. *J. Chem. Phys.*, 103: , 1995.
- [362] K. von Puttkamer and M. Quack. High resolution FTIR overtone spectra and hydrogen bond dissociation dynamics in (HF)₂. *Chimia*, 39:358–360, 1985.
- [363] K. von Puttkamer and M. Quack. High resolution interferometric FTIR spectroscopy of (HF)₂: Analysis of a low frequency fundamental near 400 cm⁻¹. *Mol. Phys.*, 62:1047–1064, 1987.
- [364] Katharina von Puttkamer, Martin Quack, and Martin Suhm. Observation and assignment of tunnelling-rotational transitions in the far infrared spectrum of (HF)₂. *Mol. Phys.*, 65:1025–1045, 1988.
- [365] Katharina von Puttkamer and Martin Quack. Vibrational spectra of (HF)₂, (HF)_n, and their D-isotopomers: Mode selective rearrangements and nonstatistical unimolecular decay. *Chem. Phys.*, 139:31–53, 1989.
- [366] Katharina von Puttkamer, Martin Quack, and Martin A. Suhm. Infrared spectrum and dynamics of the hydrogen bonded dimer (HF)₂. *Infrared Phys.*, 29:535–539, 1989.

- [367] Sarah A. Walter and Thomas A. Stephenson. Vibrational branching ratios from the dissociation of the NeIBr van der Waals molecule. *J. Chem. Phys.*, 96:3536-3541, 1992.
- [368] Robert L. Waterland, John M. Skene, and Marsha I. Lester. Rotational rainbows in the vibrational predissociation of ICl-He complexes. *J. Chem. Phys.*, 89:7277-7286, 1988.
- [369] James K. G. Watson. Determination of centrifugal distortion coefficients of assymmetric-top molecules. *J. Chem. Phys.*, 46:1935-1949, 1967.
- [370] James K. G. Watson. Approximations for the inertial defects in planar molecules. *J. Chem. Phys.*, 98:5302-5309, 1993.
- [371] Alfons Weber, editor. *Structure and Dynamics of Weakly Bound Molecular Complexes*, Vol. 212 of NATO Advanced Study Insititute, Series C:Mathematical and Physical Sciences. D. Reidel, Dordrecht, 1987.
- [372] Miles J. Weida and David J. Nesbitt. Collisional alignment of CO₂ rotational angular momentum states in a supersonic expansion. *J. Chem. Phys.*, 100:6372-6385, 1994.
- [373] Miles J. Weida, Jeanette Sperhac, and David J. Nesbitt. The structure of small (CO₂)_n clusters formed via condensation. Manuscript in preparation.
- [374] B. Wellegehausen, D. Friede, H. Vogt, and S. Shahdin. Generation of tunable cw infrared radiation by difference frequency mixing. *Appl. Phys.*, 11:363-370, 1976.
- [375] John U. White. Long optical paths of large aperture. *J. Opt. Soc. Am.*, 32:285-288, 1942.
- [376] Robert M. Whitnell, Kent R. Wilson, and James T. Hynes. Fast vibrational relaxation for a dipolar molecule in a polar solvent. *J. Phys. Chem.*, 94:8625-8628, 1990.
- [377] Robert M. Whitnell, Kent R. Wilson, and James T. Hynes. Vibrational relaxation of a dipolar molecule in water. *J. Chem. Phys.*, 96:5354-5369, 1992.
- [378] E. P. Wigner. *Soc. Ind. Appl. Phys.*, 9:1, 1967.
- [379] E. Bright Wilson, J. C. Decius, and Paul C. Cross. *Molecular Vibrations*. Dover, New York, 1980.
- [380] C. Wittig. Photoinitiated reactions in weakly bound complexes. *Acc. Chem. Res.*, 21:341-347, 1988.
- [381] Qian Wu, Dong H. Zhang, and John Z. H. Zhang. 6D quantum calculations on energy levels for HF stretching excited (HF)₂. Submitted to *J. Chem. Phys.*, 1995.

- [382] Yunjie Xu, M. C. L. Gerry, J. P. Connelly, and B. J. Howard. The microwave spectrum, structure, and harmonic force field of the van der Waals trimer Ar₂-OCS. *J. Chem. Phys.*, 98:2735-2741, 1993.
- [383] Yunjie Xu, Wolfgang Jäger, and M. C. L. Gerry. Pulsed molecular beam microwave Fourier transform spectroscopy of the van der Waals trimer Ar₂-CO₂. *J. Molec. Spectrosc.*, 157:132-140, 1993.
- [384] Richard N. Zare. *Angular Momentum*. Wiley Interscience, New York, 1988.
- [385] Warren T. Zemke, William C. Stwalley, Stephen R. Langhoff, Giuseppe L. Valderrama, and Michael J. Berry. Radiative transition probabilities for all vibrational levels in the X¹Σ⁺ state of HF. *J. Chem. Phys.*, 95:7846-7853, 1991.
- [386] Dong H. Zhang and John Z. H. Zhang. Total and partial decay widths in vibrational predissociation of HF dimer. *J. Chem. Phys.*, 98:5978:5981, 1993.
- [387] Dong H. Zhang and John Z. H. Zhang. Photofragmentation of HF dimer: Quantum dynamics studies on *ab initio* potential energy surfaces. *J. Chem. Phys.*, 99:6624:6633, 1993.
- [388] Dong H. Zhang, Qian Wu, and John Z. H. Zhang. A time-dependent approach to flux calculation in molecular photofragmentation: Vibrational predissociation of HF-DF. *J. Chem. Phys.*, 102:124-132, 1995.
- [389] Dong H. Zhang, Qian Wu, John Z. H. Zhang, Michael von Dirke, and Zlatko Bačić. Exact full-dimensional bound state calculations for (HF)₂, (DF)₂, and HFDF. *J. Chem. Phys.*, 102:2315-2325, 1995.